# QUANTITATIVE CHARACTERIZATION OF PHYSICO-CHEMICAL PROPERTIES OF THE ACTIVE LAYERS OF REVERSE OSMOSIS AND NANOFILTRATION MEMBRANES, AND THEIR RELATION TO MEMBRANE PERFORMANCE

BY

ORLANDO CORONELL NIETO

DISSERTATION

Submitted in partial fulfillment of the requirements
for the degree of Doctor of Philosophy in Environmental Engineering in Civil Engineering
in the Graduate College of the
University of Illinois at Urbana-Champaign, 2010

Urbana, Illinois

Doctoral Committee:

Professor Benito J. Mariñas, Chair
Professor David G. Cahill
Professor Menachem Elimelech, Yale University
Associate Professor Timothy J. Strathmann

# ABSTRACT

The main objectives of this dissertation were: (i) to develop experimental and analytical procedures to quantify different physico-chemical properties of the ultra-thin (~ 100 nm) active layers of reverse osmosis (RO) and nanofiltration (NF) membranes and their interactions with contaminants; (ii) to use such procedures to evaluate the similarities and differences between the active layers of different RO/NF membranes; and (iii) to relate characterization results to membrane performance. Such objectives were motivated by the current limited understanding of the physico-chemical properties of active layers as a result of traditional characterization techniques having limitations associated with the nanometer-scale spatial resolution required to study these ultra-thin films.

Functional groups were chosen as the main active layer property of interest. Specific accomplishments of this study include the development of procedures to quantify in active layers as a function of pH: (1) the concentration of both negatively and positively ionized functional groups; (2) the stoichiometry of association between ions (i.e., barium) and ionized functional groups (i.e., carboxylate and sulfonate); and (3) the steric effects experienced by ions (i.e., barium). Conceptual and mathematical models were developed to describe experimental results. The depth heterogeneity of the active layer physico-chemical properties and interactions with contaminants studied in this dissertation was also characterized. Additionally, measured concentrations of ionized functional groups in the polyamide active layers of several commercial RO/NF membranes were used as input in a simplified RO/NF transport model to predict the rejection of a strong electrolyte (i.e., potassium iodide) and a weak acid (i.e., arsenious acid) at different pH values based on

rejection results at one pH condition. The good agreement between predicted and experimental results showed that the characterization procedures developed in this study serve as useful tools in the advancement of the understanding of the properties and structure of the active layers of RO/NF membranes, and the mechanisms of contaminant transport through them.

*To Orla and Dolly,*

*Jeanne and the dindos*

# ACKNOWLEDGMENTS

I would like to express my deepest gratitude to my advisor, Professor Benito J. Mariñas, who always supported me during the course of my doctoral studies, and whose advice and sharing of experiences have gone a long way in preparing me for the road ahead.

I would also like to give special thanks to Professor David G. Cahill for bringing into my research his point of view as a scientist. The experience of being advised by an engineer while receiving great input from a scientist has enriched my doctoral studies.

I am also grateful to Professors Menachem Elimelech and Timothy Strathmann for their acceptance in being part of my Ph.D. committee, and for providing feedback that not only helped me improve my dissertation, but also stirred ideas for future research.

Special thanks go to Baoxia Mi not only for initiating me in the field of membranes while she was still a Ph.D. student, but also for enduring my emails asking her for experimental details about her potassium iodide and arsenic permeation data which I used in Chapter 6 of this dissertation. Also, special thanks to Tasuma Suzuki for our long discussions about membranes, and for living with me the experience of repeatedly snacking at 2 am at Perkins in between sampling times. I also thank Mari Gonzalez who, as an undergraduate researcher, helped me with sample analysis when the number of samples grew exponentially. A sincere thank you to Jeanne Luh and Gorie Ster, who during the course of my Ph.D. studies provided constant feedback and help when I most needed it.

I am also indebted to Doug Jeffers, Richard Haasch, Timothy Spila, and Scott MacLaren, at the Center for Microanalysis of Materials, University of Illinois at Urbana-Champaign,

who trained me in the use of equipment for materials characterization or helped me in the analysis of samples.

In addition, a big thank you to Professor Vernon L. Snoeyink whose Cultural Awareness and Speech Enhancement (CASE) program broadened and enriched my learning experience at Illinois.

The work in this dissertation was supported by the National Science Foundation Environmental Engineering and Technology program under agreement number BES-0332217, and the WaterCAMPWS, a Science and Technology Center of Advanced Materials for the Purification of Water with Systems under agreement number CTS-0120978. The financial support provided by the funding agencies is gratefully acknowledged.

# TABLE OF CONTENTS

# CHAPTER 1

# INTRODUCTION

## 1.1. Background and Motivation

The drinking water and water pollution control industries have been driven to use multi-barrier water treatment trains in which various separation and oxidation processes are used to comply with increasingly stringent regulations on both the removal of contaminants and the generation of disinfection and oxidation byproducts [1-5]. The multi-barrier approach, however, is progressively becoming more impractical and cost-prohibitive because of the wide range of contaminants (e.g., microorganisms, organic pollutants, arsenic, etc.) that need to be addressed, and the growing concern of byproducts formation (e.g., trihalomethanes, haloacetic acids, bromate, nitrogenous disinfection byproducts, etc.). In this scenario, reverse osmosis (RO) and nanofiltration (NF) membranes have become increasingly attractive technologies because they provide effective control against a broad range of water contaminants without the need for the addition of chemicals that would promote the formation of disinfection or oxidation byproducts [6, 7].

Most commercially successful RO/NF membranes have a thin-film composite structure, which includes a top ultra-thin (~50–200 nm) layer usually made of polyamide and referred to as the "active layer", an intermediate porous polysulfone support (~50 μm), and a backing fabric commonly made of non-woven polyester fibers (~200 μm) [7]. The top ultrathin active layer constitutes the main barrier to water and solute permeation, with

active layer physico-chemical properties playing important roles in transport phenomena [7-10]. Unfortunately, the characterization of the physico-chemical structure of the active layer has remained challenging due to limitations associated with the nanometer-scale spatial resolution required to study these ultrathin (~100 nm) films, as they cannot be detached from their significantly thicker (~50 μm) polysulfone supports without chemical treatment. As a result of the limited knowledge of the active layer properties and structure, there is also limited understanding of how these structure and properties affect the performance of RO/NF membranes in terms of water permeability and solute rejection [11], which hinders the systematic development of new improved membranes. Accordingly, there is a research need for: (i) the development of experimental and analytical procedures that enable the quantitative characterization of active layer properties and contaminant-active layer interactions; (ii) the use of such procedures to evaluate the similarities and differences between the active layers of different commercial RO/NF membranes; and (iii) the study of the relationship between active layer characterization results and membrane performance.

Among the active layer properties that affect membrane performance, ionizable functional groups and their interactions with ionic contaminants are of special interest because not only do they affect the permeation of water and solutes by producing pH-dependent charges in the active layer [7, 12], but also because they are directly related to the structure of the active layer [7, 13]. In particular, ionizable functional groups in polyamide active layers are related to the degree of polymer crosslinking [7] because each carboxylic (R–COOH) and amine ($R–NH_2$) group in the polyamide structure corresponds to an amide link not formed during the polyamide polymerization reaction

[7]. For these reasons, ionizable functional groups were selected as the primary active layer property of interest in this study.

### 1.2. Objectives

Consistent with the preceding discussion, and towards the goal of advancing the understanding of how the structure and properties of active layers affect membrane performance, the general objectives of this dissertation are:

1. To develop procedures that enable the quantitative characterization of functional groups and their interactions with ionic solutes in the active layers of commercial RO/NF membranes.

2. To evaluate the similarities and differences between the active layers of different RO/NF membranes in terms of their physico-chemical properties and interactions with ionic solutes.

3. To demonstrate that the quantification of the physico-chemical properties of active layers is a useful tool in the prediction of the effect that changing operational parameters such as pH have on membrane performance.

To accomplish the three general objectives mentioned above, the following specific objectives were used to guide this work:

- To develop a procedure for the quantification of negatively and positively ionized functional groups in the active layers of RO/NF membranes as a function of solution pH.

- To develop a procedure for the quantification of the stoichiometry of association between ionic species (e.g., $Ba^{2+}$) and ionized functional groups in active layers, where the stoichiometry of association also serves as a relative descriptor of the homogeneity of the spatial distribution of functional groups in the polymer structure.

- To develop a procedure for the quantification of the steric effects experienced by ionic species (e.g., $Ba^{2+}$) in the active layers.

- To develop conceptual and mathematical models that describe the characterization results obtained with the procedures developed in this work and various commercial RO/NF membranes.

- To evaluate quantitatively whether physico-chemical properties and interactions with ionic contaminants are homogeneous or heterogeneous throughout the depth of active layers.

- To predict the rejections of a strong electrolyte (i.e., potassium iodide) and a weak acid (i.e., arsenious acid) as a function of pH based on rejection results at one pH condition, and the measured concentrations of ionized functional groups in the active layers of commercial RO/NF membranes.

### 1.3. Thesis Organization

This thesis is composed of eight chapters and four appendices. Chapters 1, 7 and 8 correspond to the present introduction, conclusions, and future work, respectively, and Chapters 2–6 are stand-alone papers (i.e., with their own introduction, materials and

methods, and results and discussion sections) where each chapter builds on the results of the previous ones. Chapters 2 through 6 are briefly described below:

- Chapter 2: A methodology for the quantification of positively and negatively ionized functional groups in active layers is presented together with results of the concentration of negatively ionized carboxylic ([R–$COO^-$]) and positively ionized amine ([R–$NH_3^+$]) groups in the active layer of the commercial FT30 RO membrane as a function of solution pH. The ionization behavior of functional groups is also modeled assuming acid-base equilibrium between functional groups and aqueous solution. Additionally, the degree of crosslinking of the polyamide active layer of the FT30 membrane is quantified using a descriptor introduced as the degree of polymer crosslinking (DPC) which is calculated based on the measured elemental ratios of functional groups and nitrogen in the active layer.

- Chapter 3: Modified versions of the experimental procedures used in Chapter 2 are introduced to quantify as a function of pH in the active layer of thin-film polyamide RO/NF membranes: (i) the concentration of barium ion ([$Ba^{2+}$]) that associates with ionized carboxylic groups (R–$COO^-$), and (ii) the stoichiometry of association (NN) between R–$COO^-$ groups and $Ba^{2+}$ ions. A conceptual and mathematical model is proposed that enables the calculation of the fraction (AR) of R–$COO^-$ groups accessible to $Ba^{2+}$ ion in the active layer, where AR serves as a descriptor of the steric effects experienced by $Ba^{2+}$. AR is calculated based on

the experimentally measured [$Ba^{2+}$], [$R–COO^{-}$], and NN. Corresponding results for the FT30 RO membrane are reported.

- Chapter 4: The experimental and analytical procedures introduced in Chapters 2 and 3 are used to characterize the active layers of seven different RO/NF membranes, six of them with polyamide active layers and one of them with a sulfonated polyethersulfone active layer. Characterization results are compared, conclusions regarding what differentiates one membrane from another are drawn, and measured charge densities are used to calculate the relative differences between membranes with respect to the electric exclusion of ionic contaminants.

- Chapter 5: This chapter presents a quantitative study of the depth heterogeneity/ homogeneity in polyamide active layers of the physico-chemical properties and interactions with $Ba^{2+}$ ion studied in Chapter 2–4.

- Chapter 6: The concentrations of ionized functional groups in the active layers of several commercial RO/NF membranes, measured using the procedures developed in the previous chapters, are used as input in a modified version [14] of the solution-diffusion model for the transport of solutes through RO/NF membranes, to predict the rejection of a strong electrolyte (i.e., KI) and a weak acid (i.e., arsenious acid) in the pH range of 5.8–10.2 based on rejection data at pH = 6.3.

The four appendices follow Chapter 8, and are labeled A through D. Appendices A.1, B.1, C.1 and D present “Supporting Information” referenced in the main text of Chapters

2, 3, 4 and 5, respectively, with each of these chapters having a section (i.e., Sections 2.5, 3.5, 4.5 and 5.5) that lists the contents of such "Supporting Information". The remaining sections of the appendices show, for illustrative purposes, representative raw and modeled Rutherford backscattering spectrometry data obtained with the FT30 RO membrane.

### 1.4. References


1. United States Environmental Protection Agency (U.S. EPA), *Guidance manual for compliance with the filtration and disinfection requirements for public water systems using surface water sources*. U.S. EPA: Washington, D.C., 1991.

2. United States Environmental Protection Agency (U.S. EPA), National Primary Drinking Water Regulations: Long Term 2 Enhanced Surface Water Treatment Rule; Proposed Rule. In Federal Register: 1993; Vol. 68(154), pp 47640-47795.

3. United States Environmental Protection Agency (U.S. EPA), Drinking Water Contaminant Candidate List 2: Final Notice. In Federal Register: 2005; Vol. 70(36), pp 9071-9077

4. United States Environmental Protection Agency (U.S. EPA), National Primary Drinking Water Regulations: Stage 2 Disinfectants and Disinfection Byproducts Rule; Final Rule. In Federal Register: 2006; Vol. 71(2), pp 388-493.

5. Pontius, F., *Drinking water regulation and health*. John Wiley & Sons: New York, N.Y., 2003.

6. Mulder, M., *Principles of Membrane Technology*. Second ed.; Kluwer Academic: Boston, MA, 1996.

7. Petersen, R. J., Composite reverse osmosis and nanofiltration membranes. *J. Mem. Sci.* **1993,** *83*, 81-150.

8. Bellona, C.; Drewes, J. E.; Xu, P.; Amy, G., Factors affecting the rejection of organic solutes during NF/RO treatment-a literature review. *Water Res.* **2004,** *38*, 2795-2809.

9. Childress, A. E.; Elimelech, M., Relating nanofiltration membrane performance to membrane charge (electrokinetic) characteristics. *Environ. Sci. Technol.* **2000,** *34*, 3710-3716.

10. Szymczyk, A.; Fievet, P., Investigating transport properties of nanofiltration membranes by means of a steric, electric and dielectric exclusion model. *J. Mem. Sci.* **2005**, (252), 77-88.

11. Cahill, D. G.; Freger, V.; Kwak, S.-Y., Microscopy and microanalysis of reverse osmosis and nanofiltration membranes. *MRS Bull.* **2008,** *33*, 27-32.

12. Bowen, W. R.; Welfoot, J. S., Modelling the performance of membrane nanofiltration-critical assessment and model development. *Chem. Eng. Sci.* **2002,** *57*, 1121-1137.

13. Freger, V., Nanoscale heterogeneity of polyamide membranes formed by interfacial polymerization. *Langmuir* **2003,** *19*, 4791-4797.

14. Urama, R. I.; Mariñas, B. J., Mechanistic interpretation of solute permeation through a fully aromatic polyamide reverse osmosis membrane. *J. Mem. Sci.* **1997,** *123*, 267-280.

# CHAPTER 2

# QUANTIFICATION OF FUNCTIONAL GROUPS AND MODELING OF THEIR IONIZATION BEHAVIOR IN THE ACTIVE LAYER OF FT30 REVERSE OSMOSIS MEMBRANE[1]

**Abstract:** A new experimental approach was developed to measure the concentration of charged functional groups (FGs) in the active layer of thin-film composite reverse osmosis (RO) and nanofiltration (NF) membranes as a function of solution pH. FT30 RO membrane, with a fully aromatic polyamide (PA) active layer sandwiched between a polysulfone support and a coating layer, was used. The experiments consisted of saturating charged FGs with heavy ion probes, and determining the ion probe concentration by Rutherford Backscattering Spectrometry (RBS). Deprotonated carboxylic groups were saturated with $Ag^+$, and protonated amine groups with $WO_4^{2-}$. The ionization behavior of carboxylic and amine groups was modeled based on acid-base equilibrium theory. While the ionization behavior of amine groups was satisfactorily described by one dissociation constant ($pK_a$=4.74), two $pK_a$ values (5.23 and 8.97) were necessary to describe the titration curve of carboxylic groups. These results were consistent with the bimodal pore size distribution (PSD) of FT30 active layer reported in the literature. The calculated total concentrations of carboxylic and amine groups in the active layer of the FT30 RO membrane were 0.43 M and 0.036 M, respectively, and the isoelectric point (IEP) was 4.7. The total concentration of carboxylic and amine groups revealed that the degree of cross-linking of the PA active layer of the FT30 RO membrane studied was 94%.

[1] Reproduced with permission from Coronell, O.; Mariñas, B.J.; Zhang, X.; Cahill, D.G., Quantification of functional groups and modeling of their ionization behavior in the active layer of FT30 reverse osmosis membrane. *Environ. Sci. Technol.* **2008**, *42*, 5260-5266. Copyright 2008 American Chemical Society.

**Key Words:** amine groups, carboxylic groups, polyamide, reverse osmosis, RO membrane, Rutherford backscattering spectrometry, RBS, thin film composite membrane, TFC, ion probing

## 2.1. Introduction

Nanofiltration (NF) and reverse osmosis (RO) membranes are widely used in water quality control, and in a variety of industrial applications [1, 2]. Most commercially available RO and NF membranes have a thin-film composite structure consisting of a non-woven polyester layer that backs an intermediate layer of polysulfone (PSf) with asymmetric porosity, which in turn supports an active layer (~100 nm) commonly made of polyamide (PA) [2]. Several physico-chemical properties of the active layer affect solute-membrane interactions, and therefore impact membrane performance [2, 3]. Among these properties, the type and concentration of functional groups (FGs) that result from incomplete polymerization and crosslinking of PA [2, 4, 5] are of particular importance. The type and concentration of FGs affect the permeation of water and solutes [2, 3, 5], by producing pH-dependent charges, both negative and positive [4, 6, 7]. Additionally, since FGs are the result of incomplete polymer crosslinking, the type and concentration of the FGs created (i.e., the type and number of active groups in the reactants that did not convert into amide links) impact the resulting pore size distribution (PSD) of the active layer [2, 3, 5]. Consequently, quantification of the concentration of FGs in the active layer of NF/RO membranes is of importance for elucidating the transport mechanisms of water and solutes.

Even though titration methods are commonplace for the quantification of the concentration of FGs in monomers in solution [8] and ion exchange resins [9], the same procedures cannot be applied to the active layer of NF/RO membranes because of interference from the much thicker PSf support. The charge of NF/RO membrane active layers has been studied by streaming potential and tangential streaming potential analysis [6]. However, although these methods enable an estimate of the membrane charge density using electrokinetic modeling [6], they do not provide a direct or quantitative measurement. Contact angle titration methods have been successfully used for the detection of membrane surface FGs [4, 10, 11], and confirmation of different group functionalities on opposite sides of interfacially polymerized PA films [4]. Nonetheless, contact angle titration provides information on the relative degree of ionization of FGs rather than absolute values for FG concentrations [4, 10]. Consequently, there is a need for a new approach that enables the quantification of the concentrations of FGs, both positive and negative, in the active layer of NF/RO membranes.

The objective of this study was to develop a new method for the quantification of the concentrations of deprotonated carboxylic ($R–COO^-$) and protonated amine ($R\text{-}NH_3^+$) groups in the PA active layer of FT30 RO membrane, as a function of pH. Rutherford Backscattering Spectrometry (RBS) was used as the quantification tool. The methodology for the quantification of the concentrations of FGs and the modeling of their ionization behavior are also presented.

## 2.2. Materials and Methods

***2.2.1. Membrane.*** Experiments were performed with thin-film composite FT30 RO membrane (Dow Liquid Separation, Midland, MI) which has an active layer made of fully aromatic PA. Membrane samples were obtained by cutting 2.5×5.0 $cm^2$ coupons from a spiral-wound element obtained from the manufacturer. Samples of PSf support, i.e., membrane samples lacking the active layer, (Hydranautics, Oceanside, CA) were also analyzed to obtain their elemental composition.

***2.2.2. Approach for Determining the Concentration of Functional Groups***. A procedure was developed to characterize the concentration of ionized FGs in the active layer of NF/RO membranes as a function of pH. The method included two major steps: (i) sample preparation, and (ii) sample analysis. The goal of the sample preparation step was to saturate the target ionized FGs, $R\text{-}COO^-$ or $R\text{-}NH_3^+$, with high atomic-number counter-ion probes, $Ag^+$ or $WO_4^{2-}$, respectively. The goal of the sample analysis step was to quantify the concentration of ion probes in the active layer. The concentration of the ion probes was assumed to match that of accessible ionized FGs. The concentration of ionized FGs as a function of pH was determined by performing the sample preparation step with ion-probe solutions at various pH. All experiments were performed in triplicate and at room temperature (22±2$^o$C). Details about ion-probe solution composition, sample preparation procedures, and sample analysis methods are presented in subsequent sections.

***2.2.3. Ion-Probe Solutions.*** All ion-probe salts used were A.C.S. grade with 99% or greater purity (Sigma-Aldrich, St. Louis, MO). Silver nitrate was used as a source of

silver ions ($Ag^+$) for saturation of accessible deprotonated carboxylic groups, and sodium tungstate dihydrate was used as a source of tungstate ions ($WO_4^{2-}$) for saturation of accessible protonated amine groups. All solutions were prepared in nanopure water (NPW) produced from a Barnstead D4741 nanopure deionization system (Barnstead/Thermolyne Corp., Dubuque, IA). The concentrations of silver and tungstate in the ion-probe solutions were in the ranges of $5\times10^{-5}$–$10^{-1}$ M and $5\times10^{-6}$–$10^{-3}$ M, respectively, and were always below their solubility limit at the pH tested [12]. The pH of silver and tungstate solutions was adjusted to the desired value by addition of $HNO_3$ or NaOH, and HCl or NaOH, respectively.

***2.2.4. Sample Preparation.*** Membrane samples were prepared in four steps: (i) initial cleaning, (ii) equilibration with ion-probe solution, (iii) removal of excess ion probes, and (iv) drying. Details for these steps are illustrated for the saturation of deprotonated carboxylic groups with $Ag^+$. The membrane coupons cut from the spiral-wound element were thoroughly rinsed with NPW through six consecutive immersions, each lasting at least 6 h. The goal of this step was to remove contamination from manufacturing and handling that could potentially interfere with the ion-probing procedure. The cleaned coupons were immersed twice, each time for 10 min, in $AgNO_3$ solution prepared at the highest possible concentration of the specific experimental pH. This step was performed to saturate with $Ag^+$, according to ion exchange theory [9], all accessible deprotonated carboxylic groups. The use of the highest possible concentration of $AgNO_3$ served the purpose of circumventing potential kinetic limitations during the initial saturation of ionized carboxylic groups. Next, the $Ag^+$-treated samples were immersed four consecutive times, each for 7 min, in a $10^{-6}$ M $AgNO_3$ solution at the same pH used in the

saturation step. This rinsing step at relatively dilute ion-probe concentration ($10^{-6}$ M) was performed to reduce the excess $Ag^+$, not ionically bound to R–$COO^-$ groups, to a concentration several orders of magnitude below the concentration of $Ag^+$ at ion exchange equilibrium with R–$COO^-$ groups). The dilute ionic concentration in the final rinsing step also ensured negligible effects of ionic strength on the ionization of FGs. The rinsed samples were finally dried by pressing them between two Whatman qualitative-grade filter-papers (Fisher Scientific, Hampton, NH), followed by air-drying at room temperature for at least 24 h. A similar procedure was used for the saturation of accessible protonated amine groups with $WO_4^{2-}$. All sample preparation steps with $Ag^+$ were performed under dark conditions to avoid photochemical reactions.

***2.2.5. Sample Analysis.*** Rutherford Backscattering Spectrometry (RBS), previously used for quantifying arsenic [13] and heavy ions [14] in the active layer of commercial NF/RO membranes, was used in the present study to quantify the ion probes in the active layer of FT30 RO membrane samples prepared as described in the preceding section. RBS analyses were performed at room temperature with a circular, 3-mm diameter, 2-MeV $He^+$ beam generated with a Van de Graaff accelerator (High Voltage Engineering Corp., Burlington, MA). Incident, exit and scattering angles were set at $22.5^o$, $52.5^o$ and $150^o$, respectively. By scanning the beam over the membrane coupon, the $He^+$ ion fluence was kept under $1.5\times10^{14}$ $He^+/cm^2$. This value was below the threshold of $3\times10^{14}$ $He^+/cm^2$ for PA active layers on PSf supports above which the physico-chemical integrity of PSf is compromised [15]. The commercial software SIMNRA® [16] was used for RBS data analysis [13, 15, 17]. Additional details on RBS experimental setup [17], RBS use on

polymeric membranes [15, 17], and calculation of elemental concentrations from RBS spectra [13] were reported previously.

***2.2.6. Control Experiments.*** Control experiments were performed to confirm that the $10^{-6}$ M ion probe solutions used in the third step of sample preparation (i.e., excess ion probe removal) did not give false positive results with respect to the concentrations of FGs. A false positive result would correspond to a detectable ion-probe signal in the RBS spectra resulting from the deposition of ion probes onto the membrane surface during the drying step (i.e., as opposed to ion probes ionically bound to ionized FGs). The experiments were run in triplicate. Sample preparation was performed similarly to that of ion-probing experiments but without the second step (i.e., equilibration with ion-probe solution). Briefly, FT30 RO membrane coupons were rinsed with NPW, then immersed in $10^{-6}$ M $Na_2WO_4$ solution at pH~7.5 for 10 min, and finally dried with filter paper as detailed above. All samples were analyzed by RBS.

The control experiments were performed using tungstate as ion probe because the RBS signal is directly proportional to the square of the atomic number of the target element. As a result, RBS is 2.5 times more sensitive for tungsten than for silver atoms, and therefore the absence of false positive results for tungstate treatment would also ensure the absence of false positive results for silver treatment. Additionally, the experiments were performed at pH~7.5 because based on the study of the acid-base behavior of benzoamine in aqueous solutions [8] at this pH no more than 1% of the amine groups in the active layer was expected to be positively ionized, thus ensuring negligible ionic binding of $WO_4^{2-}$ to the PA active layer.

## 2.3. Results and Discussion

***2.3.1. Physico-Chemical Characterization of the Membrane.*** The elemental composition and thickness of the FT30 RO membrane active layer was obtained from RBS analysis of untreated samples (see Figure 2.1). In our previous work [13, 17], the FT30 membrane was simulated as an active layer of pure PA on top of a PSf support. However, a more recent study [18] has revealed that, consistent with our RBS spectra, the outer surface of the PA active layer of FT30 membrane is coated with another polymer. Nitrogen peaks in the RBS spectra of FT30 membrane predicted with (green continuous line) and without (blue dashed line) the presence of a coating layer are compared to the experimental spectrum (green squares) in the enlarged insert of Figure 2.1. The ~15-keV shift between the two lines indicated that the $He^+$ beam lost energy traversing an extra layer before reaching the nitrogen-rich active layer. Based on results obtained for TEM, XPS and ATR-FTIR analyses, Tang et al. [18] concluded that the coating material was a neutral aliphatic polymeric alcohol, a finding that was consistent with literature reports [2] that polyvinyl alcohol (PVA) derivatives have been used as coating material for NF/RO membranes. Accordingly, the structure of the FT30 RO membrane was simulated as a PA layer sandwiched between a top PVA layer and a support PSf layer. In general, the simulation was performed using the same procedure as reported previously [17] by fitting the spectra obtained from six untreated PSf support and six untreated FT30 RO membrane samples (each with an approximate surface area of 6 $cm^2$).

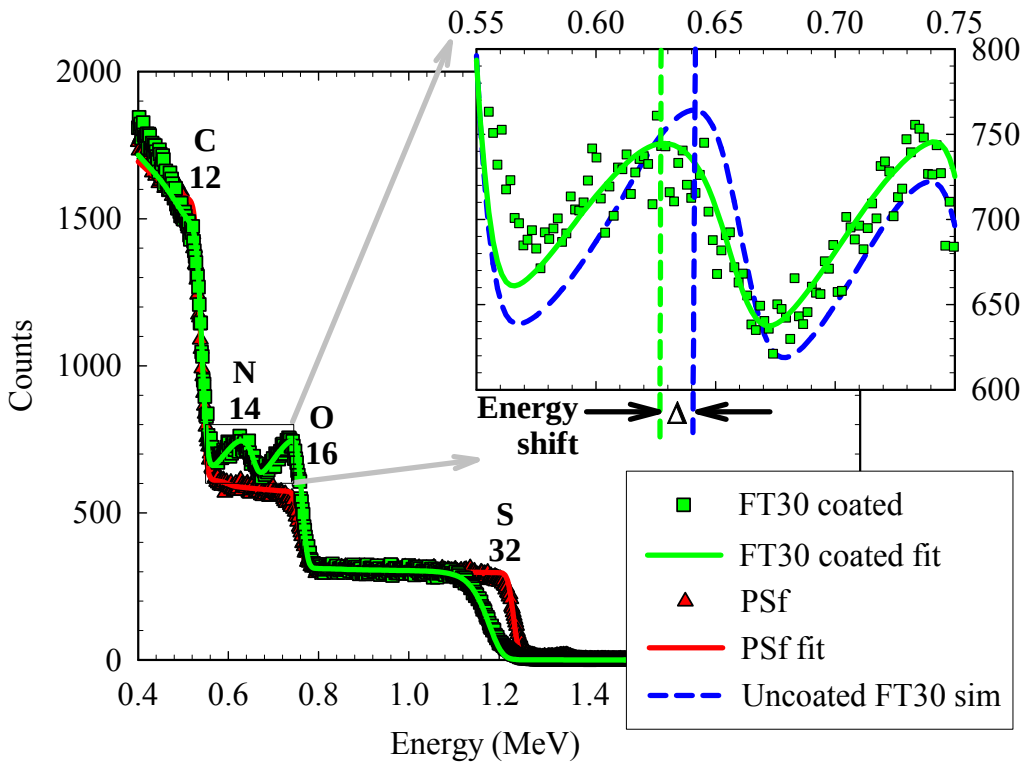


**Figure 2.1.** RBS spectra of untreated FT30 RO membrane and polysulfone (PSf) support samples. Symbols represent data. Lines represent the fit obtained using the software SIMNRA® as described previously [13, 17]. The main four elements present in the membrane (C, N, O, S), other than hydrogen, are easily discernible in the spectra. The occurrence of a coat layer on top of the PA active layer is supported by the energy shift, shown in the enlarged insert, between the fitted continuous green spectra of the FT30 RO membrane and the simulated dashed blue spectra obtained assuming that there is no coat layer.

The resulting fitting spectra are shown as continuous red (PSf support only) and green (FT30 membrane) lines in Figure 2.1. The average thicknesses (δ) and standard deviations (σ) of the PA and coat layers, and the elemental compositions of the PSf support, and PA and coat layers resulting in the best match between simulated and experimental spectra are shown in Figure 2.2.

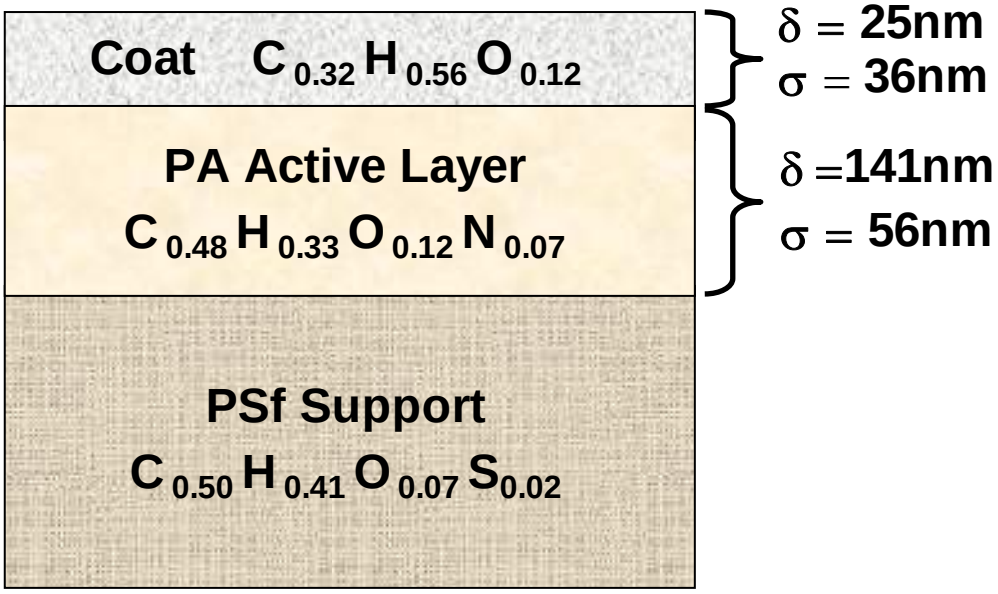


**Figure 2.2.** Elemental composition of polysulfone (PSf) support, and elemental compositions, average thicknesses (δ) and standard deviations (σ) of the coat and polyamide (PA) active layers of FT30 RO membrane obtained from RBS analyses.

The standard deviations (σ) of the thicknesses of the different layers provide indirect quantification of their roughness [16, 17]. The composition of the PSf support was consistent with that of theoretical PSf ($C_{27}H_{22}O_4S_1$) and the composition of the coat layer matched that of 50% ester-crosslinked PVA [19]. The O/N ratio of 1.77 obtained for the PA active layer was within 26% of that of 1.41 reported based on XPS analysis of an FT30-equivalent thin film with no coating prepared using *m*-phenylenediamine in aqueous phase and trimesoyl chloride in organic phase (*n*-hexane) [3]. The high Gamma distribution standard deviation of the PVA layer thickness (σ = 36 nm) was consistent with reported TEM analyses revealing that the coating material fills the valleys in the typical ridge-and-valley structure of aromatic PA active layers [18].

***2.3.2. Control Experiments.*** RBS spectra of control samples treated with tungstate as ion probe were undistinguishable from those of the untreated FT30 in Figure 2.1, thus confirming that the ion-probe concentration in the active layer was below detection limit (data not shown). These results ensured that the final rinsing step of sample preparation with a $10^{-6}$ M solution of tungstate, or silver which has a lower atomic number than tungsten, did not introduce false positive results with respect to the concentrations of FGs.

***2.3.3. Functional Groups Quantification.*** The RBS spectra of FT30 RO membrane samples treated with $AgNO_3$ at various pH levels are compared to that of an untreated sample in Figure 2.3. The carbon, nitrogen, oxygen and sulfur peaks and plateaus characteristic of the PA and coat layers and PSf support for the treated sample matched those of the untreated. An additional peak corresponding to $Ag^+$ bound to the deprotonated carboxylic groups in the PA active layer of samples treated with $AgNO_3$ appeared at ~1.75 MeV. A good match between experimental and fitted $Ag^+$ peaks was obtained with the assumption that $Ag^+$ was present in the PA active layer while absent in the coat layer, consistent with $Ag^+$ being bound to the deprotonated carboxylic groups of the PA active layer. As also depicted in Figure 2.3, the height of the $Ag^+$ peak increased with increasing pH, consistent with a corresponding increase in the concentration of deprotonated carboxylic groups ($R\text{-}COO^-$). The $Ag^+$ content in the PSf support layer also increased with pH with a measured maximum of 0.006% atom/atom, indicating the presence of a minute concentration of negatively ionizable FGs. Analysis of spectra obtained for samples treated with $WO_4^{2-}$ (Figure A.1 of Supporting Information) showed similar trends, i.e., $WO_4^{2-}$ peak present in the PA active layer but absent in the PVA coat,

and peak height increasing with decreasing pH consistent with a corresponding increase in protonated amine groups (R-$NH_3^+$). In this case, however, $WO_4^{2-}$ was not detected in the PSf support layer indicating the absence of positively ionizable FGs.

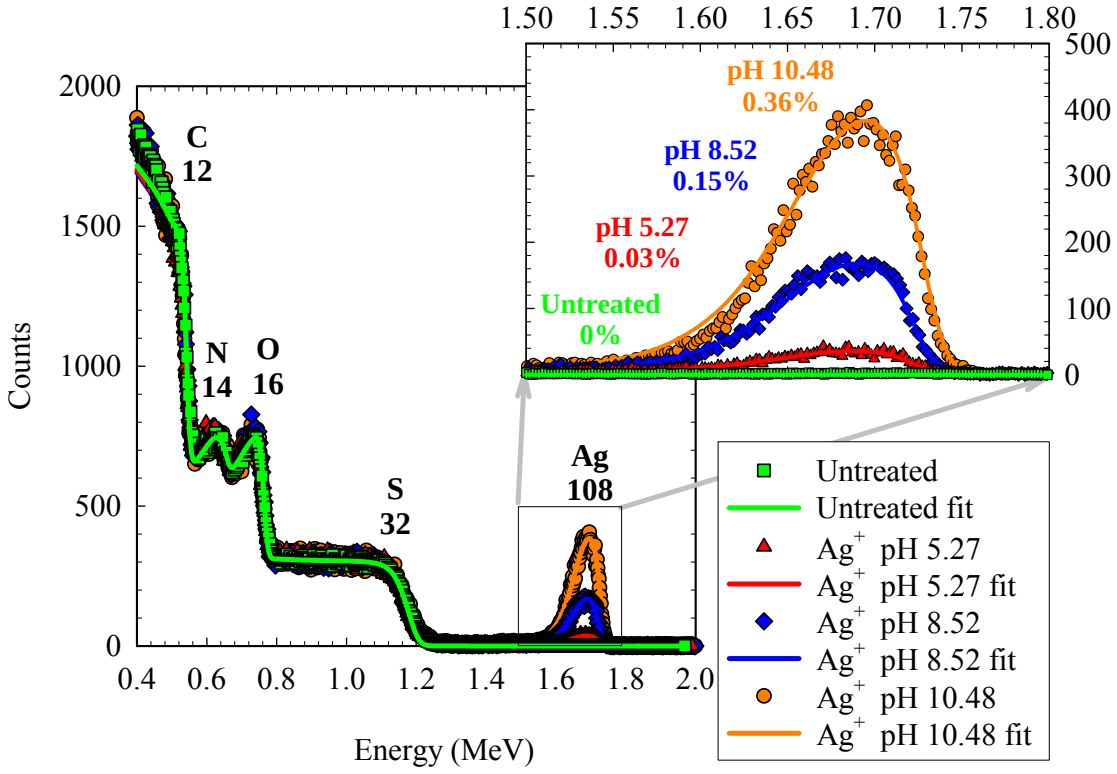


**Figure 2.3.** RBS spectra of FT30 RO membrane samples before and after $Ag^+$ probing of deprotonated carboxylic (R–$COO^-$) functional groups. $Ag^+$ peaks correspond to the $Ag^+$ ionically bound to R–$COO^-$ in the membrane active layer. Symbols represent data. Lines represent the fit obtained using the software SIMNRA® as described previously [13, 17]. Percentage values correspond to $Ag^+$ concentration in atomic percent. Higher $Ag^+$ concentrations at higher pH correspond to higher fractions of carboxylic groups in the R–$COO^-$ form. The untreated sample corresponds to a sample thoroughly rinsed with nanopure water (pH~6.8).

In addition to $Ag^+$ and $WO_4^{2-}$, the corresponding competing ions $Na^+$ and $Cl^-$ were also present in the final rinse solutions due to pH adjustment with Na(OH) and HCl.

However, the concentration of the competing ion in solution was generally similar or lower than that of the ion probe, except for the samples treated with silver and tungstate at the highest and lowest pH conditions, respectively. Taking this into account, and based on general counterion selectivity phenomena by ion exchangers, particularly the strong affinity for $Ag^+$ over $Na^+$ [9], the preference for divalent cations, e.g., $WO_4^{2-}$, over monovalent ones, e.g., $Cl^-$ [9], and the increasing selectivity with dilution of the solution [9], we neglect the competition of $Na^+$ and $Cl^-$ for ion exchange sites in the active layer.

Figure 2.4a shows the $Ag^+$ and $WO_4^{2-}$ concentrations in the FT30 RO active layer (symbols) as a function of ion-probe solution pH. Data were obtained in the 3.5-10.5 pH range. Treatment with $AgNO_3$ above pH 10.5 and $Na_2WO_4$ below pH 3.5 was not performed because of low solubility of the corresponding salts at those conditions. Consistent with the preceding discussion on RBS spectra, the increase in $Ag^+$ and decrease in $WO_4^{2-}$ concentrations with increasing pH shown in Figure 2.4a are consistent with the increase in deprotonated carboxylic and amine groups, respectively, present in the PA active layer. The spread of the titration curve for the carboxylic groups (i.e., $Ag^+$), however, was wider than that expected if there was only one dissociation constant ($pK_a$). This wider spread is consistent with that reported in the literature for contact angle titration (CAT) measurements in interfacially-polymerized PA films [4]. Wamser and Gilbert [4] reported that CAT results on the carboxylate-rich side of different PA films, including an FT30-equivalent prepared using *m*-phenylenediamine in aqueous phase and trimesoyl chloride in organic phase (chloroform), could only be explained by a distribution of effective $pK_a$ values in the range of 6-9. We note that values within this $pK_a$ distribution are higher than those reported for carboxylic groups in aqueous

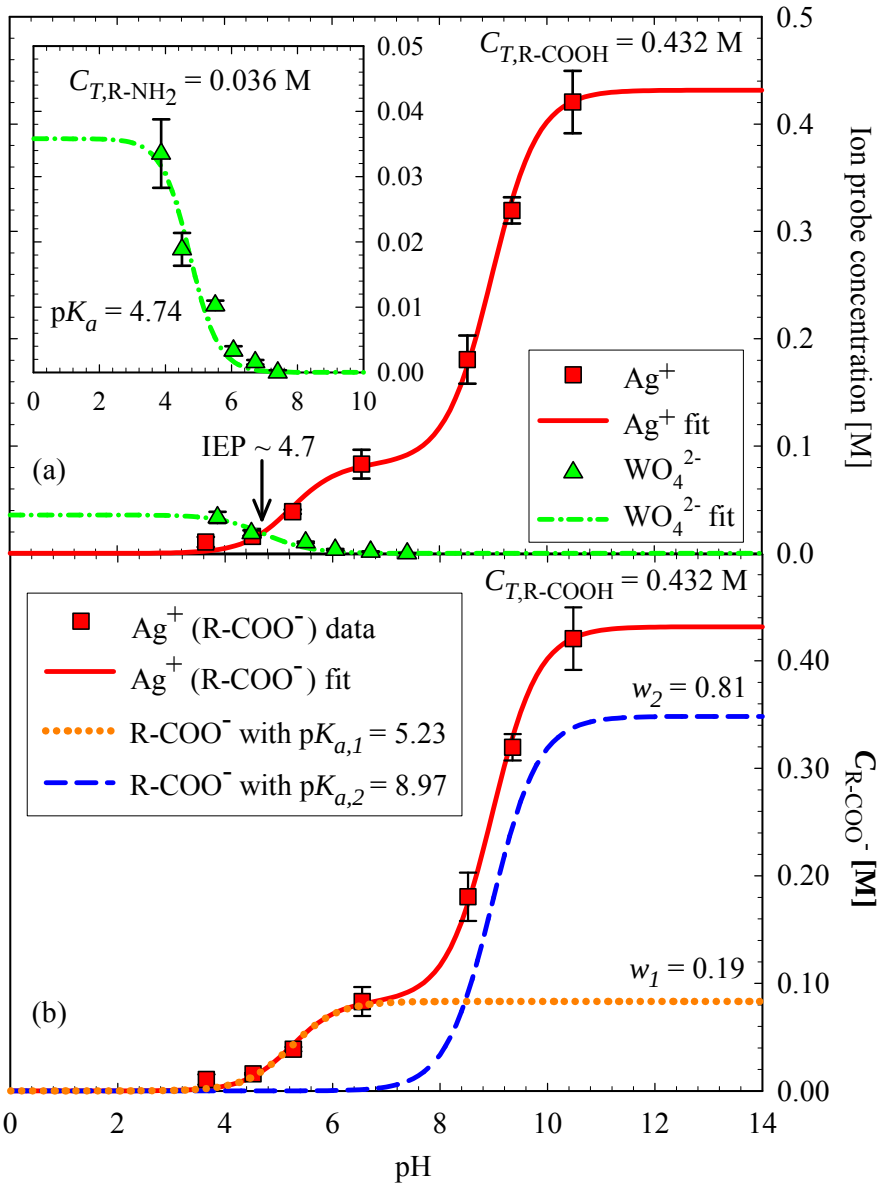


**Figure 2.4.** Concentration of ionized functional groups (FGs) as a function of pH in the polyamide (PA) active layer of FT30 RO membrane. (a) $Ag^+$ (red squares) and $WO_4^{2-}$ (green triangles) are assumed to correspond to the concentration of deprotonated carboxylic groups (R–$COO^-$) and protonated amine groups (R–$NH_3^+$), respectively. Error bars indicate standard deviation, generally within 15% of the corresponding average ion-probe concentration, obtained for replicate samples. The intersection between $Ag^+$ and $WO_4^{2-}$ corresponds to the isoelectric point (IEP) of the membrane active layer. The continuous red and dashed green curves represent the model fitting for the concentrations of respective R–$COO^-$ and R–$NH_3^+$ groups. (b) The (orange) dotted line and (blue) dashed line represent the R–$COO^-$ concentrations of carboxylic groups with lower (p$K_a$=5.23) and higher (p$K_a$=8.97) dissociation constants, respectively, and were calculated using the mathematical described in this study. The total concentration of R–$COO^-$ (red squares and continuous line) is reproduced from (a).

solution, e.g., p$K_a$=4.2 for benzoic acid at 25°C [8]. The higher p$K_a$ values in the FT30 RO membrane active layer are consistent with the relative dielectric constants of PA ($\varepsilon_{PA}$~3) [6] and water inside Angstrom-sized pores in the active layer [7] being lower than that of dilute aqueous solution ($\varepsilon_w$ = 78.3 at 25°C) [7, 8, 20]. In general, the low dielectric constant region surrounding the FGs in the active layer of FT30 RO membrane increases the energy needed for ionization [20], and thus increases the p$K_a$ of carboxylic groups and decreases the p$K_a$ of amine groups [8, 20].

Also, as depicted in Figure 2.4a, the minimum measured concentrations of $Ag^+$ and $WO_4^{2-}$ in the active layer were 0.01 M (pH =3.65) and 0.002 M (pH = 6.72), respectively. Based on the concentration ($10^{-6}$ M) of the ion-probe solutions in the final rinsing step during sample preparation, and our previous studies [14] on the partitioning of ions into the active layer of the FT30 RO membrane, it can be estimated that in this study the contribution of physi-sorption to the measured ion-probe concentration in the active layer is negligible, and therefore the measured $Ag^+$ and $WO_4^{2-}$ concentrations are accurate estimates of the concentrations of ionized carboxylic and amine groups, respectively.

***2.3.4. Isoelectric Point (IEP).*** The IEP of the active layer of FT30 RO membrane can be obtained from the intersection of the two curves in Figure 2.4a, which occurs at pH~4.7. This value is generally consistent with the IEP range of pH 4-5 reported based on zeta potential measurements on four uncoated RO aromatic PA membranes by Tang et al. [18], and two RO/NF PA membranes by Childress and Elimelech [21]. This generally good agreement was obtained even though zeta potential measurements, and the IEP values obtained from them, are known to depend on the characteristics of the solution in

which the samples are analyzed [11, 21, 22]; 0.01 M NaCl was used in both of these former studies [18, 21].

***2.3.5. Modeling of FG Ionization.*** We modeled the ionization behavior of the FGs in the PA active layer of the FT30 RO membrane based on three main assumptions: (i) FGs were at acid-base equilibrium [9] with the ion-probe solution, (ii) ionized FGs were accessible to the ion probes, and (iii) there was a one-to-one correspondence between ion probe and FG. In the first assumption, the protonation/deprotonation of FGs is the result of their equilibrium with the ion-probe solution surrounding the membrane. As a result, the acid-base equilibrium equations were written in terms of the pH of the ion-probe solution. Also, consistent with the relatively wide titration curves for deprotonated carboxylic groups obtained in this study (Figure 2.4a) and reported by Wamser and Gilbert [4], the acid-base equilibrium equations included more than one p$K_a$ constant as fitting parameters. Validity of the second assumption - that ionized FGs are present in relatively large pores accessible to the ion probe - is quantitatively addressed in the following section. The third and final assumption of one-to-one correspondence between ion probe and FG, i.e., each $Ag^+$ and $WO_4^{2-}$ ion is assumed to neutralize only one ionized site, is clearly valid for *monovalent* $Ag^+$ association with monovalent carboxylic groups. Additionally, it should also be valid for *divalent* tungstate because amine groups are present in the active layer at a relatively low concentration (up to ~0.04 M), and assuming that their distribution throughout the PA film is uniform, the minimum average distance between them can be estimated at ~3 nm. This distance is more than ten times the estimated ionic radius of tungstate ion (0.267 nm) [23], and thus the second charge of $WO_4^{2-}$ would likely be balanced by $Na^+$.

***2.3.6. Accessibility of Ion Probes to Functional Groups.*** To verify the accessibility of $Ag^{+}$ and $WO_4^{2-}$ to the membrane pores, and thus to the ionized FGs, a comparison needs to be made between the pore radii and the ion probe radii. The PSD of FT30-equivalent thin-films - prepared using *m*-phenylenediamine in aqueous phase and trimesoyl chloride in organic phase (*n*-hexane) - was recently characterized by positron annihilation lifetime spectroscopy (PALS) [3]. The PALS analyses revealed that the PSD of these films was bimodal, consistent with the interstitial-void model previously proposed by Sourirajan et al. [24] for RO thin films. In this model, the active layer was composed of a conglomerate of polymer aggregates with two types of pores, those resulting from the void space between polymer aggregates (i.e., aggregate pores), and relatively smaller pores associated with the interstitial space between polymer branches within an aggregate (i.e., network pores). The corresponding radii for aggregate and network pores in the FT30-equivalent samples studied [3] were in the ~3.5-4.1 Å and ~1.4-2.3 Å ranges, respectively.

Regarding the radii of the ion probes in the PA active layer, in general, from the existing literature on ion exchange resins [9], it appears that when the pores in the ion exchanger are large enough to accommodate the hydrated ions or when the resin structure is flexible enough to open up space for the hydrated ions, hydrated radii are the dominant ionic dimension to consider in the analysis of resin-ion interaction. However, when the rigidity of the material is high, as in zeolites or highly crosslinked polymers, and the pores are smaller than the hydrated ions, the nonsolvated ionic radii become the relevant dimension [9]. For instance, it has been reported [9] that ion hydration may be incomplete in highly crosslinked polymers, that hydration numbers lower than unity occur in ion exchangers,

e.g., 0.3 for $Ag^+$ in a sulfonated polystyrene cation exchange resin [9], and that sieve exclusion mechanisms in the rigid structure of zeolites are dominated by the nonhydrated radii of counterions [9]. As a result, because the PA active layers of RO membranes are also highly crosslinked, we assume that the ionic dimension of interest to assess the accessibility of the ion probes to the FGs in the active layer of FT30 RO membrane is the nonhydrated radius. Shannon [25] also reported that the appropriate ionic dimension to consider when an ion diffuses within a solid is the crystal ionic radius which for the case of $Ag^+$ is in the 0.81 - 1.42 Å range [25]. This range is below the radius of the smaller network pores (1.4 - 2.3 Å) in the PA film, indicating that $Ag^+$ ions should be able to access all carboxylic groups in the active layer. Accordingly, we assumed that the $Ag^+$ concentration measured in the active layer of treated membranes corresponds to that of total concentration of deprotonated carboxylic groups.

In contrast, the ionic radius of $WO_4^{2-}$ has been estimated as 0.267 nm [23]. This value is larger than the typical radius of network pores (1.4 - 2.3 Å) but lower than that of aggregate pores (3.5 - 4.1 Å). Consequently, the concentration of protonated amine groups measured through probing with $WO_4^{2-}$ ions might not take into account amine groups present in the network pores.

***2.3.7. FG Acid-Base Equilibrium.*** We used the following acid-base equilibrium expressions to represent the concentration of deprotonated carboxylic ($[R\text{-}COO^-]$) and protonated amine ($[R\text{-}NH_3^+]$) groups in the PA active layer of the FT30 membrane samples:

$$[\mathrm{R-COO^-}] = C_{T,\mathrm{R-COOH}} \sum_{i=1}^{n} \left( w_i \frac{K_{a,i}}{[\mathrm{H^+}] + K_{a,i}} \right) \quad (2.1)$$

$$[\mathrm{R-NH_3^+}] = C_{T,\mathrm{R-NH_2}} \sum_{i=1}^{n} \left( w_i \frac{[\mathrm{H^+}]}{[\mathrm{H^+}] + K_{a,i}} \right) \quad (2.2)$$

$C_{T,\mathrm{R-COOH}}$ and $C_{T,\mathrm{R-NH_2}}$ represent the total concentrations of carboxylic and amine groups, respectively, in the PA active layer, $[\mathrm{H^+}]$ is the hydrogen ion concentration of the ion-probe solution, $K_{a,i}$ is the *i*-th acid-base equilibrium constant of carboxylic or amine groups, *n* is the number of dissociation constants necessary to accurately fit the data, and $w_i$ is the fraction of carboxylic or amine groups with dissociation constant $K_{a,i}$ (i.e., $w_1+w_2+\ldots+w_n = 1$).

Experimental $[\mathrm{R-COO^-}]$ and $[\mathrm{R-NH_3^+}]$ values obtained from RBS analyses of the corresponding ion-probes (Figure 2.4a) were fit by Equations 2.1 and 2.2. Two dissociation constants ($n$=2) were sufficient to accurately describe the titration curve for the deprotonated carboxylic groups (i.e., $Ag^+$ data in Figure 2.4a). Accordingly, the fitting parameters used for model fitting were $C_{T,\mathrm{R-COOH}}$, $w_1$, $\mathrm{p}K_{a,1}$ and $\mathrm{p}K_{a,2}$. In contrast, one dissociation constant ($n$=1) was sufficient to accurately model the data for protonated amine groups (i.e., $WO_4^{2-}$ data in Figure 2.4a), and therefore the corresponding fitting parameters were $C_{T,\mathrm{R-NH_2}}$ and $\mathrm{p}K_{a,1}$ (i.e., $w_1 = 1$).

***2.3.8. Modeling Results.*** Figure 2.4a shows the results of the least-squares fitting to Equations 2.1 and 2.2 of the experimentally-determined concentrations of total deprotonated carboxylic groups (i.e., $Ag^+$ data) and accessible protonated amine groups

(i.e., $WO_4^{2-}$ data) as continuous (red) and dashed (green) lines, respectively. As depicted in the figure, the model provided a good representation of both experimental curves. Furthermore, both fitted curves were generally consistent with findings from previously reported CAT analyses [4] in which ~99% of the amine and carboxylic groups in FT30-equivalent thin films were ionized at pH~2 and pH~11, respectively. The fitting parameters obtained were $C_{T,\mathrm{R-COOH}}$ = 0.432 M, $w_1$ = 0.19 ($w_2$ = 0.81), p$K_{a,1}$ = 5.23 and p$K_{a,2}$ = 8.97 for the carboxylic groups, and $C_{T,\mathrm{R-NH_2}}$ = 0.036 M and p$K_{a,1}$ = 4.74 for the amine groups. The value obtained for $C_{T,\mathrm{R-COOH}}$ was ~2.6 times higher than that experimentally measured by CAT for a PA film made from trimesoyl chloride and hexamethylenediamine [4]. In addition to the different chemicals used to produce the PA, the discrepancy in $C_{T,\mathrm{R-COOH}}$ values could arise from the fact that the CAT procedure is a surface-sensitive technique that does not detect all the FGs present throughout the depth of the PA film [4, 10]. Although the $C_{T,\mathrm{R-COOH}}$ obtained in this study was also ~4.4 times higher than that predicted by the Freger-Srebnik (FS) model [5], the ratio $C_{T,\mathrm{R-COOH}} / C_{T,\mathrm{R-NH_2}}$ =12 was only 20% higher than the ratio of 10 predicted by the FS model [5]. A comparison between the ionization behaviors of the fractions of carboxylic groups with different p$K_a$ values is shown in Figure 2.4b. As depicted in the figure, at the pH at which 99% of the more acidic fraction (p$K_{a,1}$ = 5.23, $w_1$ = 0.19) of carboxylic groups is ionized, the degree of dissociation of the lesser acidic fraction (p$K_{a,2}$ = 8.97, $w_2$ = 0.81) is less than 2%.

The existence of two p$K_a$ values among the carboxylic groups was generally consistent with the bimodal PSD reported for the FT30-equivalent thin-films studied by Kim et al.

[3] and a corresponding decreasing dielectric constant with decreasing active layer pore size [7]. The smaller the pore, the smaller the dielectric constant in the pore environment [6, 7], and therefore the higher the p$K_a$ of the carboxylic groups in it [8, 26]. To illustrate the dielectric constant effect on the p$K_a$ of carboxylic groups, consider that at 25$^o$C the p$K_a$ of benzoic acid ($C_6H_5$-COOH) in water is 4.2 ($\varepsilon$ = 78.3) but it increases to 5.5 ($\varepsilon$ = 51.6) and 9.4 ($\varepsilon$ = 32.64) in 60% and 100% methanol-water mixtures, respectively [8, 26]. The values $w_1$ = 0.19 and $w_2$ = 0.81 of the model fitting results of deprotonated carboxylic groups are in reasonably good agreement with the PALS results reported in the literature [3], from which it can be calculated that 30% of the pores in the PA active layer are the bigger aggregate pores, while the other 70% are the smaller network pores. Finally, the assumption that the concentration of amine groups measured did not take into account those present in the smaller network pores was supported by (i) the suitability of one single p$K_a$ to describe their ionization behavior and (ii) the similarity of the fitted p$K_a$ (4.74) to the p$K_a$ (4.6) of benzoamine ($C_6H_5$-$NH_2$) in water at 25$^o$C ($\varepsilon$ = 78.3) [26].

***2.3.9. Degree of Polymer Crosslinking (DPC).*** We also used the RBS data obtained in this study to calculate a parameter describing the degree of polymer crosslinking (DPC) in the PA active layer of the FT30 RO membrane. The concentrations of carboxylic group (CG), amine group (AG) and total nitrogen (N) were used for this purpose. The DPC was defined as the ratio between the amide link (AL) concentration in the active layer and the theoretical maximum AL concentration in a fully crosslinked PA (Equation 2.3). The numerator in Equation 2.3 represents the AL concentration in the PA film, while the denominator represents the theoretical maximum AL content expressed as the sum of AL and FG concentrations. For a *fully* crosslinked film, CG=AG=0 and therefore

the DPC equals unity. Also, if no AL formation occurred, N=AG and therefore the DPC equals zero. Consequently, the DPC is theoretically bound by the limits $0 \leq DPC \leq 1$. Using the elemental atomic fractions of 0.0037, 0.00031 and 0.06948 obtained by RBS for CG, AG, and N, respectively, the calculated DPC was 0.945, indicating that 94.5% of the ALs were formed.

$$DPC = \frac{\text{Amide links}}{\text{Potential amide links}} = \frac{N - AG}{N + CG} \tag{2.3}$$

An alternative way to express the degree of polymer crosslinking is to indicate the fractions of PA repeating units that do not contain FGs ($n$), and those that contain CG ($x$) and AG ($y$), where $n+x+y=1$. The chemical formula for a *fully* cross-linked fully aromatic PA is $(C_{36}H_{24}N_6O_6)_n$. Note that the repeating unit contains six amide links (ALs). A *partially* cross-linked fully aromatic PA would have a carboxylic or amine group present in some of the repeating units, with chemical formula $(C_{36}H_{25}N_6O_7)_x$ or $(C_{36}H_{25}N_6O_6)_y$, respectively. While each repeating unit in the $y$ fraction have five ALs (i.e., one out of the six nitrogen atoms is an amine nitrogen), those in the $x$ fraction have six ALs because all nitrogen atoms that did not form ALs are already included in the $y$ fraction. Although the nitrogen-to-oxygen ratio N/O has been previously used [3] for the purpose of calculating the different repeating unit fractions, the nitrogen-to-functional groups (N/FG) ratio is used here instead. The N/FG ratio is considered to be a more accurate ratio because both functional groups and nitrogen are present *only* in the PA active layer. In contrast, oxygen is found not only in the PA active layer, but also in the coat layer and the PSf support, and therefore measurements of (relative) oxygen content

may introduce error. The chemical formulas of the three PA fractions given above were used to obtain the following expression:

$$\frac{\mathrm{N}}{\mathrm{FG}} = \frac{6(n+x+y)}{x+y} = \frac{6}{x+y} \tag{2.4}$$

Using the elemental atomic fractions obtained from RBS, N=0.06948, CG=Ag=0.0037 and AG=W=0.00031, the N/FG ratio was calculated as N/FG=0.06948/(0.0037+0.00031)=17.33. The corresponding value resulting from Equation 2.4 is $x+y$=0.346. Furthermore, $x/y$ = CG/AG = 11.94. These expressions together with $n+x+y$=1 were used to obtain $n$=0.654, $x$=0.319 and $y$=0.027. These results reveal that the fraction of PA repeating units that is fully cross-linked is 65%, and that the rest contains either a carboxylic (32%) or an amine (3%) group. Because the concentration of amine groups in the network pores could not be quantified in the present study, the fraction of repeating units with amine groups might be higher with corresponding lower values for the fully-crosslinked units and those with carboxylic groups. The DPC as defined by Equation 2.3 was calculated based on the $n$, $x$ and $y$ fractions and their corresponding content of ALs and FGs. The calculated value (0.945) matched the one calculated above indicating that the appropriate polymer repeating units have been chosen to describe the composition of the PA layer, and that both methodologies used for describing the DPC are equivalent.

Finally, the (n, x, y) values were used to estimate the chemical formula for PA ($C_{0.50}H_{0.34}N_{0.08}O_{0.09}$), and compared to that indicated in Figure 2.2 ($C_{0.48}H_{0.33}N_{0.07}O_{0.12}$) determined independently through RBS analysis assuming a theoretical H/C ratio of 0.67

[17]. As observed, while the carbon, hydrogen and nitrogen contents obtained by both methods are in good agreement, the oxygen content is approximately 25% different. Consistent with our previous discussion, this discrepancy is likely due to the presence of oxygen in all the layers of the membrane which introduces experimental error when determining its relative content in the PA layer alone. The same type of variability is not found in the carbon content, for example, which is also present in all layers, because the error introduced is negligible when compared to its very high abundance in the PA active layer, i.e., approximately 50% of the atoms are carbon atoms. In consequence, the discrepancy found in the oxygen content estimated by both methods supports our choice of using the N/FG rather than the N/O ratio to estimate the DPC of the PA active layer.

### 2.4. Acknowledgments

RBS analyses were carried out in the Center for Microanalysis of Materials, University of Illinois, partially supported by the U.S. Department of Energy under grant DEFG02-91-ER45439. The authors acknowledge Doug Jeffers for assistance in RBS analyses, Jeanne Luh for assistance in experimental procedures, and Hydranautics, Oceanside, CA for providing the polysulfone support membrane. This work was supported by the National Science Foundation Environmental Engineering and Technology program under agreement number BES-0332217, and the WaterCAMPWS, a Science and Technology Center of Advanced Materials for the Purification of Water with Systems under agreement number CTS-0120978. The opinions in this paper do not necessarily reflect those of the sponsor.

## 2.5. Supporting Information Available

The RBS spectra of FT30 RO membrane samples before and after $WO_4^{2-}$ probing of protonated amine ($R–NH_3^+$) functional groups are presented. This information is available free of charge via the Internet at http://pubs.acs.org, and in Appendix A.1.

## 2.6. References


(1) Mulder, M. *Basic Principles of Membrane Technology*; 2nd ed.; Kluwer Academic: Boston, MA, 1996

(2) Petersen, R.J. Composite reverse osmosis and nanofiltration membranes. *J. Mem. Sci.* **1993**, *83*, 81-150

(3) Kim, S.H.; Kwak, S.-Y.; Suzuki, T. Positron annihilation spectroscopic evidence to demonstrate the flux-enhancement mechanism in morphology-controlled thin-film-composite (TFC) membrane. *Environ. Sci. Technol.* **2005**, *39*, 1764-1770

(4) Wamser, C.C.; Gilbert, M.I. Detection of surface functional group asymmetry in interfacially-polymerized films by contact angle titrations. *Langmuir* **1992**, *8*, 1608-1614

(5) Freger, V. Nanoscale heterogeneity of polyamide membranes formed by interfacial polymerization. *Langmuir* **2003**, *19*, 4791-4797

(6) Szymczyk, A.; Fievet, P. Investigating transport properties of nanofiltration membranes by means of a steric, electric and dielectric exclusion model. *J. Mem. Sci.* **2005**, *252*, 77-88

(7) Bowen, W.R.; Welfoot, J.S. Modelling the performance of membrane nanofiltration-critical assessment and model development. *Chem. Eng. Sci.* **2002**, *57*, 1121-1137

(8) Conway, B.E.; Barradas, R.G. *Chemical Physics of Ionic Solutions*; John Wiley & Sons: New York, 1966

(9) Helfferich, F. *Ion exchange*; McGraw-Hill: New York, 1962

(10) Holmes-Farley, S.R.; Reamey, R. H.; McCarthy T.J.; Deutch, J.; Whitesides, G.M. Acid-base behavior of carboxylic acid groups covalently attached at the surface of polyethylene: the usefulness of contact angle in following the ionization of surface functionality. *Langmuir* **1985**, *1*, 725-740

(11) Brant, J.A.; Johnson, K.M.; Childress, A.E. Characterizing NF and RO membrane surface heterogeneity using chemical force microscopy. *Colloids Surf. A: Physicochem. Eng. Aspects* **2006**, *280*, 45-57

(12) Pourbaix, M. *Atlas of electrochemical equilibria in aqueous solutions*, 1st english ed.; Pergamon Press: Great Britain, 1966

(13) Mi, B.; Mariñas, B.J.; Cahill, D.G. RBS characterization of arsenic (III) partitioning from aqueous phase into the active layers of thin-film composite NF/RO membranes. *Environ. Sci. Technol.* **2007**, *41*, 3290-3295

(14) Zhang, X.; Cahill, D.G.; Coronell, O.; Mariñas, B.J. Partitioning of salt ions in FT30 reverse osmosis membranes. *Appl. Phys. Lett.* **2007**, *91*, 181904

(15) Mi, B.; Cahill, D.G.; Mariñas, B.J. Physico-chemical integrity of nanofiltration/reverse osmosis membranes during characterization by Rutherford backscattering spectrometry. *J. Mem. Sci.* **2007**, *291*, 77-85

(16) Mayer, M.; Duggan, J.L.; Morgan, I.L. SIMNRA, a simulation program for the analysis of NRA, RBS and ERDA. *Proceedings of the 15th International Conference on the Application of Accelerators in Research and Industry*. Denton, TX, **1998**, 541.

(17) Mi, B.; Coronell, O.; Mariñas, B.J.; Watanabe, F.; Cahill, D.G.; Petrov, I. Physico-chemical characterization of NF/RO membrane active layers by Rutherford backscattering spectrometry. *J. Mem. Sci.* **2006**, *282*, 71-81.

(18) Tang, C.Y.; Kwon, Y.-N; Leckie, J.O. Probing the nano- and micro-scales of reverse osmosis membranes-A comprehensive characterization of physiochemical properties of uncoated and coated membranes by XPS, TEM, ATR-FTIR, and streaming potential measurements. *J. Mem. Sci.* **2007**, *287*, 146-156

(19) Immelman, E.; Sanderson, R.D.; Jacobs, E.P.; van Reenen, A.J. Poly(vinyl alcohol) gel sublayers for reverse osmosis. I. Insolubilization by acid-catalyzed dehydration. *J. Appl. Polym. Sci.* **1993**, *50*, 1013-1034

(20) Marshall, J. The interaction of ions with nylon. Part I. Absorption of simple acids. *J. Polym. Sci. Part A-1: Polym. Chem.* **1968**, *6*, 1583-1595

(21) Childress A.E., Elimelech, M. Effect of solution chemistry on the surface charge of polymeric reverse osmosis and nanofiltration membranes. *J. Mem. Sci.* **1996**, *119*, 253-268

(22) Childress A.E., Elimelech, M. Relating nanofiltration membrane performance to membrane charge (electrokinetic) characteristics. *Environ. Sci. Technol.* **2000**, *34*, 3710-3716

(23) Marcus, Y. Ionic radii in aqueous solution. *Chem. Rev.* **1988**, *88*, 1475-1498

(24) Nguyen, T.D.; Chan, K.; Matsuura, T.; Sourirajan, S. Viscoelastic and statistical thermodynamic approach to the study of the structure of polymer film casting solutions for making RO/UF membranes. *Ind. Eng. Chem. Prod. Res. Dev.* **1985**, *24*, 655-665

(25) Shannon, R.D. Revised effective ionic radii and systematic studies of interatomic distances in halides and chalcogenides. *Acta Cryst.* **1976**, *A32*, 751-767

(26) Bacarella, A.L.; Grunwald, E.; Marshall, H.P.; Purlee, E.L. The potentiometric measurements of acid dissociation constants and pH in the system methanol-water. $pK_A$ values for carboxylic acids and anilinium ions. *J. Org. Chem.* **1955**, *20*, 747-762

# CHAPTER 3

# ACCESSIBILITY AND ION EXCHANGE STOICHIOMETRY OF IONIZED CARBOXYLIC GROUPS IN THE ACTIVE LAYER OF FT30 REVERSE OSMOSIS MEMBRANE[1]

**Abstract:** We have experimentally determined the concentration of $Ba^{2+}$ that associates with the accessible ionized R–$COO^-$ groups in the polyamide active layer of the FT30 reverse osmosis membrane in the pH range 3.42-10.30. $Ba^{2+}$ concentrations in the active layer ([$Ba^{2+}$]) were measured using the ion-probing/Rutherford backscattering spectrometry procedure reported in our previous work. We found that at all but the lowest experimental pH=3.42, [$Ba^{2+}$] was lower than the corresponding total concentrations of R–$COO^-$ groups; their difference was consistent with steric and charge effects determining the accessibility and association, respectively, of $Ba^{2+}$ to R–$COO^-$ groups. Accordingly, we propose two descriptors, the *accessibility ratio* (AR) and the *neutralization number* (NN), to account for the observed difference. AR, the fraction of R–$COO^-$ groups accessible to $Ba^{2+}$ ions, and NN, the average number of R–$COO^-$ groups neutralized per $Ba^{2+}$ ion, were determined experimentally performing $Ag^+$-$Ba^{2+}$ ion-exchange tests. The resulting AR=0.40 indicated that on average only 40% of ionizable carboxylic groups were accessible to $Ba^{2+}$. [$Ba^{2+}$] values calculated using R–$COO^-$ concentrations and the AR and NN concepts were in agreement with experimental [$Ba^{2+}$] results.

[1] Reproduced with permission from Coronell, O.; Mariñas, B.J.; Cahill, D.G., Accessibility and ion exchange stoichiometry of ionized carboxylic groups in the active layer of FT30 reverse osmosis membrane. *Environ. Sci. Technol.* **2009**, *43*, 5042-5048. Copyright 2009 American Chemical Society.

**Key Words:** accessibility ratio, neutralization number, steric effects, reverse osmosis, nanofiltration, polyamide, Rutherford backscattering spectrometry, carboxylic groups

### 3.1. Introduction

Most commercially available reverse osmosis (RO) and nanofiltration (NF) membranes have a thin-film composite structure consisting of a top thin polyamide active layer (~50-200 nm), an intermediate polysulfone support (~50 μm) and a backing (~200 μm) of non-woven polyester fibers [1]. Some membranes also have a protective surface coating designed to produce a more hydrophilic, fouling-resistant surface [1, 2]. The active layer of RO/NF membranes is the main barrier controlling contaminant rejection which is the result of solute-active layer interactions determining the ability of contaminants to partition into and move through the active layer [1, 3], with active layer pore size and charge distribution, and contaminant size and charge playing important roles in transport phenomena [3-5]. Accordingly, comparing how solutes with different sizes and charges interact with active layers would improve our understanding of the mechanisms controlling contaminant transport through RO/NF membranes.

Unfortunately, characterizing contaminant-active layer interactions has remained challenging due to limitations associated with the nanometer-scale spatial resolution required to study these ultrathin active layers. Several groups have addressed this challenge by characterizing the physico-chemical properties of active layers and the concentration of contaminants within them through different thin-film characterization procedures [6-13]. In one of these procedures of interest for the present study, we quantified the concentrations of ionized functional groups in the polyamide active layer

of the FT30 reverse osmosis (RO) membrane as a function of pH [14]. While ionized carboxylic groups ($R–COO^-$) were above detection limit (~0.01 M) in the pH range studied (~3.5-10.3), ionized amine groups ($R–NH_3^+$) decreased below detection limit above pH=6.0. Total concentrations of carboxylic (≈0.43 M) and amine (≈0.04 M) groups were in the same order of magnitude of theoretical predictions by Freger and Srebnik [15], and of experimental volumetric charge densities and ion exchange capacities obtained from streaming potential analysis and titration methods, respectively, for various polyamide active layers [4, 16].

The procedure for quantification of $R–COO^-$ groups involved their neutralization with $Ag^+$ as ion probe followed by the quantification of $Ag^+$ by Rutherford backscattering spectrometry (RBS). $Ag^+$ was chosen as probe because it fulfilled two requirements: (i) smaller ionic radius ($r_{Ag^+}$ =0.81-1.42 Å [17]) than the radii of the smallest pores in the active layer of FT30 membrane ($r_{Pore\ min}$ =1.4-2.3 Å [8]); and (ii) accurate quantification by RBS [18] at the concentrations that $R–COO^-$ is present in polyamide active layers (i.e., RBS signal is proportional to the square of the atomic number of the element detected). The size of the smallest pores in the active layer of the FT30 membrane was previously determined by Kim et al. [8] in a positron annihilation lifetime spectroscopy (PALS) study that found a bimodal pore size distribution with larger and smaller pore radii in the ranges of 3.5-4.1 Å and 1.4-2.3 Å, respectively. The results from Kim et al. are consistent with later results of similar PALS studies for different RO/NF membranes [9].

The concentration of $Ag^+$ in the active layer ($[Ag^+]$) measured by RBS was assumed to be equivalent to that of $R–COO^-$ groups based on two premises [14]: (i) accessibility of $Ag^+$

to all R–$COO^-$ groups due to $r_{Ag^+} \leq r_{Pore\ min}$ (see Figure 3.1); and (ii) one-to-one correspondence between $Ag^+$ ions and R–$COO^-$ groups due to the monovalence of both. It was also implicitly assumed that [$Ag^+$] was not significantly affected by formation of $Ag^+$-amine complexes; this assumption was supported by a 10-fold difference between the calculated total concentrations of carboxylic (≈0.43 M) and amine (≈0.04 M) groups in FT30 membrane [14, 15]. Additionally, the stability constants for $Ag^+$-amine complexes in aqueous solutions [19] indicate that no more than ~75% and ~1% of R–$NH_2$ would complex with $Ag^+$ to form $(amine)_2Ag^+$ and $(amine)Ag^+$ complexes, respectively. As amine groups are in relatively low concentrations and relatively fixed positions in the polymer matrix, it seems unlikely that $(amine)_2Ag^+$ complexes form; however, in a worst case scenario, each $Ag^+$ would complex with two R–$NH_2$ groups, and therefore the uncertainty in the concentration of R–$COO^-$ groups measured with our ion-probe method should not exceed (0.04 M×0.75)÷2=0.015 M.

The ion-probing/RBS procedure previously developed to quantify the concentration of R–$COO^-$ groups in the active layer of FT30 membrane [14] opens the possibility to study the accessibility and ion-exchange stoichiometry of R–$COO^-$ groups by using ion probes of varying size and charge. Accordingly, the objectives of this study are to quantify as a function of pH in the active layer of the FT30 membrane: (i) the accessibility of $Ba^{2+}$ ion ($r_{Ba^{2+}}$ =1.49-1.75 Å [17]) to R–$COO^-$ groups; and (ii) the ion-exchange stoichiometry between (divalent) $Ba^{2+}$ ion and R–$COO^-$ groups. To accomplish these objectives, we measured the concentration of $Ba^{2+}$ that associates as a function of pH with the accessible R–$COO^-$ groups in the active layer of the FT30 membrane, and compared the results to

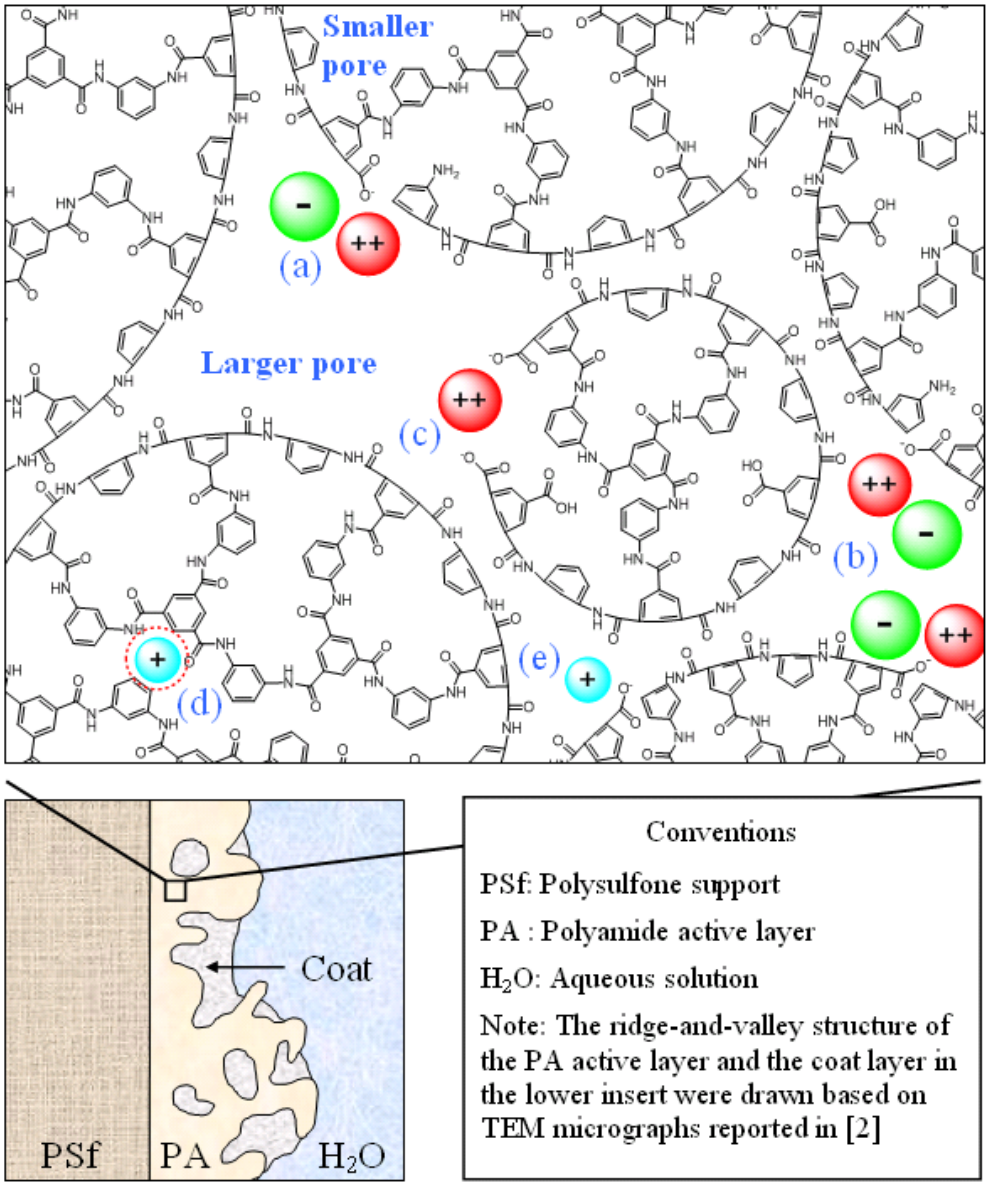


**Figure 3.1.** Top: Schematic representation of the accessibility and association of counterions to ionized carboxylic groups ($R–COO^-$) in the bulk polyamide active layer of the FT30 RO membrane. The figure is not intended as an exact representation of the molecular structure of the polyamide network, but as a visual aid to the accessibility and stoichiometry of association concepts discussed in this manuscript. Larger and smaller pores represent the bimodal pore size distribution reported by Kim et al. [8]. Monovalent (blue) positive and (green) negative circles represent silver and chloride ions, respectively. Divalent (red) circles represent barium ions. Bottom: Composite structure of the FT30 RO membrane showing the open ridge-and-valley structure of its polyamide active layer where steric effects may be negligible for counterions accessing ionized functional groups located in the vicinity of the surface. The cartoon also shows the coat layer on top of the active layer which was previously reported [14] to have a composition consistent with that of 50% ester-crosslinked polyvinyl alcohol.

those previously obtained with the relatively smaller and monovalent $Ag^+$. The results from this study constitute the first direct quantification of the steric effects and stoichiometry of association of ionic contaminants within the active layers of RO/NF membranes. We also developed a conceptual and mathematical model describing the results.

**3.2. Materials and Methods** (See extended version in Supporting Information)

***3.2.1. Target Membrane.*** All experiments were performed with coupons ($2.5\times5.0$ $cm^2$) of the thin-film composite FT30 RO membrane (Dow Liquid Separation, Midland, MI) cut from a spiral-wound element.

***3.2.2. Ion-Probe Solutions.*** All chemicals used were A.C.S. grade with 99%+ purity. Silver nitrate ($AgNO_3$), barium nitrate ($Ba(NO_3)_2$), and barium chloride dihydrate ($BaCl_2{\cdot}2H_2O$) were used as sources of $Ag^+$ and $Ba^{2+}$. All ion-probe solutions were prepared with nanopure water. The concentrations of silver ($5\times10^{-5}$-$10^{-3}$ M) and barium ($10^{-6}$-0.32 M) in solution were always below their solubility limit at the pH tested. The pH of barium and silver solutions was adjusted to the desired value by addition of HCl or NaOH, and $HNO_3$ or NaOH, respectively.

***3.2.3. Sample Preparation for Ion Probing with $Ba^{2+}$.*** Membrane coupons previously rinsed with nanopure water were immersed in 0.1 M $BaCl_2{\cdot}2H_2O$ solution at the pH of interest to saturate accessible $R–COO^-$ groups with $Ba^{2+}$. Then, to reduce excess $Ba^{2+}$ not associated to $R–COO^-$ groups to a concentration below the detection limit of our sample analysis procedure, the samples underwent four immersions in $10^{-6}$ M $BaCl_2{\cdot}2H_2O$ solution at the same pH used in the saturation step. Finally, the samples were dried by

pressing them between two filter-papers and air-dried at room temperature for ≥24 h. Each experimental pH condition was tested in triplicate. All membrane coupons used for $Ba^{2+}$-probing tests were cut from approximately the same location (FT30-L1) of the spiral-wound element.

***3.2.4. Sample Preparation for $Ag^{+}/Ba^{2+}$ Ion Exchange.*** Ion-exchange experiments in the pH range 7.5-10.3 were performed to study the displacement of $Ag^{+}$ by $Ba^{2+}$ from the $R–COO^{-}$ groups in the active layer of FT30 membrane. Sample preparation was similar to that for $Ba^{2+}$-probing tests with some modifications. After rinsing with nanopure water, the coupons were immersed in concentrated $AgNO_3$ solution at the target pH to saturate $R–COO^{-}$ groups with $Ag^{+}$. Next, exchange of $Ag^{+}$ by $Ba^{2+}$ was effected by sequential immersions in 0.32 M and 0.10 M $Ba(NO_3)_2$ solutions at the same target pH used in the $Ag^{+}$-saturation step. Then, to reduce excess ions not associated to $R–COO^{-}$ groups to a concentration several orders of magnitude below the detection limit of our sample analysis procedure, the samples underwent four immersions in $10^{-6}$ M $Ba(NO_3)_2$ solution at the same target pH of the previous steps. Coupons used as test samples were cut from four different locations (FT30-L2 through FT30-L5) of the spiral-wound element. Experiments were performed in triplicate at pH values of ~7.5 (FT30-L4 and FT30-L5), ~9.5 (FT30-L2 and FT30-L3), and ~10.3 (FT30-L5).

***3.2.5. Sample Analysis.*** RBS was used to quantify $Ba^{2+}$ and $Ag^{+}$ concentrations in the active layer of treated membrane samples. Extensive information on RBS theory and analysis [18, 20], and use in polymer and membrane characterization [6, 11 , 21] can be found elsewhere. In this study, immediately before sample analysis, the membrane coupons were attached to the sample holder of the RBS analysis chamber at room

temperature using a double-sided thermally conductive adhesive tape. Next, a circular, 3-mm, 2-MeV $He^+$ beam generated with a Van de Graaff accelerator was scanned over the surface of the membrane sample. Incident, exit and scattering angles of the $He^+$ beam were 22.5°, 52.5° and 150°, respectively. A detector registered the energy and counts of backscattered ions (see sample spectrum in Figure B.2 of Supporting Information). For a given incident ion, geometry of RBS setup, and energy of the incident beam, the energy of the backscattered ions reveals the elements present in the sample; the counts at each energy serve to obtain the relative concentrations of each element without the need of calibration standards [18, 20]. Only hydrogen cannot be detected directly by RBS, and so a theoretical hydrogen/carbon ratio of 0.67 was assumed [11]. The software SIMNRA® [18] was used for data analysis. For details on the calculation of ion-probe concentrations in the active layer, please see extended version of the Sample Analysis section in Supporting Information. Also, the carboxylic group concentrations in the active layer of the FT30 membrane presented in this study in Figure 3.2a were obtained using $\rho_{\text{active layer}}$ = 1.24 g/cm$^3$ [22] to improve the accuracy of the corresponding concentrations previously reported [14] where $\rho_{\text{active layer}}$ = 1.06 g/cm$^3$ was assumed. The newly calculated values are ~11% higher than those reported in [14]. See also extended version of the Sample Analysis section for details.

### 3.3. Results and Discussion

***3.3.1. Concentration of $Ba^{2+}$ Ion Associated with R–$COO^-$ Groups ([$Ba^{2+}$]).*** Figure 3.2a shows a comparison between the concentration of R–$COO^-$ groups ([R–$COO^-$]) in the polyamide active layer of FT30 RO membrane as a function of pH and the concentration

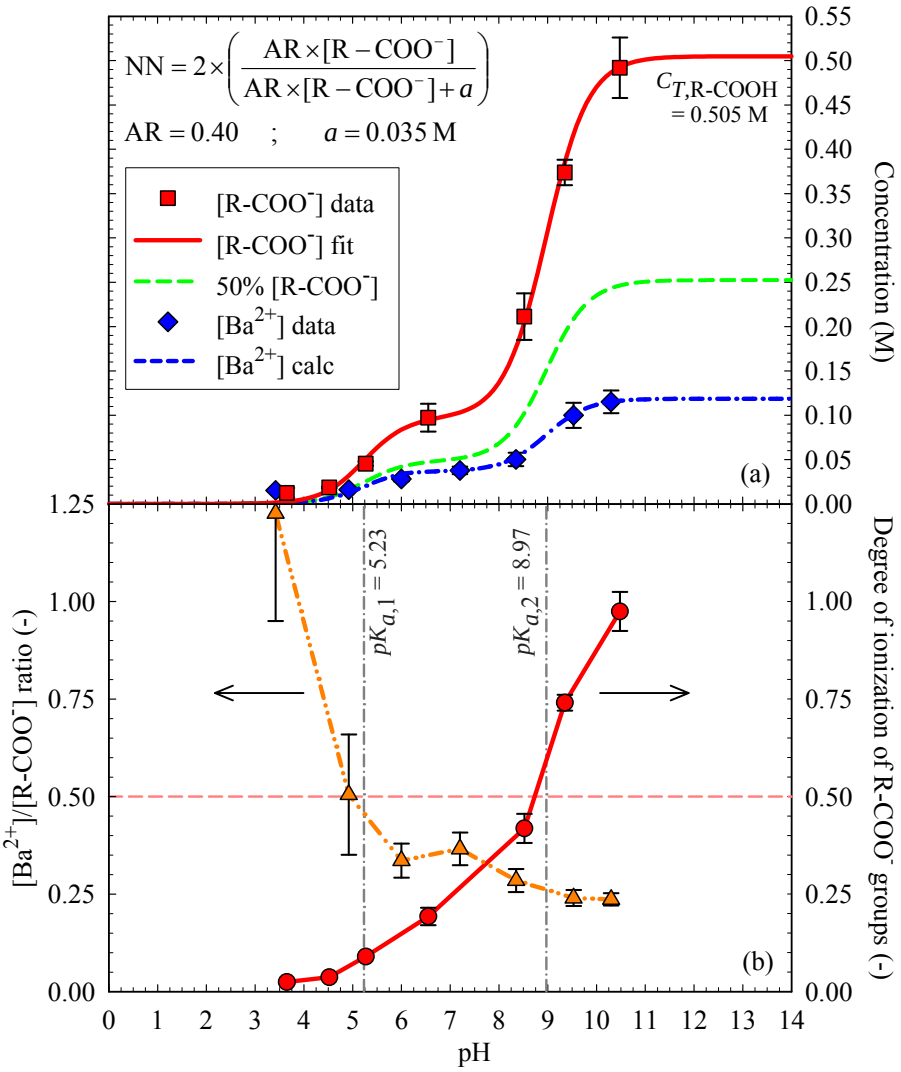


**Figure 3.2.** (a) Comparison between the total concentration of R–COO$^-$ groups ([R–COO$^-$]) in the polyamide active layer of the FT30 RO membrane as a function of pH and the concentration of barium ions that ionically associate with accessible R–COO$^-$ groups ([$Ba^{2+}$]). Error bars indicate standard deviation. The [R–COO$^-$] data points (red symbols), and corresponding model fit (continuous red curve) for the acid-base equilibrium between R–COO$^-$ groups and the aqueous solution, were obtained by using $\rho_{\text{active layer}}$ = 1.24 g/cm$^3$ [22] to improve the accuracy of the [R–COO$^-$] values previously calculated in [14] where $\rho_{\text{active layer}}$ = 1.06 g/cm$^3$ was assumed (see extended version of the Sample Analysis section in Supporting Information for details). The (blue) dashed-dotted line corresponds to the calculated [$Ba^{2+}$] as a function of pH using Equation 3.3. (b) [$Ba^{2+}$]/[R–COO$^-$] ratio as a function of pH (orange triangles) and degree of ionization of R–COO$^-$ groups (red circles). The (orange) dash-dot-dot and (red) continuous lines correspond to straight lines connecting the experimental data points. Error bars indicate standard error. The horizontal (pink) dashed line represents the minimum possible [$Ba^{2+}$]/[R–COO$^-$] ratio of 0.5 if 100% of the R–COO$^-$ groups were accessible to $Ba^{2+}$ ions.

of $Ba^{2+}$ that associates with them ($[Ba^{2+}]$). Experimental $[R–COO^-]$ concentrations (red squares) and corresponding fit line (continuous red curve) from our modeling results based on acid-base equilibrium between $R–COO^-$ groups and aqueous solution correspond to the values reported in our previous work [14] corrected using $\rho_{\text{active layer}} = 1.24$ g/cm$^3$ as detailed above. $[Ba^{2+}]$ (blue diamonds) was measured as part of the present study through ion-probing/RBS analysis. The figure shows that $[Ba^{2+}]$ was consistently lower than $[R–COO^-]$ and the (green) dashed line representing 50% of the concentration of $R–COO^-$ groups. Consequently, the $[Ba^{2+}]$ results could not be explained based solely on the assumption that, because of their divalence, each $Ba^{2+}$ ion neutralizes two $R–COO^-$ groups simultaneously.

To evaluate the possible causes for the difference between $[R–COO^-]$ and $[Ba^{2+}]$, we used the information from Figure 3.2a to calculate the $[Ba^{2+}]/[R–COO^-]$ ratio (orange triangles) as a function of pH, and plotted it in Figure 3.2b together with the degree of ionization of carboxylic groups, i.e., $[R–COO^-]/([R–COOH]+[R–COO^-])$ (red circles). The two vertical dashed-dotted lines correspond to the two p$K_a$ values that describe the ionization behavior of carboxylic groups in the active layer of FT30 membrane [14]. Figure 3.2b shows that at the lowest experimental pH=3.42, the $[Ba^{2+}]/[R–COO^-]$ ratio was not significantly different from one, which suggests that all $R–COO^-$ groups were accessible to $Ba^{2+}$, and that there was a one-to-one correspondence between *monovalent* $R–COO^-$ groups and *divalent* $Ba^{2+}$ ions (see locations (a) and (b) in Figure 3.1). Such one-to-one correspondence is consistent with the relatively low concentration (≈0.01 M) of $R–COO^-$ groups at pH=3.42. Assuming a homogeneous distribution of $R–COO^-$ groups throughout the polyamide matrix, the average distance between neighboring

ionized sites would be ≈5.5 nm making it relatively unlikely for one $Ba^{2+}$ ion to neutralize two R–$COO^-$ groups. We also estimated the average separation between R–$COO^-$ groups at a concentration of 0.50 M (i.e., the total concentration of ionizable carboxylic groups in FT30 membrane). Under the same assumption of R–$COO^-$ groups homogeneously distributed, the average distance between neighboring ionized sites would decrease to ≈1.5 nm, therefore increasing the probability of the existence of $Ba^{2+}$ ions neutralizing two R–$COO^-$ sites simultaneously (see location (c) in Figure 3.1).

Consistent with the discussion above, we expect the *average* distance between neighboring ionized sites in FT30 membrane to decrease with increasing pH (i.e., with increasing concentration of R–$COO^-$ groups), and the *average* number of R–$COO^-$ groups neutralized per $Ba^{2+}$ ion to *gradually* increase from one to two. Consequently, even though the difference between [R–$COO^-$] and [$Ba^{2+}$] in Figure 3.2a could not be explained based only on the divalence of $Ba^{2+}$, we propose that the divalence does play a role in the observed difference with a stronger effect as pH increases. Accordingly, defining the *neutralization number* (NN) for $Ba^{2+}$ at a certain solution pH as the average number of R–$COO^-$ groups neutralized per $Ba^{2+}$ ion, and assuming that $Ba^{2+}$ has access to 100% of the ionized sites in the active layer, then [$Ba^{2+}$] could be expressed by Equation 3.1.

$$[Ba^{2+}] = \frac{[R - COO^-]}{NN} \tag{3.1}$$

To evaluate the assumption of 100% accessibility of $Ba^{2+}$ to R–$COO^-$ groups, we drew a (pink) dashed line in Figure 3.2b corresponding to the theoretical minimum [$Ba^{2+}$]/[R–

$COO^-$]=0.5 ratio if $Ba^{2+}$ had access to all R–$COO^-$ groups; for 100% accessibility, all R–$COO^-$ groups would be neutralized by $Ba^{2+}$ and each $Ba^{2+}$ ion would neutralize at most two ionized sites. Figure 3.2b shows that the experimental [$Ba^{2+}$]/[R–$COO^-$] ratio was lower than the theoretical minimum value of 0.5 at all but the two lowest experimental pH values, and that there was a rapid decrease of the [$Ba^{2+}$]/[R–$COO^-$] ratio from ≈1 to less than 0.5 in the pH range 3.42-6.00. Accordingly, the results suggest that the accessibility of $Ba^{2+}$ to R–$COO^-$ groups decreased in the initial ionization stages, and that only the carboxylic groups ionizable at the lowest experimental pH=3.42 were 100% accessible to $Ba^{2+}$. Figure 3.2b also shows that the R–$COO^-$ groups ionized at pH=3.42 are only ≈2.5% of all ionizable carboxylic groups detected.

The general upper limits of the p$K_a$ values of monobasic and polybasic carboxylic groups in bulk water at 25°C are ≈5.0 and ≈6.4, respectively [23]. As a result, the relatively low pH of ionization of the carboxylic groups deprotonated at pH=3.42 suggests that they are exposed to bulk aqueous solution, and that they might be located in the vicinity of the open ridge-and-valley structure [1, 2] at the surface of the polyamide active layer (see bottom-left schematic of Figure 3.1).

As mentioned above, Figure 3.2b shows that the [$Ba^{2+}$]/[R–$COO^-$] ratio was below 0.5 at pH≥6. This indicates that in most of the pH range studied a fraction of the ionized R–$COO^-$ groups was inaccessible to $Ba^{2+}$ ($r_{Ba^{2+}}$=1.49-1.75 Å [17]) but accessible to the smaller $Ag^+$ ($r_{Ag^+}$=0.81-1.42 Å [17]). Such observation suggests that $Ba^{2+}$ ions experience steric effects in the active layer (see location (d) in Figure 3.1) that prevent their access to a fraction of the R–$COO^-$ groups (see location (e) in Figure 3.1). Since

hindered accessibility was observed in most of the pH range studied, we conclude that most of the carboxylic groups in the active layer are located in the bulk of the polyamide matrix where steric effects are important for $Ba^{2+}$ ion. Counterion exclusion by steric effects has also been reported to occur in ion-exchange resins and zeolites [24]. As counterion size increases, ion-exchange materials may show an apparent reduction in ion-exchange capacity indicating the occurrence of steric effects that limit counterion accessibility to functional groups [24].

We used the concept of hindered accessibility of $Ba^{2+}$ to carboxylic groups to modify Equation 3.1 by defining the *accessibility ratio* (AR) for $Ba^{2+}$ as the fraction of $R–COO^-$ groups accessible to $Ba^{2+}$ ion. Accordingly, $[Ba^{2+}]$ is expressed by Equation 3.2, where the product $AR \times [R–COO^-]$ represents the concentration of $R–COO^-$ groups accessible to $Ba^{2+}$ at a given solution pH. Equation 3.2 suggests that the concentration of $Ba^{2+}$ that associates with the *accessible* $R–COO^-$ groups at a certain solution pH may be predicted based on the total concentration of $R–COO^-$ groups, and the NN and AR parameters at the same pH. The following sections address the experimental determination of NN and AR.

$$[Ba^{2+}] = \frac{AR \times [R - COO^-]}{NN} \qquad (3.2)$$

***3.3.2. Experimental Determination of the Neutralization Number (NN) for $Ba^{2+}$.*** The dependence of NN (i.e., the average number of $R–COO^-$ groups neutralized per $Ba^{2+}$ ion) on the concentration of sites neutralized by $Ba^{2+}$ was studied by performing $Ag^+$-$Ba^{2+}$ ion-exchange experiments at various solution pH conditions (see Table 3.1 and Figure

**Table 3.1.** Experimental results for $Ag^+$-$Ba^{2+}$ ion-exchange experiments and corresponding values for neutralization number (NN), coefficient *a*, and accessibility ratio (AR) in the polyamide active layer of the FT30 RO membrane.

| **Col.1** | **Col.2** | **Col.3** | **Col.4** | **Col.5= Col.2-Col.3** | **Col.6 = Col.5/Col.4** | **Col.7 = 2*Col.4 – Col.5** | **Col.8**[d] | **Col.9** | **Col.10** |
|---|---|---|---|---|---|---|---|---|---|
| Exp. ($pH_1$[a]) | $Ag^+$ before IX[b] [M] | $Ag^+$ after IX[b] [M] | $Ba^{2+}$ after IX[b] [M] | $Ag^+$ displaced by $Ba^{2+}$ [M] | NN [-] | *a*[c] [M] | AR[d] [-] | $pH_2$[e] | Location in SWE[f] |
| 1 (9.51) | 0.271 | 0.163 | 0.071 | 0.108 | 1.511 | 0.035 | 0.40 | 9.53 | FT30-L2 |
| 2 (9.48) | 0.239 | 0.102 | 0.085 | 0.137 | 1.614 | 0.033 | 0.40 | 9.53 | FT30-L3 |
| 3 (7.58) | 0.115 | 0.058 | 0.046 | 0.057 | 1.236 | 0.035 | 0.39 | 7.20 | FT30-L4 |
| 4 (7.50) | 0.121 | 0.058 | 0.049 | 0.063 | 1.282 | 0.035 | 0.39 | 7.20 | FT30-L5 |
| 5 (10.26) | 0. 409 | 0.270 | 0.087 | 0.139 | 1.598 | 0.035 | 0.40 | 10.30 | FT30-L5 |
| 1-5[g] (7.50-10.26) | - | - | - | - | - | 0.035 | 0.40 | 4.92–10.30 | FT30-L2–FT30-L5 |

Notes for Table 3.1:
[a] $pH_1$ = pH of the ion-exchange experiment. [b] IX = ion exchange. [c] *a* equals the *x* and *y* values at the intercept between the lines of slope one and two in Figure 3.3a, also equivalent to the concentration of sites neutralized by $Ba^{2+}$, i.e., coordinate in Figure 3.3b, at which NN departs from unity. [d] Calculated using Equations 3.2 and 3.3, Col.7, and the [R–$COO^-$] and [$Ba^{2+}$] information in Figure 3.2a at the pH indicated in Col.9. [e] $pH_2$ = pH of the $Ba^{2+}$-probing experiment from which the [$Ba^{2+}$] value used to calculate AR in Col.8 was obtained. [f] SWE = Spiral-wound element; Col.10 indicates different locations within the SWE from which the membrane samples used in the corresponding ion-exchange experiment were taken (see also Materials and Methods section). [g] Coefficient *a* obtained through the linear fit of the data from Exps. 1-5 in Figure 3.3a. AR was calculated as the average of the AR values obtained for each of the pH conditions at which [$Ba^{2+}$] was measured in Figure 3.2a (see Figure 3.4), except for pH = 3.42 at which AR = 1 (see Figure 3.2b and corresponding discussion).

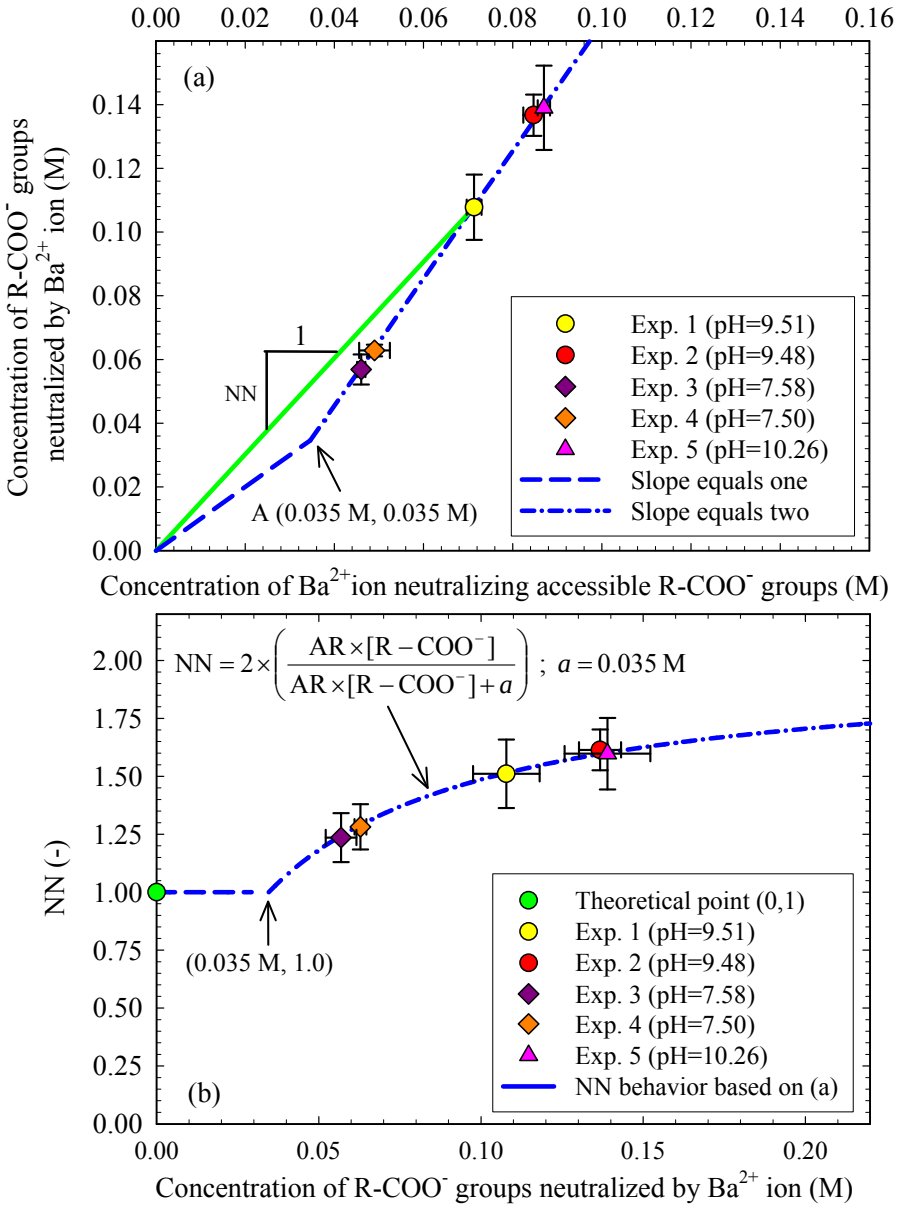


**Figure 3.3.** Stoichiometry of the association between R–COO$^-$ groups neutralized by $Ba^{2+}$ ion in the polyamide active layer of the FT30 RO membrane and the $Ba^{2+}$ ions neutralizing them. (a) Limiting one-to-one (blue dashed line) and two-to-one (blue dashed-dotted line) correspondence between accessible R–COO$^-$ groups and $Ba^{2+}$ ion. The symbols are the experimental ion-exchange data presented in Table 3.1. The neutralization number (NN) for any given point is calculated as the corresponding *y/x* ratio as illustrated by the continuous (green) line for Experiment 1. (b) Behavior of the neutralization number for $Ba^{2+}$ ion (NN) as a function of the concentration of R–COO$^-$ sites that it neutralizes. Symbols are the NN values of the five experimental sets from (a)–see also Table 3.1. The (blue) dashed and dashed-dotted lines are the NN values of the points that belong to the (blue) dashed and dashed-dotted lines in (a). Error bars indicate standard error.

3.3). The concentrations of $Ag^+$ in the active layer before (Col.2) and after (Col.3) exchange, and the concentration of $Ba^{2+}$ in the active layer after exchange (Col.4) were determined by RBS. The calculated drop in $Ag^+$ concentration in the active layer (Col.5) corresponds to the concentration of $Ag^+$ displaced by $Ba^{2+}$, and therefore to the concentration of R–$COO^-$ sites neutralized by $Ba^{2+}$ ($y$-axis in Figure 3.3a). The concentration of $Ba^{2+}$ neutralizing those sites ($x$-axis in Figure 3.3a) is given by the $Ba^{2+}$ concentration after exchange (Col.4).

Figure 3.3a shows that all experimental points obtained through the ion-exchange experiments lie on a straight (blue dashed-dotted) line with a slope of ≈2 (best fit $y$=2.032$x$-0.037). The slope of two indicates that as the degree of ionization of R–$COO^-$ groups increases in the concentration range of ionized sites at which the experiments were performed, every two additional sites that ionize are neutralized by one $Ba^{2+}$ ion (slope=$\Delta y/\Delta x \approx 2/1 \approx 2$). The ($x$,$y$) coordinates of each of the experimental points in Figure 3.3a were used to obtain the corresponding neutralization numbers (NN=$y/x$) which are presented as symbols in Figure 3.3b; the experimental NN values lie between one and two, the theoretical lower and upper limits, respectively, of NN.

Even though we were not able to obtain ion-exchange data at lower concentrations in Figure 3.3 due to the inability of our sample analysis procedure to accurately differentiate the $Ag^+$ and $Ba^{2+}$ signals at these lower concentrations, the occurrence of a one-to-one stoichiometry (NN=1) at the lower concentration limit in Figure 3.3 is confirmed by the ion-probing results in Figure 3.2 showing that [R–$COO^-$] and [$Ba^{2+}$] are approximately equal (≈0.01 M) at pH=3.42.

Accordingly, as the degree of ionization increases at these relatively low concentrations of R–$COO^-$ groups in Figure 3.3a, every two additional sites that ionize are neutralized by two $Ba^{2+}$ ions resulting in a (blue) dashed line with slope of one (slope=$\Delta y/\Delta x \approx 2/2 \approx 1$). The corresponding NN=$y/x$=1 representing the one-to-one stoichiometry of association between accessible R–$COO^-$ groups and $Ba^{2+}$ ions is depicted by the (blue) dashed line in Figure 3.3b.

Equation 3.2 and the equations of the two limiting linear behaviors depicted in Figure 3.3a for the stoichiometry of association between additional accessible carboxylic groups that ionize and the $Ba^{2+}$ ions that neutralize them, i.e., $\Delta y / \Delta x = 1 \rightarrow y = x$ and $\Delta y / \Delta x = 2 \rightarrow y = 2x - a$, were used to obtain Equation 3.3 describing the behavior of NN=$y/x$ as a function of the concentration of sites neutralized by $Ba^{2+}$ ion (AR×[R–$COO^-$]). The parameter $a$ in Equation 3.3 represents the concentration of accessible R–$COO^-$ groups at which the stoichiometry of association between the additional sites that ionize and the $Ba^{2+}$ ions that neutralize them (i.e., $\Delta y/\Delta x$) changes from one-to-one to two-to-one (see point A in Figure 3.3a); $a$ is also equal to the maximum concentration of accessible ionized sites at which NN=1 (see Figure 3.3b). The parameter $a$ is a set value for the specific membrane-counterion system studied and does not depend on pH. We note that the magnitude of $a$=0.035 M for the FT30 membrane-$Ba^{2+}$ system is higher than 0.01 M at which the ion-probing data shows that a one-to-one stoichiometry still occurs. Equation 3.3 is valid when AR×[R–$COO^-$]>$a$, otherwise NN=1.

$$\mathrm{NN} = 2 \times \left( \frac{\mathrm{AR} \times [\mathrm{R-COO^-}]}{\mathrm{AR} \times [\mathrm{R-COO^-}] + a} \right) \tag{3.3}$$

Col.2 in Table 3.1 reveals the occurrence of variability in the concentration of R–$COO^-$ groups at different locations of the spiral-wound element. R–$COO^-$ concentrations for locations FT30-L2 through FT30-L5 were 60-110% of those in location FT30-L1 at the corresponding solution pH (see Figure 3.2a). It is important to notice, however, that the variability in the concentration of R–$COO^-$ groups for different locations in the spiral-wound element at a given pH does not antagonize the purpose of Figure 3.3. The purpose of Figure 3.3 is *not* to provide ion-exchange capacity information, but information on the stoichiometry of the association between neutralized R–$COO^-$ groups and $Ba^{2+}$ ions as a function of the concentration of the former regardless of the pH at which any given concentration occurs.

***3.3.3. Experimental Determination of the Accessibility Ratio (AR) for $Ba^{2+}$.*** From the analysis above of Figure 3.2, we concluded that ≈100% of the carboxylic groups ionized at pH=3.42 were accessible to $Ba^{2+}$ ion (AR=1), and that this was not the case at the other pH conditions investigated. For the experimental pH values of 4.92 and above, we calculated the corresponding AR values using Equations 3.2 and 3.3 with $a$=0.035 M, and the corresponding experimental [$Ba^{2+}$] and [R–$COO^-$] values at each pH from Figure 3.2a. The results, shown in Figure 3.4, reveal that the accessibility ratio is approximately constant at AR=0.40 in the pH range 4.92-10.30, indicating that only ≈40% of the ionizable carboxylic groups in the active layer of FT30 membrane are accessible to $Ba^{2+}$. The inaccessible R–$COO^-$ groups would therefore be located in regions of the active layer accessible only through pores smaller than $Ba^{2+}$ ion, or of such a size and geometry that a 'two-way traffic' of incoming $Ba^{2+}$ ions and out coming protons ($H^+$) is not possible as it has been proposed to occur in other ion-exchange systems [24].

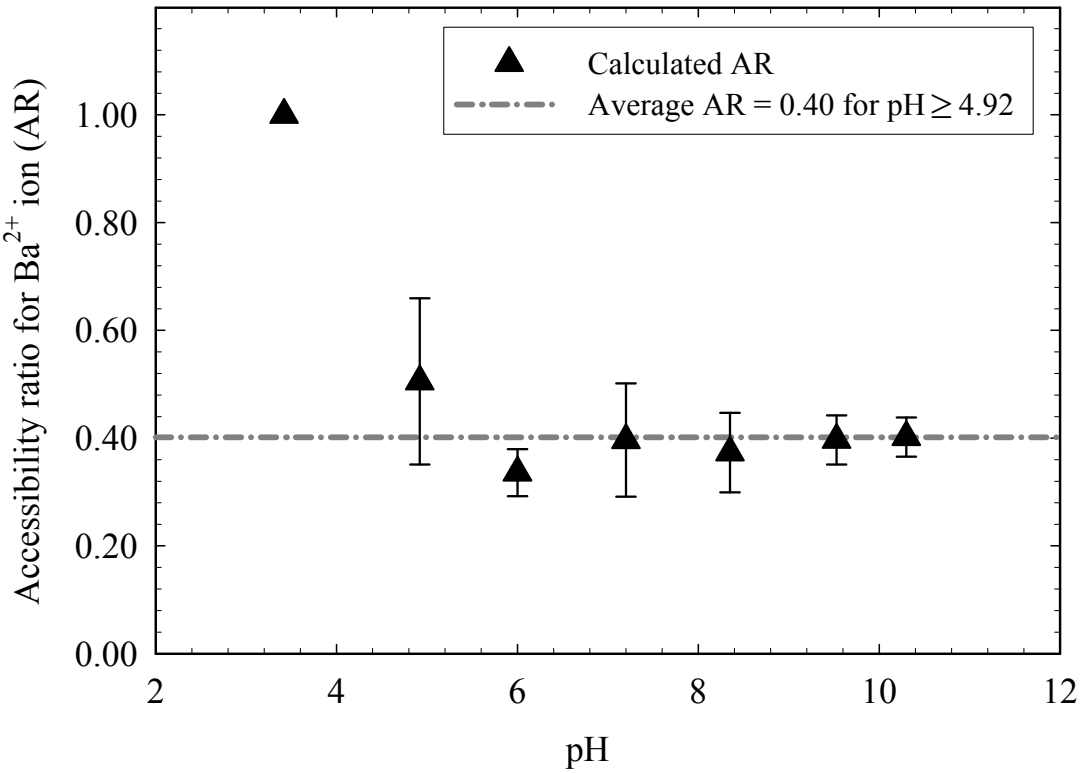


**Figure 3.4.** Accessibility ratio for $Ba^{2+}$ ion (AR) in the polyamide active layer of the FT30 RO membrane. Symbols are the values obtained by solving Equations 3.2 and 3.3 simultaneously using the [R–$COO^-$] and [$Ba^{2+}$] information in Figure 3.2a, and $a$ = 0.035 M from Figure 3.3b, where $a$ is the concentration of sites neutralized by $Ba^{2+}$ at which the neutralization number (NN) for $Ba^{2+}$ departs from unity. AR was calculated for the pH values at which [$Ba^{2+}$] was determined experimentally (see Figure 3.2a), except pH = 3.42 at which AR = 1 (see Figure 3.2b and corresponding discussion). Error bars indicate standard error. The dashed-dotted line is the average AR = 0.40 value in the pH range 4.92-10.30.

The existence of a pore size distribution in the active layer of FT30 membrane [8] is one of the factors that possibly determines the broad pH range of ionization of its R–$COO^-$ groups [14, 25] as a result of the decreasing dielectric constant of water with decreasing size of the nanopores where it is confined [4, 26, 27], and the increasing p$K_a$ value of carboxylic groups with decreasing dielectric constant of the surrounding medium [28]. Accordingly, the broad pH range of ionization of R–$COO^-$ groups (see Figure 3.2a)

suggests that R–$COO^-$ groups are distributed in pores of different sizes. The constant accessibility ratio AR=0.40 for the relatively broad experimental pH range of 4.92-10.30 therefore suggests that there is interconnectivity between pores of different sizes in the active layer. Even if carboxylic groups with different p$K_a$ values are likely located in pores of different sizes, the interconnectivity between pores makes all ionized sites approximately equally accessible (or inaccessible) to $Ba^{2+}$. Additionally, even if carboxylic groups are located in the larger pores ( $r_{\text{Larger Pore}}$ =3.5-4.1 Å [8]) which are bigger than $Ba^{2+}$ ( $r_{Ba^{2+}}$ =1.49-1.75 Å [17]), the pore may be accessible only through the smaller pores due to pore interconnectivity, which would make the functional groups located in the larger pore effectively inaccessible to $Ba^{2+}$ (see location (e) in Figure 3.1).

We used Equations 3.2 and 3.3 to calculate the concentration of $Ba^{2+}$ associated with R–$COO^-$ groups as a function of pH using as input the experimentally determined parameter $a$=0.035 M, the constant accessibility ratio AR=0.40, and the total concentration of R–$COO^-$ groups at each corresponding pH. The results, shown as a (blue) dashed-dotted line in Figure 3.2a, are in close agreement with the experimental data. We point out that the two constant parameters $a$=0.035 M and AR=0.40 describe the difference between [$Ba^{2+}$] and [R–$COO^-$] *as a function of pH* without recourse to any other parameters (e.g., a change in acid dissociation constants). Accordingly, the agreement between the calculated [$Ba^{2+}$] and the experimental data suggests that the difference between [$Ba^{2+}$] and [R–$COO^-$] is indeed primarily the result of steric and charge effects on $Ba^{2+}$ ion.

***3.3.4. Prediction of [$Ba^{2+}$].*** We have demonstrated that we can describe the stoichiometry of association between R–$COO^-$ groups and $Ba^{2+}$ as two limiting lines with

slopes of one ($y=x$) and two ($y=2x-a$) in a plot of the concentration of ionized sites neutralized by $Ba^{2+}$ as a function of the concentration of $Ba^{2+}$ neutralizing those sites (see Figure 3.3a). Such realization indicates that it is possible to obtain a good estimate of the parameter *a* from any ion-exchange experiment whose data point lies on the line of slope of two. Additionally, the demonstrated constant accessibility ratio in the pH range 4.92-10.30 reveals that we can use the estimated *a* value to determine AR (see Col.8 in Table 3.1) by plugging in Equations 3.2 and 3.3 [$R–COO^-$] and [$Ba^{2+}$] values at any *one* pH condition. Any of the resulting pairs of *a* and AR values (see Table 3.1) obtained through $Ba^{2+}$-probing and ion-exchange experiments *at one pH* can then be used with Equations 3.2 and 3.3 and the [$R–COO^-$] data in Figure 3.2a to *predict* [$Ba^{2+}$] *as a function of pH*. The results (presented in Figure B.3 in the Supporting Information) are in very close agreement with the (blue) dashed-dotted line of Figure 3.2b.

The methods developed in the present study and our previous work [14] provide tools for the *quantitative* study of the effects that functional groups in the active layer of RO/NF membranes and their interaction with ionic contaminants have on membrane performance. For example, our procedures can be used to study the effect that the concentration of functional groups in active layers has on water flux and/or ion rejection. Also, using the AR parameter as a metric of the steric effects that ionic contaminants experience in active layers, the effects of steric hindrance on ion rejection can be studied. Such studies will contribute to build a more complete understanding of the mechanisms of contaminant transport through active layers and guide the development of improved RO/NF membranes.

### 3.4. Acknowledgments

RBS analyses were carried out in the Center for Microanalysis of Materials, University of Illinois, partially supported by the U.S. Department of Energy under grant DEFG02-91-ER45439. The authors acknowledge Doug Jeffers for assistance in RBS analyses, and Tasuma Suzuki for helpful discussion. This work was supported by the National Science Foundation Environmental Engineering and Technology program under agreement number BES-0332217, and the WaterCAMPWS, a Science and Technology Center of Advanced Materials for the Purification of Water with Systems under agreement number CTS-0120978. The opinions in this paper do not necessarily reflect those of the sponsor.

### 3.5. Supporting Information Available

Materials and Methods (Extended version); Figure B.1 (Effect of the anion of the barium salt on the concentration of $Ba^{2+}$ that associates with R–$COO^-$ groups in the active layer of FT30 RO membrane); Figure B.2 (Example of a spectrum obtained from the RBS analysis of an FT30 RO membrane sample probed with $Ba^{2+}$ ion at pH=10.3); and Figure B.3 (Comparison between the prediction of [$Ba^{2+}$] as a function of pH using the six different sets of *a* and AR values shown in Table 3.1). This information is available free of charge via the Internet at http://pubs.acs.org, and in Appendix B.1.

### 3.6. References

1. Petersen, R. J., Composite reverse osmosis and nanofiltration membranes. *J. Mem. Sci.* **1993,** *83*, 81-150.

2. Tang, C. Y.; Kwon, Y.-N.; Leckie, J. O., Probing the nano- and micro-scales of reverse osmosis membranes-A comprehensive characterization of physiochemical properties of uncoated and coated membranes by XPS, TEM, ATR-FTIR, and streaming potential measurements. *J. Mem. Sci.* **2007,** *287*, 146-156.

3. Bellona, C.; Drewes, J. E.; Xu, P.; Amy, G., Factors affecting the rejection of organic solutes during NF/RO treatment-a literature review. *Water Res.* **2004,** *38*, 2795-2809.

4. Szymczyk, A.; Fievet, P., Investigating transport properties of nanofiltration membranes by means of a steric, electric and dielectric exclusion model. *J. Mem. Sci.* **2005**, (252), 77-88.

5. Childress, A. E.; Elimelech, M., Relating nanofiltration membrane performance to membrane charge (electrokinetic) characteristics. *Environ. Sci. Technol.* **2000,** *34*, 3710-3716.

6. Bartels, C. R., A surface science investigation of composite membranes. *J. Mem. Sci.* **1989,** *45*, 225-245.

7. Shimazu, A.; Ikeda, K.; Miyazaki, T.; Ito, Y., Application of positron annihilation technique to reverse osmosis membrane materials. *Radiat. Phys. Chem.* **2000,** *58*, 555-561.

8. Kim, S. H.; Kwak, S.-Y.; Suzuki, T., Positron annihilation spectroscopic evidence to demonstrate the flux-enhancement mechanism in morphology-controlled thin-film-composite (TFC) membrane. *Environ. Sci. Technol.* **2005,** *39*, 1764-1770.

9. Boussu, K.; De Baerdemaeker, J.; Dauwe, C.; Weber, M.; Lynn, K. G.; Depla, D.; Aldea, S.; Vankelecom, I. F. J.; Vandecasteele, C.; Van der Bruggen, B., Physico-

chemical characterization of nanofiltration membranes. *Chem. Phys. Chem.* **2007,** *8*, 370-379.

10. Ben-David, A.; Bason, S.; Jopp, J.; Oren, Y.; Freger, V., Partitioning of organic solutes between water and polyamide layer of RO and NF membranes: Correlation to rejection. *J. Mem. Sci.* **2006,** *281*, 480-490.

11. Mi, B.; Coronell, O.; Mariñas, B. J.; Watanabe, F.; Cahill, D. G.; Petrov, I., Physico-chemical characterization of NF/RO membrane active layers by Rutherford backscattering spectrometry. *J. Mem. Sci.* **2006,** *282*, 71-81.

12. Mi, B.; Mariñas, B. J.; Cahill, D. G., RBS characterization of arsenic (III) partitioning from aqueous phase into the active layers of thin-film composite NF/RO membranes. *Environ. Sci. Technol.* **2007,** *41*, 3290-3295.

13. Zhang, X.; Cahill, D. G.; Coronell, O.; Mariñas, B. J., Partitioning of salt ions in FT30 reverse osmosis membranes. *Appl. Phys. Lett.* **2007,** *91*, 181904.

14. Coronell, O.; Mariñas, B. J.; Zhang, X.; Cahill, D. G., Quantification of functional groups and modeling of their ionization behavior in the active layer of FT30 reverse osmosis membrane. *Environ. Sci. Technol.* **2008,** *42*, 5260-5266.

15. Freger, V., Nanoscale heterogeneity of polyamide membranes formed by interfacial polymerization. *Langmuir* **2003,** *19*, 4791-4797.

16. Afonso, M. D.; Hagmeyer, G.; Gimbel, R., Streaming potential measurements to assess the variation of nanofiltration membranes surface charge with the concentration of salt solutions. *Sep. Purif. Technol.* **2001,** *22-23*, 529-541.

17. Shannon, R. D., Revised effective ionic radii and systematic studies of interatomic distances in halides and chalcogenides. *Acta Cryst.* **1976,** *A32*, 751-767.

18. Mayer, M.; Duggan, J. L.; Morgan, I. L. In *SIMNRA, a simulation program for the analysis of NRA, RBS and ERDA*, Proceedings of the 15th International Conference on the Application of Accelerators in Research and Industry, Denton, TX, 1998; Denton, TX, 1998; p 541.

19. IUPAC *Stability constants database*, Academic Software: Yorks, UK, 2001.

20. Chu, W.-K.; Mayer, J. W.; Nicolet, M. A., *Backscattering Spectrometry*. Academic Press: New York, NY, 1978.

21. Mi, B.; Cahill, D. G.; Mariñas, B. J., Physico-chemical integrity of nanofiltration/reverse osmosis membranes during characterization by Rutherford backscattering spectrometry. *J. Mem. Sci.* **2007,** *291*, 77-85.

22. Zhang, X.; Cahill, D. G.; Coronell, O.; Mariñas, B. J., Absorption of water in the active layer of reverse osmosis membranes. *J. Mem. Sci.* **2009,** *331*, 143-151.

23. Albert, A.; Serjeant, E. P., *The determination of ionization constants*. Third ed.; Chapman and Hall: London, Great Britain, 1984.

24. Helfferich, F., *Ion exchange.* McGraw-Hill: New York, 1962.

25. Wamser, C. C.; Gilbert, M. I., Detection of surface functional group asymmetry in interfacially-polymerized films by contact angle titrations. *Langmuir* **1992,** *8*, 1608-1614.

26. Senapati, S.; Chandra, A., Dielectric constant of water confined in a nanocavity. *J. Phys. Chem. B* **2001,** *105*, 5106-5109.

27. Szymczyk, A.; Sbaï, M.; Fievet, P.; Vidonne, A., Transport properties and electrokinetic characterization of an amphoteric nanofilter. *Langmuir* **2006,** *22*, 3910-3919.

28. Bacarella, A. L.; Grunwald, E.; Marshall, H. P.; Lee Purlee, E., The potentiometric measurements of acid dissociation constants and *p*H in the system methanol-water. $pK_A$ values for carboxylic acids and anilinium ions. *J. Org. Chem.* **1955,** *20*, 747-762.

# CHAPTER 4

# IONIZATION BEHAVIOR, STOICHIOMETRY OF ASSOCIATION AND ACCESSIBILITY OF FUNCTIONAL GROUPS IN THE ACTIVE LAYERS OF REVERSE OSMOSIS AND NANOFILTRATION MEMBRANES

**Abstract:** We characterized the polyamide (PA) active layers of six commercial reverse osmosis (RO) and nanofiltration (NF) membranes and found that in contrast to their similar elemental composition, thickness, total concentration of functional groups, and degree of polymerization, the ionization behavior and spatial distribution of carboxylic (R–COOH) groups within the active layers can be significantly different. We also assessed the steric effects experienced by barium ion ($Ba^{2+}$) in the active layers by determining the fraction AR of carboxylate ($R–COO^-$) groups accessible to $Ba^{2+}$. AR was found to vary within the range AR=0.40–0.81, and to be generally independent of external solution pH. Additionally, we studied an NF membrane with a sulfonated polyethersulfone (SPES) active layer, and found that the concentration of sulfonate ($R–SO_3^-$) groups in the active layer was 1.67 M, a value that was independent of external solution pH and approximately three times higher than the maximum concentration (≈0.45±0.25 M) of carboxylate ($R–COO^-$) groups in PA active layers. The $R–SO_3^-$ groups were also found to be nearly completely accessible to $Ba^{2+}$ (AR=0.95±0.01).

**Key Words:** accessibility ratio, amine groups, carboxylate groups, nanofiltration, neutralization number, polyamide, reverse osmosis, Rutherford backscattering spectrometry, steric effects, sulfonate groups, sulfonated polyethersulfone

## 4.1. Introduction

Reverse osmosis (RO) and nanofiltration (NF) membrane processes are increasingly attractive technologies for water treatment applications because they provide effective control against a broad range of contaminants. Even though the structure of most RO/NF membranes consists of a top ultra-thin active layer (~50–200 nm) usually made of polyamide (PA), an intermediate asymmetric polysulfone porous support, and a polyester backing [1], membrane performance is mostly controlled by the interaction of water and contaminants with the active layer [1-3]. As a result, a detailed understanding of the relation between active layer physico-chemical properties and the permeation of water and solutes would enable the systematic optimization of RO/NF membranes for custom applications.

Unfortunately, despite decades of research efforts, it is currently not possible to directly relate the physico-chemical properties of active layers to RO/NF membrane performance, partly because of the limited amount of quantitative data available about key properties of the inner region of active layers and its interaction with water and contaminants. While experimental studies of the surface of active layers are abundant in the literature [4-8], the number of studies of the inner region of active layers are more limited [9]. Such disparity is due to limitations associated with the nanometer-scale spatial resolution required to characterize the ultra-thin (~100 nm) active layers as they cannot be detached from their significantly thicker (~50 μm) polysulfone supports without chemical treatment. Among the several properties and interactions with water and contaminants in the inner region of active layers that have been experimentally studied [9], only few (e.g.,

pore size distribution [10] and elemental composition [11]) have been characterized quantitatively in several commercial RO/NF membranes. As a result, there is a need in the literature to gather more data on the properties of the inner region of active layers, and their interaction with contaminants, to build a better understanding of what differentiates one RO/NF membrane from another.

Active layer properties affecting membrane performance include the concentration of ionizable functional groups and their interaction with ionic contaminants. Ionizable functional groups affect the permeation of water and solutes not only because they produce pH-dependent charges in the active layer [1, 5], but also because they are directly related to the active layer structure [12, 13]. Most notably, in PA active layers ionizable functional groups are related to the degree of polymer crosslinking [1, 12] because each carboxylic (R–COOH) and amine ($R–NH_2$) group in the PA structure corresponds to an amide link not formed during the PA polymerization reaction [1].

Accordingly, the objective of this study is to investigate various properties related to ionizable functional groups in the active layers of five RO/NF membranes with fully-aromatic PA active layers, and an NF membrane with a sulfonated polyethersulfone (SPES) active layer. Properties studied include: (i) concentration of functional groups and their ionization behavior as a function of pH; (ii) degree of polymer crosslinking; (iii) stoichiometry of association between negative functional groups and $Ba^{2+}$ ion; and (iv) steric effects experienced by $Ba^{2+}$. The findings from this study provide valuable information towards advancing the understanding of the mechanisms that control transport phenomena in RO/NF membranes.

## 4.2. Materials and Methods

***4.2.1. Target Membranes.*** Six commercial RO/NF membranes were studied: LF10 RO and NTR−7450 NF (Nitto Denko, Shimohozumi, Japan), ESPA3 RO and ESNA NF (Hydranautics, Oceanside, CA), NF90 NF (Dow Liquid Separation, Midland, MI), and TFC−S NF (Koch Membrane Systems, Wilmington, MA). NTR−7450 has a sulfonated polyethersulfone (SPES) active layer with negative sulfonate ($R–SO_3^-$) groups [1, 11], and all other membranes have fully-aromatic polyamide (PA) active layers (see spectroscopic analyses in Figure C.1 of Supporting Information) with negatively ionizable carboxylic (R–COOH) and positively ionizable amine ($R–NH_2$) groups [1, 12]. All experiments were performed at room temperature (20–22$^oC$) with 2.5×5.0-$cm^2$ coupons previously rinsed with and stored in nanopure water. In general, triplicate samples were prepared for each condition tested.

***4.2.2. Quantification of Ionized Functional Groups.*** Concentrations of ionized functional groups in the active layers of the membranes studied were determined as a function of pH using experimental methods developed in our previous studies with the FT30 RO membrane [12, 14]. Negative functional groups in active layers were quantified in the pH range 3.4–10.5 by first saturating them with silver ion ($Ag^+$), and subsequently quantifying the concentration of $Ag^+$ associated with the ionized groups using Rutherford backscattering spectrometry (RBS). The measured $Ag^+$ concentration in the active layer was considered equivalent to that of the negative functional groups. A representative RBS spectrum and simulation for a sample of LF10 RO membrane probed with $Ag^+$ is presented in Figure C.2 of Supporting Information. Positive functional

groups were quantified in the pH range 3.8–7.4 using tungstate ($WO_4^{2-}$) as ion probe. The concentration of $WO_4^{2-}$ in the active layer was considered an approximation of the concentration of positive functional groups. Additional details about experimental procedures can be found elsewhere [12, 14].

***4.2.3. Stoichiometry of Association between Negative Functional Groups and $Ba^{2+}$.*** Negative functional groups in active layers were initially saturated with $Ag^+$. Next, barium ions ($Ba^{2+}$) were used to displace $Ag^+$ ions. The concentrations of $Ag^+$ and $Ba^{2+}$ in the active layer before and after ion displacement were quantified by RBS. While the drop in $Ag^+$ concentration in the active layer ($\Delta[Ag^+]$) provided the concentration of sites neutralized by $Ba^{2+}$, the concentration of $Ba^{2+}$ neutralizing those sites was given by the $Ba^{2+}$ concentration ($[Ba^{2+}]$) after ion displacement. Consequently, the ratio $NN=\Delta[Ag^+]/[Ba^{2+}]$ represented the stoichiometry of association between neutralized negative groups and $Ba^{2+}$ at a concentration $\Delta[Ag^+]$ of neutralized sites [14]. The stoichiometry of association was studied as a function of the concentration of neutralized sites by performing $Ag^+$–$Ba^{2+}$ displacement experiments at different pH values within the range of 6.0–10.3. Additional details about methods used in $Ag^+$–$Ba^{2+}$ displacement tests can be found elsewhere [14].

***4.2.4. Ion Probing with $Ba^{2+}$ and $K^+$.*** Using the ion-probing/RBS procedure summarized above and reported in greater detail previously [14], the concentration of $Ba^{2+}$ that associates with negative functional groups in the active layers of all RO/NF membranes studied was characterized in the pH range 3.5–10.3. Additionally, the concentration of

$K^+$ that associates with $R–SO_3^-$ groups in the active layer of the NTR–7450 membrane was quantified in the pH range 5.3–8.8.

***4.2.5. Ion-Probe Solutions.*** All solutions were prepared with nanopure water and A.C.S. grade chemicals with 99%+ purity. Barium chloride dihydrate ($BaCl_2 \cdot 2H_2O$) (Fisher Scientific, Hampton, NH), and barium nitrate ($Ba(NO_3)_2$), silver nitrate ($AgNO_3$) and sodium tungstate ($Na_2WO_4$) (Sigma-Aldrich, St. Louis, MO) were used as sources of $Ba^{2+}$, $Ag^+$ and $WO_4^{2-}$. The concentrations of barium ($10^{-6}$–0.32 M), silver ($10^{-6}$–$10^{-3}$ M) and tungstate ($10^{-6}$–$10^{-3}$ M) in solution were always below their solubility limit [15]. NaOH and HCl were used for pH adjustment, except in the case of experiments involving silver for which NaOH and $HNO_3$ were used to avoid AgCl precipitation. Solutions containing silver were prepared and used under dim red light to avoid photoreactivity.

***4.2.6. RBS Analyses.*** F For any given membrane, RBS was first used to determine the elemental composition of its active layer by scanning six untreated membrane coupons (i.e., total scanned area of ≈48 $cm^2$). The obtained elemental composition was then used during the analysis of RBS spectra of treated membrane samples for the quantification of ion probes in active layers. Details on RBS theory and analysis [16], and its use to characterize the elemental composition of active layers of RO/NF membranes [4, 11, 17], and to quantify the concentration of heavy ions in active layers [14, 17], can be found elsewhere.

## 4.3. Results and Discussion

***4.3.1. Elemental Composition and Thickness of Active Layers.*** Table 4.1 shows the RBS results for the elemental composition and thickness of the active layer of each membrane studied including results previously reported for the active layer of FT30 RO membrane [12, 14]. Corresponding RBS spectra and simulations for untreated membranes are presented in Figure C.4 of Supporting Information. The analysis of the onset energy of the nitrogen peak in the RBS spectra of the LF10 RO membrane (see ref [12] for analysis details using the FT30 membrane) revealed the existence of a 58±33-nm thick coat layer with approximate composition $C_{0.28}O_{0.12}H_{0.60}Cl_{0.001}$ on top of the active layer, similar to the 25±35-nm thick coat ($C_{0.32}O_{0.12}H_{0.56}$) previously observed [12] for the FT30 RO membrane. The relatively high O:C ratios in the reported coats is consistent with the use of cross-linked polyvinyl alcohol as coating material [1, 18]. Analyses of the RBS spectra of all other membranes showed that they did not have coating layers, thus indicating that among the membranes studied only some of the RO membranes, but none of the NF membranes, had coats. These observations were consistent with attenuated total reflectance Fourier transform infrared (ATR-FTIR) studies [19, 20] reporting that only four RO membranes out of a pool of nine RO and four NF membranes had coats. A proposed reason for coat layers not being used in NF membranes is that even though coats provide benefits such as increase in fouling resistance [18], they also have the detrimental effect of reducing water permeability before fouling, therefore decreasing the maximum achievable water production at a given operating pressure [18].

**Table 4.1.** Summary of results for the RBS and ion-probing/RBS analyses of the active layers of the membranes studied. Uncertainties represent standard error.

| **Membrane** | **FT30** [a,b] **RO** | **LF10** [b] **RO** | **ESPA3 RO** | **TFC−S NF** | **ESNA NF** | **NF90 NF** | **NTR−7450 NF** |
|---|---|---|---|---|---|---|---|
| C | 0.48 | 0.48 | 0.49 | 0.49 | 0.49 | 0.50 | 0.47 |
| O | 0.12 | 0.13 | 0.09 | 0.09 | 0.09 | 0.08 | 0.15 |
| N | 0.07 | 0.06 | 0.08 | 0.08 | 0.09 | 0.08 | - |
| S | - | - | - | - | - | - | 0.04 |
| Cl | 0.00 | 0.008 | 0.008 | 0.006 | 0.012 | 0.002 | - |
| H [c] | 0.32 | 0.32 | 0.33 | 0.33 | 0.33 | 0.33 | 0.34 |
| O:N ratio | 1.77 | 2.34 | 1.12 | 1.25 | 1.00 | 0.96 | - |
| Thickness [d] (nm) | 120±47 | 116±55 | 98±57 | 72±41 | 87±53 | 111±56 | 142±65 |
| $C_{T,\mathrm{R–COOH}}$ (M) | 0.54±0.02 | 0.50±0.02 | 0.64±0.01 | 0.54±0.01 | 0.51±0.01 | 0.24±0.02 | 1.67±0.02 [g] |
| p$K_{a,1}$ | 5.39±0.23 | 5.23±0.16 | 3.91±1.06 | 5.38±0.11 | 5.42±0.13 | 5.72±0.06 | - |
| p$K_{a,2}$ | 9.03±0.08 | 8.46±0.17 | 5.86±0.10 | 8.66±0.06 | 8.67±0.11 | 9.87±0.23 | - |
| $w_1$ | 0.22±0.03 | 0.49±0.05 | 0.08±0.07 | 0.33±0.02 | 0.45±0.03 | 0.60±0.04 | - |
| $w_2$ | 0.78±0.03 | 0.51±0.05 | 0.92±0.07 | 0.67±0.02 | 0.55±0.03 | 0.40±0.04 | - |
| $C_{T,\mathrm{R–NH2}}$ (M) | 0.04±0.01 | 0.01±0<.005 | 0.01±<0.005 | 0.02±<0.005 | 0.01±<0.005 | 0.08±0.04 | - |
| p$K_{a,\ \mathrm{R–NH2}}$ | 4.62±0.28 | 4.07±0.09 | 3.68±0.21 | 3.63 [h] | 3.63 [h] | 3.63±0.35 | - |
| $C_{T,\mathrm{R–COOH}}/C_{T,\ \mathrm{R–NH2}}$ | 0.08±0.02 | 0.03±0.002 | 0.01±0.005 | 0.03±0.004 | 0.03±0.001 | 0.33±0.18 | 0.00 [i] |
| Isoelectric point | 4.5 | 4.1 | 3.3 | 3.4 | 3.5 | 4.3 | - |
| DPC [e] | 0.94±0.07 [j] | 0.94±0.06 [j] | 0.95±0.07 [j] | 0.95±0.07 [j] | 0.96±0.07 [j] | 0.97±0.07 [j] | - |
| $a$ [e] (M) | 0.03±<0.01 | 0.17±0.01 | 0.28±0.02 | 0.14±0.01 | 0.12±0.02 | NN=1.98±0.20 [k] | NN=1.96±0.05 [k] |
| AR [e] | 0.40±0.04 | 0.58±0.03 | 0.62±0.04 | 0.81±0.03 | 0.44±0.02 | 0.58±0.03 | 0.95±0.01 |
| $n$ [f] | 0.64±0.07 | 0.59±0.04 | 0.66±0.11 | 0.68±0.04 | 0.73±.02 | 0.84±0.07 | k = 2.00 [l] |
| $x$ [f] | 0.34±0.07 | 0.40±0.04 | 0.34±0.11 | 0.31±0.04 | 0.26±.02 | 0.12±0.07 | l = 1.08 [l] |
| $y$ [f] | 0.03±0.01 | 0.01±0.001 | 0.005±0.002 | 0.01±.001 | 0.01±.001 | 0.04±0.02 | i = 0.75 [l] |

Notes for Table 4.1:

[a] For consistency with the RBS data analysis performed for the other membranes in Table 4.1, the RBS data previously reported in references [12, 14] for the FT30 RO membrane was re-analyzed taking into account the recently obtained density (1.24 g/cm$^3$) of its polyamide (PA) active layer [31] and other minor improvements to RBS simulation. The results presented in Table 4.1 are only slightly different from those reported before [12, 14], and do not affect any of the conclusions reported in previous publications [12, 14].

[b] The PA active layers of the FT30 RO and LF10 RO membranes were found to have active layer coatings of approximate composition and thickness $C_{0.32}O_{0.12}H_{0.56}$ and 25±35 nm, and $C_{0.28}O_{0.12}H_{0.60}Cl_{0.001}$ and 58±33nm, respectively.

[c] Because RBS spectra do not have a hydrogen signal, but are affected by the hydrogen content of the sample, analysis of RBS data for polymers requires the input of their H:C ratio [11]. The ratio assumed for the sulfonated polyethersulfone (SPES) active layer of the NTR−7450 NF membrane was H:C = 0.69 [28] (see Figure C.3 of Supporting Information), and that for fully aromatic PA active layers was H:C = 0.67 [11].

[d] For the calculation of active layer thickness, the density of the active layer is needed [14, 31]; we used 1.24g/cm$^3$ [31] and 1.37 g/cm$^3$ [32] for PA and SPES, respectively. For coat layers, we used the density of amorphous polyvinyl alcohol (PVA) (1.26 g/cm$^3$) [33] consistent with reports of the use of PVA as coating material [1, 18].

[e] DPC (degree of polymer crosslinking), AR (accessibility ratio) and *a* parameter in Equations 4.3, 4.4 and 4.5, respectively.

[f] Fractions of polymer repeating units that are fully crosslinked (*n*), contain a carboxylic group (*x*), and contain an amine group (*y*). Uncertainties are mainly determined by the error-to-value ratio of the fitted total concentration of amine groups which is high due to the inability to obtain $WO_4^{2-}$-probing data below pH≈3.8.

[g] Concentration of sulfonate groups ($C_{T,R-SO3^-}$) in the SPES active layer.

[h] Given the limited number of data points for the probing of R–$NH_3^+$ with $WO_4^{2-}$ in the TFC–S NF and ESNA NF membranes, for these two membranes we only fitted $C_{T,\,R-NH2}$ using $pK_{a,R-NH2} = 3.63$ obtained through the fitting of the data of the third PA nanofiltration membrane, NF90.

[i] The concentration of positive sites in the SPES active layer was quantified in the pH range 4.00–5.67 and was found to be zero.

[j] Uncertainty was calculated assuming a 5% error in nitrogen content.

[k] For the NF90 NF membrane, *a* = 0.00±<0.01, and as a result, we report the experimental NN. For the NTR−7450 NF membrane, the *a* parameter lacks practical physical meaning because the concentration of ionized sulfonate groups was constant across the pH range studied. Accordingly, we report the experimental NN.

[l] Fractions of repeating units k, l and i making up the composition of the SPES active layer as defined in Figure C.3 of Supporting Information.

Table 4.1 also shows that there are no major differences between RO and NF membranes with respect to the elemental compositions of uncoated PA active layers; however, oxygen contents in coated active layers are distinctly higher than in uncoated ones. We reported previously [12] that the relatively high oxygen content obtained by RBS analysis may result from the RBS simulation being unable to accurately differentiate the oxygen in the PA active layer from that in the coat layer. We did not test this hypothesis experimentally as it was not possible to perform RBS analysis in the absence of the coats because it is not possible to remove them without chemical treatment.

Thickness values in Table 4.1 suggest that fully-aromatic PA RO active layers are in general thicker than their NF counterparts with the average thickness of PA active layers in RO and NF membranes being 111 nm and 90 nm, respectively, and the thinnest RO and NF active layers being 98-nm and 72-nm thick, respectively. Since water flux is inversely proportional to active layer thickness [3, 5], it is likely that thinner fully-aromatic polyamide RO active layers are not used because a minimum thickness is required to obtain salt rejection at RO levels. The relatively high standard deviation of the thickness of fully-aromatic PA active layers shown in Table 4.1, and reported elsewhere [11, 13, 20], supports this assertion as thinner membranes would increase the probability of imperfections that would prevent the level of solute rejection needed for RO applications. In contrast, the SPES active layer of the NTR–7450 NF membrane was approximately 15% thicker than the thickest PA active layer, and in particular about 40% thicker than that of the ESPA3 RO membrane; however, water permeability for the NTR–7450 membrane is higher ($2.1–6.4\times10^{-11}$ $m\cdot s^{-1}\cdot Pa^{-1}$[21]) than that for the ESPA3

membrane ($\approx 1.7\times10^{-11}$ m·s$^{-1}$·Pa$^{-1}$ [22]) indicating that active layer resistance to water transport per unit thickness of PA is higher than per unit thickness of SPES.

***4.3.2. Ionization Behavior of Functional Groups.*** Figure 4.1a shows the experimental data and model lines for the concentration of ionized functional groups in the active layer of the LF10 RO membrane as a function of pH. The corresponding plots for the other membranes studied can be found in Figure C.5 of Supporting Information. For PA active layers, the ionization of functional groups was modeled assuming acid-base equilibrium with the aqueous ion-probe solution in accordance with Equations 4.1 and 4.2 [12], where $C_{T,\text{R–COOH}}$ and $C_{T,\text{ R–NH2}}$ are the total concentrations of carboxylic and amine groups, respectively, and $w_i$ represents the fraction of functional groups having p$K_a$=p$K_{a,i}$ where $\sum_{i=1}^{n} w_i = 1$. The fitted values for all membranes are summarized in Table 4.1.

Two p$K_a$ values were needed to describe the ionization behavior of carboxylic groups in the PA active layers studied (i.e., $n$=2 in Equation 4.1), which is consistent with what we previously reported for the FT30 RO membrane [12], and with the bimodal pore size distribution reported for PA active layers [10, 23, 24]; the size of the nanopores where water is contained affects its dielectric constant [25] which, in turn, affects the p$K_a$ of carboxylic groups [26]. The ESPA3 RO membrane, however, had a p$K_a$ distribution heavily biased towards one value ($w_2$=0.92±0.07), and a fitted dominant p$K_a$=5.86±0.10 between the p$K_{a,1}$ and p$K_{a,2}$ values of the other membranes, which is consistent with the use of additives such as dimethyl sulfoxide (DMSO) during the production of the PA active layer. Kim et al. [10, 23, 24] showed that the use of DMSO during the interfacial

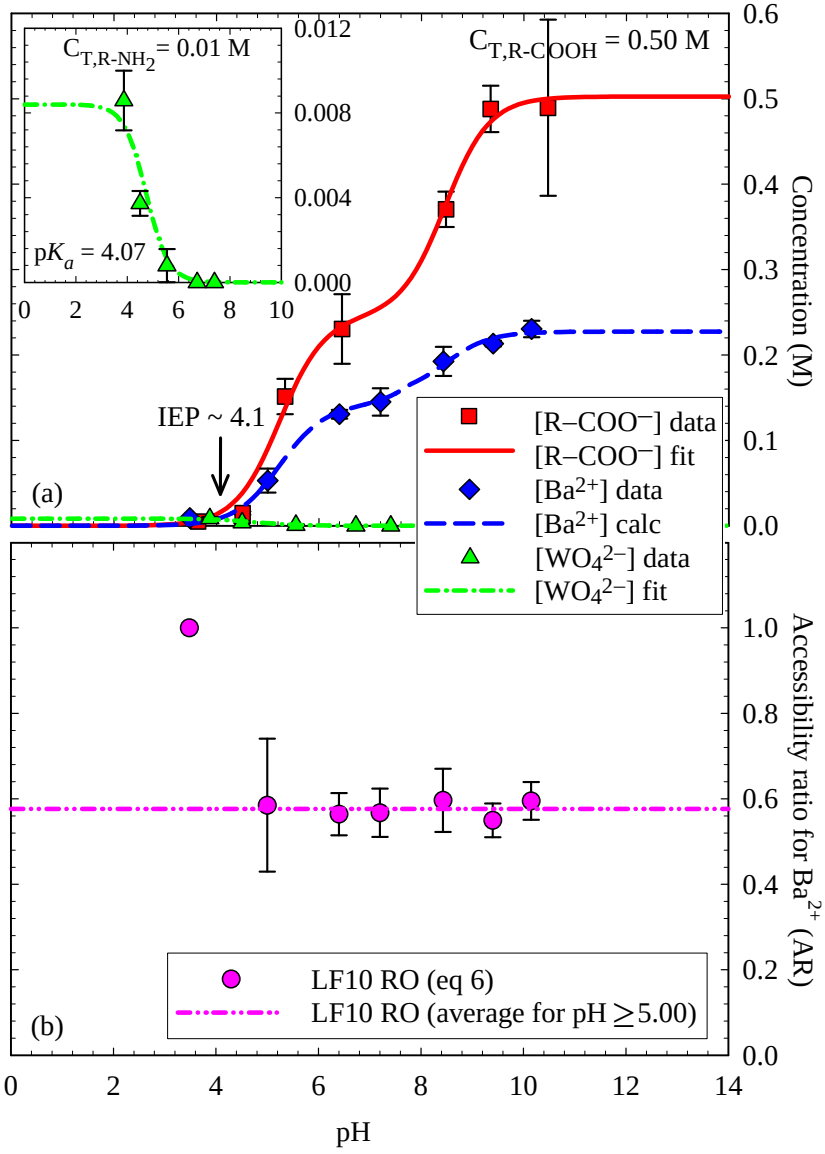


**Figure 4.1.** (a) Concentrations of R–$COO^-$ ([R–$COO^-$]) and R–$NH_3^+$ ([R–$NH_3^+$]) groups in the polyamide active layer of the LF10 RO membrane measured using $Ag^+$ and $WO_4^{2-}$, respectively, as ion probes. The concentration of $Ba^{2+}$ ([$Ba^{2+}$]) that associates with accessible R–$COO^-$ groups in the active layer is also shown. Symbols represent experimental data. Error bars indicate standard deviation. The (red) continuous and (green) dot-dash lines are the fit lines of [R–$COO^-$] with Equation 4.1, and [R–$NH_3^+$] with Equation 4.2, respectively. The (blue) dashed line is the calculated [$Ba^{2+}$] using Equations 4.4 and 4.5 with *a* and AR values in Table 4.1. (b) Accessibility ratio for $Ba^{2+}$ ion (AR) in the active layer of the LF10 RO membrane. Circles correspond to AR values calculated by solving Equations 4.4 and 4.5 using the [R–$COO^-$] and [$Ba^{2+}$] information in (a), and the *a* parameter from Table 4.1. At the lowest experimental pH of 3.48, we found that AR ≈ 1. Error bars indicate standard error. The dash-dot-dot line is the average AR = 0.58±0.03 for the pH range of 5.00–10.15.

polymerization reaction results in high-flux RO membranes with active layers having pore size distributions biased towards a pore size intermediate between those two that would result in the absence of the additive. Consistent with the discussion above on the relation between pore size, water dielectric constant, and p$K_a$ values, an intermediate dominant pore size would also result in an intermediate dominant p$K_a$ value.

$$[\mathrm{R-COO^-}] = C_{T,\mathrm{R-COOH}} \sum_{i=1}^{n} \left( w_i \times \frac{10^{-\mathrm{p}Ka,\,i}}{10^{-\mathrm{pH}} + 10^{-\mathrm{p}Ka,\,i}} \right) \tag{4.1}$$

$$[\mathrm{R-NH_3^+}] = C_{T,\mathrm{R-NH2}} \sum_{j=1}^{n} \left( w_j \times \frac{10^{-\mathrm{pH}}}{10^{-\mathrm{pH}} + 10^{-\mathrm{p}Ka,\,j}} \right) \tag{4.2}$$

Table 4.1 shows that while the ESPA3 RO membrane had the highest $C_{T,\mathrm{R-COOH}}$= 0.64 M, the lowest p$K_a$ values (p$K_{a,1}$=3.91, p$K_{a,2}$=5.86) and the lowest fraction $w_1$=0.08±0.07, the NF90 NF membrane had the lowest $C_{T,\mathrm{R-COOH}}$= 0.24 M, the highest p$K_a$ values (p$K_{a,1}$=5.72, p$K_{a,2}$=9.87) and the highest fraction $w_1$=0.60±0.07. On the other hand, the other four PA membranes had intermediate parameters values, including similar total concentrations of carboxylic groups ($C_{T,\mathrm{R-COOH}}$=0.50–0.54 M), relatively similar equilibrium constants (p$K_{a,1}$=5.23–5.42, p$K_{a,2}$=8.46–9.03), and $w_1$ fractions in the 0.22–0.49 range. Consistent with these values, the ESPA3 RO membrane reached 94% ionization by pH=7, the NF90 NF membrane had a relatively stable intermediate charge density of ≈0.14 M in the pH range 7.0–9.0, and the other four PA membranes underwent a relatively steady charge increase across the whole pH range. Accordingly, our results revealed that for the fully-aromatic polyamide RO/NF membranes studied: (i) total concentrations of carboxylic groups were in the 0.45±0.25 M range; (ii) while the highest

and lowest $C_{T,\mathrm{R-COOH}}$ values were obtained for RO and NF membranes, respectively, some RO and NF membranes had almost identical $C_{T,\mathrm{R-COOH}}$; (iii) membranes with similar $C_{T,\mathrm{R-COOH}}$ values still had relatively different ionization behaviors as a result of their relatively different p$K_a$ and $w_1$ values; and (iv) the membranes with the highest and lowest $C_{T,\mathrm{R-COOH}}$ had the lowest and highest, respectively, p$K_{a.1}$, p$K_{a.2}$ and $w_1$ values.

For the case of amine groups, one p$K_a$ value sufficed to describe their ionization behavior. Table 4.1 shows that p$K_a$ values for amine groups were in the 3.63–4.62 range, and that $C_{T,\mathrm{R-NH2}}$ values were in the 0.01–0.08 M range with $C_{T,\mathrm{R-NH2}}$:$C_{T,\mathrm{R-COOH}} \leq 0.08$ except for the NF90 NF membrane ($C_{T,\mathrm{R-NH2}}$:$C_{T,\mathrm{R-COOH}} = 0.33$). The combination of relatively low total concentrations and p$K_a$ values for amine groups made the concentration of positive charges in the PA active layers studied negligible (≤ 0.005 M) in the pH range of interest for water treatment (pH≈6–10). While the highest total concentration of amine groups (0.08 M) occurred in an NF membrane (NF90), the second highest (0.04 M) occurred in an RO membrane (FT30), thus indicating that there is no particular correlation between the concentration of amine groups and membrane rating (i.e., RO or NF). We also obtained the isoelectric point in PA active layers as the intersection of [R–COO$^-$] and [$WO_4^{2-}$] curves in Figure 4.1a and Figure C.5 of Supporting Information. All isoelectric points fell in the pH≈3–5 range consistent with the range of values reported in the literature from zeta potential analyses [7, 20, 27].

RBS characterization of the SPES active layer of the NTR–7450 NF membrane revealed that its concentration of sulfonic groups was 1.67 M=1.22 meq/g which is consistent with the range of ion exchange capacities (1.0–1.6 meq/g) reported [28] for SPES copolymers

with compositions similar to that of the active layer of NTR−7450. In contrast to carboxylic groups in PA active layers, sulfonic groups remained ionized in the entire pH range investigated (5.31−8.75), an observation consistent with their relatively low p$K_a$ < 4 [29]. The concentration of sulfonate groups in the SPES active layer of the NTR−7450 NF membrane was 2.6 times higher than the highest total concentration of carboxylic groups measured in PA active layers (i.e., 0.64 M for the ESPA3 RO membrane).

***4.3.3. Degree of Polymer Crosslinking (DPC).*** We used the RBS data to calculate the degree of polymer crosslinking (DPC) in PA active layers, defined as the ratio between the measured concentration of amide links and the concentration of amide links in an equivalent fully-crosslinked active layer. We calculated the DPC using Equation 4.3 [12], where N, AG and CG represent the concentrations of nitrogen, amine groups and carboxylic groups, respectively, in the active layer. The results in Table 4.1 show that the DPC was 94−95% and 95−97% for RO and NF membranes, respectively. We also characterized the degree of crosslinking by calculating the *n*, *x* and *y* fractions of polymer repeating units in the PA structure that were fully crosslinked $(C_{36}H_{24}N_6O_6)_n$, contained a carboxylic group $(C_{36}H_{25}N_6O_7)_x$, or contained an amine group $(C_{36}H_{25}N_6O_6)_y$, respectively [12]. We calculated *n*, *x* and *y* using the information in Table 4.1 and the relations $x+y = 6\times(CG+AG)/N$, $x/y = CG/AG$, and $n+x+y = 1$ [12]. The *n* fraction of fully crosslinked repeating units for RO and NF membranes was 59−66% and 68−84%, respectively. These DPC and *n* values indicate that the degree of crosslinking in NF membranes was higher than in RO membranes.

$$DPC = \frac{\text{Amide links}}{\text{Potential amide links}} = \frac{N - AG}{N + CG} \quad (4.3)$$

### *4.3.4. Stoichiometry of Association between Negative Functional Groups and $Ba^{2+}$.*

Figure 4.2a shows the results for the stoichiometry of association between R–$COO^-$ groups and barium ion ($Ba^{2+}$) in the active layers of the PA membranes studied. The *y*-axis represents the concentration of R–$COO^-$ groups neutralized by $Ba^{2+}$, and the *x*-axis represents the concentration of $Ba^{2+}$ ions neutralizing those sites. Accordingly, the average number of R–$COO^-$ groups neutralized per barium ion ($Ba^{2+}$), referred to as the neutralization number NN [14], at a given concentration *y* of neutralized R–$COO^-$ groups is given by NN=*y*/*x* for any given (*x*,*y*) experimental point. Figure 4.2b presents the calculated NN values as a function of the concentration of R–$COO^-$ groups neutralized by $Ba^{2+}$ (i.e., the *x*-axis in Figure 4.2b is the same as the *y*-axis in Figure 4.2a).

In a previous study [14], we modeled the experimental data for the FT30 RO membrane reproduced in Figure 4.2a based on one single parameter *a* such that $\Delta y/\Delta x=1 \rightarrow y=x$ for $x \le a$, and $\Delta y/\Delta x=2 \rightarrow y = 2x-a$ for $x>a$. Accordingly, the *a* parameter represented the concentration of neutralized R–$COO^-$ groups at which the stoichiometry of association between the additional R–$COO^-$ sites ($\Delta y$) that ionized as pH increased and the $Ba^{2+}$ ions ($\Delta x$) that neutralized them changed from 1:1 to 2:1. We used the same model to fit the experimental data for all other PA membranes studied and obtained the corresponding *a* values and fitted lines shown in Table 4.1 and Figure 4.2a, respectively. The corresponding NN curves were also calculated and plotted in Figure 4.2b. As depicted in the figures, fitted lines described well the experimental data sets with multiple data

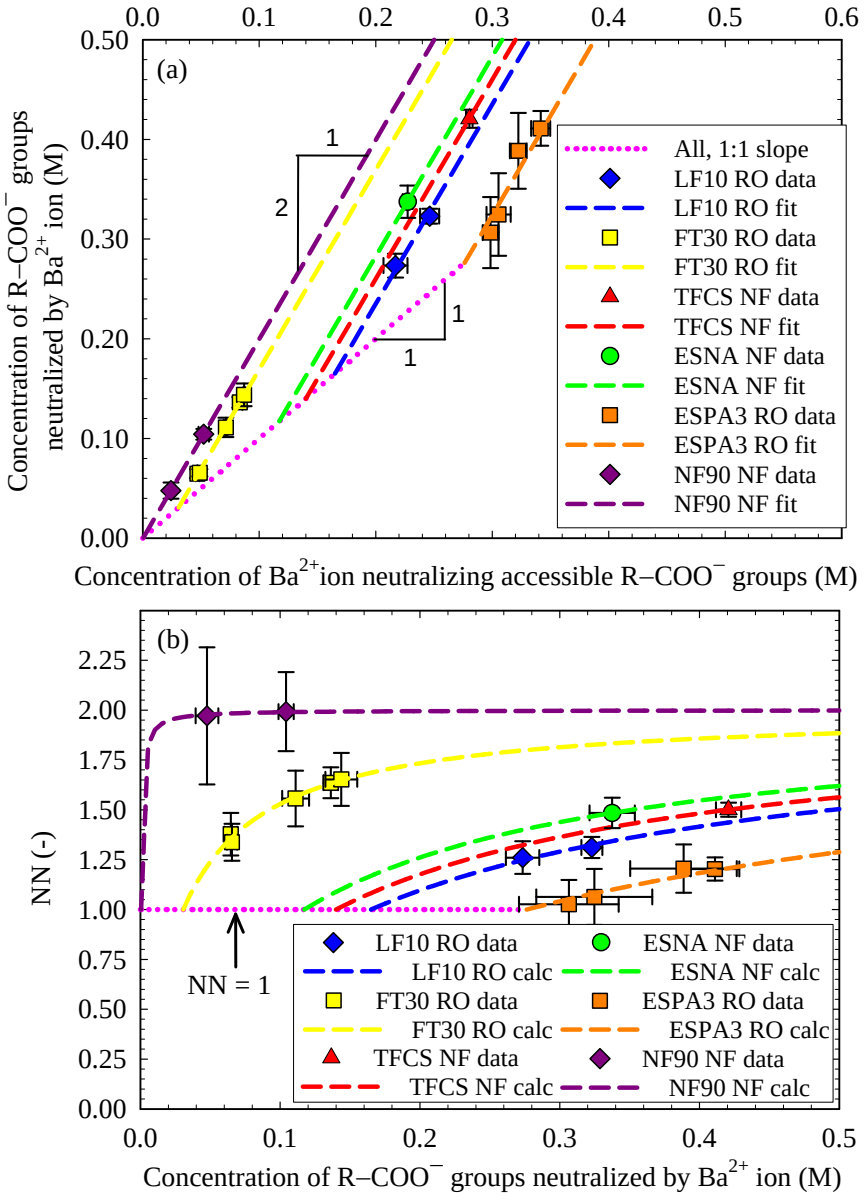


**Figure 4.2.** Stoichiometry of association between R–COO$^-$ groups neutralized by $Ba^{2+}$ in the polyamide (PA) active layers of the membranes studied and the $Ba^{2+}$ ions neutralizing them. (a) Limiting one-to-one (pink dotted line) and two-to-one (color dashed lines) correspondence between neutralized R–COO$^-$ groups and $Ba^{2+}$ ion. Symbols are experimental data obtained from $Ag^+$–$Ba^{2+}$ ion-displacement tests. The coordinates $(x,y) = (a,a)$ of the intersection of the 2:1 line of any membrane with the 1:1 line correspond to the value of the $a$ parameter in Table 4.1 and Equation 4.5. The neutralization number for $Ba^{2+}$ ion (NN) for any given $(x,y)$ point is calculated as its corresponding $y/x$ ratio. (b) NN as a function of the concentration of R–COO$^-$ sites neutralized by $Ba^{2+}$ ion in the PA active layers of the membranes studied. Symbols and lines are the NN values calculated from their corresponding plots in (a). Error bars indicate standard error.

points, thus supporting the validity of the model. Figure 4.2 and Table 4.1 show that the *a* parameter was different for all membranes studied. Since a higher *a* indicates a lower average number of R–$COO^-$ groups neutralized per $Ba^{2+}$ ion at a given concentration of neutralized R–$COO^-$ groups (e.g., $a_{ESPA3}$=0.28 M > $a_{FT30}$=0.03 M and thus $NN_{ESPA3} \leq NN_{FT30}$), then a higher *a* also indicates a larger average distance between ionized functional groups in the active layer. Accordingly, since $a_{Max} = a_{ESPA3\ RO} > a_{LF10\ RO} > a_{TFC-S\ NF} > a_{ESNA\ NF} > a_{FT30\ RO} > a_{NF90\ NF} = a_{Min}$, then the spatial distribution of carboxylic groups in the PA active layers of the membranes studied is generally different for each membrane with ESPA3 RO and NF90 NF having the most and the least, respectively, homogeneously distributed carboxylic groups in their active layers. Additionally, since RO membranes had both the largest and the second-lowest *a* values, there seems to be no correlation between the value of the *a* parameter and membrane rating.

We also performed an $Ag^+$–$Ba^{2+}$ displacement test at pH=5.96 with the NTR–7450 NF membrane to study the stoichiometry of association between the R–$SO_3^-$ groups in its SPES active layer and $Ba^{2+}$ ion, and found that NN=1.96±0.05. Since the concentration of R–$SO_3^-$ groups in NTR–7450 as a function of pH is constant, then NN ≈ 2.0 at any pH.

***4.3.5. Accessibility of $Ba^{2+}$ Ion to Negative Functional Groups.*** In a previous study [14], we demonstrated that the concentration of barium ion ([$Ba^{2+}$]) that associated with accessible carboxylic groups in the PA active layer of the FT30 RO membrane as a function of pH was given by Equation 4.4, where the accessibility ratio AR represents the

fraction of $R–COO^-$ groups accessible to $Ba^{2+}$ ions. We also showed that NN was given by Equation 4.5 for $AR\times[R–COO^-] > a$, and NN=1 for $AR\times[R–COO^-] \leq a$. Accordingly, in this study, we used Equations 4.4 and 4.5 together with the experimental ion-probing/RBS data for $[R–COO^-]$ and $[Ba^{2+}]$ as a function of pH, and the *a* parameter values obtained in the previous section, to calculate AR as a function of pH. The $[Ba^{2+}]$ data and calculated AR values as a function of pH are presented in Figure 4.1 for LF10 RO, and shown in Figure C.5 of Supporting Information for all other membranes studied. The results show that in general, and consistent with our previous findings for FT30 RO [14], AR was approximately constant as a function of pH except at the lowest pH values tested (pH≈3.5) at which AR=1. Average AR values were in the 0.40–0.81 range (see Table 4.1). The only membrane that perhaps deviated significantly from a constant AR across the whole pH range was NF90 NF for which AR varied from 0.45±0.04 at pH=3.5–6.6 to 0.69±0.05 at pH=7.5–10.4; however, an AR=0.58±0.03 satisfactorily described the average steric effects experienced by $Ba^{2+}$ ion.

$$[Ba^{2+}] = \frac{AR \times [R - COO^-]}{NN} \tag{4.4}$$

$$NN = 2 \times \left( \frac{AR \times [R - COO^-]}{AR \times [R - COO^-] + a} \right) \tag{4.5}$$

The average AR and *a* values of each membrane were used to calculate $[Ba^{2+}]$ as a function of pH (see dashed blue lines in Figure 4.1a and Figure C.5 of Supporting Information) using Equations 4.4 and 4.5. As observed in the figures, the calculated $[Ba^{2+}]$ matches well the experimental data, thus indicating that for any given PA active

layer, the two constant parameters AR and *a* describing the accessibility and stoichiometry of association, respectively, of carboxylic groups, suffice to describe adequately the difference between [R–$COO^-$] and [$Ba^{2+}$] as a function of pH. Since carboxylic groups are likely to have different p$K_a$ values in pores of different sizes for a given active layer (see discussion above and in reference [14]), constant AR values for the entire pH range investigated are consistent with what we previously proposed based on the studies with the FT30 RO membrane [14], i.e., that pores of different sizes in PA active layers are interconnected thus forming a network of pores that makes carboxylic groups equally accessible (or inaccessible) regardless of the size of the pore where they are located.

For the case of the SPES active layer of the NTR–7450 membrane, [$Ba^{2+}$]=0.81±0.02 M was approximately constant at all pH values studied. Using Equation 4.4 and NN=1.96±0.05 ≈ 2.0 (see previous section), we calculated AR as a function of pH. The results, presented in Figure C.5 of Supporting Information, show that AR = 0.95±0.01 ≈ 1 indicating that $Ba^{2+}$ ions have access to ≈100% of the R–$SO_3^-$ groups in the active layer. Accordingly, the steric effects experienced by $Ba^{2+}$ ions and other solutes of equal or greater size in fully-aromatic PA active layers are greater than in the SPES active layer of the NTR–7450 NF membrane.

***4.3.6. Implications of Results on Membrane Performance.*** The effect of the net charge of the active layer on the partitioning of ions into it when the membrane is in equilibrium with an aqueous solution of a symmetrical electrolyte is described by Equations 4.6 [5] and 4.7 [5, 30]. In Equation 4.6, $K_{AL/Water}$ is the active layer-water partition coefficient of

the ion of interest, and Φ, $\gamma$ and $\mathbb{D}$ are terms related to steric effects, activity coefficients, and the electrical Donnan exclusion mechanism, respectively. In Equation 4.7, $C_{net}$ =[R–$NH_3^+$]–[R–$COO^-$], $C_{ion}$ and $z_{ion}$ are the net charge density of the active layer due to ionized functional groups, the concentration of the symmetrical electrolyte solution, and the valence of the ion of interest, respectively. We used the Donnan exclusion ratio $\left(\mathbb{D}_j / \mathbb{D}_l\right)^{-1}$ as a quantitative descriptor of how many more times membrane *j* excludes a given ion *by the Donnan mechanism* compared to membrane *l*. Because of the higher negative charge density in its active layer, the NTR–7450 NF membrane excludes anions by the Donnan mechanism more effectively than all the PA membranes investigated. For example, the lowest and highest Donnan exclusion ratios for chloride ion in NaCl solution at a concentration of 1,500 mg/L and pH=10 are $\left(\mathbb{D}_{\text{NTR}-7450\text{ NF}} / \mathbb{D}_{\text{ESPA3 RO}}\right)^{-1} = 2.6$ and $\left(\mathbb{D}_{\text{NTR}-7450\text{ NF}} / \mathbb{D}_{\text{NF90 NF}}\right)^{-1} = 8.2$, respectively. Additionally, since sulfonate groups remain ionized as a function of pH, but carboxylic groups protonate with decreasing pH, the $\left(\mathbb{D}_{\text{NTR}-7450\text{ NF}} / \mathbb{D}_{\text{PA membrane}}\right)^{-1}$ ratio increases steadily as pH decreases reaching values as high as 173, where values above 64 occur when PA membranes acquire a net positive charge because of the protonation of amine groups.

$$\mathrm{K}_{\text{AL/Water}} = \Phi \times \gamma \times \mathbb{D} \tag{4.6}$$

$$\mathbb{D} = \exp\left(-\operatorname{arcsinh}\left(\frac{C_{\text{net}}}{2 \times z_{\text{ion}} \times C_{\text{ion}}}\right)\right) \tag{4.7}$$

In contrast, the $\left(\mathbb{D}_j / \mathbb{D}_l\right)^{-1}$ ratio does not increase or decrease steadily with pH when both *j* and *l* membranes have PA active layers. We used $\mathbb{D}_{\text{NF90 NF}}$ as baseline, and plotted in Figure 4.3 the $\left(\mathbb{D}_j / \mathbb{D}_{\text{NF90 NF}}\right)^{-1}$ ratios for the other five PA membranes as a function of pH to compare the relative benefits that adjusting the solution pH has on the Donnan exclusion of chloride by PA membranes. Figure 4.3 shows that, in the pH range 5.0–9.5, PA membranes exclude chloride by the Donnan mechanism in the order ESPA3 RO>LF10 RO>ESNA NF> TFC–S NF>FT30 RO>NF90 NF, with the exception of $\left(\mathbb{D}_{\text{FT30 RO}} / \mathbb{D}_{\text{NF90 NF}}\right)^{-1} < 1$ in the pH range 6.0–7.9. Figure 4.3 also shows that $\left(\mathbb{D}_j / \mathbb{D}_{\text{NF90 NF}}\right)^{-1}$ peaked at pH ≈ p$K_{a,1}$ and pH ≈ p$K_{a,2}$ for all PA membranes except for ESPA3 RO. The peaks occur because the p$K_{a,1}$ and p$K_{a,2}$ values of the NF90 active layer are higher than the corresponding values for the other PA active layers, and as a result, pH ranges in which ($C_{\text{net,i}} - C_{\text{net,NF90}}$) increases are always followed by pH ranges in which ($C_{\text{net,i}} - C_{\text{net,NF90}}$) decreases. Also, even though the FT30, LF10, TFC–S, and ESNA membranes have relatively similar $C_{T,\text{R–COOH}}$, p$K_{a,1}$ and p$K_{a,2}$ values, and similar $\left(\mathbb{D}_j / \mathbb{D}_{\text{NF90 NF}}\right)^{-1}$ behavior as a function of pH, Figure 4.3 shows that at pH < p$K_{a,2}$ − 1 ≈ 8.0 the differences in their $\mathbb{D}_j$ values are significant. Such differences occur mainly because their active layers have different fractions $w_1$ and $w_2$ of carboxylic groups which makes the concentrations of ionized sites significantly different at pH < p$K_{a,2}$ − 1 below which $C_{\text{net}}$ does not exceed ≈ $w_1 \times C_{T,\text{R–COOH}}$. Finally, because the total concentration of carboxylic groups in the ESPA3 RO membrane (0.64 M) is significantly higher than in the NF90 NF membrane (0.24 M), and the p$K_{a,2}$=5.86 of ESPA3 membrane is

approximately equal to the p$K_{a,1}$=5.74 of NF90 membrane, $\left(\mathbb{D}_{\text{ESPA3 RO}} / \mathbb{D}_{\text{NF90 NF}}\right)^{-1}$ decreases only at pH > p$K_{a,2,\text{NF90}}$ − 2 = 7.87 at which the charge in ESPA3 membrane has already stabilized and the charge in NF90 membrane increases. The result is the bell-shaped curve in Figure 4.3.

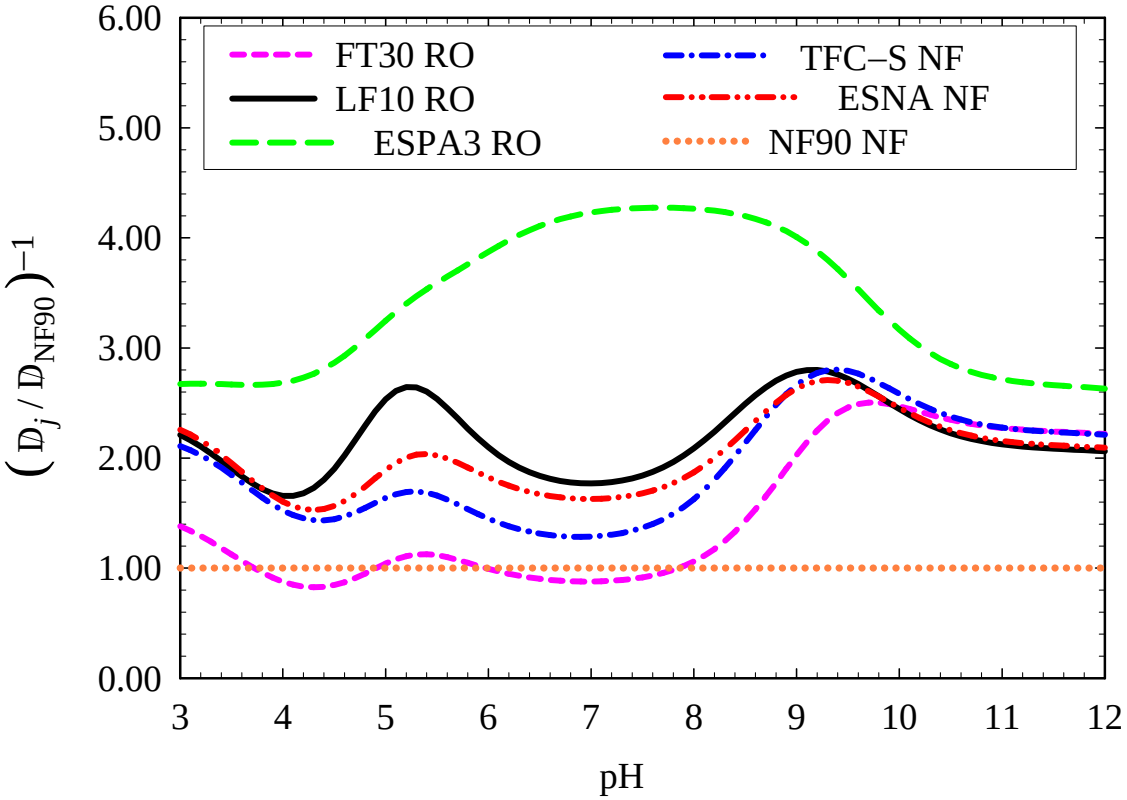


**Figure 4.3.** Quantitative description, using the $\left(\mathbb{D}_j / \mathbb{D}_{\text{NF90 NF}}\right)^{-1}$ ratio, of the relative Donnan exclusion of chloride ion by polyamide (PA) membrane *j* compared to by the polyamide NF90 membrane, for the partitioning of chloride from a feed sodium chloride solution with a concentration of 1,500 mg/L.

## 4.4. Acknowledgments

RBS analyses were carried out in the Center for Microanalysis of Materials, University of Illinois at Urbana-Champaign, partially supported by the U.S. Department of Energy under grant DEFG02-91-ER45439. The authors acknowledge Mari Gonzalez and Doug Jeffers for assistance in RBS analyses, Gorie Ster and Jeanne Luh for helpful discussions, and the companies Nitto Denko, Hydranautics and Koch Membrane Systems for providing membrane materials and related information. This work was supported by the National Science Foundation Environmental Engineering and Technology program under agreement number BES-0332217, and the WaterCAMPWS, a Science and Technology Center of Advanced Materials for the Purification of Water with Systems under agreement number CTS-0120978. The opinions in this paper do not necessarily reflect those of the sponsor.

## 4.5. Supporting Information Available

Figure C.1 (Attenuated total reflectance Fourier transform infrared (ATR-FTIR) spectrometry analyses of membranes with polyamide (PA) active layers); Figure C.2 (Rutherford backscattering spectrometry (RBS) spectrum of a sample of LF10 RO membrane probed with $Ag^{+}$ at pH=9.85); Figure C.3 (Repeating units in the polymer structure of the sulfonated polyethersulfone (SPES) active layer of NTR–7450 NF); Figure C.4 (RBS spectra and corresponding simulations for: (a) FT30 RO (see note ‘a’ in Table 4.1), (b) LF10 RO, (c) ESPA3 RO, (d) TFC–S NF, (e) ESNA NF, (f) NF90 NF, (g) NTR–7450 NF); Figure C.5 (Concentration of ionizable functional groups, concentration of $Ba^{2+}$ ion that associates with accessible $R–COO^{-}$ groups, and accessibility ratio for

$Ba^{2+}$ ion as a function of pH in the active layers of FT30 RO (see note 'a' in Table 4.1), ESPA3 RO, TFC–S NF, ESNA NF, NF90 NF, and NTR–7450 NF). This information is available in Appendix C.1.

### 4.6. References


1. Petersen, R. J., Composite reverse osmosis and nanofiltration membranes. *J. Mem. Sci.* 1993, *83*, 81-150.

2. Szymczyk, A.; Fievet, P., Investigating transport properties of nanofiltration membranes by means of a steric, electric and dielectric exclusion model. *J. Mem. Sci.* 2005, (252), 77-88.

3. Wijmans, J. G.; Baker, R. W., The solution-diffusion model: a review. *J. Mem. Sci.* 1995, *107*, 1-21.

4. Bartels, C. R., A surface science investigation of composite membranes. *J. Mem. Sci.* 1989, *45*, 225-245.

5. Bowen, W. R.; Welfoot, J. S., Modelling the performance of membrane nanofiltration-critical assessment and model development. *Chem. Eng. Sci.* 2002, *57*, 1121-1137.

6. Brant, J. A.; Johnson, K. M.; Childress, A. E., Characterizing NF and RO membrane surface heterogeneity using chemical force microscopy. *Colloids Surf. A: Physicochem. Eng. Aspects* 2006, *280*, 45-57.

7. Childress, A. E.; Elimelech, M., Relating nanofiltration membrane performance to membrane charge (electrokinetic) characteristics. *Environ. Sci. Technol.* 2000, *34*, 3710-3716.

8. Elimelech, M.; Zhu, X.; Childress, A. E.; Hong, S., Role of membrane surface morphology in colloidal fouling of cellulose acetate and composite aromatic polyamide reverse osmosis membranes. *J. Mem. Sci.* 1997, *127*, 101-109

9. Cahill, D. G.; Freger, V.; Kwak, S.-Y., Microscopy and microanalysis of reverse osmosis and nanofiltration membranes. *MRS Bull.* 2008, *33*, 27-32.

10. De Baerdemaeker, J.; Boussu, K.; Djourelov, N.; Van der Bruggen, B.; Dauwe, C.; Weber, M.; Lynn, K. G., Investigation of nanopores in nanofiltration membranes using slow positron beam techniques. *Phys. Stat. Sol.* 2007, *4*, 3804-3809.

11. Mi, B.; Coronell, O.; Mariñas, B. J.; Watanabe, F.; Cahill, D. G.; Petrov, I., Physico-chemical characterization of NF/RO membrane active layers by Rutherford backscattering spectrometry. *J. Mem. Sci.* 2006, *282*, 71-81.

12. Coronell, O.; Mariñas, B. J.; Zhang, X.; Cahill, D. G., Quantification of functional groups and modeling of their ionization behavior in the active layer of FT30 reverse osmosis membrane. *Environ. Sci. Technol.* 2008, *42*, 5260-5266.

13. Freger, V., Nanoscale heterogeneity of polyamide membranes formed by interfacial polymerization. *Langmuir* 2003, *19*, 4791-4797.

14. Coronell, O.; Mariñas, B. J.; Cahill, D. G., Accessibility and ion exchange stoichiometry of ionized carboxylic groups in the active layer of FT30 reverse osmosis membrane. *Environ. Sci. Technol.* 2009, *43*, 5042-5048.

15. Pourbaix, M., *Atlas of electrochemical equilibria in aqueous solutions.* First English ed.; Pergamon Press: Great Britain, 1966.

16. Mayer, M.; Duggan, J. L.; Morgan, I. L. In *SIMNRA, a simulation program for the analysis of NRA, RBS and ERDA*, Proceedings of the 15th International Conference

on the Application of Accelerators in Research and Industry, Denton, TX, 1998; Denton, TX, 1998; p 541.

17. Mi, B.; Mariñas, B. J.; Cahill, D. G., RBS characterization of arsenic (III) partitioning from aqueous phase into the active layers of thin-film composite NF/RO membranes. *Environ. Sci. Technol.* 2007, *41*, 3290-3295.

18. Hachisuka, H.; Ikeda, K. Reverse osmosis composite membrane and reverse osmosis treatment method for water using the same. US Patent, US 6,413,425 B1, 2002.

19. Tang, C. Y.; Kwon, Y.-N.; J.O., L., Effect of membrane chemistry and coating layer on physiochemical properties of thin film composite polyamide RO and NF membranes I. FTIR and XPS characterization of polyamide and coating layer chemistry. *Desalination* 2009, *242*, (149-167), 149.

20. Tang, C. Y.; Kwon, Y.-N.; Leckie, J. O., Probing the nano- and micro-scales of reverse osmosis membranes-A comprehensive characterization of physiochemical properties of uncoated and coated membranes by XPS, TEM, ATR-FTIR, and streaming potential measurements. *J. Mem. Sci.* 2007, *287*, 146-156.

21. Bargeman, G.; Vollenbroek, J. M.; Straatsma, J.; Schroën, C. G. P. H.; Boom, R. M., Nanofiltration of multi-component feeds. Interactions between neutral and charged components and their effect on retention. *J. Mem. Sci.* 2005, *247*, 11-20.

22. Louie, J. S.; Pinnau, I.; Ciobanu, I.; Ishida, K. P.; Ng, A.; Reinhard, M., Effects of polyether-polyamide block copolymer coating on performance and fouling of reverse osmosis membranes. *J. Mem. Sci.* 2006, *280*, 762-770.

23. Harder, E.; Walters, D. E.; Bodnar, Y. D.; Faibish, R. S.; Roux, B., Molecular dynamics study of a polymeric reverse osmosis membrane. *J. Phys. Chem. B* 2009, *113*, 10177-10182.

24. Kim, S. H.; Kwak, S.-Y.; Suzuki, T., Positron annihilation spectroscopic evidence to demonstrate the flux-enhancement mechanism in morphology-controlled thin-film-composite (TFC) membrane. *Environ. Sci. Technol.* 2005, *39*, 1764-1770.

25. Senapati, S.; Chandra, A., Dielectric constant of water confined in a nanocavity. *J. Phys. Chem. B* 2001, *105*, 5106-5109.

26. Bacarella, A. L.; Grunwald, E.; Marshall, H. P.; Lee Purlee, E., The potentiometric measurements of acid dissociation constants and *p*H in the system methanol-water. $pK_A$ values for carboxylic acids and anilinium ions. *J. Org. Chem.* 1955, *20*, 747-762.

27. Childress, A. E.; Elimelech, M., Effect of solution chemistry on the surface charge of polymeric reverse osmosis and nanofiltration membranes. *J. Mem. Sci.* 1996, *119*, 253-268.

28. Ikeda, K.; Yamamoto, S.; Ito, H. Sulfonated polysulfone composite semipermeable membranes. European Patent, EP 0 165 077 B2, 1998.

29. Vaidya, B.; Soper, S. A.; McCarley, R. L., Surface modification and characterization of microfabricated poly(carbonate) devices: manipulation of electroosmotic flow. *Analyst* 2002, *127*, 1289-1292.

30. Ohshima, H.; Ohki, S., Donnan potential and surface potential of a charged membrane. *Biophys. J.* 1985, *47*, 673-678.

31. Zhang, X.; Cahill, D. G.; Coronell, O.; Mariñas, B. J., Absorption of water in the active layer of reverse osmosis membranes. *J. Mem. Sci.* 2009, *331*, 143-151.

32. Solvay Membranes: Product Information. Available at., http://www.solvayadvancedpolymers.com/products/byproducttype/sulf/0,,53267-2-0,00.htm. (Accessed October 30, 2009).

33. Van Krevelen, D. W., *Properties of Polymers*. 3rd Completely Revised ed.; Elsevier Publishing Company: New York, N.Y., 1990; p 875.

# CHAPTER 5

# DEPTH HETEROGENEITY OF THE ELEMENTAL COMPOSITION, CONCENTRATION OF NEGATIVE CHARGES, DEGREE OF POLYMER CROSSLINKING, AND STERIC EFFECTS IN FULLY AROMATIC POLYAMIDE ACTIVE LAYERS OF REVERSE OSMOSIS AND NANOFILTRATION MEMBRANES

**Abstract:** We studied the depth heterogeneity of fully-aromatic polyamide (PA) active layers in commercial reverse osmosis (RO) and nanofiltration (NF) membranes based on quantitative analyses of the surface (i.e., top ≈6 nm) and average properties of the active layers using X-ray photoelectron spectrometry (XPS) and Rutherford Backscattering spectrometry (RBS), respectively. Results show that while one group of membranes (e.g., ESPA3 RO) had active layers that were depth homogeneous with respect to the concentration of carboxylic groups, degree of crosslinking and concentration of barium ion that associated with ionized carboxylic groups, another group of membranes (e.g., NF90 NF) had active layers that were depth heterogeneous with respect to all properties just mentioned. Additionally, while the p$K_a$ distribution of carboxylic groups and steric effects experienced by $Ba^{2+}$ ion were depth homogeneous in ESPA3 RO membrane, they were depth heterogeneous in NF90 NF membrane. Our study thus provides quantitative results supporting that while some active layers operate as single layers with homogeneous properties, other active layers have a least two distinct sub-layers.

**Key Words:** reverse osmosis, nanofiltration, fully aromatic, polyamide, RBS, XPS, negative charges, steric effects, depth heterogeneity

## 5.1. Introduction

Reverse osmosis (RO) and nanofiltration (NF) membranes have become attractive technologies for water treatment applications because in contrast to conventional treatment processes they are capable of removing a broad range of contaminants within a single treatment step [1]. In RO/NF membranes, water and contaminant transport is mainly controlled by a top ultra-thin (~50–200 nm) selective barrier, commonly referred to as the active layer, that sits on a porous polysulfone support (~50 μm) backed by a non-woven polyester fabric (~200 μm) [2]. The most common material for active layers is polyamide (PA) with its fully-aromatic crosslinked version being the polymer of choice in most RO and many NF membranes [2-4].

PA active layers are produced by the process of interfacial polymerization where, for fully-aromatic PA, *m*-phenylenediamine (MPD) reacts with trimesoyl chloride (TMC) when an organic solvent solution of TMC is brought into contact with a polysulfone support whose surface has been previously wetted with an aqueous solution of MPD [2, 5]. The resulting active layer structure has been proposed to be highly heterogeneous throughout its depth [2, 5-7]. In particular, Wamser et al. [7] showed through contact angle titration studies of active layers prepared in Petri dishes that carboxylic ($R–COO^-$) and amine ($R–NH_3^+$) groups dominated the TMC and MPD sides, respectively. Also, Freger et al. proposed based on a mathematical model describing the kinetics of the interfacial polymerization reaction [6], and on transmission electron microscope (TEM) images of commercial membranes [5], that the carboxylic-rich and amine-rich sub-layers are loosely crosslinked and separated by a densely crosslinked core. Such studies thus

indicate that the properties in the surface of PA active layers, which controls the approach and entrance of water and contaminants into the membrane, are different from the properties in the inner region of the active layer, which controls the subsequent transport of penetrants to the permeate side. As a result, in order to improve and validate existing mathematical models [8-11] describing solute transport through RO/NF membranes, there is a need to characterize the differences in physico-chemical properties and interactions with contaminants between the surface and the inner region of the active layers of commercial RO/NF membranes.

Accordingly, the objectives of this study were to characterize both in the surface and in average throughout the fully-aromatic PA active layers of eight commercial RO/NF membranes their: (i) elemental composition, (ii) concentration of carboxylic groups, (iii) degree of polymer crosslinking, and (iv) concentration of barium ion ($Ba^{2+}$) that associated with $R–COO^-$ groups at pH≈10. Similarly, we also characterized in the active layers of one RO and one NF membrane as a function of pH their: (v) ionization behavior of carboxylic groups; and (v) steric effects experienced by $Ba^{2+}$ ion. To accomplish our objectives, we analyzed membrane samples using X-ray photoelectron spectroscopy (XPS) and Rutherford backscattering spectrometry (RBS) which provided surface and average, respectively, quantitative information about the active layers.

## 5.2. Materials and Methods

***5.2.1. Target Membranes.*** All experiments were performed with coupons (2.5×5.0-$cm^2$) cut from spiral-wound elements or flat sheets of the RO/NF membranes ESPA3 RO, SWC5 RO, ESPAB RO and ESNA NF from Hydranautics (Oceanside, CA), SW30 RO

and NF90 NF from Dow Liquid Separation (Midland, MI), TFC–S NF from Koch Membrane Systems (Wilmington, MA), and LF10 RO from Nitto Denko (Japan). All membranes studied have fully-aromatic polyamide (PA) active layers (see Figure D.1 of the Supporting Information and ref [4] for spectroscopy evidence). While FT30 and LF10 are produced by the manufacturers with a hydrophilic, nitrogen-free coat on top of their active layers [4, 12, 13], none of the other membranes have a coat (see Figure D.2 of the Supporting Information and ref [4]). Prior to sample preparation, membrane coupons were always thoroughly rinsed with and stored in nanopure water from a Barnstead D4741 nanopure deionization system (Barnstead/Thermolyne Corp., Dubuque, IA) as detailed in our previous work [14]. All experiments were performed at room temperature (20–22$^{o}$C), and a minimum of two replicates were prepared for each experimental condition (see Table 5.1 for details). In general, after sample preparation by any of the procedures described below, a 2.5×1-cm$^2$ piece was carefully cut from each sample for XPS analyses while the rest of the sample was used for RBS analyses.

***5.2.2. Ion-Probe Solutions and Chemicals.*** All ion-probe solutions were prepared with nanopure water and A.C.S. grade chemicals with 99%+ purity. Silver nitrate ($AgNO_3$) from Sigma-Aldrich (St. Louis, MO) and barium chloride dihydrate ($BaCl_2{\cdot}2H_2O$) from Fisher Scientific (Hampton, NH) were used as sources of silver ($Ag^+$) and barium ($Ba^{2+}$) ions, respectively, in probing experiments. Barium nitrate ($Ba(NO_3)_2$) from Sigma-Aldrich (St. Louis, MO) was used instead of $BaCl_2{\cdot}2H_2O$ in $Ag^+$–$Ba^{2+}$ displacement tests to avoid precipitation of silver salts. (We showed in our previous work [14] that the anion of the barium salt does not affect the concentration of $Ba^{2+}$ that associates with accessible ionized carboxylic groups (R–$COO^-$) in PA active layers.) The concentrations

**Table 5.1.** Summary of results from XPS, RBS, $Ag^{+}$-probing//XPS/RBS, and AFM analyses of the un-coated membranes ESPA3 RO, SWC5 RO, TFC–S NF, ESNA NF, NF90 NF, and ESPAB RO, and the coated membranes FT30 RO and LF10 RO. Uncertainties represent standard deviation[a] between samples tested.

| **Membrane** | | **ESPA3** | **SWC5** | **TFC–S** | **ESNA** | **ESPAB** | **NF90** | **FT30** [b] | **LF10** [b] |
|---|---|---|---|---|---|---|---|---|---|
| Rating [c] | | BW RO | SW RO | NF | NF | BW RO | NF | SW RO | BW RO |
| Coated? | | No | No | No | No | No | No | Yes | Yes |
| %C | XPS [i] | 74.16±0.40 | 77.82±0.59 | 73.04±0.92 | 73.64±0.74 | 73.60±0.64 | 76.00±0.45 | 70.97±1.57 | 77.92±2.83 |
| | RBS [i] | 71.57±1.13 | 72.67±1.29 | 72.46±0.42 | 71.79±0.70 | 73.66±1.50 | 74.20±1.85 | 70.99±1.20 | 71.11±1.49 |
| | XPS2 [j] | 74.27±1.02 | - | - | - | 73.86±0.86 | - | - | - |
| %O | XPS [i] | 13.92±0.46 | 11.27±0.74 | 15.17±0.85 | 13.71±0.54 | 15.61±0.59 | 13.34±0.20 | 26.25±1.73 | 20.21±2.77 |
| | RBS [i] | 14.16±0.50 | 12.99±0.51 | 13.92±0.14 | 13.16±0.41 | 13.08±0.70 | 13.16±0.86 | 17.43±0.39 | 18.14±1.02 |
| | XPS2 [j] | 14.21±0.80 | - | - | - | 15.24±0.88 | - | - | - |
| %N | XPS [i] | 11.08±0.08 | 10.32±0.31 | 10.91±0.28 | 11.33±0.23 | 10.69±0.13 | 10.58±0.23 | 2.77±1.72 | 1.68±0.22 |
| | RBS [i] | 12.95±0.66 | 12.81±0.66 | 12.43±0.32 | 13.13±0.43 | 13.07±0.89 | 12.40±1.07 | 11.49±0.59 | 9.33±0.61 |
| | XPS2 [j] | 10.71±0.41 | - | - | - | 10.82±0.29 | - | - | - |
| %Cl | XPS [i] | 0.84±0.04 | 0.59±0.06 | 0.88±0.11 | 1.32±0.06 | 0.11±0.03 | 0.08±0.10 | 0.01±0.04 | 0.19±0.03 |
| | RBS [i] | 1.33±0.11 | 1.53±0.08 | 1.19±0.09 | 1.92±0.06 | 0.19±0.06 | 0.24±0.06 | 0.09±0.02 | 1.42±0.03 |
| | XPS2 [j] | 0.81±0.08 | - | - | - | 0.08±0.05 | - | - | - |
| O:N ratio [d] | XPS [i] | 1.26±0.04 | 1.09±0.09 | 1.39±0.07 | 1.21±0.05 | 1.46±0.07 | 1.26±0.03 | 16.26±14.29 | 12.15±2.11 |
| | RBS [i] | 1.10±0.05 | 1.01±0.02 | 1.12±0.02 | 1.00±0.003 | 1.00±0.04 | 1.06±0.06 | 1.52±0.05 | 1.95±0.08 |
| | XPS2 [j] | 1.33±0.09 | - | - | - | 1.41±0.10 | - | - | - |
| $\%R-COO^{-}$ [e] | XPS [k] | 0.69±0.02 | 0.42±0.04 | 0.54±0.09 | 0.52±0.03 | 0.43±0.01 | 0.57±0.01 | 0.24±0.07 | 0.32±0.05 |
| | RBS [l] | 0.71±0.01 | 0.41±0.001 | 0.55±0.01 | 0.54±0.004 | 0.23±0.02 | 0.43±0.01 | 0.48±0.02 | 0.53±0.01 |
| $\frac{\%R-COO^{-}}{\%N}$ | XPS [k] | 0.063±0.002 | 0.040±0.003 | 0.049±0.008 | 0.046±0.003 | 0.040±0.001 | 0.054±0.001 | 0.092±0.048 | 0.178±0.013 |
| | RBS [l] | 0.054±0.004 | 0.031±0.001 | 0.043±0.002 | 0.042±0.000 | 0.018±0.003 | 0.034±0.005 | 0.040±0.003 | 0.059±0.006 |
| $DPC_{pH\approx10}$ [f] | XPS [k] | 94.1±0.15 | 96.2±0.30 | 95.3±0.71 | 95.6±0.29 | 96.1±0.11 | 94.9±0.05 | 91.7± 3.89 | 84.9±0.95 |
| | RBS [l] | 94.9±0.34 | 97.0±0.07 | 95.9±0.13 | 96.0±0.02 | 98.3±0.27 | 96.7±0.36 | 96.2±0.20 | 94.4±0.46 |
| $n$ [g] | XPS [k] | 0.62±0.01 | 0.76±0.02 | 0.70±0.05 | 0.73±0.02 | 0.76±0.01 | 0.68±0.003 | 0.45±0.29 | 0.00±0.08 |
| | RBS [l] | 0.68±0.02 | 0.81±0.005 | 0.74±0.01 | 0.75±0.001 | 0.89±0.02 | 0.79±0.02 | 0.76±0.01 | 0.64±0.02 |
| $x$ [g] | XPS [k] | 0.38±0.01 | 0.24±0.02 | 0.30±0.05 | 0.27±0.02 | 0.24±0.01 | 0.32±0.003 | 0.55±0.29 | 1.00±0.08 |
| | RBS [l] | 0.32±0.02 | 0.19±0.005 | 0.26±0.01 | 0.25±0.001 | 0.11±0.02 | 0.21±0.02 | 0.24±0.01 | 0.36±0.02 |
| $R_{rms}$ [h] (nm) | | 77.3±19.6 | 100±0.7 | 21.8±0.7 | 43.3±2.8 | 140.3±33.9 | 58.2±2.8 | 75.5±3.8 | 71.1±11.8 |

Notes for Table 5.1:

[a] For experimental conditions where only duplicates (A and B) were run, the standard deviation was calculated as the difference between either A or B and their average value.

[b] We previously reported [4] the PA active layers of FT30 RO and LF10 RO to have coats of approximate composition and thickness $C_{0.32}O_{0.12}H_{0.56}$ and 25±35 nm, and $C_{0.28}O_{0.12}H_{0.60}Cl_{0.001}$ and 58±33 nm, respectively.

[c] RO: reverse osmosis; NF: nanofiltration; BW: brackish water; SW: seawater

[d] Average O:N ratios were calculated as the average between the O:N ratios of the replicates (not as the ratio between their average %O and the average %N).

[e] $\%R{-}COO^- = \%Ag$ values were measured at pH≈10.

[f] $DPC \approx DPC_{pH\approx10}$ was calculated from Equation 5.4 using the $\%R{-}COO^- / \%N$ values at pH≈10 shown in this table.

[g] *n* and *x* represent the fraction of fully-aromatic polyamide repeating units that are fully crosslinked, and that contain a carboxylic group, respectively, and were calculated assuming that the concentration of amine groups in the active layer is negligible compared to that of carboxylic groups (i.e., $n + x = 1$).

[h] The root mean square roughness ($R_{rms}$) value for each membrane is the average of at least two replicates, each of which was obtained by scanning a 10×10-$\mu m^2$ area with an Atomic Force Microscope (AFM) in tapping mode. In particular, five replicates were obtained for brackish water RO membranes ESPA3 and ESPAB whose roughness was found to be highly dependent on the location of the spot analyzed.

[i] Values in this row are the average of 4–6 replicates (i.e., total analysis area of 0.15–0.23 $mm^2$ and 32–48 $cm^2$ for XPS and RBS analyses, respectively).

[j] Values in this row are the average of 50 replicates (i.e., total analysis area of 1.90 $mm^2$).

[k] Values in this row are the average of 4 replicates (i.e., total analysis area of 0.15 $mm^2$).

[l] Values in this row are the average of 2–3 replicates (i.e., total analysis area of 16–24 $cm^2$).

of silver ($10^{-6}$–$10^{-3}$ M) and barium ($10^{-6}$–0.32 M) in solution were always below their solubility limit [15, 16]. The pH of ion-probe solutions during $Ba^{2+}$-probing experiments was adjusted to the desired value by addition of HCl or NaOH. For all other experiments, $HNO_3$ was used instead of HCl. Silver solutions were prepared and used under dim red light to avoid photoreactivity.

***5.2.3. Ion Probing with Silver ($Ag^+$) and Barium ($Ba^{2+}$).*** Ion probing with $Ag^+$ and $Ba^{2+}$ was performed to study the concentration of $R–COO^-$ groups and the concentration of $Ba^{2+}$ that associates with accessible $R–COO^-$ groups, respectively, in the active layers studied. Extensive details on sample preparation procedures for ion-probing tests can be found elsewhere [12, 14]. In brief, for the case of $Ag^+$-probing, rinsed coupons were immersed three times, each time for ≈10 minutes, in concentrated $AgNO_3$ solution at the pH of interest. The purpose of this first round of immersions was to saturate $R–COO^-$ groups with $Ag^+$ ions. Next, four consecutive ≈7-min immersions were performed in dilute $AgNO^3$ $10^{-6}$ M solution at the same pH of the saturation step with the purpose of bringing below the detection level of our sample analysis procedures the concentration of $Ag^+$ ions not ionically associated with $R–COO^-$ groups. Then, the samples were dried by applying fingertip pressure between two qualitative-grade filter-papers, and air-dried at room temperature for ≥24 h. Ion-probing with $Ba^{2+}$ was performed in a similar fashion to ion probing with $Ag^+$, but using $BaCl_2$ as ion-probe solution. Samples of all membranes studied were probed with $Ag^+$ and $Ba^{2+}$ at pH ≈ 10. Additionally, samples of ESPA3 RO and NF90 NF were probed in the pH range 3.43–10.33.

***5.2.4. $Ag^{+}$–$Ba^{2+}$ Displacement Tests.*** Ion-displacement tests in which $Ag^{+}$ ions were initially used to saturate R–$COO^{-}$ groups, and $Ba^{2+}$ ions were subsequently used to displace $Ag^{+}$ ions, were employed to study the stoichiometry of association between $Ba^{2+}$ ion and R–$COO^{-}$ groups in the active layer of ESPA3 RO membrane. Extensive details on sample preparation procedures for ion-displacement tests can be found elsewhere [14]. In brief, sample preparation resembled that of ion probing with $Ba^{2+}$ with the difference that before the first round of immersions in $Ba^{2+}$-probing solution, the membrane coupons were immersed three times, each time for ≈10 minutes, in concentrated $AgNO_3$ solution. While the concentration of $Ag^{+}$ ion displaced from the active layer ($\Delta[Ag^{+}]$) provided the concentration of sites neutralized by $Ba^{2+}$, the concentration of $Ba^{2+}$ neutralizing those sites was given by the $Ba^{2+}$ concentration ($[Ba^{2+}]$) after ion displacement. Accordingly, the stoichiometry of association between R–$COO^{-}$ groups and $Ba^{2+}$ ion at a concentration $\Delta[Ag^{+}]$ of neutralized sites was calculated as NN = $\Delta[Ag^{+}]/[Ba^{2+}]$ where NN is referred to as the neutralization number. $Ag^{+}$–$Ba^{2+}$ displacement tests were performed in the pH range 8.02–10.33.

***5.2.5. XPS Analyses.*** We analyzed membrane samples with XPS to quantify their surface elemental composition including the surface elemental fraction of ion probe(s). For illustrative purposes, we present in Figure D.3 in Supporting Information, for a sample of ESPA3 RO membrane used in $Ag^{+}$–$Ba^{2+}$ displacement tests, the XPS signal of chlorine (Cl2p) which to the best of our knowledge had only been detected by XPS analyses in chlorine-treated membranes [17], and the signals of silver (Ag3d) and barium (Ba3d) which we used as ion probes. Prior to XPS analysis, samples were vacuum-dried

for ≈72 hours. XPS analyses were performed with a Kratos AXIS Ultra photoelectron spectrometer (Kratos Analytical, England) employing a Mg Kα X-ray source (1,253.6 eV) with high voltage and emission current of 15kV and 7mA, respectively, and a $90^{o}$ take-off angle. Membrane samples were mounted on the sample holder of the spectrometer chamber using double-sided carbon tape. Sample charging was minimized using a charge neutralizer operating with filament current, bias and charge balance of 1.8 A, 2.54 V and 1 V, respectively. For each sample analyzed, we averaged four survey scans in the 0–1,100 eV binding energy range with a resolution of 1 eV and pass energy of 160 eV. High resolution scans of the carbon (C1s), oxygen (O1s), nitrogen (N1s), chlorine (Cl2p), silver (Ag3d), and barium (Ba3d) signals allowed the quantification of the corresponding elemental fractions, and were performed with pass energy of 40 eV and resolution of 0.1 eV. Data was collected from a circular area with a diameter of 0.22 mm (0.04 $mm^2$). Based on our experimental settings, it can be shown (see Section D.1 in Supporting Information) that ≈95% of the XPS signal was collected from within ≈6 nm of the membrane sample surface or less.

***5.2.6. RBS Analyses.*** RBS is a thin-film analytical technique [18] with sufficient depth resolution to discern the active layer of RO/NF membranes from their polysulfone support [4, 12, 19, 20], and accordingly, we used it to quantify the average elemental composition throughout the active layer including the average concentration of ion probe(s) in it. For the coated membranes FT30 RO and LF10 RO, the RBS results reported in this study describe the PA active layer having already taken into account that there exists a coat on top of it. Accordingly, for all membranes studied, the differences between XPS and RBS results provide a quantitative description of the differences

between the properties in the surface of the membrane and the average properties throughout the active layer; however, only in uncoated membranes these differences are attributed to depth heterogeneity in the PA active layer. Details on RBS experimental procedures and data analysis were reported in our previous work [14]. In brief, we mounted each sample on the RBS chamber sample holder using a double-sided conductive tape. Next, a 2-MeV $He^+$ beam, with a diameter of 3 mm, generated with a Van de Graaff accelerator (High Voltage Engineering Corp., Burlington, MA) was scanned over ≈8 $cm^2$ of the sample surface keeping the $He^+$ ion fluence under $1.5\times10^{14}$ $He^+/cm^2$ to avoid compromising the integrity of the polymer structure [21]. The incident, exit and scattering angles of the $He^+$ beam were $22.5^o$, $52.5^o$ and $150^o$, respectively. The commercial software SIMNRA® [18] was used for raw data analysis. The RBS results for ESPA3 RO and NF90 NF have been reproduced from our previous studies [4] in order to compare them to their corresponding XPS results. All other RBS results were obtained for this study.

***5.2.7. AFM Analyses.*** AFM analyses were performed to characterize the surface roughness of the membranes studied. Samples consisted of virgin membrane coupons rinsed with and stored in nanopure water, and air-dried for ≈48 hours. An MFP-3D AFM from Asylum Research (Santa Barbara, CA) equipped with Tap300Al tips from BudgetSensors (Sofia, Bulgaria) was used in tapping mode to scan at least two areas of $10\times10$ $\mu m^2$ on the surface of each membrane. Surface roughness was reported as root-mean-square roughness ($R_{rms}$) and was calculated as reported elsewhere [22].

## 5.3. Results and Discussion

***5.3.1. Elemental Composition.*** Table 5.1 shows the average elemental compositions obtained by XPS and RBS analyses. Elemental percentages shown in the table include chlorine which was previously [4, 12] shown to be present in the PA active layers of commercial RO/NF membranes, and exclude hydrogen because XPS spectra do not have a hydrogen signal nor are affected by the hydrogen content of the sample. Values in rows labeled "XPS" and "RBS" correspond to the average ± standard deviation of 4–6 replicates, and values in rows labeled "XPS2" correspond to average ± standard deviation of 50 replicates. In particular, four replicates were used in the rows labeled "XPS" for ESPA3 RO and NF90 NF. As shown in the table, there was no significant difference between the elemental compositions obtained with 4 replicates and those obtained with 50 replicates, thus indicating that a relatively low number of replicates by XPS analyses were sufficient to provide a representative elemental composition of the surface of uncoated membranes.

We focus our attention on the nitrogen and chlorine contents, and the O:N ratio, which are directly related to the content of amide links, and therefore to the PA structure [2]. Table 5.1 shows that for uncoated membranes the nitrogen content measured in the surface by XPS was 14–20% lower than the corresponding average value throughout the active layer measured by RBS. Similarly, even though the oxygen contents measured by XPS and RBS did not show any specific trend, the O:N ratio measured by XPS was 8–46% higher than the value measured by RBS. Given that in PA active layers the nitrogen content contributed by amine groups is ≤1% of the total nitrogen [4, 12], the

lower nitrogen content (and higher O:N ratios) obtained by XPS indicate a reduced surface concentration of amide links.

The combination of previous results [4, 12, 20] indicating that the chlorine content in the PA active layers of commercial RO/NF membranes is not of ionic nature, the results in Table 5.1 showing higher nitrogen and chlorine contents in the surface of the PA active layers, and results in the literature from studies on the effect of chlorination on PA active layers [2, 23-25] indicate that permanently-bound chlorine in the PA active layers of as-sold membranes may be the result of a controlled treatment with hypochlorite by the manufacturer. It has been reported [2, 23, 24] that chlorination of PA results in chlorine substitution of the amidic hydrogen and/or chlorine addition to the meta and ortho positions in the nitrogen benzene rings. Additionally, when performed at relatively high pH values (pH~9) and at the appropriate chlorine concentration and exposure time (~100 ppm·h), chlorination increases water flux without significant loss of salt rejection [24, 25]. Accordingly, if manufacturers chlorinated their membranes to improve performance, regions in the active layers with lower concentrations of amide links would acquire lower concentrations of permanently-bound chlorine atoms, which is consistent with our XPS and RBS measurements showing lower nitrogen and chlorine contents in the surface of all uncoated membranes. Consequently, both the nitrogen and chlorine results for uncoated membranes in Table 5.1 support the fact that the concentration of amide links in the surface of fully-aromatic PA active layers is lower than the corresponding average value throughout their depth.

For the coated FT30 RO and LF10 RO membranes, we attribute the relatively higher standard deviations obtained by XPS analyses, when compared to those obtained for

uncoated membranes, to the un-even thicknesses of their coat layers. We previously reported [4] that the coats of FT30 and LF10 have approximate thicknesses 25±35 nm and 58±33 nm, respectively. The significantly high standard deviations of the thicknesses of the coats indicate that while some areas of the PA active layers are covered by the coat, some are not, which is also observed in the transmission electron microscope (TEM) images of the coated BW30 RO membrane reported by Tang et al. [13]. The presence of the coat and the un-even coverage it provides therefore results in (i) a relatively high variability of the membrane surface composition [13], (ii) significantly lower surface content of nitrogen and chlorine, and (iii) significantly higher surface O:N ratio (see Table 5.1). The higher variability of the surface nitrogen content for FT30 compared to the corresponding variability for LF10 is consistent with the thicker coat of LF10; a thicker coat likely ensures a more even coverage of the PA active layer.

***5.3.2. Concentration of Ionized R–COO$^-$ Groups.*** In our previous studies [4, 12] we measured the average concentration of ionized carboxylic groups in the PA active layers of RO/NF membranes by probing the R–COO$^-$ groups with $Ag^+$ ion, and quantifying the resulting $Ag^+$ content ([$Ag^+$]) in the active layer by RBS. It was considered that the measured [$Ag^+$] equaled [R–COO$^-$] based on: (i) the one-to-one correspondence between $Ag^+$ and R–COO$^-$ because of their monovalence, and (ii) the fact that $Ag^+$ ion is smaller than the smallest pores in PA active layers [12]. In this study, we used the $Ag^+$-probing procedure at pH≈10 together with XPS and RBS analyses to quantify the content of ionized carboxylic groups (%R–COO$^-$ = %Ag) both in the membrane surface and in average throughout the active layers. We chose pH≈10 for sample preparation based on

our previous research [4, 12] that showed that at pH=10, 93–100% of the carboxylic groups were ionized in the membranes studied, with the exception of those in the NF90 NF membrane in which the degree of ionization was 84%. Accordingly, performing $Ag^+$-probing/XPS/RBS experiments at pH≈10 allowed us not only to characterize the depth heterogeneity of carboxylic groups in the active layers, but also to quantify the approximate total content of carboxylic groups in them.

The results for the content of R–$COO^-$ groups are presented in Table 5.1 as elemental fractions, and in Figure 5.1a as molar concentrations calculated using Equation 5.1, where $\varepsilon_i^{'}$, $M_i$, and $\rho_{PA}$ = 1.24 g/cm$^3$ [26] are the elemental fraction excluding hydrogen of element i, molar mass of element i, and dry density of polyamide, respectively, and the subscripts Ag, C, and H indicate silver, carbon and hydrogen, respectively. The derivation of Equation 5.1 is presented in Section D.2 in Supporting Information. The results show that for uncoated membranes the content of R–$COO^-$ groups in the active layer was depth heterogeneous in two of them (i.e., ESPAB RO and NF90 NF) with an R–$COO^-$ content more than 33% higher in the active layer surface, but depth homogeneous in the other four (i.e., ESPA3 RO, SWC5 RO, TFC–S NF, and ESNA NF). As a result, even though the results in the preceding section showed that PA active layers had in general lower nitrogen content indicating lower surface concentrations of amide links, this did not translate for some membranes in a corresponding depth heterogeneity of the concentration of carboxylic groups. For coated membranes, all the charge density detected was attributed to the R–$COO^-$ groups of the PA active layer based on reports [2, 27] indicating that coat layers are made of non-ionic polymers. The measured surface

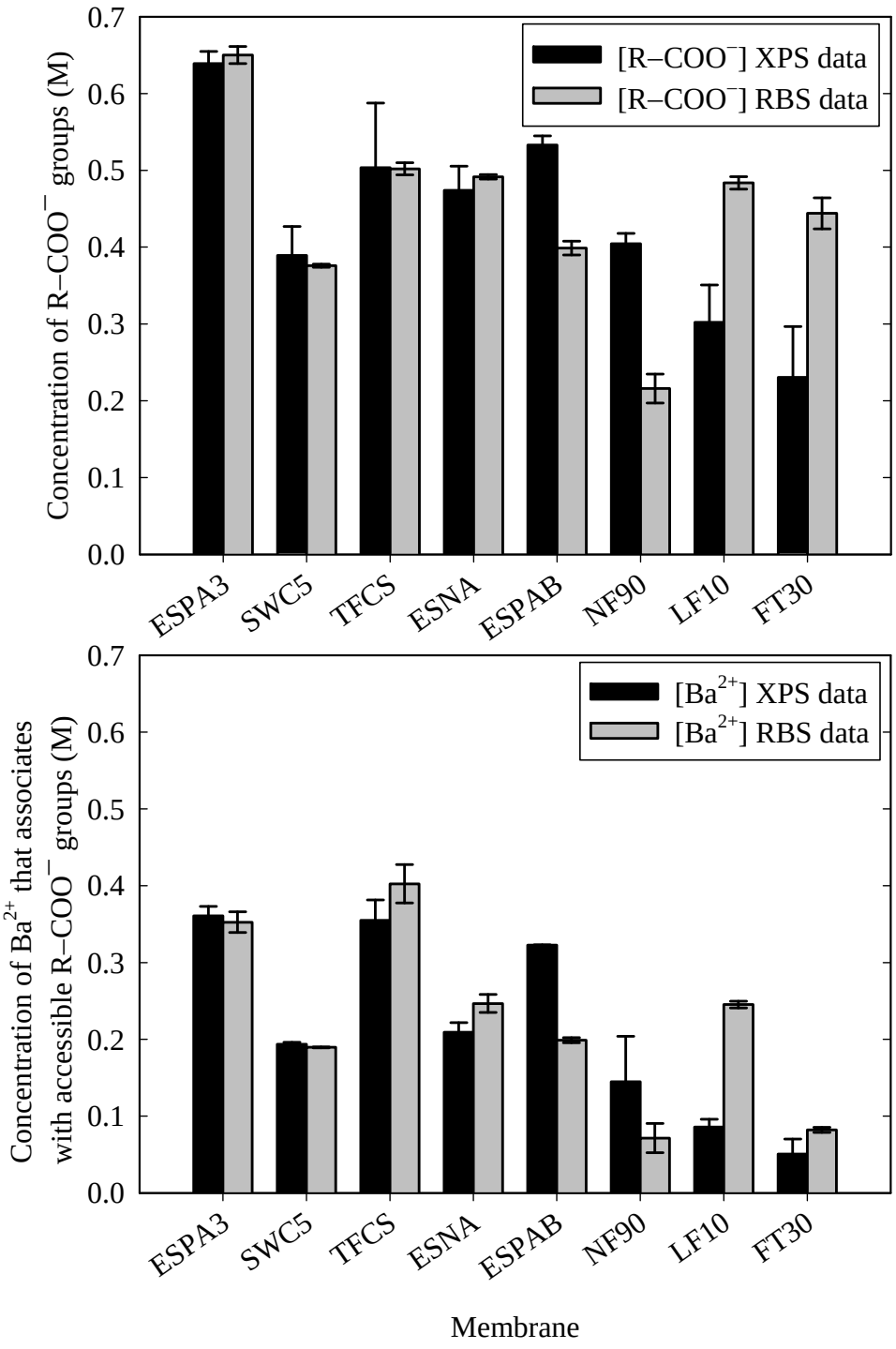


**Figure 5.1.** Concentrations of (a) ionized carboxylic groups ([R–COO$^-$]) and (b) barium ions ([$Ba^{2+}$]) that associate with them at pH ≈ 10 at the surface (i.e., XPS data, solid bars) of the polyamide active layers of eight commercial RO/NF membranes and in average throughout the active layer depth (i.e., RBS data, open bars). Error bars indicate standard deviation.

charge then indicates that the R–$COO^-$ content in the surface was more than 40% lower than the average content in the PA active layer, which is explained by the uneven coverage that the coats provides to the PA active layers (see discussion above).

$$[R-COO^-] = \varepsilon'_{Ag} \times \frac{\rho_{PA}}{\sum_{C,O,N,Cl}\left(\varepsilon'_i \times M_i\right) + 0.67 \times \varepsilon'_C \times M_H} \quad (5.1)$$

Given that 95% of the silver signal in our XPS analyses comes from within ≈3 nm of the membrane surface or less (see Section D.1 of Supporting Information), and that the electric exclusion of ionic contaminants approaching a charged film permeable to them is determined by the charge density within the top ≈2 nm of the film [28], then our results provide quantitative evidence that in some PA active layers the surface region that controls the electric exclusion of ionic contaminants may have a different charge density than the average value throughout the active layer.

***5.3.3. Ionization Behavior of Carboxylic Groups.*** We studied by XPS and RBS the content of ionized carboxylic groups as a function of pH in ESPA3 RO and NF90 NF membranes which, as discussed above, showed to be depth homogeneous and depth heterogeneous, respectively, at pH≈10. While the XPS data was obtained for this study, the RBS data was reproduced from our previous studies [4]. The results in Figure 5.2 reveal that, consistent with the $Ag^+$-probing results at pH≈10, the concentration of ionized sites was consistently depth homogeneous and depth heterogeneous for ESPA3 RO and NF90 NF, respectively, across the pH range studied, thus confirming that there exists both depth homogeneous and depth heterogeneous PA active layers with respect to the concentration of carboxylic groups. The results also confirm that depth heterogeneity

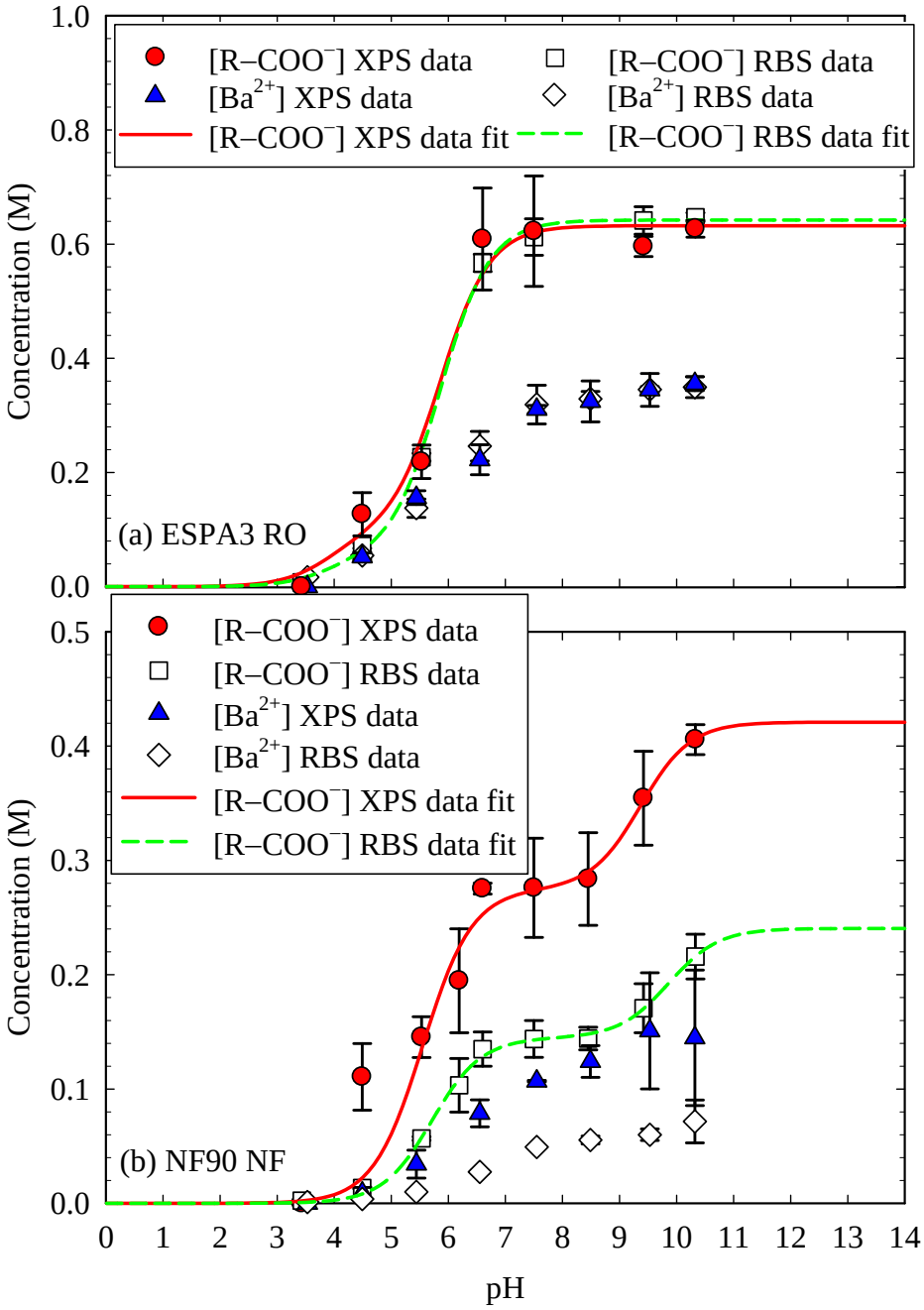


**Figure 5.2.** Concentrations of ionized carboxylic groups ([R–COO$^-$]) and barium ions ([$Ba^{2+}$]) that associate with them as a function of pH at the surface (i.e., XPS data, solid symbols) of the polyamide active layers of (a) ESPA3 RO and (b) NF90 NF membranes and in average throughout the active layers depth (i.e., RBS data, open symbols). Error bars indicate standard deviation. (Red) Continuous and (green) dashed lines represent the fit to Equation 5.2 of the XPS and RBS data, respectively, for the concentration of ionized carboxylic groups. XPS data was obtained for this study. RBS data was reproduced from our previous work [4].

of the nitrogen content in PA active layers does not necessarily imply depth heterogeneity of the concentration of ionizable sites. It is difficult to explain why this is so, as limited information is provided by manufacturers about the protocols used to produce their proprietary PA active layers.

We also fitted to Equation 5.2 [4] the XPS and RBS data for the concentration of $R–COO^-$ groups as a function of pH in ESPA3 RO and NF90 NF membranes to study the depth variability of the total concentration ($C_{T,R–COOH}$) and p$K_a$ distribution of carboxylic groups. In Equation 5.2, $w_i$ represents the fraction of carboxylic groups with p$K_a$ = p$K_{a,i}$, where $\sum w_i = 1$. The values of the fitted parameters are presented in Table 5.2, and the corresponding fitted lines are shown in Figure 5.2. The fitted parameters for the RBS data were reproduced from our previous study [4]. The results show that two p$K_a$ values were needed to describe the ionization behavior of carboxylic groups in accordance with our previous work [4, 12], and with the bimodal pore size distribution reported in the literature for PA active layers [29-31]; the dielectric constant of water both depends on the size of the nanopores where water is contained [32], and affects the p$K_a$ of carboxylic groups [33], and therefore a bimodal p$K_a$ distribution is consistent with a bimodal pore size distribution. Nevertheless, the relatively low $w_1$ value, and relatively high standard error of the fitted $w_1$ and p$K_{a,1}$ parameters for both the XPS and RBS data in the ESPA3 RO membrane indicate a pore size distribution heavily biased towards one value, which has been shown to occur [31] in the production of high-flux PA membranes, of which ESPA3 RO is an example, when additives such as dimethyl sulfoxide (DMSO) are used during the interfacial polymerization reaction to increase the miscibility of the aqueous amine and organic acyl-chloride phases.

**Table 5.2.** Fitted parameters for the modeling of the concentration of R–$COO^-$ groups measured by $Ag^+$-probing/XPS/RBS analyses in the polyamide (PA) active layers of the ESPA3 RO and NF90 NF membranes as a function of pH. Uncertainties indicate standard error. RBS results were reproduced from our previous studies [4].

| Membrane | | $C_{T,R-COOH}$ | $pK_{a,1}$ | $w_1$ | $pK_{a,2}$ | $w_2$ |
|---|---|---|---|---|---|---|
| ESPA3 RO | XPS | 0.63±0.03 | 3.91±1.95 | 0.14±0.22 | 5.86±0.35 | 0.86±0.22 |
| | RBS | 0.64±0.01 | 3.91±1.06 | 0.08±0.07 | 5.86±0.10 | 0.92±0.07 |
| NF90 NF | XPS | 0.42±0.03 | 5.55±0.13 | 0.65±0.05 | 9.37±0.36 | 0.35±0.05 |
| | RBS | 0.24±0.02 | 5.72±0.06 | 0.60±0.04 | 9.87±0.23 | 0.40±0.04 |

As expected from the depth homogeneous R–$COO^-$ content as a function of pH obtained for the ESPA3 RO membrane, the $C_{T,R-COOH}$ and $pK_a$ distribution of carboxylic groups were also depth homogeneous in its active layer. In contrast, for NF90 NF, the $C_{T,R-COOH}$ was ≈1.75 times larger in the surface of the active layer than the corresponding average value throughout the active layer depth. Additionally, both $pK_a$ values were lower at the active layer surface, and the surface fraction $w_1$ of carboxylic groups with the lower $pK_a$ value ($pK_{a,1}$) increased. Consistent with the discussion above on the relation between pore size, water dielectric constant and $pK_a$ values, while the results for ESPA3 RO suggest that a relatively invariant pore size distribution exists throughout its active layer, the results for NF90 NF indicate that relatively larger pores exist in its active layer surface compared to in average throughout the active layer depth.

$$[R-COO^-] = C_{T,R-COOH}\sum_{i=1}^{n}\left(w_i \times \frac{10^{-pKa,i}}{10^{-pH}+10^{-pKa,i}}\right) \quad (5.2)$$

***5.3.4. Degree of Polyamide Crosslinking.*** We used the nitrogen and R–$COO^-$ content at pH≈10, measured by XPS and RBS analyses, to quantify the depth heterogeneity of the

degree of polyamide crosslinking. In our previous studies [4, 12], we proposed Equation 5.3 as a quantitative descriptor of the degree of polymer crosslinking (DPC) defined as the ratio between the measured concentration of amide links and the concentration of amide links in an equivalent fully-crosslinked active layer. In Equation 5.3, N, AG and CG represent the content of nitrogen, amine groups and carboxylic groups, respectively, in the active layer. Consistent with our previous results [4] that showed that AG<<N, we have simplified Equation 5.3 to Equation 5.4, where CG/N = %R–$COO^-$ / %N, and in which we have used the %R–$COO^-$ at pH≈10 to calculate an approximate DPC ($DPC_{pH\approx10}$) in the active layers studied. The calculated DPC as defined by Equations 5.3 and 5.4 takes into account only elements present in the PA active layer, and not in the polysulfone support or coat layers. As a result, the surface DPC calculated for coated membranes already accounts for the presence of the coat, and thus describes the DPC of the polyamide surface.

The DPC results presented in Table 5.1 show that: (i) for uncoated membranes that were depth homogeneous with respect to the content of R–$COO^-$ groups, the $DPC_{pH\approx10}$ values obtained by XPS and RBS were only 0.4–0.8% units different; (ii) for uncoated membranes that were depth heterogeneous with respect to the content of R–$COO^-$ groups, the $DPC_{pH\approx10}$ obtained by XPS was 1.8–2.2% units lower than that obtained by RBS; and (iii) coated membranes showed the greatest depth heterogeneity in crosslinking with XPS results being 4.5–9.5% units lower than RBS results. In particular, the fact that the active layer of ESPA3 RO showed a lower DPC difference (0.8±0.4%) between XPS and RBS results than the active layer of NF90 NF (1.8±0.4%) is consistent with the fact

that ESPA3 RO is the membrane with a depth homogeneous p$K_a$ distribution (which suggests a depth homogeneous pore size distribution), and NF90 NF is the membrane with surface p$K_a$ values lower than the average p$K_a$ values throughout the active layer (which suggests relatively larger pores in the active layer surface).

$$\mathrm{DPC} = \frac{\text{Amide links}}{\text{Potential amide links}} = \frac{\mathrm{N} - \mathrm{AG}}{\mathrm{N} + \mathrm{CG}} \tag{5.3}$$

$$\mathrm{DPC} \approx \frac{1}{1 + \mathrm{CG/N}} \tag{5.4}$$

The degree of crosslinking in the active layers can also be described in terms of the fractions of polymer repeating units *n*, *x* and *y* in the PA structure that are fully crosslinked $(C_{36}H_{24}N_6O_6)_n$, that contain a carboxylic group $(C_{36}H_{25}N_6O_7)_x$ and that contain an amine group $(C_{36}H_{25}N_6O_6)_y$, respectively [4, 12]. The values of the *n*, *x*, and *y* fractions are more sensitive to the content of functional groups in the active layer than the DPC parameter, and therefore, expose more easily differences in degrees of crosslinking. Given that the concentration of amine groups is negligible, we assumed $y \approx 0$, and calculated *n* and *x* using the relations $x = 6 \times \mathrm{CG/N}$, and $n + x = 1$ with the information in Table 5.1. In agreement with the DPC results, the fraction *n* of fully-crosslinked polymer repeating units in the polyamide surface is lower than the corresponding average value throughout the active layer, with the lowest difference between XPS and RBS results occurring for the uncoated membranes that were depth homogeneous with respect to the content of $R{-}COO^-$ groups, and the greatest difference occurring for coated membranes.

***5.3.5. Surface Roughness.*** Table 5.1 presents the root-mean-square roughness ($R_{rms}$) values obtained from atomic force microscopy (AFM) analyses of the surfaces of the membranes studied. A representative AFM image of each membrane is presented in Figure D.4 of Supporting Information. The results show that there is no correlation between roughness and depth heterogeneity of any of the active layer properties studied.

***5.3.6. Steric Effects Experienced by Barium ($Ba^{2+}$) Ion.*** The depth heterogeneity of the steric effects experienced by $Ba^{2+}$ ion in the active layers of ESPA3 RO and NF90 NF membranes were characterized by quantifying the fraction AR of ionized carboxylic groups accessible to $Ba^{2+}$ as a function of pH, both in the active layer surface and in average throughout the active layers. The fraction AR was calculated using Equation 5.5, where $[Ba^{2+}]$ is the concentration of barium ion that associates with the accessible ionized carboxylic groups ($AR\times [R–COO^-]$), and NN is the average stoichiometry of association between $R–COO^-$ groups and $Ba^{2+}$ ion calculated using Equation 5.6 for $AR\times [R–COO^-] \geq a$, otherwise NN = 1. $[Ba^{2+}]$ and NN were obtained from $Ba^{2+}$-probing and $Ag^+–Ba^{2+}$ displacement tests, respectively, followed by XPS and RBS analyses of the prepared samples. While the XPS data was obtained for this study, the RBS data has been reproduced from our previous work [4]. The analysis of the $Ag^+–Ba^{2+}$ displacement data for the calculation of NN as a function of pH was done as detailed elsewhere [4], and is briefly described in Figure D.5 of Supporting Information. For ESPA3 RO, in Equation 5.6, $a = 0.13\pm0.01$ M and $a = 0.14\pm0.01$ M [4] for the XPS and RBS analyses, respectively. For NF90 NF, NN = 1.98±0.20 (i.e., $a \approx 0$) in all the pH range studied [4].

Results for the ESPA3 RO membrane in Figures 5.2a and 5.3a show that [$Ba^{2+}$] and AR were depth homogeneous in the pH range studied, and that as a result, the steric effects experienced by $Ba^{2+}$ ion in the active layer were also depth homogeneous, suggesting a depth homogeneous pore size distribution consistent with the results from the study of the degree of polymer crosslinking, and concentrations and ionization behavior of carboxylic groups. On the other hand, for the NF90 NF membrane, Figure 5.2b shows that [$Ba^{2+}$] was always higher in the surface of the active layer when compared to the corresponding average value throughout the active layer, and Figure 5.3b shows that the AR values obtained by XPS analyses were also relatively higher than those obtained by RBS analyses. The [$Ba^{2+}$] and AR results therefore indicate that $Ba^{2+}$ experiences steric effects at a lesser extent in the surface of the active layer of the NF90 NF membrane suggesting a relatively larger pore size in the surface, which is consistent with the findings of the previous sections.

$$[Ba^{2+}] = \frac{AR \times [R - COO^{-}]}{NN} \tag{5.5}$$

$$NN = 2 \times \left( \frac{AR \times [R - COO^{-}]}{AR \times [R - COO^{-}] + a} \right) \tag{5.6}$$

The concentration of $Ba^{2+}$ that associated with R–$COO^{-}$ groups in the active layers of the other membranes studied was also quantified to assess whether all membranes showed trends consistent with those shown by ESPA3 RO and NF90 NF, namely that depth homogeneity and heterogeneity in the content of R–$COO^{-}$ groups occurred together with depth homogeneity and heterogeneity, respectively, of [$Ba^{2+}$]. The results in Figure 5.1b

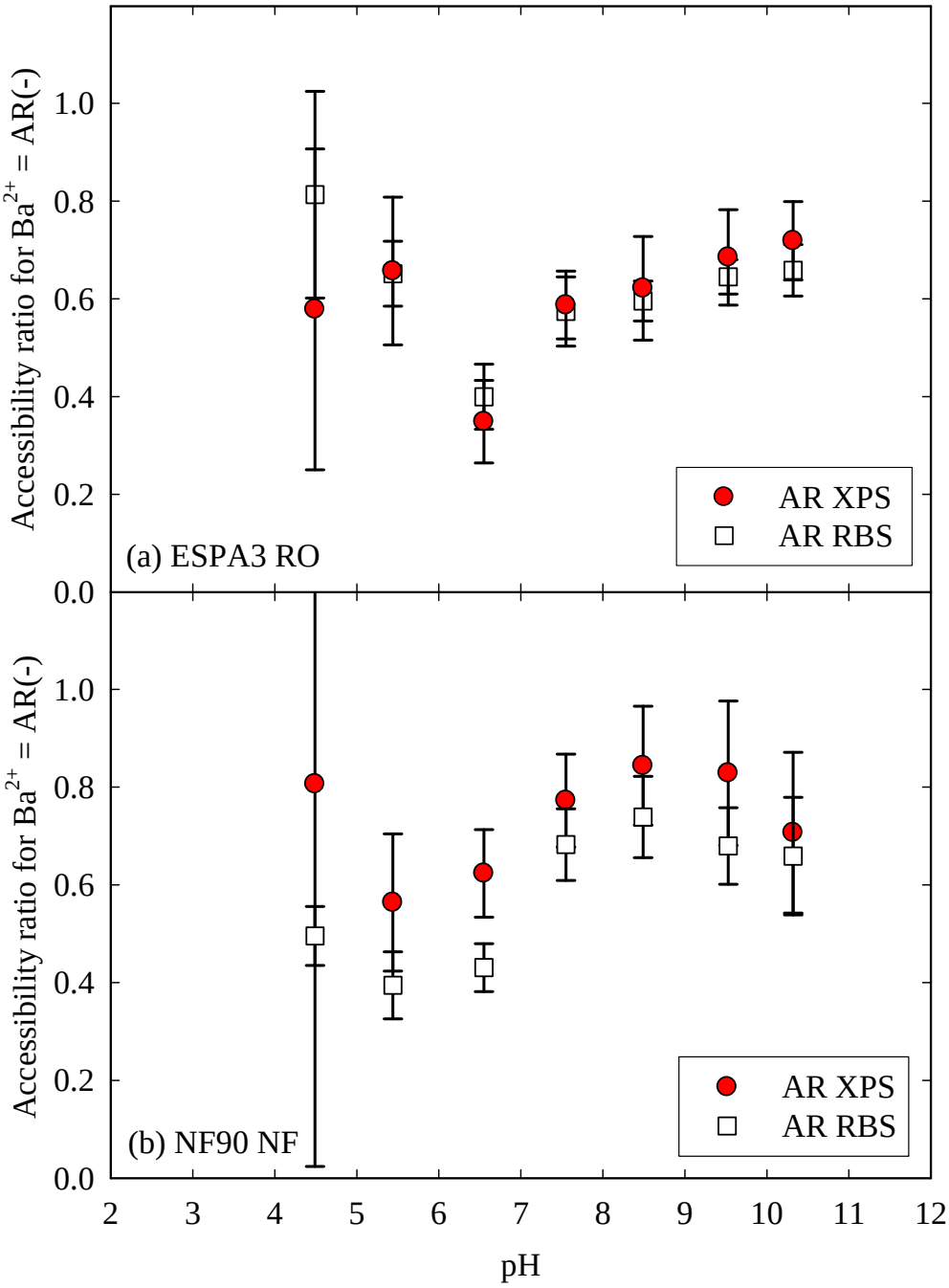


**Figure 5.3.** Fraction AR of ionized carboxylic groups accessible to barium ion ($Ba^{2+}$) at the surface (i.e., XPS data, solid symbols) of the polyamide active layers of (a) ESPA3 RO and (b) NF90 NF membranes and in average throughout the active layers depth (i.e., RBS data, open symbols). Error bars indicate standard error.

show that this was the case as the XPS and RBS results were only 2–15% different for SWC5 RO, TFC–S NF, and ESNA NF membranes, but 62% different for ESPAB RO. Additionally, the coated FT30 RO and LF10 RO membranes showed differences in the 52–62% range between XPS and RBS results.

***5.3.7. Implications of Depth Heterogeneity on Mechanisms of Solute Transport.*** This work showed that the content and p$K_a$ distribution of carboxylic groups, the concentration of $Ba^{2+}$ ion ([$Ba^{2+}$]) that associated with R–$COO^-$ groups, and the fraction AR of R–$COO^-$ groups accessible to $Ba^{2+}$ ion (i.e., steric effects experienced by $Ba^{2+}$) were either all depth homogeneous or depth heterogeneous in the fully-aromatic PA active layers studied. Our results therefore indicate that the transport of contaminants through uncoated RO/NF membranes occurs through either of the following: (i) a depth homogeneous active layer that can be modeled as a single layer with thickness equal to that of the whole active layer and with homogeneous properties and interactions with contaminants throughout its depth; or (ii) a depth heterogeneous active layer having at least two sub-layers in which the top sub-layer has a higher charge density that controls the electric exclusion of ionic species, and the bottom sub-layer (with relatively smaller pores) presents increased steric hindrance to solute transport. While the thickness of each sub-layer is important [5, 8-11], and TEM imaging [5] and RBS analysis [20] can be used to study the total thickness of the active layer, a method to determine the individual thickness of each sub-layer remains to be developed. For membrane development, the concept of an engineered depth heterogeneous active layer is advantageous as the electric exclusion provided by the top sub-layer and steric hindrance provided by the bottom sub-layer could be tuned independently from each other. Regarding the third sub-layer rich in

amine groups and adjacent to the polysulfone support reported elsewhere [5, 7], its properties remain to be characterized quantitatively and its relevance to contaminant rejection remains to be assessed. Coated membranes, on the other hand, were shown to have PA active layers unevenly covered by the coats, and lower charge densities in their surfaces. Accordingly, coated active layers have at least two distinct sub-layers in which the top sub-layer is a mixture of coat and PA that, despite the benefits brought by the coat layer [2, 27], comes at the cost of a reduced surface charge and a corresponding reduced electric exclusion of ionic contaminants.

### 5.4. Acknowledgments

RBS analyses were carried out in the Center for Microanalysis of Materials, University of Illinois, partially supported by the U.S. Department of Energy under grant DEFG02-91-ER45439. The authors acknowledge Doug Jeffers and Richard Haasch for training and assistance in RBS and XPS analyses, respectively, Tasuma Suzuki and Jeanne Luh for helpful discussions, and the companies Nitto Denko, Hydranautics and Koch Membrane Systems for providing membrane materials and related information. Scott MacLaren is also gratefully acknowledged for acquiring the AFM images. This work was supported by the National Science Foundation Environmental Engineering and Technology program under agreement number BES-0332217, and the WaterCAMPWS, a Science and Technology Center of Advanced Materials for the Purification of Water with Systems under agreement number CTS-0120978. The opinions in this paper do not necessarily reflect those of the sponsor.

## 5.5. Supporting Information Available

Section D.1 (Calculation of the analysis depth of X-ray photoelectron spectroscopy (XPS) tests); Section D.2 (Derivation of Equation 5.1 used to calculate the molar concentration of ionized carboxylic groups ($R–COO^-$) in the active layers); Figure D.1 (Attenuated total reflectance Fourier transform infrared (ATR-FTIR) spectrometry analyses of SWC5 and ESPAB reverse osmosis (RO) membranes); Figure D.2 (Rutherford backscattering spectrometry (RBS) spectra and corresponding simulations of virgin (a) SWC5 RO and (b) ESPAB RO membranes); Figure D.3 (XPS signals of the (a) chlorine Cl2p, (b) silver Ag3d, and (c) barium Ba3d photoelectrons in a sample of ESPA3 RO membrane used for $Ag^+$–$Ba^{2+}$ displacement tests); Figure D.4 (Atomic force microscopy (AFM) images (10×10 μm) of (a) ESPA3 RO, (b) SWC5 RO, (c) TFC–S NF, (d) ESNA NF, (e) ESPAB RO, (f) NF90 NF, (g) FT30 RO, and (h) LF10 RO membranes); Figure D.5 (Stoichiometry of association between the $R–COO^-$ groups neutralized by $Ba^{2+}$ ion in the polyamide (PA) active layers of ESPA3 RO and NF90 NF membranes and the $Ba^{2+}$ ions neutralizing them). This information is available in Appendix D.

## 5.6. References

1. Mulder, M., *Principles of Membrane Technology*. Second ed.; Kluwer Academic: Boston, MA, 1996.

2. Petersen, R. J., Composite reverse osmosis and nanofiltration membranes. *J. Mem. Sci.* **1993,** *83*, 81-150.

3. Tang, C. Y.; Kwon, Y.-N.; J.O., L., Effect of membrane chemistry and coating layer on physiochemical properties of thin film composite polyamide RO and NF membranes I. FTIR and XPS characterization of polyamide and coating layer chemistry. *Desalination* **2009,** *242*, (149-167), 149.

4. Coronell, O., Ionization behavior, stoichiometry of association and accessibility of functional groups in the active layers of reverse osmosis and nanofiltration membranes. *Chapter 4 of this dissertation*.

5. Freger, V., Nanoscale heterogeneity of polyamide membranes formed by interfacial polymerization. *Langmuir* **2003,** *19*, 4791-4797.

6. Freger, V.; Srebnik, S., Mathematical model of charge and density distributions in interfacial polymerization of thin films. *J. Appl. Polym. Sci.* **2003,** *88*, 1162-1169.

7. Wamser, C. C.; Gilbert, M. I., Detection of surface functional group asymmetry in interfacially-polymerized films by contact angle titrations. *Langmuir* **1992,** *8*, 1608-1614.

8. Bowen, W. R.; Welfoot, J. S., Modelling the performance of membrane nanofiltration-critical assessment and model development. *Chem. Eng. Sci.* **2002,** *57*, 1121-1137.

9. Szymczyk, A.; Fievet, P., Investigating transport properties of nanofiltration membranes by means of a steric, electric and dielectric exclusion model. *J. Mem. Sci.* **2005**, (252), 77-88.

10. Urama, R. I.; Mariñas, B. J., Mechanistic interpretation of solute permeation through a fully aromatic polyamide reverse osmosis membrane. *J. Mem. Sci.* **1997,** *123*, 267-280.

11. Yaroshchuk, A. E.; Boiko, Y. P.; Makovetskiy, A. L., Filtration potential across membranes containing selective layers. *Langmuir* **2002,** *18,* 5154-5162.

12. Coronell, O.; Mariñas, B. J.; Zhang, X.; Cahill, D. G., Quantification of functional groups and modeling of their ionization behavior in the active layer of FT30 reverse osmosis membrane. *Environ. Sci. Technol.* **2008,** *42,* 5260-5266.

13. Tang, C. Y.; Kwon, Y.-N.; Leckie, J. O., Probing the nano- and micro-scales of reverse osmosis membranes-A comprehensive characterization of physiochemical properties of uncoated and coated membranes by XPS, TEM, ATR-FTIR, and streaming potential measurements. *J. Mem. Sci.* **2007,** *287,* 146-156.

14. Coronell, O.; Mariñas, B. J.; Cahill, D. G., Accessibility and ion exchange stoichiometry of ionized carboxylic groups in the active layer of FT30 reverse osmosis membrane. *Environ. Sci. Technol.* **2009,** *43,* 5042-5048.

15. Aghaie, M.; Aghaie, H.; Ebrahimi, A., Thermodynamics of the solubility of barium nitrate in the mixed solvent, ethanol+water, and the related ion-association. *J. Mol. Liq.* **2007,** *135*, 72-74.

16. Pourbaix, M., *Atlas of electrochemical equilibria in aqueous solutions.* First English ed.; Pergamon Press: Great Britain, 1966.

17. Kwon, Y.-N.; Tang, C. Y.; Leckie, J. O., Change of chemical composition and hydrogen bonding behavior due to chlorination of crosslinked polyamide membranes. *J. Appl. Polym. Sci.* **2008,** *108*, 2061-2066.

18. Mayer, M.; Duggan, J. L.; Morgan, I. L. In *SIMNRA, a simulation program for the analysis of NRA, RBS and ERDA*, Proceedings of the 15th International Conference

on the Application of Accelerators in Research and Industry, Denton, TX, 1998; Denton, TX, 1998; p 541.

19. Bartels, C. R., A surface science investigation of composite membranes. *J. Mem. Sci.* **1989,** *45*, 225-245.

20. Mi, B.; Coronell, O.; Mariñas, B. J.; Watanabe, F.; Cahill, D. G.; Petrov, I., Physico-chemical characterization of NF/RO membrane active layers by Rutherford backscattering spectrometry. *J. Mem. Sci.* **2006,** *282*, 71-81.

21. Mi, B.; Cahill, D. G.; Mariñas, B. J., Physico-chemical integrity of nanofiltration/reverse osmosis membranes during characterization by Rutherford backscattering spectrometry. *J. Mem. Sci.* **2007,** *291*, 77-85.

22. Kwak, S. Y.; Jung, S. G.; Yoon, Y. S.; Ihm, D. W., Details of surface features in aromatic polyamide reverse osmosis membranes characterized by scanning electron and atomic force microscopy. *J. Polym. Sci., Part B: Polym. Phys.* **1999,** *37*, 1429-1440.

23. Glater, J.; Hong, S.-k.; Elimelech, M., The search for a chlorine-resistant reverse osmosis membrane. *Desalination* **1994,** *95*, 325-345.

24. Kwon, Y.-N.; Leckie, J. O., Hypochlorite degradation of crosslinked polyamide membranes II. Changes in hydrogen bonding behavior and performance. *J. Mem. Sci.* **2006,** *282*, 456-464.

25. Kwon, Y.-N.; Tang, C. Y.; Leckie, J. O., Change of membrane performance due to chlorination of crosslinked polyamide membranes. *J. Appl. Polym. Sci.* **2006,** *102*, 5895-5902.

26. Zhang, X.; Cahill, D. G.; Coronell, O.; Mariñas, B. J., Absorption of water in the active layer of reverse osmosis membranes. *J. Mem. Sci.* **2009,** *331*, 143-151.

27. Hachisuka, H.; Ikeda, K. Reverse osmosis composite membrane and reverse osmosis treatment method for water using the same. US Patent, US 6,413,425 B1, 2002.

28. Ohshima, H.; Kondo, T., Potential and pH distribution across a membrane with a surface layer of ionizable groups. *J. Theor. Biol.* **1987,** *124*, 191-198.

29. De Baerdemaeker, J.; Boussu, K.; Djourelov, N.; Van der Bruggen, B.; Dauwe, C.; Weber, M.; Lynn, K. G., Investigation of nanopores in nanofiltration membranes using slow positron beam techniques. *Phys. Stat. Sol.* **2007,** *4*, 3804-3809.

30. Harder, E.; Walters, D. E.; Bodnar, Y. D.; Faibish, R. S.; Roux, B., Molecular dynamics study of a polymeric reverse osmosis membrane. *J. Phys. Chem. B* **2009,** *113*, 10177-10182.

31. Kim, S. H.; Kwak, S.-Y.; Suzuki, T., Positron annihilation spectroscopic evidence to demonstrate the flux-enhancement mechanism in morphology-controlled thin-film-composite (TFC) membrane. *Environ. Sci. Technol.* **2005,** *39*, 1764-1770.

32. Senapati, S.; Chandra, A., Dielectric constant of water confined in a nanocavity. *J. Phys. Chem. B* **2001,** *105*, 5106-5109.

33. Bacarella, A. L.; Grunwald, E.; Marshall, H. P.; Lee Purlee, E., The potentiometric measurements of acid dissociation constants and *p*H in the system methanol-water. $pK_A$ values for carboxylic acids and anilinium ions. *J. Org. Chem.* **1955,** *20*, 747-762.

# CHAPTER 6

# RELATING CHARGE DENSITY IN THE ACTIVE LAYERS OF REVERSE OSMOSIS AND NANOFILTRATION MEMBRANES TO ARSENIC (III) AND POTASSIUM IODIDE REJECTION AS A FUNCTION OF PH

**Abstract:** We used the solution-diffusion model, the theory of Donnan potential in permeable charged films, and charge density measurements in the active layers of reverse osmosis (RO) and nanofiltration (NF) membranes to predict the rejection of a weak acid (i.e., arsenious acid) and a strong electrolyte (i.e., potassium iodide) at two different pH values based on the rejection at a third pH condition. Predictions of solute rejection were in agreement with experimental data indicating that for RO/NF membranes: (i) the solution-diffusion model coupled with the theory of Donnan potential satisfactorily describe the effect that the pH of the feed solution has on solute rejection; and (ii) the experimental procedures reported in our previous work for the quantification of ionized functional groups in active layers provide data that adequately describe the active layer charge density that determines the electric exclusion of ionic contaminants from the membrane. Additionally, results showed that the activity coefficients of solutes in active layers may be significantly different from unity, and that as a result they should not be neglected in transport models for an accurate description of transport phenomena. The ratio between the activity coefficients of the neutral arsenious acid and the monovalent arsenite ion was estimated as equal to ≈9 in polyamide active layers.

**Key Words:** reverse osmosis, nanofiltration, polyamide, performance, rejection, arsenic, strong electrolyte, RBS, XPS, negative charges, depth heterogeneity, solution diffusion

## 6.1. Introduction

Reverse osmosis (RO) and nanofiltration (NF) membranes are technologies of interest to the water treatment industry because they are capable of removing a wide variety of contaminants including salts, small neutral molecules, and pathogens [1] without recourse to additional treatment steps, or chemical addition to the feed water. Most commercially successful RO/NF membranes have a thin-film composite structure with a bottom polyester backing (~200 μm), an intermediate polysulfone layer (~50 μm), and a top ultrathin (~50–200 nm) "active layer" usually made of polyamide (PA) that constitutes the main barrier to the permeation of water and solutes [2]. Accordingly, mathematical models describing transport phenomena in RO/NF membranes most commonly assume that membrane performance is the result of the interactions between the active layer and water and solutes [3-6].

Existing models can be classified based on whether they assume a solution-diffusion or pore-flow permeation mechanism. In solution-diffusion type models, the active layer is non-porous, and permeation is the result of partitioning into and diffusion through the active layer [4, 6]. In some variations of the solution-diffusion model, an advection term is included that accounts for imperfections or pores in the active layer that allow transport of bulk feed water through the membrane [7, 8]. In pore-flow type models, the active layer is considered porous, and therefore permeation occurs by a combination of hindered diffusion, advection and electro-migration through the active layer pores [3, 5, 9]. Even though both types of models have been used successfully to fit experimental data of water and solute permeation through RO/NF membranes [3, 6, 8, 9], they have not been used to make *a priori* predictions of membrane performance based on independent measurements

of the physico-chemical properties of the active layers (e.g., pore size distribution, active layer charge, etc.) or their interactions with water and contaminants (e.g., partition coefficients, diffusion coefficients, etc). One of the reasons for the absence of *a priori* predictions of membrane performance in the literature is that, only until recently, there has been advancement in the development of characterization procedures [10-16] that allow the direct, independent quantification of some of the active layer properties and solute-active layer interactions that serve as key parameters in the current mathematical models for RO/NF transport. Such quantitative characterization procedures have opened the door to start using the quantitative results as input in the existing mathematical models for predictive purposes.

Accordingly, the objective of this study was to use the charge densities measured [17, 18] in the active layers of four commercial RO/NF membranes as input in the solution-diffusion model [8], to predict the corresponding rejections of a weak acid (i.e., arsenious acid) and a strong electrolyte (i.e., potassium iodide) at two different pH conditions based on rejection results at a third pH value. In addition to the experimental and predicted results, we present the procedures and corresponding sets of equations used to calculate the predicted values.

## 6.2. Rejection Experiments

***6.2.1. Source of Rejection Data.*** The permeation data analyzed in this chapter has been reproduced from the Ph.D. dissertation of Mi, B. [19] with permission. Such data was chosen for the present study because in our previous work [11, 12, 17, 18] we quantified the concentration of ionized functional groups as a function of pH in the active layers of

membrane samples obtained from the same spiral-wound elements and flat sheets from which Mi, B. [19] obtained the membrane coupons used in the permeation experiments. Relevant experimental details of the permeation experiments [19, 20], as well as additional information relevant to the mathematical analysis performed in this chapter are provided below.

***6.2.2. Target Membranes.*** The following four commercially available RO/NF membranes with PA active layers [17] were studied: ESNA NF (Hydranautics, Oceanside, CA), TFC–S NF (Koch Membrane Systems, Wilmington, MA), FT30 RO (Dow Liquid Separation, Midland, MI), and LF10 RO (Nitto Denko, Shimohozumi, Japan). The FT30 RO and LF10 RO membranes have neutral, fouling-resistant [21] coating layers on top of their PA active layers [17] that present additional resistance to water and solute transport [21], and result in a different surface charge density from the average charge density throughout the PA active layer [18]. The ESNA NF and TFC–S NF membranes are uncoated.

***6.2.3. Target Solutes and Feed Waters.*** Trivalent arsenic (As(III)), a relatively common water contaminant in the United States [22], and potassium iodide (KI) were used to test solute rejection by the membranes studied. While the relatively high p$K_a$ = 9.2 of As(III) makes the neutral arsenious acid ($H_3AsO_3$) the predominant species in the typical pH = 6–9 range of natural waters, arsenite ion ($H_2AsO_3^-$) becomes predominant at pH above 9.2. Experimental pH values of feed waters were 6.3, 8.0 and 10.2 [19]. In arsenic rejection experiments, feed waters had a background KI concentration of 0.01 mM [19], and As(III) concentrations of 4 mM for TFC–S NF and LF10 RO membranes [20], and 2

mM for ESNA NF and FT30 RO membranes [20]. In iodide rejection experiments, the feed water concentration of both As(III) and KI was 4 mM [19, 20].

***6.2.4. Experimental Setup.*** Permeation experiments were performed using a flat-sheet, closed-loop, cross-flow, high-pressure membrane system (see ref [19] for details) with two SEPA™ cells connected in series to allow the simultaneous study of two membrane specimens. Membrane coupons used as test samples were cut from spiral-wound elements of the TFC–S NF, ESNA NF and FT30 RO membranes, and from flat sheets of the LF10 RO membrane [20]. Plastic feed spacers cut from spiral wound elements were used in the feed channels and served as turbulence promoters. The feed pressure was varied within the range of 0.5–3.5 MPa in each experiment [19]. All experiments were performed at 20$^{o}$C. [19]

***6.2.5. Quantification of As(III) and Iodide ($I^-$) in Solution.*** The As(III) concentration in feed and permeate samples was quantified by a colorimetric method [19, 23] using a UV/visible 1601 spectrophotometer (Shimadzu, Japan) [19]. The rejection of KI by the membranes tested was assessed based on the concentrations of iodide ($I^-$) in the feed and permeate samples. Iodide concentration in solution was quantified by ion chromatography with a Dionex ICS-2000 ion chromatograph using an IonPac AS18 4mm analytical column (4×250mm) (Dionex Corporation, Westmont, IL) [20].

## 6.3. Background on the Modeling of RO/NF Transport Phenomena

***6.3.1. Solution-Diffusion Theory with Advective Transport.*** In this study, we assumed solution-diffusion as the main permeation mechanism, and accounted for the possibility

that small pores in the active layer allow the passage of bulk feed solution [24] by using a modified version [8] of the solution-diffusion model that incorporates advective transport through imperfections or pores in the active layer as depicted in Figure 6.1. Assuming thermodynamic equilibrium at the interfaces between the active layer and the feed and permeate solutions, solute passage can be expressed by [8]

$$J_S = J_V \times c_P = B \times (c_W - c_P) + \overline{\alpha} \times J_V \times c_W, \tag{6.1}$$

where $J_S$ [mol/(m$^2$·d)] and $J_V$ [m$^3$/(m$^2$·d)] are the solute and permeate water fluxes, respectively, c [M] is the solute concentration in aqueous solution, B [m/d] is the solute diffusive permeation coefficient, $\overline{\alpha}$ [-] is a transport coefficient related to the fraction of water that permeates by advection, and subscripts P and W refer to the bulk permeate and feed next to the membrane wall, respectively.

The solute concentration next to the membrane wall ($c_W$) is higher from that in the bulk feed ($c_F$) because of the phenomenon of concentration polarization (CP) [25]. At steady state, $c_F$ and $c_W$ are related by the expression [25]

$$\frac{c_W - c_P}{c_F - c_P} = \exp\left(\frac{J_V}{k_S}\right), \tag{6.2}$$

where $k_S$ [m/d] is the mass transfer coefficient of the solute of interest in the CP layer. Equations 6.1 and 6.2 can be combined to eliminate $c_W$, which can not be readily measured experimentally, to obtain [8]

$$\frac{c_P}{c_F - c_P} = \left( \frac{B}{1-\bar{\alpha}} \times \frac{1}{J_V} + \frac{\bar{\alpha}}{1-\bar{\alpha}} \right) \times \exp\left( \frac{J_V}{k_S} \right), \tag{6.3}$$

where $c_F$, $c_P$ and $J_V$ are measured experimentally, and B, $\bar{\alpha}$ and $k_S$ serve as fitting parameters. The $c_P/(c_F - c_P)$ value is related to the more commonly reported percentage solute rejection (%R) by the expression

$$\%R = 100 \times \left( \frac{c_F - c_P}{c_F} \right) = 100 \times \left( 1 + \frac{c_P}{c_F - c_P} \right)^{-1}. \tag{6.4}$$

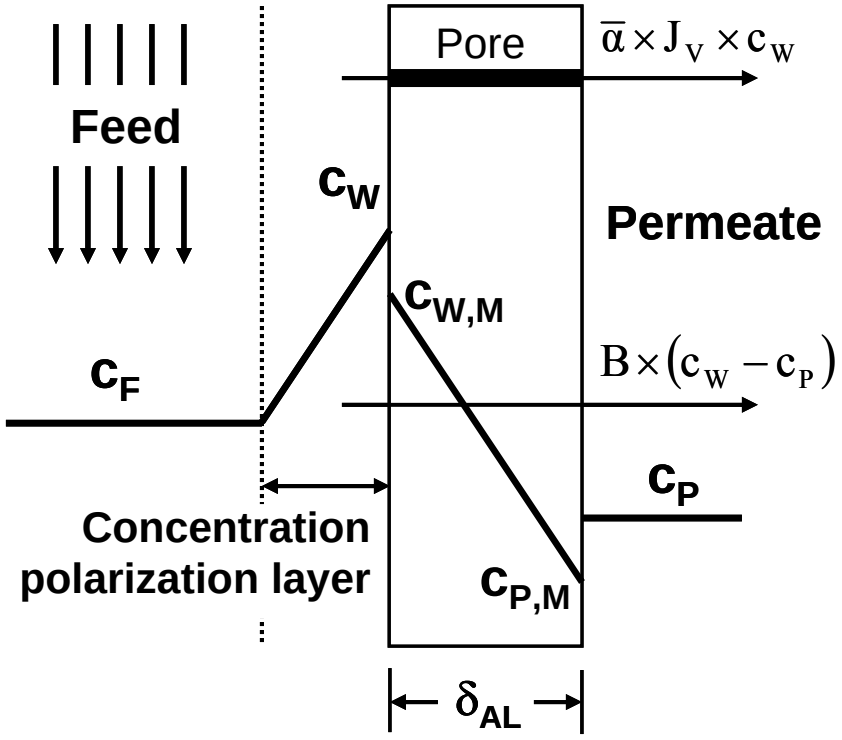


**Figure 6.1**. Schematic of transport phenomena through the active layer of RO/NF membranes. Solute transport from the feed to the permeate side occurs by diffusion ($B \times (c_W - c_P)$) through the active layer polymer matrix and advection ($\bar{\alpha} \times J_V \times c_W$) through pores.

***6.3.2. Effect of Active Layer Charge on Ion Partitioning.*** Assuming that the solute-active layer system is an ideal solution and that the active layer is homogeneous, the solute diffusive permeation coefficient B in Equations 6.1 and 6.3 is defined as [6, 8]

$$B = \frac{K_S \times D_S}{\delta_{AL}}, \tag{6.5}$$

where $K_S$ is the active layer-water partition coefficient of the solute of interest, $D_S$ is the solute diffusion coefficient in the active layer, and $\delta_{AL}$ is the active layer thickness. The partition coefficient $K_S$ can be expressed as $K_S = c_{W,M} / c_W = c_{P,M} / c_P$ where $c_{W,M}$ and $c_{P,M}$ correspond to the solute concentrations in the membrane next to the feed and permeate walls, respectively (see Figure 6.1). Assuming local thermodynamic equilibrium at the membrane-solution interface, $K_S$ is also given by [3, 5, 18]

$$K_S = \Phi \times \frac{\gamma_{S,H2O}}{\gamma_{S,M}} \times \exp\left(f(\psi_D)\right) = \Phi \times \frac{\gamma_{S,H2O}}{\gamma_{S,M}} \times \mathbb{D}, \tag{6.6}$$

in which $\Phi$ is a coefficient that accounts for the steric effects experienced by the solute in the active layer, $\gamma_{S,H2O}$ and $\gamma_{S,M}$ are the solute activity coefficients in the aqueous solution and membrane, respectively, at their interface, $\psi_D$ is the Donnan potential, and we define $\mathbb{D} = \exp\left(f(\psi_D)\right)$ as the Donnan exclusion coefficient. The dependence of $\mathbb{D}$ on the active layer net charge density is given by the theory of Donnan potential in a system where a symmetrical electrolyte is in equilibrium with a charge film permeable to the electrolyte ions [18, 26]. The Donnan exclusion coefficient can be calculated as [3, 18, 26]

$$\mathbb{D} = \exp\left(-\operatorname{arcsinh}\left(\frac{C_{net}}{2 \times z_{ion} \times C_{ion}}\right)\right), \tag{6.7}$$

where $C_{net}$, $C_{ion}$ and $z_{ion}$ are the net charge density at the membrane surface, the concentration of the symmetrical electrolyte solution, and the charge of the ion of interest, respectively. The charge density $C_{net}$ can be obtained by direct measurements of the concentration of ionized functional groups in the active layers as a function of pH using the methods reported in our previous work [18]. For neutral solutes, $\mathbb{D} = 1$.

## 6.4. Results and Discussion

***6.4.1. Arsenic (III) Rejection Data.*** Figure 6.2 shows the percentage rejection (%R) of arsenic (III) as a function of permeate flux ($J_V$) by the TFC–S NF, LF10 RO, ESNA NF and FT30 RO membranes. The experiments were performed at pH values of 6.3, 8.0 and 10.2. The figure shows that the range of arsenic rejection was 35–97% with only the TFC–S NF membrane having rejections below 50%. The figure depicts how in each of the membranes studied As(III) rejection increased as permeate flux (i.e., trans-membrane pressure) increased, before reaching a plateau at the highest fluxes tested. Equations 6.3 and 6.4 predict that at higher trans-membrane pressures, As(III) rejection would have decreased due to the concentration polarization effect. Figure 6.2 also shows that As(III) rejection is relatively constant at pH≤8.0, which is qualitatively explained by the relatively high p$K_a$ = 9.2 value of arsenious acid that makes the neutral $H_3AsO_3$ species account for 94% of the arsenic in solution at pH = 8.0. Since changing the pH of the feed

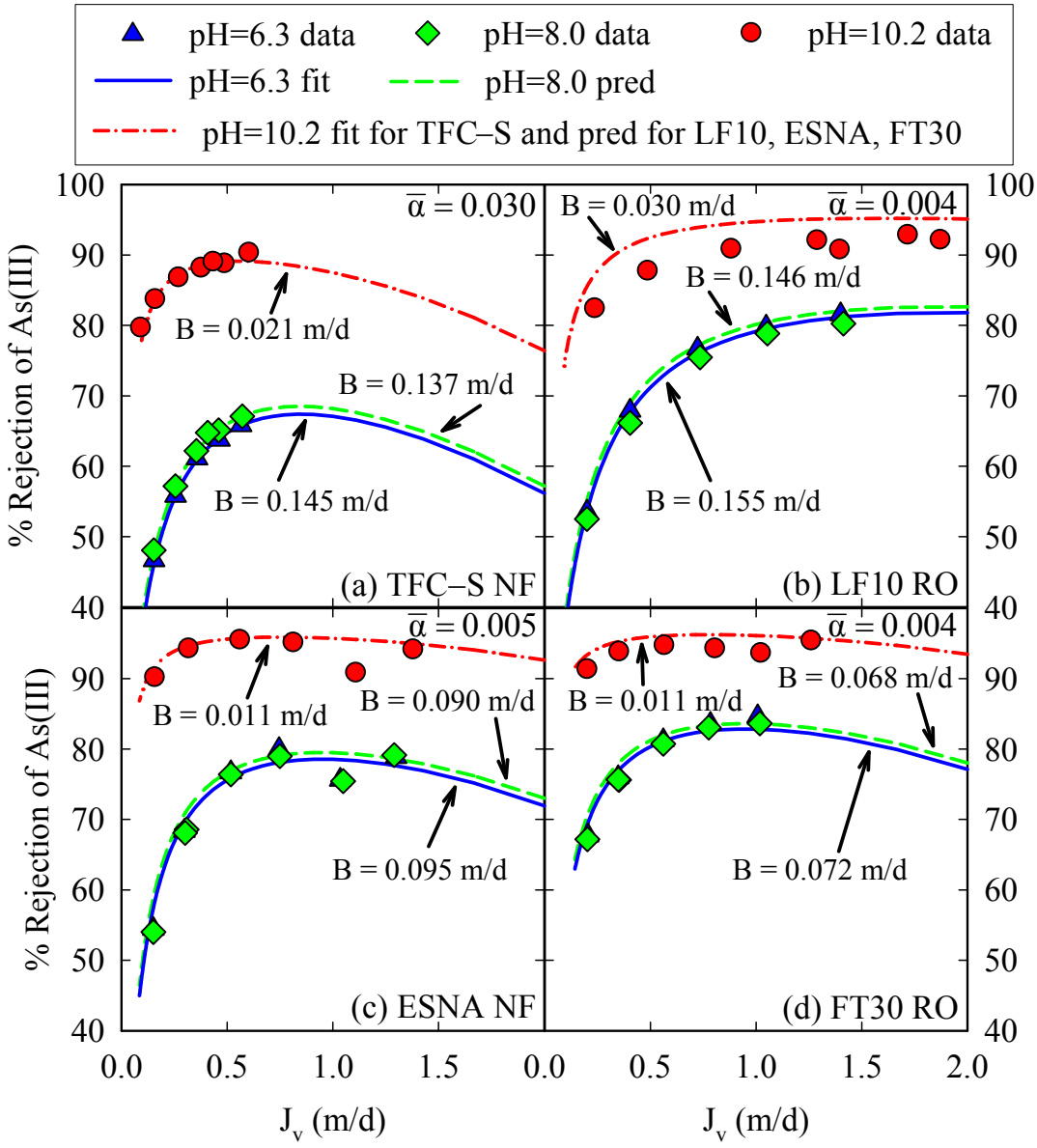


**Figure 6.2**. Rejection of arsenic (III) as a function of pH by the (a) TFC–S NF, (b) LF10 RO, (c) ESNA NF and (d) FT30 RO membranes. Continuous (blue) lines at pH = 6.3 for all membranes, and the dashed-dotted (red) line at pH = 10.2 for the TFC–S NF membrane correspond to model fitting (Equations 6.3 and 6.4). The fitted B parameters obtained from the fitting of the data for the TFC–S NF membrane at pH = 6.3 and 10.2 were used in Equation 6.14 to obtain $\bar{\gamma}_{As,M} = 9$. Dashed (green) lines at pH = 8.0 for all membranes, and dashed-dotted (red) lines at pH = 10.2 for all membranes except TFC–S NF were predicted using Equation 6.14, $\bar{\gamma}_{As,M} = 9$, and the corresponding charge density values in Table 6.1. The mass transfer coefficient ($k_{As}$) in the feed solution was equal to 1.0 m/d in all cases. A summary of fitted and predicted model parameters is presented in Table 6.1.

solution changes the charge density in the active layer, but the latter only affects the rejection of the ionic species $H_2AsO_3^-$ which at pH = 8.0 accounts for only 6% of the arsenic in solution, then at pH values lower than ≈8.0, the change in As(III) rejection is relatively similar to the experimental error. In contrast, at pH = 10.2, approximately 91% of the arsenic in solution is in the ionic $H_2AsO_3^-$ form, and as a result, the increase in As(III) rejection observed in Figure 6.2 reflects both the electric exclusion of $H_2AsO_3^-$ and the reduced concentration of the neutral $H_3AsO_3$ species.

***6.4.2. Potassium Iodide (KI) Rejection Data.*** Figure 6.3 shows the percentage rejection (%R) of KI, measured as rejection of $I^-$, in the TFC–S NF and LF10 RO membranes as a function of $J_V$. The experiments were performed at pH values of 6.3, 8.0 and 10.2. The figure shows that the range of rejection of iodide was significantly smaller than the corresponding range for As(III), with $I^-$ rejection being in the 88–96% and 95–99% range for the TFC–S NF and LF10 RO membranes, respectively. As it was the case for As(III), the rejection of KI initially increased with increasing permeate flux, before reaching a plateau at higher water fluxes. For the LF10 RO membrane, KI rejection decreased at the highest permeate fluxes tested due to the concentration polarization effect as expected from Equations 6.3 and 6.4. In contrast to the results obtained with As(III), the rejection of KI consistently increased with increasing pH. Such results are consistent with the increasing negative charge density in the surface of the membranes studied as pH increases [17, 18], and the corresponding increasing electric exclusion of anions such as iodide by the Donnan effect (see Equation 6.7).

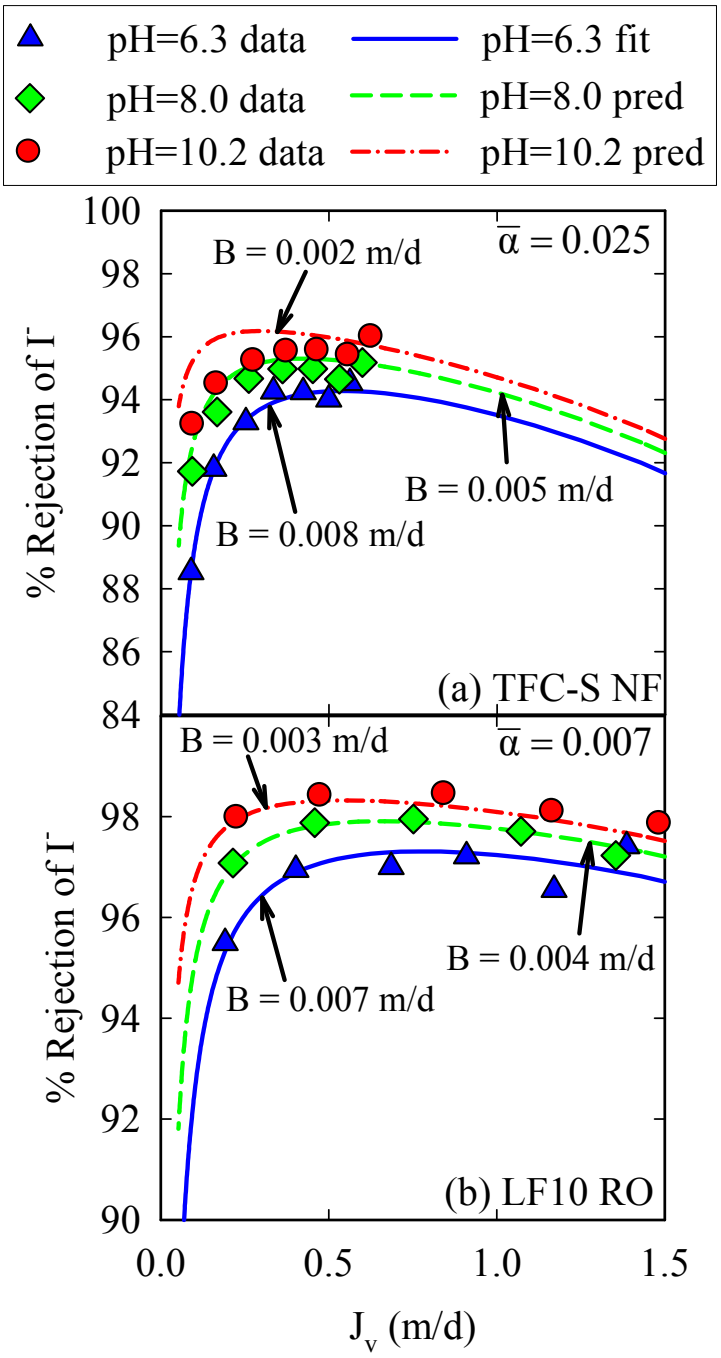


**Figure 6.3**. Rejection of potassium iodide (KI), measured as iodide ($I^-$), as a function of pH by the (a) TFC–S NF and (b) LF10 RO membranes. Continuous (blue) lines at pH = 6.3 correspond to model fitting (Equations 6.3 and 6.4). Dashed (green) lines at pH = 8.0 and dashed-dotted (red) lines at pH = 10.2 were predicted using Equation 6.15. The mass transfer coefficient ($k_{KI}$) in the feed solution was equal to 1.4 m/d in all cases. A summary of fitted and predicted model parameters is presented in Table 6.1.

***6.4.3. Approach for the Prediction of As(III) Rejection at $pH_j$ Based on Rejection at $pH_i$.*** At any given pH of the feed solution, As(III) dissociates into a fraction $\alpha_0$ of $H_3AsO_3$, and a fraction $\alpha_1$ of $H_2AsO_3^-$, where $\alpha_0 + \alpha_1 = 1$ [27]. The passage of As(III) through an RO/NF membrane can then be expressed as

$$J_S = J_{S,0} + J_{S,1}, \tag{6.8}$$

where the subscripts 0 and 1 indicate $H_3AsO_3$ and $H_2AsO_3^-$, respectively. Similarly, the concentrations $c_W$ and $c_P$ are given by

$$c_W = c_{W,0} + c_{W,1}, \tag{6.9}$$

and

$$c_P = c_{P,0} + c_{P,1}, \tag{6.10}$$

where $c_{W,0} = \alpha_0 \times c_W$, $c_{W,1} = \alpha_1 \times c_W$, $c_{P,0} = \alpha_0 \times c_P$, and $c_{P,1} = \alpha_1 \times c_P$.

Based on the similar molecular radii (0.236–0.237 nm) and molar mobility [28] of $H_3AsO_3$ and $H_2AsO_3^-$, we assume that the parameters $\overline{\alpha}$, $D_S$ and $\Phi$ in Equations 6.1, 6.5 and 6.6, respectively, have similar values for the permeation of $H_3AsO_3$ and $H_2AsO_3^-$ (i.e., $\overline{\alpha} = \overline{\alpha}_0 = \overline{\alpha}_1$, $D_S = D_{S,0} = D_{S,1}$, and $\Phi = \Phi_0 = \Phi_1$). Accordingly, from Equations 6.1, 6.8, 6.9 and 6.10, the diffusive transport coefficients B, $B_0$ and $B_1$ are related by

$$B = \alpha_0 \times B_0 + \alpha_1 \times B_1, \tag{6.11}$$

and

$$B_1 = B_0 \times \left( \frac{\gamma_{1,H2O}}{\gamma_{0,H2O}} \right) \times \left( \frac{\gamma_{0,M}}{\gamma_{1,M}} \right) \times \frac{\mathbb{D}_1}{\mathbb{D}_0}. \tag{6.12}$$

Remembering that $\mathbb{D}_0 = 1$, and defining $\bar{\gamma}_{As,M} = \gamma_{0,M} / \gamma_{1,M}$, we have from Equations 6.11 and 6.12 that

$$B = B_0 \times \left( \alpha_0 + \alpha_1 \times \left( \frac{\gamma_{1,H2O}}{\gamma_{0,H2O}} \right) \times \bar{\gamma}_{As,M} \times \mathbb{D}_1 \right). \tag{6.13}$$

Permeation results at any given pH can be used to fit the parameters B, $\bar{\alpha}$, and $k_{As}$ in Equation 6.3. Since $\bar{\alpha}$ is related to advective transport, $k_{As}$ is related to the hydrodynamic conditions and the As(III) diffusion coefficient in the feed, and $H_3AsO_3$ and $H_2AsO_3^-$ have similar mobilities [28], then only B depends on pH, and the parameters $\bar{\alpha}$ and $k_{As}$ are valid at any pH. Additionally, from Equation 6.13, the B parameters at two different pH values $pH_i$ and $pH_j$ are related by the expression

$$\frac{B_{pHj}}{B_{pHi}} = \frac{\left( \alpha_0 + \alpha_1 \times \left( \frac{\gamma_{1,H2O}}{\gamma_{0,H2O}} \right) \times \bar{\gamma}_{As,M} \times \mathbb{D}_1 \right)_{pHj}}{\left( \alpha_0 + \alpha_1 \times \left( \frac{\gamma_{1,H2O}}{\gamma_{0,H2O}} \right) \times \bar{\gamma}_{As,M} \times \mathbb{D}_1 \right)_{pHi}}, \tag{6.14}$$

where $\alpha_0$ and $\alpha_1$, $\gamma_{0,H20}$ and $\gamma_{1,H20}$, and $\mathbb{D}_1$ are calculated at any pH of the feed solution based on weak acid-base chemistry theory [27], the Debye-Hückel theory [27], and Equation 6.7, respectively.

The solute activity coefficient $\gamma_{S,M}$ in Equation 6.6 is generally assumed to be equal to one, or to be implicitly included in other "effective" parameters of the transport models

(e.g., "effective" charge density of the active layer) [3, 9, 28-31]. If we assumed $\gamma_{S,M} = 1$ in Equation 6.6, then $\bar{\gamma}_{As,M} = 1$ in Equations 6.13 and 6.14, and the prediction of $B_{pHj}$ could be easily performed using Equation 6.14 and a fitted $B_{pHi}$; however, our preliminary analysis (not shown) of the data in Figure 6.2 indicates that $\bar{\gamma}_{As,M} \neq 1$ in Equations 6.13 and 6.14. This result is not surprising as the conditions inside the active layer are not those of an ideal solution (i.e., $\gamma_{S,M} \neq 1$). Unfortunately, analytical procedures for the calculation of activity coefficients in polymers [30] require a number of assumptions regarding the polymer structure and its interaction with the solute, therefore making unfeasible the calculation of $\bar{\gamma}_{As,M}$ from first principles. Nevertheless, remembering that for all membranes and experimental conditions tested the $\bar{\gamma}_{As,M}$ parameter is a ratio between the activity coefficients of the same two species (i.e., the neutral $H_3AsO_3$ and the monovalent $H_2AsO_3^-$), and that the active layer material (i.e., polyamide) in all membranes is relatively similar, we assume that the $\bar{\gamma}_{As,M}$ parameter is approximately the same for all experiments and all membranes. As a result, it is necessary to calculate $\bar{\gamma}_{As,M}$ with only one membrane using fitted B parameters at only two pH values; the calculated $\bar{\gamma}_{As,M}$ can then be used for any membrane with a polyamide active layer, as well as for any pH condition.

Accordingly, we first calculated $\bar{\gamma}_{As,M}$ from Equation 6.14 using B, $\bar{\alpha}$, and $k_{As}$ parameters obtained from the fitting to Equation 6.3 of the permeation results with TFC−S NF membrane at pH values of 6.3 and 10.2, where only B was pH dependent.

Then, we predicted the rejection of As(III) by the membranes studied at feed solution $pH_j$ values of 8.0 and 10.2 based on corresponding results at $pH_i$ =6.3 as follows:

1. We fitted the parameters $B_{pHi}$, $\bar{\alpha}$, and $k_{As}$ in Equation 6.3 to the permeation results at $pH_i$ = 6.3.
2. We calculated $B_{pHj}$ using Equations 6.7 and 6.14, $\bar{\gamma}_{As,M}$, and $B_{pHi}$ from Step 1.
3. We predicted As(III) rejection at $pH_j$ using Equations 6.3 and 6.4, $B_{pHj}$ from Step 2, and $\bar{\alpha}$ and $k_{As}$ from Step 1.

***6.4.4. Approach for the Prediction of Iodide Rejection at $pH_j$ Based on Rejection at $pH_i$.*** KI rejection is determined by the electric exclusion of the co-ion iodide ($I^-$). In contrast to the arsenic case in which a change in the pH of the feed solution changes the speciation of the solute of interest, pH changes do not affect the concentration of iodide in solution. Equation 6.14 can then be rewritten for iodide as

$$\frac{B_{pHj}}{B_{pHi}} = \frac{\left(\gamma_{I^-,H2O} \times \mathbb{D}_{I^-}\right)_{pHj}}{\left(\gamma_{I^-,H2O} \times \mathbb{D}_{I^-}\right)_{pHi}}, \tag{6.15}$$

where $\gamma_{I^-,M}$ for iodide cancels out in the numerator and denominator consistent with our assumption of approximately constant $\gamma_{S,M}$ in the active layers (see previous section). Accordingly, we predicted the rejection of iodide by the TFC–S NF and LF10 RO membranes at $pH_j$ values of 8.0 and 10.2 based on results at $pH_i$ =6.3 as follows:

1. We fitted parameters $B_{pHi}$, $\bar{\alpha}$, and $k_{KI}$ in Equation 6.3 to the permeation results at $pH_i$ = 6.3.
2. We calculated $B_{pHj}$ using Equations 6.7 and 6.15, and $B_{pHi}$ from Step 1.

3. We predicted $I^-$ rejection using Equations 6.3 and 6.4, $B_{pHj}$ from Step 2, and $\bar{\alpha}$ and $k_{KI}$ from Step 1.

***6.4.5. Prediction of Iodide Rejection at $pH_j$ = 8.0 and 10.2 Based on Rejection at $pH_i$ = 6.3.*** Figure 6.3 shows the model fit to Equations 6.3 and 6.4 of the percentage rejection of iodide at $pH_i$ = 6.3 in the TFC−S NF and LF10 RO membranes. Since the two cells that contained the membrane coupons tested had the same configuration and hydrodynamic conditions, the concentration polarization coefficient $k_{KI}$ was fitted as a common value for the TFC−S NF and LF10 RO membranes, resulting in $k_{KI}$ = 1.4 m/d. For the TFC−S NF membrane, we obtained $B_{pHi=6.3}$ = 0.0084 m/d and $\bar{\alpha}$ = 0.0247 ; for the LF10 RO membrane, we obtained $B_{pHi=6.3}$ = 0.0068 m/d and $\bar{\alpha}$ = 0.0070 (see Table 6.1). Fitted curves are plotted as continuous (blue) lines in Figure 6.3. The values of the fitted parameters indicate that both diffusive and advective transport of KI is larger in the TFC−S membrane than in the LF10 membrane.

The Donnan exclusion coefficients $\mathbb{D}_{I^-}$ for both membranes at pH values of 6.3, 8.0 and 10.2 were calculated using Equation 6.7, and the membrane charge densities ($C_{net}$) shown in Table 6.1 and obtained in our previous work [18]. Since the electric exclusion of ionic solutes approaching a charged film permeable to them is determined by the charge density within the top ≈2 nm of the film [32], the $C_{net}$ values in Table 6.1 correspond to charge densities at the membrane surfaces and not to the average values in their active layers. The calculated $\mathbb{D}_{I^-}$ values were used in Equation 6.15 to calculate $B_{pHj}$ at $pH_j$ values of 8.0 and 10.2 (see Table 6.1). Corresponding iodide rejection curves at both pH

**Table 6.1.** Summary of parameters related to the prediction of the rejection of arsenic (III) and potassium iodide (KI) by the TFC–S NF, LF10 RO, ESNA NF and FT30 RO membranes at pH values in the 6.3–10.2 range based on rejection results at pH = 6.3.

| Parameter | pH | TFC–S NF | LF10 RO | ESNA NF | FT30 RO |
|---|---|---|---|---|---|
| $C_{net}$ [a] (M) | 6.3 | -0.16 | -0.14 | -0.21 | -0.06 |
| | 8.0 | -0.24 | -0.19 | -0.28 | -0.08 |
| | 10.2 | -0.53 | -0.30 | -0.50 | -0.26 |
| **Analysis of the rejection of iodide ($I^-$)** | | | | | |
| B (m/d) | 6.3 [b] | 0.009 | 0.007 | - | - |
| | 8.0 | 0.005 | 0.004 | - | - |
| | 10.2 | 0.002 | 0.003 | - | - |
| $\bar{\alpha}$ [b] (-) | All | 0.025 | 0.007 | - | - |
| $k_{KI}$ [b] (m/d) | All | 1.4 | 1.4 | - | - |
| $\mathbb{D}_{I^-}$ (-) | 6.3 | 0.063 | 0.073 | - | - |
| | 8.0 | 0.034 | 0.044 | - | - |
| | 10.2 | 0.015 | 0.026 | - | - |
| $\lvert\Delta\%R_{Max}\rvert$ | 8.0 | 0.79 | 0.18 | - | - |
| | 10.2 | 2.00 | 0.32 | - | - |
| $\lvert\Delta\%R_{Ave}\rvert$ | 8.0 | 0.51 | 0.07 | - | - |
| | 10.2 | 0.98 | 0.18 | - | - |
| **Analysis of the rejection of arsenic (III) ($\bar{\gamma}_{As,M} = 9$)** | | | | | |
| B (m/d) | 6.3 [b] | 0.145 | 0.155 | 0.095 | 0.072 |
| | 8.0 | 0.132 | 0.146 | 0.090 | 0.068 |
| | 10.2 | 0.021 [b] | 0.030 | 0.012 | 0.011 |
| $\bar{\alpha}$ [b] (-) | All | 0.030 | 0.004 | 0.005 | 0.004 |
| $k_{As}$ [b] (m/d) | All | 1.0 | 1.0 | 1.0 | 1.0 |
| $\mathbb{D}_1$ (-) | 6.3 | 0.0001 | 0.0001 | 0.0001 | 0.0002 |
| | 8.0 | 0.0011 | 0.0014 | 0.0004 | 0.0017 |
| | 10.2 | 0.0073 | 0.0129 | 0.0040 | 0.0077 |
| $\lvert\Delta\%R_{Max}\rvert$ | 8.0 | 0.81 | 2.89 | 2.33 | 2.11 |
| | 10.2 | 2.10 | 4.95 | 4.75 | 2.48 |
| $\lvert\Delta\%R_{Ave}\rvert$ | 8.0 | 0.56 | 2.16 | 1.53 | 1.08 |
| | 10.2 | 0.67 | 3.72 | 1.44 | 1.63 |

Notes for Table 6.1:

[a] $C_{net}$ : net charge density in the membrane surface obtained from our previous work [18]. The negative sign indicates a net negative charge.

[b] The B, $\bar{\alpha}$ and $k_S$ parameters at pH = 6.3 for all membranes for both $I^-$ and As(III) rejection analysis were obtained by fitting the corresponding experimental data to Equation 6.3 . The B parameter at pH = 10.2 for the TFC–S NF membrane for As(III) rejection analysis was also fitted in order to calculate the value of $\bar{\gamma}_{As,M}$ using Equation 6.14; $\bar{\gamma}_{As,M}$ was found to be equal to 9. The values of the B parameter at all other conditions were predicted.

conditions were then predicted as a function of permeate flux using Equations 6.3 and 6.4. Prediction lines are shown in Figure 6.3 as dashed (green) and dashed-dotted (red) lines for the pH values of 8.0 and 10.2, respectively. The prediction lines show that there was a good agreement between predicted and experimental values, with predictions for the LF10 RO membrane being in general more accurate than predictions for the TFC–S NF membrane. Also, predictions at pH = 8.0 for both membranes matched better the experimental data than predictions at pH = 10.2. The maximum and average differences at pH = 10.2 between predicted and experimental results were 2% and 0.98%, and 0.79% and 0.51% for the TFCS and LF10 membranes, respectively. Corresponding maximum and average values at pH = 8.0 were 1.8–2.6 times lower for both membranes.

***6.4.6. Prediction of Arsenic (III) Rejection at $pH_j$ = 8.0 and 10.2 Based on Rejection at $pH_i$ = 6.3.*** Given that the feed channel configuration and hydrodynamic conditions for As(III) rejection experiments were the same as those for iodide rejection experiments, the concentration polarization coefficients for As(III) and potassium iodide are related by [8]

$$k_{As} = k_{KI} \times \left( \frac{D_{As,H2O}}{D_{KI,H2O}} \right)^{2/3}, \qquad (6.16)$$

where $D_{As,\,H2O} = 1.0\times10^{-9}$ m$^2$/s and $D_{KI,\,H2O} = 2.0\times10^{-9}$ m$^2$/s are the solute diffusion coefficients in aqueous solution for $H_3AsO_3$ and KI, respectively. Using $k_{As}$ = 1.4 m/d obtained in the previous section, we calculated $k_{As}$ = 1.0 m/d, which was used for all membranes at all pH conditions.

For all membranes, the As(III) rejection data at pH = 6.3 was fitted to Equations 6.3 and 6.4 using $k_{As}$ = 1.0 m/d to obtain the values of the $\bar{\alpha}$ and $B_{pHi=6.3}$ parameters (see Table

6.1). The model fit lines are shown in Figure 6.2 as continuous (blue) lines. Values of the fitted B and $\bar{\alpha}$ parameters indicate that the TFC–S NF membrane had approximately 6–7 times more advective permeation of arsenic than the other membranes, and that the TFC–S NF and LF10 RO membranes had approximately 1.5–2.0 times more diffusive permeation of arsenic than the ESNA NF and FT30 RO membranes.

For the TFC–S NF membrane, $k_{As}$ = 1.0 m/d and the fitted $\bar{\alpha} = 0.03$ were used to fit the experimental data at pH = 10.2 (dashed-dotted red line in Figure 6.2a), obtaining $B_{pH=10.2}$ = 0.0211 m/d. The values of the B parameter for the TFC–S NF membrane at pH values of 6.3 and 10.2, and the corresponding Donnan exclusion coefficients $\mathbb{D}_1$ calculated with Equation 6.7 (see Table 6.1) were used in Equation 6.14 to obtain $\bar{\gamma}_{As,M} = 9$. Given that the activity coefficient of the neutral species $H_3AsO_3$ is likely approximately one ($\gamma_{0,M} \approx 1$), the $\bar{\gamma}_{As,M} = 9$ value indicates that $\gamma_{1,M} \approx 0.1$. The relatively low activity coefficient of the monovalent $H_2AsO_3^-$ in the polymer matrix ($\gamma_{1,M} \approx 0.1$) is consistent with the $\gamma_M < 0.1$ reported [30] for monovalent electrolytes in a crosslinked phenol sulfonated resin.

B parameters at $pH_j$ = 8.0 for all membranes, and $pH_j$ = 10.2 for all membranes except the TFC–S NF membrane were calculated using corresponding $B_{pHi=6.3}$ parameters, $\bar{\gamma}_{As,M} = 9$ and $\mathbb{D}_1$ coefficients at the corresponding pH conditions (see Table 6.1). The calculated $B_{pHj}$ were used to predict As(III) rejection as a function of permeate flux using Equations 6.3 and 6.4. Prediction curves are shown in Figure 6.2 as dashed (green) lines for pH = 8.0, and dashed-dotted (red) lines for pH = 10.2. The prediction lines show that

there was a good agreement between predicted and experimental values. In general, the predictions reproduced the relatively small variation in As(III) rejection in the pH range of 6.3–8.0, and the relatively significant variation at pH = 10.2.

A factor that may have played a role in the observed deviations between predicted and experimental rejection values is the variability in charge density between membrane coupons obtained from different locations of the same spiral-wound element or flat sheet (see Section 6.2.1). In our previous work [11] we reported that the concentrations of ionized carboxylic groups at a given pH in different locations of a spiral-wound membrane element of the FT30 RO membrane were up to 40% different. A sensitivity analysis (not shown) of the effect that a 40% difference in $C_{net}$ would have in the percent rejection of As(III) at pH = 10.2 indicates that such difference would account for the observed deviation between predicted and experimental results for both FT30 RO and LF10 RO membranes.

Another factor that may have had an effect in the observed deviations between predicted and experimental results is the presence of the coat in coated membranes. While the ESNA NF membrane is uncoated and had the smallest deviation between predicted and experimental results at pH = 10.2, the LF10 RO membrane is the membrane with the thickest coat and had the largest deviations at the same pH value. In our previous work [17], we reported that LF10 RO and FT30 RO membranes had coat layers with thicknesses of 58±33nm and 25±35 nm, respectively. Rejection predictions relied on the validity of the $\bar{\gamma}_{As,M} = 9$ value as representative for all active layers; however, $\bar{\gamma}_{As,M} = 9$ was obtained from the analysis of the permeation data of the uncoated TFC–S membrane,

and as a result, while $\bar{\gamma}_{As,M} = 9$ may be representative for uncoated polyamide active layers such as that of the ESNA NF membrane, it may be less representative of active layers with thick coats such as that of the LF10 RO membrane.

***6.4.7. Implications of This Work on the Study of RO/NF Transport Phenomena.*** We have showed that the effect of the pH of the feed solution on the rejection of a strong electrolyte and a monoprotic weak acid by RO/NF membranes can be satisfactorily modeled using a modified solution-diffusion model that includes advective permeation [8], and the theory of Donnan potential in charged films permeable to ions [26]. Nevertheless, predicting the effect of pH on the rejection of strong electrolytes and weak acids requires the knowledge of the charge density in the active layer as a function of pH. The satisfactory agreement between predicted and experimental values of solute rejection as a function of pH found in the present study indicates that the experimental methods that we previously reported [18] for the quantification of the concentration of ionized functional groups in active layers provide a valuable characterization of their charge density. Additionally, the present work indicates that solute activity coefficients in the active layers may be significantly different from unity, and that as a result, they should not be neglected in transport models. We found that for uncoated polyamide active layers the representative ratio between the activity coefficient of the neutral species $H_3AsO_3$ and that of the conjugate ionic species $H_2AsO_3^-$ is $\bar{\gamma}_{As,M} = \gamma_{0,M} / \gamma_{1,M} = 9$. Finally, our results indicate that, for the purpose of predicting the effect that changing the pH of the feed solution has on solute rejection, it is reasonable to assume that solute activity coefficients in the active layer are approximately constant as a function of pH.

## 6.5. Acknowledgments

RBS analyses were carried out in the Center for Microanalysis of Materials, University of Illinois, partially supported by the U.S. Department of Energy under grant DEFG02-91-ER45439. The authors acknowledge Gorie Ster and Jeanne Luh for helpful discussions, and the companies Nitto Denko, Hydranautics and Koch Membrane Systems for providing membrane materials and related information. This work was supported by the National Science Foundation Environmental Engineering and Technology program under agreement number BES-0332217, and the WaterCAMPWS, a Science and Technology Center of Advanced Materials for the Purification of Water with Systems under agreement number CTS-0120978. The opinions in this paper do not necessarily reflect those of the sponsor.

## 6.6. References

1. Mulder, M., *Principles of Membrane Technology*. Second ed.; Kluwer Academic: Boston, MA, 1996.

2. Petersen, R. J., Composite reverse osmosis and nanofiltration membranes. *J. Mem. Sci.* **1993,** *83*, 81-150.

3. Bowen, W. R.; Welfoot, J. S., Modelling the performance of membrane nanofiltration-critical assessment and model development. *Chem. Eng. Sci.* **2002,** *57*, 1121-1137.

4. Paul, D. R., Reformulation of the solution-diffusion theory of reverse osmosis. *J. Mem. Sci.* **2004,** *241*, 371-386.

5. Szymczyk, A.; Fievet, P., Investigating transport properties of nanofiltration membranes by means of a steric, electric and dielectric exclusion model. *J. Mem. Sci.* **2005**, (252), 77-88.

6. Wijmans, J. G.; Baker, R. W., The solution-diffusion model: a review. *J. Mem. Sci.* **1995,** *107*, 1-21.

7. Spiegler, K. S.; Kedem, O., Thermodynamics of hyperfiltration (reverse osmosis): criteria for efficient membranes. *Desalination* **1966,** *1*, 311-326.

8. Urama, R. I.; Mariñas, B. J., Mechanistic interpretation of solute permeation through a fully aromatic polyamide reverse osmosis membrane. *J. Mem. Sci.* **1997,** *123*, 267-280.

9. Schaep, J.; Vandecasteele, C.; Mohammad, A. W.; Bowen, W. R., Analysis of the salt retention of nanofiltration membranes using the Donnan-steric partitioning pore model. *Sep. Sci. Technol.* **1999,** *34*, 3009-3030.

10. Bason, S.; Oren, Y.; Freger, V., Characterization of ion transport in thin films using electrochemical impedance spectroscopy II: Examination of the polyamide layer of RO membranes. *J. Mem. Sci.* **2007,** *302*, 10-19.

11. Coronell, O.; Mariñas, B. J.; Cahill, D. G., Accessibility and ion exchange stoichiometry of ionized carboxylic groups in the active layer of FT30 reverse osmosis membrane. *Environ. Sci. Technol.* **2009,** *43*, 5042-5048.

12. Coronell, O.; Mariñas, B. J.; Zhang, X.; Cahill, D. G., Quantification of functional groups and modeling of their ionization behavior in the active layer of FT30 reverse osmosis membrane. *Environ. Sci. Technol.* **2008,** *42*, 5260-5266.

13. De Baerdemaeker, J.; Boussu, K.; Djourelov, N.; Van der Bruggen, B.; Dauwe, C.; Weber, M.; Lynn, K. G., Investigation of nanopores in nanofiltration membranes using slow positron beam techniques. *Phys. Stat. Sol.* **2007,** *4*, 3804-3809.

14. Freger, V., Swelling and morphology of the skin layer of polyamide composite membranes: an atomic force microscopy study. *Environ. Sci. Technol.* **2004,** *38*, 3168-3175.

15. Kim, S. H.; Kwak, S.-Y.; Suzuki, T., Positron annihilation spectroscopic evidence to demonstrate the flux-enhancement mechanism in morphology-controlled thin-film-composite (TFC) membrane. *Environ. Sci. Technol.* **2005,** *39*, 1764-1770.

16. Zhang, X.; Cahill, D. G.; Coronell, O.; Mariñas, B. J., Absorption of water in the active layer of reverse osmosis membranes. *J. Mem. Sci.* **2009,** *331*, 143-151.

17. Coronell, O., Ionization behavior, stoichiometry of association and accessibility of functional groups in the active layers of reverse osmosis and nanofiltration membranes. *Chapter 4 of this dissertation*.

18. Coronell, O., Depth heterogeneity of the elemental composition, concentration of negative charges, degree of polymer crosslinking, and steric effects in the fully aromatic polyamide active layers of reverse osmosis and nanofiltration membranes. *Chapter 5 of this dissertation*.

19. Mi, B. Ph.D. dissertation, University of Illinois at Urbana-Champaign, Urbana, IL, 2006.

20. Mi, B., Personal communication. In 2009.

21. Hachisuka, H.; Ikeda, K. Reverse osmosis composite membrane and reverse osmosis treatment method for water using the same. US Patent, US 6,413,425 B1, 2002.

22. United States Environmental Protection Agency (USEPA), National primary drinking water regulations; Arsenic and clarificatoins to compliance and new source contaminants monitoring; Final rule. In Federal Register: 2001; Vol. 66(14), pp 6975-7066.

23. Johnson, D. L.; Pilson, M. E. Q., Spectrophotometric determination of arsenite, arsenate, and phosphate in natural waters. *Anal. Chim. Acta* **1972,** *58*, 289-299.

24. Adham, S. S.; Trussell, R. S.; Gagliardo, P. F.; Trussell, R. R., Rejection of MS-2 virus by RO membranes. *J. Am. Water Works Assn.* **1998,** *9*.

25. Matthiason, E.; Sivik, B., Concentration polarization and fouling. *Desalination* **1980,** *35*, 59-103.

26. Ohshima, H.; Ohki, S., Donnan potential and surface potential of a charged membrane. *Biophys. J.* **1985,** *47*, 673-678.

27. Snoeyink, V. L.; Jenkins, D., *Water Chemistry*. John Wiley & Sons: United States of America, 1980; p 463.

28. Oh, J. I.; Urase, T.; Kitawaki, H.; Rahman, M. M.; Rhahman, M. H.; Yamamoto, K., Modeling of arsenic rejection considering affinity and steric hindrance effect in nanofiltration membranes. *Water Sci. Technol.* **2000,** *42*, 173-180.

29. Bowen, W. R.; Mukhtar, H., Characterisation and predictoin of separation performance of nanofiltration membranes. *J. Mem. Sci.* **1996,** *112*, 263-274.

30. Lakshminarayanaiah, N., Activity coefficients of small ions in ion-exchange resins. *J. Polym. Sci., Part A: Polym. Chem.* **1963,** *1*, 139-149.

31. Tsuru, T.; Urairi, M. N.; Nakao, S.-I.; Kimura, S., Negative rejection of anions in the loose reverse osmosis separation of mono- and divalent ion mixtures. *Desalination* **1991,** *81*, 219-227.

32. Ohshima, H.; Kondo, T., Potential and pH distribution across a membrane with a surface layer of ionizable groups. *J. Theor. Biol.* **1987,** *124*, 191-198.

# CHAPTER 7

# CONCLUSIONS

This dissertation focused on: (i) the development of experimental and analytical procedures to quantify physico-chemical properties of the active layers of RO/NF membranes and interactions with ionic solutes; (ii) the use of such procedures to assess the relative differences and similarities between different RO/NF membranes; and (iii) the use of measured charge densities in active layers to predict solute rejection as a function of pH in commercial RO/NF membranes. Experimental procedures were based on the probing with heavy ions of target ionized functional groups in the active layers and the subsequent quantification of the heavy ions. Average values of physico-chemical properties throughout the active layers were quantified using Rutherford backscattering spectrometry (RBS) as analytical tool. Corresponding surface values were measured using X-ray photoelectron spectrometry (XPS). Conceptual and mathematical models were developed to describe experimental findings. Major outcomes of this dissertation are:

1. An experimental procedure was developed to quantify negatively and positively ionized functional groups in the active layers of RO/NF membranes as a function of solution pH. For polyamide (PA) active layers, the average total concentration of ionizable carboxylic groups (R–COOH) was 0.44±0.20 M, which was approximately an order of magnitude higher than the total concentration of ionizable amine groups ($R–NH_2$). For the sulfonated polyethersulfone (SPES)

active layer of the NTR−7450 NF membrane the concentration of sulfonate ($R–SO_3^-$) groups was 1.68±0.02 M.

2. The ionization behavior of functional groups in PA active layers was successfully modeled assuming acid-base equilibrium between functional groups and the aqueous solution. Two dissociation constants (i.e., $pK_{a,1}$ and $pK_{a,2}$) were necessary to adequately describe the ionization behavior of carboxylic groups, which was consistent with the reported bimodal pore size distribution in PA active layers. The $R–SO_3^-$ groups in the SPES active layer of the NTR−7450 NF membrane remained ionized across the pH range studied of 3.38–10.15.

3. An experimental and analytical procedure was developed to quantify the stoichiometry of association between negatively ionized functional groups and barium ion ($Ba^{2+}$), where the average number of ionized functional groups neutralized per $Ba^{2+}$ ion was referred to as the neutralization number (NN). For the SPES active layer of the NTR−7450 NF membrane, NN=1.96±0.05 at all pH values. For polyamide active layers, NN was found to be a function of pH, and this function was mathematically expressed in terms of one parameter *a*. The parameter *a* represents the concentration of neutralized $R–COO^-$ groups at which the stoichiometry of association between additional $R–COO^-$ sites that ionize as pH increases and the $Ba^{2+}$ ions that neutralize them changes from 1:1 to 2:1. The value of the parameter *a* was found to be in the 0.00–0.28 M range.

4. A conceptual and mathematical model was proposed that relates as a function of pH the concentration of $Ba^{2+}$ ion ($[Ba^{2+}]$) that associates with $R–COO^-$ groups,

[R–COO$^-$], NN, and AR, where AR (accessibility ratio) is the fraction of R–COO$^-$ groups accessible to $Ba^{2+}$ ion in the active layer. Experimental data for [$Ba^{2+}$], [R–COO$^-$], and NN was used to calculate AR as a function of pH. AR was found to be approximately constant in the pH range of ≈3.5–10.5 except sometimes at the lowest experimental pH of ≈3.5. Consistent with the relationship between the dissociation constants of carboxylic groups, water dielectric constant, and the size of the pores where the carboxylic groups are located, the constant AR as a function of pH indicates that pores of different sizes in PA active layers are interconnected, therefore creating a network of pores that makes carboxylic groups in smaller and bigger pores equally accessible (or inaccessible) to barium ion. The value of the AR parameter was found to be in the 0.40–0.81 range for PA active layers. For the SPES active layer of the NTR–7450 NF membrane, AR = 0.95±0.01 indicating that approximately 100% of sulfonate groups were accessible to barium ion.

5. The characterization of the active layers of different RO/NF membranes resulted in the following observations:

    - Membrane rating (i.e., RO or NF) was not strongly correlated to the total concentration of carboxylic groups, total concentration of amine groups, dissociation constants of carboxylic groups (i.e., p$K_{a,1}$ and p$K_{a,2}$), iso-electric point, *a* parameter or AR parameter.
    - The degree of polymer crosslinking of the polyamide active layers of RO membranes was higher than the degree of crosslinking of NF membranes.

- While the total concentration of functional groups and p$K_{a,1}$ and p$K_{a,2}$ values were sometimes similar for different membranes, the *a* and AR parameters were in general different.
- Even though different membranes sometimes had similar total concentrations of carboxylic groups and p$K_{a,1}$ and p$K_{a,2}$ values, the fractions $w_1$ and $w_2$ of carboxylic groups with dissociation constants p$K_{a,1}$ and p$K_{a,2}$ , respectively, were in general different, thus resulting in different ionization behavior as a function of pH.
- The highest and lowest concentrations of ionizable carboxylic groups occurred for the membranes with the lowest and highest, respectively, p$K_{a,1}$ and p$K_{a,2}$ values.

6. Results showed that the PA active layers of some membranes (e.g., ESPA3 RO) were depth homogeneous with respect to the concentration of carboxylic groups, p$K_a$ values, degree of crosslinking, concentration of barium ion that associated with ionized carboxylic groups, and steric effects experienced by $Ba^{2+}$ ion. In contrast, other group of PA membranes (e.g., NF90 NF) had active layers that were depth heterogeneous with respect to all properties just mentioned.

7. Depth homogeneous and depth heterogeneous active layers were found for both RO and NF membranes, and as a result, depth homogeneity/heterogeneity is not correlated to membrane rating.

8. When an active layer was found to be depth heterogeneous, surface properties compared to average properties throughout the active layer in the following ways:

(i) the surface concentration of ionizable functional groups were higher, (ii) the surface degree of crosslinking was lower, and (iii) contaminants experienced steric effects to a lesser extent at the surface.

9. The measured surface concentration of ionized carboxylic groups in coated polyamide membranes was lower (i.e., ~50%) than the average concentration of ionized carboxylic groups throughout the polyamide active layer.

10. The joint analysis of rejection data of arsenic (III) and the measured charge density in active layers indicated that the activity coefficients of solutes in active layers may be significantly different from one in contrast to what is commonly assumed in the literature.

11. The percentage rejection of a strong electrolyte (i.e., KI) and a weak acid (i.e., arsenious acid) as a function of pH by commercial RO/NF membranes were predicted using the measured concentrations of ionized functional groups in the active layers of the membranes tested, and solute rejection results at one pH value. The good agreement between predicted and experimental rejections indicated that: (i) the experimental procedures developed in this dissertation for the quantification of ionized functional groups in active layers provide results that adequately describe the active layer charge density that determines the electric exclusion of ionic contaminants from the membrane, and (ii) the quantification of the physico-chemical properties of active layers is a useful tool in the prediction of the effect that changing operational parameters such as pH have on membrane performance.

# CHAPTER 8

# FUTURE WORK

The results obtained and conclusions drawn from this dissertation have provided tools and raised questions that open avenues for future research. Three of the research questions that arouse from this study are listed below:

1. How does the value of the accessibility ratio (AR) relate to membrane performance? The AR parameter is, by definition, related to the steric effects that solutes experience in active layers, where lower AR values indicate a stronger steric exclusion of solutes from the active layers. Data such as that in Chapter 6 showing that the rejection of the neutral contaminant arsenious acid by the uncoated TFC–S NF membrane with AR = 0.81 was lower than its rejection by the also uncoated ESNA NF membrane with AR = 0.44 encourages the further study of the relationship between AR and solute rejection. (Rejection data for the coated membranes should not be directly compared to that of the uncoated membranes because while coats likely play a role in contaminant rejection, they do not play a role in the AR value obtained for coated active layers.)

2. In RO/NF membranes with polyamide active layers, what is the depth distribution of positive charges (i.e., ionized amine groups)? In this dissertation, the depth heterogeneity of negative charges (i.e., ionized carboxylic groups) was studied in polyamide active layers in a quantitative fashion. Similar studies remain to be performed for positive charges. The effect that different levels of depth

heterogeneity in the concentration of positive charges have on membrane performance also remains to be assessed.

3. Can the depth heterogeneity of active layers be tailored to maximize electric exclusion of ionic contaminants? Membrane preparation procedures should be explored with the goal of producing active layers with tailored depth heterogeneity. In such active layers, the charge density in the top sub-layer would be optimized to maximize electric exclusion of ionic contaminants, while the rest of the active layer would provide the desired level of rejection of neutral contaminants. Tailored depth heterogeneous active layers would be especially beneficial for NF applications where the ionic strength of feed waters is not high enough to significantly screen the charges in the active layers.

# APPENDIX A

# APPENDICES FOR CHAPTER 2

## Appendix A.1. Supporting Information for Chapter 2

**Summary of contents:**

- Two pages
- Figure A.1. RBS spectra of FT30 RO membrane samples before and after $WO_4^{2-}$ probing of protonated amine ($R–NH_3^+$) functional groups.
- **Note:** Bibliographic information for references cited in Appendix A.1 can be found in Section 2.6 of this dissertation.

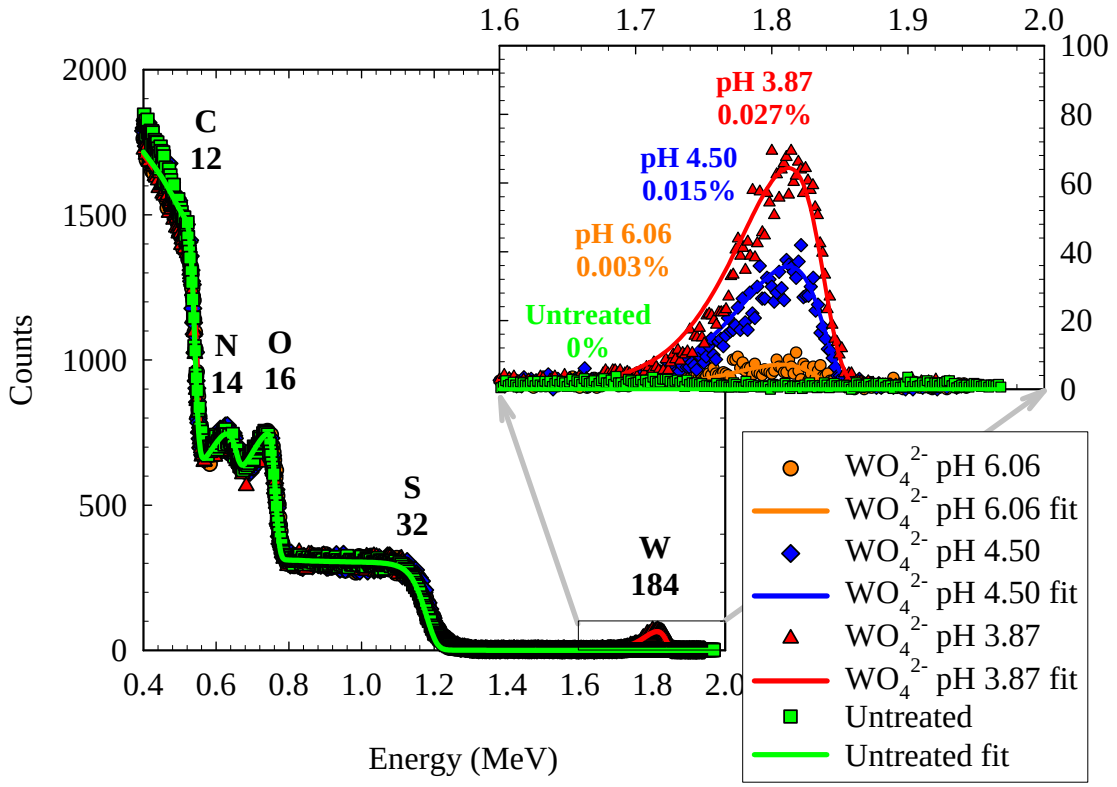


**Figure A.1**. RBS spectra of FT30 RO membrane samples before and after $WO_4^{2-}$ probing of protonated amine ($R–NH_3^+$) functional groups. $WO_4^{2-}$peaks correspond to the $WO_4^{2-}$ ionically bound to $R–NH_3^+$ in the membrane active layer. Symbols represent data. Lines represent the fit obtained using the software SIMNRA® as described previously [13, 17]. Percentage values correspond to W concentration in atomic percent. Higher $WO_4^{2-}$ concentrations at lower pH correspond to higher fraction of amine groups in $R–NH_3^+$ form.

**Appendix A.2. Results of Rutherford Backscattering Spectrometry (RBS) Analyses of FT30 Reverse Osmosis (RO) Membrane Samples Probed with Silver ($Ag^{+}$) Ion**

**Note:** Appendices A.2, A.3, B.2, B.3 and C.2 present representative results obtained when thin-film composite RO/NF membranes are characterized using the ion-probing/RBS analysis procedures developed in this dissertation. The results obtained with the FT30 RO membrane were chosen as representative for illustrative purposes. RBS spectra, fitted lines, and summary tables of calculated concentrations of ion probes in the active layers of samples probed with silver ($Ag^{+}$), barium ($Ba^{2+}$) and tungstate ($WO_4^{2-}$) ions, and used in $Ag^{+}$–$Ba^{2+}$ ion-displacement tests are provided.

| | **pH = 5.27** | | | |
|---|---|---|---|---|
| | **Treatment** | **pH max/pH min/pH final** | **Elemental ratio** | **Concentration [M]** |
| **1Ag** | **FT30+Ag 5.5** | 5.43/5.27/5.27 | 0.00032 | 0.03764 |
| **2Ag** | | 5.43/5.27/5.27 | 0.00035 | 0.04117 |
| **3Ag** | | 5.43/5.27/5.27 | 0.00032 | 0.03764 |
| | | | **Average** | 0.03882 |
| | | | **Std deviation** | 0.00204 |
| | | | **(Std dev/Mean)x100** | 5.25 |

| | **pH = 6.55** | | | |
|---|---|---|---|---|
| | **Treatment** | **pH max/pH min/pH final** | **Elemental ratio** | **Concentration [M]** |
| **4Ag** | **FT30+Ag 6.5** | 6.8/6.55/6.55 | 0.00058 | 0.06823 |
| **5Ag** | | 6.8/6.55/6.55 | 0.00074 | 0.08705 |
| **6Ag** | | 6.8/6.55/6.55 | 0.00080 | 0.09411 |
| | | | **Average** | 0.08313 |
| | | | **Std deviation** | 0.01338 |
| | | | **(Std dev/Mean)x100** | 16.09 |

| | **pH = 4.52** | | | |
|---|---|---|---|---|
| | **Treatment** | **pH max/pH min/pH final** | **Elemental ratio** | **Concentration [M]** |
| **7Ag** | **FT30+Ag 4.5** | 4.83/4.5/4.52 | 0.00014 | 0.01647 |
| **8Ag** | | 4.83/4.5/4.52 | 0.00013 | 0.01529 |
| | | | **Average** | 0.01588 |
| | | | **Std deviation** | 0.00083 |
| | | | **(Std dev/Mean)x100** | 5.24 |

| | **pH = 3.65** | | | |
|---|---|---|---|---|
| | **Treatment** | **pH max/pH min/pH final** | **Elemental ratio** | **Concentration [M]** |
| **9Ag** | **FT30+Ag 3.5** | 3.75/3.55/3.65 | 0.00005 | 0.00588 |
| **10Ag** | | 3.75/3.55/3.65 | 0.00009 | 0.01059 |
| **11Ag** | | 3.75/3.55/3.65 | 0.00013 | 0.01529 |
| | | | **Average** | 0.01059 |
| | | | **Std deviation** | 0.00471 |
| | | | **(Std dev/Mean)x100** | 44.44 |

| | pH = 8.52 | | | |
|---|---|---|---|---|
| | Treatment | pH max/pH min/pH final | Elemental ratio | Concentration [M] |
| 12Ag | FT30+Ag 8.5 | 8.56/8.40/8.52 | 0.00167 | 0.19646 |
| 13Ag | | 8.56/8.40/8.52 | 0.00140 | 0.16470 |
| | | | Average | 0.18058 |
| | | | Std deviation | 0.02246 |
| | | | (Std dev/Mean)x100 | 12.44 |

| | pH =10.48 | | | |
|---|---|---|---|---|
| | Treatment | pH max/pH min/pH final | Elemental ratio | Concentration [M] |
| 14Ag | FT30+Ag 10.5 | 10.6/10.48/10.48 | 0.00340 | 0.39998 |
| 15Ag | | 10.6/10.48/10.48 | 0.00375 | 0.44115 |
| | | | Average | 0.42056 |
| | | | Std deviation | 0.02911 |
| | | | (Std dev/Mean)x100 | 6.92 |

| | pH = 9.35 | | | |
|---|---|---|---|---|
| | Treatment | pH max/pH min/pH final | Elemental ratio | Concentration [M] |
| 16Ag | FT30+Ag 9.5 | 9.35/9.31/9.35 | 0.00275 | 0.32351 |
| 17Ag | | 9.35/9.31/9.35 | 0.00280 | 0.32939 |
| 18Ag | | 9.35/9.31/9.35 | 0.00260 | 0.30586 |
| | | | Average | 0.31959 |
| | | | Std deviation | 0.01224 |
| | | | (Std dev/Mean)x100 | 3.83 |

**1Ag**

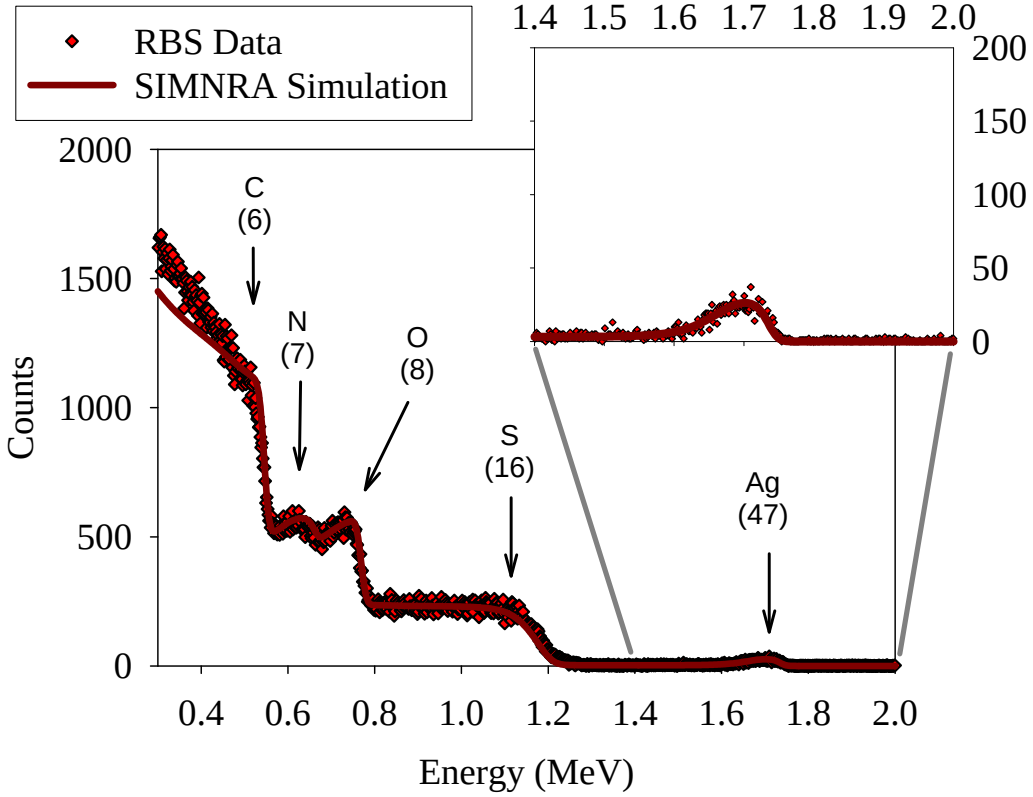
RBS Data
SIMNRA Simulation
Counts
Energy (MeV)
C (6)
N (7)
O (8)
S (16)
Ag (47)

**2Ag**

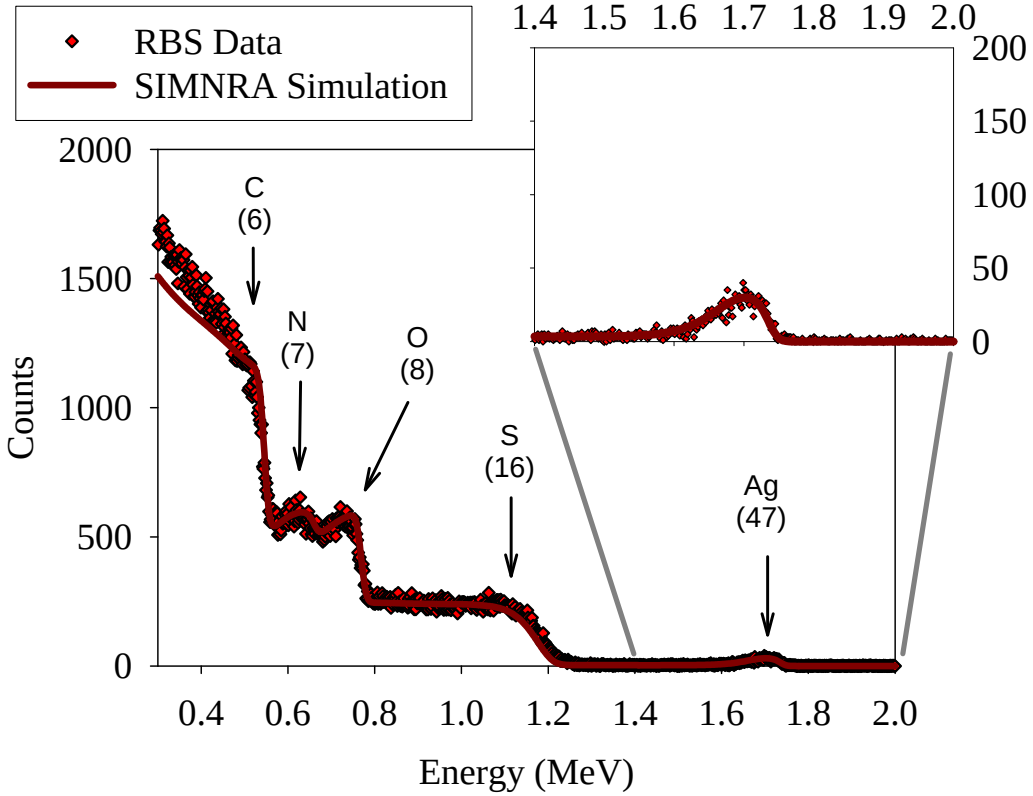
RBS Data
SIMNRA Simulation
Counts
Energy (MeV)
C (6)
N (7)
O (8)
S (16)
Ag (47)

**3Ag**

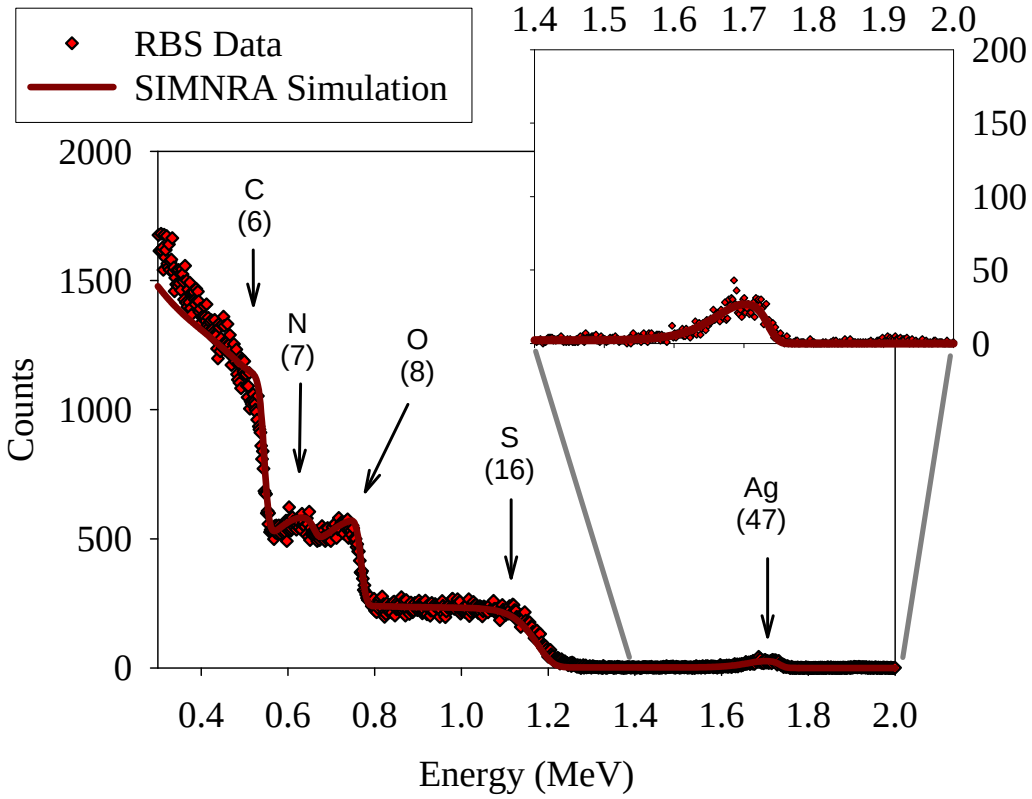
RBS Data
SIMNRA Simulation
Counts
Energy (MeV)
C (6)
N (7)
O (8)
S (16)
Ag (47)

**4Ag**

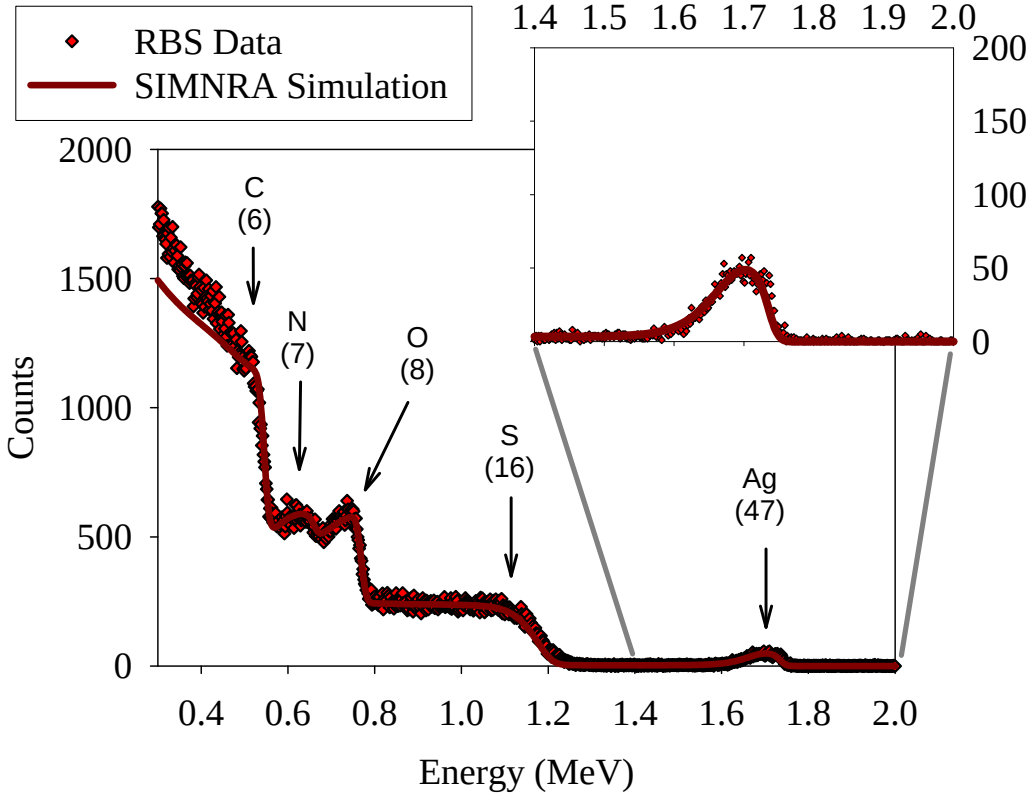
RBS Data
SIMNRA Simulation
Counts
Energy (MeV)
C (6)
N (7)
O (8)
S (16)
Ag (47)

**5Ag**

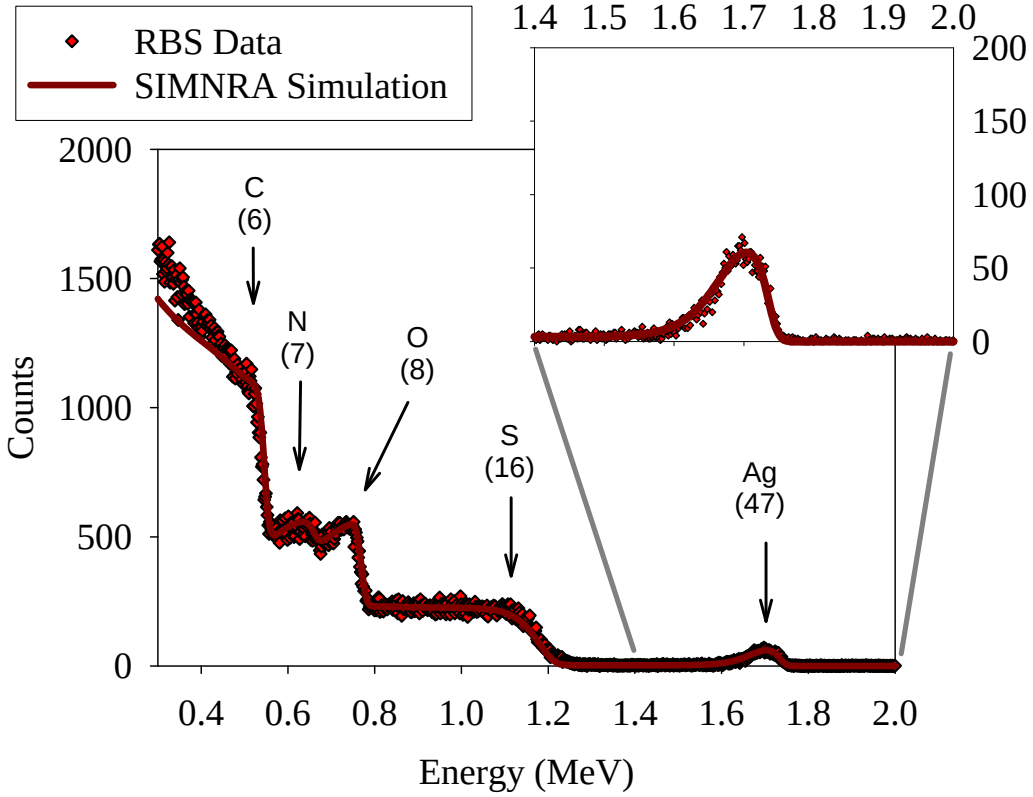
RBS Data
SIMNRA Simulation
Counts
Energy (MeV)
C (6)
N (7)
O (8)
S (16)
Ag (47)

**6Ag**

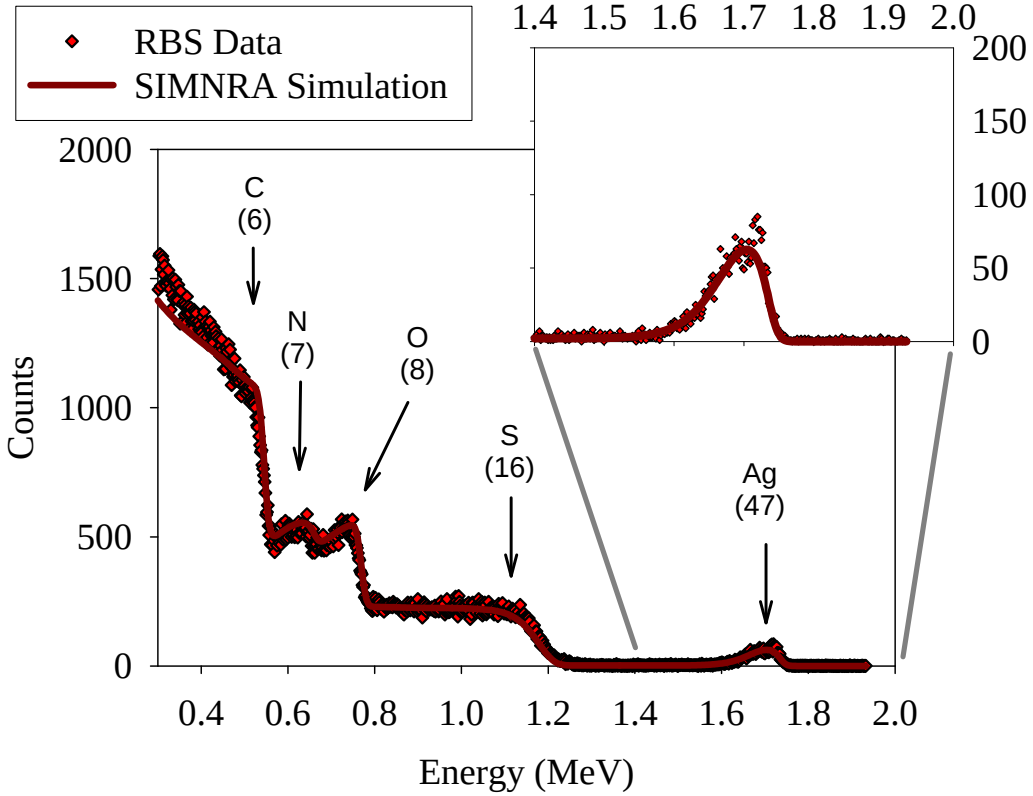
RBS Data
SIMNRA Simulation
Counts
Energy (MeV)
C (6)
N (7)
O (8)
S (16)
Ag (47)

**7Ag**

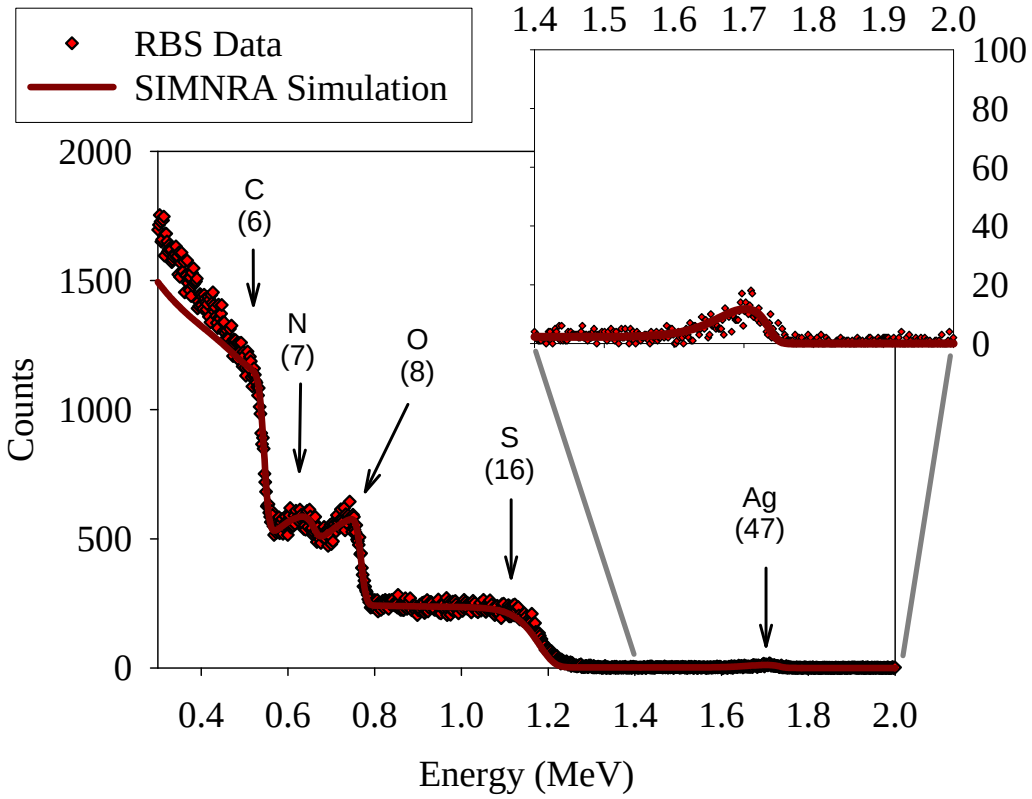
RBS Data
SIMNRA Simulation
Counts
Energy (MeV)
C (6)
N (7)
O (8)
S (16)
Ag (47)

**8Ag**

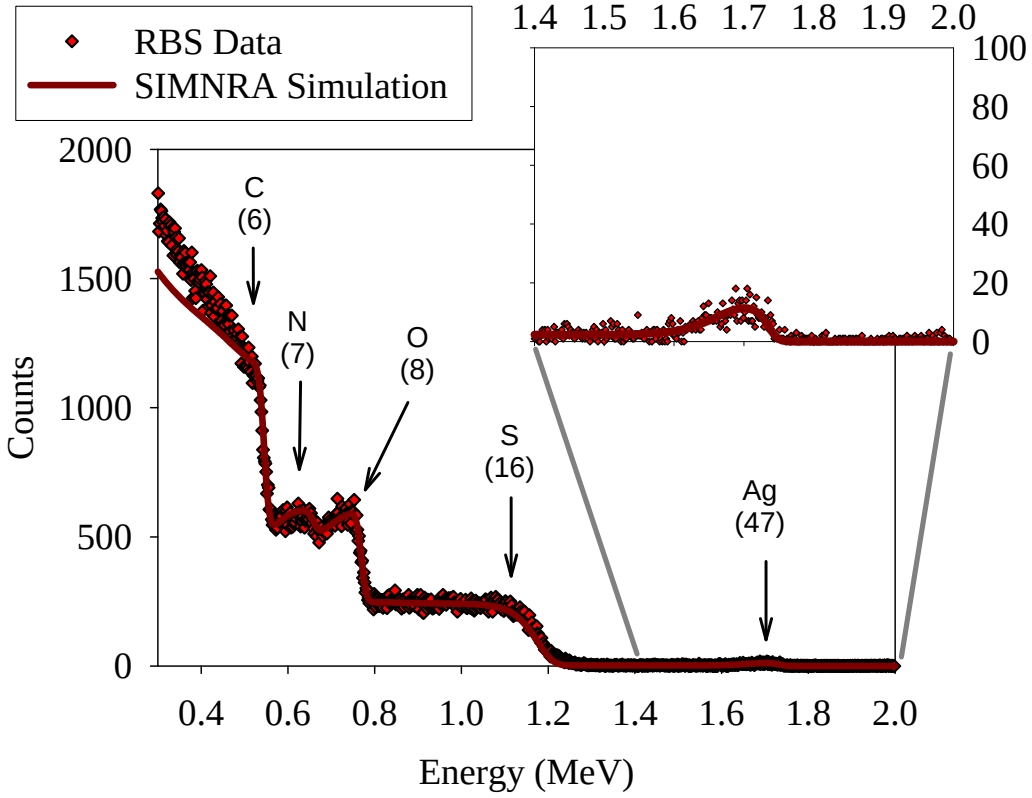
RBS Data
SIMNRA Simulation
Counts
Energy (MeV)
C (6)
N (7)
O (8)
S (16)
Ag (47)

**9Ag**

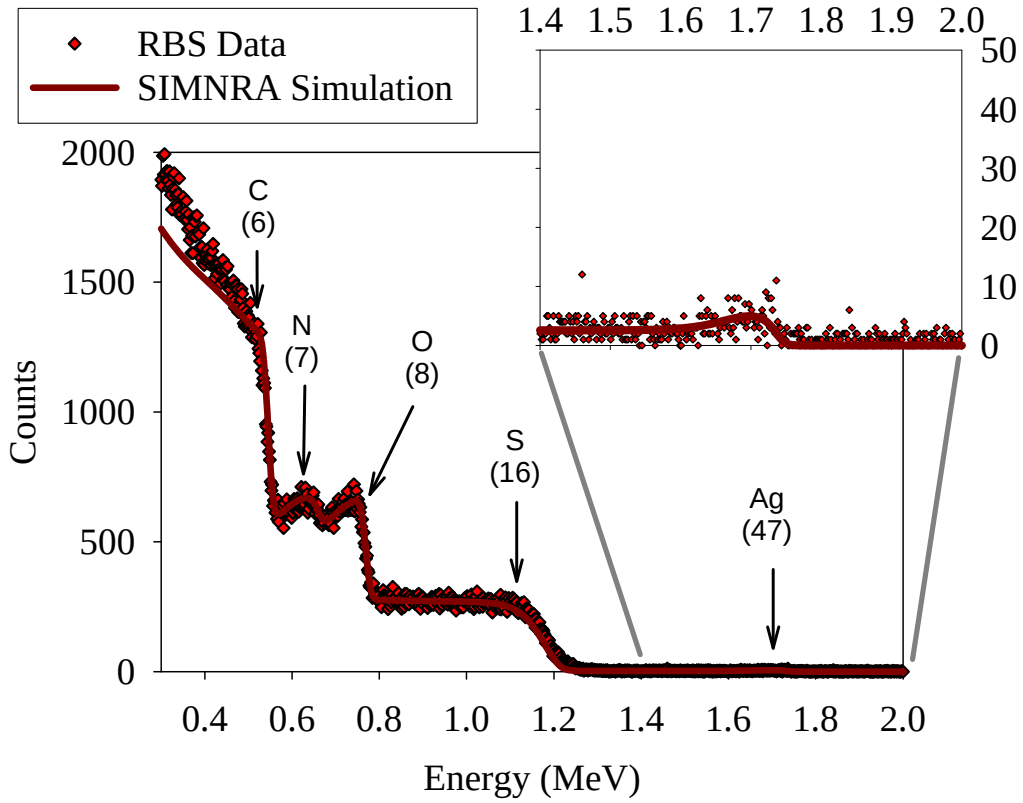
RBS Data
SIMNRA Simulation
Counts
Energy (MeV)
C (6)
N (7)
O (8)
S (16)
Ag (47)

**10Ag**

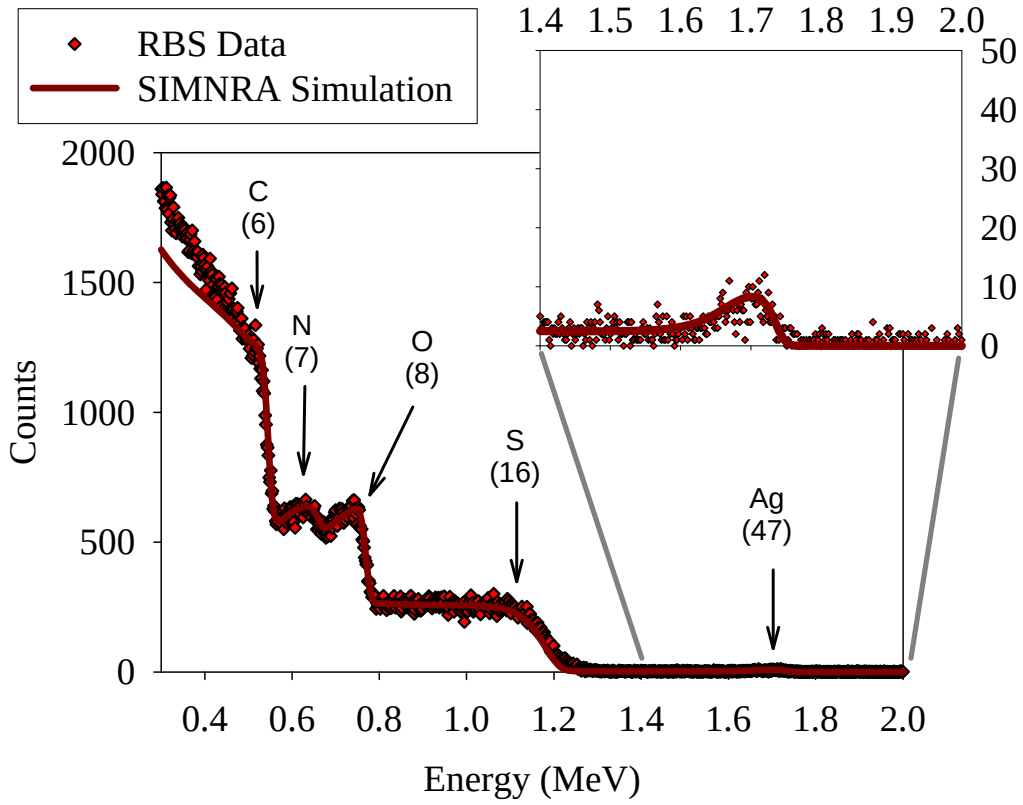
RBS Data
SIMNRA Simulation
Counts
Energy (MeV)
C (6)
N (7)
O (8)
S (16)
Ag (47)

**11Ag**

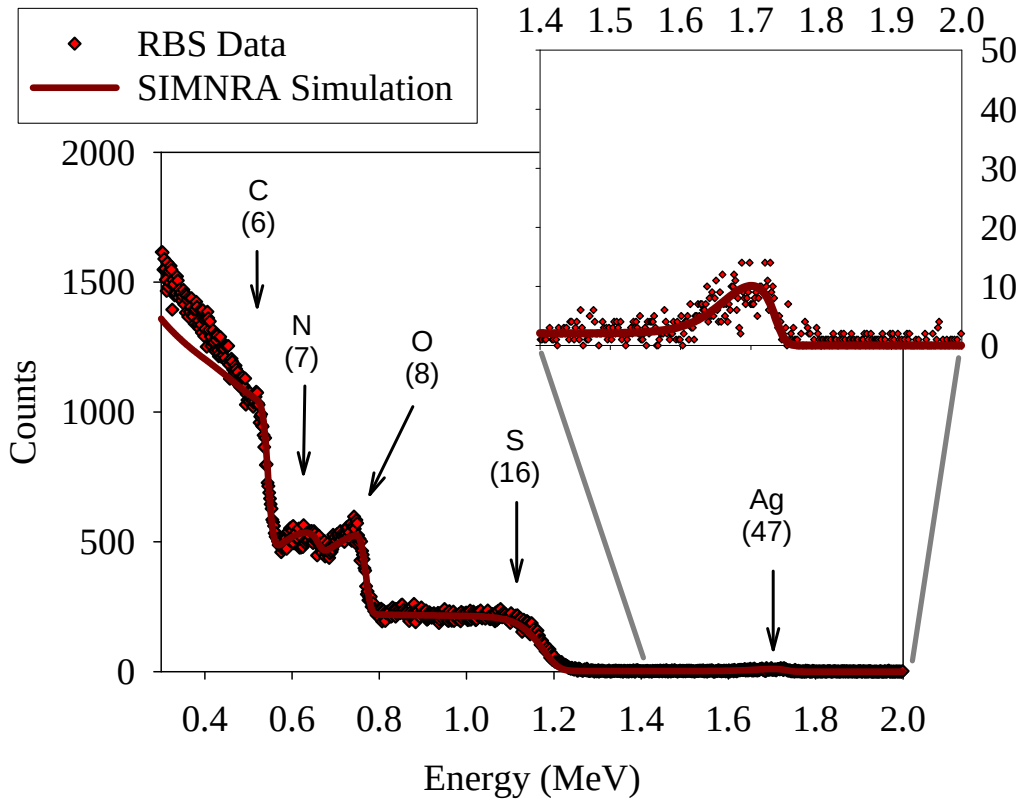
RBS Data
SIMNRA Simulation
Counts
Energy (MeV)
C (6)
N (7)
O (8)
S (16)
Ag (47)

**12Ag**

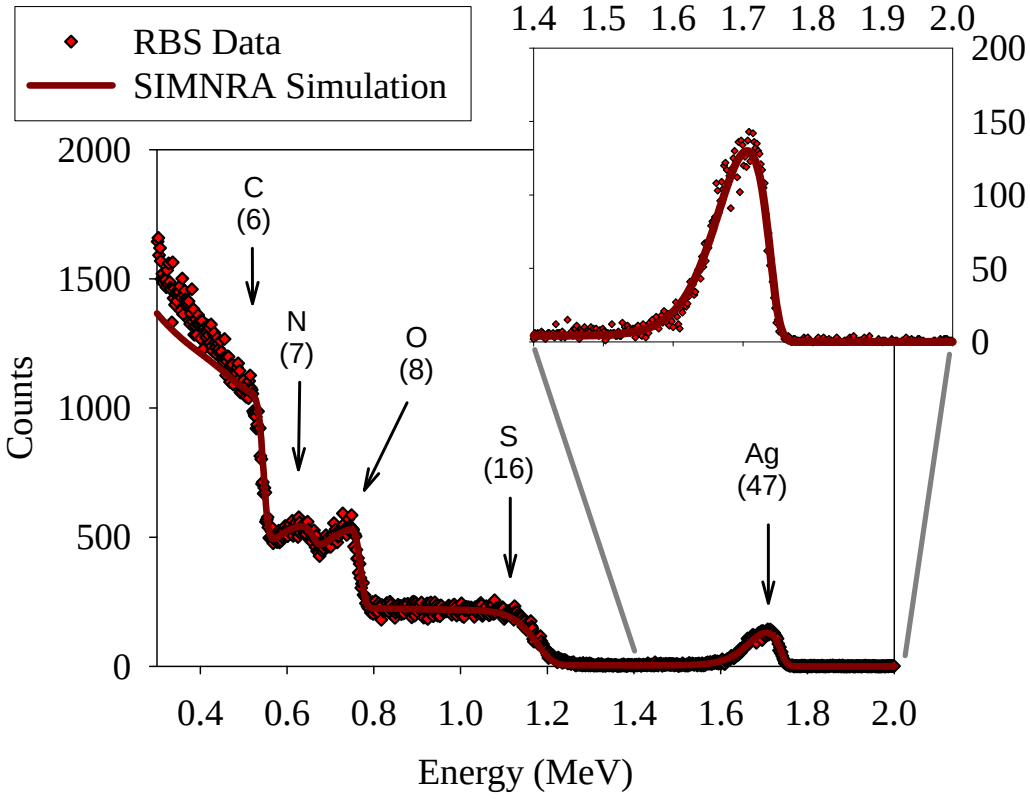
RBS Data
SIMNRA Simulation
Counts
Energy (MeV)
C (6)
N (7)
O (8)
S (16)
Ag (47)

**13Ag**

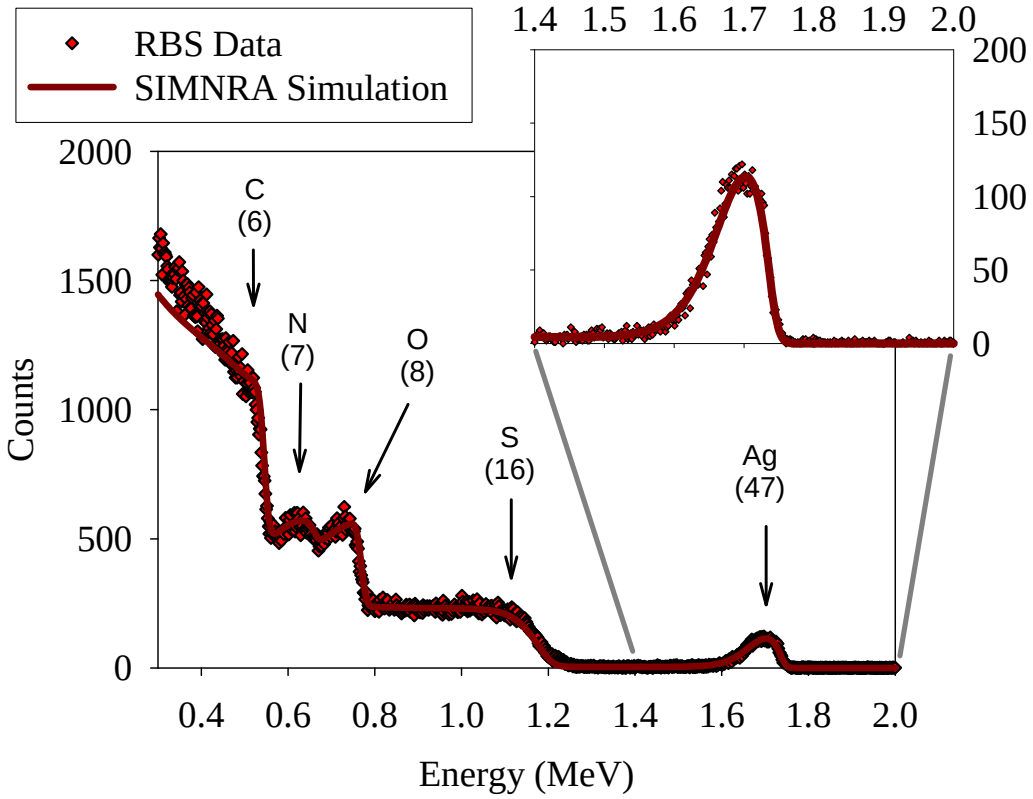
RBS Data
SIMNRA Simulation
Counts
Energy (MeV)
C (6)
N (7)
O (8)
S (16)
Ag (47)

**14Ag**

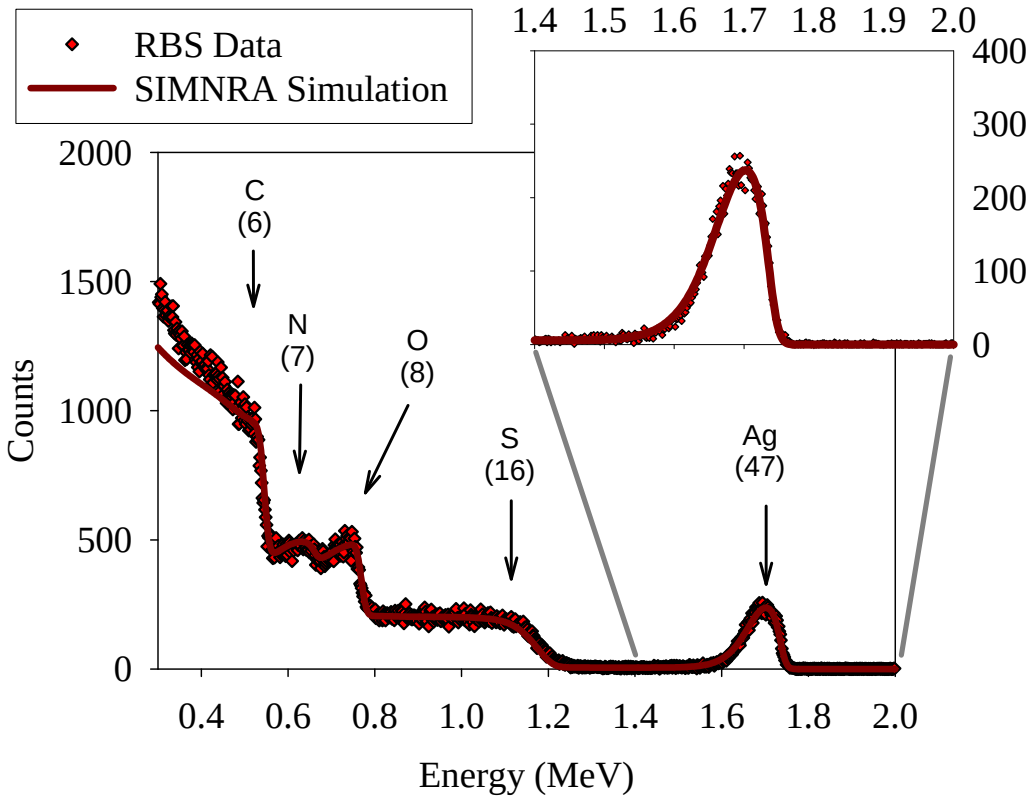
RBS Data
SIMNRA Simulation
Counts
Energy (MeV)
C (6)
N (7)
O (8)
S (16)
Ag (47)

**15Ag**

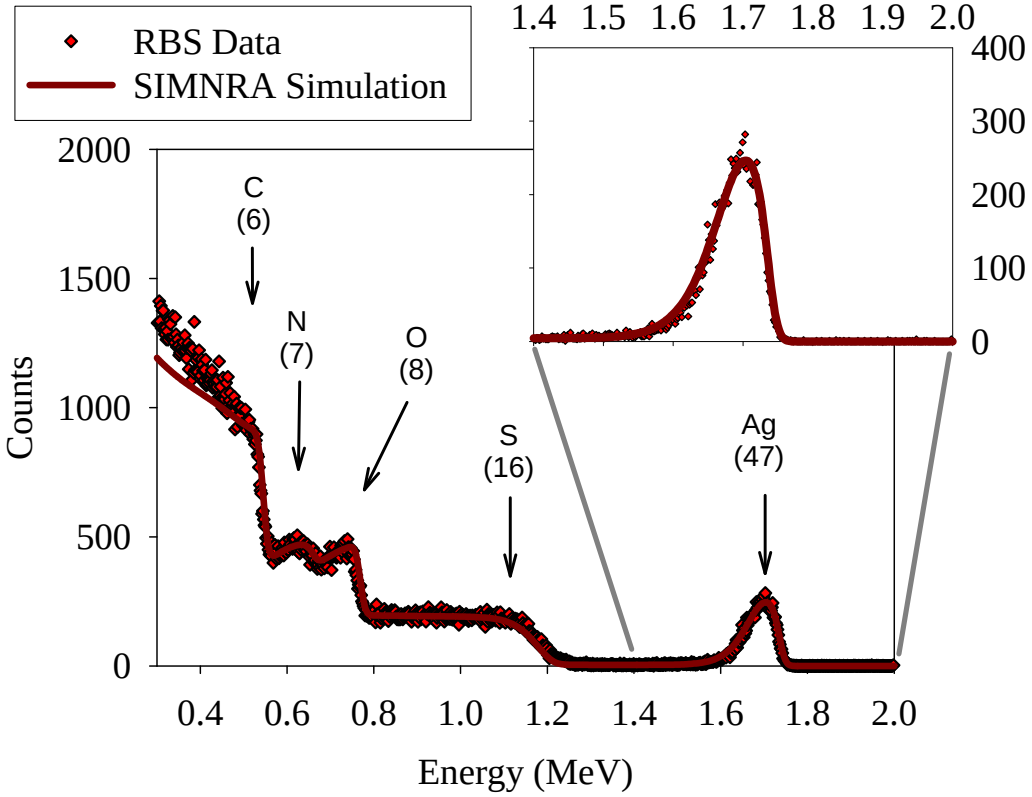
RBS Data
SIMNRA Simulation
Counts
Energy (MeV)
C (6)
N (7)
O (8)
S (16)
Ag (47)

**16Ag**

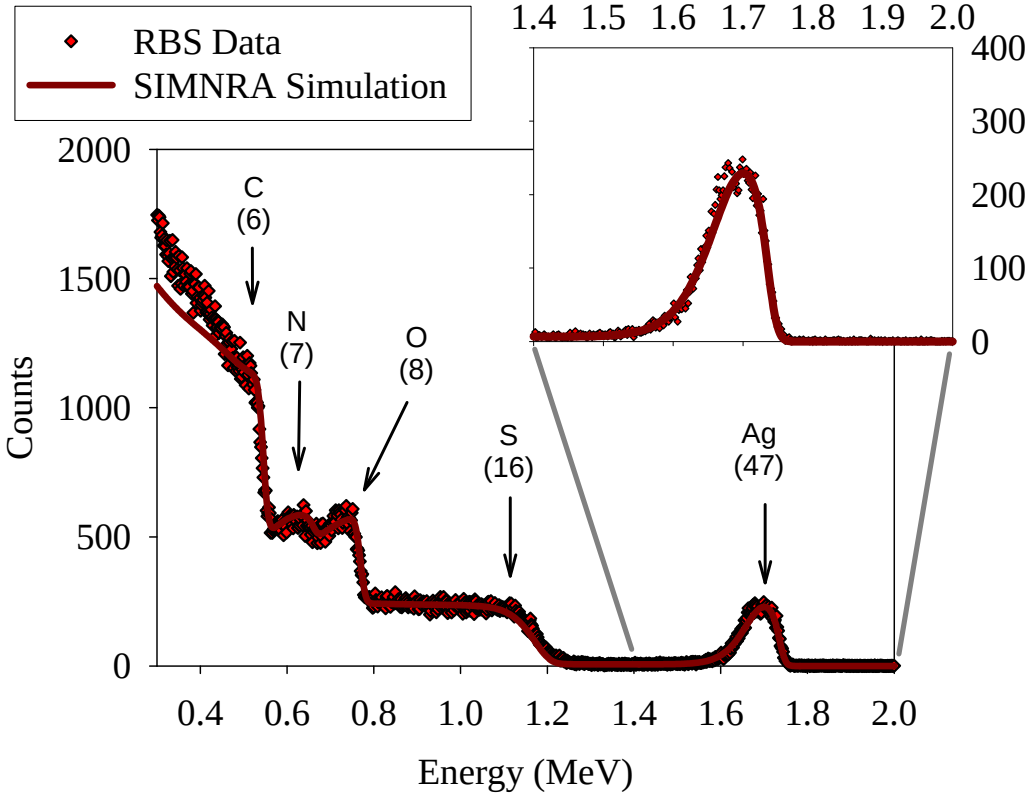
RBS Data
SIMNRA Simulation
Counts
Energy (MeV)
C (6)
N (7)
O (8)
S (16)
Ag (47)

**17Ag**

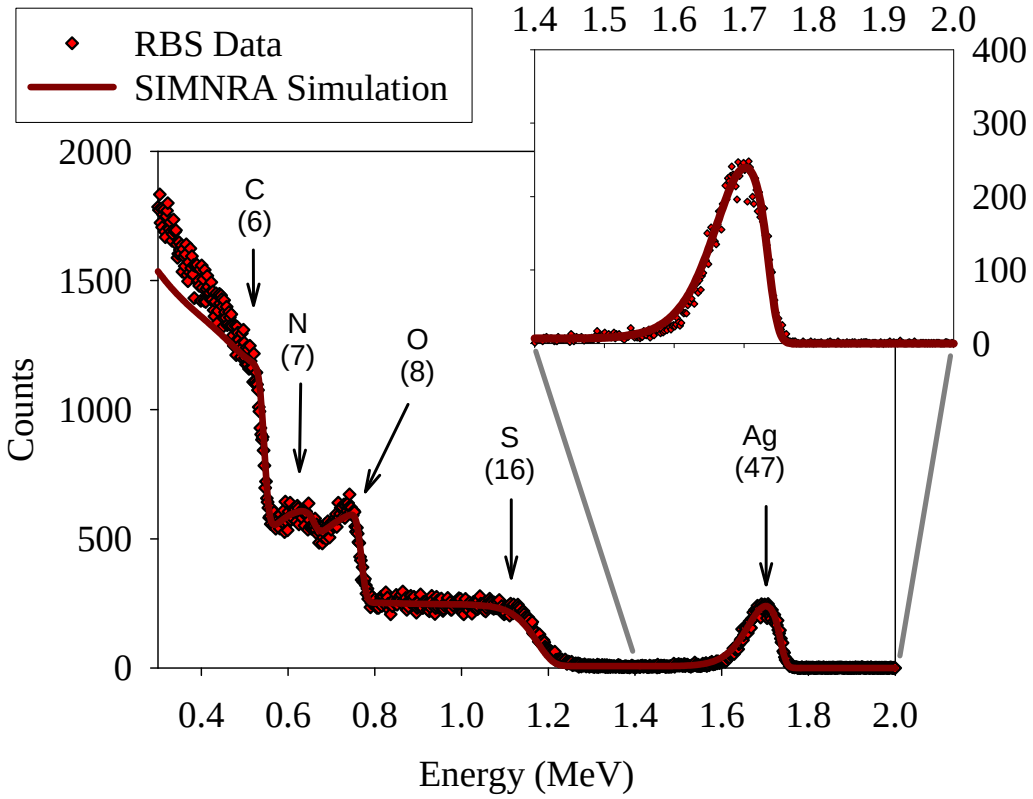
RBS Data
SIMNRA Simulation
Counts
Energy (MeV)
C (6)
N (7)
O (8)
S (16)
Ag (47)
2000
1500
1000
500
0
0.4
0.6
0.8
1.0
1.2
1.4
1.6
1.8
2.0
400
300
200
100
0

**18Ag**

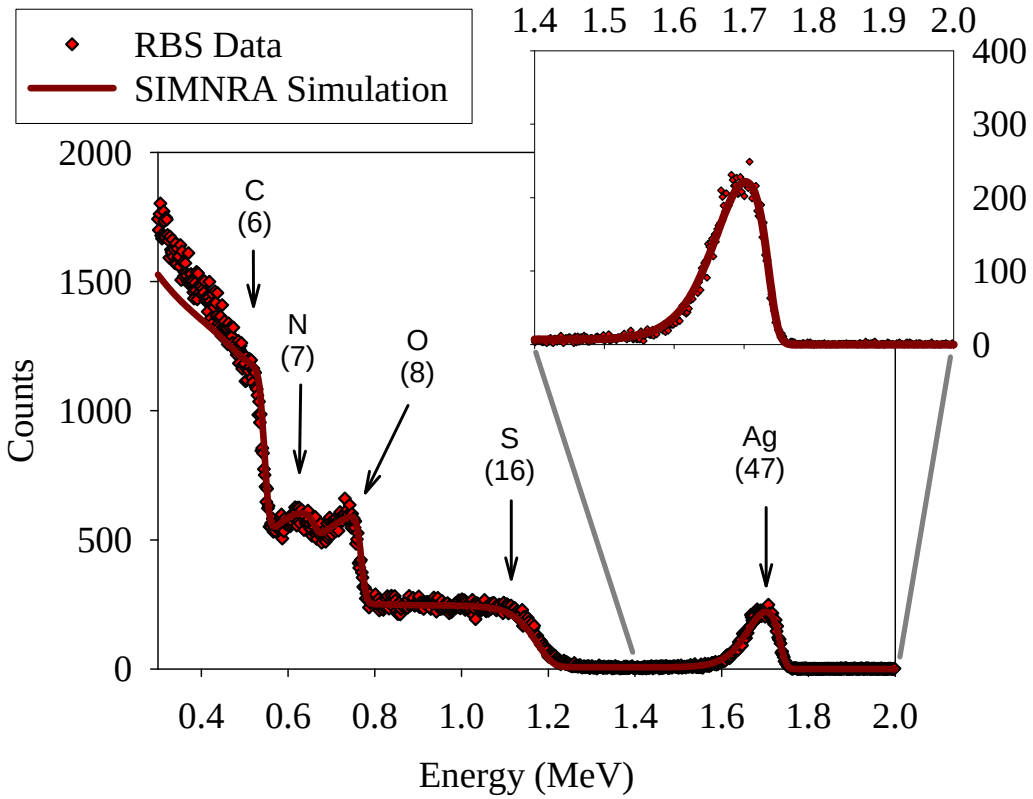
RBS Data
SIMNRA Simulation
Counts
Energy (MeV)
C (6)
N (7)
O (8)
S (16)
Ag (47)
2000
1500
1000
500
0
0.4
0.6
0.8
1.0
1.2
1.4
1.6
1.8
2.0
400
300
200
100
0

**Appendix A.3. Results of Rutherford Backscattering Spectrometry (RBS) Analyses of FT30 Reverse Osmosis (RO) Membrane Samples Probed with Tungstate ($WO_4^{2-}$) Ion**

| | pH = 5.65 and 5.51 | | | |
|---|---|---|---|---|
| | Treatment | pH max/pH min/pH final | Elemental ratio | Concentration [M] |
| 1W | FT30+W 5.5 | 5.65/5.62/5.65 | 0.000075 | 0.00943 |
| 2W | | 5.65/5.62/5.65 | 0.000085 | 0.01069 |
| 3W | | 5.65/5.51/5.51 | 0.000085 | 0.01069 |
| | | | Average | 0.01027 |
| | | | Std deviation | 0.00073 |
| | | | (Std dev/Mean)x100 | 7.07 |

| | pH = 4.50 | | | |
|---|---|---|---|---|
| | Treatment | pH max/pH min/pH final | Elemental ratio | Concentration [M] |
| 4W | FT30+W 4.5 | 4.62/4.48/4.50 | 0.00017 | 0.02137 |
| 5W | | 4.62/4.48/4.50 | 0.00015 | 0.01886 |
| 6W | | 4.62/4.48/4.50 | 0.00013 | 0.01634 |
| | | | Average | 0.01886 |
| | | | Std deviation | 0.00251 |
| | | | (Std dev/Mean)x100 | 13.33 |

| | pH = 6.72 | | | |
|---|---|---|---|---|
| | Treatment | pH max/pH min/pH final | Elemental ratio | Concentration [M] |
| 7W | FT30+W 6.5 | 6.73/6.61/6.72 | 0.000015 | 0.00189 |
| 8W | | 6.73/6.61/6.72 | 0.000015 | 0.00189 |
| 9W | | 6.73/6.61/6.72 | 0.000010 | 0.00126 |
| | | | Average | 0.00168 |
| | | | Std deviation | 0.00036 |
| | | | (Std dev/Mean)x100 | 21.65 |

| | pH = 7.40 | | | |
|---|---|---|---|---|
| | Treatment | pH max/pH min/pH final | Elemental ratio | Concentration [M] |
| 10W | FT30+W 7.5 | 7.60/7.10/7.40 | 0.000005 | 0.00063 |
| 11W | | 7.60/7.10/7.40 | 0.000005 | 0.00063 |
| 12W | | 7.60/7.10/7.40 | 0.000000 | 0.00000 |
| | | | Average | 0.00042 |
| | | | Std deviation | 0.00036 |
| | | | (Std dev/Mean)x100 | 86.60 |

| | pH = 6.06 | | | |
|---|---|---|---|---|
| | Treatment | pH max/pH min/pH final | Elemental ratio | Concentration [M] |
| 13W | FT30+W 6.0 | 6.25/6.04/6.06 | 0.000025 | 0.00314 |
| 14W | | 6.25/6.04/6.06 | 0.000035 | 0.00440 |
| 15W | | 6.25/6.04/6.06 | 0.000025 | 0.00314 |
| | | | Average | 0.00356 |
| | | | Std deviation | 0.00073 |
| | | | (Std dev/Mean)x100 | 20.38 |

| | pH = 3.87 | | | |
|---|---|---|---|---|
| | Treatment | pH max/pH min/pH final | Elemental ratio | Concentration [M] |
| 16W | FT30+W 4.0 | 4.06/3.89/3.87 | 0.00022 | 0.02766 |
| 17W | | 4.06/3.89/3.87 | 0.00030 | 0.03771 |
| 18W | | 4.06/3.89/3.87 | 0.00028 | 0.03520 |
| | | | **Average** | 0.03352 |
| | | | **Std deviation** | 0.00523 |
| | | | **(Std dev/Mean)x100** | 15.61 |

**1W**

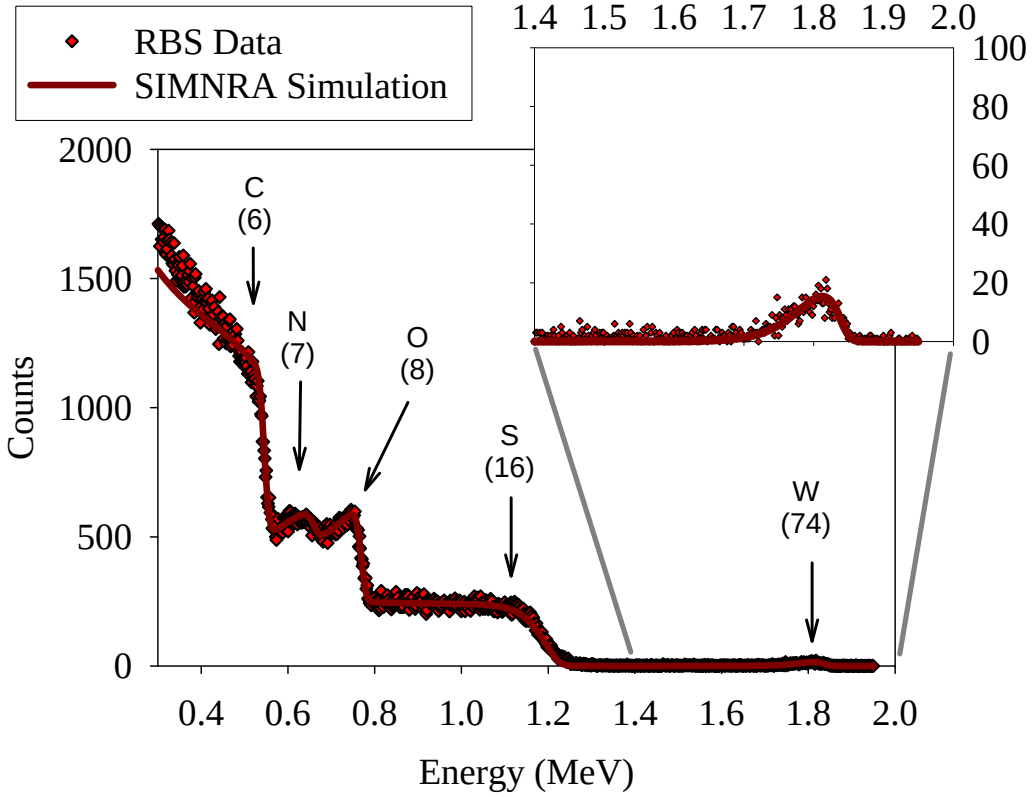
RBS Data
SIMNRA Simulation
Counts
Energy (MeV)
C (6)
N (7)
O (8)
S (16)
W (74)

**2W**

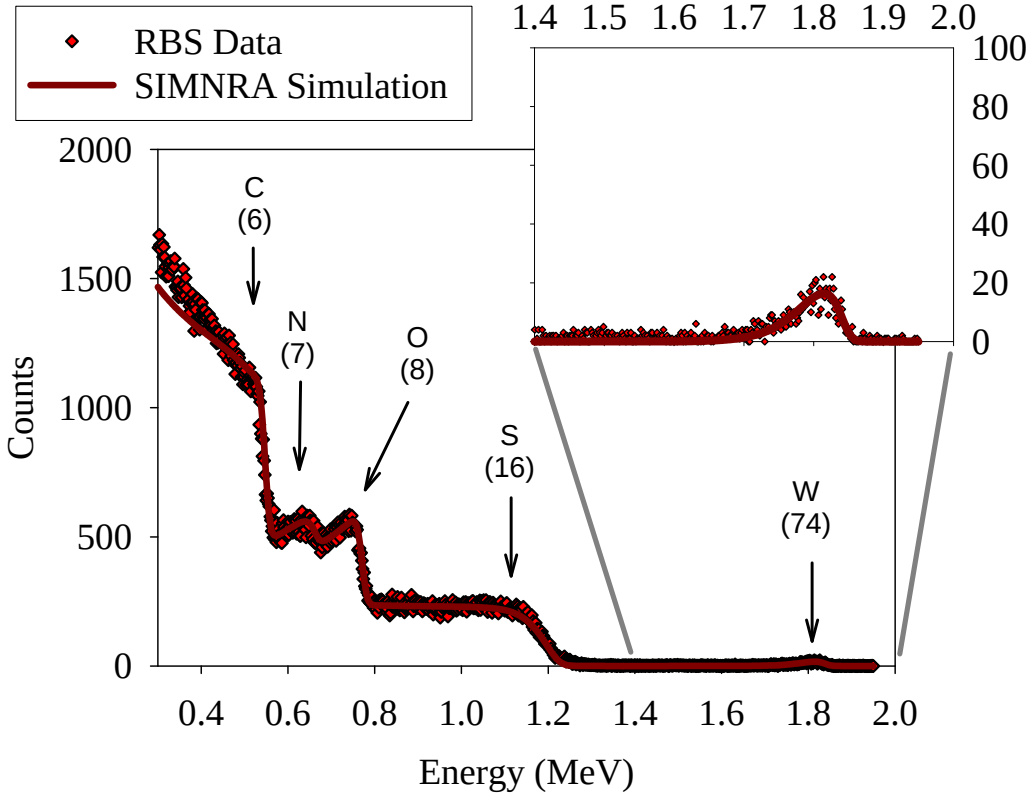
RBS Data
SIMNRA Simulation
Counts
Energy (MeV)
C (6)
N (7)
O (8)
S (16)
W (74)

**3W**

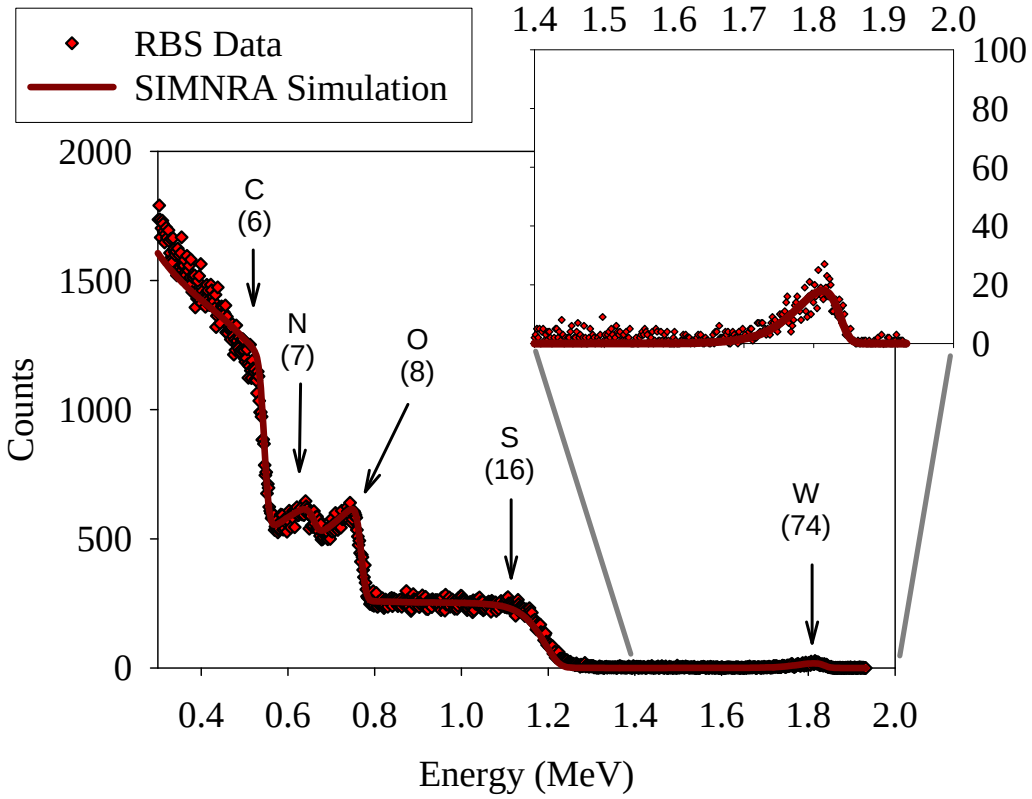
RBS Data
SIMNRA Simulation
Counts
Energy (MeV)
C (6)
N (7)
O (8)
S (16)
W (74)

**4W**

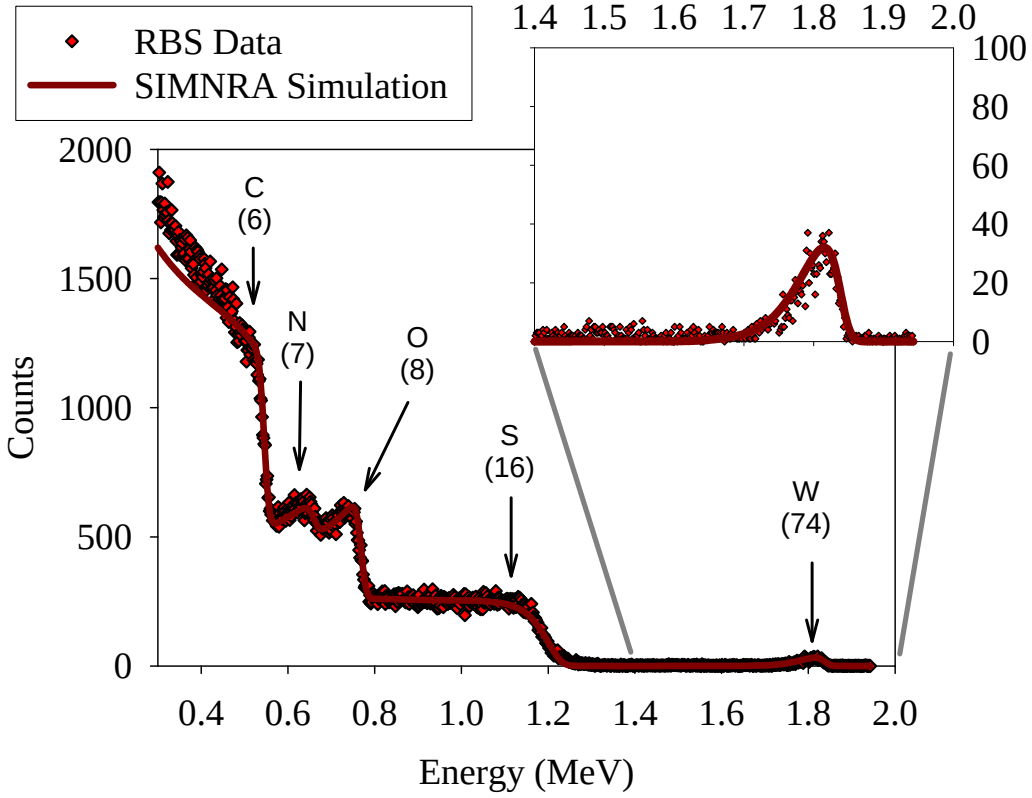
RBS Data
SIMNRA Simulation
Counts
Energy (MeV)
C (6)
N (7)
O (8)
S (16)
W (74)

**5W**

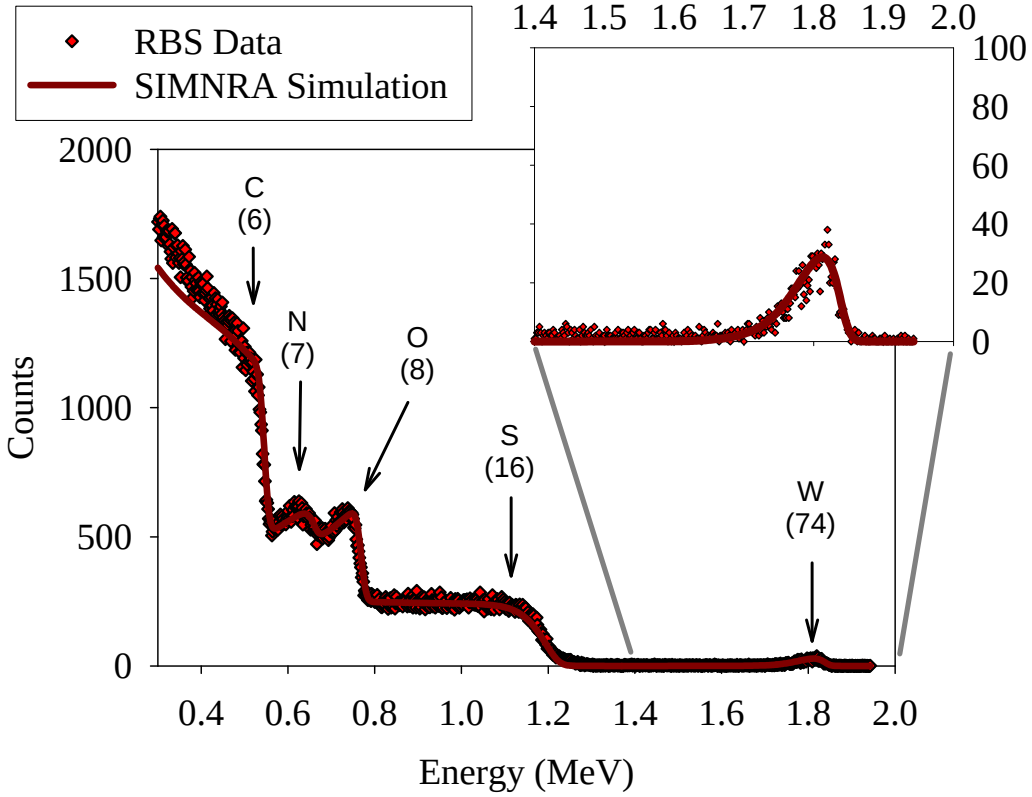
RBS Data
SIMNRA Simulation
Counts
Energy (MeV)
C (6)
N (7)
O (8)
S (16)
W (74)

**6W**

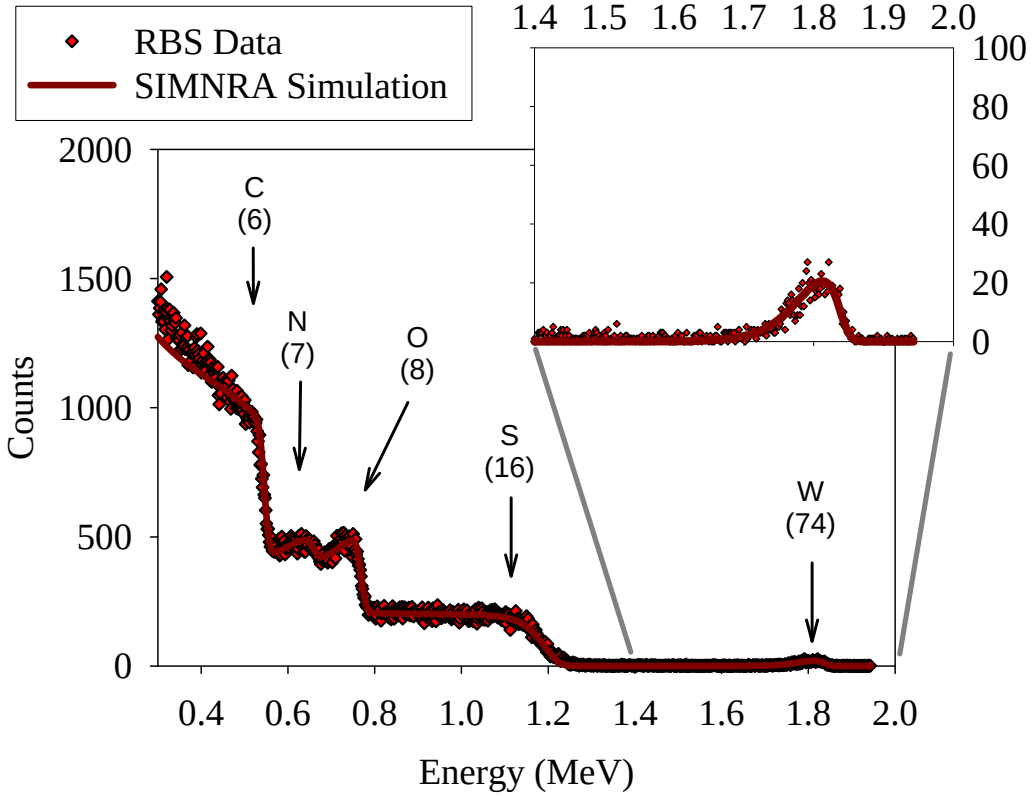
RBS Data
SIMNRA Simulation
Counts
Energy (MeV)
C (6)
N (7)
O (8)
S (16)
W (74)

**7W**

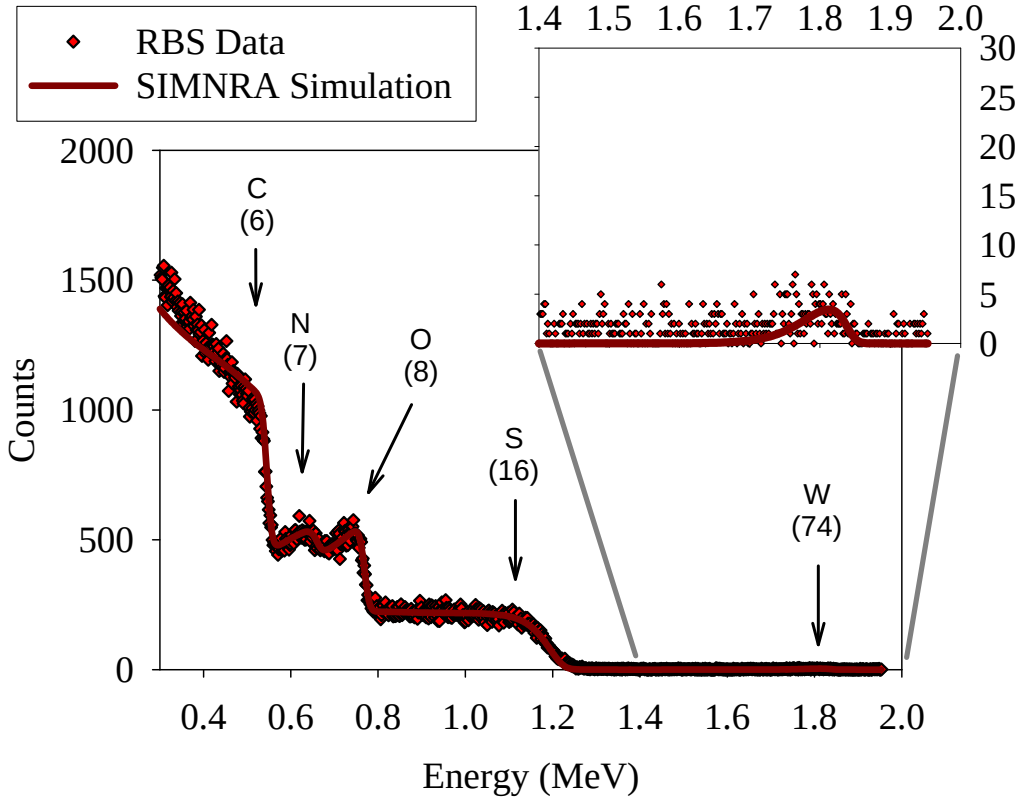
RBS Data
SIMNRA Simulation
Counts
Energy (MeV)
C (6)
N (7)
O (8)
S (16)
W (74)

**8W**

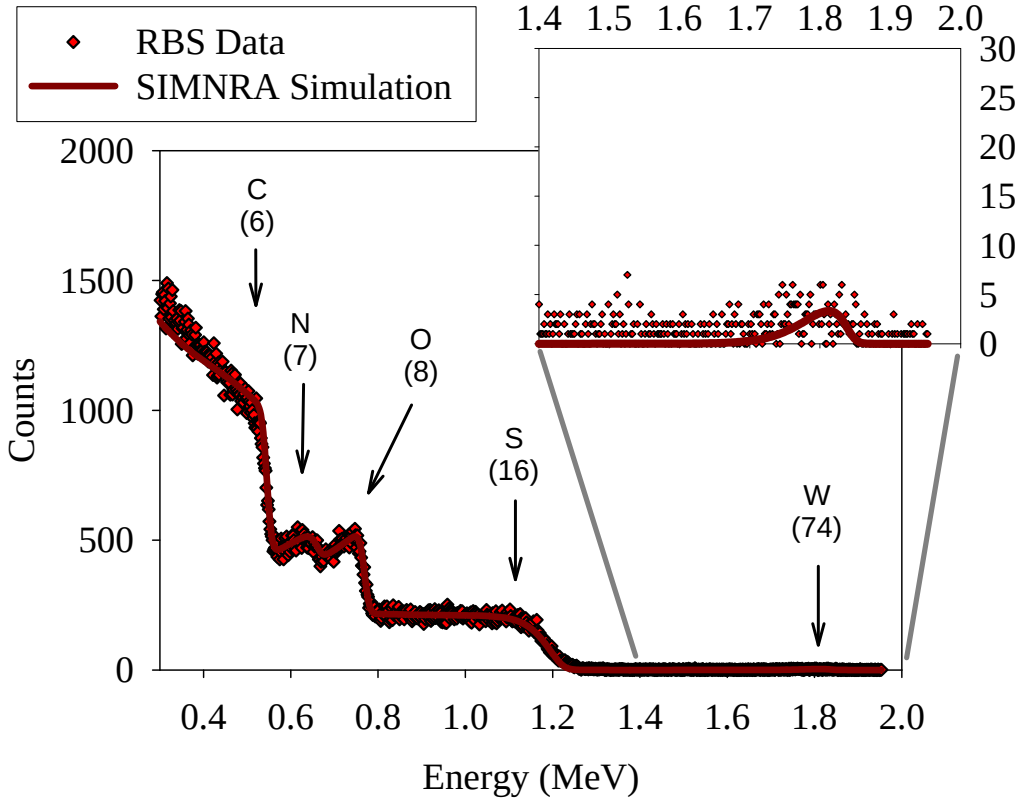
RBS Data
SIMNRA Simulation
Counts
Energy (MeV)
C (6)
N (7)
O (8)
S (16)
W (74)

**9W**

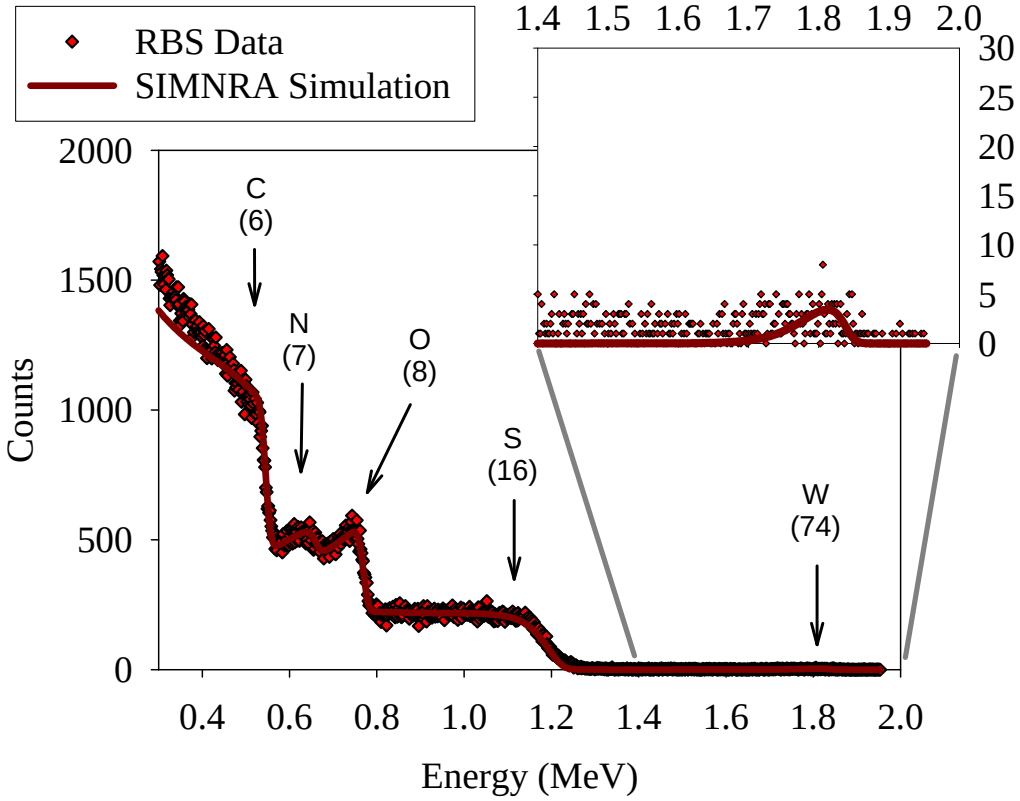
RBS Data
SIMNRA Simulation
Counts
Energy (MeV)
C (6)
N (7)
O (8)
S (16)
W (74)

**10W**

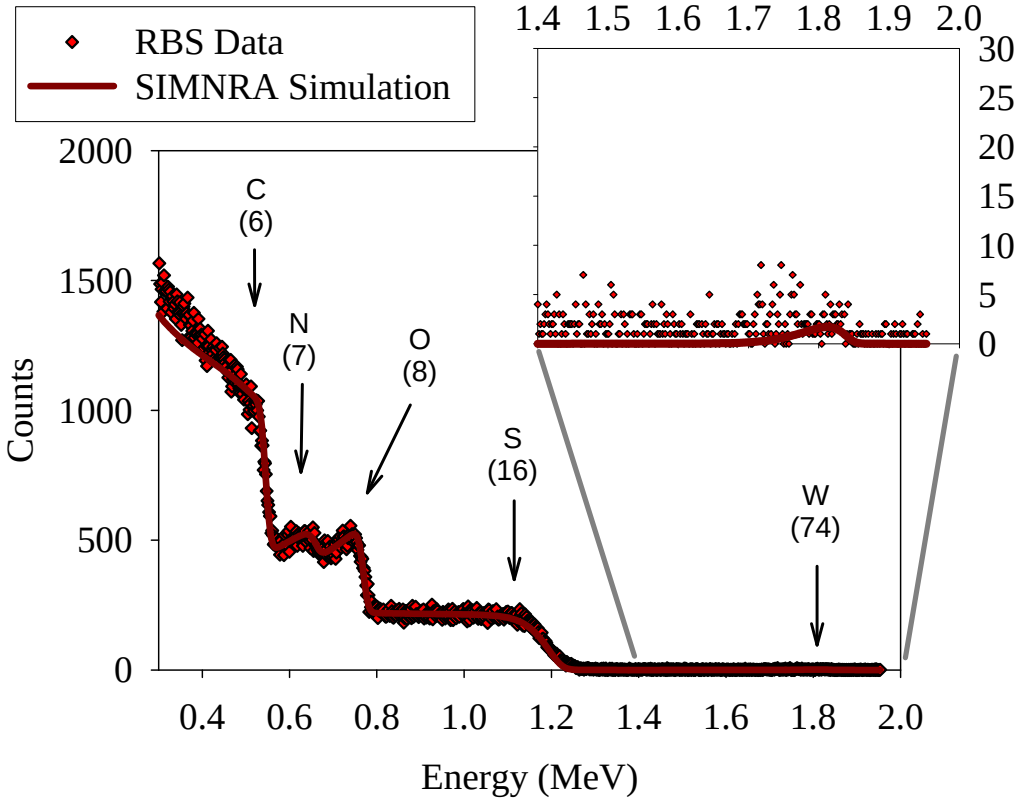
RBS Data
SIMNRA Simulation
Counts
Energy (MeV)
C (6)
N (7)
O (8)
S (16)
W (74)

**11W**

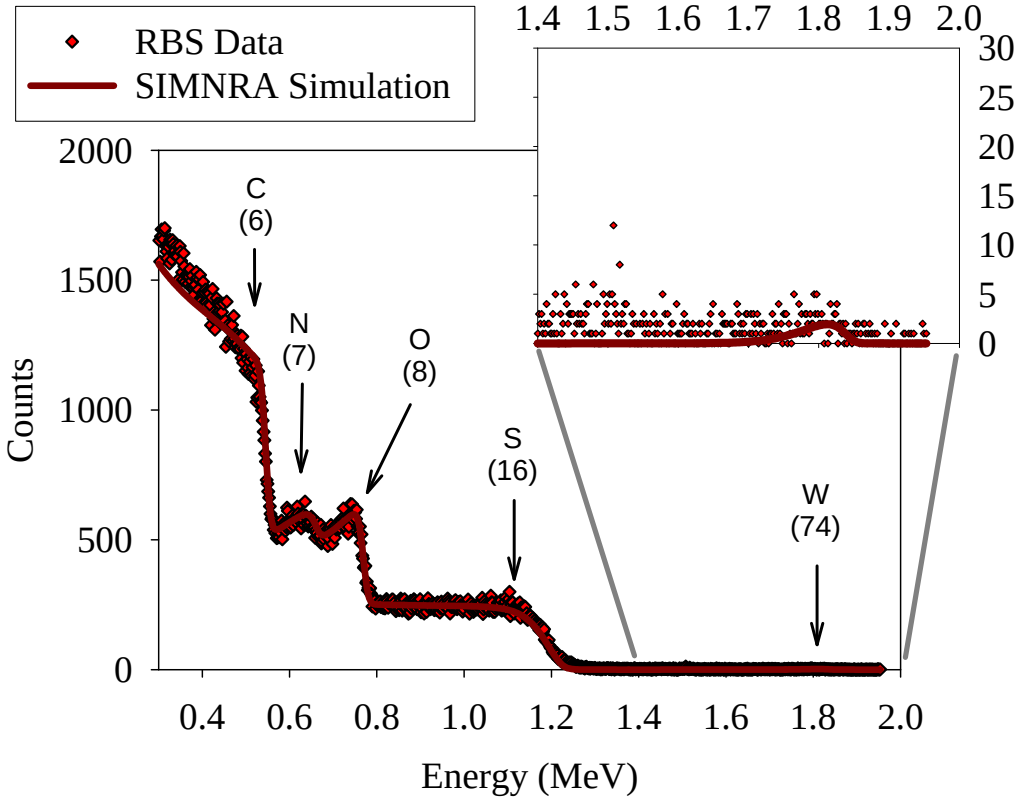
RBS Data
SIMNRA Simulation
Counts
Energy (MeV)
C (6)
N (7)
O (8)
S (16)
W (74)

**12W**

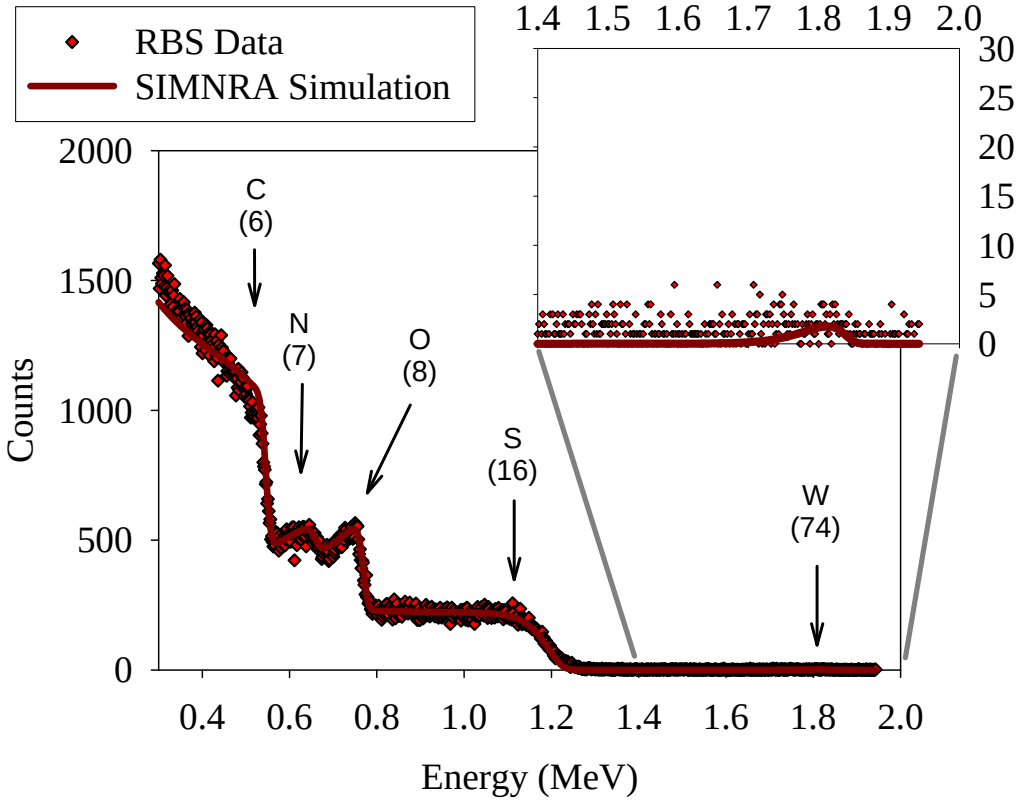
RBS Data
SIMNRA Simulation
Counts
Energy (MeV)
C (6)
N (7)
O (8)
S (16)
W (74)

**13W**

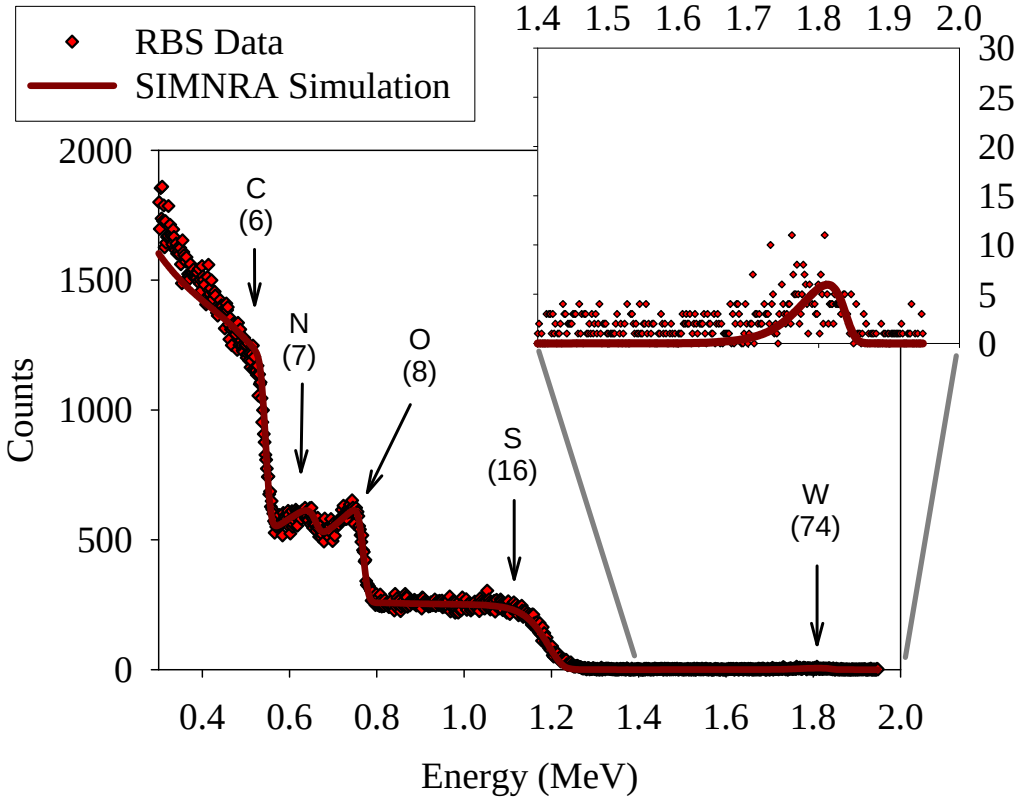
RBS Data
SIMNRA Simulation
Counts
Energy (MeV)
C (6)
N (7)
O (8)
S (16)
W (74)

**14W**

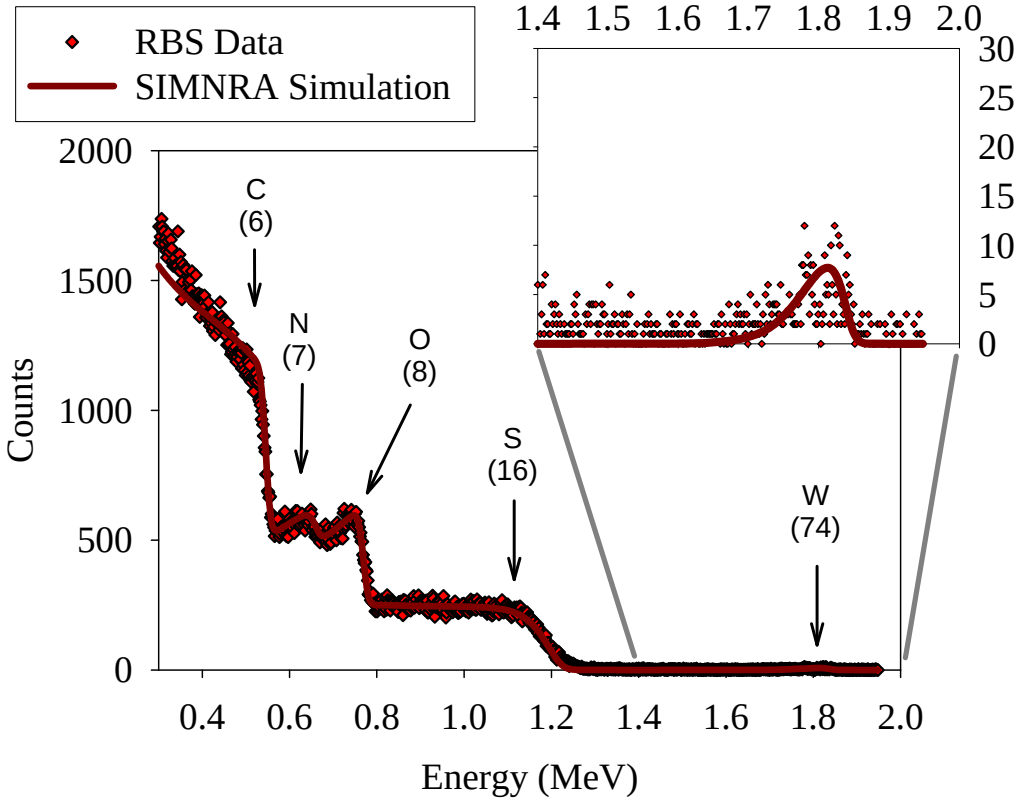
RBS Data
SIMNRA Simulation
Counts
Energy (MeV)
C (6)
N (7)
O (8)
S (16)
W (74)

**15W**

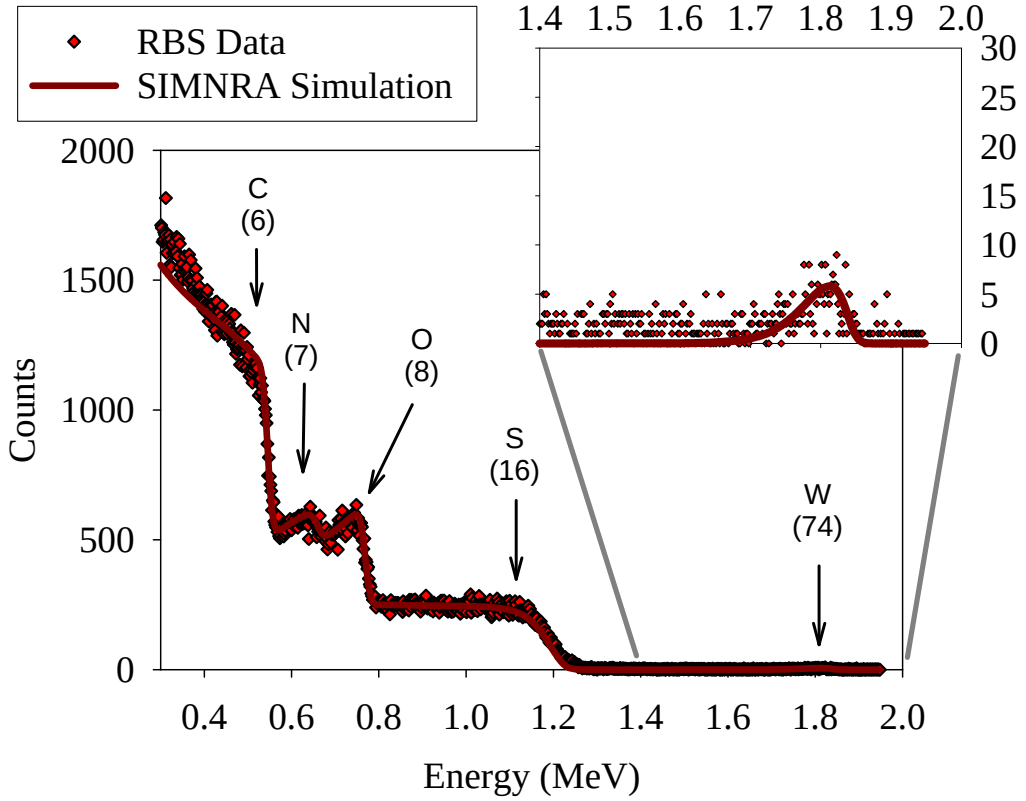
RBS Data
SIMNRA Simulation
Counts
Energy (MeV)
C (6)
N (7)
O (8)
S (16)
W (74)

**16W**

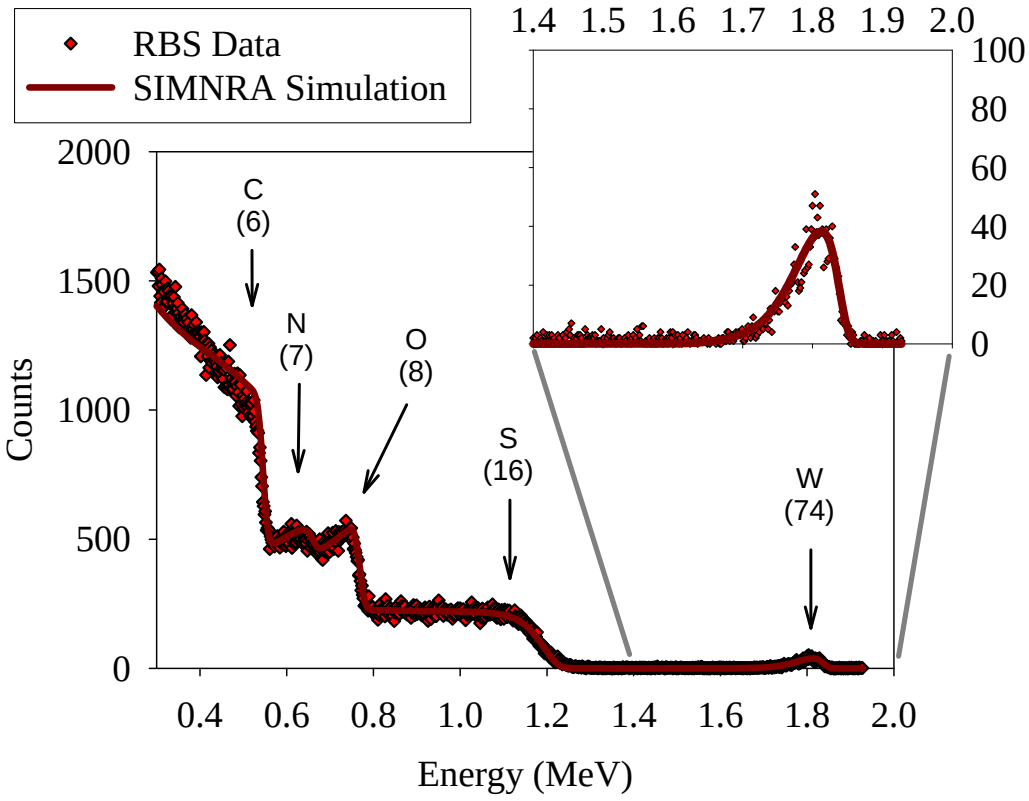
RBS Data
SIMNRA Simulation
Counts
Energy (MeV)
C (6)
N (7)
O (8)
S (16)
W (74)

**17W**

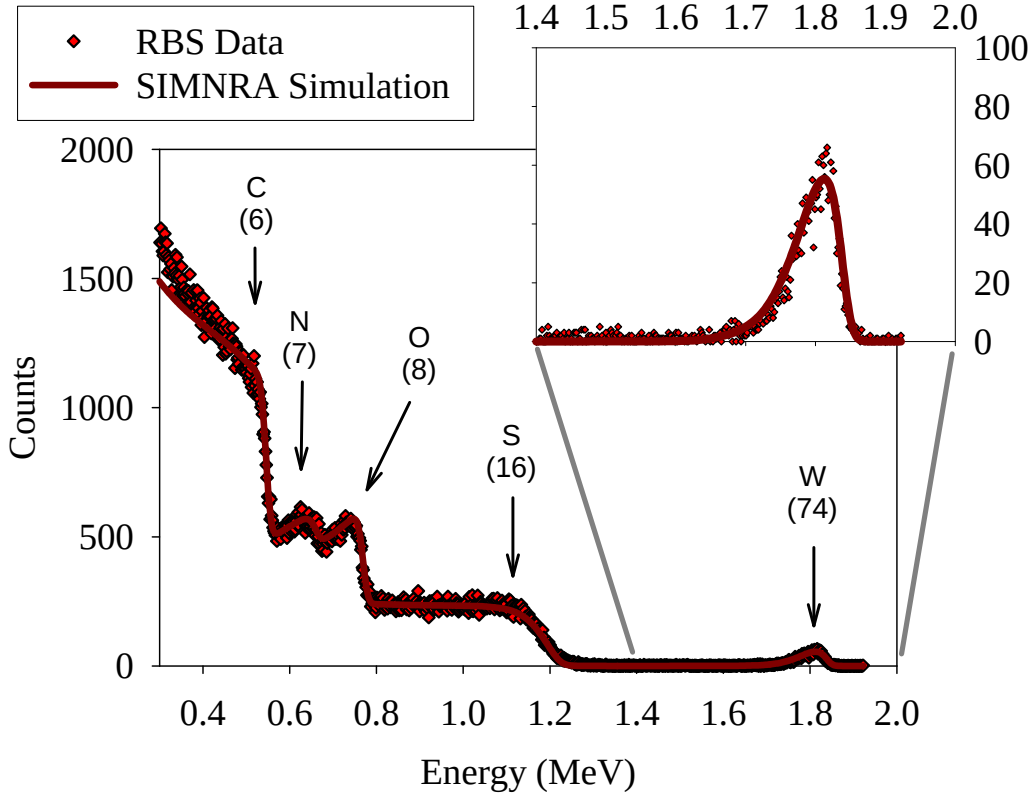
RBS Data
SIMNRA Simulation
Counts
Energy (MeV)
C (6)
N (7)
O (8)
S (16)
W (74)

**18W**

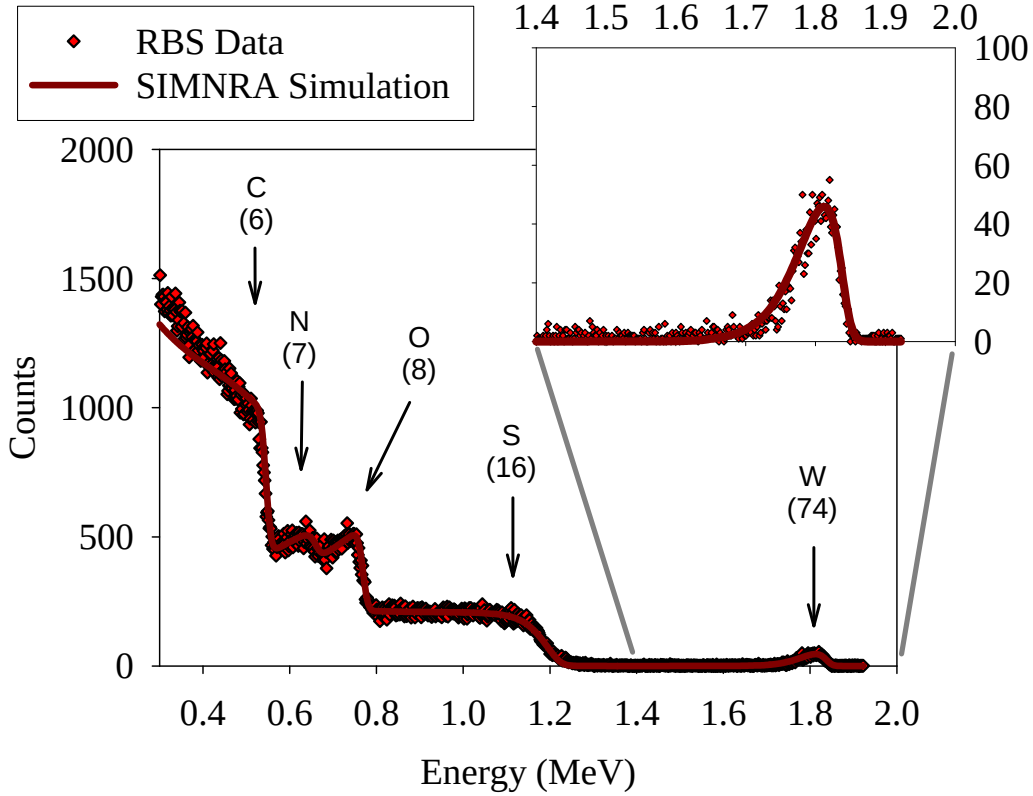
RBS Data
SIMNRA Simulation
Counts
Energy (MeV)
C (6)
N (7)
O (8)
S (16)
W (74)

# APPENDIX B

# APPENDICES FOR CHAPTER 3

## Appendix B.1. Supporting Information for Chapter 3

**Summary of Contents:**

- Seven pages
- Materials and Methods (Extended version)
- Figure B.1. Effect of the anion of the barium salt on the concentration of $Ba^{2+}$ that associates with $R–COO^-$ groups in the active layer of FT30 RO membrane.
- Figure B.2. Example of a spectrum obtained from the RBS analysis of an FT30 RO membrane sample probed with $Ba^{2+}$ ion at pH=10.3.
- Figure B.3. Comparison between the prediction of $[Ba^{2+}]$ as a function of pH using the six different sets of *a* and AR values shown in Table 3.1.
- **Note:** Bibliographic information for references cited in Appendix B.1 can be found in Section 3.6 of this dissertation.

**Materials and Methods** (Extended version)

***Target Membrane.*** All experiments were performed with coupons (2.5×5.0 $cm^2$) of the thin-film composite FT30 RO membrane (Dow Liquid Separation, Midland, MI) cut from a spiral-wound element obtained from the manufacturer. The elemental compositions of the polyamide active layer ($C_{0.48}H_{0.33}O_{0.12}N_{0.07}$) and coat layer ($C_{0.32}H_{0.56}O_{0.12}$) of the FT30 RO membrane were obtained in a previous study [14] with samples from the same membrane element used in this study; the composition of the coat layer was consistent with that of 50% ester-crosslinked polyvinyl alcohol. The coupons were rinsed with nanopure water from a Barnstead D4741 nanopure deionization system (Barnstead/Thermolyne Corp., Dubuque, IA) to avoid contamination that could potentially interfere with the sample preparation procedure. The coupons rinsing procedure started with three consecutive immersions in nanopure water, each time for ~1 minute. Next, the following sequence was repeated a minimum of six times: coupons immersion in nanopure water for ≥8 hours, followed by three consecutive immersions of ~1 minute each. The rinsed coupons were stored in nanopure water until needed for use.

***Ion-Probe Solutions.*** All chemicals used were A.C.S. grade with 99%+ purity. Silver nitrate ($AgNO_3$) and barium nitrate ($Ba(NO_3)_2$) from Sigma-Aldrich (St. Louis, MO), and barium chloride dihydrate ($BaCl_2 \cdot 2H_2O$) from Fisher Scientific (Hampton, NH) were used as sources of $Ag^+$ and $Ba^{2+}$. All ion-probe solutions were prepared with nanopure water. The concentrations of silver ($5\times10^{-5}$-$10^{-3}$ M) and barium ($10^{-6}$-0.32 M) in solution were always below their solubility limit at the pH tested [Aghaie, et al., *J. Mol. Liq.* **2007,** *135*, 72-74; Pourbaix, M., *Atlas of electrochemical equilibria in aqueous solutions.* Pergamon Press: Great Britain, 1966]. The pH of barium, and silver solutions was adjusted to the desired value by addition of HCl or NaOH, and $HNO_3$ or NaOH, respectively. Silver solutions were prepared and used under dark conditions to avoid photoreactivity.

***Sample Preparation for Ion Probing with $Ba^{2+}$.*** The procedure reported previously [14] for the probing with $Ag^+$ of R–$COO^-$ groups in the active layer of the FT30 membrane was used in this study for probing with $Ba^{2+}$. Membrane coupons previously rinsed with nanopure water were immersed twice, each time for ≈10 min, in 0.1 M solution of $BaCl_2 \cdot 2H_2O$ at the pH of interest to saturate accessible R–$COO^-$ groups with $Ba^{2+}$. Then, to reduce excess $Ba^{2+}$ not associated to R–$COO^-$ groups to a concentration below the detection limit of our sample analysis procedure, the samples underwent four consecutive immersions, each lasting ≈7 min, in a $10^{-6}$ M solution of $BaCl_2 \cdot 2H_2O$ at the same pH used in the saturation step. Finally, the samples were dried by pressing them between two Whatman qualitative-grade filter-papers (Fisher Scientific, Hampton, NH), and air-dried at room temperature for ≥24 h. Each experimental pH condition was tested in triplicate. Prepared samples were analyzed by RBS (see below). All membrane coupons used for $Ba^{2+}$-probing tests were cut from approximately the same location (FT30-L1) of the spiral-wound element. All locations in the spiral-wound element from where membrane samples were obtained for testing were ≥20 cm away from the glue lines and permeate collector.

***Sample Preparation for $Ag^+/Ba^{2+}$ Ion Exchange.*** Ion-exchange experiments in the pH range 7.5-10.3 were performed to study the displacement of $Ag^+$ by $Ba^{2+}$ from the R–$COO^-$ groups in the active layer of the FT30 membrane. Sample preparation was similar to that for $Ba^{2+}$-probing tests with some modifications. After rinsing with nanopure water, the coupons were immersed twice, each time for ≈10 min, in concentrated $AgNO_3$ solution at the target pH to saturate R–$COO^-$ groups with $Ag^+$. Next, exchange of $Ag^+$ for $Ba^{2+}$ was effected by sequential immersions, each lasting ≈10 min, in $Ba(NO_3)_2$ solutions at the same target pH used in the $Ag^+$-saturation step starting with two immersions in 0.32 M $Ba(NO_3)_2$ solution followed by two immersions in 0.10 M $Ba(NO_3)_2$ solution. Then, to reduce excess ions not associated to R–$COO^-$ groups to a concentration several orders of magnitude below the detection limit of our sample analysis procedure, the samples underwent four consecutive immersions, each time for ≈7 min, in $10^{-6}$ M $Ba(NO_3)_2$ solution at the same target pH of the previous steps. Finally, the coupons were dried as described above for $Ba^{2+}$-probing samples, and analyzed by RBS (see below). Coupons used as test samples were cut from four different locations (FT30-L2 through FT30-L5) of the FT30 RO spiral-wound element. Experiments were performed in triplicate at pH values of ~7.5 (FT30-L4 and FT30-L5), ~9.5 (FT30-L2 and FT30-L3), and ~10.3 (FT30-L5). In the ion-exchange tests, $Ba(NO_3)_2$ was used instead of $BaCl_2$ to avoid precipitation of AgCl. We verified through $Ba^{2+}$-probing experiments at pH≈9.5 with $Ba(NO_3)_2$ and $BaCl_2$ that the anion (i.e., $Cl^-$ or $NO_3^-$) of the barium salt did not affect the concentration of $Ba^{2+}$ that associated with R–$COO^-$ groups (see Figure B.1).

***Sample Analysis.*** Rutherford backscattering spectrometry (RBS) was used to quantify $Ba^{2+}$ and $Ag^+$ concentrations in the active layer of treated membrane samples. Extensive information on RBS theory and analysis [18, 20], and use in polymer and membrane characterization [6, 11 , 21] can be found elsewhere. In this study, immediately before sample analysis, the membrane coupons were attached to the sample holder of the RBS analysis chamber at room temperature using a double-sided thermally conductive adhesive tape (T410 material, Marian, Chicago, IL). Next, a circular, 3-mm, 2-MeV $He^+$ beam generated with a Van de Graaff accelerator (High Voltage Engineering Corp., Burlington, MA) was scanned over the surface of the membrane sample keeping the $He^+$ ion fluence under $1.5\times10^{14}$ $He^+/cm^2$ which is below the threshold of $3\times10^{14}$ $He^+/cm^2$ above which the integrity of polysulfone is compromised [21]. Incident, exit and scattering angles of the $He^+$ beam were $22.5^o$, $52.5^o$ and $150^o$, respectively. A detector registered the energy and counts of backscattered ions (see sample spectrum in Figure B.2). For a given incident ion, geometry of RBS setup, and energy of the incident beam, the energy of the backscattered ions reveals the elements present in the sample; the counts at each energy serve to obtain the relative concentration of each element without the need of calibration standards [18, 20]. Only hydrogen cannot be detected directly by RBS, and so a hydrogen:carbon ratio of 0.67 was assumed [11]. The software SIMNRA® [18] was used for data analysis yielding the elemental ratios (composition) and total areal atomic density (atoms/$cm^2$) of the active layer. During data analysis, the carbon, oxygen and sulfur content associated with the polysulfone support were properly taken into account for the calculation of the polyamide elemental composition by using in the SIMNRA® simulations the elemental composition of polysulfone obtained from RBS spectra of polysulfone supports without the active layer [14].

The concentration of a given ion probe in the active layer of the sample tested was calculated as $[\text{ion}] = (\varepsilon_{\text{ion}} / \sum(\varepsilon \cdot \text{M})) \times \rho_{\text{active layer}}$ where $[\text{ion}]$ and $\varepsilon_{\text{ion}}$ correspond to the molar concentration and elemental ratio of the ion probe in the active layer, respectively, and $\sum(\varepsilon \cdot \text{M})$ and $\rho_{\text{active layer}}$ correspond the summation of the products of the elemental ratio and molar mass of each element (i.e., N, C, O, H) in the active layer, and the average mass bulk density of the dry active layer, respectively. The ion-probe concentration so calculated is an average value over the whole thickness of the active layer.

In a previous study [11], we estimated $\rho_{\text{active layer}}$ = 1.06 g/cm$^3$ from an experimental hydrated density of FT30 of 1.38 g/cm$^3$ [Kotelyanskii, et al., *J. Mem. Sci.* **1998**, *139*, 1-16], and a corresponding reported value of 23 wt% of water absorbed in the active layer estimated by molecular modeling [Kotelyanskii, et al., *J. Mem. Sci.* **1998**, 139, 1-16]. Accordingly, we used $\rho_{\text{active layer}}$ = 1.06 g/cm$^3$ in reference [14] to calculate the concentration of R–COO$^-$ groups as a function of pH in the active layer of the FT30 membrane; however, in a subsequent study [22], we calculated a corrected $\rho_{\text{active layer}}$ = 1.24 g/cm$^3$ using an experimentally measured value of 11.2% for the mass of water absorbed per dry mass of active layer in the FT30 membrane [22]. As a result, the $\rho_{\text{active layer}}$ = 1.24 g/cm$^3$ value has been used in the present study not only for all relevant calculations, but also to improve the accuracy of the values previously reported in [14] for the concentration of R–COO$^-$ groups as a function of pH in the active layer of the FT30 membrane. The newly calculated values (see Figure 3.2a) are ~11% higher than those reported in [14].

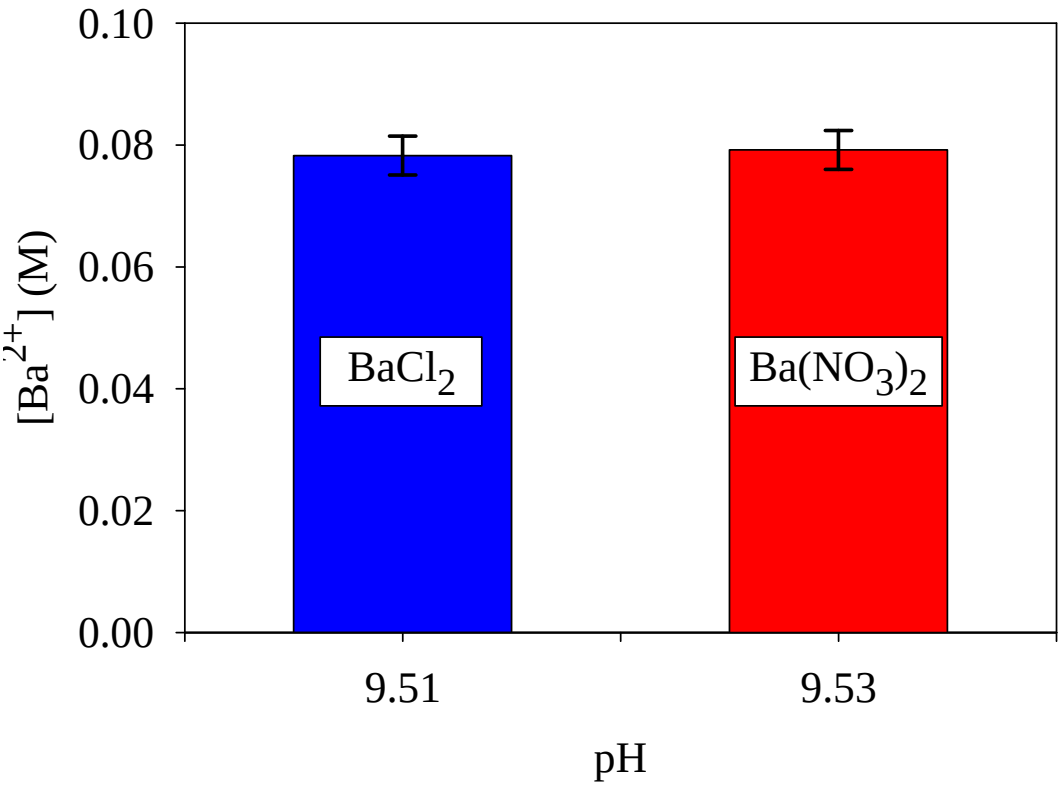


**Figure B.1**. Effect of the anion of the barium salt on the concentration of $Ba^{2+}$ that associates with R–$COO^-$ groups in the active layer of the FT30 RO membrane at pH~9.5 during $Ba^{2+}$-probing experiments. Membrane coupons used for this test were cut from location six (FT30-L6) in the spiral-wound element which was ≥20 cm away from glue lines and permeate collector. The blue and red bars correspond to samples probed with $BaCl_2$ and $Ba(NO_3)_2$ solutions, respectively, using the $Ba^{2+}$-probing procedure described in the Materials and Methods section of the manuscript and the Materials and Methods (Extended version) section of the Supporting Information. Each condition was tested in triplicate. Error bars indicate standard deviation. As depicted in the figure, the effect of the anion (i.e., $Cl^-$ or $NO_3^-$) of the barium salt on the concentration of $Ba^{2+}$ that associated with R–$COO^-$ groups was negligible.

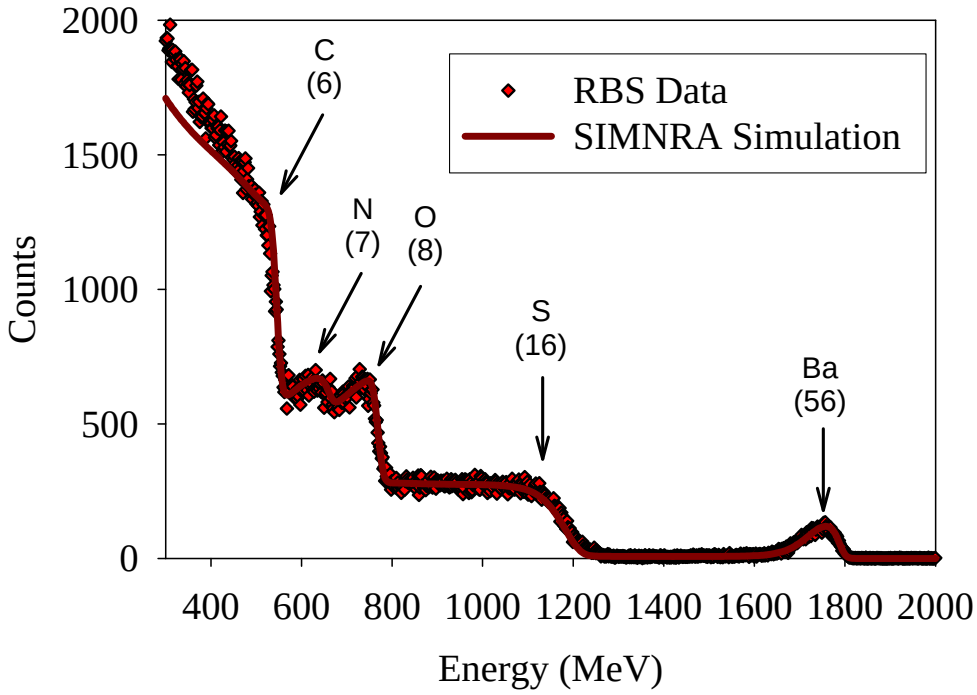


**Figure B.2**. Rutherford backscattering spectrometry (RBS) spectrum of an FT30 RO membrane sample after probing of ionized carboxylic ($R–COO^-$) groups at pH = 10.3 with $Ba^{2+}$ ion. Symbols represent RBS data. Lines represent the fit obtained using the software SIMRA®. Details of the procedure used for RBS data analysis can be found elsewhere [11, 14]. The main four elements present in the membrane (C, N, O, S), other than hydrogen, are easily identified in the spectra. The ion probe ($Ba^{2+}$), neutralizing ionized $R–COO^-$ groups, is also easily discerned. The sulfur signal corresponds to the sulfur present in the polysulfone support layer.

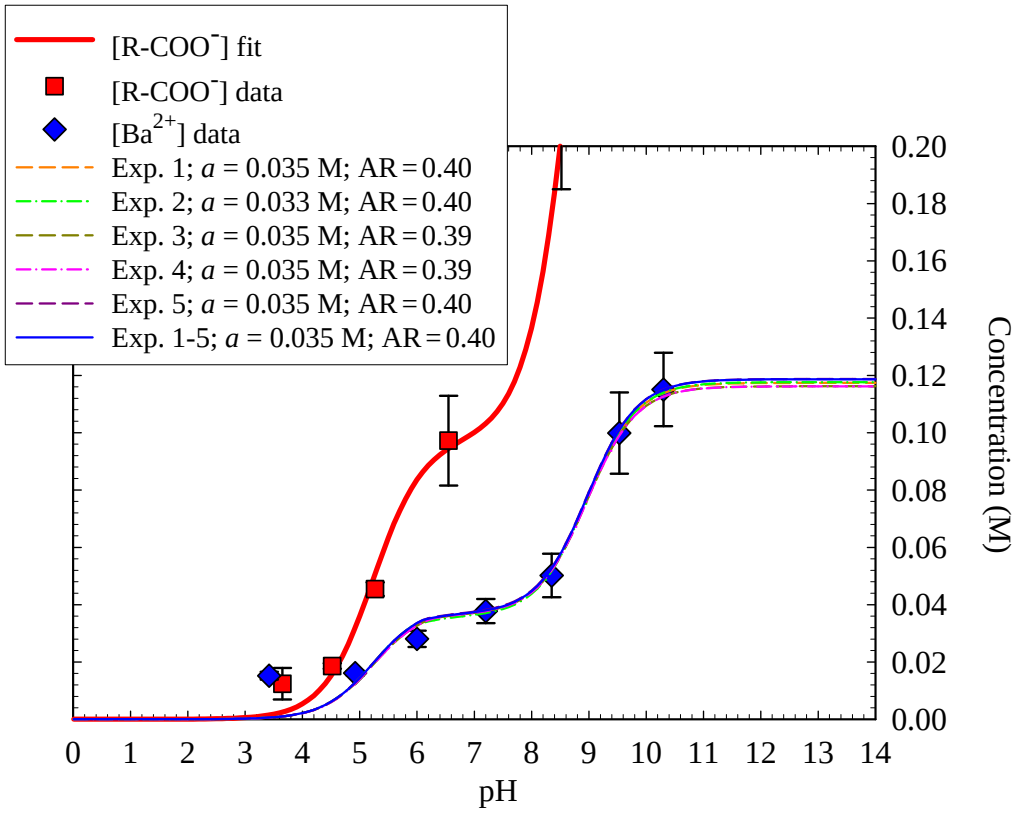


**Figure B.3**. Prediction of the concentration of $Ba^{2+}$ ion [$Ba^{2+}$] that associates with R–$COO^-$ groups in the active layer of the FT30 membrane as a function of pH. (Blue) diamonds and (red) squares represent experimental data for [$Ba^{2+}$] and the concentration of ionized carboxylic groups [R–$COO^-$], respectively. [R–$COO^-$] is reproduced from our previous work [14]. Error bars indicate standard deviation. The continuous (red) curve corresponds to the model fit for [R–$COO^-$] based on acid-base equilibrium between the R–$COO^-$ groups and the aqueous solution [14]. The five different (interrupted line) predictions of [$Ba^{2+}$] *as a function of pH* were calculated based on Equations 3.2 and 3.3, and the five different sets of *a* and AR values indicated in the figure legend and shown in Table 3.1. Each set of *a* and AR values was obtained based on $Ag^+$-$Ba^{2+}$ ion exchange experiments and $Ba^{2+}$-probing experiments at *one pH* (see Table 3.1). The predictions are in close agreement with the continuous (blue) line labeled Exp. 1-5 which corresponds to the (blue) dashed-dotted line of Figure 3.2b previously obtained using the $a$ = 0.035 M value determined from the linear fit of *all* ion-exchange experiments in Figure 3.3a and the AR = 0.40 calculated as the average of *all* AR values in the pH range 4.92-10.30. The satisfactory prediction of [$Ba^{2+}$] as a function of pH reveals that satisfactory estimates of the *a* parameter and AR value are obtained by performing ion-probing and ion-exchange experiments at *one pH*.

**Appendix B.2. Results of Rutherford Backscattering Spectrometry (RBS) Analyses of FT30 Reverse Osmosis (RO) Membrane Samples Probed with Barium ($Ba^{2+}$) Ion**

| | pH = 10.3 | | | |
|---|---|---|---|---|
| | Treatment | pH max/pH min/pH final | Elemental ratio | Concentration [M] |
| 1Ba | FT30+Ba 10.5 | 10.31/10.10/10.3 | 0.00091 | 0.12566 |
| 2Ba | | 10.31/10.10/10.3 | 0.00086 | 0.11876 |
| 3Ba | | 10.31/10.10/10.3 | 0.00073 | 0.10081 |
| | | | Average | 0.11508 |
| | | | Std deviation | 0.01283 |
| | | | (Std dev/Mean)x100 | 11.15 |

| | pH = 9.53 | | | |
|---|---|---|---|---|
| | Treatment | pH max/pH min/pH final | Elemental ratio | Concentration [M] |
| 4Ba | FT30+Ba 9.5 | 9.54/9.45/9.53 | 0.00075 | 0.10357 |
| 5Ba | | 9.54/9.45/9.53 | 0.00061 | 0.08424 |
| 6Ba | | 9.54/9.45/9.53 | 0.00081 | 0.11185 |
| | | | Average | 0.09989 |
| | | | Std deviation | 0.01417 |
| | | | (Std dev/Mean)x100 | 14.19 |

| | pH = 8.35 | | | |
|---|---|---|---|---|
| | Treatment | pH max/pH min/pH final | Elemental ratio | Concentration [M] |
| 7Ba | FT30+Ba 8.5 | 8.51/8.35/8.35 | 0.00036 | 0.04971 |
| 8Ba | | 8.51/8.35/8.35 | 0.00042 | 0.05800 |
| 9Ba | | 8.51/8.35/8.35 | 0.00031 | 0.04281 |
| | | | Average | 0.05017 |
| | | | Std deviation | 0.00761 |
| | | | (Std dev/Mean)x100 | 15.16 |

| | pH = 7.2 | | | |
|---|---|---|---|---|
| | Treatment | pH max/pH min/pH final | Elemental ratio | Concentration [M] |
| 10Ba | FT30+Ba 7.5 | 7.53/7.1/7.2 | 0.00028 | 0.03867 |
| 11Ba | | 7.53/7.1/7.2 | 0.00024 | 0.03314 |
| 12Ba | | 7.53/7.1/7.2 | 0.00030 | 0.04143 |
| | | | Average | 0.03775 |
| | | | Std deviation | 0.00422 |
| | | | (Std dev/Mean)x100 | 11.18 |

| | pH = 6.0 | | | |
|---|---|---|---|---|
| | Treatment | pH max/pH min/pH final | Elemental ratio | Concentration [M] |
| 13Ba | FT30+Ba 6.0 | 6.01/5.95/6.0 | 0.00022 | 0.03038 |
| 14Ba | | 6.01/5.95/6.0 | 0.00021 | 0.02900 |
| 15Ba | | 6.01/5.95/6.0 | 0.00018 | 0.02486 |
| | | | Average | 0.02808 |
| | | | Std deviation | 0.00287 |
| | | | (Std dev/Mean)x100 | 10.24 |

| | pH = 4.92 | | | |
|---|---|---|---|---|
| | Treatment | pH max/pH min/pH final | Elemental ratio | Concentration [M] |
| 16Ba | FT30+Ba 5.0 | 5.00/4.92/4.92 | 0.00011 | 0.01519 |
| 17Ba | | 5.00/4.92/4.92 | 0.00012 | 0.01657 |
| 18Ba | | 5.00/4.92/4.92 | 0.00012 | 0.01657 |
| | | | **Average** | 0.01611 |
| | | | **Std deviation** | 0.00080 |
| | | | **(Std dev/Mean)x100** | 4.95 |

| | pH = 3.42 | | | |
|---|---|---|---|---|
| | Treatment | pH max/pH min/pH final | Elemental ratio | Concentration [M] |
| 19Ba | FT30+Ba 3.5 | 3.5/3.35/3.42 | 0.00011 | 0.01519 |
| 20Ba | | 3.5/3.35/3.42 | 0.00010 | 0.01381 |
| 21Ba | | 3.5/3.35/3.42 | 0.00012 | 0.01657 |
| | | | **Average** | 0.01519 |
| | | | **Std deviation** | 0.00138 |
| | | | **(Std dev/Mean)x100** | 9.09 |

**1Ba**

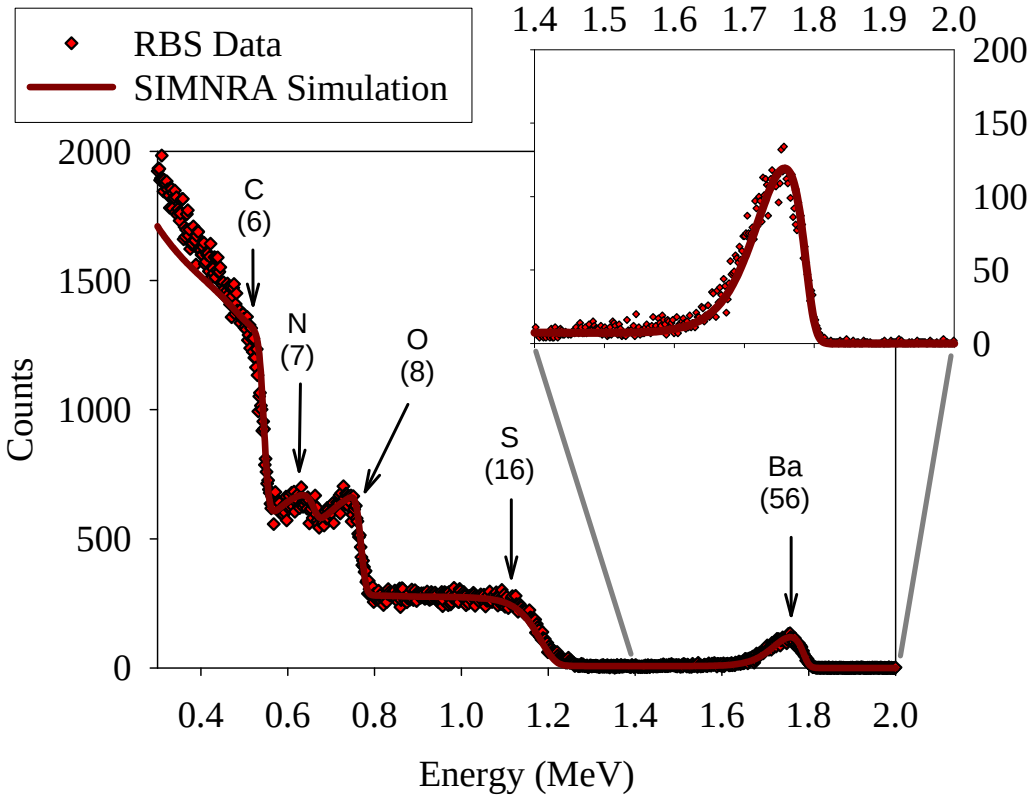
RBS Data
SIMNRA Simulation
Counts
Energy (MeV)
C (6)
N (7)
O (8)
S (16)
Ba (56)

**2Ba**

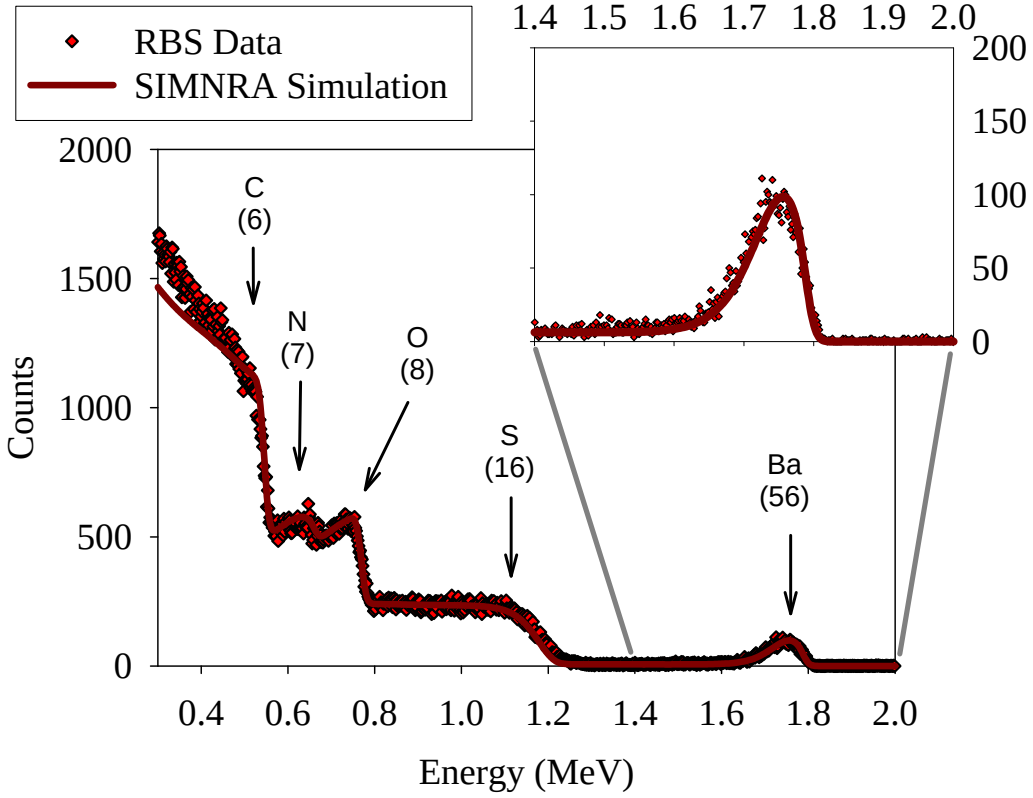
RBS Data
SIMNRA Simulation
Counts
Energy (MeV)
C (6)
N (7)
O (8)
S (16)
Ba (56)

**3Ba**

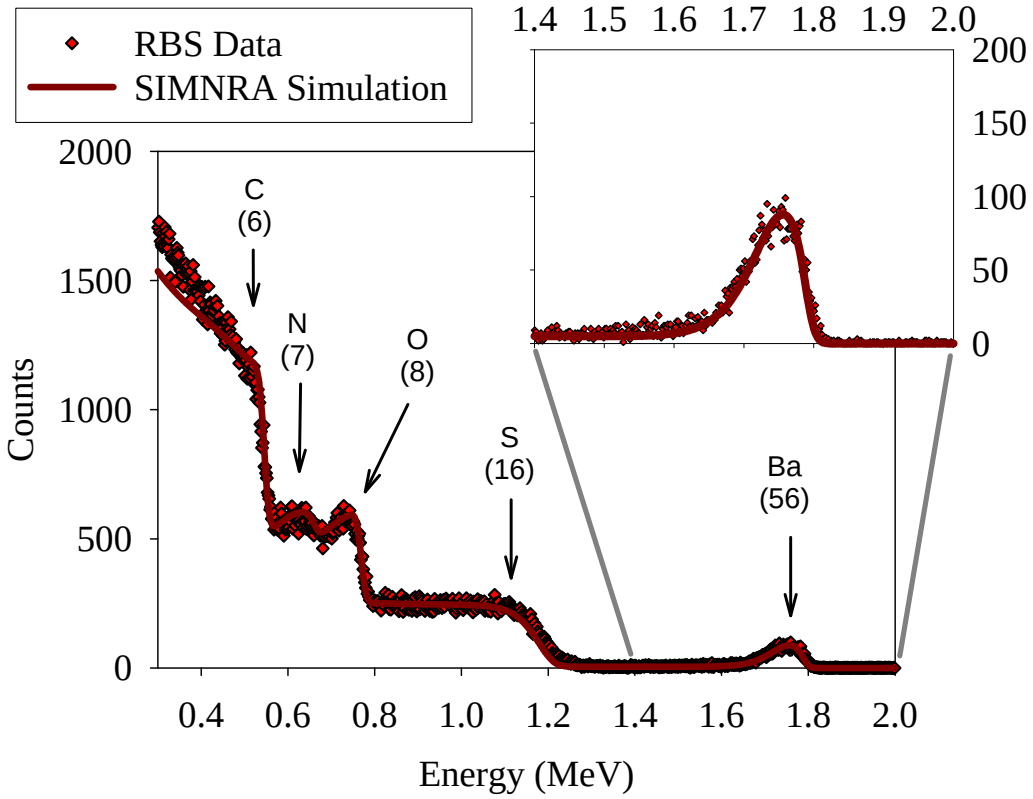
RBS Data
SIMNRA Simulation
Counts
Energy (MeV)
C (6)
N (7)
O (8)
S (16)
Ba (56)

**4Ba**

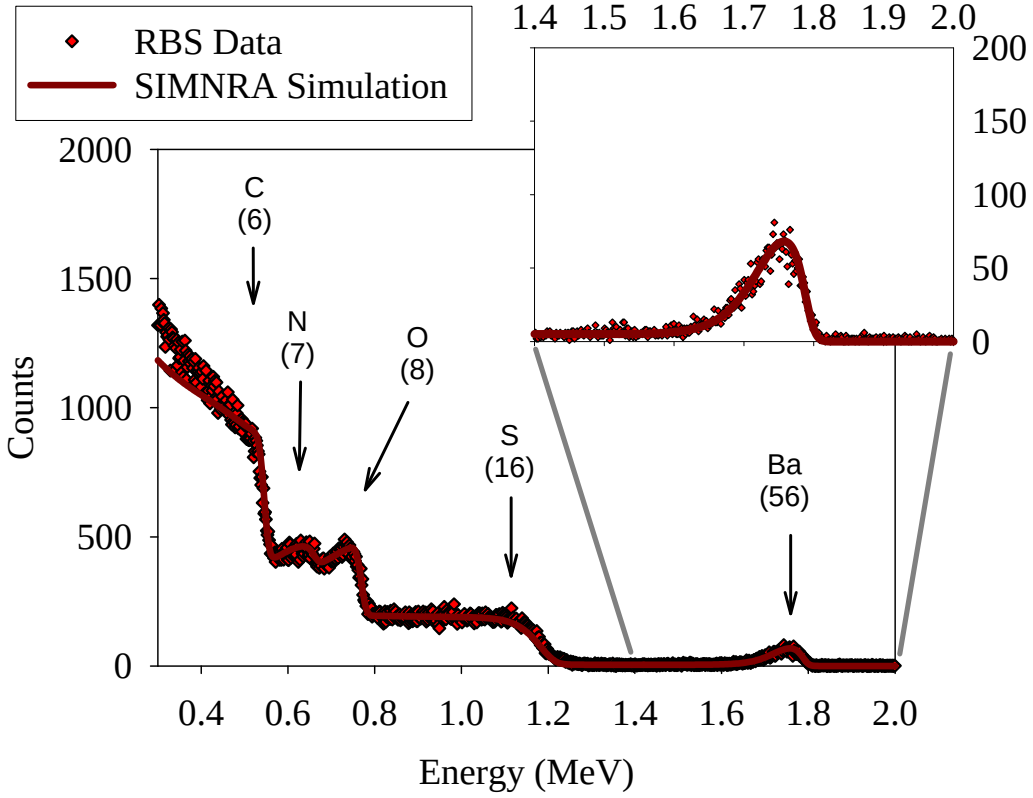
RBS Data
SIMNRA Simulation
Counts
Energy (MeV)
C (6)
N (7)
O (8)
S (16)
Ba (56)

**5Ba**

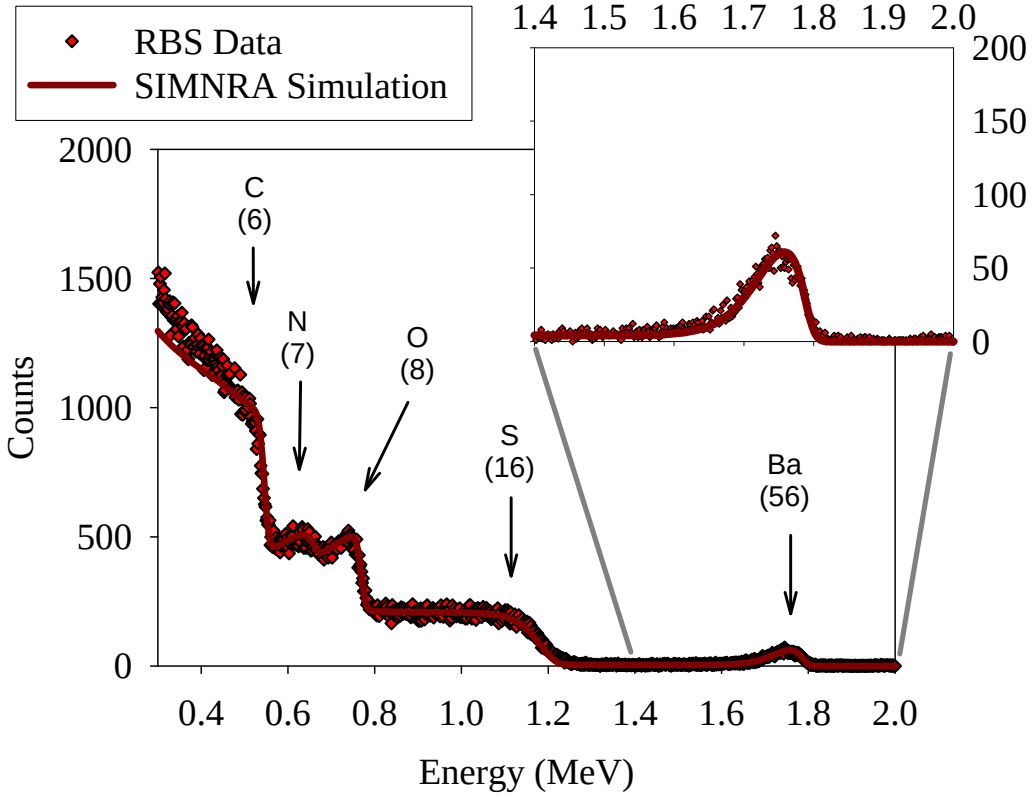
RBS Data
SIMNRA Simulation
Counts
Energy (MeV)
C (6)
N (7)
O (8)
S (16)
Ba (56)

**6Ba**

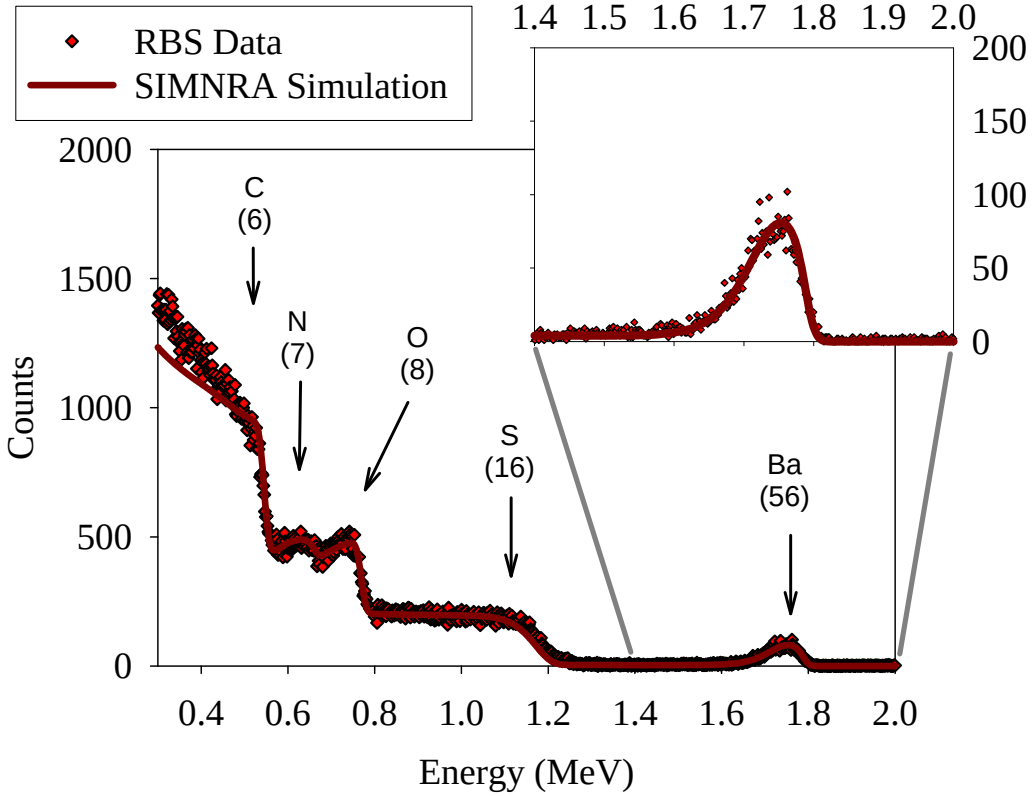
RBS Data
SIMNRA Simulation
Counts
Energy (MeV)
C (6)
N (7)
O (8)
S (16)
Ba (56)

**7Ba**

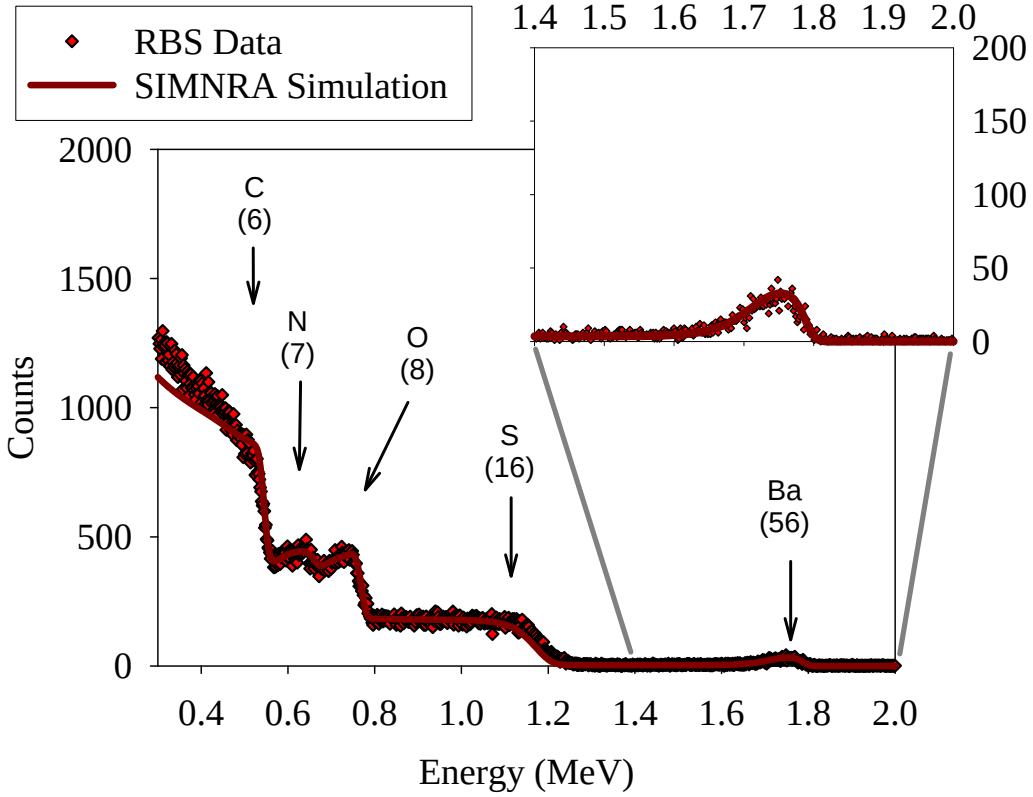
RBS Data
SIMNRA Simulation
Counts
Energy (MeV)
C (6)
N (7)
O (8)
S (16)
Ba (56)

**8Ba**

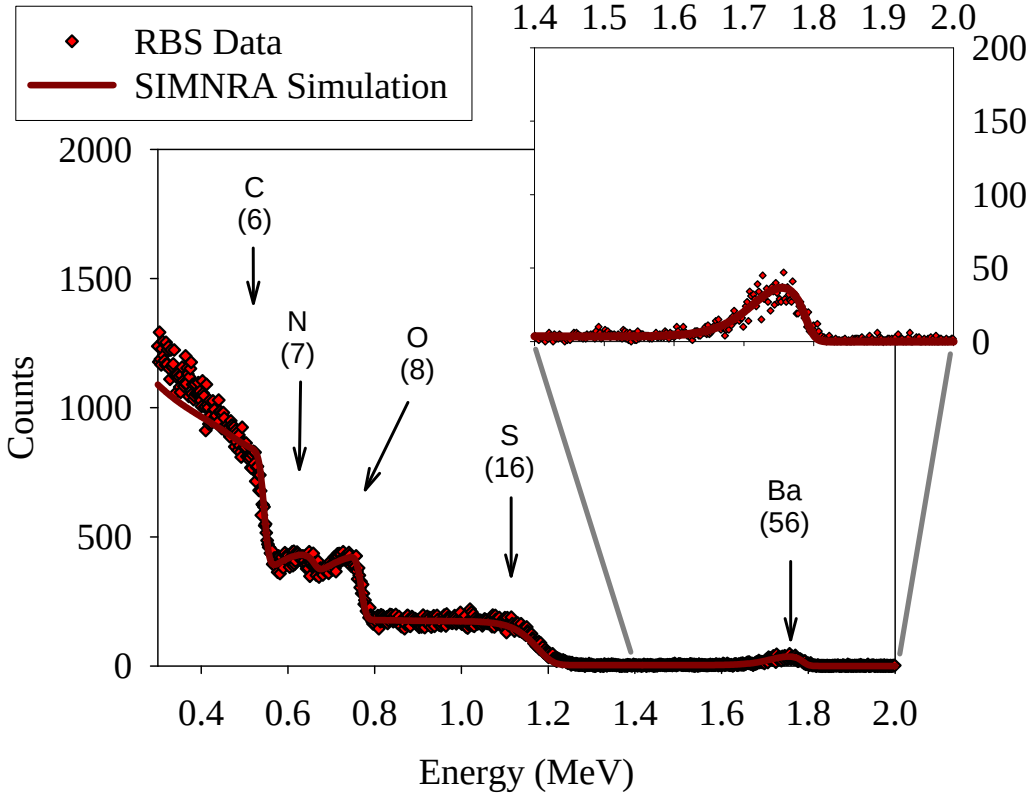
RBS Data
SIMNRA Simulation
Counts
Energy (MeV)
C (6)
N (7)
O (8)
S (16)
Ba (56)

**9Ba**

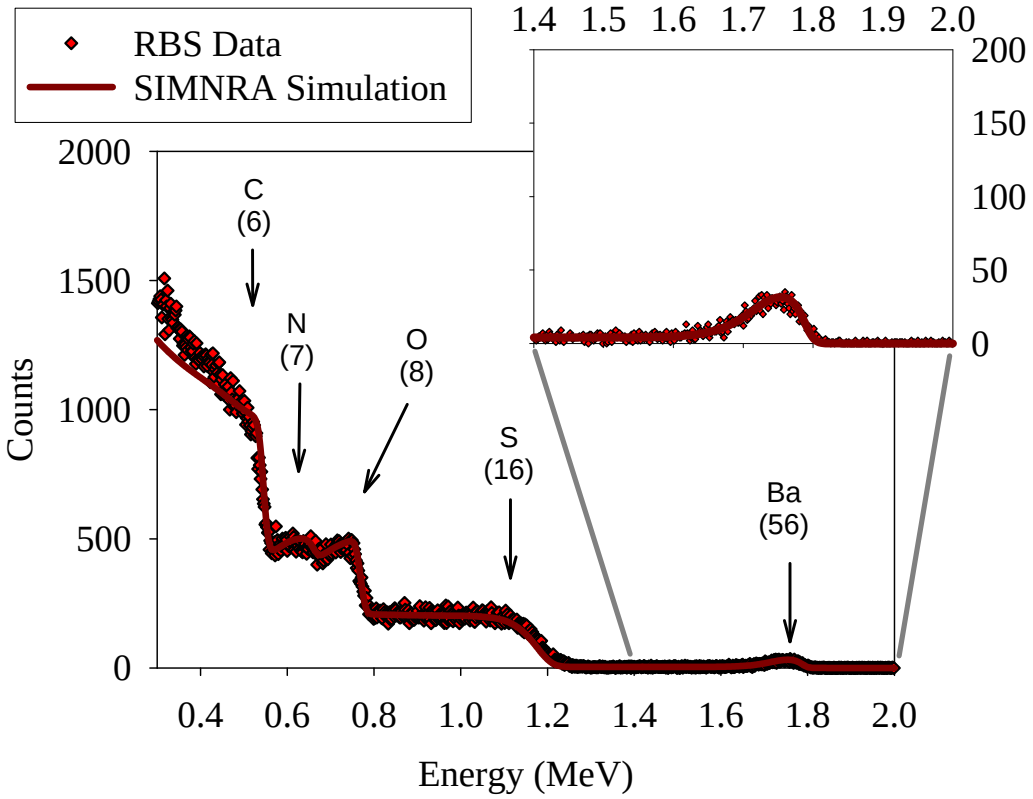
RBS Data
SIMNRA Simulation
Counts
Energy (MeV)
C (6)
N (7)
O (8)
S (16)
Ba (56)

**10Ba**

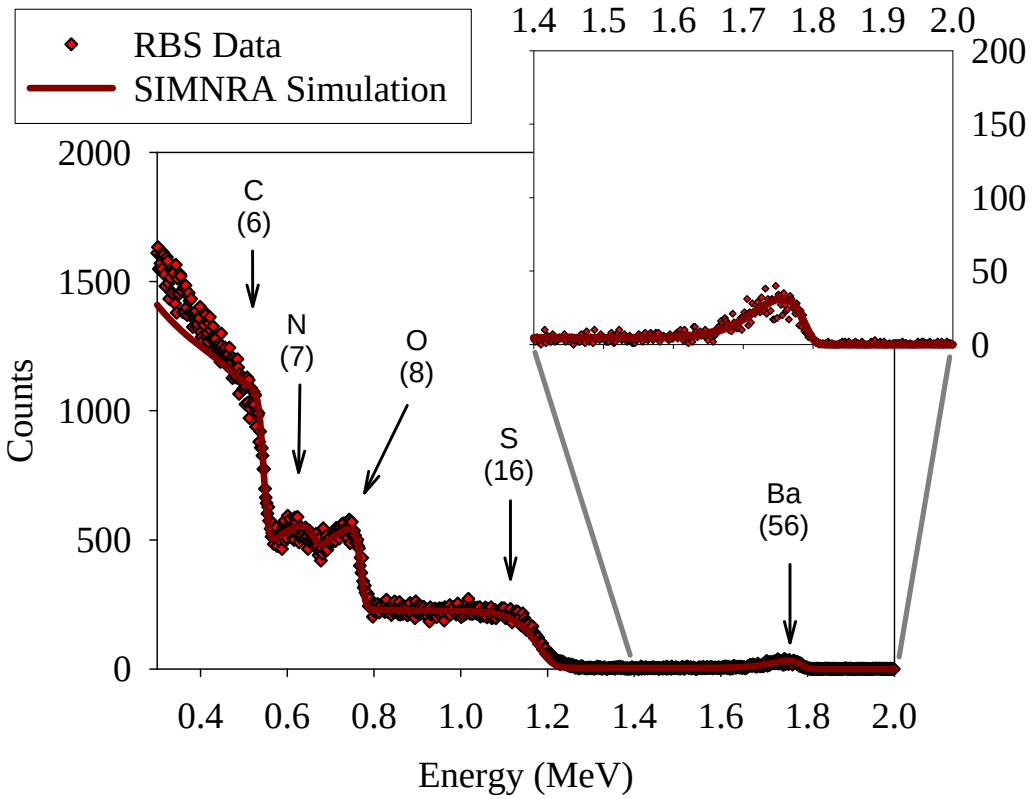
RBS Data
SIMNRA Simulation
Counts
Energy (MeV)
C (6)
N (7)
O (8)
S (16)
Ba (56)

**11Ba**

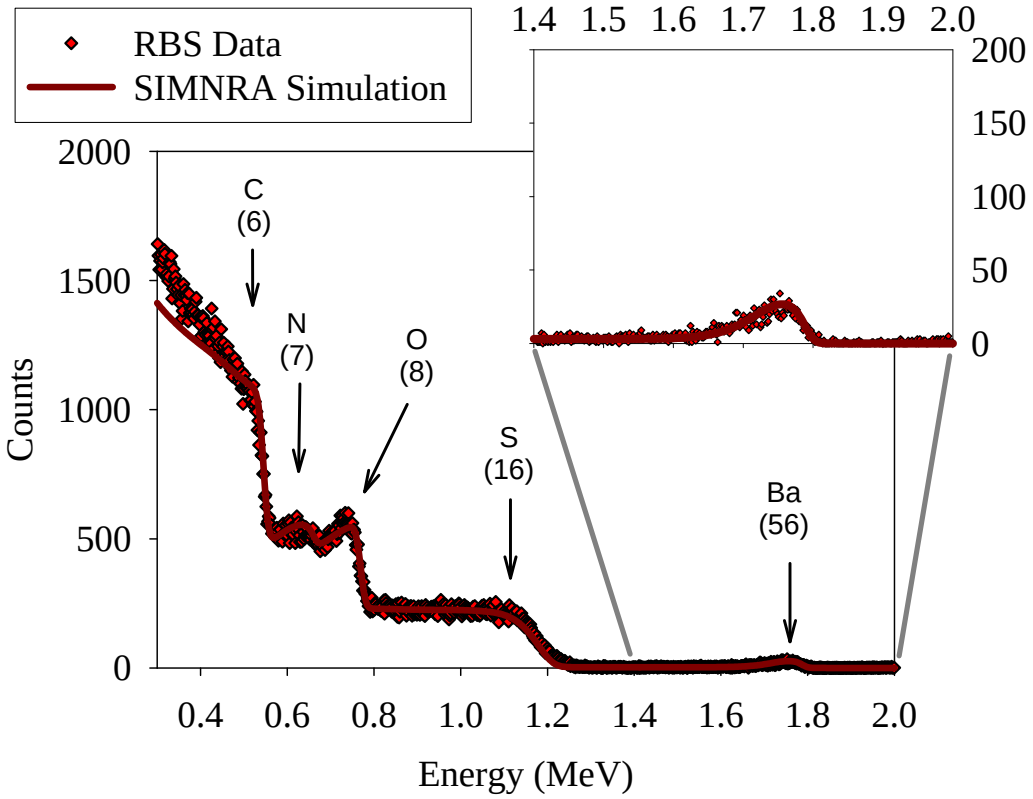
RBS Data
SIMNRA Simulation
Counts
Energy (MeV)
C (6)
N (7)
O (8)
S (16)
Ba (56)

**12Ba**

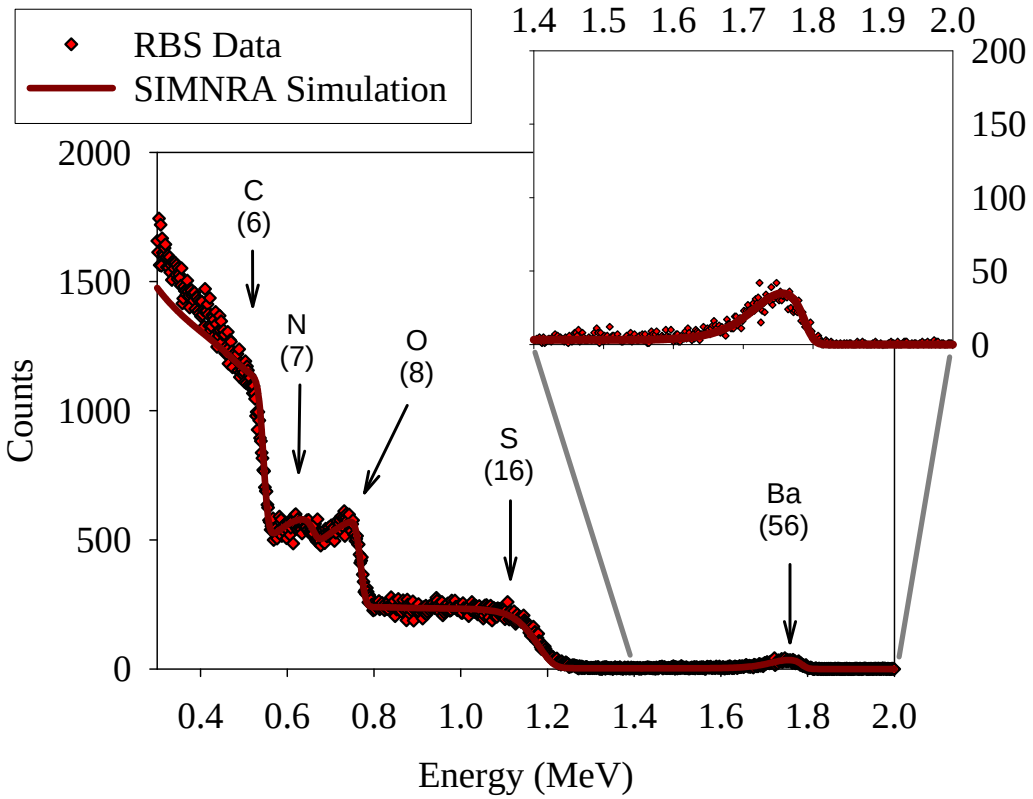
RBS Data
SIMNRA Simulation
Counts
Energy (MeV)
C (6)
N (7)
O (8)
S (16)
Ba (56)

**13Ba**

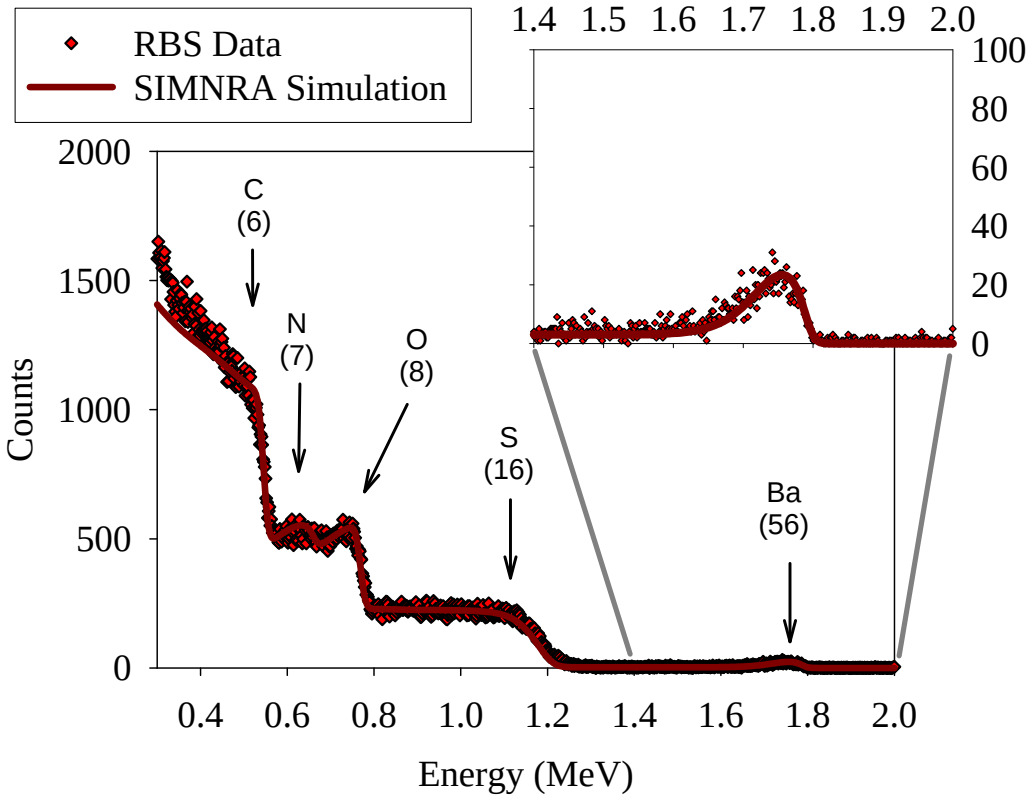
RBS Data
SIMNRA Simulation
Counts
Energy (MeV)
C (6)
N (7)
O (8)
S (16)
Ba (56)

**14Ba**

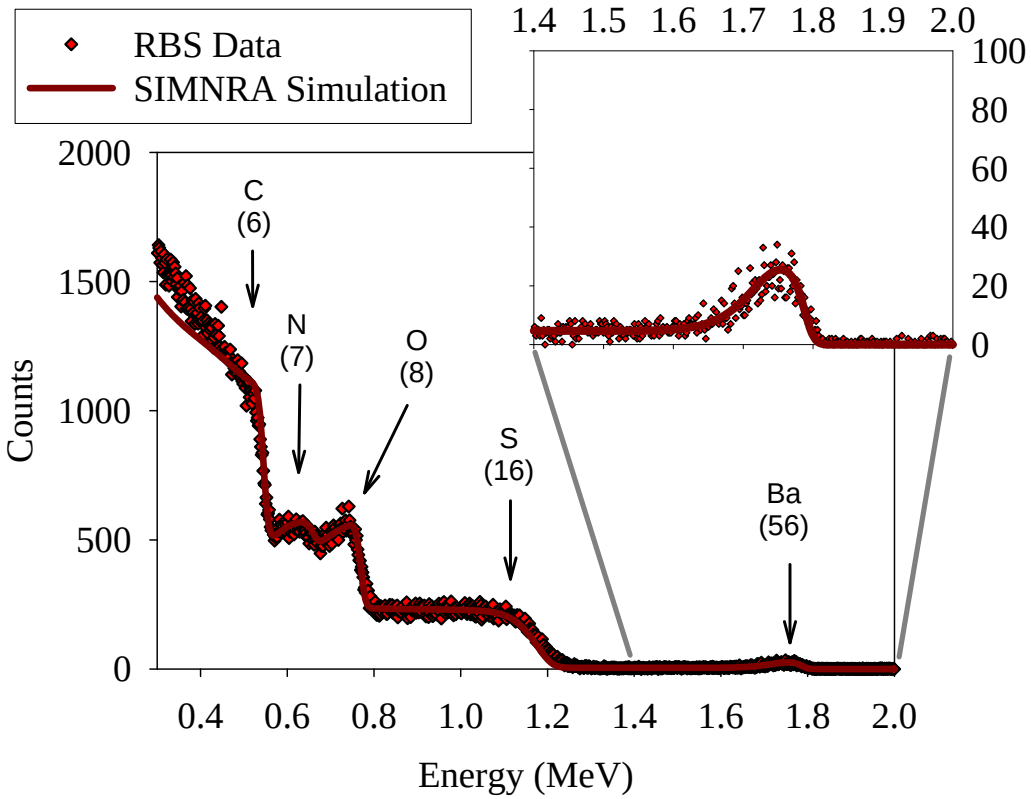
RBS Data
SIMNRA Simulation
Counts
Energy (MeV)
C (6)
N (7)
O (8)
S (16)
Ba (56)

**15Ba**

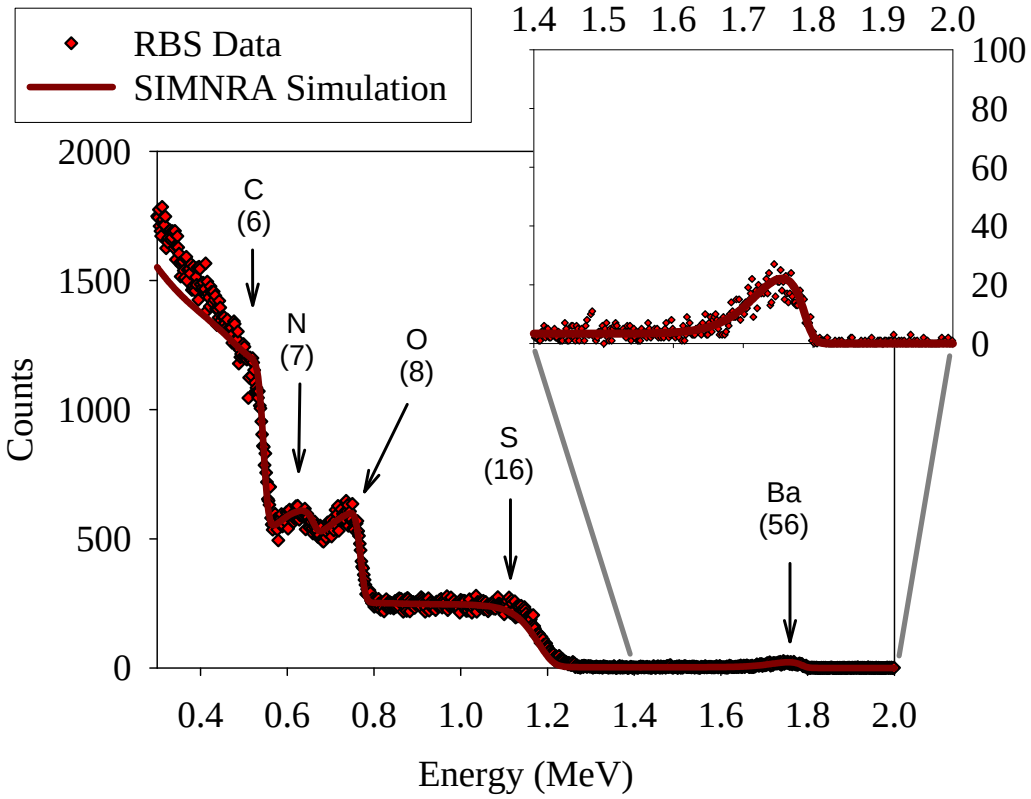
RBS Data
SIMNRA Simulation
Counts
Energy (MeV)
C (6)
N (7)
O (8)
S (16)
Ba (56)

**16Ba**

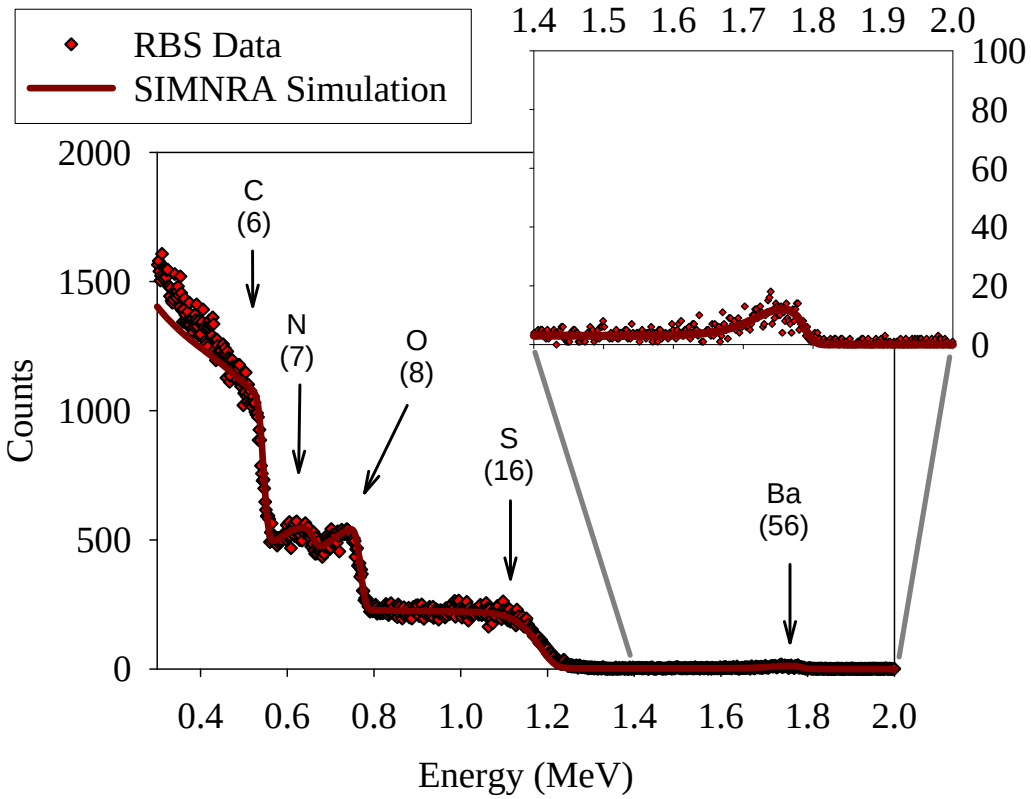
RBS Data
SIMNRA Simulation
Counts
Energy (MeV)
C (6)
N (7)
O (8)
S (16)
Ba (56)

**17Ba**

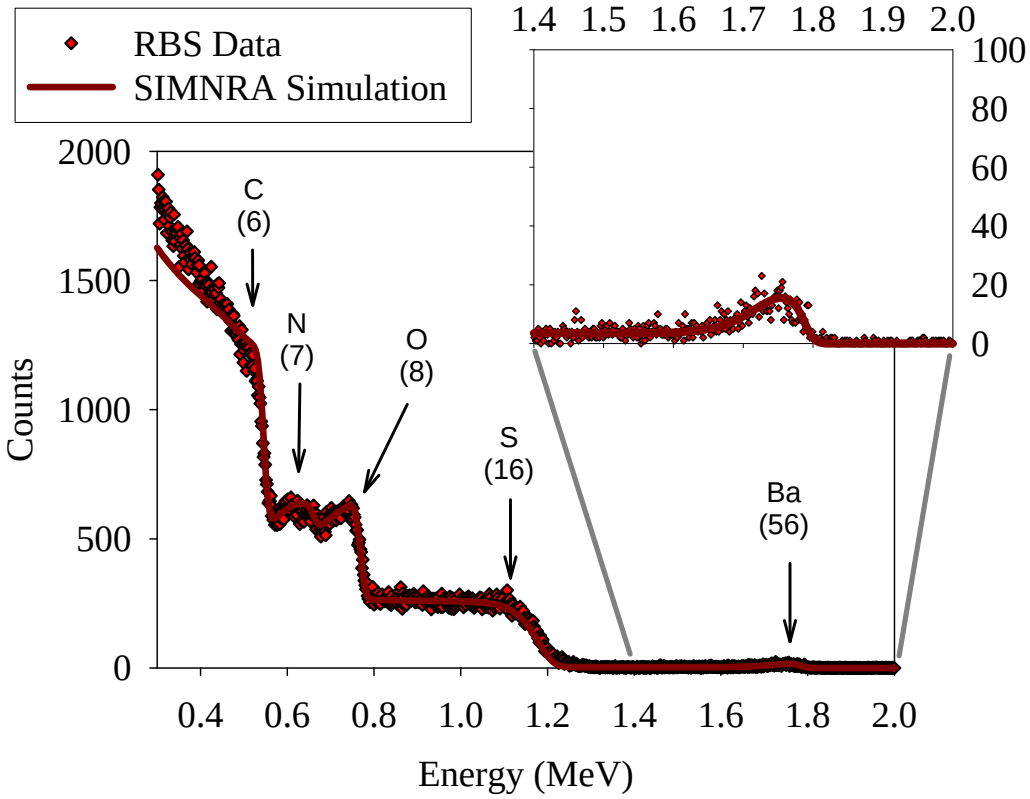
RBS Data
SIMNRA Simulation
Counts
Energy (MeV)
C (6)
N (7)
O (8)
S (16)
Ba (56)

**18Ba**

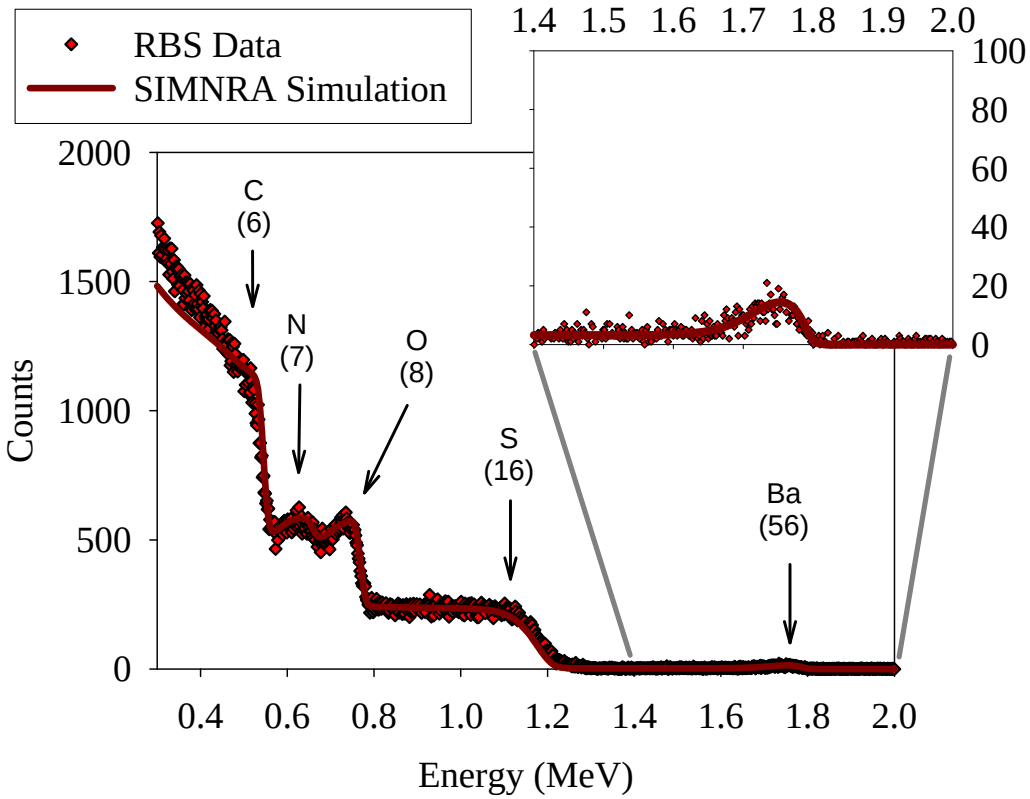
RBS Data
SIMNRA Simulation
Counts
Energy (MeV)
C (6)
N (7)
O (8)
S (16)
Ba (56)

**19Ba**

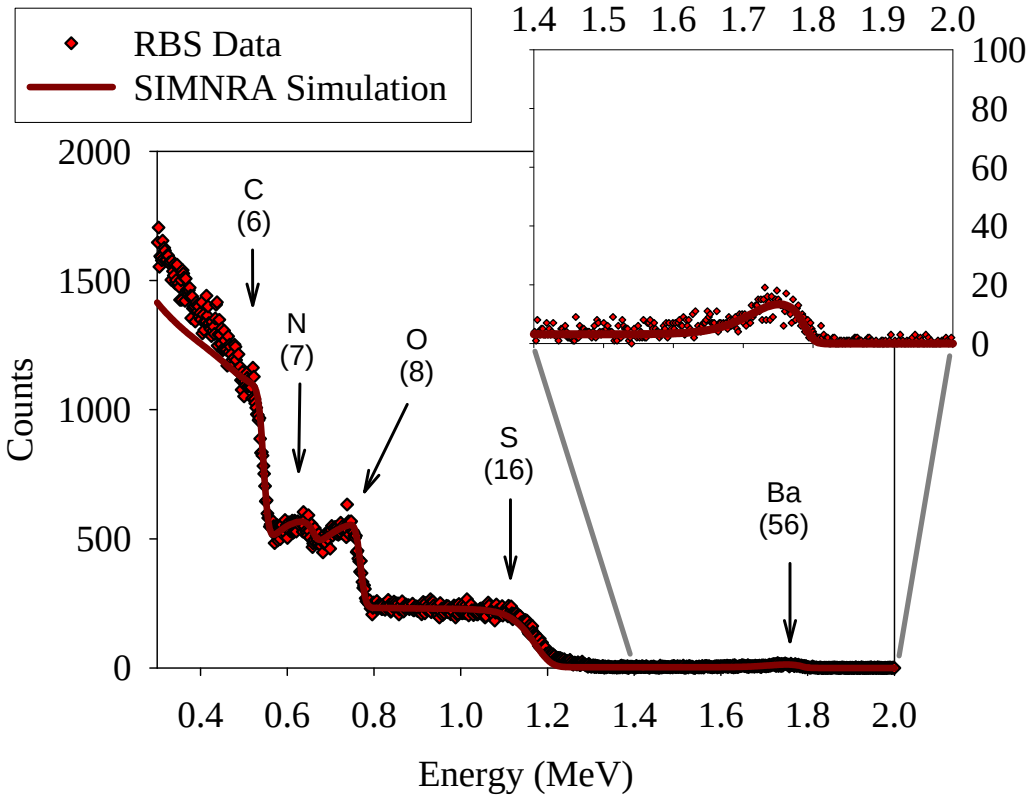
RBS Data
SIMNRA Simulation
Counts
Energy (MeV)
C (6)
N (7)
O (8)
S (16)
Ba (56)

**20Ba**

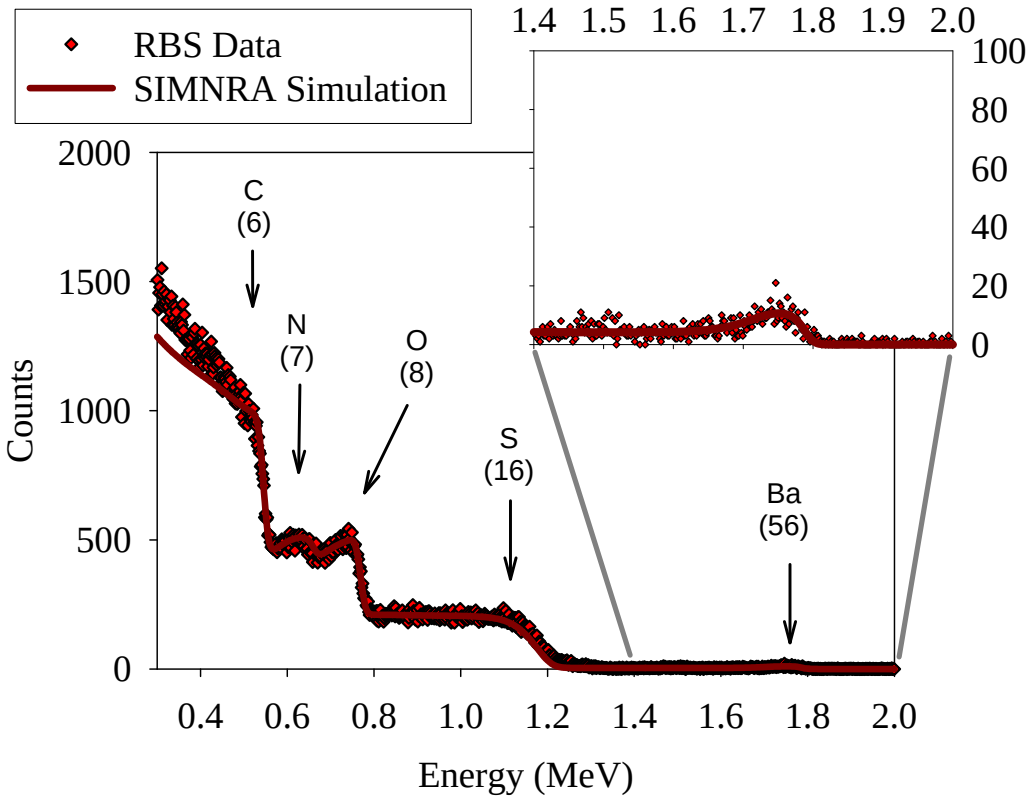
RBS Data
SIMNRA Simulation
Counts
Energy (MeV)
C (6)
N (7)
O (8)
S (16)
Ba (56)

**21Ba**

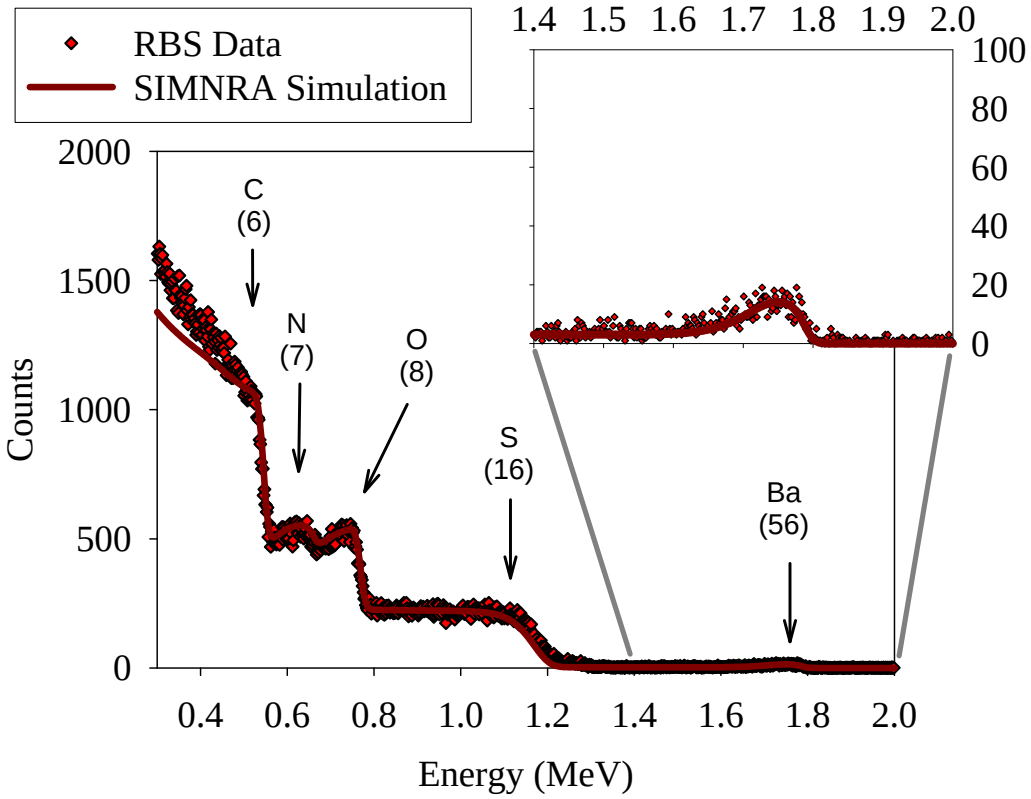
RBS Data
SIMNRA Simulation
Counts
Energy (MeV)
C
(6)
N
(7)
O
(8)
S
(16)
Ba
(56)
2000
1500
1000
500
0
0.4
0.6
0.8
1.0
1.2
1.4
1.6
1.8
2.0
1.4
1.5
1.6
1.7
1.8
1.9
2.0
100
80
60
40
20
0

**Appendix B.3. Results of Rutherford Backscattering Spectrometry (RBS) Analyses of FT30 Reverse Osmosis (RO) Membrane Samples Used for the Study of the Stoichiometry of Association between Barium ($Ba^{2+}$) Ion and Carboxylate ($R-COO^{-}$) Groups**

| | FT30-L2 | | | | | |
|---|---|---|---|---|---|---|
| | **Ionic exchange of Ag+ for Ba++ pH = 9.51** | | | | | |
| | **Treatment** | **pH max/pH min/pH final** | **Ba++ elemental ratio** | **Ba++ concentration [M]** | **Ag+ elemental ratio** | **Ag+ concentration [M]** |
| **1IX** | **FT30+IX 9.5** | 9.75/9.37/9.56 | 0.00050 | 0.06905 | 0.00115 | 0.15881 |
| **2IX** | | 9.75/9.37/9.56 | 0.00051 | 0.07043 | 0.00110 | 0.15190 |
| **3IX** | | 9.75/9.37/9.56 | 0.00054 | 0.07457 | 0.00130 | 0.17952 |
| | | | **Average** | 0.07135 | **Average** | 0.16341 |
| | | | **Std deviation** | 0.00287 | **Std deviation** | 0.01437 |
| | | | **(Std dev/Mean) x100** | 4.03 | **(Std dev/Mean) x100** | 8.80 |

| | **Ag+ pH = 9.53** | | | |
|---|---|---|---|---|
| | **Treatment** | **pH max/pH min/pH final** | **Ag+ elemental ratio** | **Ag+ concentration [M]** |
| **4IX** | **FT30+Ag 9.5** | 9.56/9.50/9.50 | 0.00190 | 0.26237 |
| **5IX** | | 9.60/9.48/9.53 | 0.00205 | 0.28309 |
| **6IX** | | 9.60/9.48/9.53 | 0.00195 | 0.26928 |
| | | | **Average** | 0.27158 |
| | | | **Std deviation** | 0.01055 |
| | | | **(Std dev/Mean)x100** | 3.88 |

| FT30-L3 |
|---|

| Ionic exchange of Ag+ for Ba++ pH = 9.48 | | | | | | |
|---|---|---|---|---|---|---|
| | Treatment | pH max/pH min/pH final | Ba++ elemental ratio | Ba++ concentration [M] | Ag+ elemental ratio | Ag+ concentration [M] |
| 7IX | FT30+IX 9.5 | 9.90/9.44/9.52 | 0.00063 | 0.08700 | 0.00080 | 0.11047 |
| 8IX | | 9.90/9.44/9.52 | 0.00063 | 0.08700 | 0.00076 | 0.10495 |
| 9IX | | 9.90/9.44/9.52 | 0.00058 | 0.08009 | 0.00066 | 0.09114 |
| | | | **Average** | 0.08470 | **Average** | 0.10219 |
| | | | **Std deviation** | 0.00399 | **Std deviation** | 0.00996 |
| | | | **(Std dev/Mean) x100** | 4.71 | **(Std dev/Mean) x100** | 9.74 |

| Ag+ pH = 9.52 | | | | |
|---|---|---|---|---|
| | Treatment | pH max/pH min/pH final | Ag+ elemental ratio | Ag+ concentration [M] |
| 10IX | FT30+Ag 9.5 | 9.52/9.35/9.52 | 0.00176 | 0.24304 |
| 11IX | | 9.52/9.35/9.52 | 0.00169 | 0.23337 |
| 12IX | | 9.52/9.35/9.52 | 0.00175 | 0.24166 |
| | | | **Average** | 0.23936 |
| | | | **Std deviation** | 0.00523 |
| | | | **(Std dev/Mean)x100** | 2.18 |

**FT30-L4**

**Ionic exchange of Ag+ for Ba++ pH = 7.58**

| | Treatment | pH max/pH min/pH final | Ba++ elemental ratio | Ba++ concentration [M] | Ag+ elemental ratio | Ag+ concentration [M] |
|---|---|---|---|---|---|---|
| 13IX | FT30+IX 7.5 | 8.25/6.92/7.72 | 0.00034 | 0.04695 | 0.00037 | 0.05109 |
| 14IX | | 8.25/6.92/7.72 | 0.00034 | 0.04695 | 0.00041 | 0.05662 |
| 15IX | | 8.25/6.92/7.72 | 0.00032 | 0.04419 | 0.00048 | 0.06628 |
| | | | **Average** | 0.04603 | **Average** | 0.05800 |
| | | | **Std deviation** | 0.00159 | **Std deviation** | 0.00769 |
| | | | **(Std dev/Mean) x100** | 3.46 | **(Std dev/Mean) x100** | 13.26 |

**Ag+ pH = 7.54**

| | Treatment | pH max/pH min/pH final | Ag+ elemental ratio | Ag+ concentration [M] |
|---|---|---|---|---|
| 16IX | FT30+Ag 7.5 | 7.54/6.60/7.54 | 0.00084 | 0.11600 |
| 17IX | | 7.54/6.60/7.54 | 0.00085 | 0.11738 |
| 18IX | | 7.54/6.60/7.54 | 0.00081 | 0.11185 |
| | | | **Average** | 0.11508 |
| | | | **Std deviation** | 0.00287 |
| | | | **(Std dev/Mean)x100** | 2.50 |

**FT30-L5**

**Ionic exchange of Ag+ for Ba++ pH = 7.50**

| | Treatment | pH max/pH min/pH final | Ba++ elemental ratio | Ba++ concentration [M] | Ag+ elemental ratio | Ag+ concentration [M] |
|---|---|---|---|---|---|---|
| 19IX | FT30+IX 7.5 | 8.25/6.85/7.51 | 0.00033 | 0.04557 | 0.00041 | 0.05662 |
| 20IX | | 8.25/6.85/7.51 | 0.00038 | 0.05247 | 0.00043 | 0.05938 |
| | | | **Average** | 0.04902 | **Average** | 0.05800 |
| | | | **Std deviation** | 0.00488 | **Std deviation** | 0.00195 |
| | | | **(Std dev/Mean) x100** | 9.96 | **(Std dev/Mean) x100** | 3.37 |

**Ag+ pH = 7.4**

| | Treatment | pH max/pH min/pH final | Ag+ elemental ratio | Ag+ concentration [M] |
|---|---|---|---|---|
| 21IX | FT30+Ag 7.5 | 7.65/7.05/7.4 | 0.00088 | 0.12152 |
| 22IX | | 7.65/7.05/7.4 | 0.00089 | 0.12290 |
| 23IX | | 7.65/7.05/7.4 | 0.00086 | 0.11876 |
| | | | **Average** | 0.12106 |
| | | | **Std deviation** | 0.00211 |
| | | | **(Std dev/Mean)x100** | 1.74 |

| | Ionic exchange of Ag+ for Ba++ pH = 10.26 | | | | | |
|---|---|---|---|---|---|---|
| | Treatment | pH max/pH min/pH final | Ba++ elemental ratio | Ba++ concentration [M] | Ag+ elemental ratio | Ag+ concentration [M] |
| 24IX | FT30+IX 10.5 | 10.40/10.25/10.27 | 0.00062 | 0.08562 | 0.00198 | 0.27342 |
| 25IX | | 10.40/10.25/10.27 | 0.00064 | 0.08838 | 0.00195 | 0.26928 |
| | | | **Average** | 0.08700 | **Average** | 0.27135 |
| | | | **Std deviation** | 0.00195 | **Std deviation** | 0.00293 |
| | | | **(Std dev/Mean) x100** | 2.24 | **(Std dev/Mean) x100** | 1.08 |

| | Ag+ pH = 10.29 | | | |
|---|---|---|---|---|
| | Treatment | pH max/pH min/pH final | Ag+ elemental ratio | Ag+ concentration [M] |
| 26IX | FT30+Ag 10.5 | 10.35/10.20/10.29 | 0.00288 | 0.39770 |
| 27IX | | 10.35/10.20/10.29 | 0.00307 | 0.42394 |
| | | | **Average** | 0.41082 |
| | | | **Std deviation** | 0.01855 |
| | | | **(Std dev/Mean)x100** | 4.52 |

**1IX**

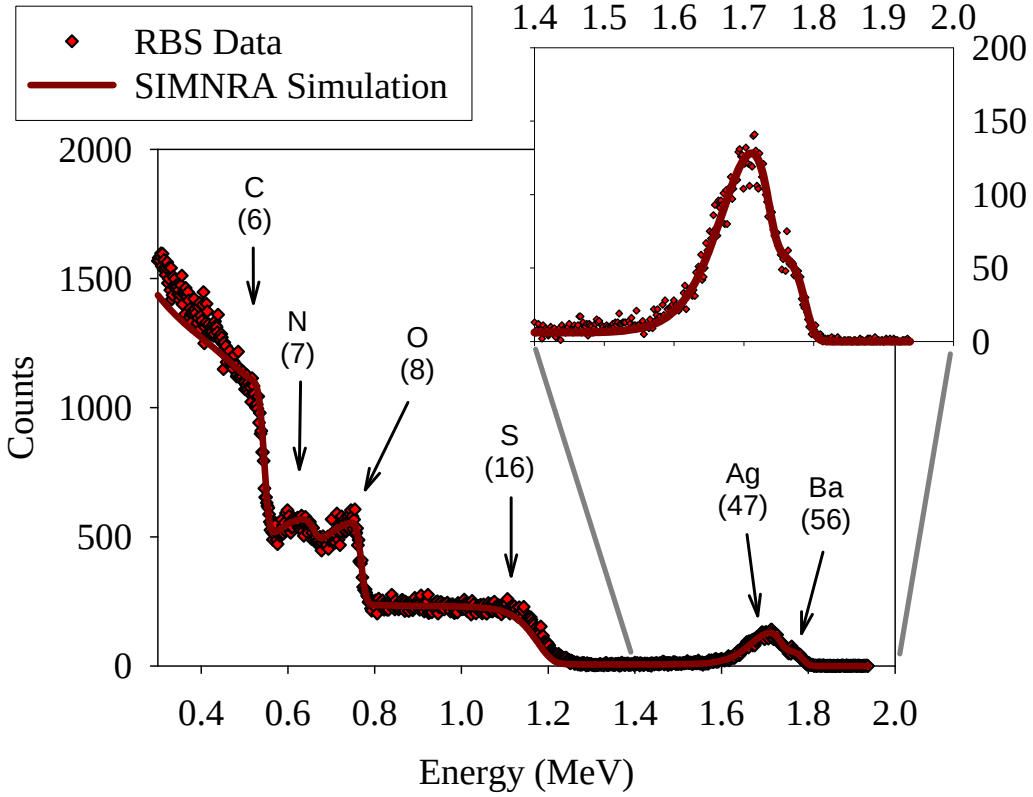
RBS Data
SIMNRA Simulation
Counts
Energy (MeV)
C (6)
N (7)
O (8)
S (16)
Ag (47)
Ba (56)

**2IX**

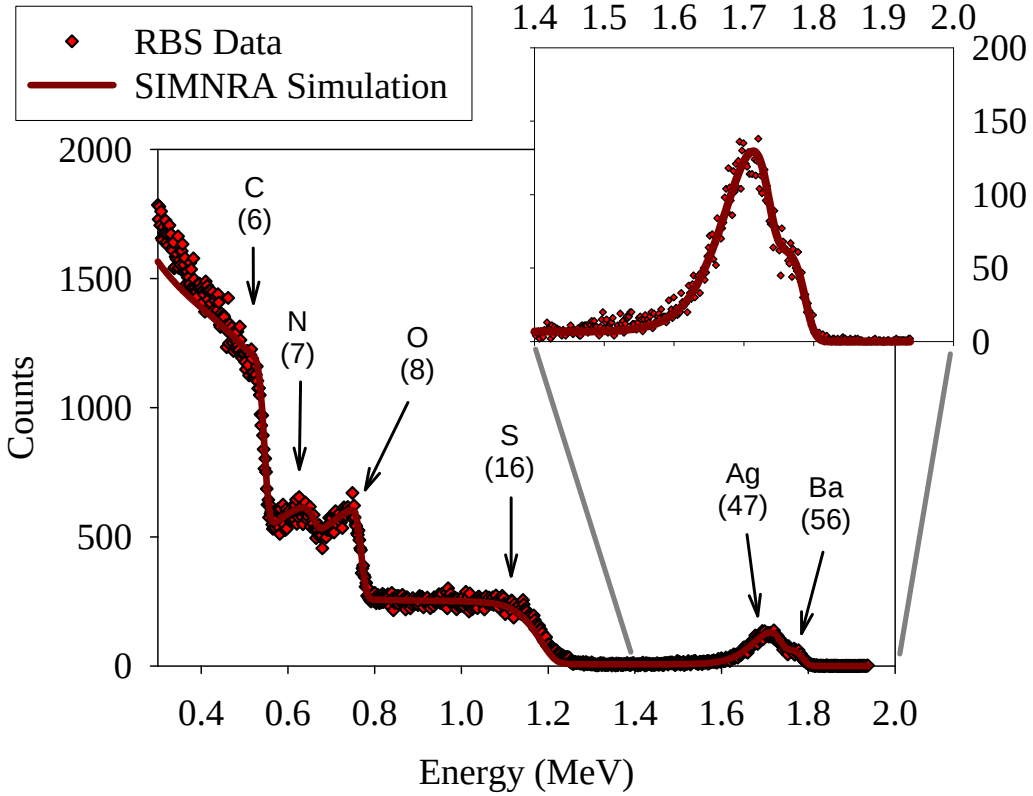
RBS Data
SIMNRA Simulation
Counts
Energy (MeV)
C (6)
N (7)
O (8)
S (16)
Ag (47)
Ba (56)

**3IX**

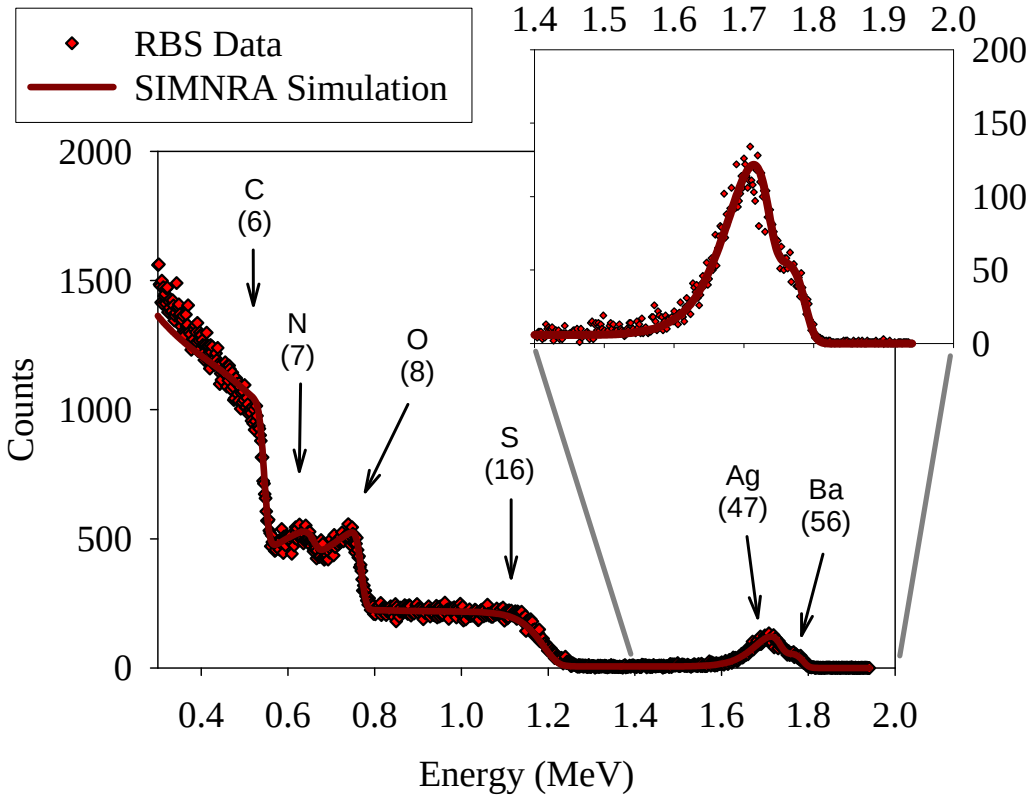
RBS Data
SIMNRA Simulation
Counts
Energy (MeV)
C (6)
N (7)
O (8)
S (16)
Ag (47)
Ba (56)

**4IX**

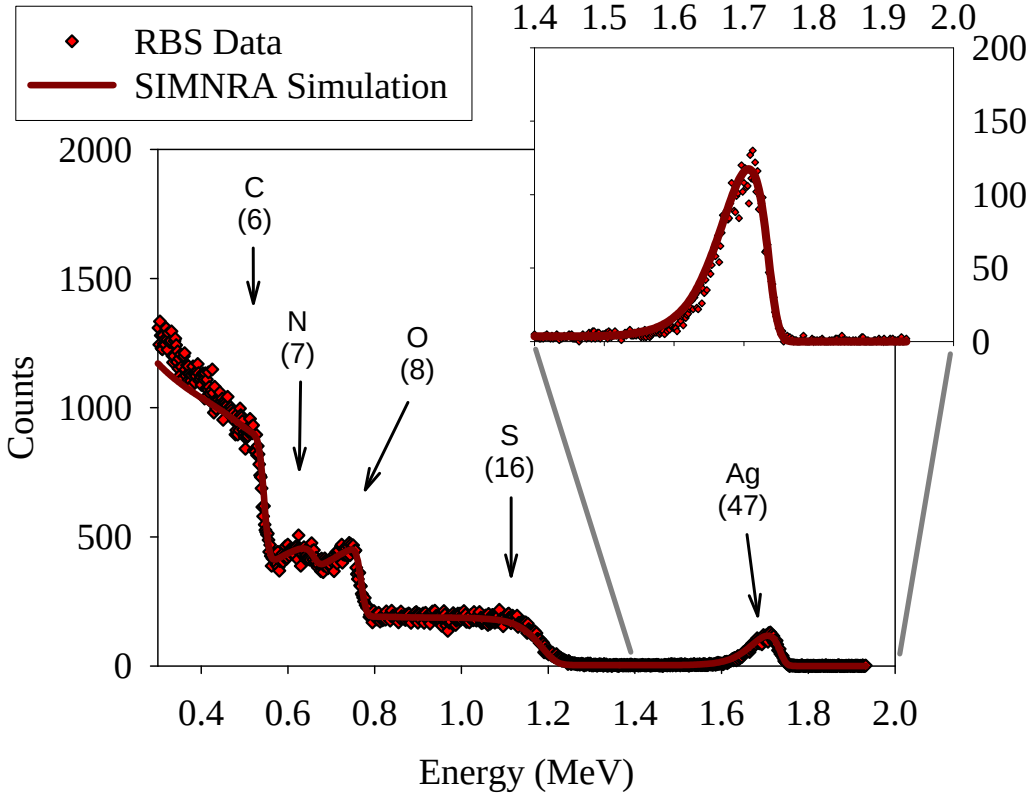
RBS Data
SIMNRA Simulation
Counts
Energy (MeV)
C (6)
N (7)
O (8)
S (16)
Ag (47)

**5IX**

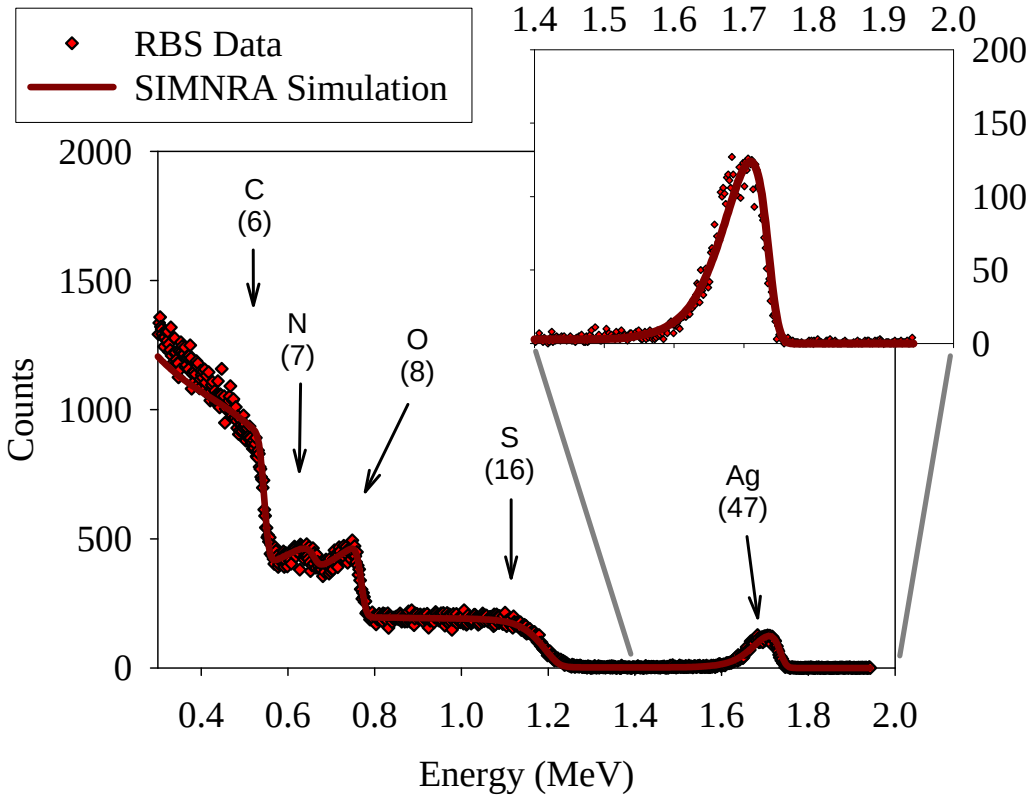
RBS Data
SIMNRA Simulation
Counts
Energy (MeV)
C (6)
N (7)
O (8)
S (16)
Ag (47)

**6IX**

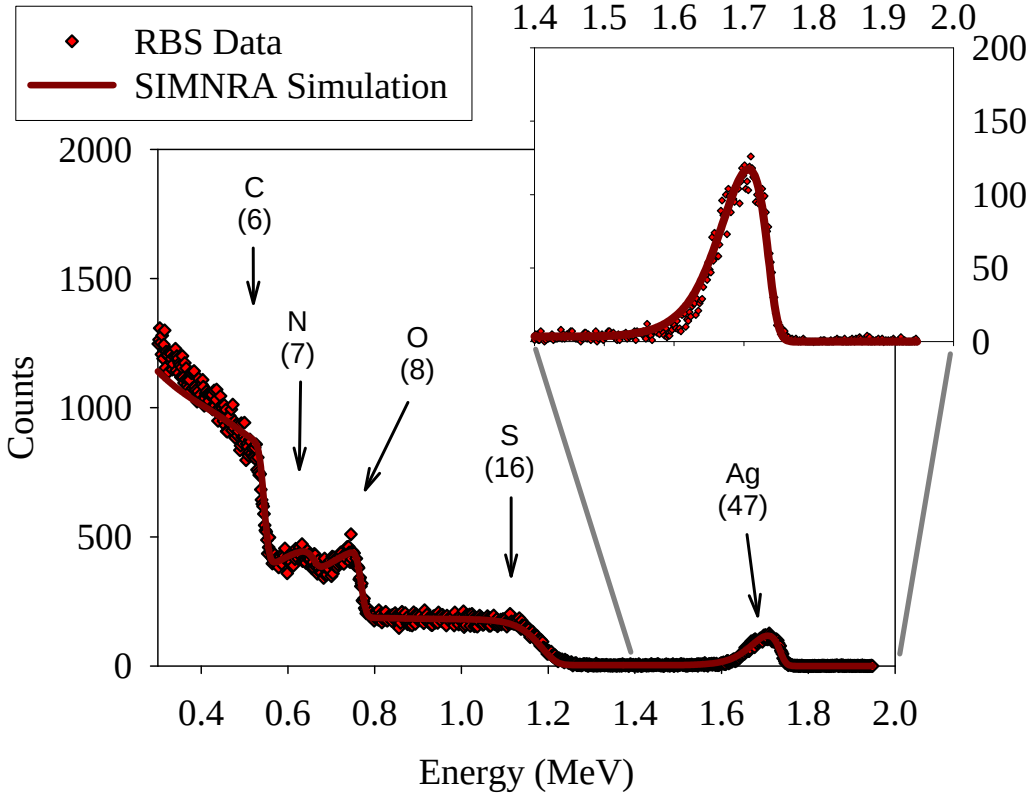
RBS Data
SIMNRA Simulation
Counts
Energy (MeV)
C (6)
N (7)
O (8)
S (16)
Ag (47)

**7IX**

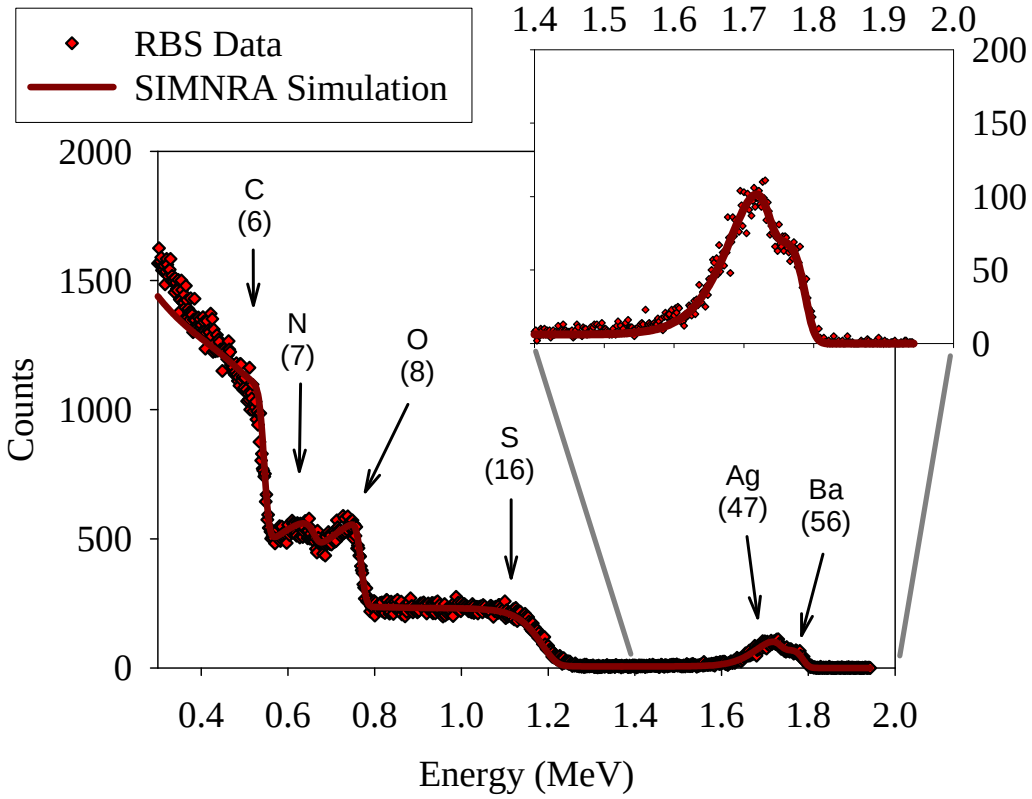
RBS Data
SIMNRA Simulation
Counts
Energy (MeV)
C (6)
N (7)
O (8)
S (16)
Ag (47)
Ba (56)

**8IX**

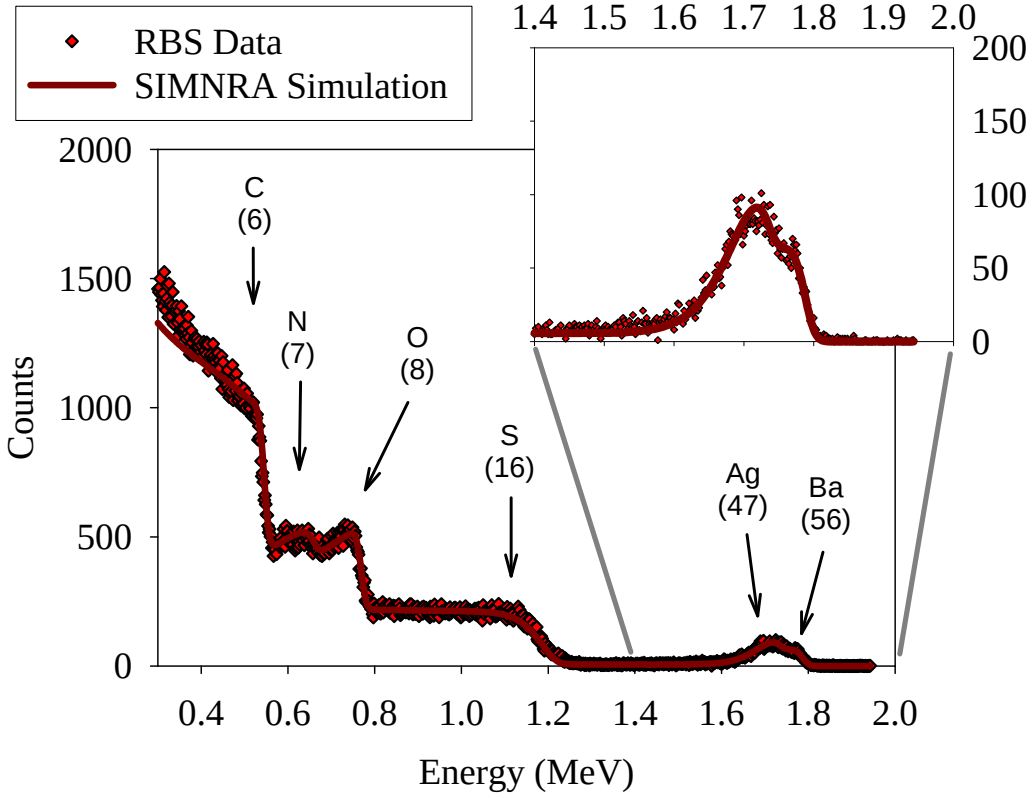
RBS Data
SIMNRA Simulation
Counts
Energy (MeV)
C (6)
N (7)
O (8)
S (16)
Ag (47)
Ba (56)

**9IX**

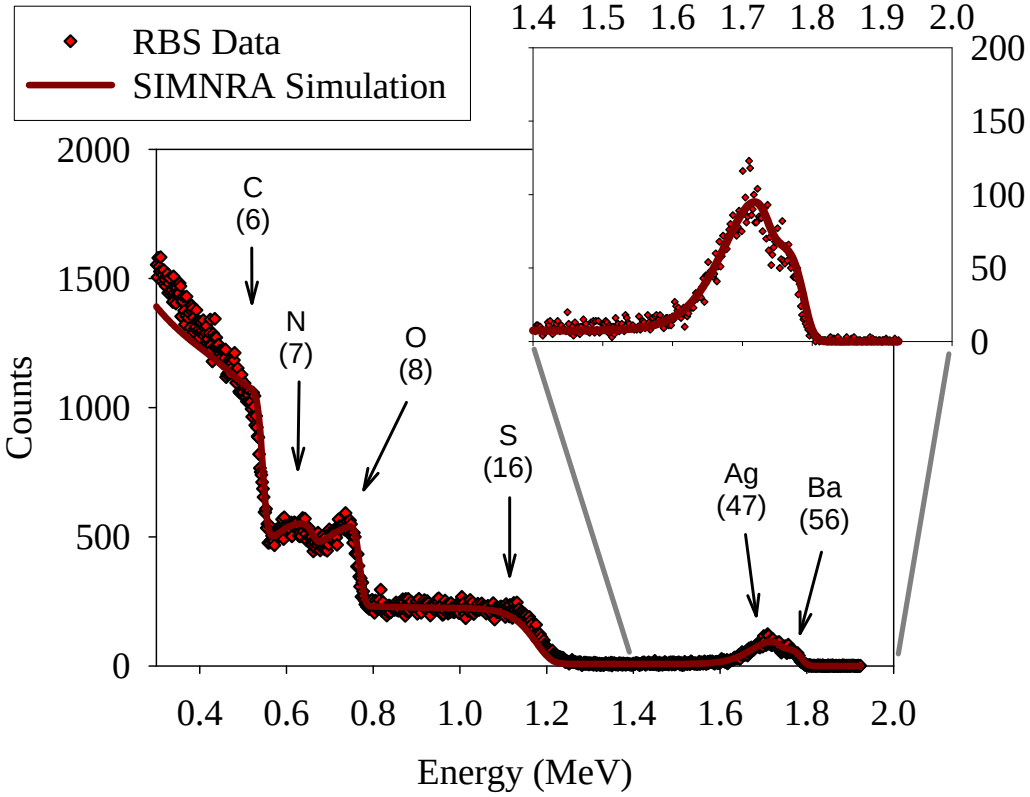
RBS Data
SIMNRA Simulation
Counts
Energy (MeV)
C (6)
N (7)
O (8)
S (16)
Ag (47)
Ba (56)

**10IX**

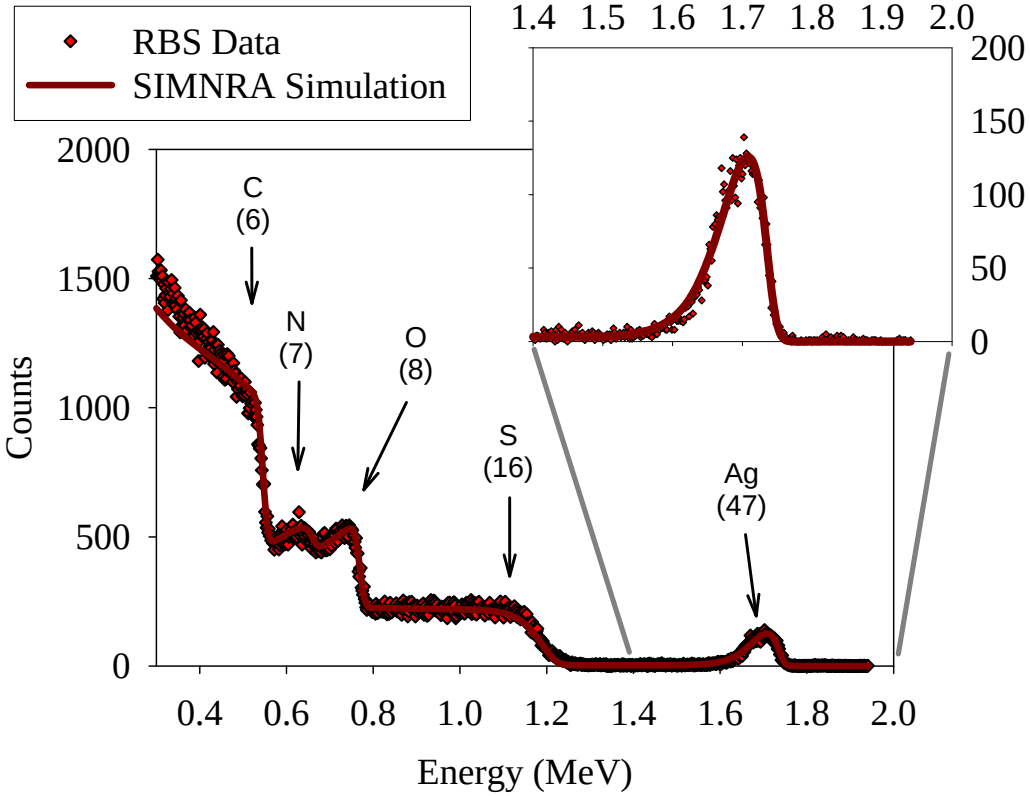
RBS Data
SIMNRA Simulation
Counts
Energy (MeV)
C (6)
N (7)
O (8)
S (16)
Ag (47)

**11IX**

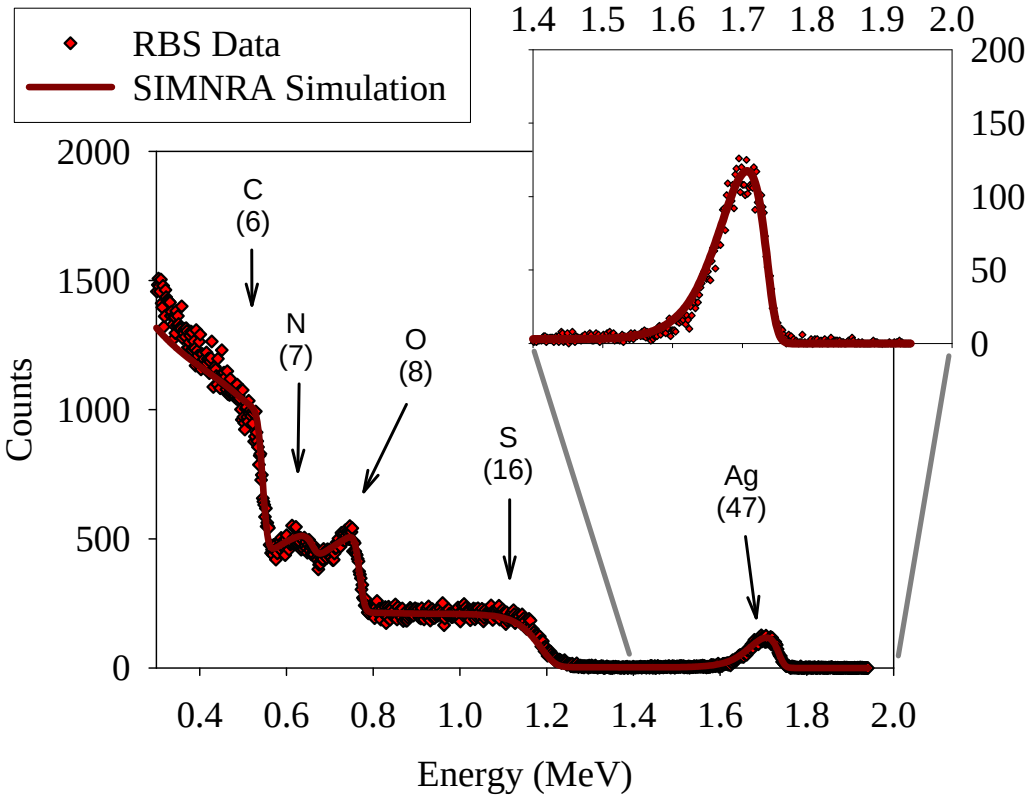
RBS Data
SIMNRA Simulation
Counts
Energy (MeV)
C (6)
N (7)
O (8)
S (16)
Ag (47)

**12IX**

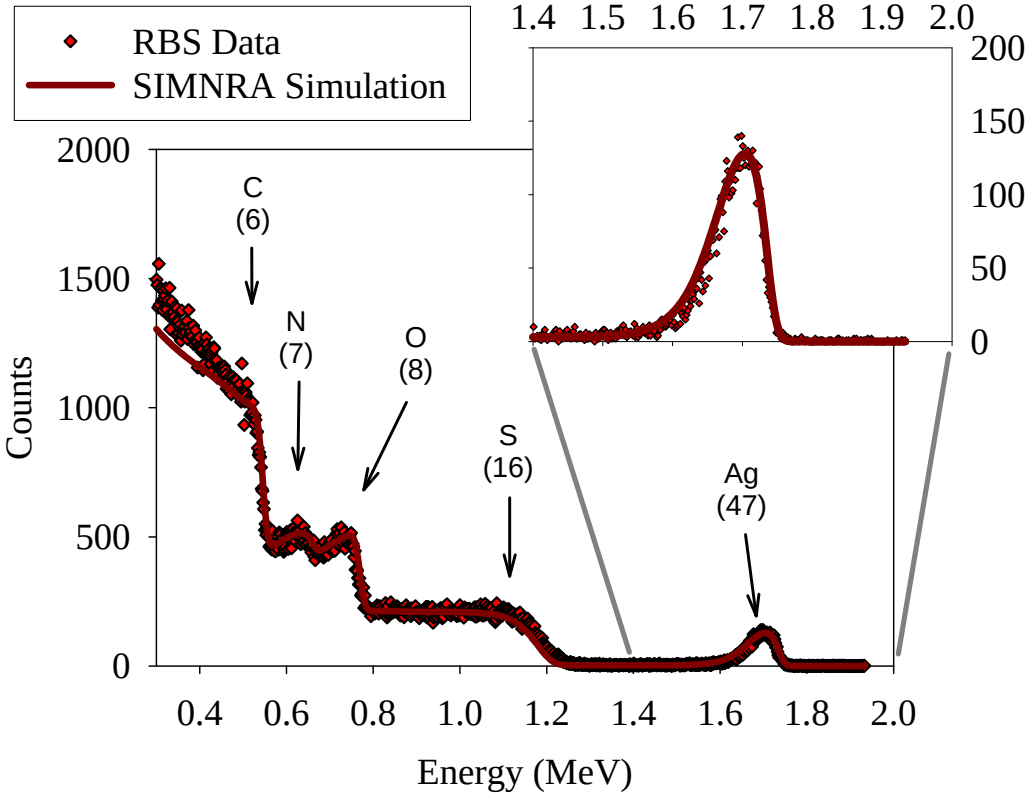
RBS Data
SIMNRA Simulation
Counts
Energy (MeV)
C (6)
N (7)
O (8)
S (16)
Ag (47)

**13IX**

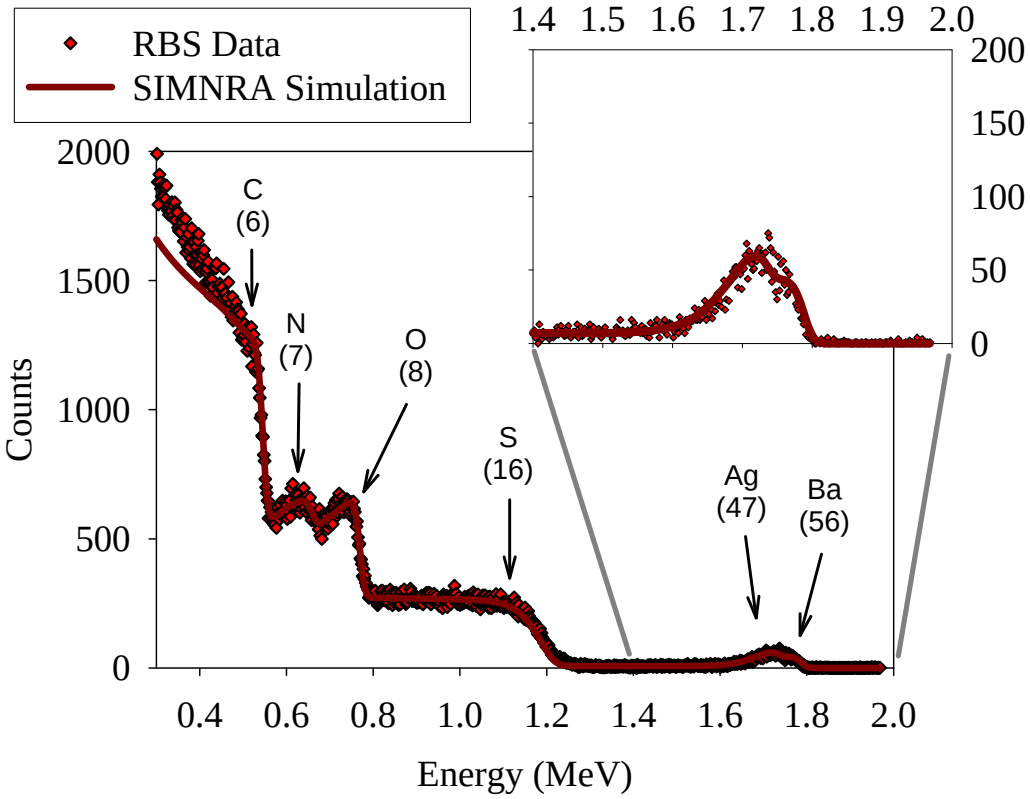
RBS Data
SIMNRA Simulation
Counts
Energy (MeV)
C (6)
N (7)
O (8)
S (16)
Ag (47)
Ba (56)

**14IX**

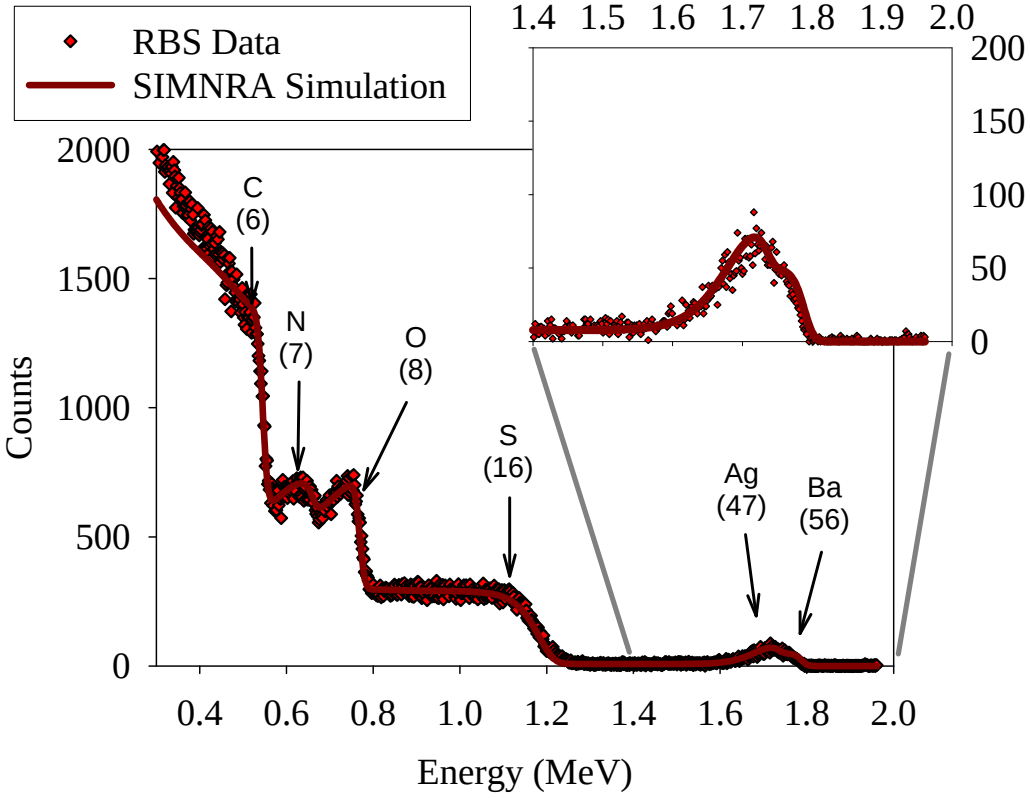
RBS Data
SIMNRA Simulation
Counts
Energy (MeV)
C (6)
N (7)
O (8)
S (16)
Ag (47)
Ba (56)

**15IX**

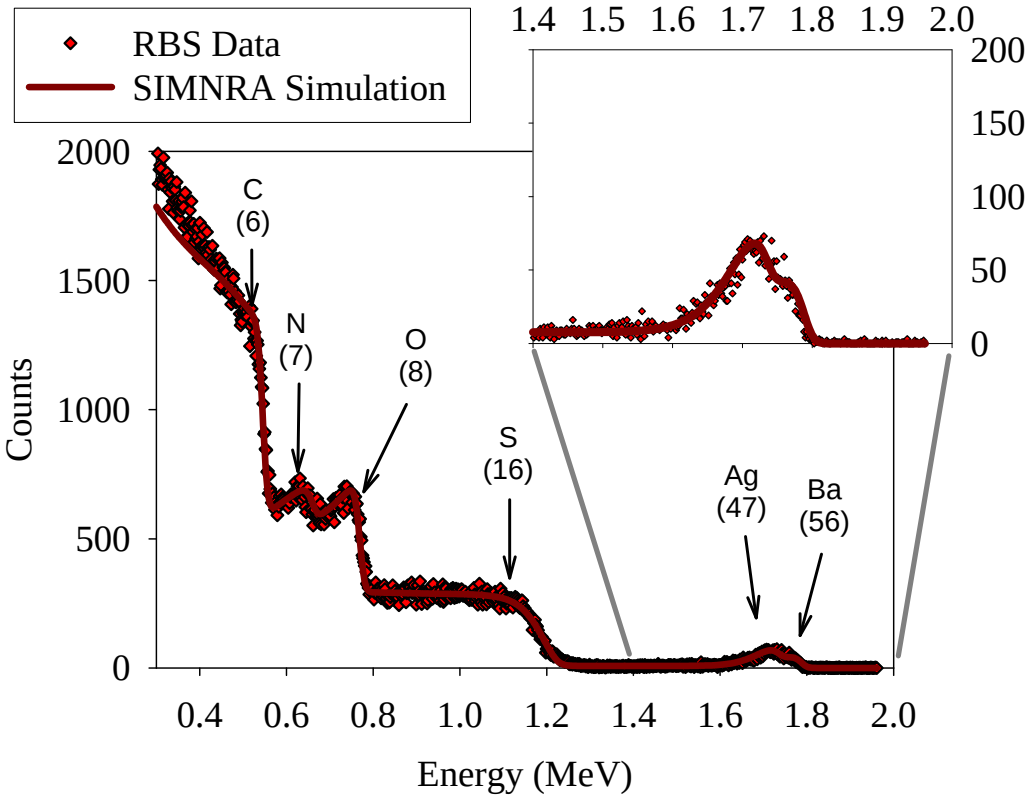
RBS Data
SIMNRA Simulation
Counts
Energy (MeV)
C (6)
N (7)
O (8)
S (16)
Ag (47)
Ba (56)

**16IX**

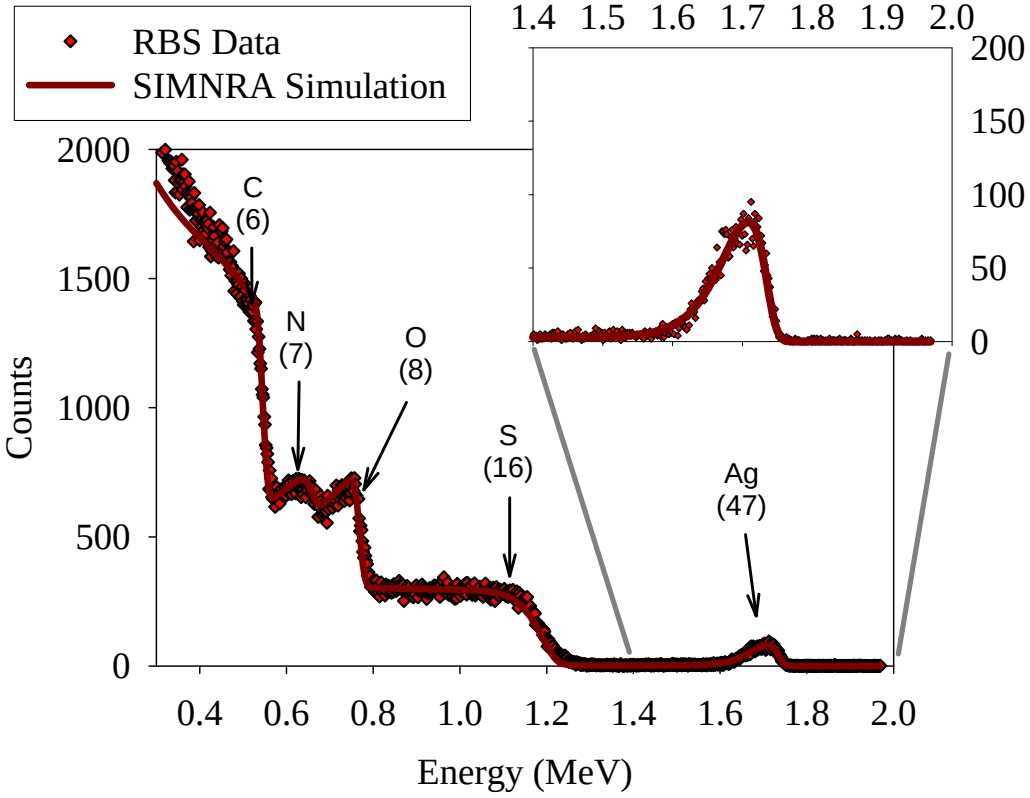
RBS Data
SIMNRA Simulation
Counts
Energy (MeV)
C (6)
N (7)
O (8)
S (16)
Ag (47)

**17IX**

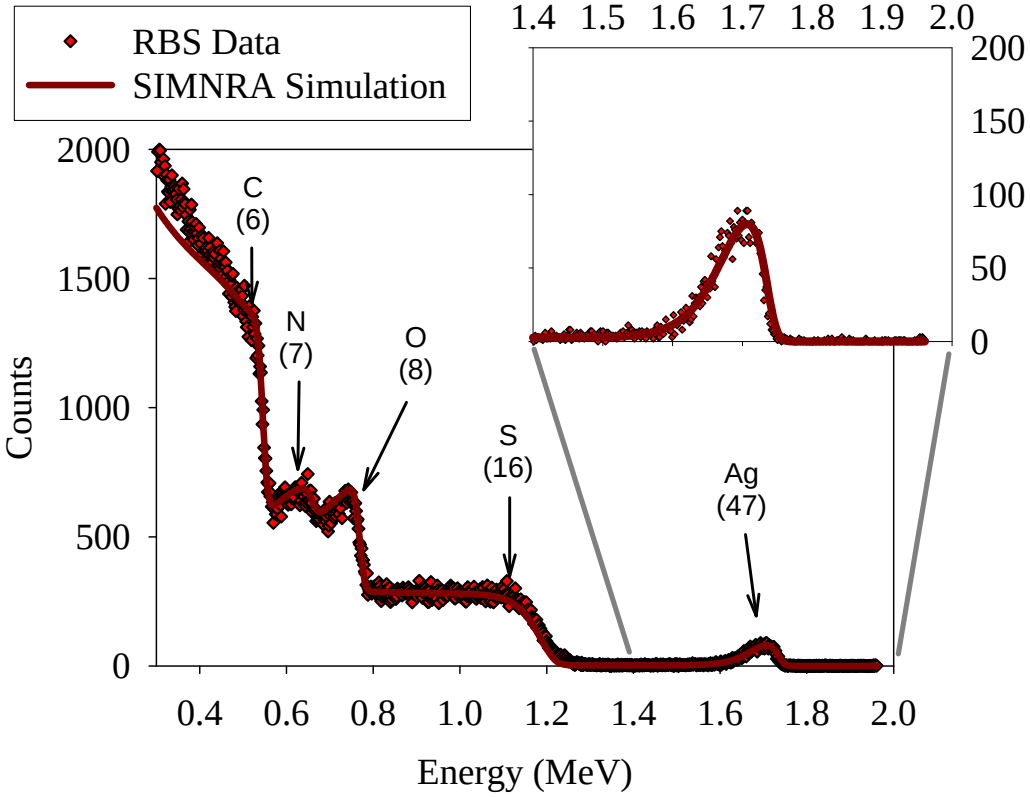
RBS Data
SIMNRA Simulation
Counts
Energy (MeV)
C (6)
N (7)
O (8)
S (16)
Ag (47)

**18IX**

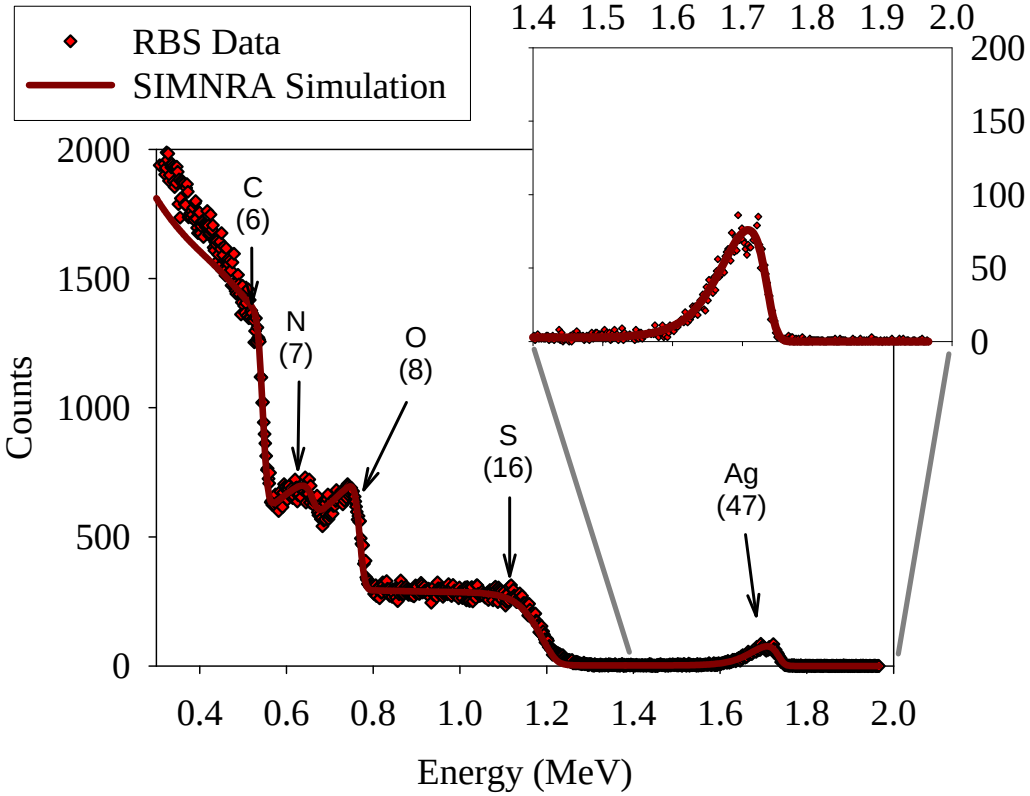
RBS Data
SIMNRA Simulation
Counts
Energy (MeV)
C (6)
N (7)
O (8)
S (16)
Ag (47)

**19IX**

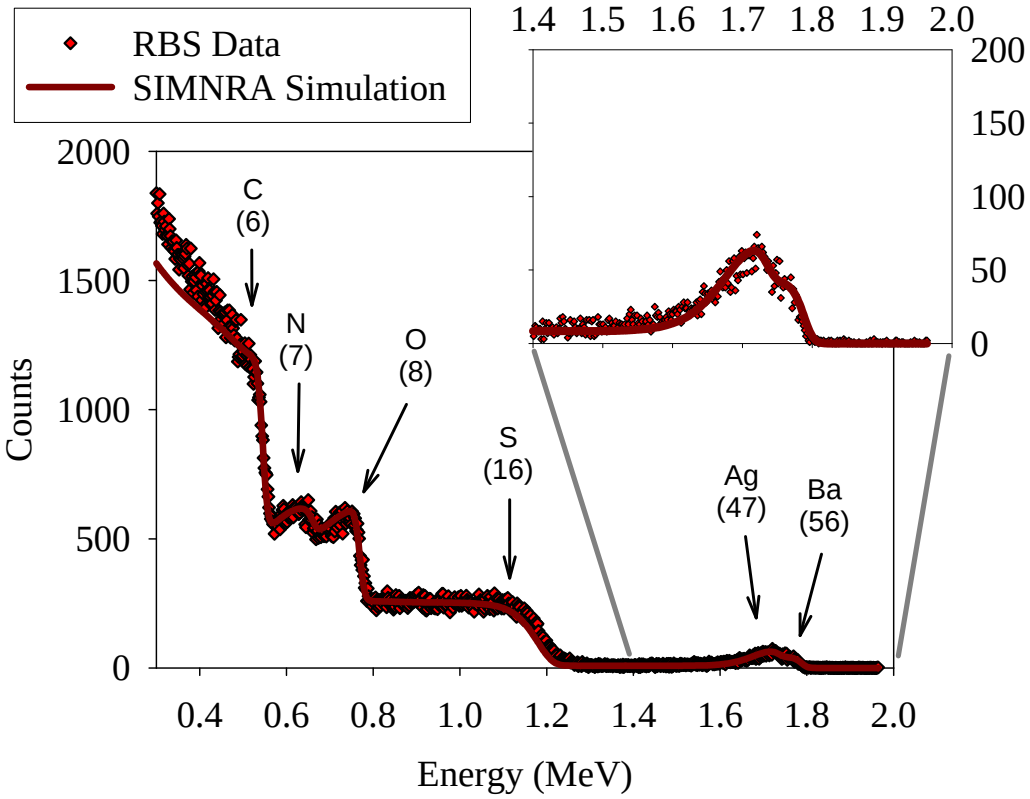
RBS Data
SIMNRA Simulation
Counts
Energy (MeV)
C (6)
N (7)
O (8)
S (16)
Ag (47)
Ba (56)

**20IX**

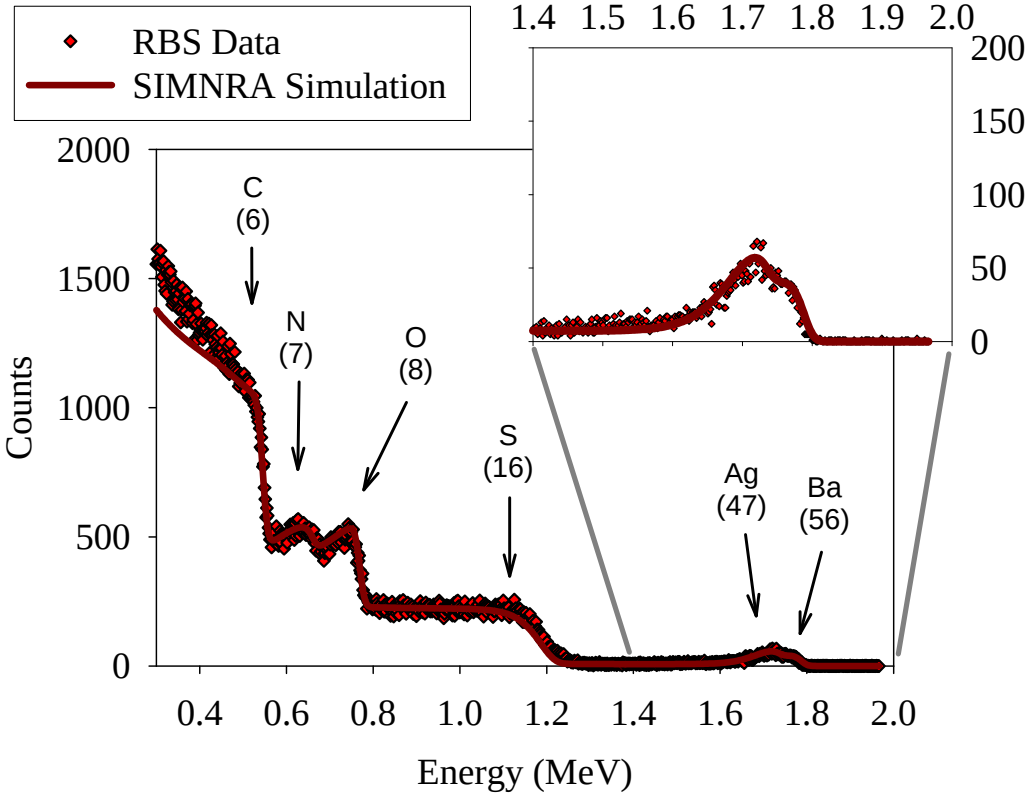
RBS Data
SIMNRA Simulation
Counts
Energy (MeV)
C (6)
N (7)
O (8)
S (16)
Ag (47)
Ba (56)

**21IX**

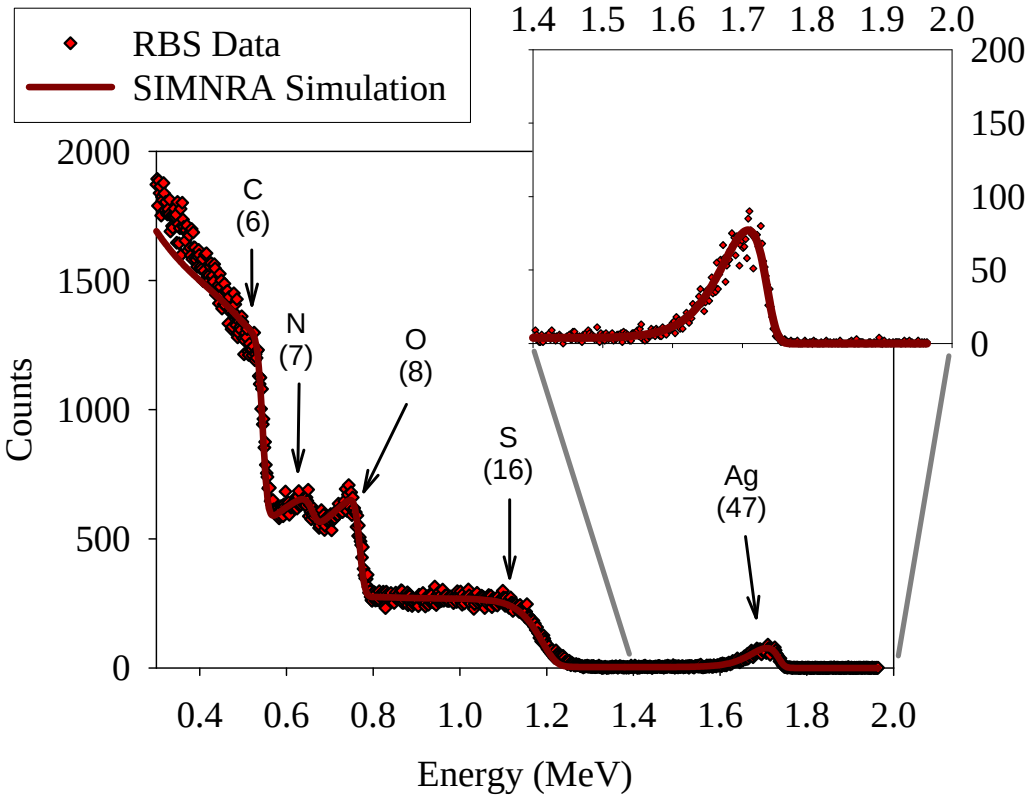
RBS Data
SIMNRA Simulation
Counts
Energy (MeV)
C (6)
N (7)
O (8)
S (16)
Ag (47)

**22IX**

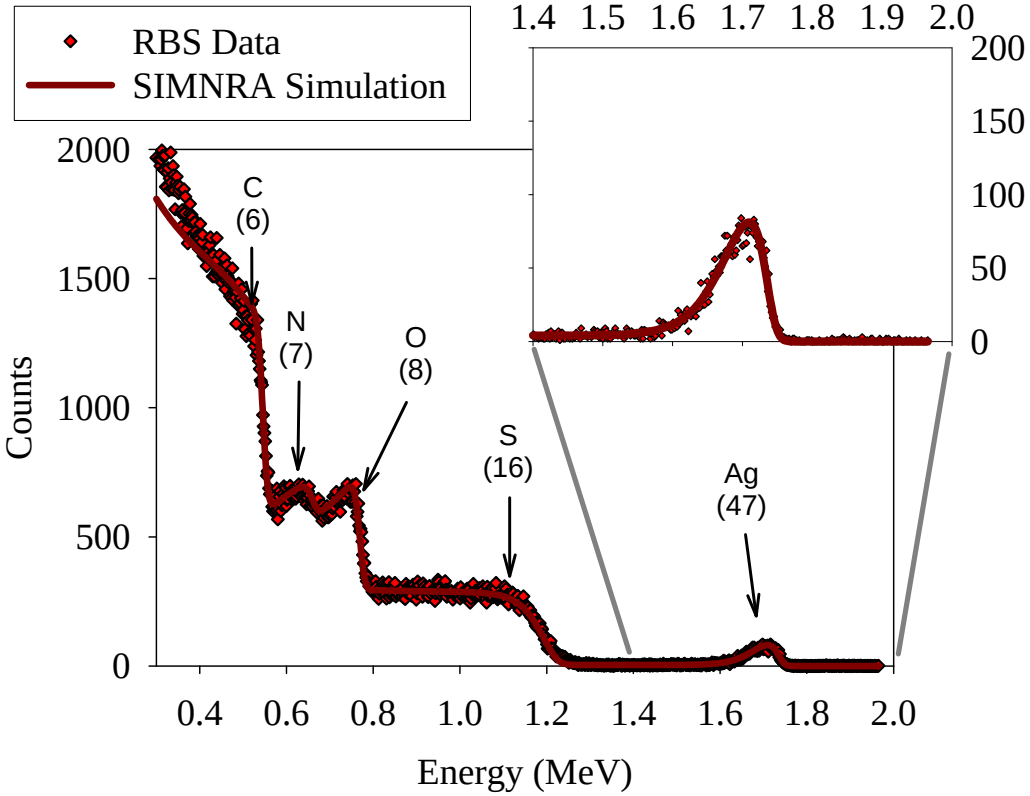
RBS Data
SIMNRA Simulation
Counts
Energy (MeV)
C (6)
N (7)
O (8)
S (16)
Ag (47)

**23IX**

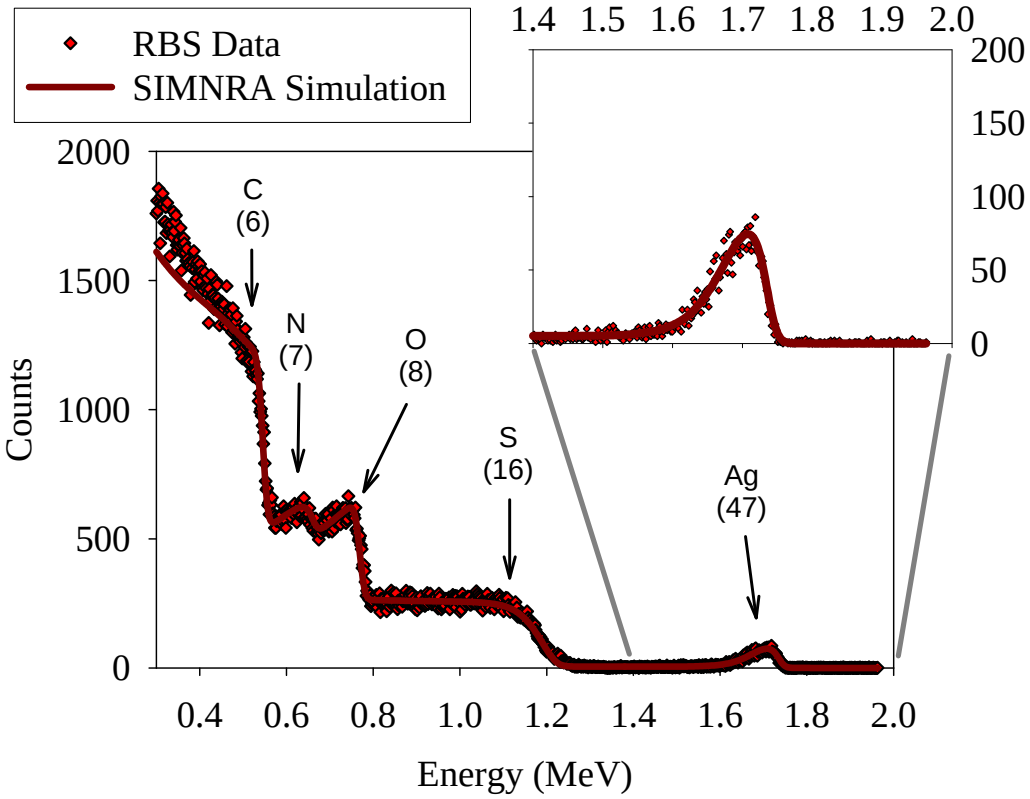
RBS Data
SIMNRA Simulation
Counts
Energy (MeV)
C (6)
N (7)
O (8)
S (16)
Ag (47)

**24IX**

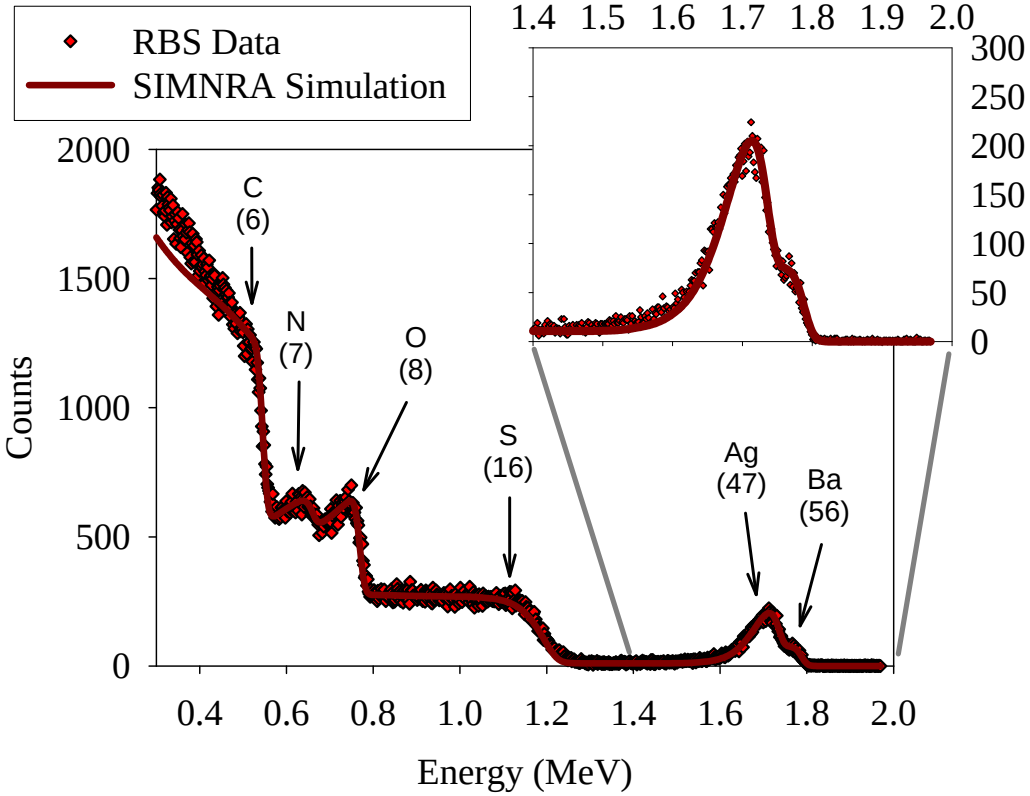
RBS Data
SIMNRA Simulation
Counts
Energy (MeV)
C (6)
N (7)
O (8)
S (16)
Ag (47)
Ba (56)

**25IX**

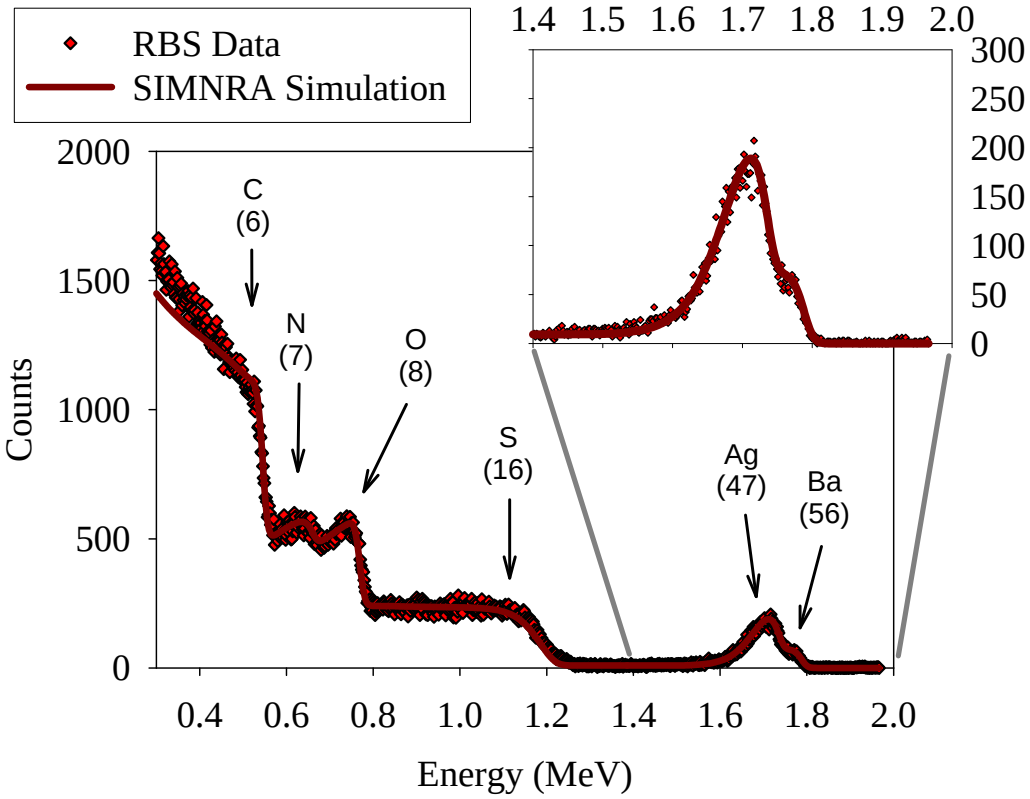
RBS Data
SIMNRA Simulation
Counts
Energy (MeV)
C (6)
N (7)
O (8)
S (16)
Ag (47)
Ba (56)

**26IX**

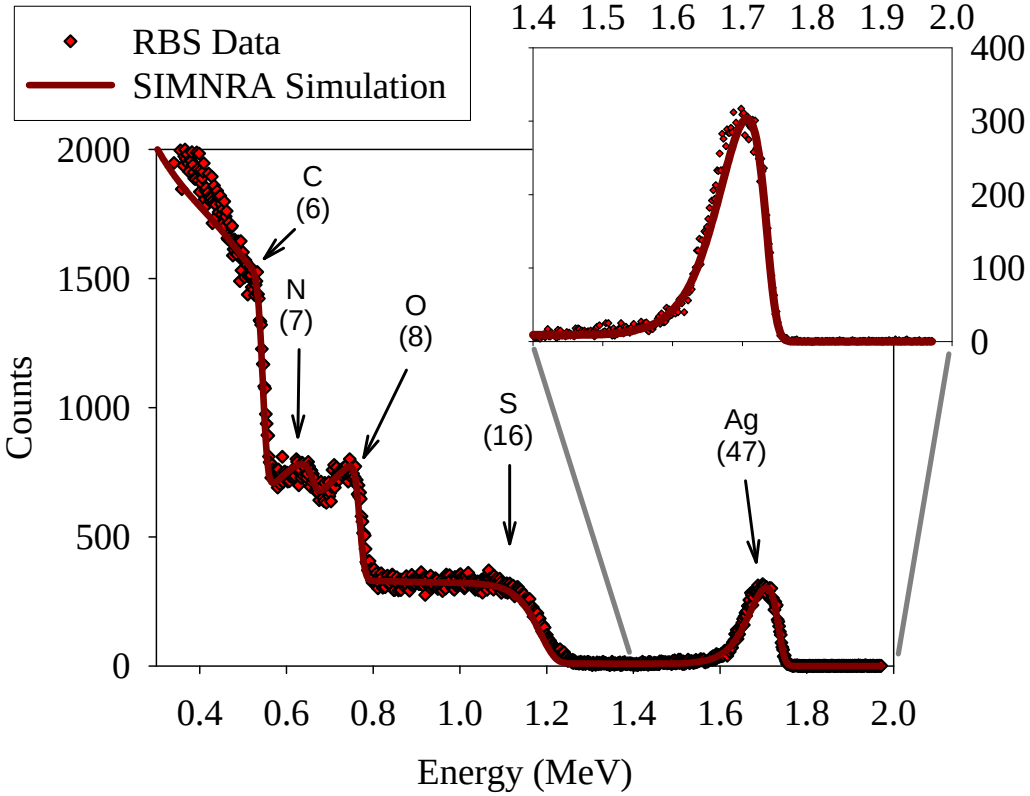
RBS Data
SIMNRA Simulation
Counts
Energy (MeV)
C (6)
N (7)
O (8)
S (16)
Ag (47)

**27IX**

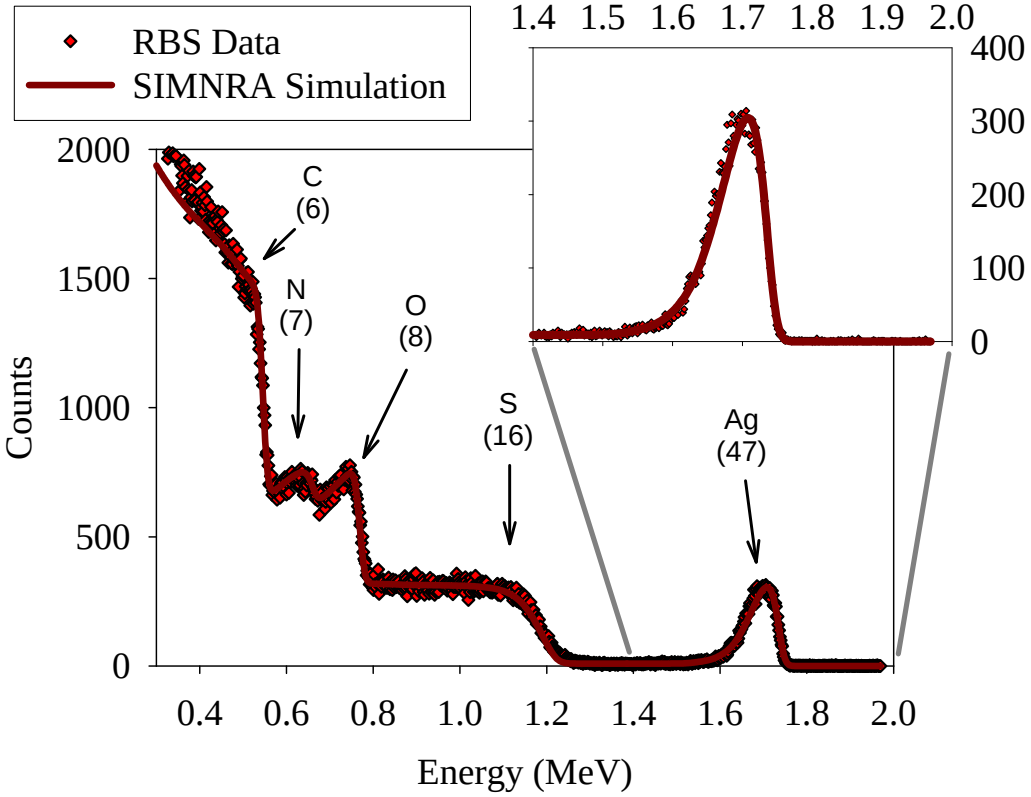
RBS Data
SIMNRA Simulation
Counts
Energy (MeV)
C
(6)
N
(7)
O
(8)
S
(16)
Ag
(47)
2000
1500
1000
500
0
0.4
0.6
0.8
1.0
1.2
1.4
1.6
1.8
2.0
400
300
200
100
0

# APPENDIX C

# APPENDICES FOR CHAPTER 4

## Appendix C.1. Supporting Information for Chapter 4

**Summary of contents:**

- Fifteen pages
- Figure C.1. Attenuated total reflectance Fourier transform infrared (ATR-FTIR) spectrometry analyses of membranes with polyamide (PA) active layers.
- Figure C.2. Rutherford backscattering spectrometry (RBS) spectrum of a sample of LF10 RO membrane probed with $Ag^{+}$ at pH = 9.85.
- Figure C.3. Repeating units in the polymer structure of the sulfonated polyethersulfone (SPES) active layer of NTR−7450 NF.
- Figure C.4. RBS spectra and corresponding simulations for: (a) FT30 RO (see note 'a' in Table 4.1), (b) LF10 RO, (c) ESPA3 RO, (d) TFC−S NF, (e) ESNA NF, (f) NF90 NF, (g) NTR−7450 NF.
- Figure C.5. Concentration of ionizable functional groups, concentration of $Ba^{2+}$ ion that associates with accessible $R{-}COO^{-}$ groups, and accessibility ratio for $Ba^{2+}$ ion as a function of pH in the active layers of (a) FT30 RO (see note 'a' in Table 4.1), (b) ESPA3 RO, (c) TFC−S NF, (d) ESNA NF, (e) NF90 NF, and (f) NTR−7450 NF.
- **Note:** Bibliographic information for references cited in Appendix C.1 can be found in Section 4.6 of this dissertation.

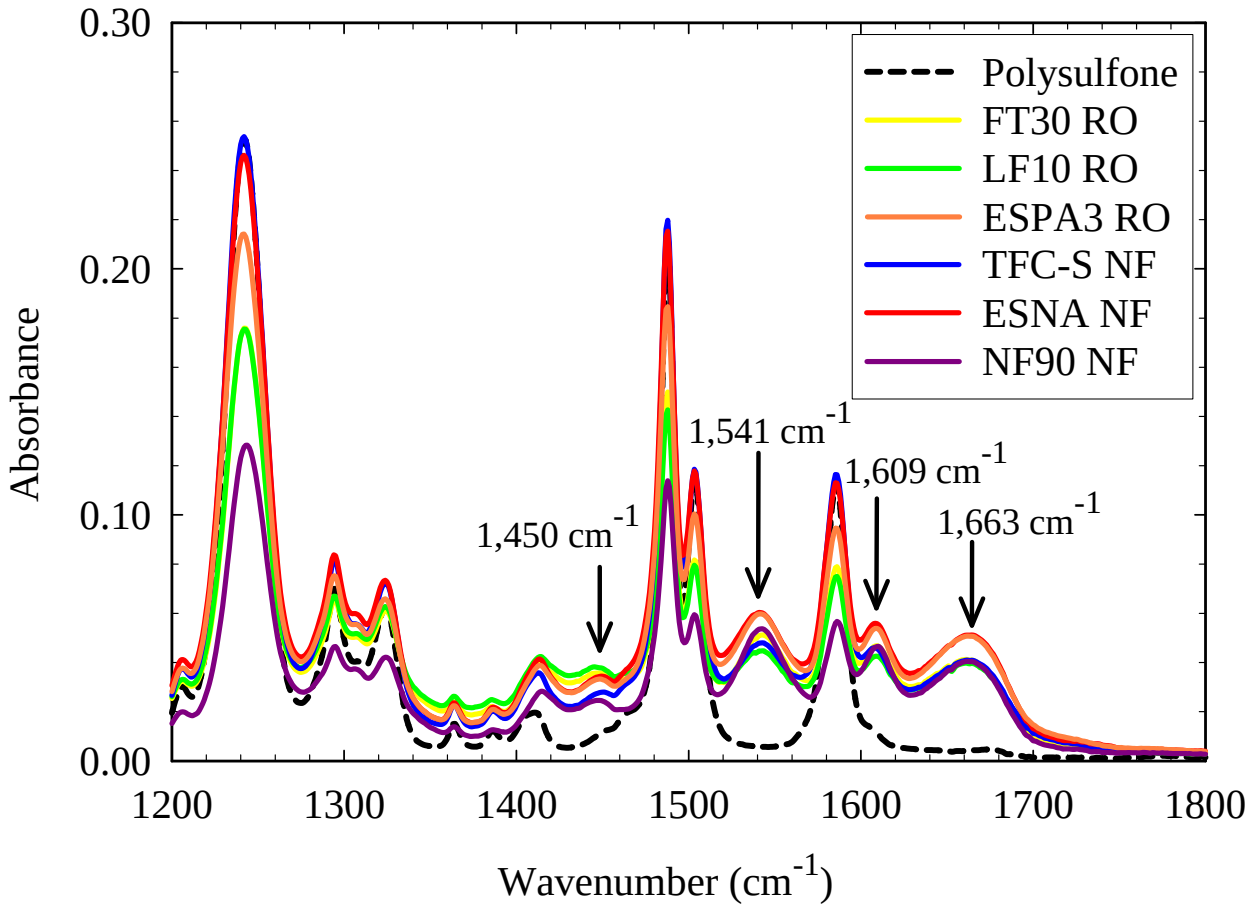


**Figure C.1.** Attenuated total reflectance Fourier transform infrared (ATR-FTIR) spectrometry analyses of membranes with polyamide (PA) active layers.

**Commentary:** The spectra reveal that all PA membranes used have the three characteristic peaks of fully-aromatic PA [19] at wavenumbers 1,663 $cm^{-1}$ (amide I band, secondary amide groups: C=O stretching, C–N stretching, and C–C–N deformation vibration), 1,609 $cm^{-1}$ (aromatic amide groups: N–H deformation vibration, and C=C ring stretching vibration), and 1,541 $cm^{-1}$ (amide II band, amide groups: N–H in-plane bending and N–C stretching vibration). The spectra also show the 1,450 $cm^{-1}$ peak associated with carboxylic acid groups corresponding to C–O stretching/O–H bending (Rao et al., *J. Mem. Sci.* 2003, *211*, 13-24). Each spectrum in the figure was obtained as the average of five replicate ATR–FTIR spectra, with each spectrum being collected as the average of 256 scans in the 650–4000 $cm^{-1}$ wavenumber range at 2 $cm^{-1}$ resolution. Membrane samples were first dried by pressing them between two qualitative-grade filter-paper circles, and then dried in vacuum for ≥72 hours before performing ATR–FTIR analyses using a Nexus 670 FTIR spectrometer (Thermo Nicolet Corporation, Madison, WI) equipped with an IR source with incident angle of 45°, a Smart Golden Gate diamond ATR accessory that samples a circular area of ≈2 mm in diameter, a DTGS-KBr detector, and a KBr beam-splitter.

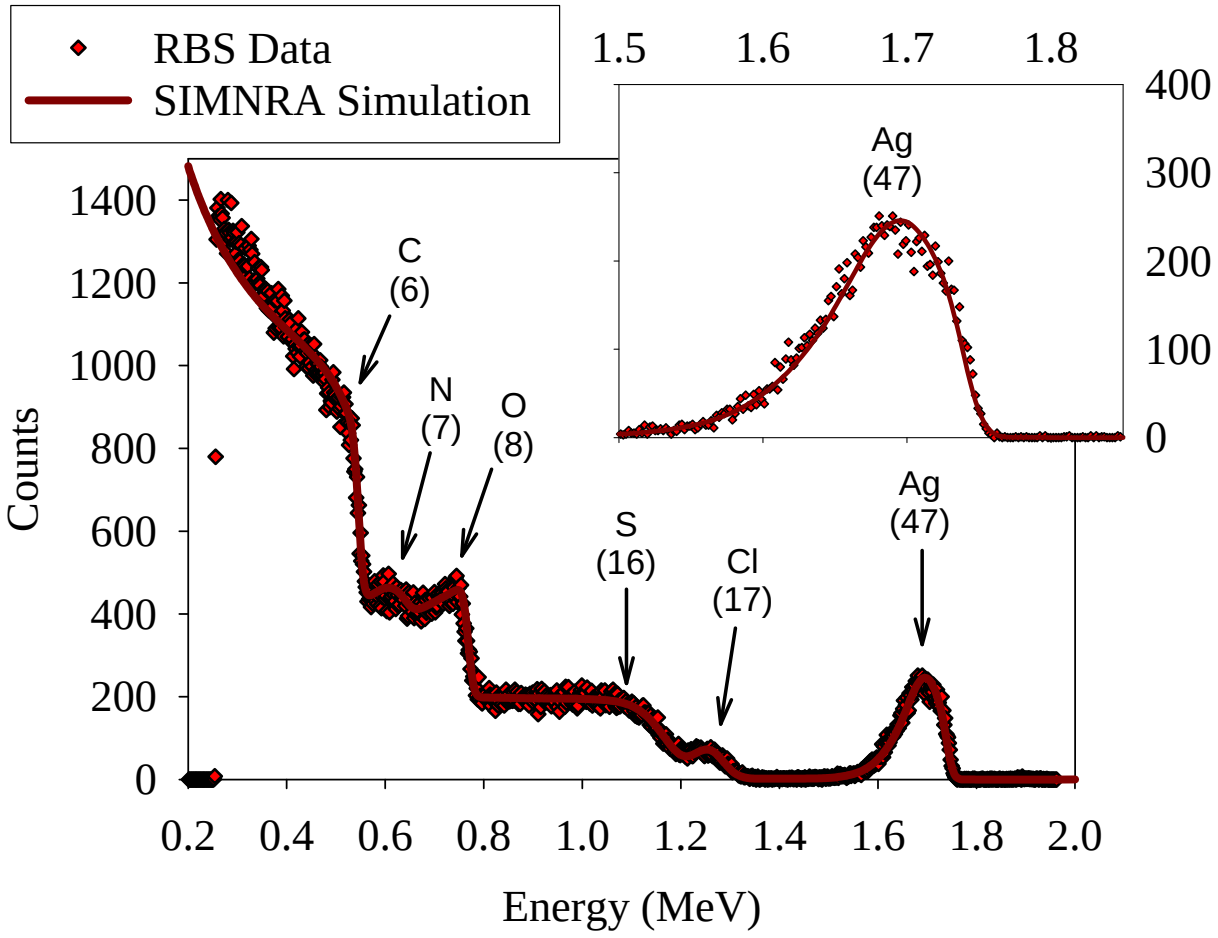


**Figure C.2.** Rutherford backscattering spectrometry (RBS) spectrum of a sample of LF10 RO membrane probed with $Ag^{+}$ at pH = 9.85. Symbols represent RBS data. Lines represent the fit obtained using the software SIMNRA® [16]. The number in parentheses below the symbol of each element corresponds to its atomic number. The main four elements present in the membrane (C, N, O, S), other than hydrogen, are easily identified in the spectrum. Hydrogen content in the membrane affects the spectrum but does not have a signal in it (see commentary in Figure C.4 below). The ion probe ($Ag^{+}$), neutralizing ionized $R–COO^{-}$ groups, is also easily discerned.

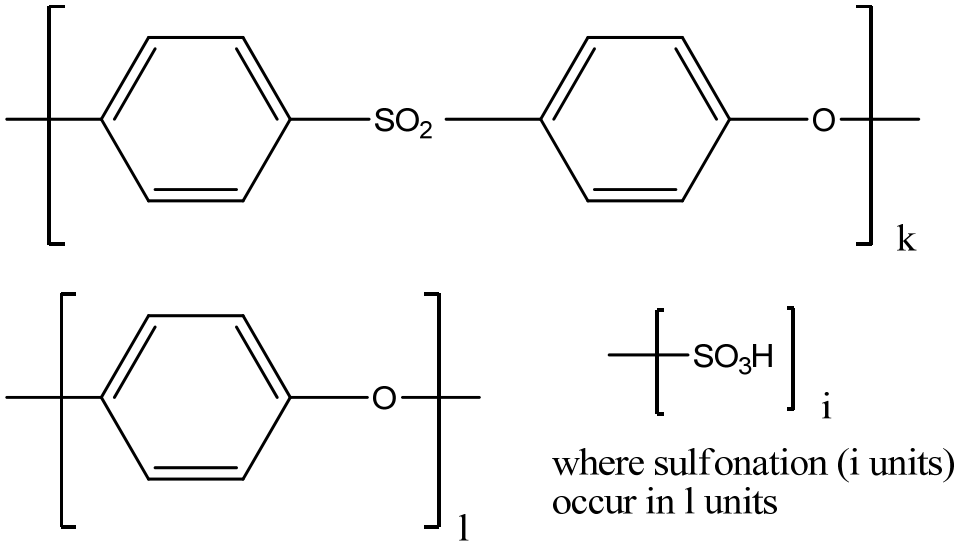


**Figure C.3.** Repeating units in the polymer structure of the sulfonated polyethersulfone (SPES) active layer of NTR–7450 NF [28].

**Commentary:** The values of the fractions for each repeating unit shown in the figure are k = 2.00, l = 1.08 and i = 0.75 for the active layer of NTR–7450 NF membrane. The concentration of sulfonate ($R–SO3^-$) groups in the SPES polymer was found to be 1.67±0.02 M using the ion-probing/RBS procedure with $Ag^+$ and $K^+$ as probes. The 1.67 M concentration of sulfonate groups corresponds to an elemental fraction of 0.0125 for a monovalent ion probe (i.e., $Ag^+$ or $K^+$) neutralizing the sulfonate groups, where the summation of the elemental fractions of all elements present in the active layer equals one. (See also H:C ratio discussion in the commentary of Figure C.4 below)

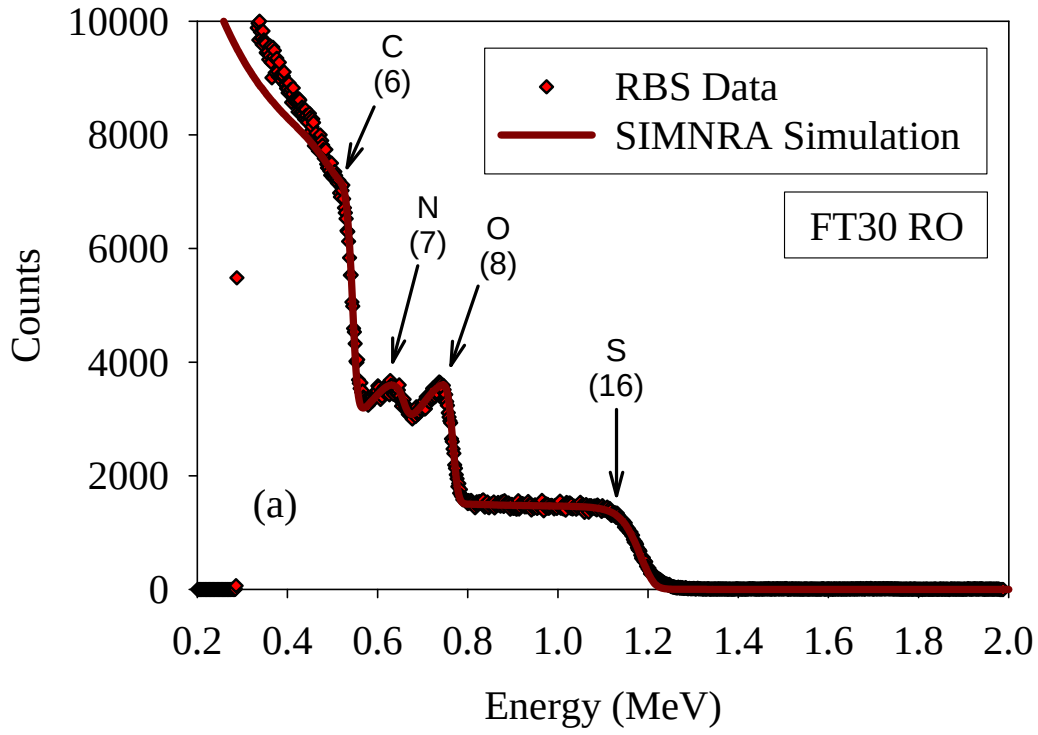


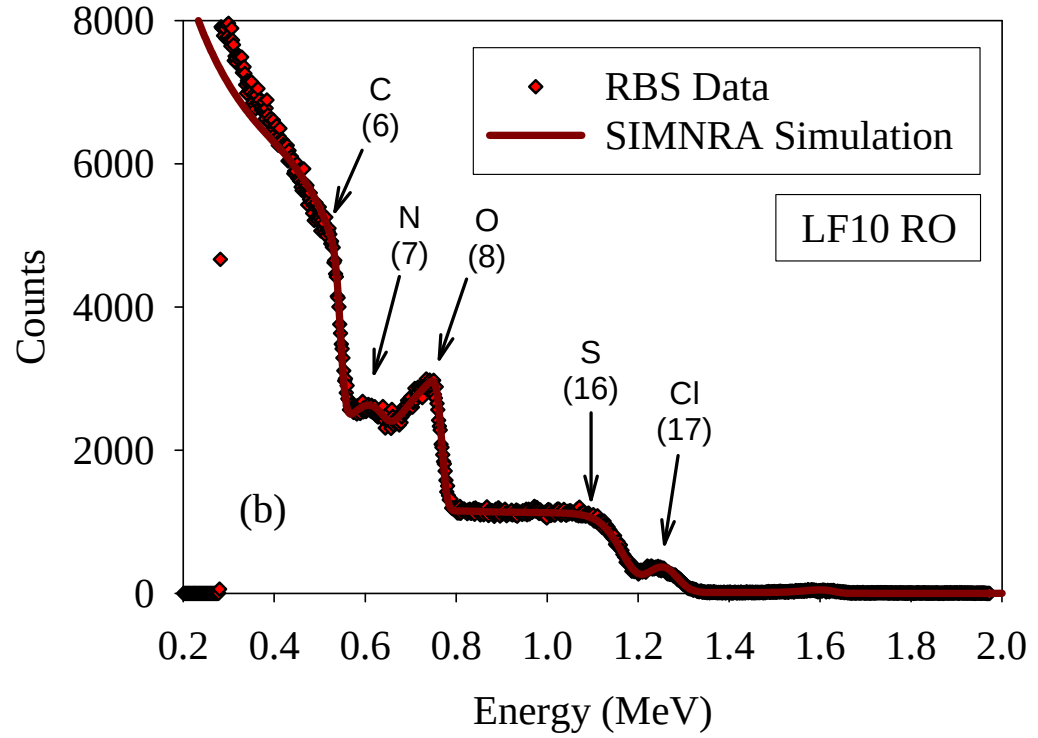


**Figure C.4a and C.4b**

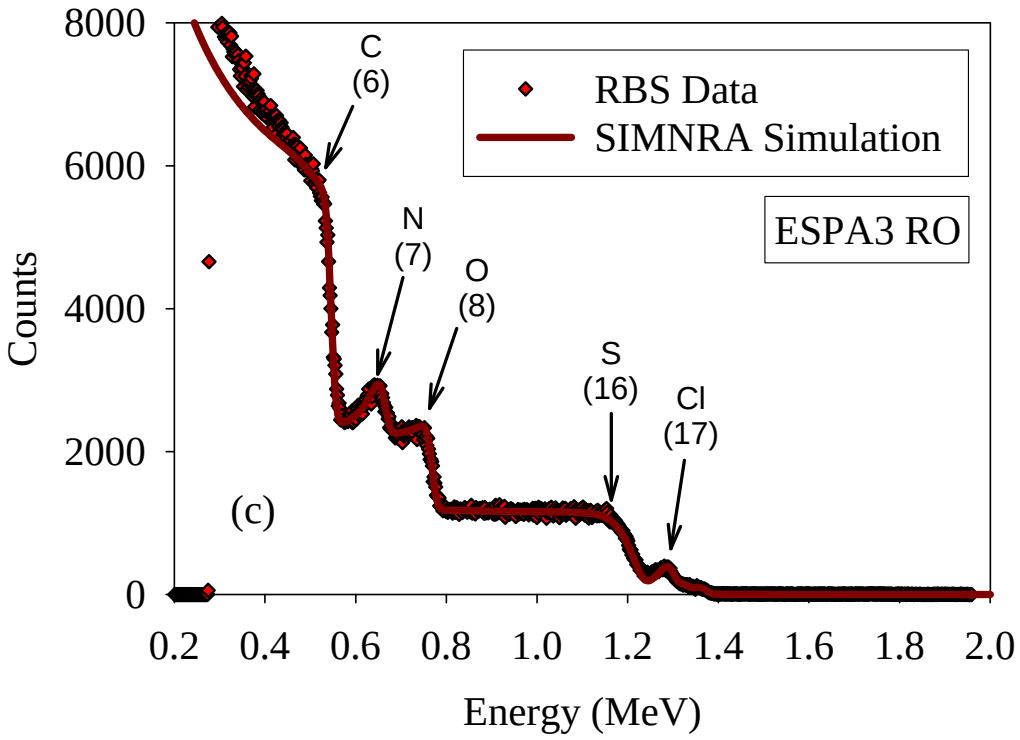


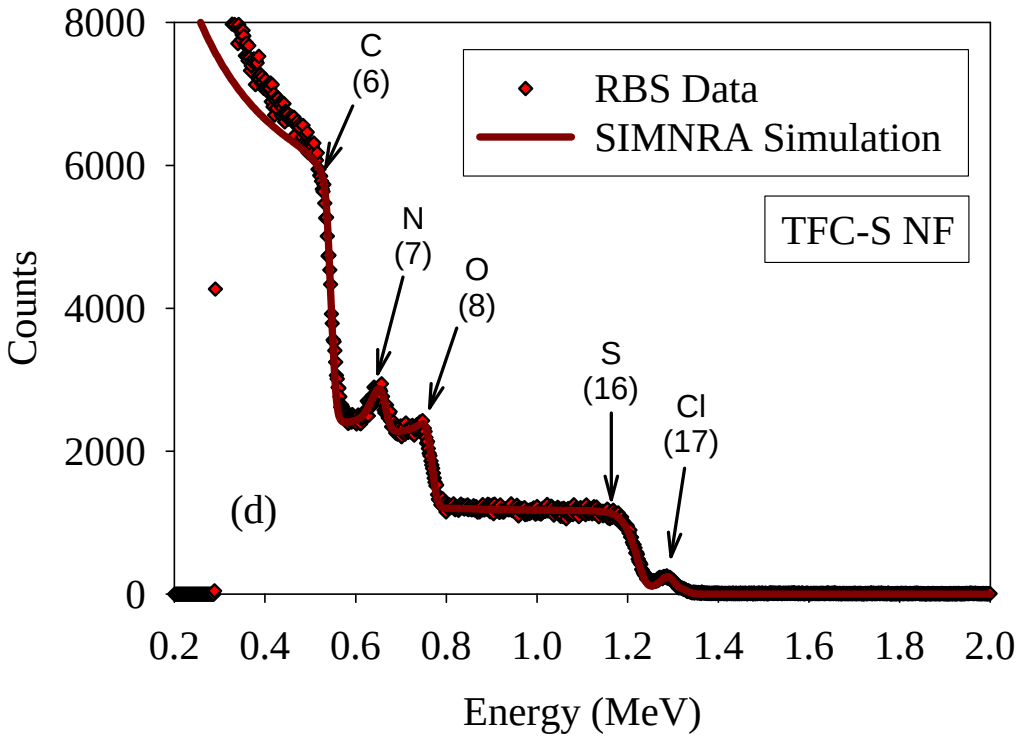


**Figure C.4c and C.4d**

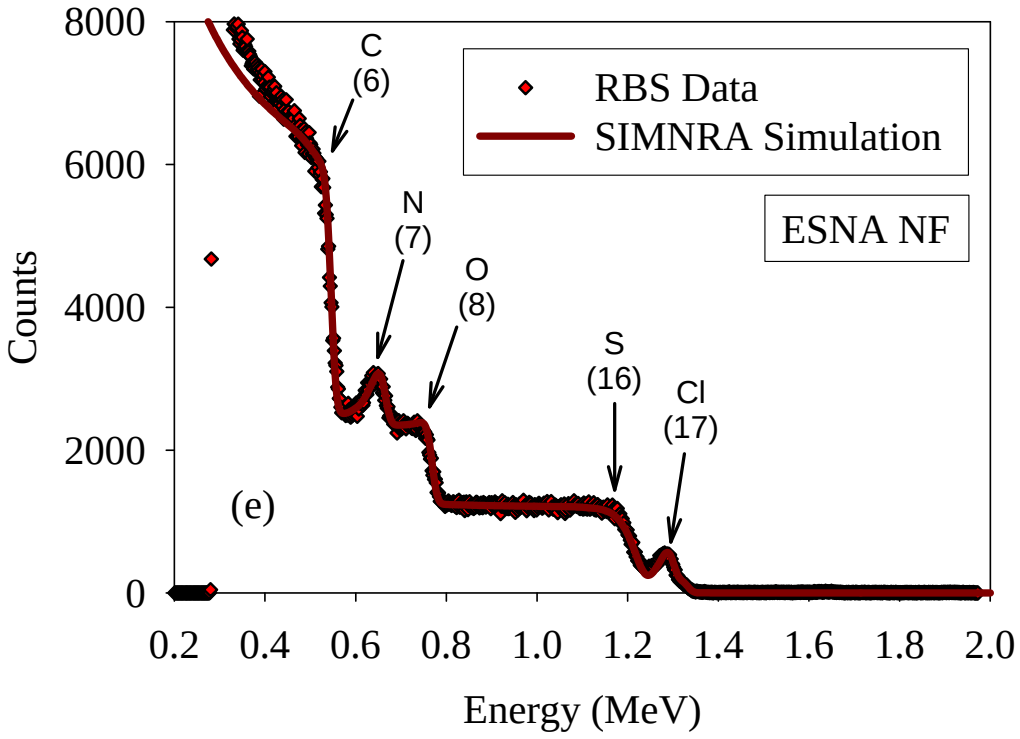


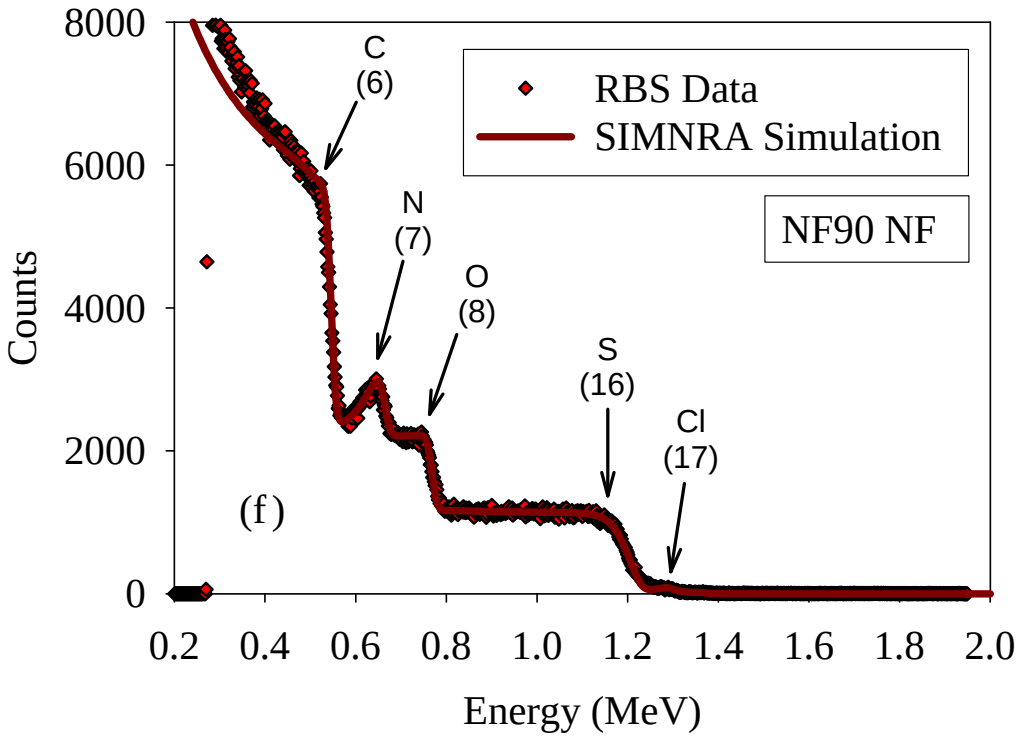


**Figure C.4e and C.4f**

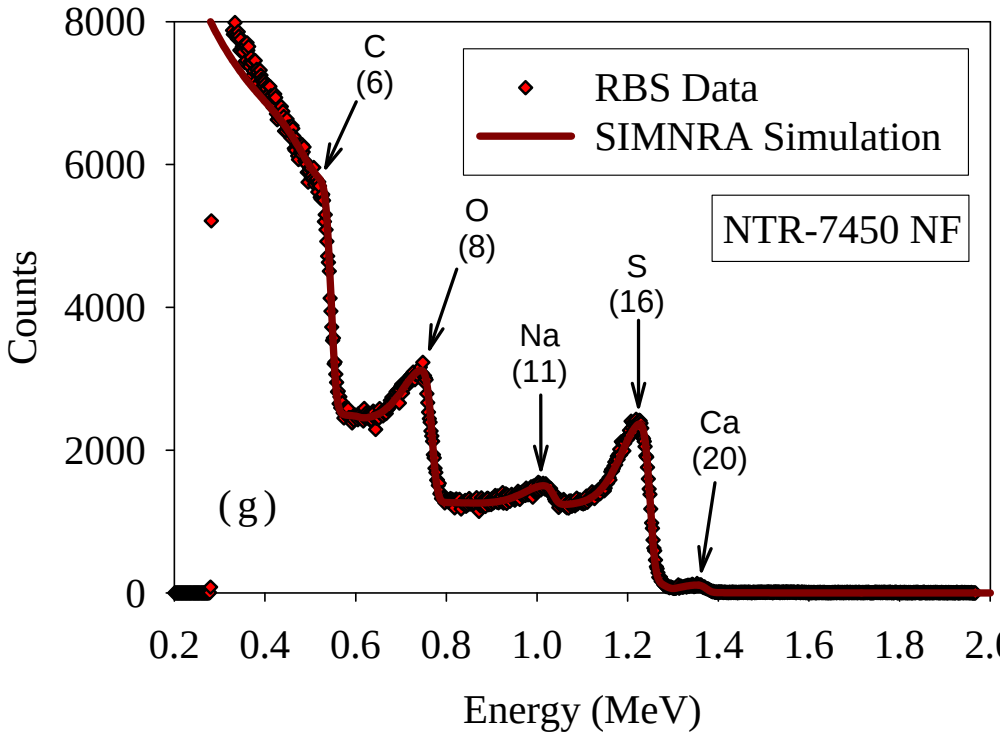


**Figure C.4.** RBS spectra and corresponding simulations for: (a) FT30 RO (see note 'a' in Table 4.1), (b) LF10 RO, (c) ESPA3 RO, (d) TFC–S NF, (e) ESNA NF, (f) NF90 NF, (g) NTR–7450 NF. Symbols represent RBS data. Lines represent the fit obtained using the software SIMNRA® [16].

**Commentary:** Because RBS spectra do not have a hydrogen signal, but are affected by the hydrogen content of the sample, fitting of the elemental compositions required the input of the H:C ratio in the active and support layers [11]. For the sulfonated polyethersulfone (SPES) active layer of NTR–7450 NF, H:C = 0.72 which is in close agreement with the theoretical H:C = 0.69 calculated from the composition of the repeating units of its polymer structure and its 1.67 M concentration of sulfonate groups (see Figure C.3 in Supporting Information). For polyamide (PA) active layers, H:C = 0.67 based on the composition of the repeating unit of fully-crosslinked, fully-aromatic PA ($C_{0.50}O_{0.08}N_{0.08}H_{0.33}$) [11]. For the polysulfone supports, H:C = 0.81 based on the theoretical composition of polysulfone ($C_{27}O_4S_1H_{22}$) [11]. (The polysulfone support of NTR–7450 NF was found to be sulfonated with 0.0125 sulfonate groups ($-SO_3^-$) per polysulfone repeating unit). While for PA membranes the sulfur signal corresponds to the sulfur present in the polysulfone supports, for NTR–7450 NF it corresponds to the sulfur in both the polysulfone support and in the SPES active layer. In most PA active layers, chlorine was also detected. The chlorine association to the PA active layers is likely covalent in nature as membrane immersion in and rinsing with 1 M NaBr [11] or 0.01 M $Na_2WO_4$ (this study) solutions did not make the chlorine peak decrease in the RBS spectra. The calcium and sodium content in NTR–7450 NF corresponds to calcium and sodium ions neutralizing the sulfonate groups in the SPES active layer.

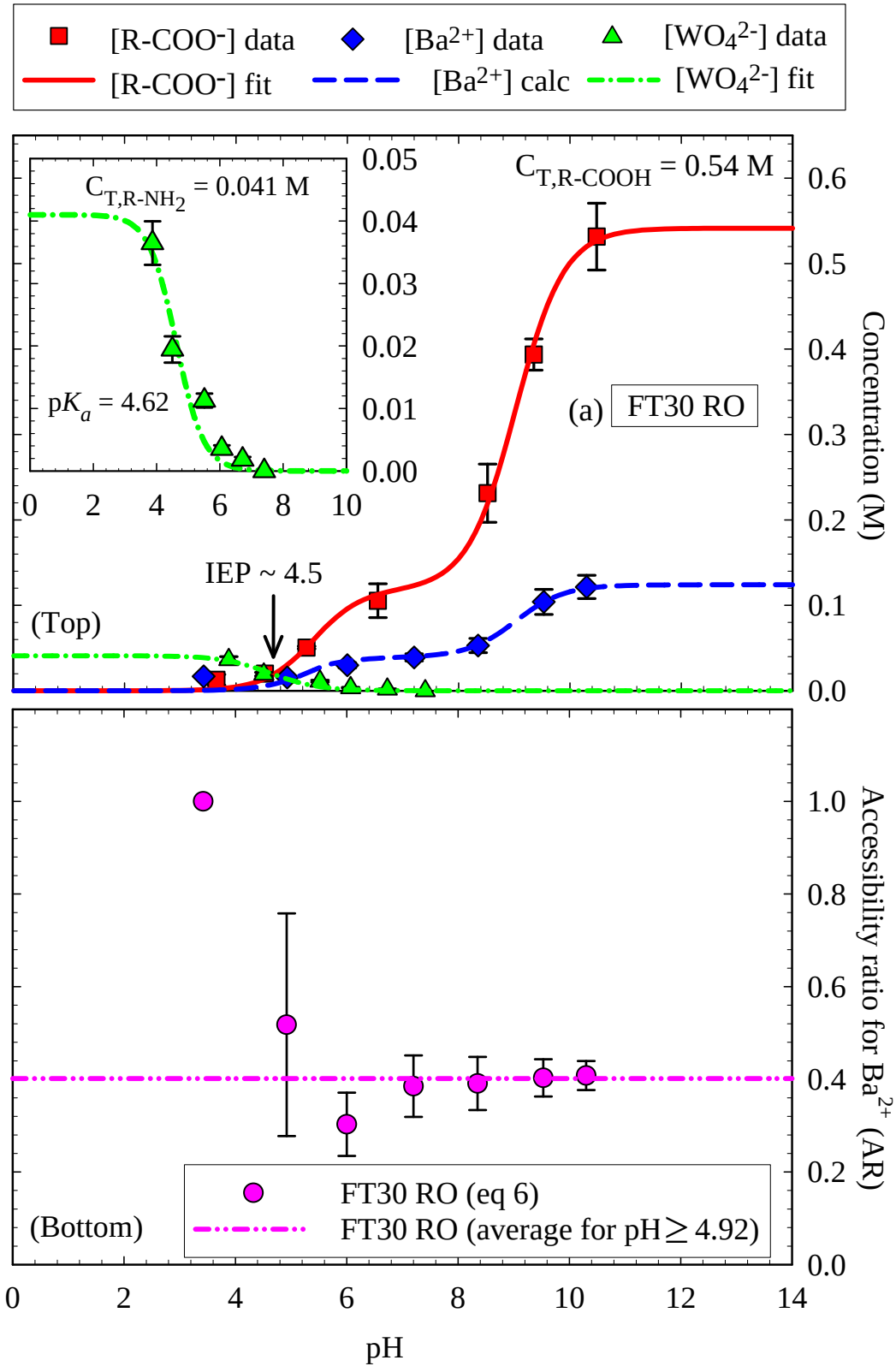
[R-COO-] data
[Ba2+] data
[WO4 2-] data
[R-COO-] fit
[Ba2+] calc
[WO4 2-] fit
C T,R-NH2 = 0.041 M
pKa = 4.62
C T,R-COOH = 0.54 M
(a) FT30 RO
IEP ~ 4.5
(Top)
Concentration (M)
(Bottom)
FT30 RO (eq 6)
FT30 RO (average for pH ≥ 4.92)
Accessibility ratio for Ba2+ (AR)
pH

**Figure C.5a**

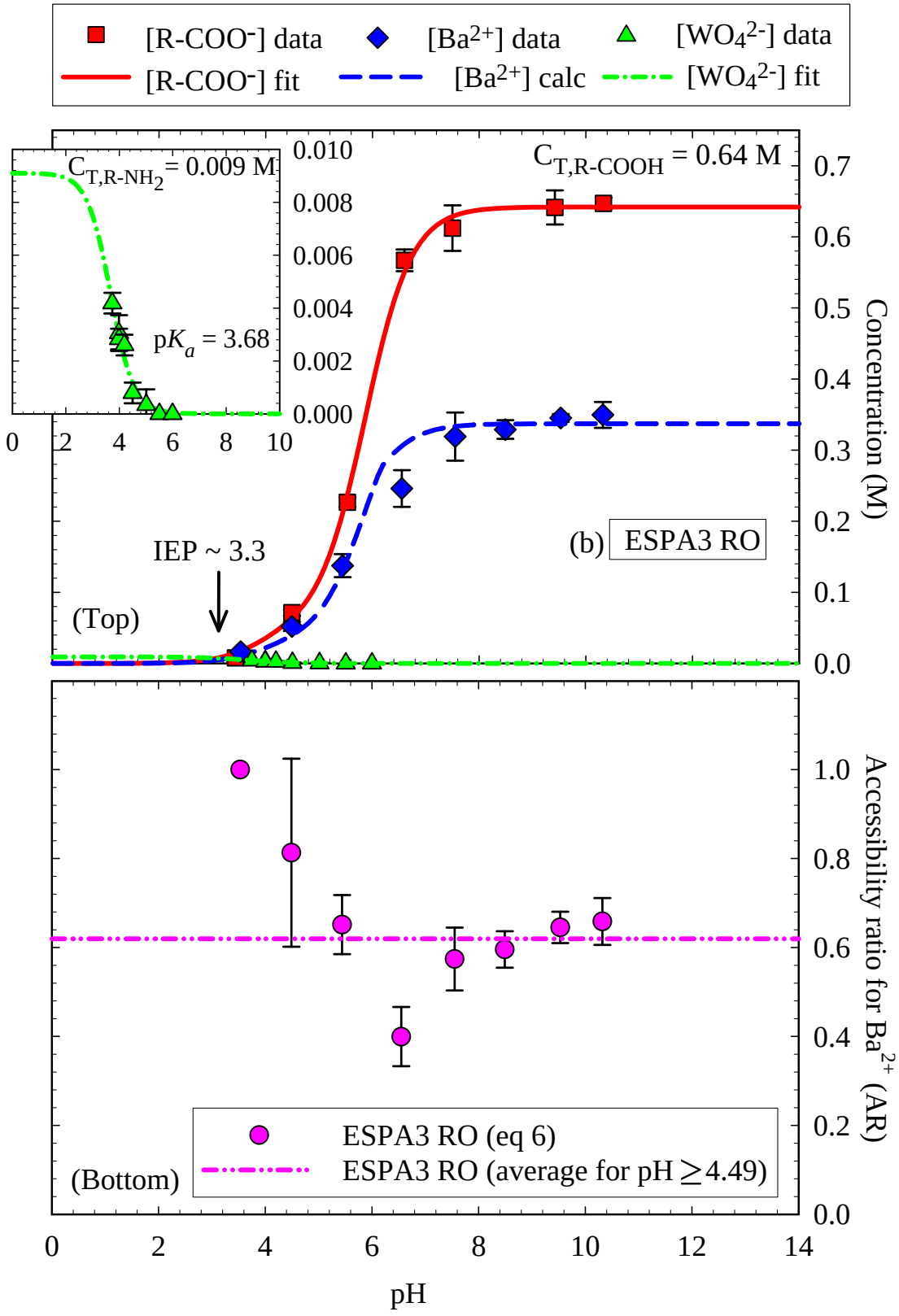
[R-COO-] data
[Ba2+] data
[WO42-] data
[R-COO-] fit
[Ba2+] calc
[WO42-] fit
CT,R-NH2 = 0.009 M
pKa = 3.68
CT,R-COOH = 0.64 M
IEP ~ 3.3
(Top)
(b) ESPA3 RO
Concentration (M)
(Bottom)
ESPA3 RO (eq 6)
ESPA3 RO (average for pH ≥4.49)
Accessibility ratio for Ba2+ (AR)
pH

**Figure C.5b**

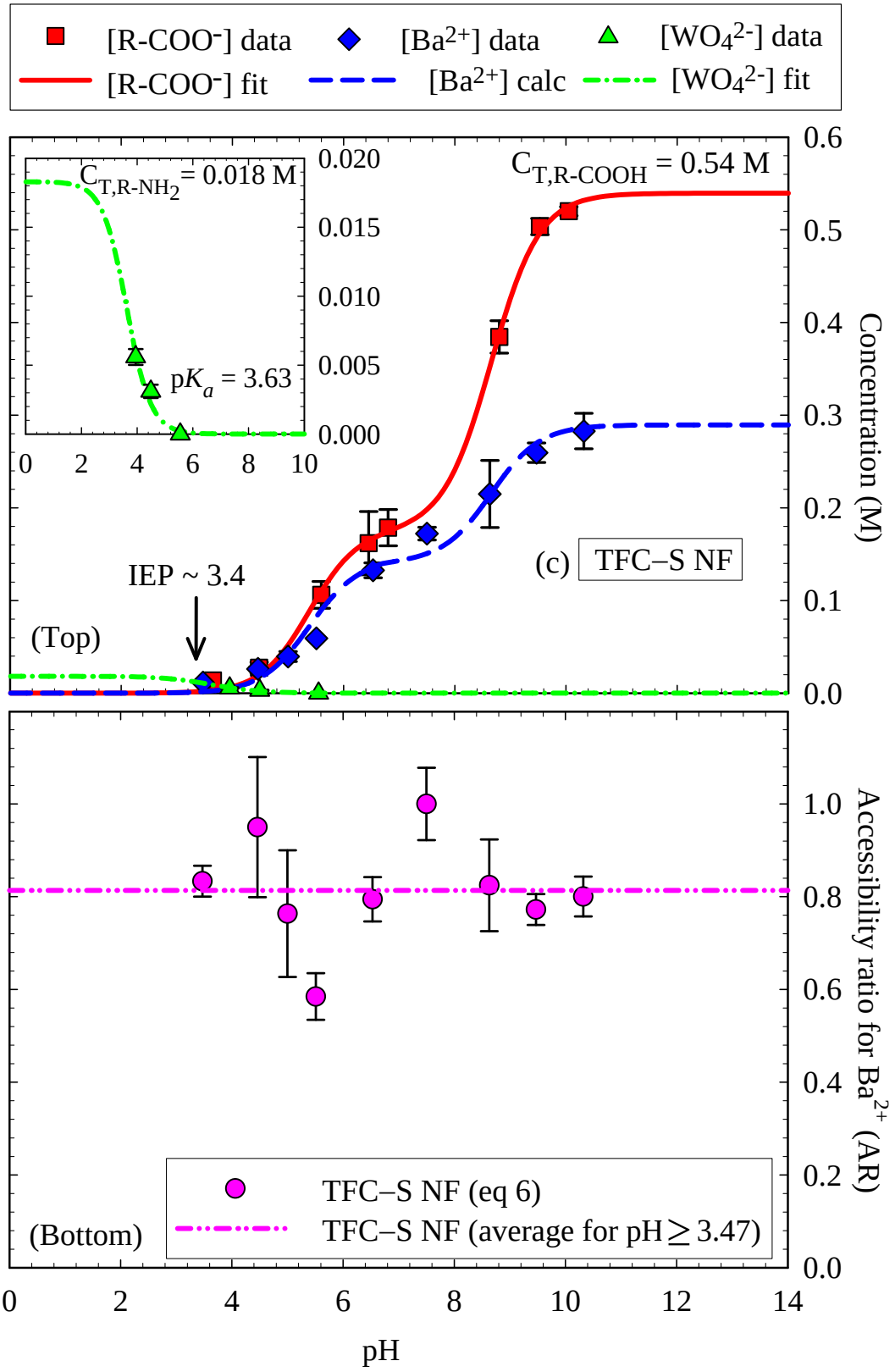
[R-COO-] data
[Ba2+] data
[WO42-] data
[R-COO-] fit
[Ba2+] calc
[WO42-] fit
CT,R-NH2 = 0.018 M
pKa = 3.63
CT,R-COOH = 0.54 M
IEP ~ 3.4
(Top)
(c) TFC–S NF
Concentration (M)
(Bottom)
TFC–S NF (eq 6)
TFC–S NF (average for pH ≥ 3.47)
Accessibility ratio for Ba2+ (AR)
pH

**Figure C.5c**

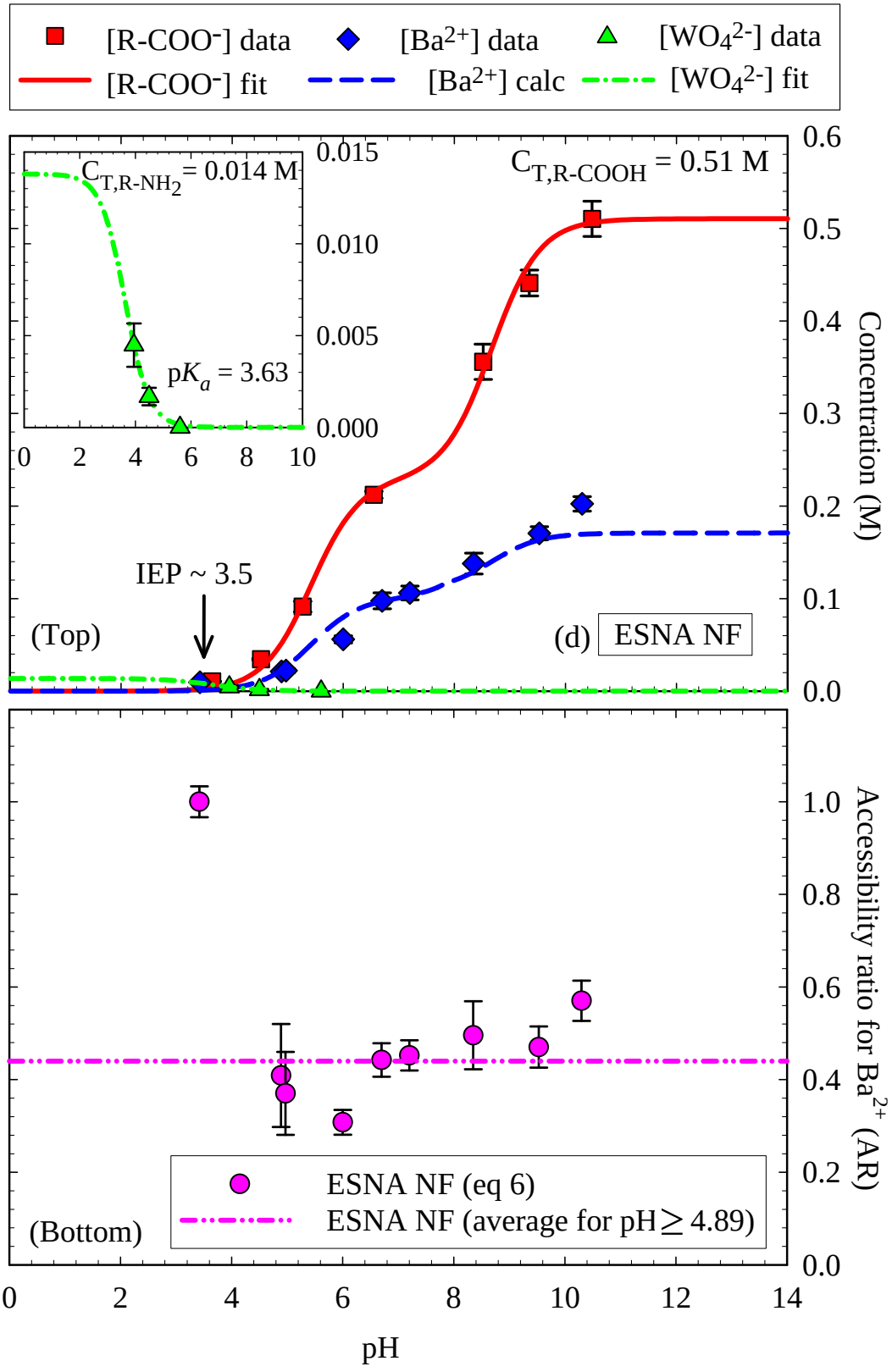
[R-COO-] data
[Ba2+] data
[WO42-] data
[R-COO-] fit
[Ba2+] calc
[WO42-] fit
CT,R-NH2 = 0.014 M
pKa = 3.63
CT,R-COOH = 0.51 M
IEP ~ 3.5
(Top)
(d) ESNA NF
Concentration (M)
(Bottom)
ESNA NF (eq 6)
ESNA NF (average for pH≥ 4.89)
Accessibility ratio for Ba2+ (AR)
pH

**Figure C.5d**

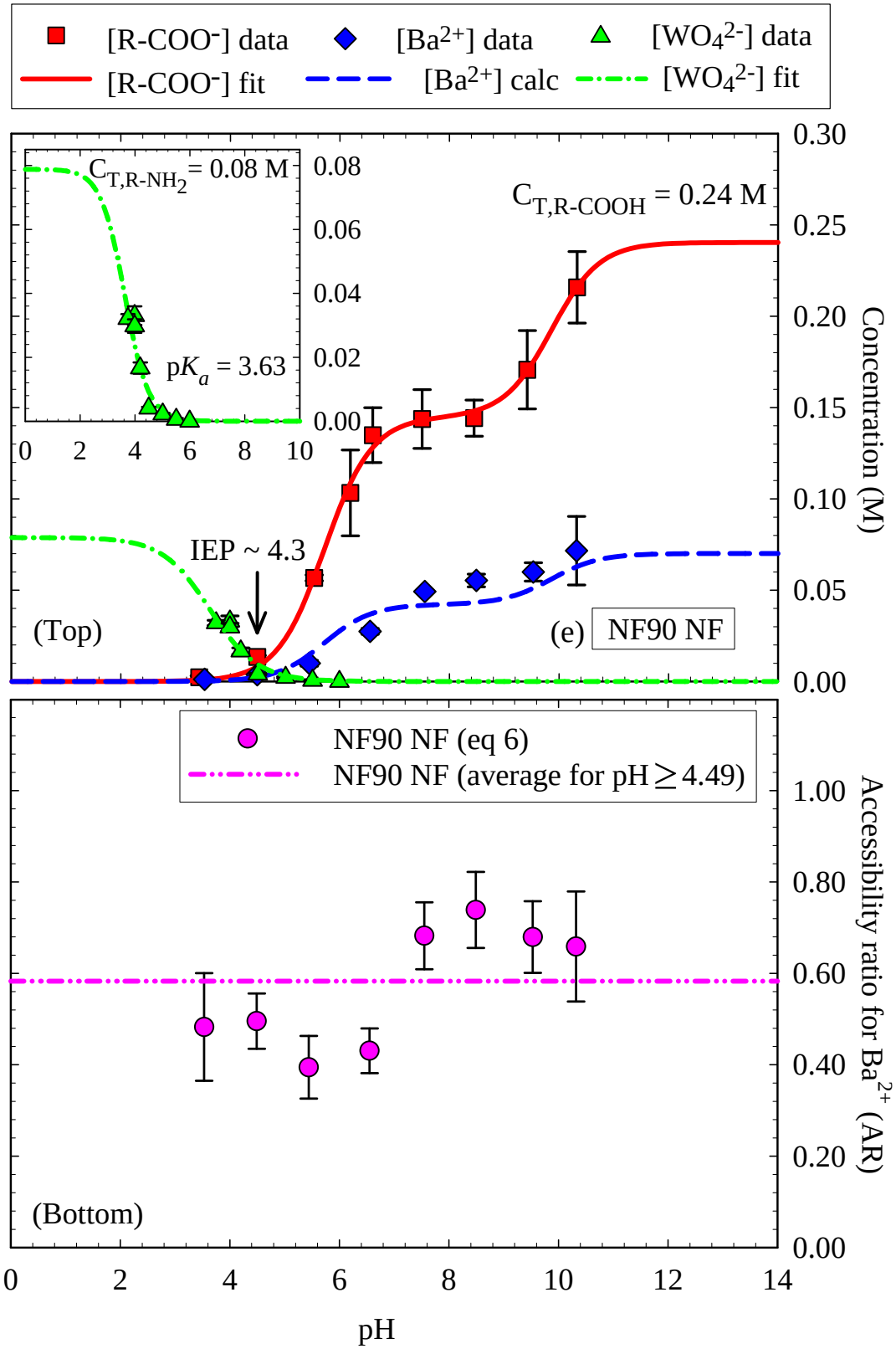
[R-COO-] data
[Ba2+] data
[WO4 2-] data
[R-COO-] fit
[Ba2+] calc
[WO4 2-] fit
CT,R-NH2 = 0.08 M
pKa = 3.63
CT,R-COOH = 0.24 M
IEP ~ 4.3
(Top)
(e) NF90 NF
Concentration (M)
NF90 NF (eq 6)
NF90 NF (average for pH ≥ 4.49)
(Bottom)
Accessibility ratio for Ba2+ (AR)
pH

**Figure C.5e**

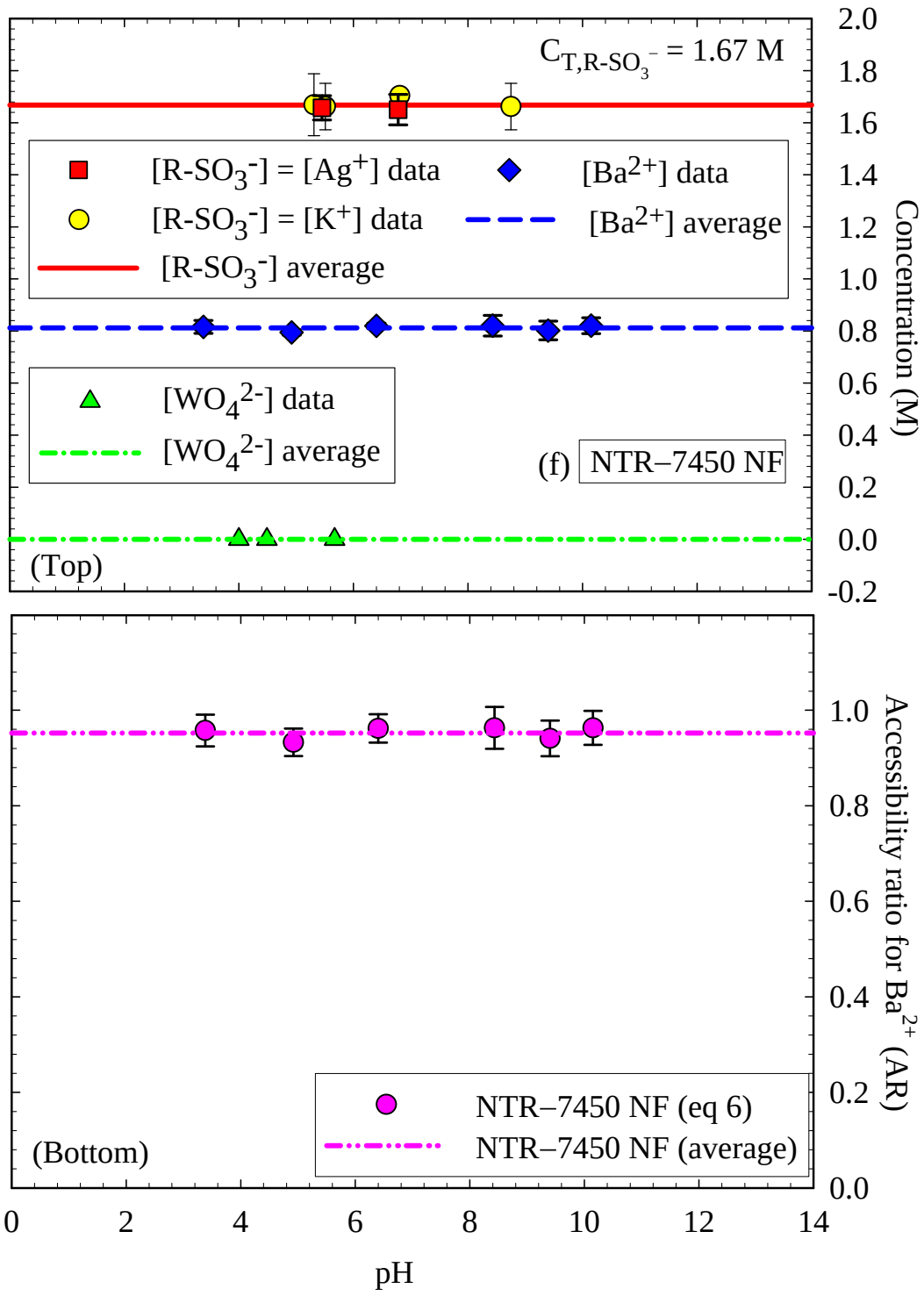


**Figure C.5.** Concentration of ionizable functional groups, concentration of $Ba^{2+}$ ion that associates with accessible R–$COO^-$ groups, and accessibility ratio for $Ba^{2+}$ ion as a function of pH in the active layers of (a) FT30 RO (see note 'a' in Table 4.1), (b) ESPA3 RO, (c) TFC–S NF, (d) ESNA NF, (e) NF90 NF, and (f) NTR–7450 NF. For membranes other than NTR–7450 NF: Top: Concentration of carboxylic ([R–$COO^-$] = [$Ag^+$]) and

amine ([R–$NH_2$] ≈ [$WO_4^{2-}$]) groups in the active layer. Also, concentration of $Ba^{2+}$ ([$Ba^{2+}$]) that associates with accessible R–$COO^-$ groups in the active layer. Symbols represent experimental data. Error bars indicate standard deviation. The (red) continuous and (green) dot-dash lines correspond to the fit lines of [R–$COO^-$] with Equation 4.1 and [$WO_4^{2-}$] with Equation 4.2, respectively. The (blue) dashed line corresponds to the calculated [$Ba^{2+}$] using Equations 4.4 and 4.5, and the *a* and AR values in Table 4.1. Bottom: Accessibility ratio for $Ba^{2+}$ ion (AR) in the active layer. Circles are the values obtained by solving Equations 4.4 and 4.5 using the [R–$COO^-$] and [$Ba^{2+}$] information in the top panel, and the *a* parameter from Table 4.1. For NF90 NF, $a = 0.00 \pm < 0.01$, and as a result the measured NN=1.98±0.20 was used for the calculations of AR. Error bars indicate standard error. The dash-dot-dot line is the average AR value in the pH range ≈5.0–10.5. For the NTR–7450 NF membrane: Top: Concentration of sulfonate groups ([R–$SO_3^-$]) in the active layer. [R–$SO_3^-$] was measured using $Ag^+$ and $K^+$ as ion probes. Also, concentration of $Ba^{2+}$ ([$Ba^{2+}$]) that associates with R–$SO_3^-$ groups in the active layer. Symbols represent experimental data. Error bars indicate standard deviation. The (red) continuous and (blue) dashed lines correspond to the average [R–$SO_3^-$] and [$Ba^{2+}$], respectively. Bottom: Accessibility ratio for $Ba^{2+}$ ion (AR) in the active layer. Circles are the values obtained by solving Equation 4.4 using the average [R–$SO_3^-$] and experimental [$Ba^{2+}$] points in the top panel, and NN = 1.96±0.05 from Table 4.1. Error bars indicate standard error. The dash-dot-dot line is the average AR value in the pH range tested.

**Appendix C.2. Re-analysis of Rutherford Backscattering Spectrometry (RBS) Data in Appendices A and B for FT30 Reverse Osmosis (RO) Membrane (See Note 'a' in Table 4.1)**

***Appendix C.2.1. Re-analysis of Rutherford Backscattering Spectrometry (RBS) Data in Appendix A.2 for FT30 Reverse Osmosis (RO) Membrane Samples Probed with Silver ($Ag^+$) Ion***

| | pH = 3.65 | | | |
|---|---|---|---|---|
| | Treatment | pH max/pH min/pH final | Elemental ratio | Concentration [M] |
| 9Ag | FT30+Ag 3.5 | 3.75/3.55/3.65 | 0.00005 | 0.00690 |
| 10Ag | | 3.75/3.55/3.65 | 0.00009 | 0.01243 |
| 11Ag | | 3.75/3.55/3.65 | 0.00014 | 0.01933 |
| | | | Average | 0.01289 |
| | | | Std deviation | 0.00623 |
| | | | (Std dev/Mean)x100 | 48.31 |

| | pH = 4.52 | | | |
|---|---|---|---|---|
| | Treatment | pH max/pH min/pH final | Elemental ratio | Concentration [M] |
| 7Ag | FT30+Ag 4.5 | 4.83/4.5/4.52 | 0.00015 | 0.02071 |
| 8Ag | | 4.83/4.5/4.52 | 0.00014 | 0.01933 |
| | | | | |
| | | | Average | 0.02002 |
| | | | Std deviation | 0.00098 |
| | | | (Std dev/Mean)x100 | 4.88 |

| | pH = 5.27 | | | |
|---|---|---|---|---|
| | Treatment | pH max/pH min/pH final | Elemental ratio | Concentration [M] |
| 1Ag | FT30+Ag 5.5 | 5.43/5.27/5.27 | 0.00036 | 0.04971 |
| 2Ag | | 5.43/5.27/5.27 | 0.00038 | 0.05247 |
| 3Ag | | 5.43/5.27/5.27 | 0.00036 | 0.04971 |
| | | | Average | 0.05063 |
| | | | Std deviation | 0.00159 |
| | | | (Std dev/Mean)x100 | 3.15 |

| | pH = 6.55 | | | |
|---|---|---|---|---|
| | Treatment | pH max/pH min/pH final | Elemental ratio | Concentration [M] |
| 4Ag | FT30+Ag 6.5 | 6.8/6.55/6.55 | 0.00060 | 0.08285 |
| 5Ag | | 6.8/6.55/6.55 | 0.00082 | 0.11323 |
| 6Ag | | 6.8/6.55/6.55 | 0.00087 | 0.12013 |
| | | | Average | 0.10540 |
| | | | Std deviation | 0.01983 |
| | | | (Std dev/Mean)x100 | 18.82 |

| | pH = 8.52 | | | |
|---|---|---|---|---|
| | Treatment | pH max/pH min/pH final | Elemental ratio | Concentration [M] |
| 12Ag | FT30+Ag 8.5 | 8.56/8.40/8.52 | 0.00185 | 0.25545 |
| 13Ag | | 8.56/8.40/8.52 | 0.00150 | 0.20712 |
| | | | | |
| | | | Average | 0.23128 |
| | | | Std deviation | 0.03417 |
| | | | (Std dev/Mean)x100 | 14.78 |

| | pH = 9.35 | | | |
|---|---|---|---|---|
| | Treatment | pH max/pH min/pH final | Elemental ratio | Concentration [M] |
| 16Ag | FT30+Ag 9.5 | 9.35/9.31/9.35 | 0.00290 | 0.40043 |
| 17Ag | | 9.35/9.31/9.35 | 0.00295 | 0.40734 |
| 18Ag | | 9.35/9.31/9.35 | 0.00270 | 0.37282 |
| | | | Average | 0.39353 |
| | | | Std deviation | 0.01827 |
| | | | (Std dev/Mean)x100 | 4.64 |

| | pH = 10.48 | | | |
|---|---|---|---|---|
| | Treatment | pH max/pH min/pH final | Elemental ratio | Concentration [M] |
| 14Ag | FT30+Ag 10.5 | 10.6/10.48/10.48 | 0.00365 | 0.50399 |
| 15Ag | | 10.6/10.48/10.48 | 0.00405 | 0.55922 |
| | | | | |
| | | | Average | 0.53161 |
| | | | Std deviation | 0.03905 |
| | | | (Std dev/Mean)x100 | 7.35 |

**1Ag**

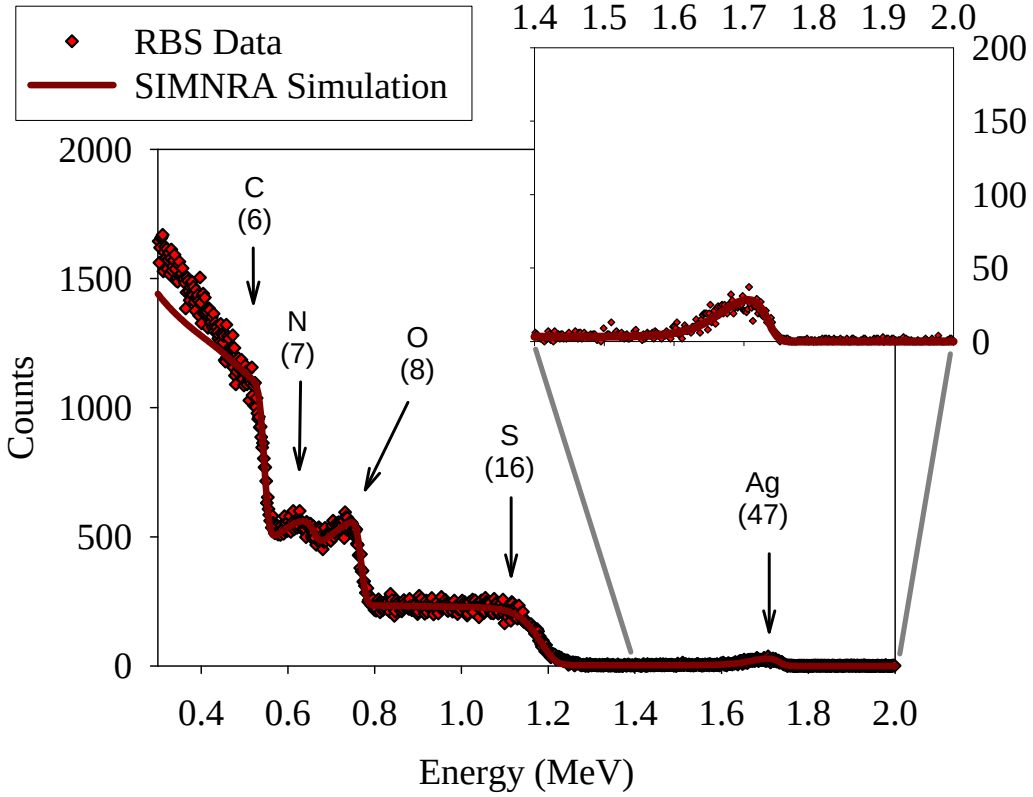
RBS Data
SIMNRA Simulation
Counts
Energy (MeV)
C (6)
N (7)
O (8)
S (16)
Ag (47)

**2Ag**

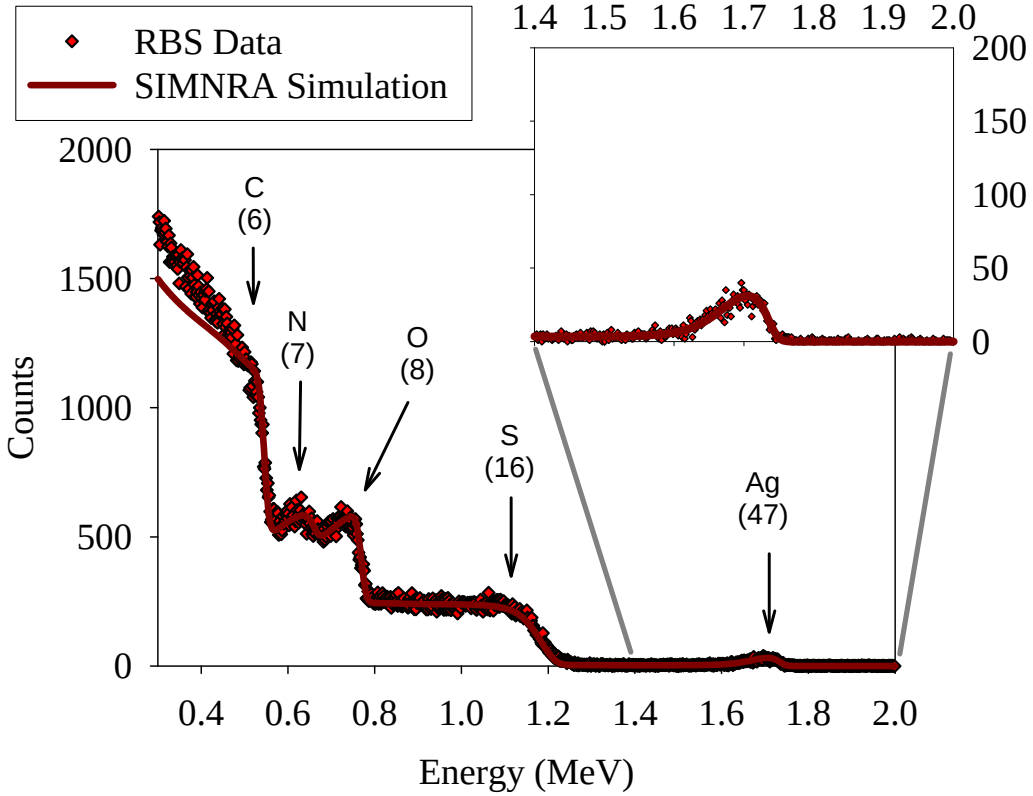
RBS Data
SIMNRA Simulation
Counts
Energy (MeV)
C (6)
N (7)
O (8)
S (16)
Ag (47)

**3Ag**

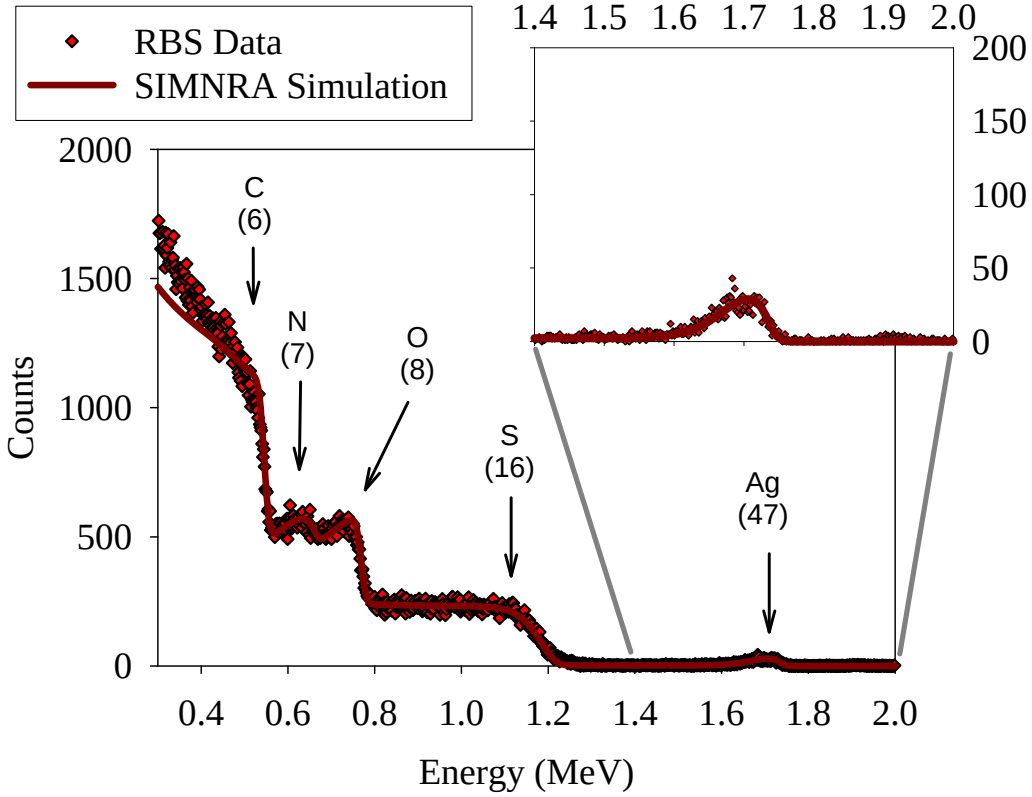
RBS Data
SIMNRA Simulation
Counts
Energy (MeV)
C (6)
N (7)
O (8)
S (16)
Ag (47)

**4Ag**

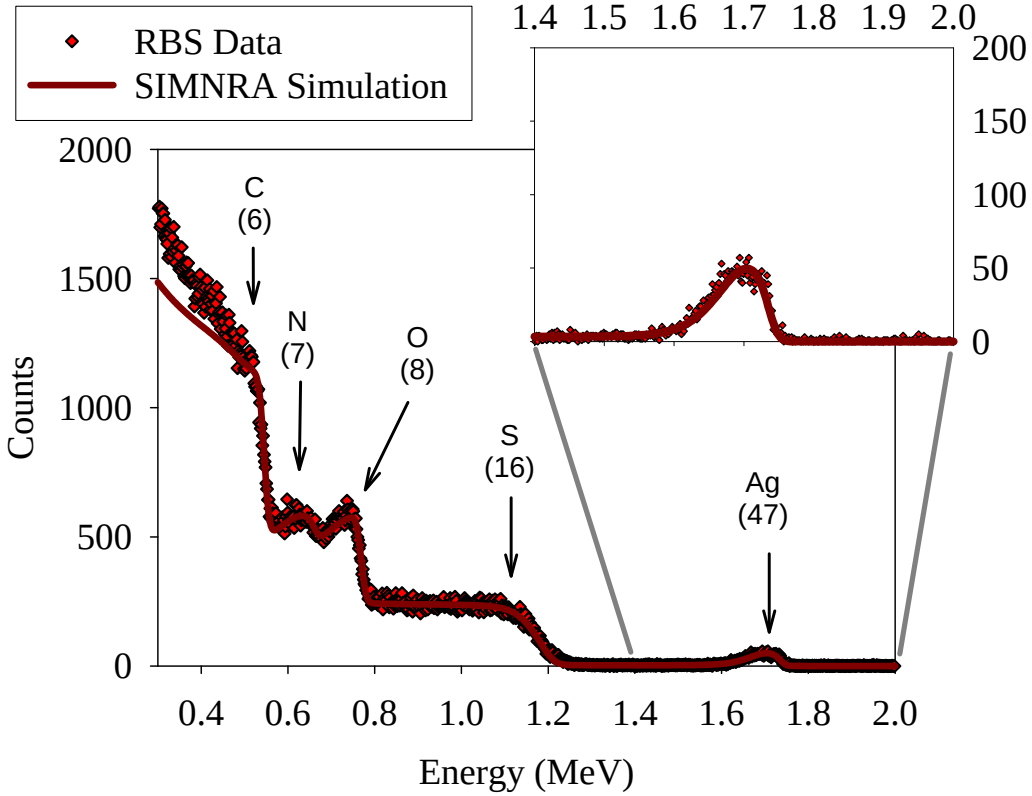
RBS Data
SIMNRA Simulation
Counts
Energy (MeV)
C (6)
N (7)
O (8)
S (16)
Ag (47)

**5Ag**

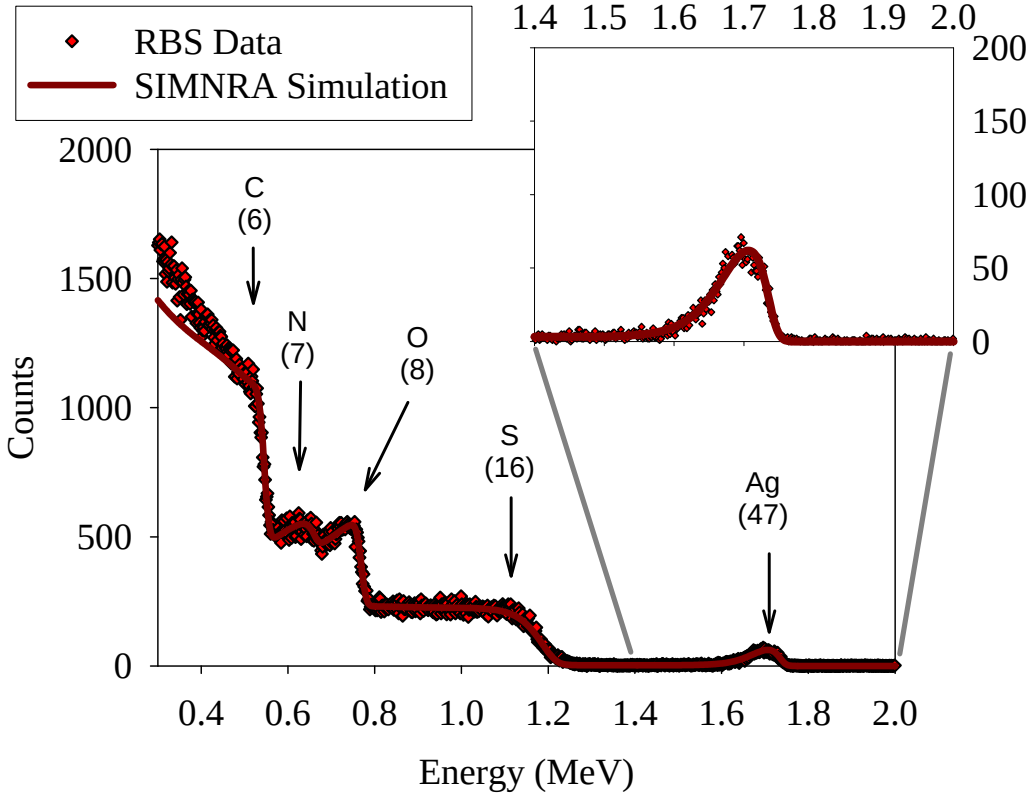
RBS Data
SIMNRA Simulation
Counts
Energy (MeV)
C (6)
N (7)
O (8)
S (16)
Ag (47)

**6Ag**

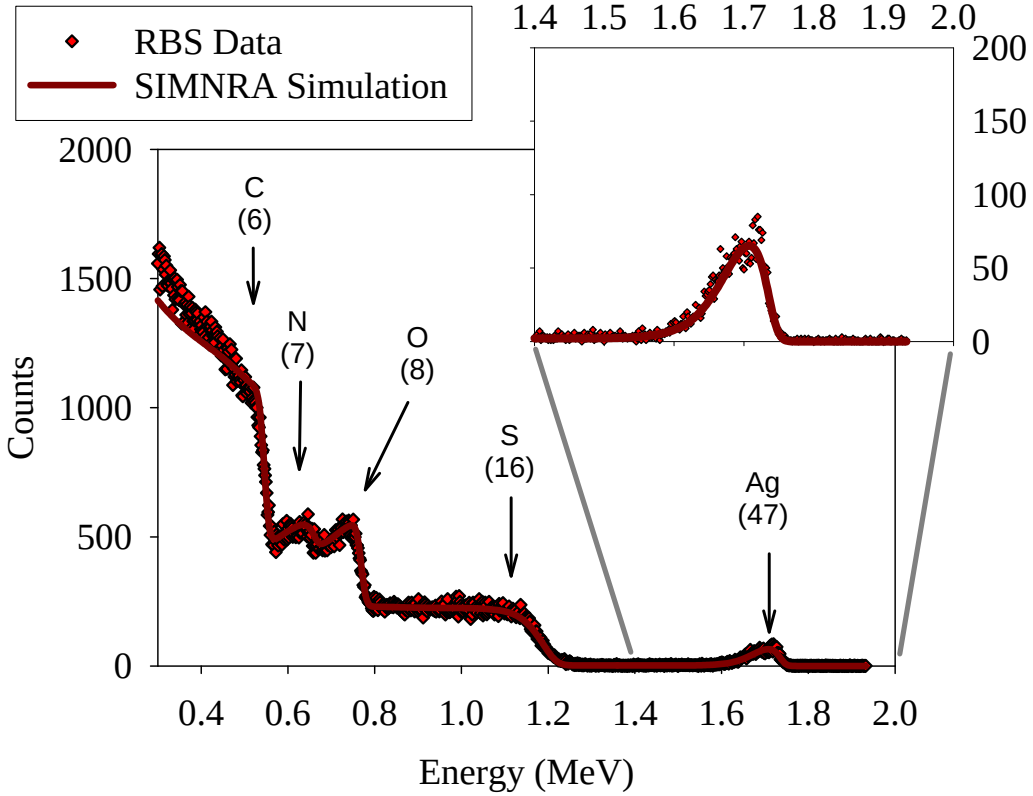
RBS Data
SIMNRA Simulation
Counts
Energy (MeV)
C (6)
N (7)
O (8)
S (16)
Ag (47)

**7Ag**

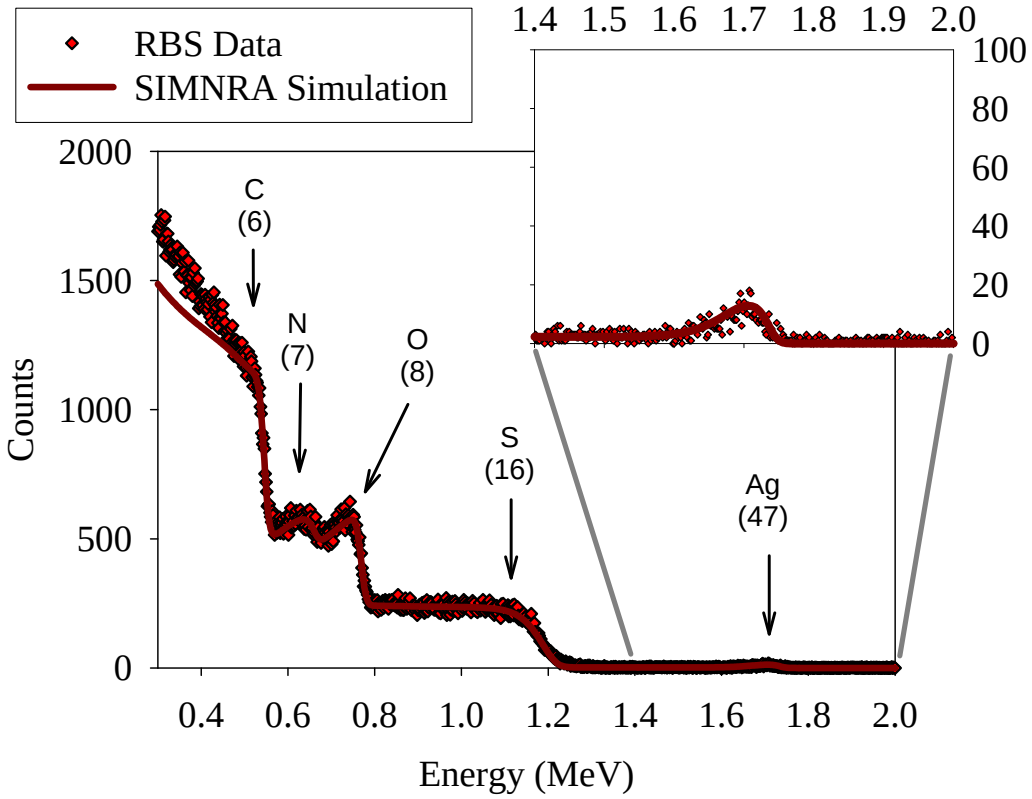
RBS Data
SIMNRA Simulation
Counts
Energy (MeV)
C (6)
N (7)
O (8)
S (16)
Ag (47)

**8Ag**

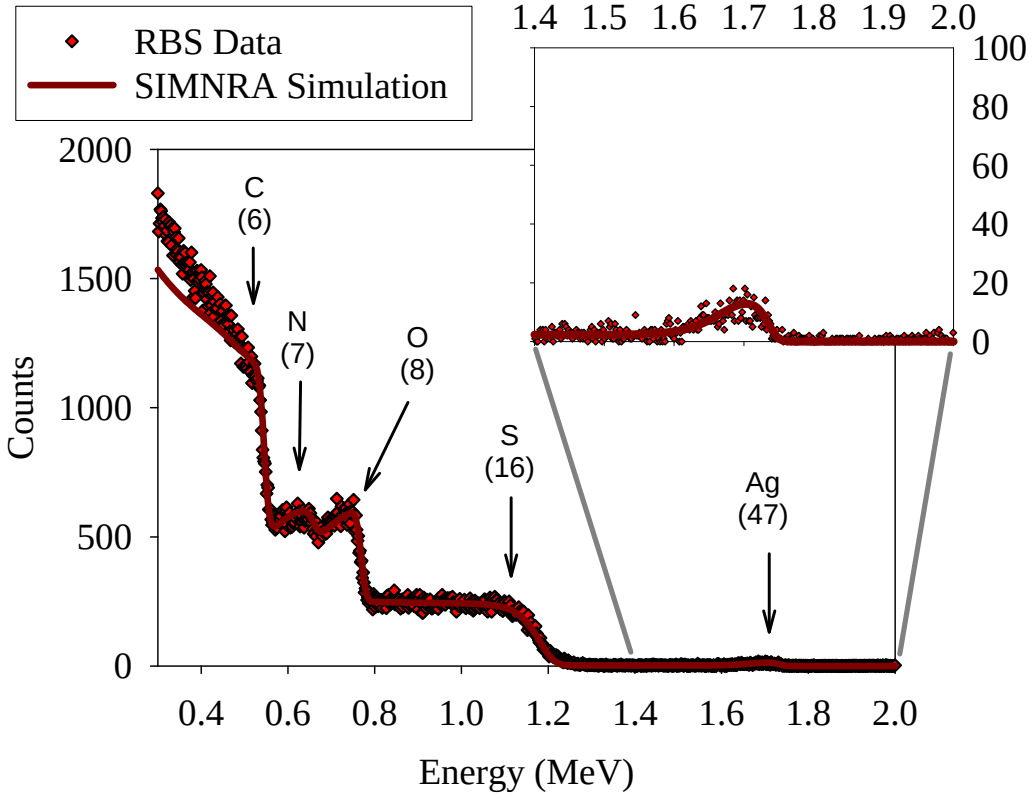
RBS Data
SIMNRA Simulation
Counts
Energy (MeV)
C (6)
N (7)
O (8)
S (16)
Ag (47)

**9Ag**

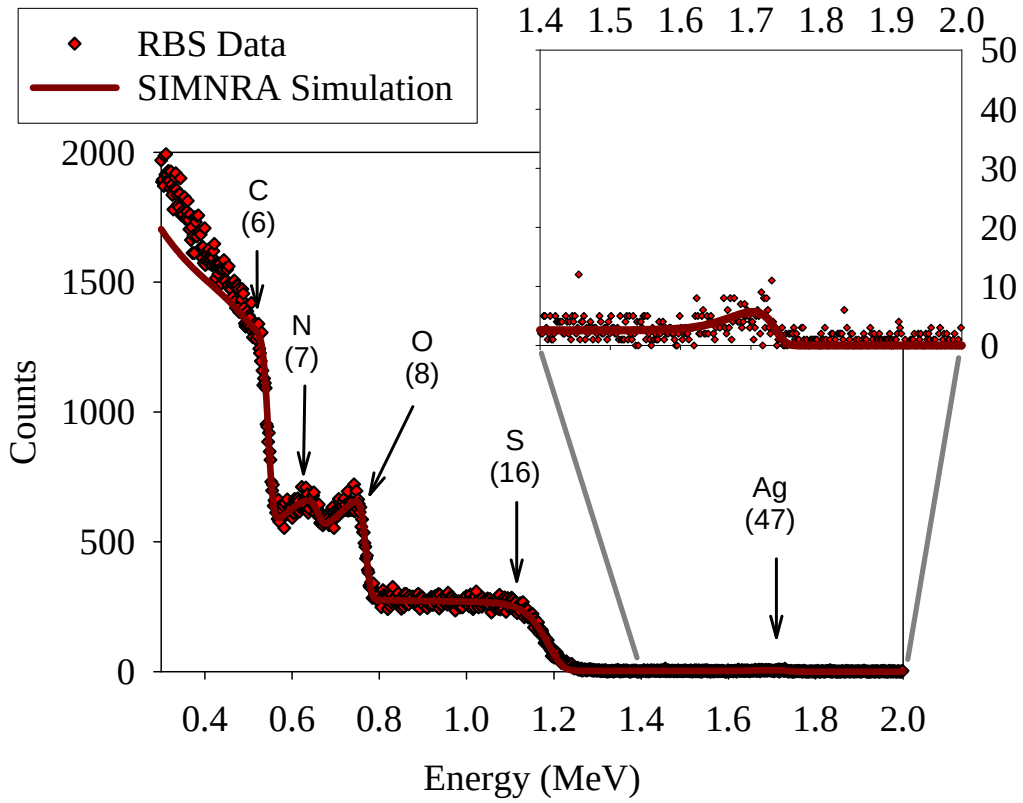
RBS Data
SIMNRA Simulation
Counts
Energy (MeV)
C (6)
N (7)
O (8)
S (16)
Ag (47)

**10Ag**

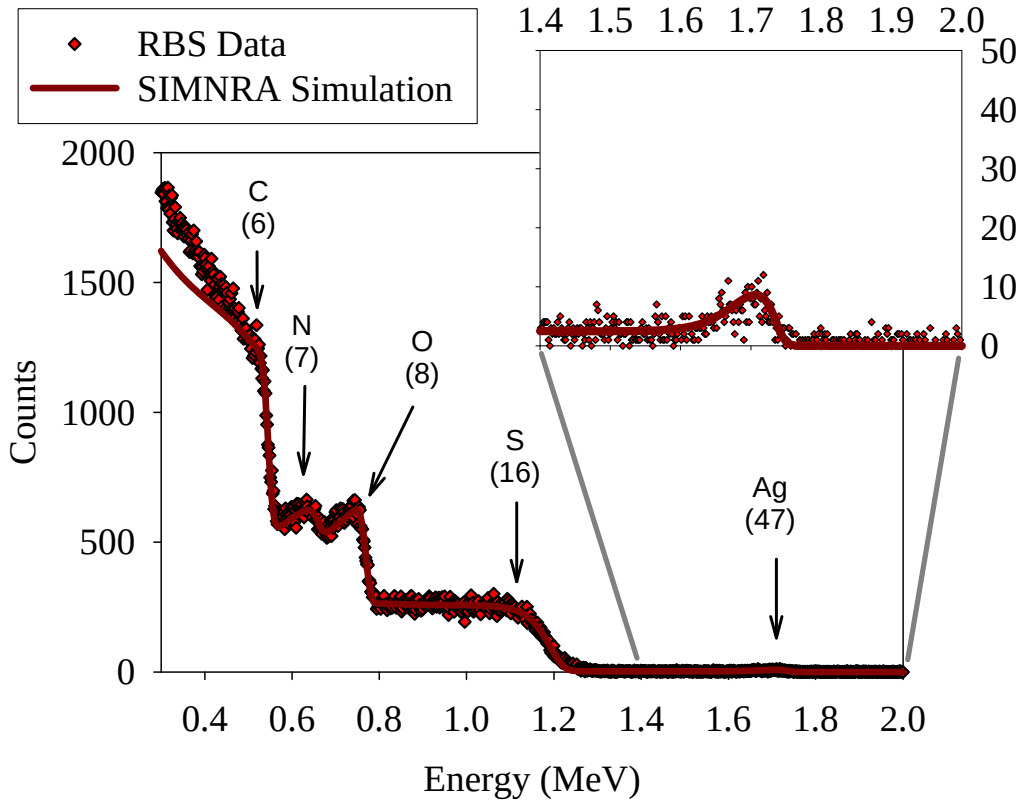
RBS Data
SIMNRA Simulation
Counts
Energy (MeV)
C (6)
N (7)
O (8)
S (16)
Ag (47)

**11Ag**

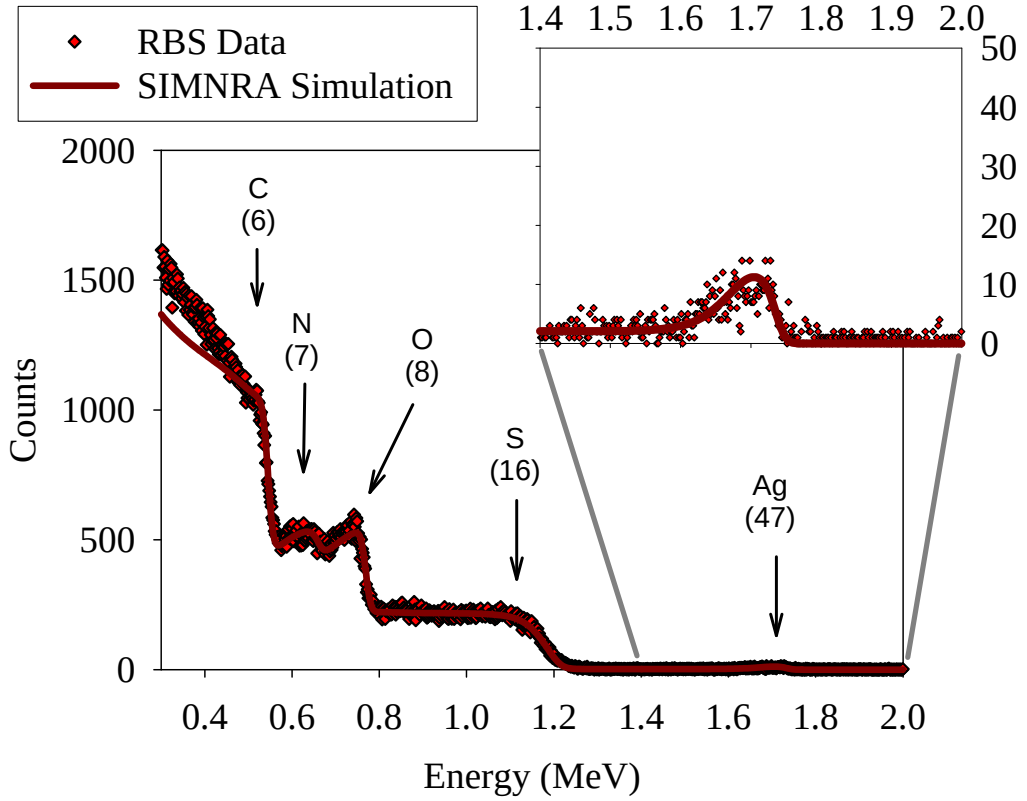
RBS Data
SIMNRA Simulation
Counts
Energy (MeV)
C (6)
N (7)
O (8)
S (16)
Ag (47)

**12Ag**

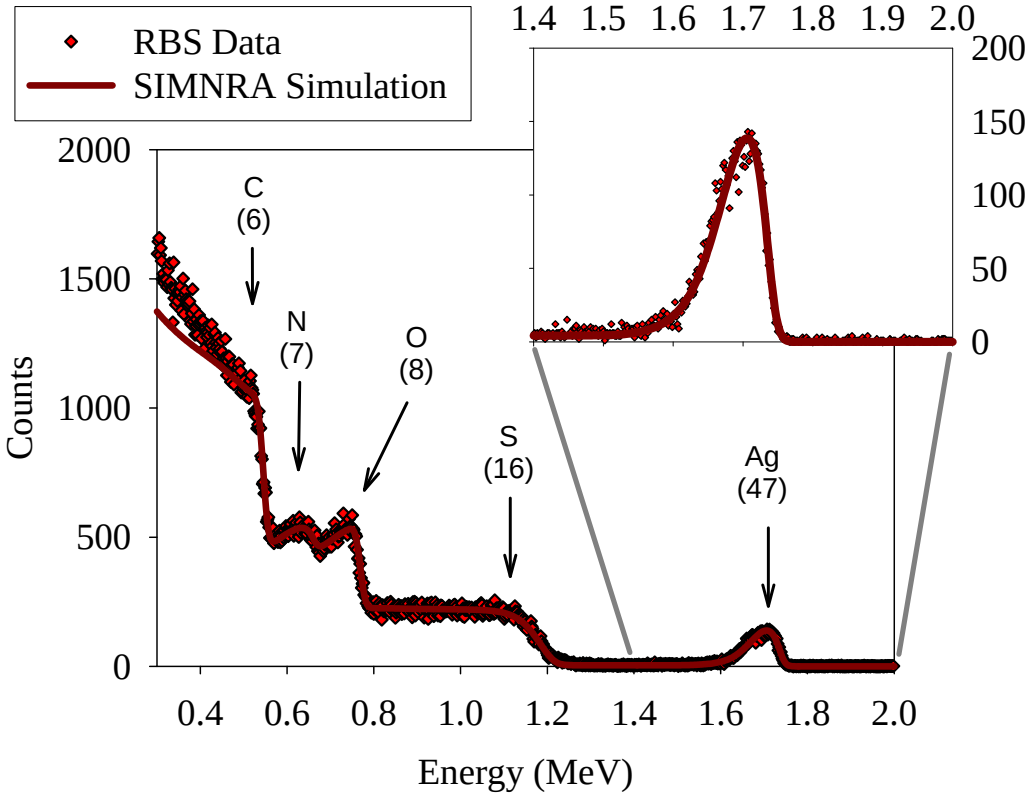
RBS Data
SIMNRA Simulation
Counts
Energy (MeV)
C (6)
N (7)
O (8)
S (16)
Ag (47)

**13Ag**

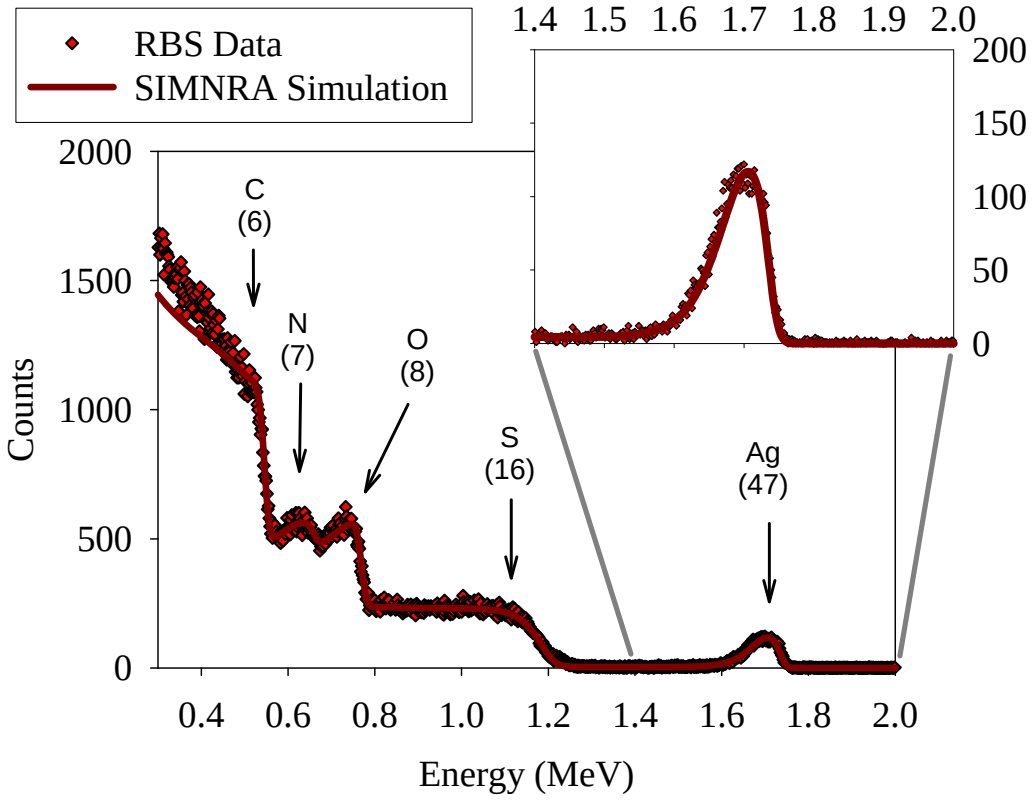
RBS Data
SIMNRA Simulation
Counts
Energy (MeV)
C (6)
N (7)
O (8)
S (16)
Ag (47)

**14Ag**

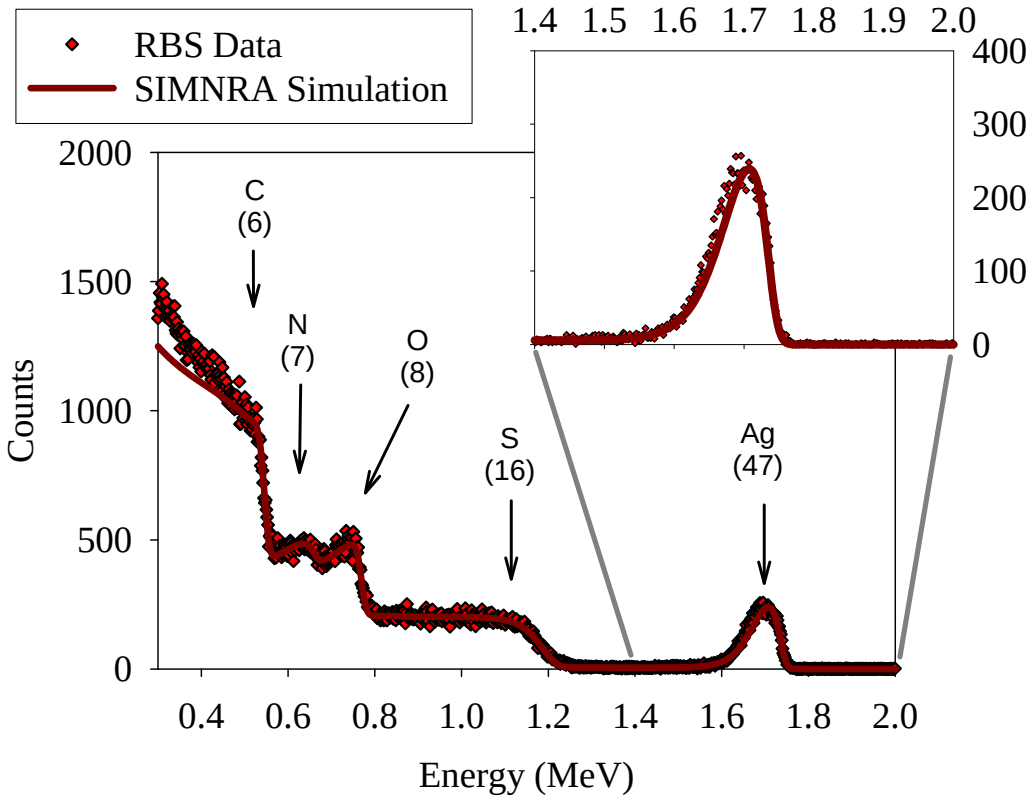
RBS Data
SIMNRA Simulation
Counts
Energy (MeV)
C (6)
N (7)
O (8)
S (16)
Ag (47)

**15Ag**

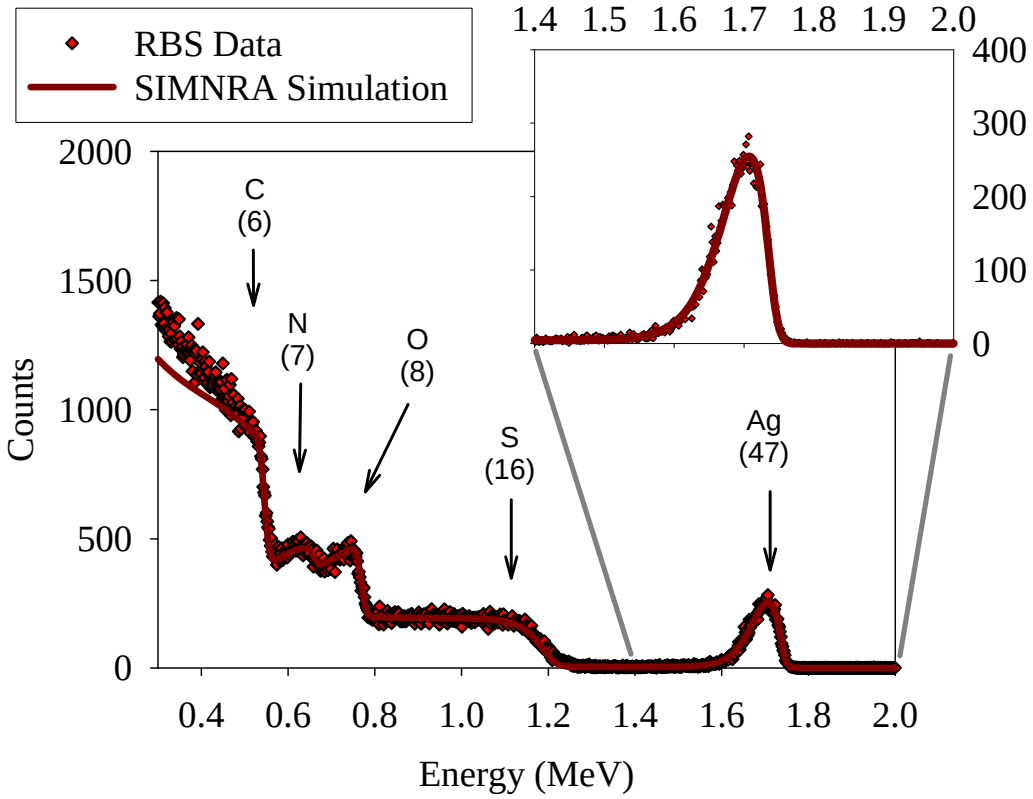
RBS Data
SIMNRA Simulation
Counts
Energy (MeV)
C (6)
N (7)
O (8)
S (16)
Ag (47)

**16Ag**

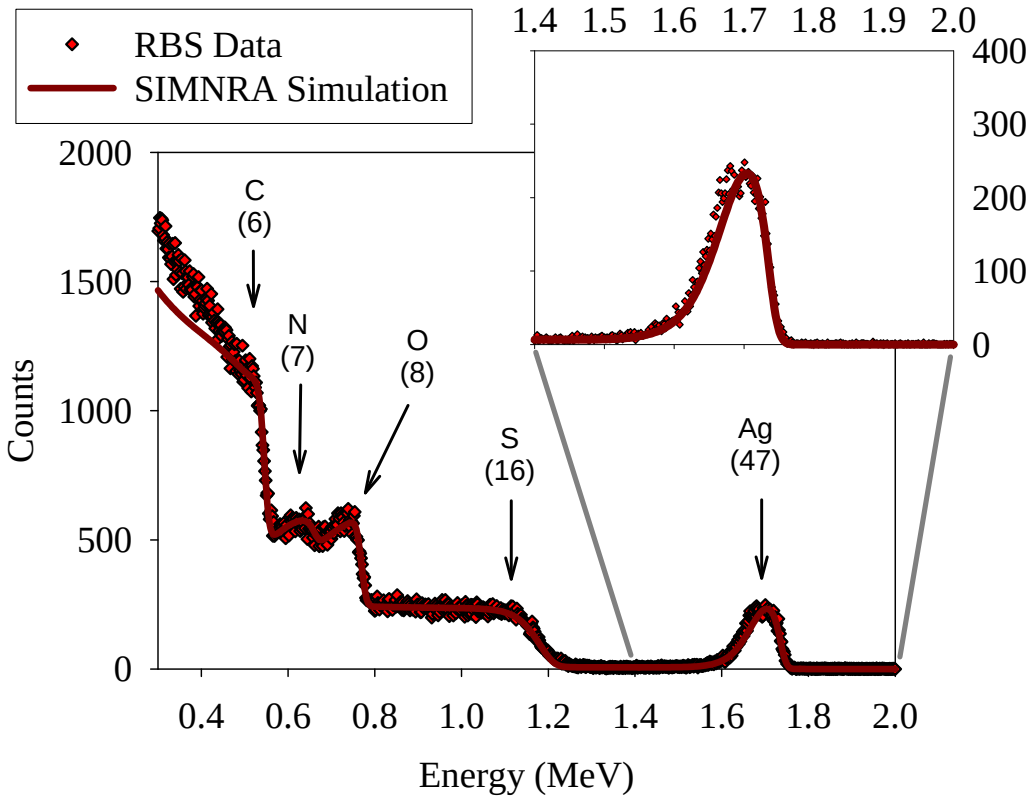
RBS Data
SIMNRA Simulation
Counts
Energy (MeV)
C (6)
N (7)
O (8)
S (16)
Ag (47)

**17Ag**

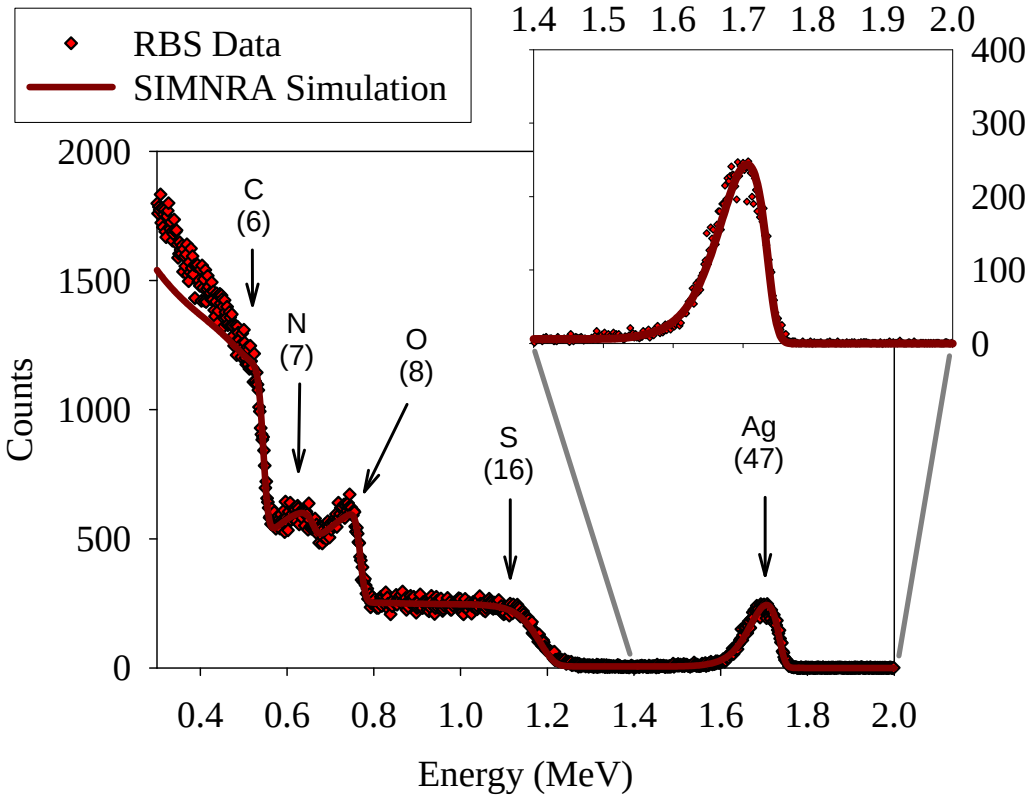
RBS Data
SIMNRA Simulation
Counts
Energy (MeV)
C (6)
N (7)
O (8)
S (16)
Ag (47)
2000
1500
1000
500
0
0.4
0.6
0.8
1.0
1.2
1.4
1.6
1.8
2.0
400
300
200
100
0

**18Ag**

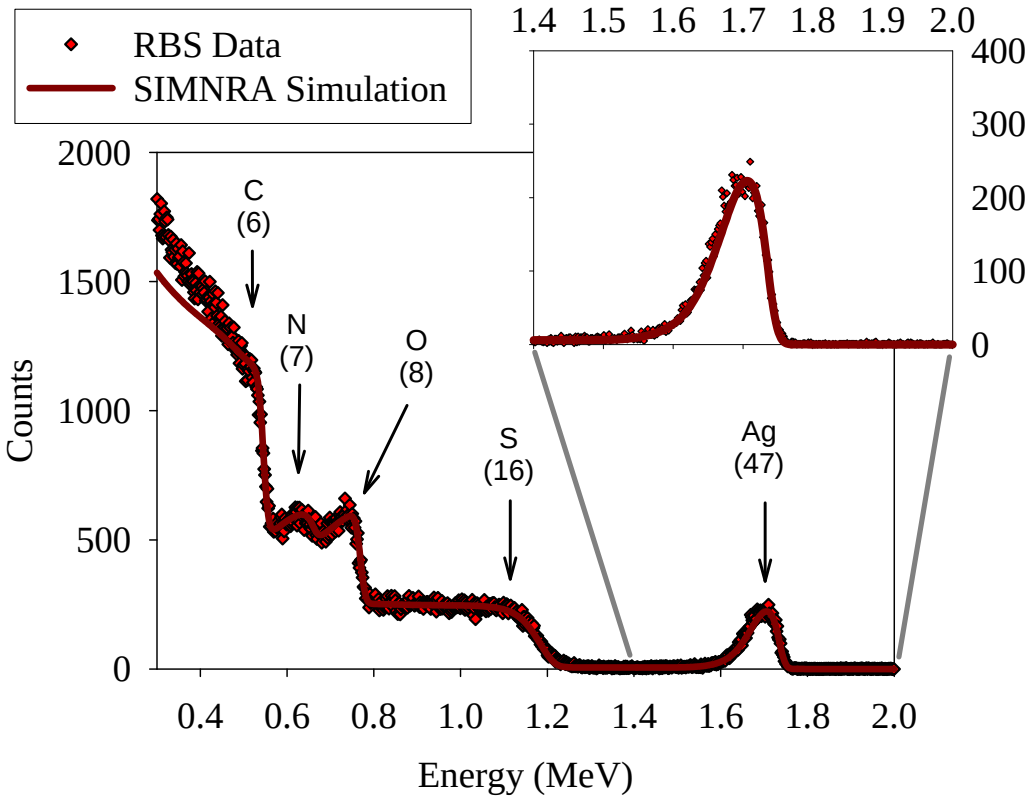
RBS Data
SIMNRA Simulation
Counts
Energy (MeV)
C (6)
N (7)
O (8)
S (16)
Ag (47)
2000
1500
1000
500
0
0.4
0.6
0.8
1.0
1.2
1.4
1.6
1.8
2.0
400
300
200
100
0

***Appendix C.2.2. Re-analysis of Rutherford Backscattering Spectrometry (RBS) Data in Appendix A.3 for FT30 Reverse Osmosis (RO) Membrane Samples Probed with Tungstate ($WO_4^{2-}$) Ion***

| | pH = 3.87 | | | |
|---|---|---|---|---|
| | Treatment | pH max/pH min/pH final | Elemental ratio | Concentration [M] |
| 16W | FT30+W 3.5 | 4.06/3.89/3.87 | 0.00024 | 0.03279 |
| 17W | | 4.06/3.89/3.87 | 0.00029 | 0.03970 |
| 18W | | 4.06/3.89/3.87 | 0.00027 | 0.03694 |
| | | | Average | 0.03648 |
| | | | Std deviation | 0.00347 |
| | | | (Std dev/Mean)x100 | 9.53 |

| | pH = 4.50 | | | |
|---|---|---|---|---|
| | Treatment | pH max/pH min/pH final | Elemental ratio | Concentration [M] |
| 4W | FT30+W 4.5 | 4.62/4.48/4.50 | 0.00016 | 0.02175 |
| 5W | | 4.62/4.48/4.50 | 0.00014 | 0.01899 |
| 6W | | 4.62/4.48/4.50 | 0.00013 | 0.01761 |
| | | | Average | 0.01945 |
| | | | Std deviation | 0.00211 |
| | | | (Std dev/Mean)x100 | 10.85 |

| | pH = 5.51 | | | |
|---|---|---|---|---|
| | Treatment | pH max/pH min/pH final | Elemental ratio | Concentration [M] |
| 1W | FT30+W 5.5 | 5.65/5.62/5.65 | 0.000073 | 0.01001 |
| 2W | | 5.65/5.62/5.65 | 0.000085 | 0.01174 |
| 3W | | 5.65/5.51/5.51 | 0.000088 | 0.01208 |
| | | | Average | 0.01128 |
| | | | Std deviation | 0.00111 |
| | | | (Std dev/Mean)x100 | 9.84 |

| | pH = 6.06 | | | |
|---|---|---|---|---|
| | Treatment | pH max/pH min/pH final | Elemental ratio | Concentration [M] |
| 13W | FT30+W 6.0 | 6.25/6.04/6.06 | 0.000023 | 0.00311 |
| 14W | | 6.25/6.04/6.06 | 0.000030 | 0.00414 |
| 15W | | 6.25/6.04/6.06 | 0.000025 | 0.00345 |
| | | | Average | 0.00357 |
| | | | Std deviation | 0.00053 |
| | | | (Std dev/Mean)x100 | 14.78 |

| | pH = 6.72 | | | |
|---|---|---|---|---|
| | Treatment | pH max/pH min/pH final | Elemental ratio | Concentration [M] |
| 7W | FT30+W 6.5 | 6.73/6.61/6.72 | 0.000015 | 0.00207 |
| 8W | | 6.73/6.61/6.72 | 0.000015 | 0.00207 |
| 9W | | 6.73/6.61/6.72 | 0.000010 | 0.00138 |
| | | | Average | 0.00184 |
| | | | Std deviation | 0.00040 |
| | | | (Std dev/Mean)x100 | 21.65 |

| | pH = 7.40 | | | |
|---|---|---|---|---|
| | Treatment | pH max/pH min/pH final | Elemental ratio | Concentration [M] |
| 10W | FT30+W 7.5 | 7.60/7.10/7.40 | 0.000000 | 0.00000 |
| 11W | | 7.60/7.10/7.40 | 0.000000 | 0.00000 |
| 12W | | 7.60/7.10/7.40 | 0.000000 | 0.00000 |
| | | | **Average** | 0.00000 |
| | | | **Std deviation** | 0.00000 |
| | | | **(Std dev/Mean)x100** | #DIV/0! |

**1W**

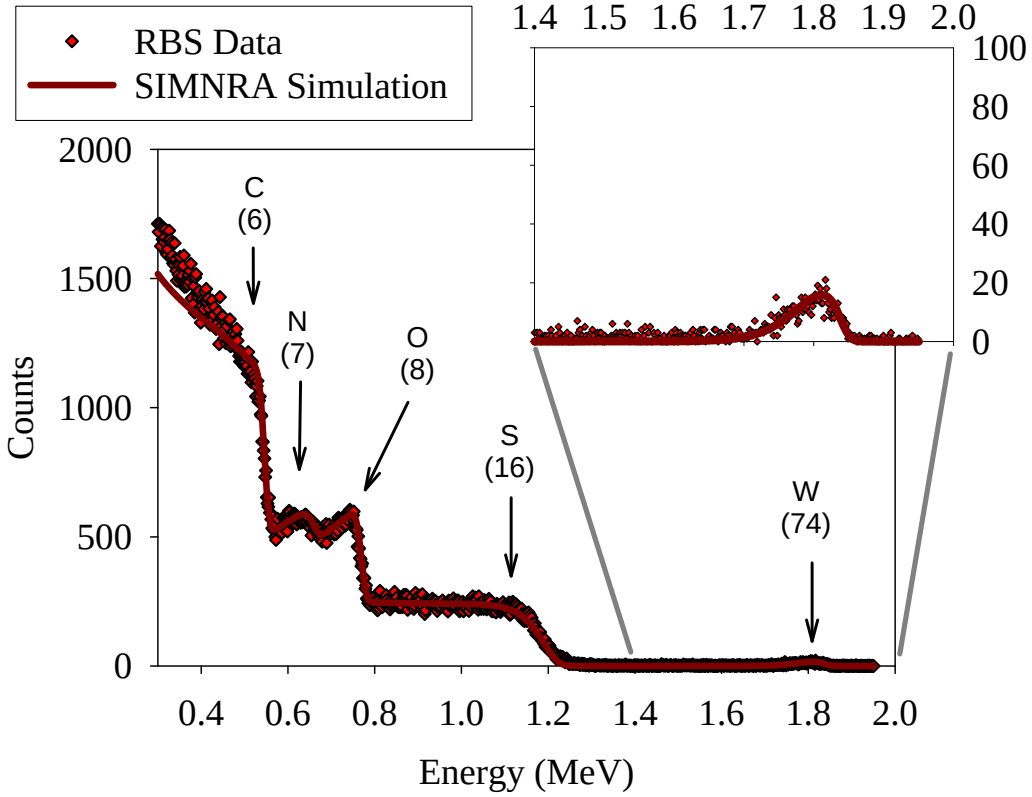
RBS Data
SIMNRA Simulation
Counts
Energy (MeV)
C (6)
N (7)
O (8)
S (16)
W (74)

**2W**

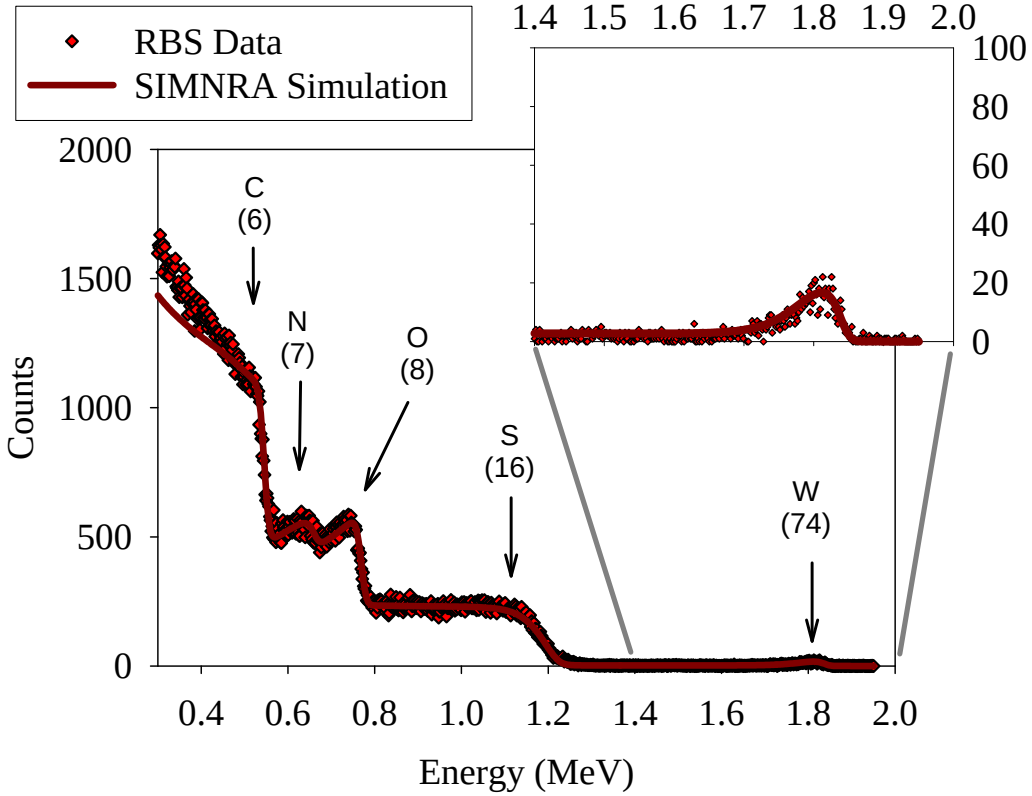
RBS Data
SIMNRA Simulation
Counts
Energy (MeV)
C (6)
N (7)
O (8)
S (16)
W (74)

**3W**

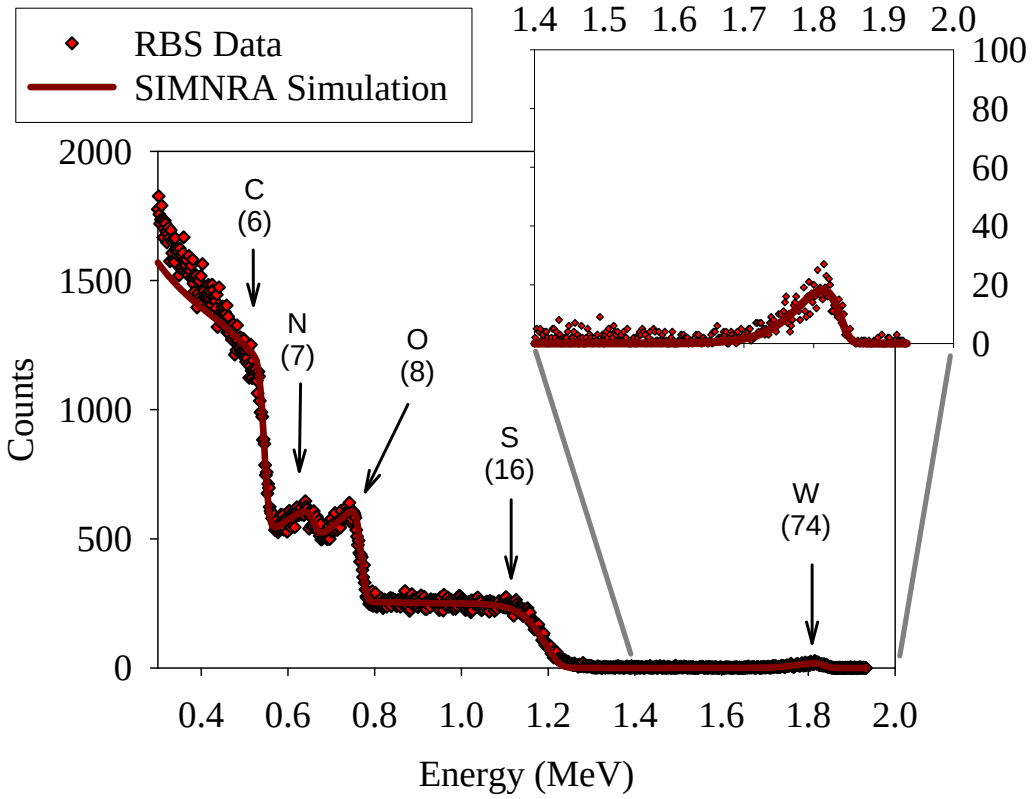
RBS Data
SIMNRA Simulation
Counts
Energy (MeV)
C (6)
N (7)
O (8)
S (16)
W (74)

**4W**

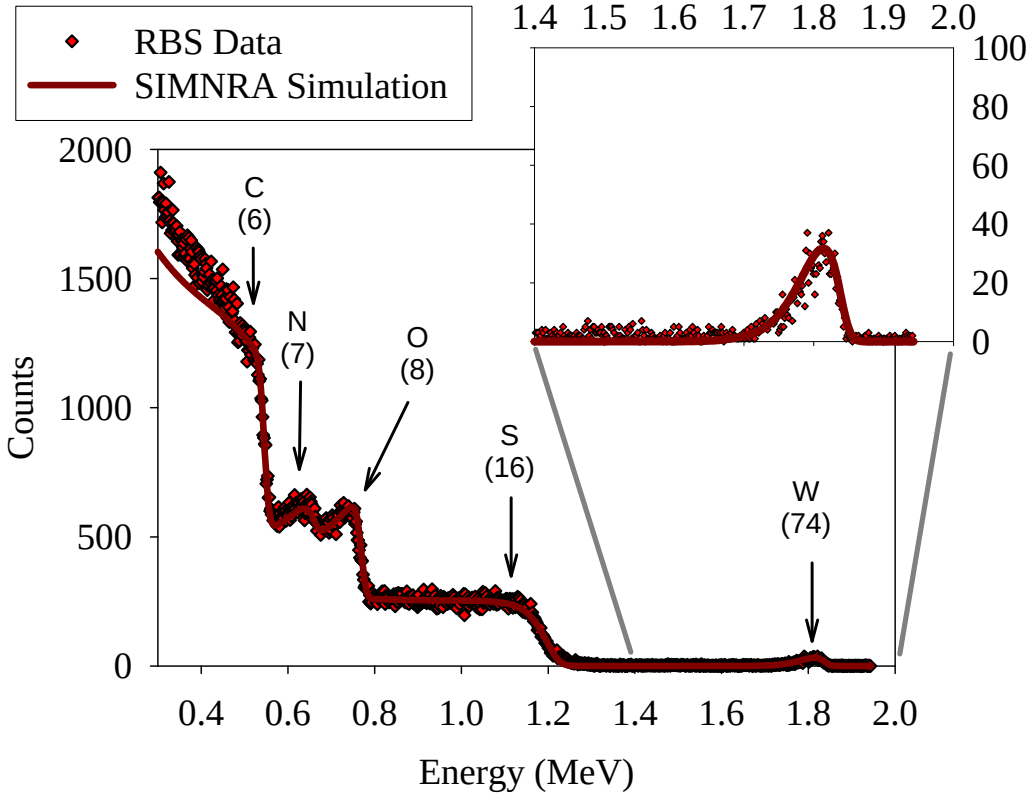
RBS Data
SIMNRA Simulation
Counts
Energy (MeV)
C (6)
N (7)
O (8)
S (16)
W (74)

**5W**

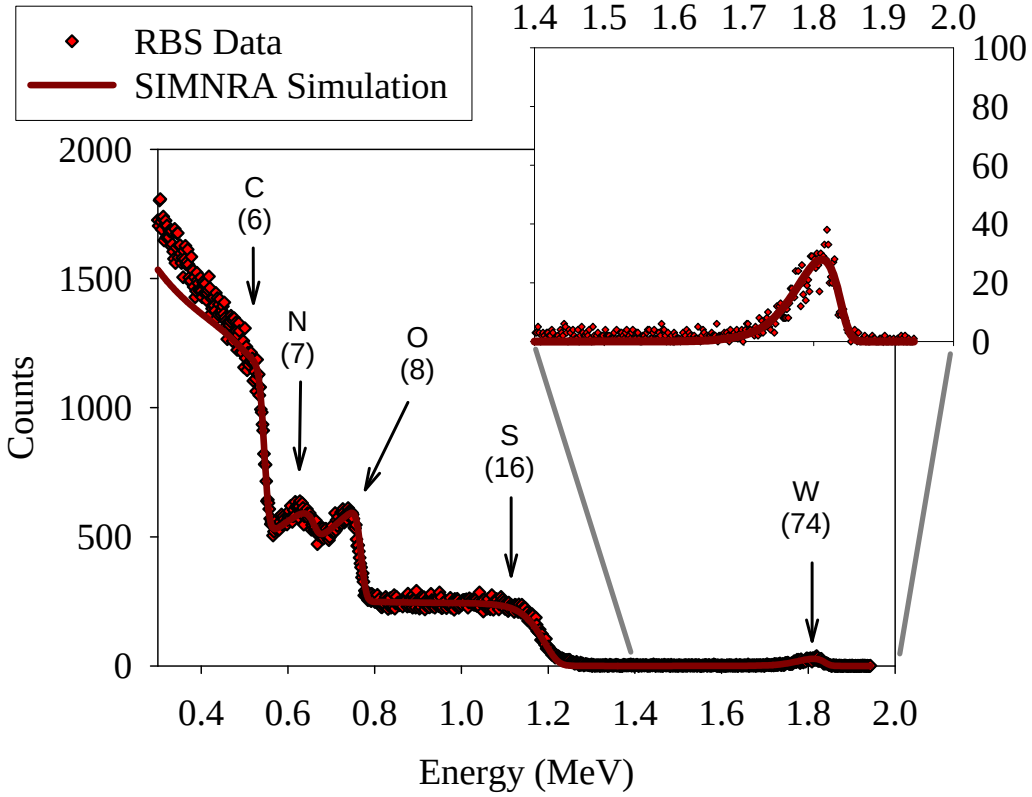
RBS Data
SIMNRA Simulation
Counts
Energy (MeV)
C (6)
N (7)
O (8)
S (16)
W (74)

**6W**

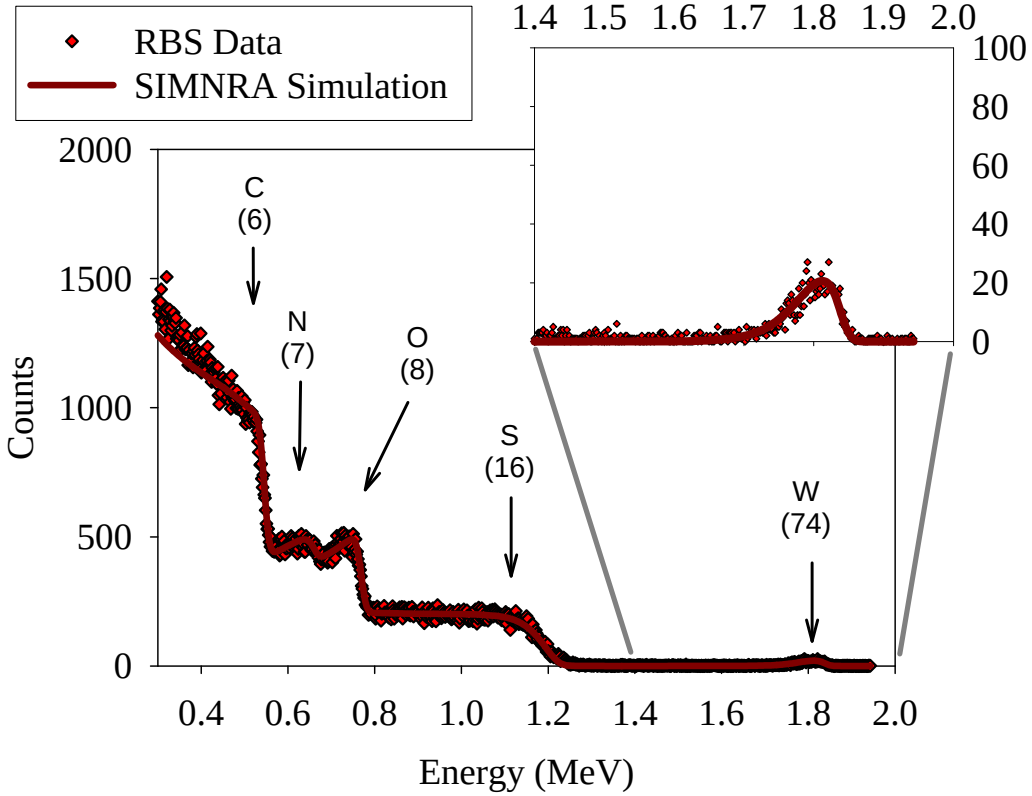
RBS Data
SIMNRA Simulation
Counts
Energy (MeV)
C (6)
N (7)
O (8)
S (16)
W (74)

**7W**

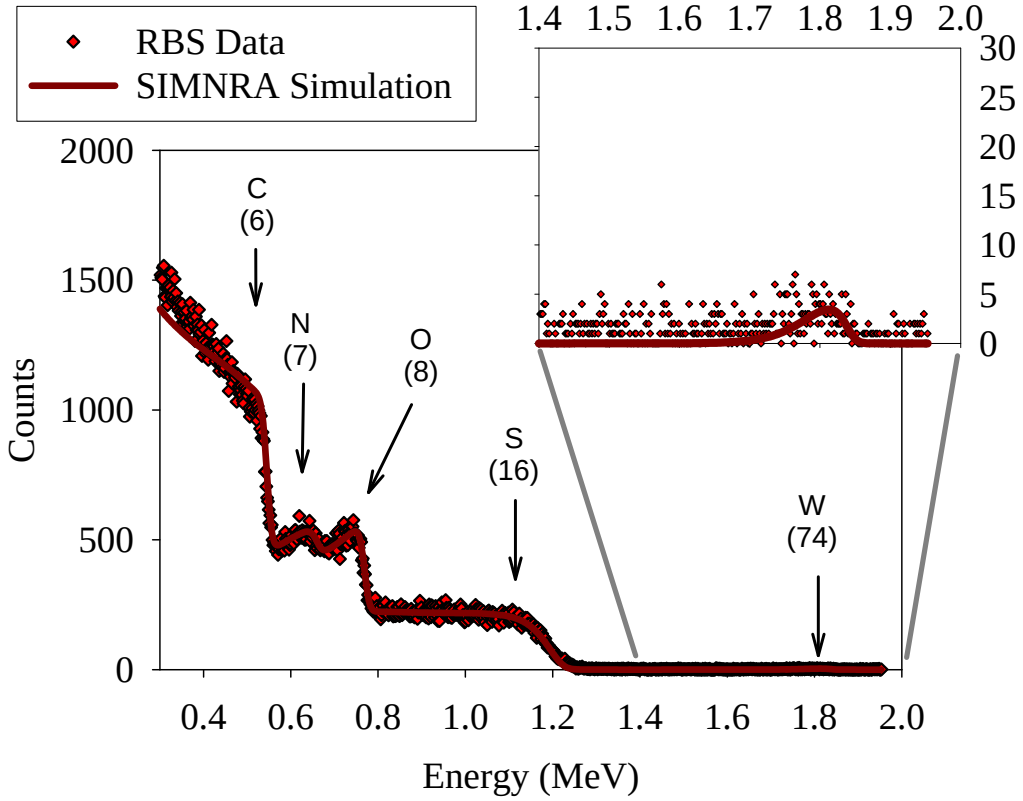
RBS Data
SIMNRA Simulation
Counts
Energy (MeV)
C (6)
N (7)
O (8)
S (16)
W (74)

**8W**

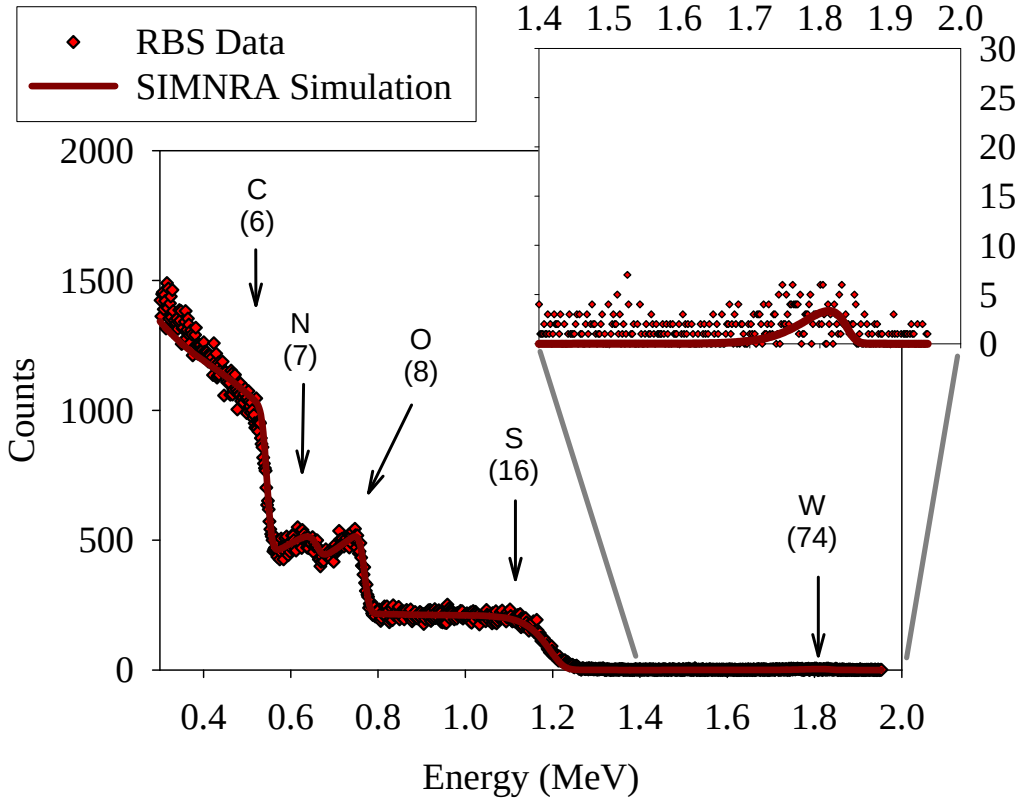
RBS Data
SIMNRA Simulation
Counts
Energy (MeV)
C (6)
N (7)
O (8)
S (16)
W (74)

**9W**

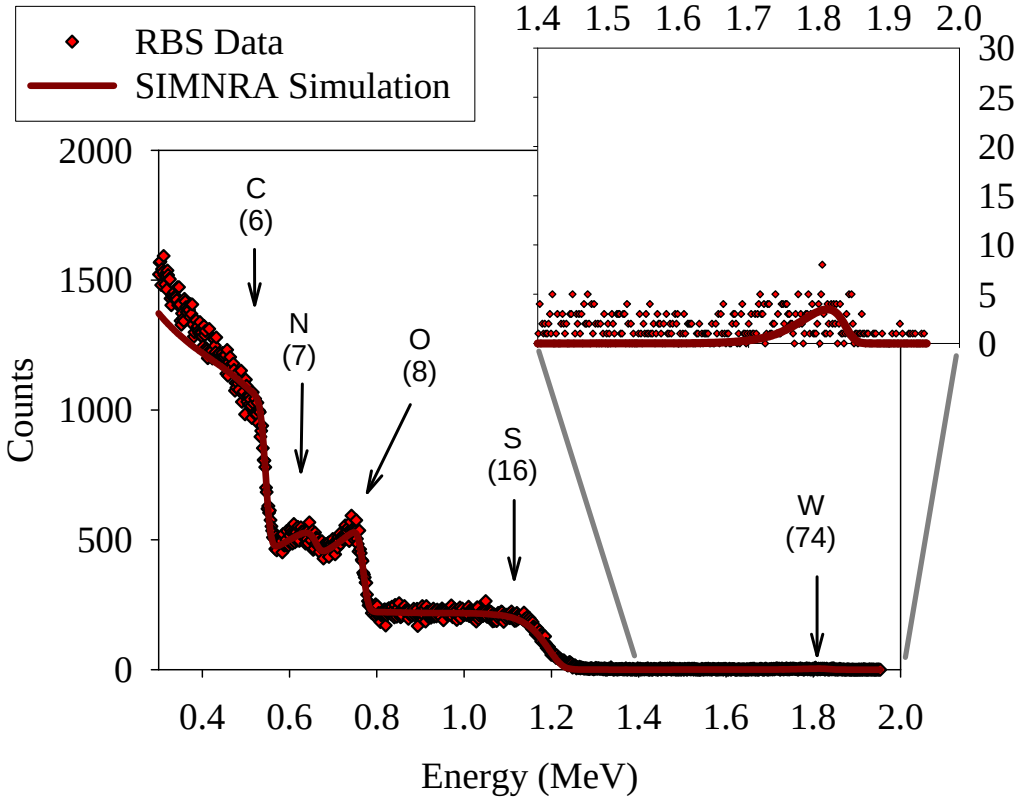
RBS Data
SIMNRA Simulation
Counts
Energy (MeV)
C (6)
N (7)
O (8)
S (16)
W (74)

**10W**

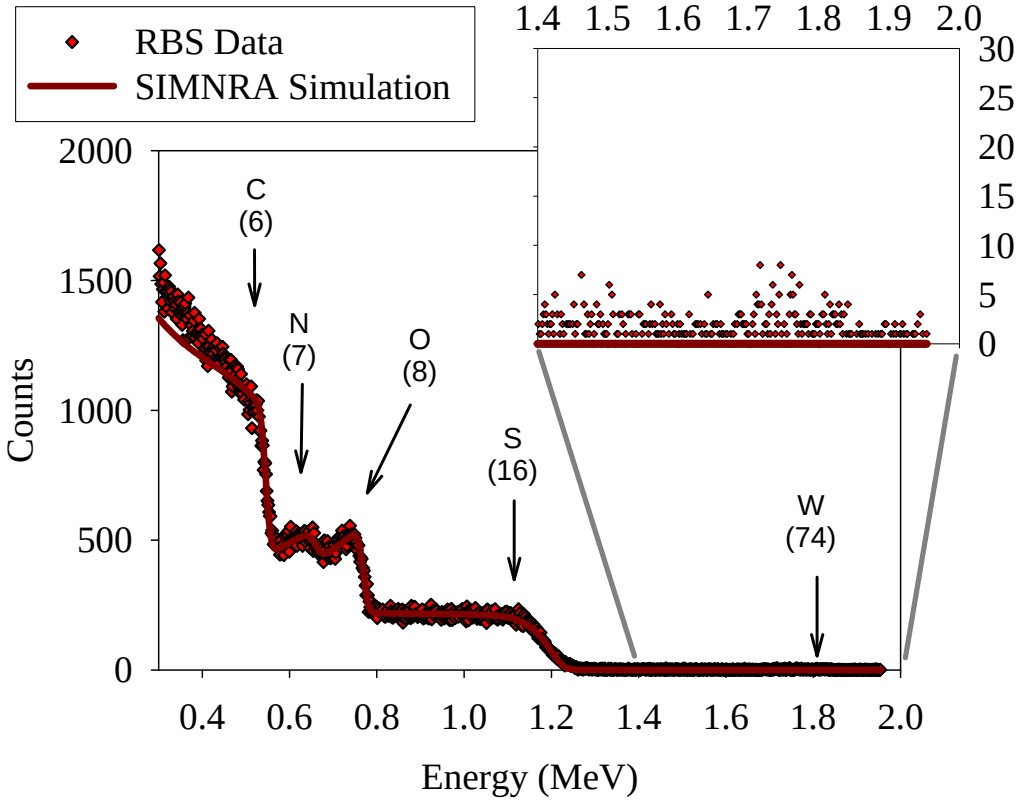
RBS Data
SIMNRA Simulation
Counts
Energy (MeV)
C (6)
N (7)
O (8)
S (16)
W (74)

**11W**

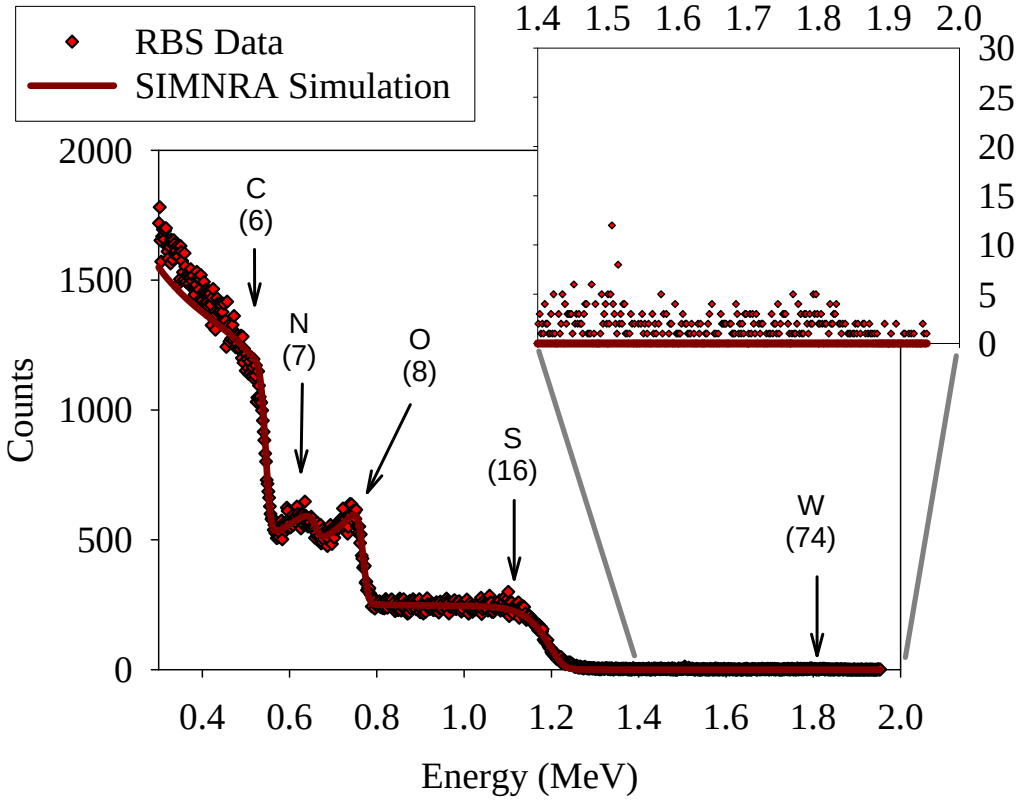
RBS Data
SIMNRA Simulation
Counts
Energy (MeV)
C (6)
N (7)
O (8)
S (16)
W (74)

**12W**

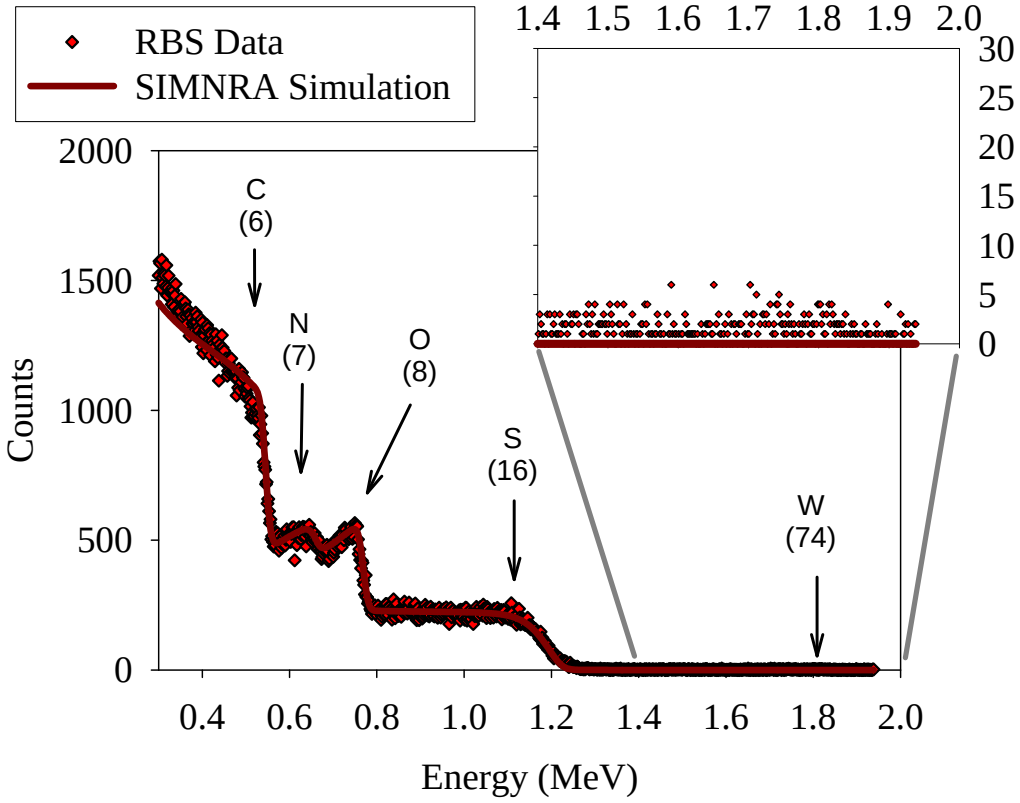
RBS Data
SIMNRA Simulation
Counts
Energy (MeV)
C (6)
N (7)
O (8)
S (16)
W (74)

**13W**

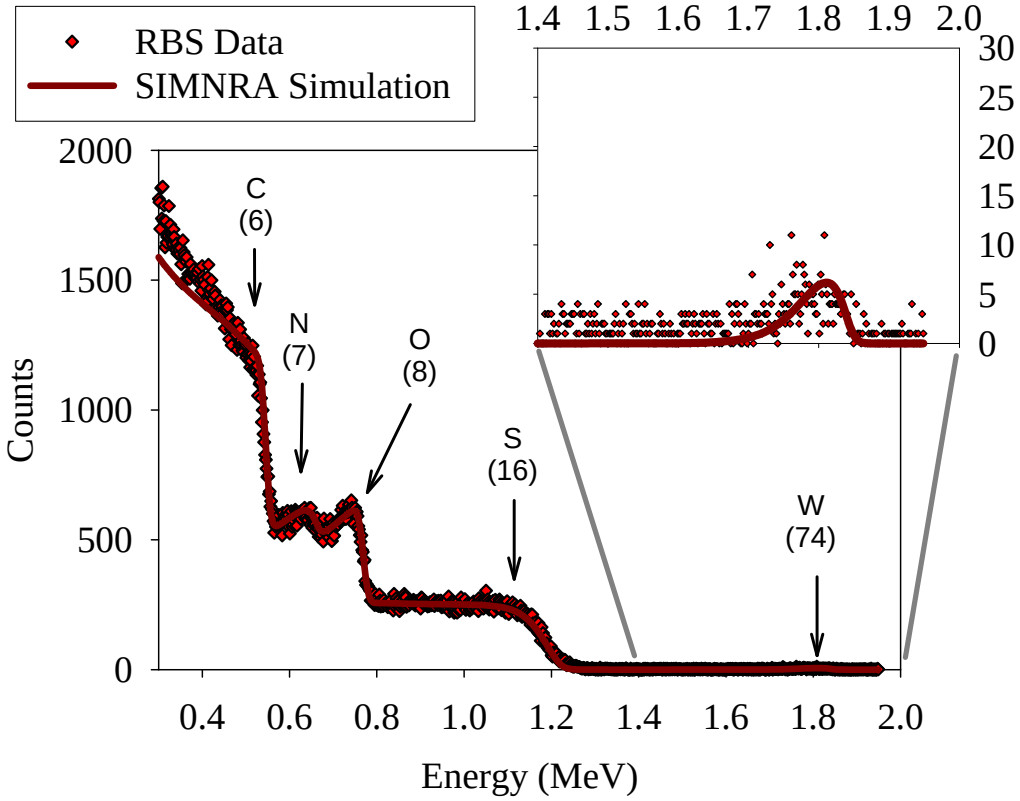
RBS Data
SIMNRA Simulation
Counts
Energy (MeV)
C (6)
N (7)
O (8)
S (16)
W (74)

**14W**

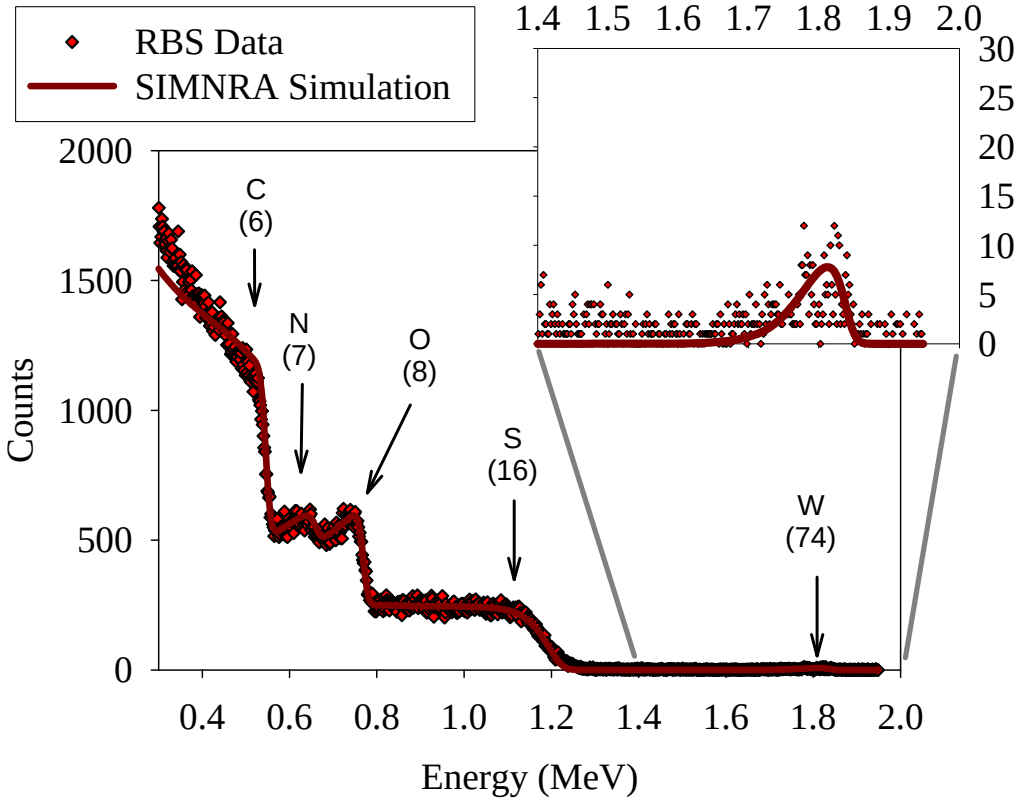
RBS Data
SIMNRA Simulation
Counts
Energy (MeV)
C (6)
N (7)
O (8)
S (16)
W (74)

**15W**

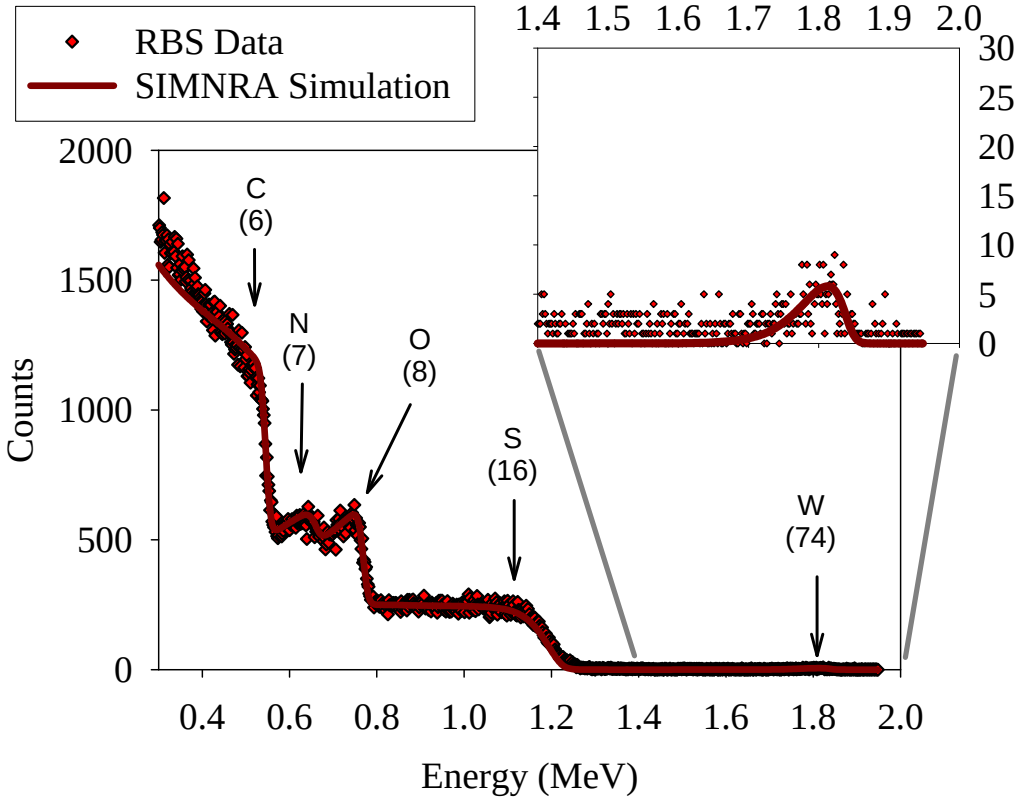
RBS Data
SIMNRA Simulation
Counts
Energy (MeV)
C (6)
N (7)
O (8)
S (16)
W (74)

**16W**

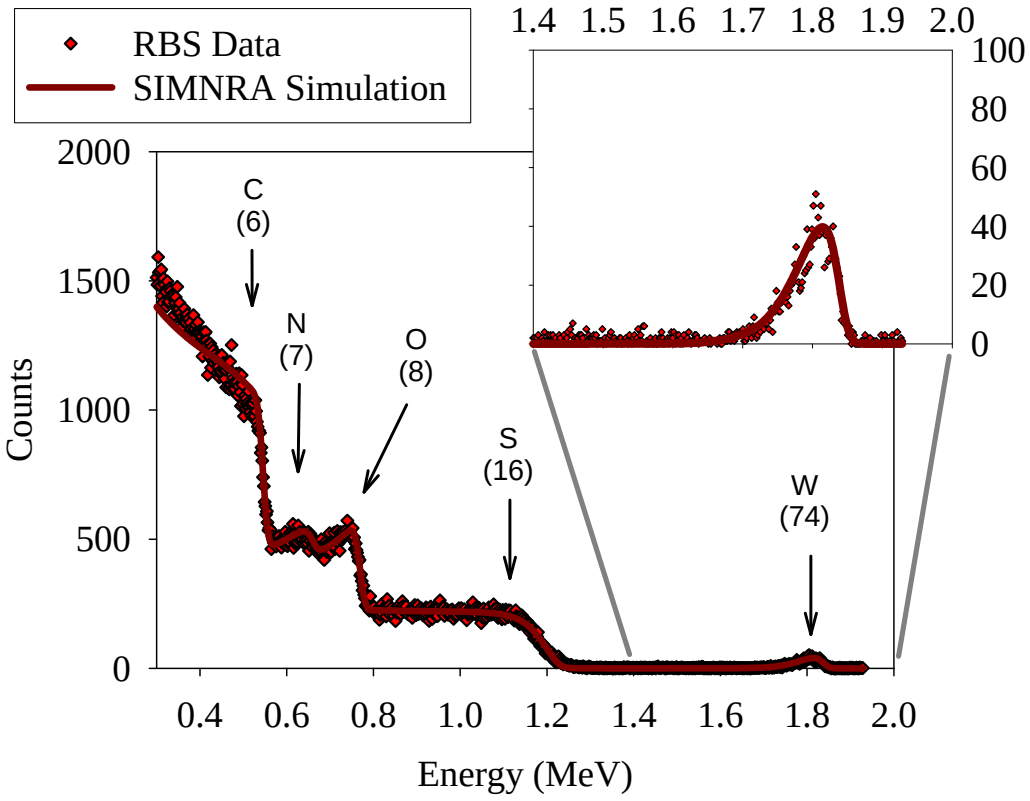
RBS Data
SIMNRA Simulation
Counts
Energy (MeV)
C (6)
N (7)
O (8)
S (16)
W (74)

**17W**

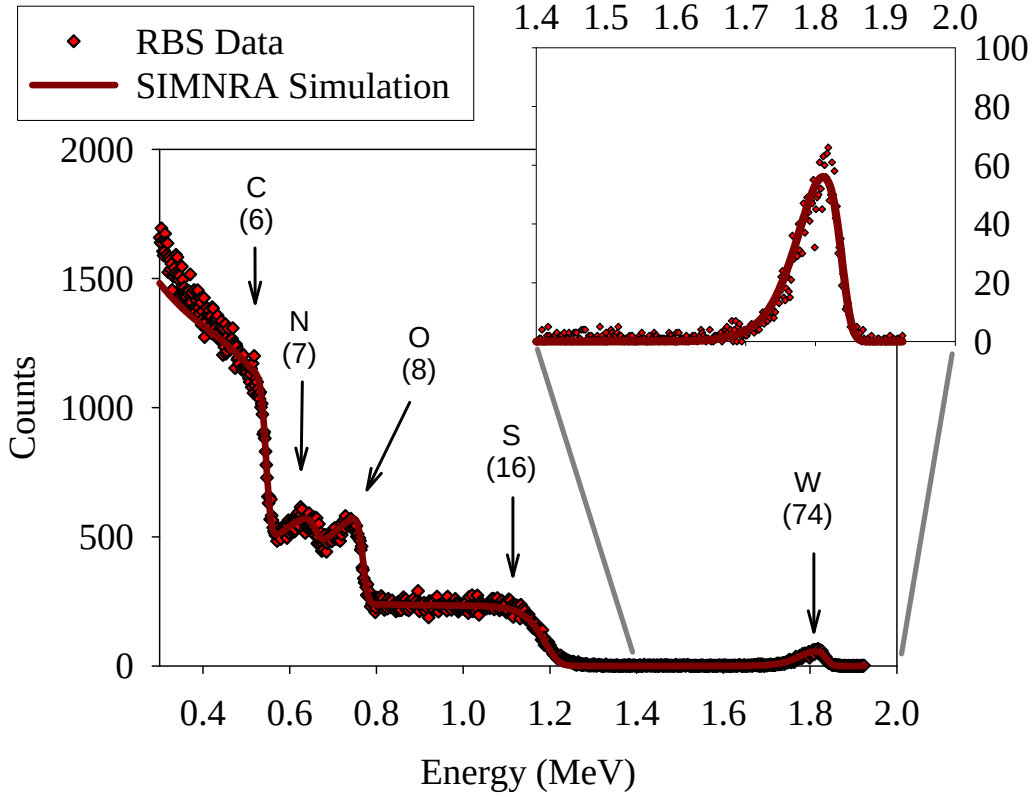
RBS Data
SIMNRA Simulation
Counts
Energy (MeV)
C (6)
N (7)
O (8)
S (16)
W (74)

**18W**

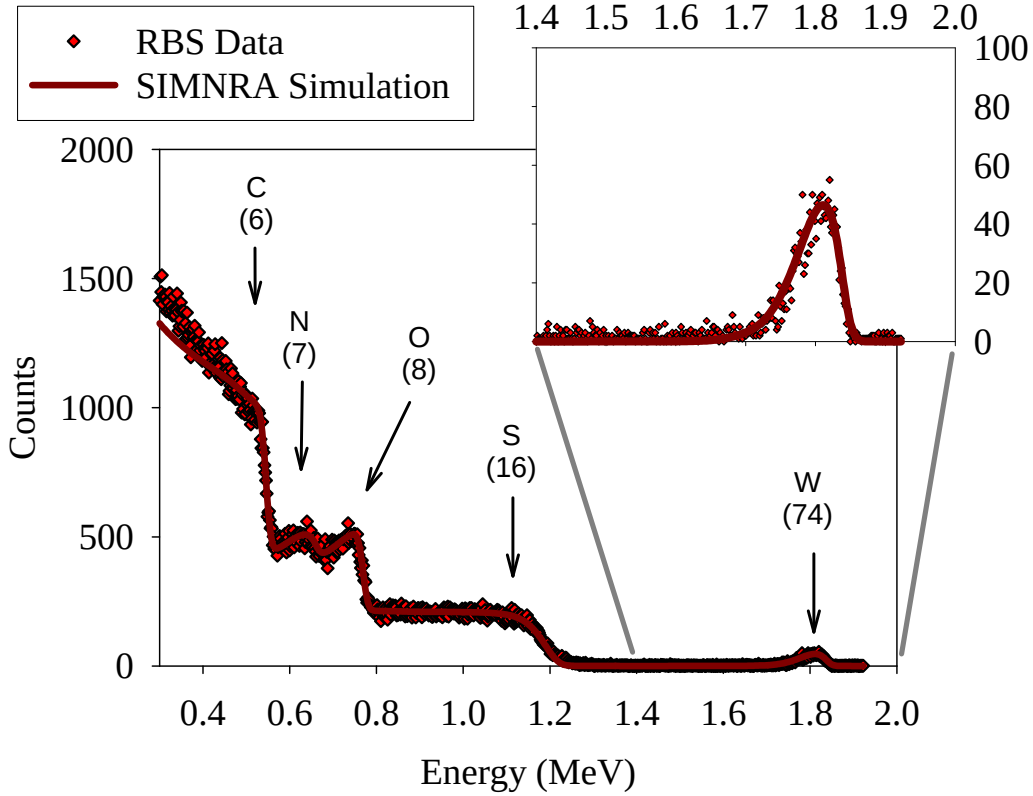
RBS Data
SIMNRA Simulation
Counts
Energy (MeV)
C (6)
N (7)
O (8)
S (16)
W (74)

***Appendix C.2.3. Re-analysis of Rutherford Backscattering Spectrometry (RBS) Data in Appendix B.2 for FT30 Reverse Osmosis (RO) Membrane Samples Probed with Barium ($Ba^{2+}$) Ion***

| | pH = 3.42 | | | |
|---|---|---|---|---|
| | Treatment | pH max/pH min/pH final | Elemental ratio | Concentration [M] |
| 19Ba | FT30+Ba 3.5 | 3.5/3.35/3.42 | 0.00012 | 0.01657 |
| 20Ba | | 3.5/3.35/3.42 | 0.00011 | 0.01519 |
| 21Ba | | 3.5/3.35/3.42 | 0.00014 | 0.01864 |
| | | | Average | 0.01680 |
| | | | Std deviation | 0.00174 |
| | | | (Std dev/Mean)x100 | 10.34 |

| | pH = 4.92 | | | |
|---|---|---|---|---|
| | Treatment | pH max/pH min/pH final | Elemental ratio | Concentration [M] |
| 16Ba | FT30+Ba 5.0 | 5.00/4.92/4.92 | 0.00011 | 0.01450 |
| 17Ba | | 5.00/4.92/4.92 | 0.00012 | 0.01657 |
| 18Ba | | 5.00/4.92/4.92 | 0.00012 | 0.01588 |
| | | | Average | 0.01565 |
| | | | Std deviation | 0.00105 |
| | | | (Std dev/Mean)x100 | 6.74 |

| | pH = 6.00 | | | |
|---|---|---|---|---|
| | Treatment | pH max/pH min/pH final | Elemental ratio | Concentration [M] |
| 13Ba | FT30+Ba 6.0 | 6.01/5.95/6.00 | 0.00023 | 0.03176 |
| 14Ba | | 6.01/5.95/6.00 | 0.00023 | 0.03176 |
| 15Ba | | 6.01/5.95/6.00 | 0.00019 | 0.02624 |
| | | | Average | 0.02992 |
| | | | Std deviation | 0.00319 |
| | | | (Std dev/Mean)x100 | 10.66 |

| | pH = 7.20 | | | |
|---|---|---|---|---|
| | Treatment | pH max/pH min/pH final | Elemental ratio | Concentration [M] |
| 10Ba | FT30+Ba 7.5 | 7.53/7.10/7.20 | 0.00029 | 0.04004 |
| 11Ba | | 7.53/7.10/7.20 | 0.00025 | 0.03452 |
| 12Ba | | 7.53/7.10/7.20 | 0.00031 | 0.04280 |
| | | | Average | 0.03912 |
| | | | Std deviation | 0.00422 |
| | | | (Std dev/Mean)x100 | 10.78 |

| | pH = 8.35 | | | |
|---|---|---|---|---|
| | Treatment | pH max/pH min/pH final | Elemental ratio | Concentration [M] |
| 7Ba | FT30+Ba 8.5 | 8.51/8.35/8.35 | 0.00039 | 0.05385 |
| 8Ba | | 8.51/8.35/8.35 | 0.00044 | 0.06076 |
| 9Ba | | 8.51/8.35/8.35 | 0.00032 | 0.04419 |
| | | | Average | 0.05293 |
| | | | Std deviation | 0.00832 |
| | | | (Std dev/Mean)x100 | 15.72 |

| | pH = 9.53 | | | |
|---|---|---|---|---|
| | Treatment | pH max/pH min/pH final | Elemental ratio | Concentration [M] |
| 4Ba | FT30+Ba 9.5 | 9.54/9.45/9.53 | 0.00077 | 0.10632 |
| 5Ba | | 9.54/9.45/9.53 | 0.00064 | 0.08837 |
| 6Ba | | 9.54/9.45/9.53 | 0.00085 | 0.11737 |
| | | | Average | 0.10402 |
| | | | Std deviation | 0.01463 |
| | | | (Std dev/Mean)x100 | 14.07 |

| | pH = 10.30 | | | |
|---|---|---|---|---|
| | Treatment | pH max/pH min/pH final | Elemental ratio | Concentration [M] |
| 1Ba | FT30+Ba 10.5 | 10.31/10.10/10.3 | 0.00096 | 0.13256 |
| 2Ba | | 10.31/10.10/10.3 | 0.00091 | 0.12565 |
| 3Ba | | 10.31/10.10/10.3 | 0.00077 | 0.10632 |
| | | | Average | 0.12151 |
| | | | Std deviation | 0.01360 |
| | | | (Std dev/Mean)x100 | 11.19 |

**1Ba**

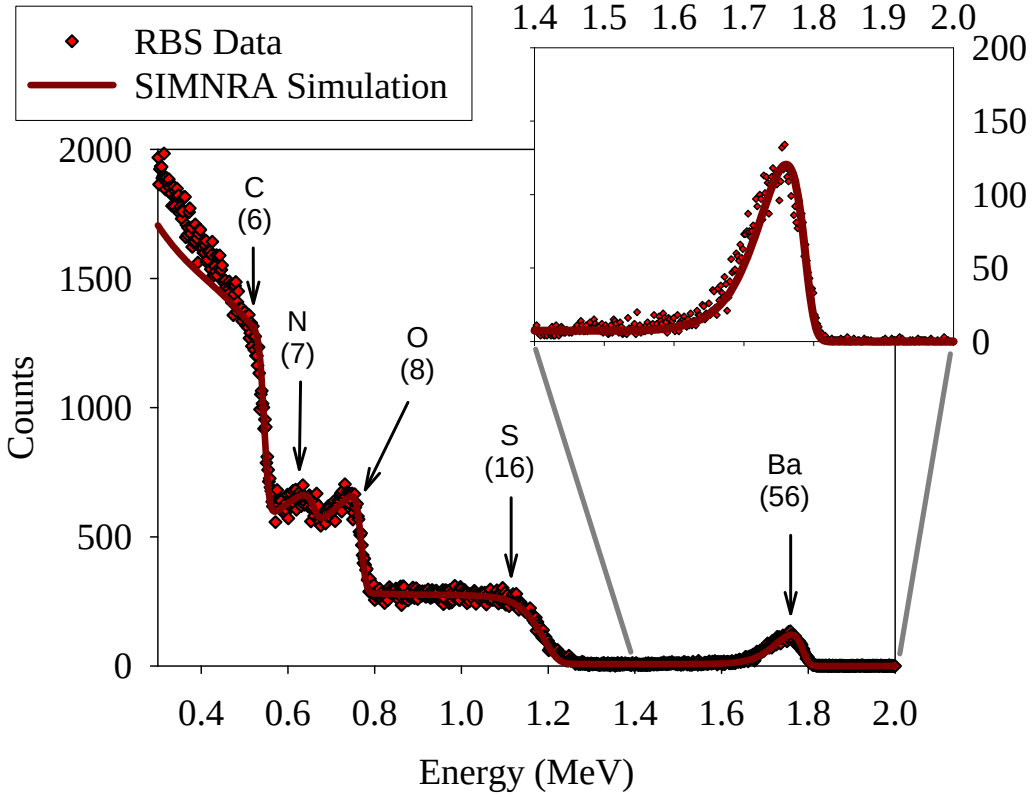
RBS Data
SIMNRA Simulation
Counts
Energy (MeV)
C (6)
N (7)
O (8)
S (16)
Ba (56)

**2Ba**

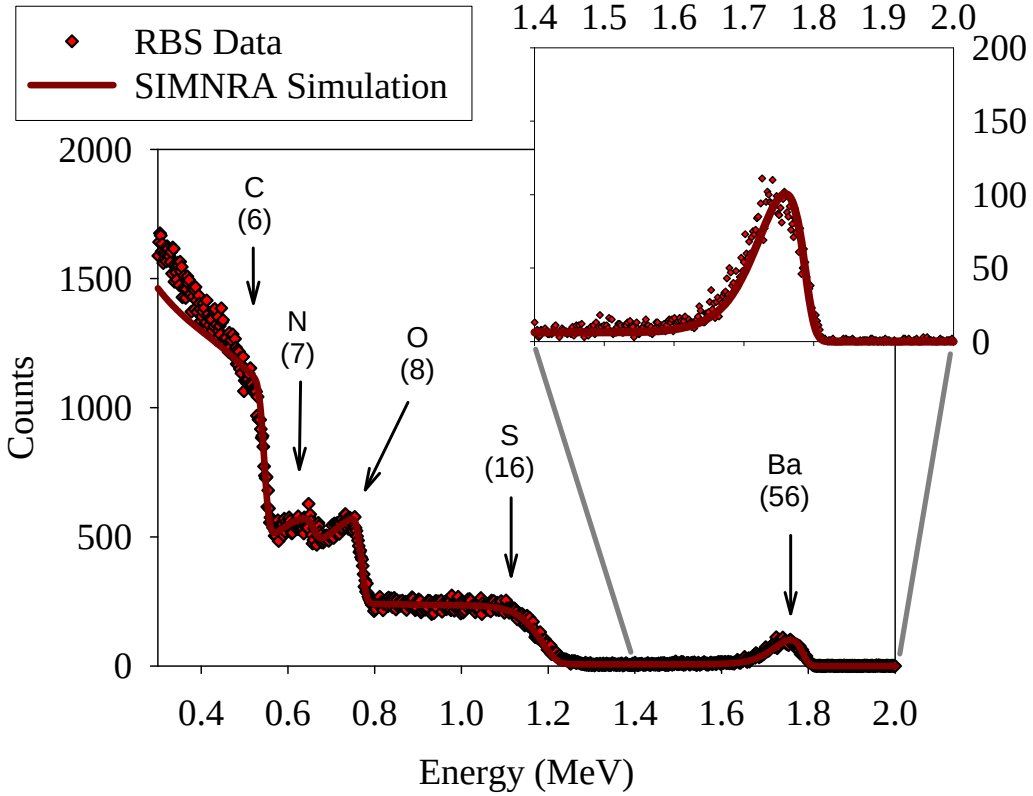
RBS Data
SIMNRA Simulation
Counts
Energy (MeV)
C (6)
N (7)
O (8)
S (16)
Ba (56)

**3Ba**

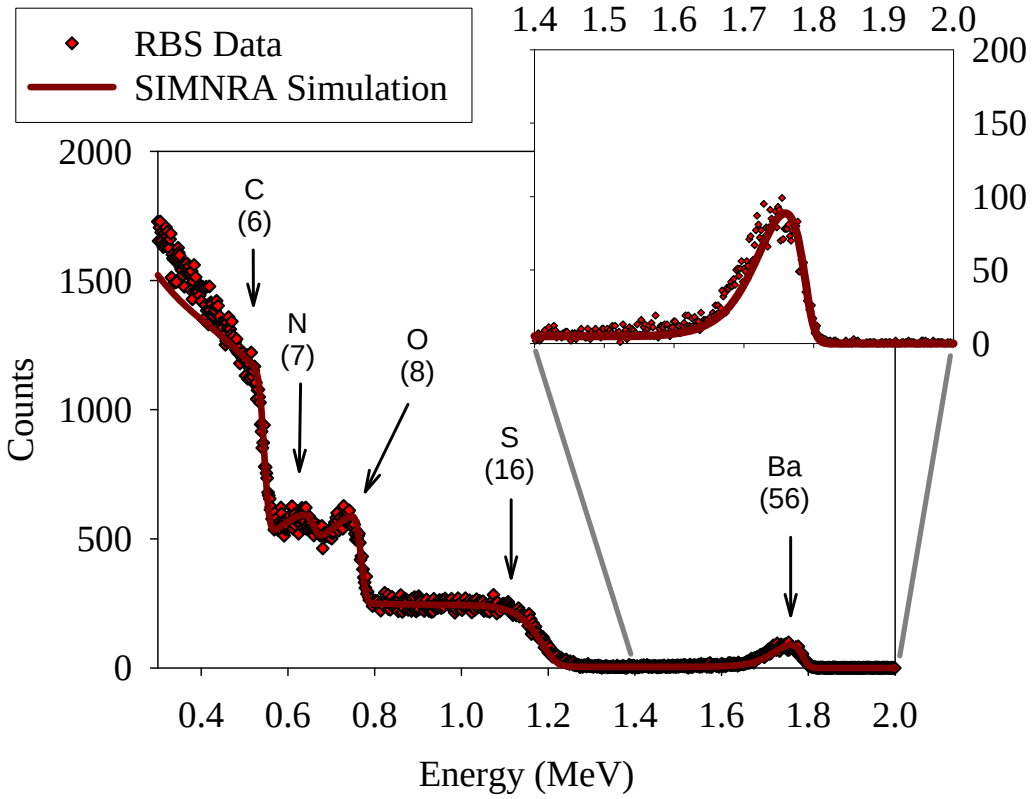
RBS Data
SIMNRA Simulation
Counts
Energy (MeV)
C (6)
N (7)
O (8)
S (16)
Ba (56)

**4Ba**

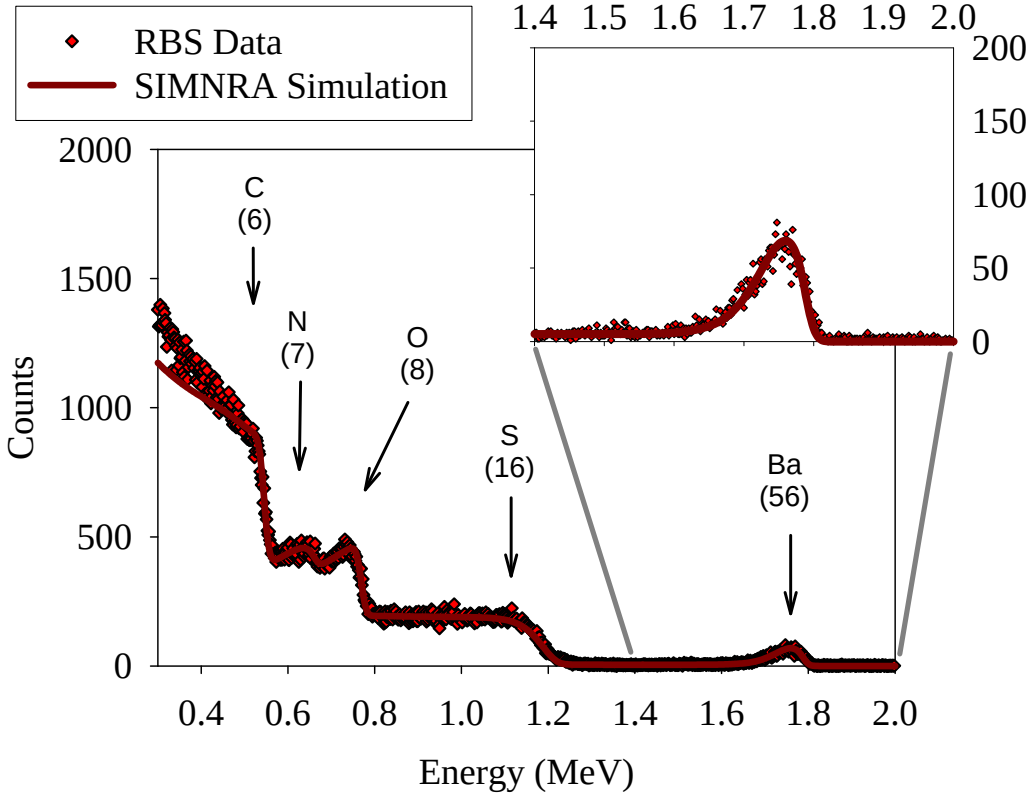
RBS Data
SIMNRA Simulation
Counts
Energy (MeV)
C (6)
N (7)
O (8)
S (16)
Ba (56)

**5Ba**

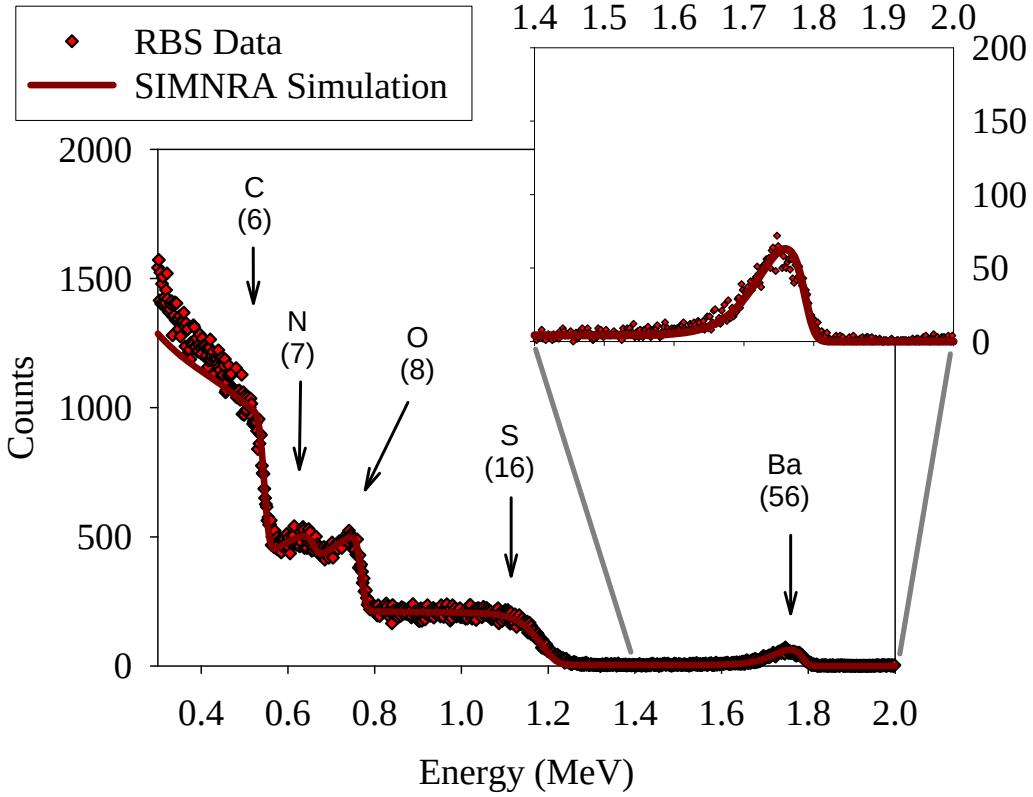
RBS Data
SIMNRA Simulation
Counts
Energy (MeV)
C (6)
N (7)
O (8)
S (16)
Ba (56)

**6Ba**

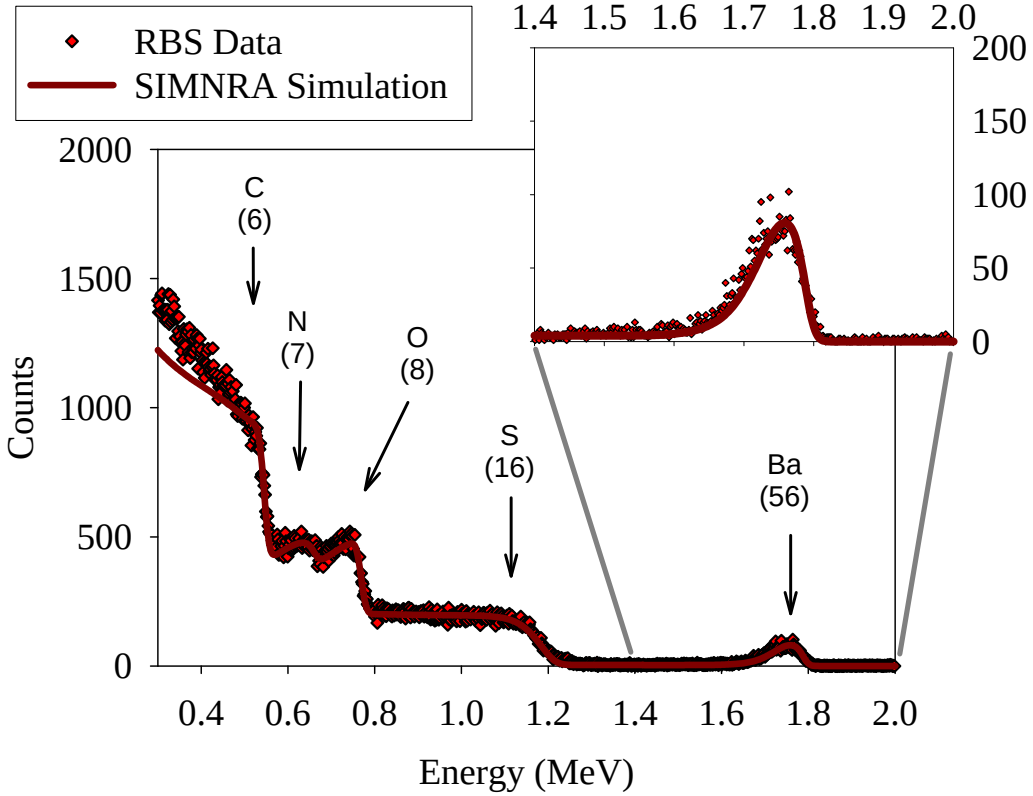
RBS Data
SIMNRA Simulation
Counts
Energy (MeV)
C (6)
N (7)
O (8)
S (16)
Ba (56)

**7Ba**

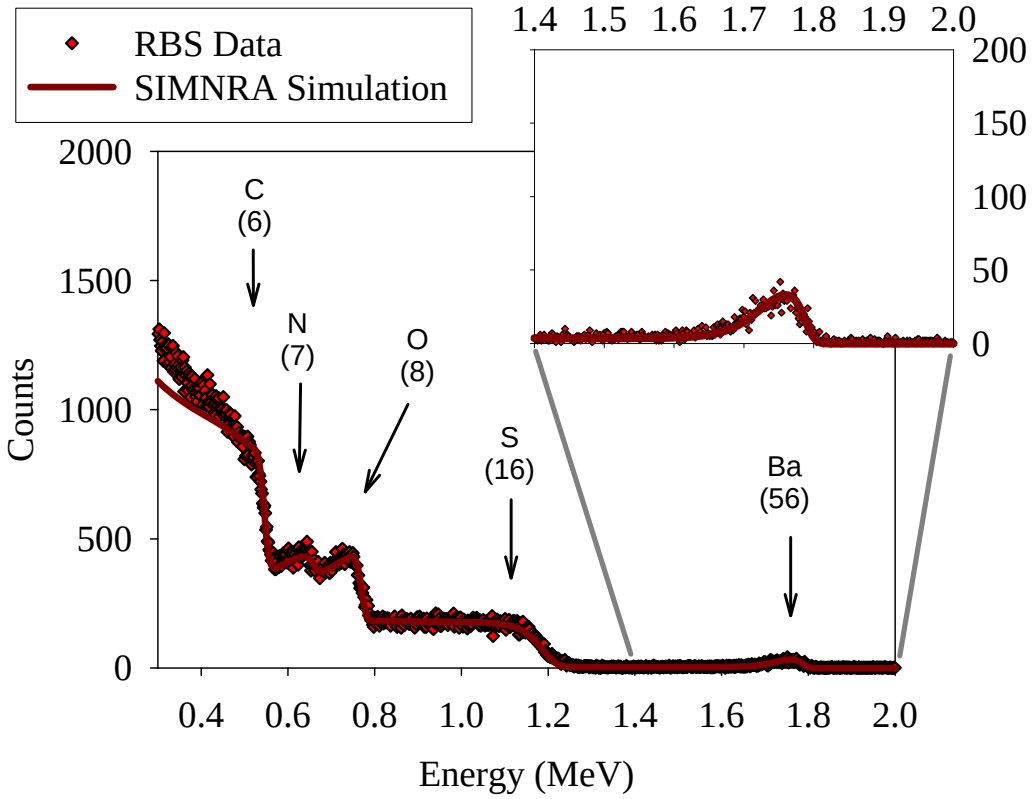
RBS Data
SIMNRA Simulation
Counts
Energy (MeV)
C (6)
N (7)
O (8)
S (16)
Ba (56)

**8Ba**

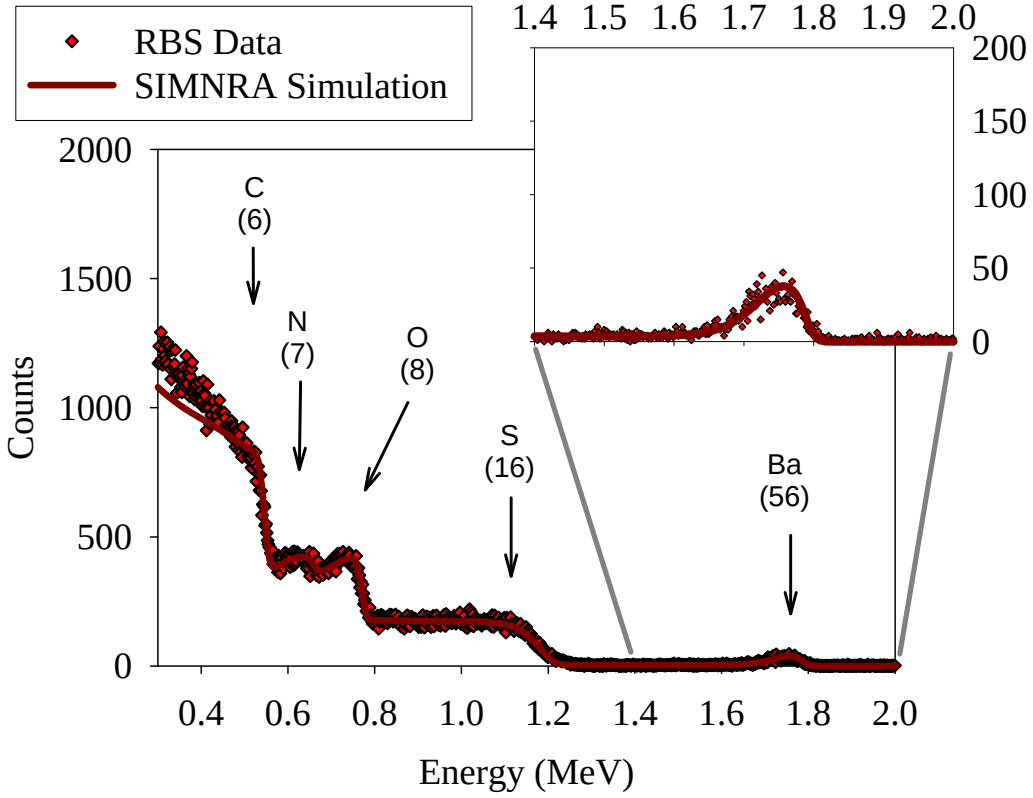
RBS Data
SIMNRA Simulation
Counts
Energy (MeV)
C (6)
N (7)
O (8)
S (16)
Ba (56)

**9Ba**

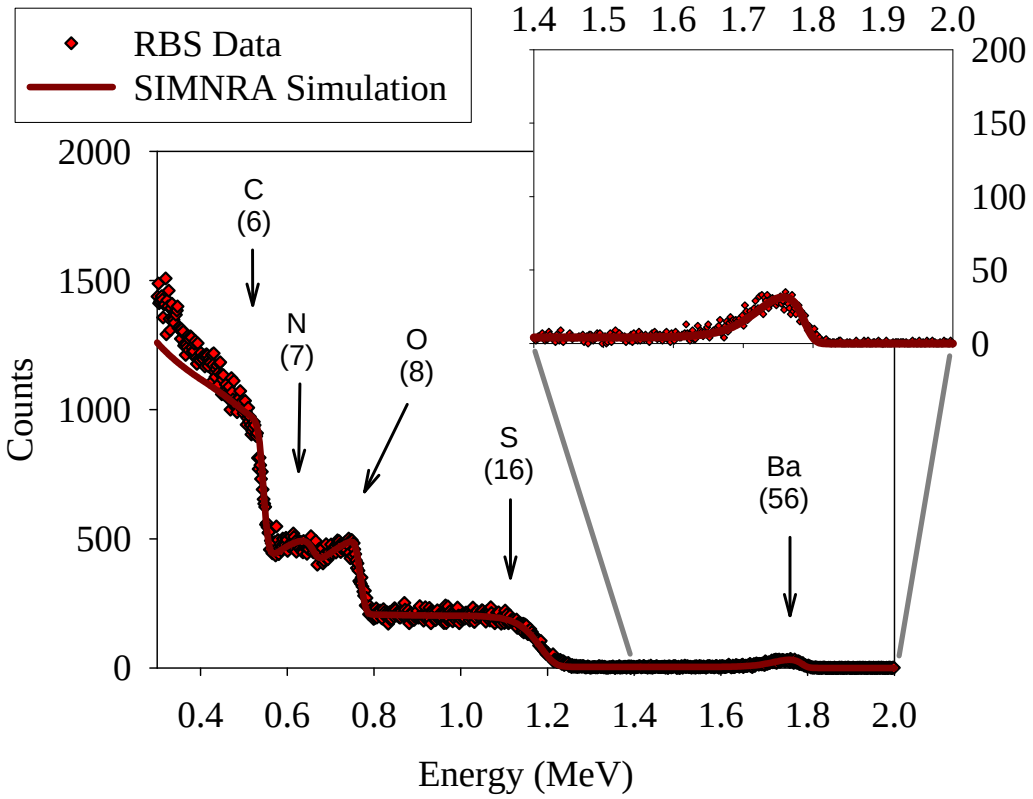
RBS Data
SIMNRA Simulation
Counts
Energy (MeV)
C (6)
N (7)
O (8)
S (16)
Ba (56)

**10Ba**

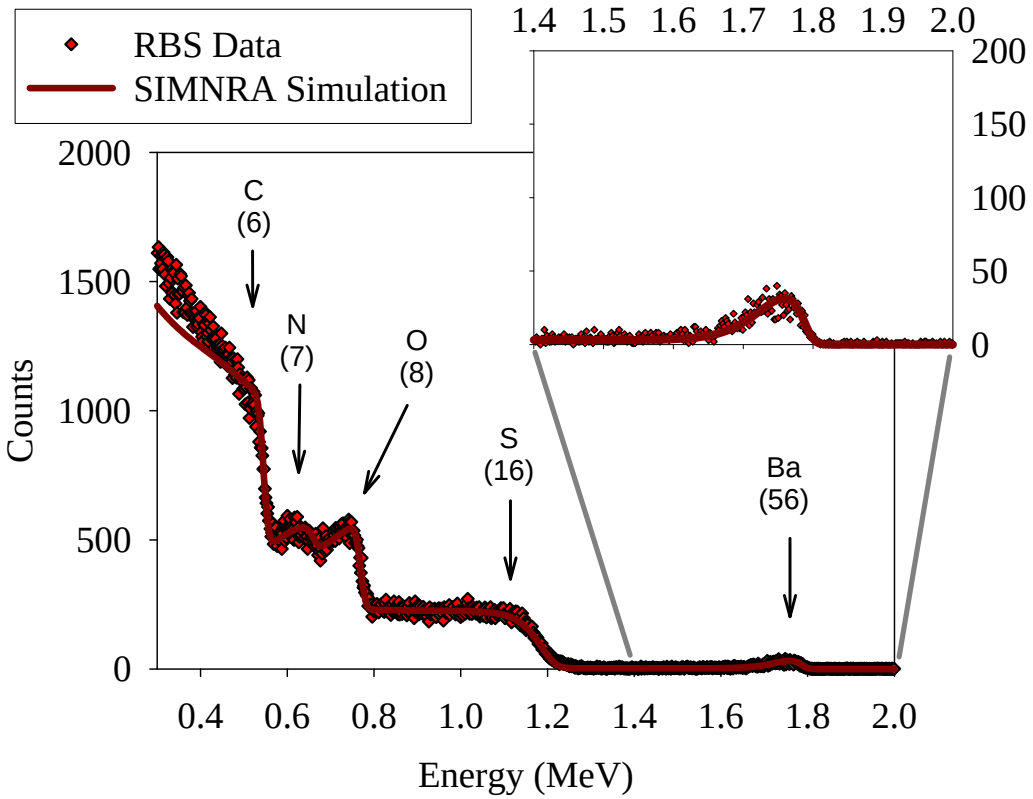
RBS Data
SIMNRA Simulation
Counts
Energy (MeV)
C (6)
N (7)
O (8)
S (16)
Ba (56)

**11Ba**

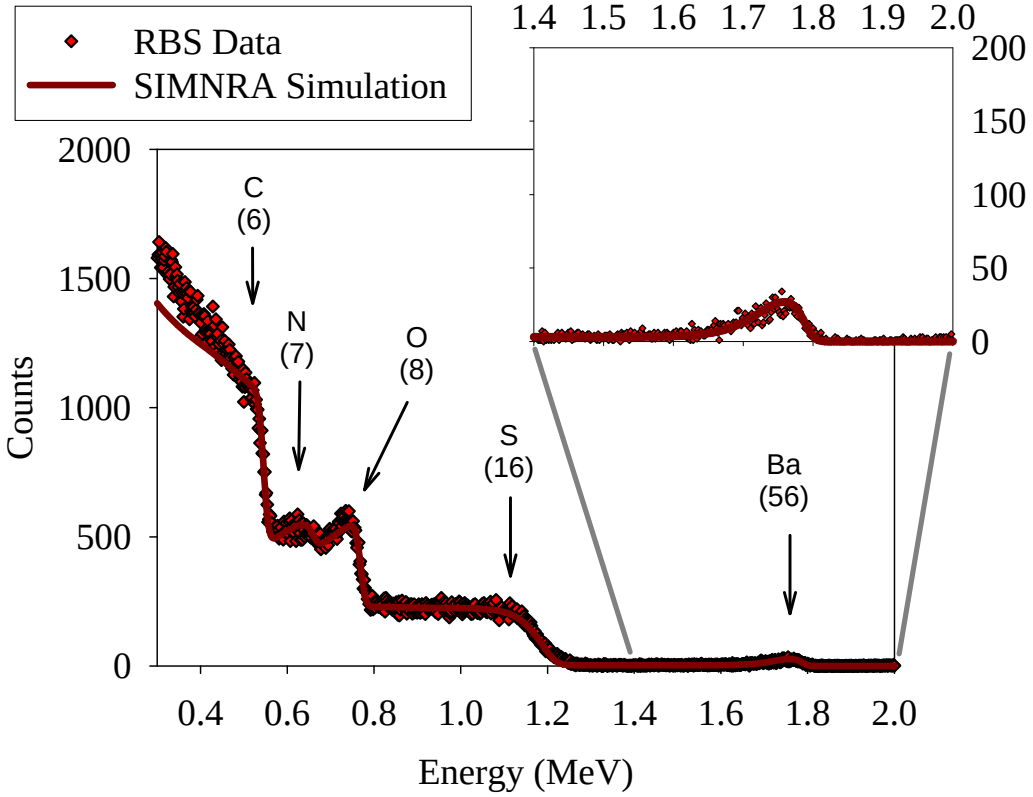
RBS Data
SIMNRA Simulation
Counts
Energy (MeV)
C (6)
N (7)
O (8)
S (16)
Ba (56)

**12Ba**

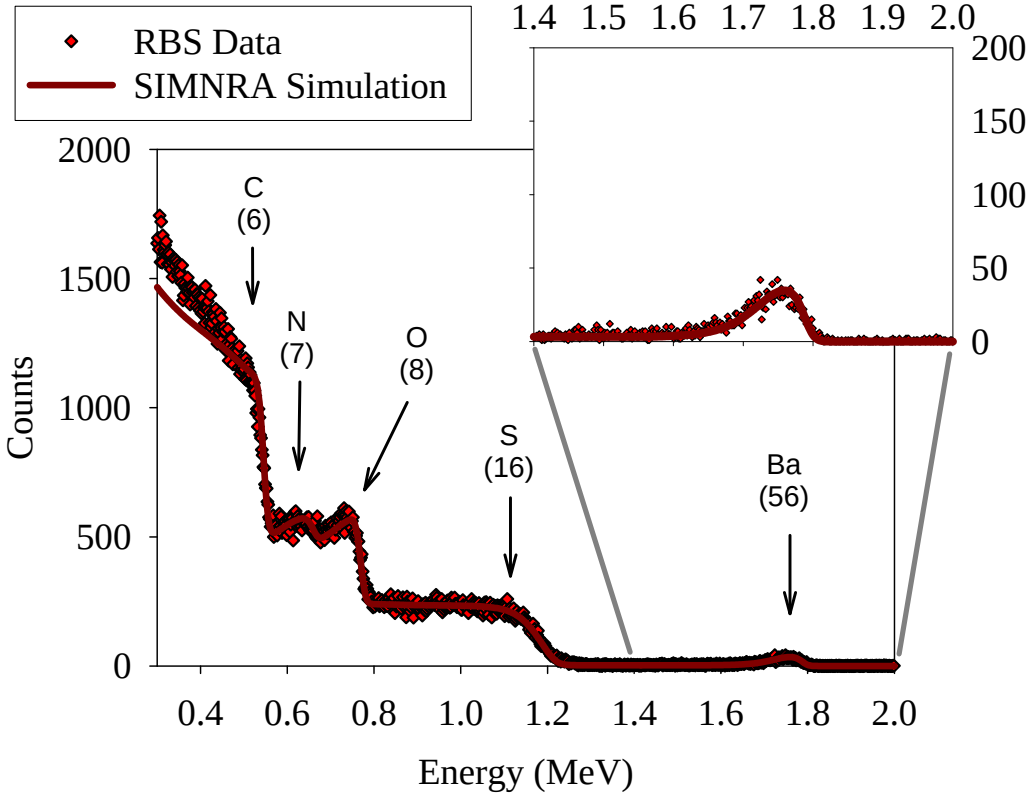
RBS Data
SIMNRA Simulation
Counts
Energy (MeV)
C (6)
N (7)
O (8)
S (16)
Ba (56)

**13Ba**

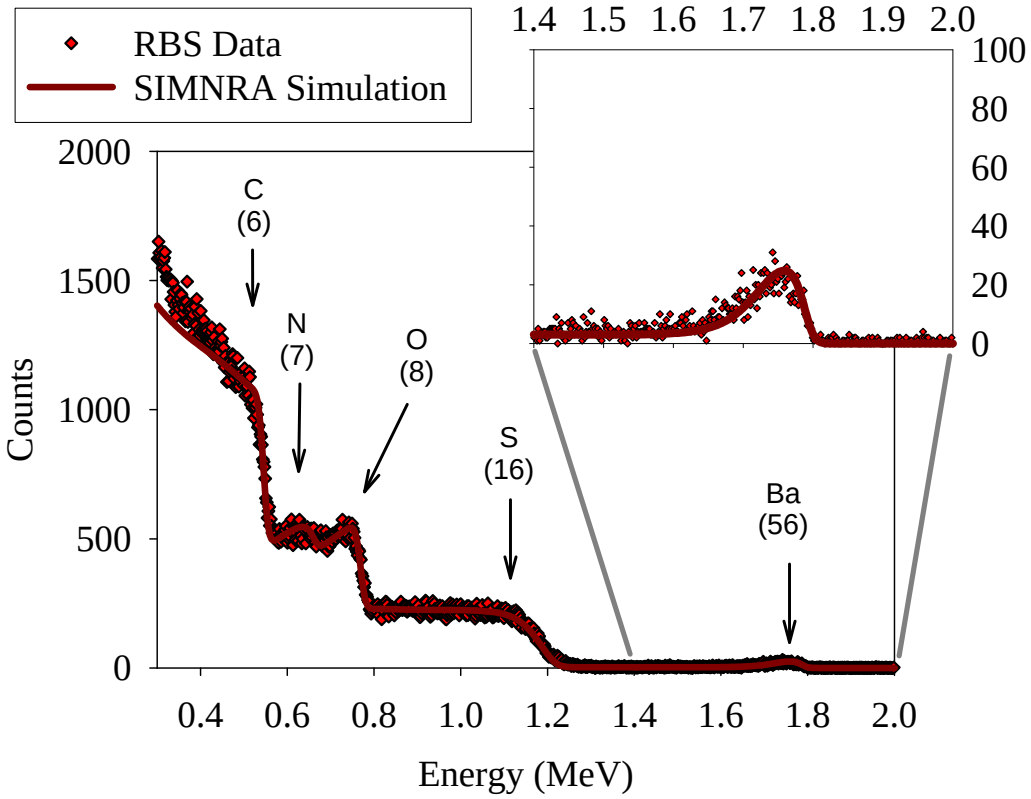
RBS Data
SIMNRA Simulation
Counts
Energy (MeV)
C (6)
N (7)
O (8)
S (16)
Ba (56)

**14Ba**

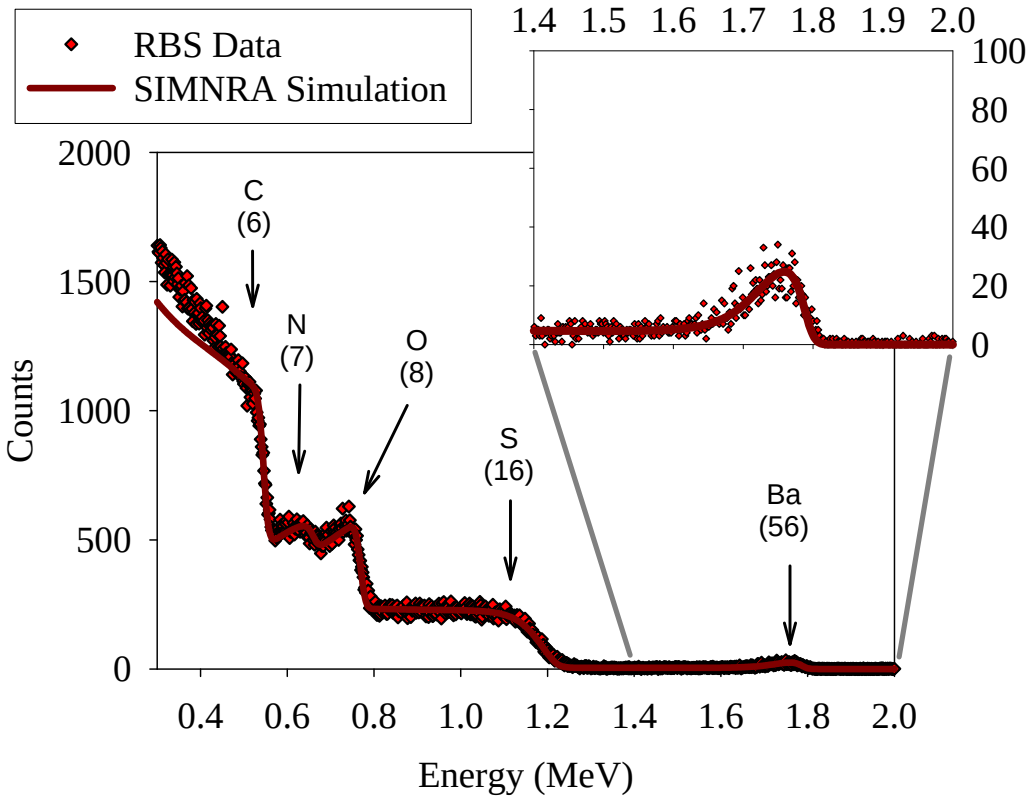
RBS Data
SIMNRA Simulation
Counts
Energy (MeV)
C (6)
N (7)
O (8)
S (16)
Ba (56)

**15Ba**

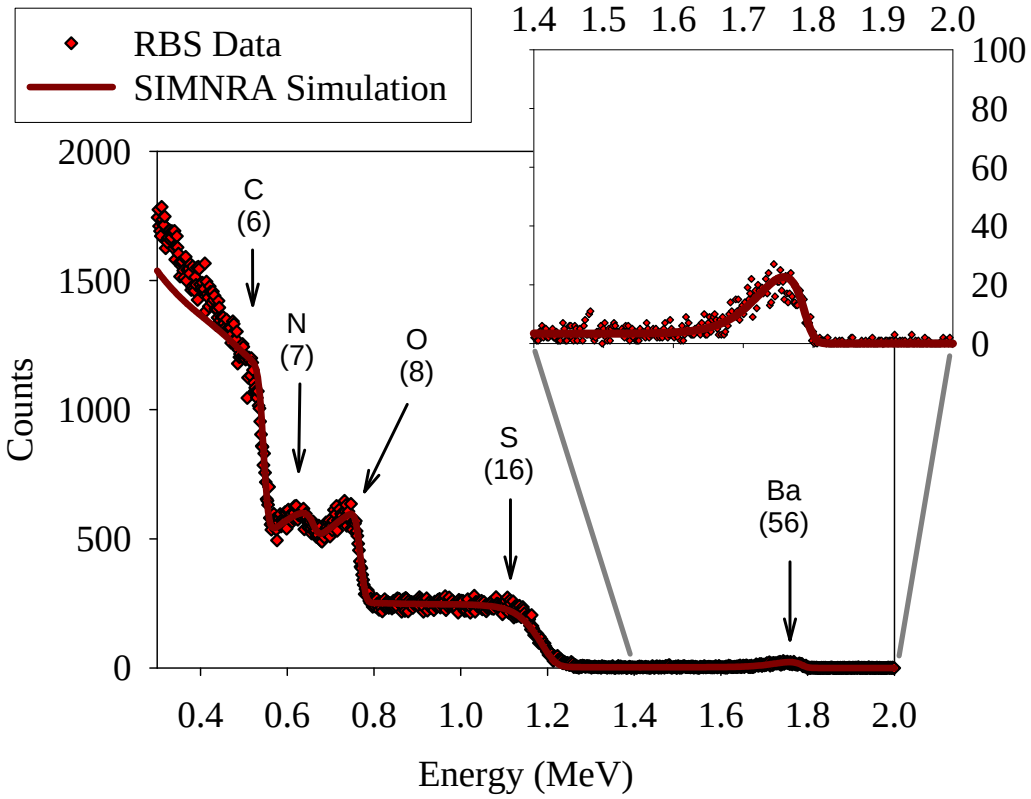
RBS Data
SIMNRA Simulation
Counts
Energy (MeV)
C
(6)
N
(7)
O
(8)
S
(16)
Ba
(56)

**16Ba**

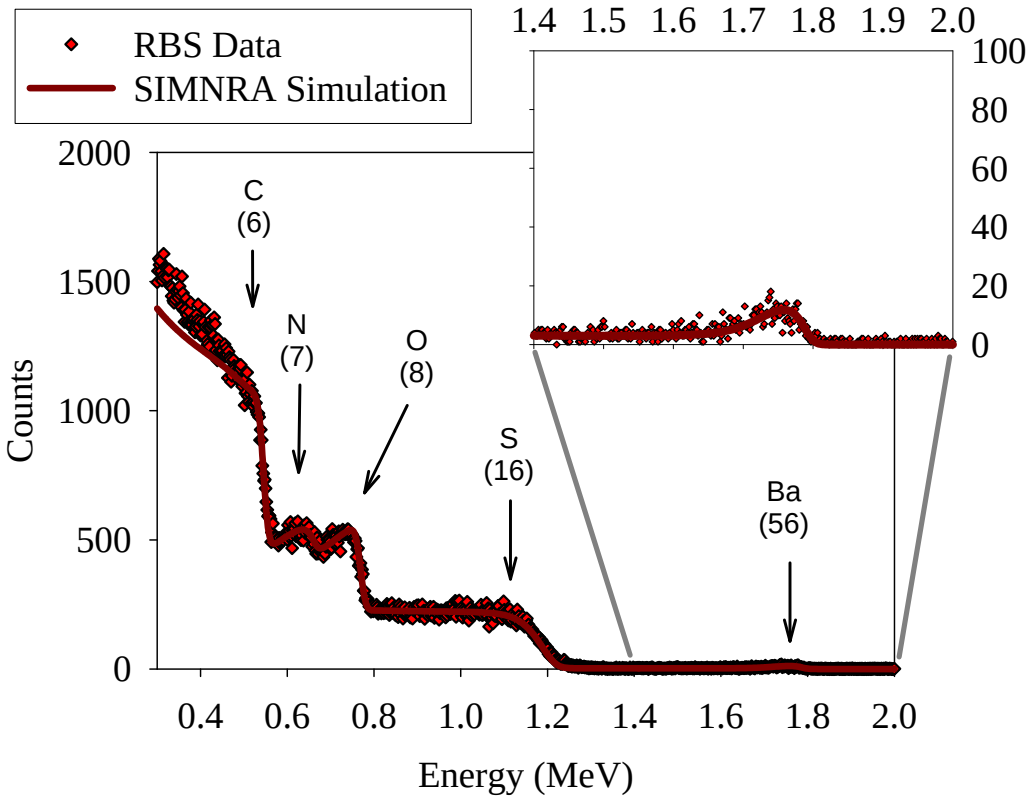
RBS Data
SIMNRA Simulation
Counts
Energy (MeV)
C
(6)
N
(7)
O
(8)
S
(16)
Ba
(56)

**17Ba**

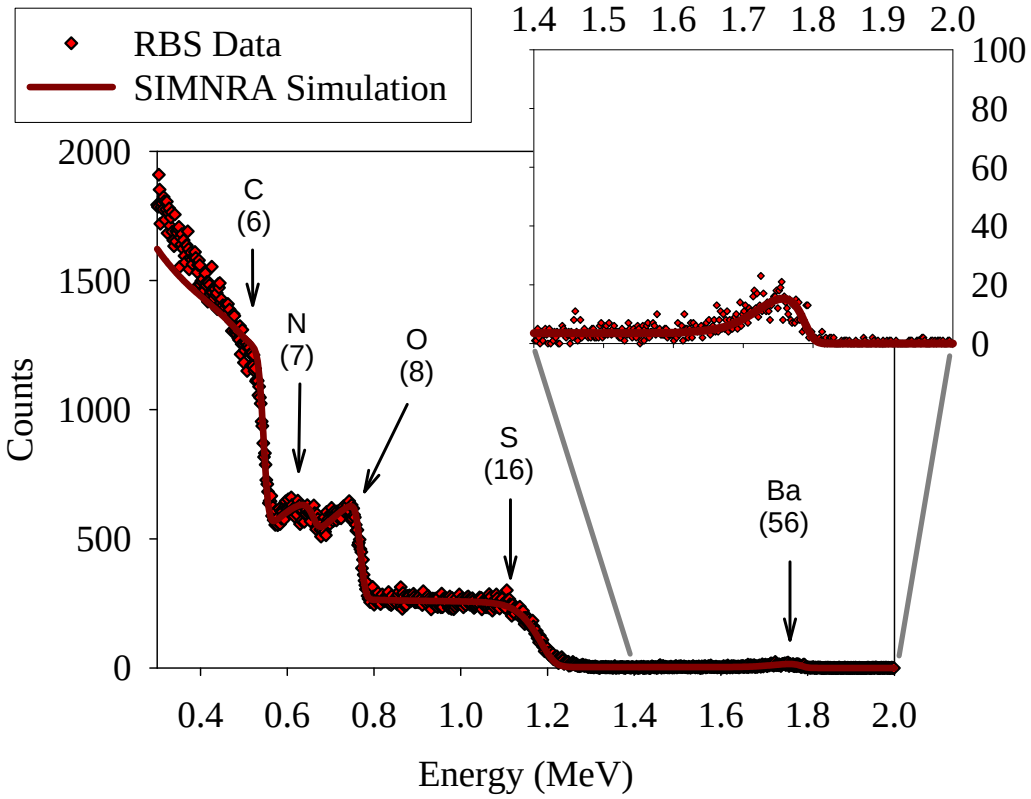
RBS Data
SIMNRA Simulation
Counts
Energy (MeV)
C (6)
N (7)
O (8)
S (16)
Ba (56)

**18Ba**

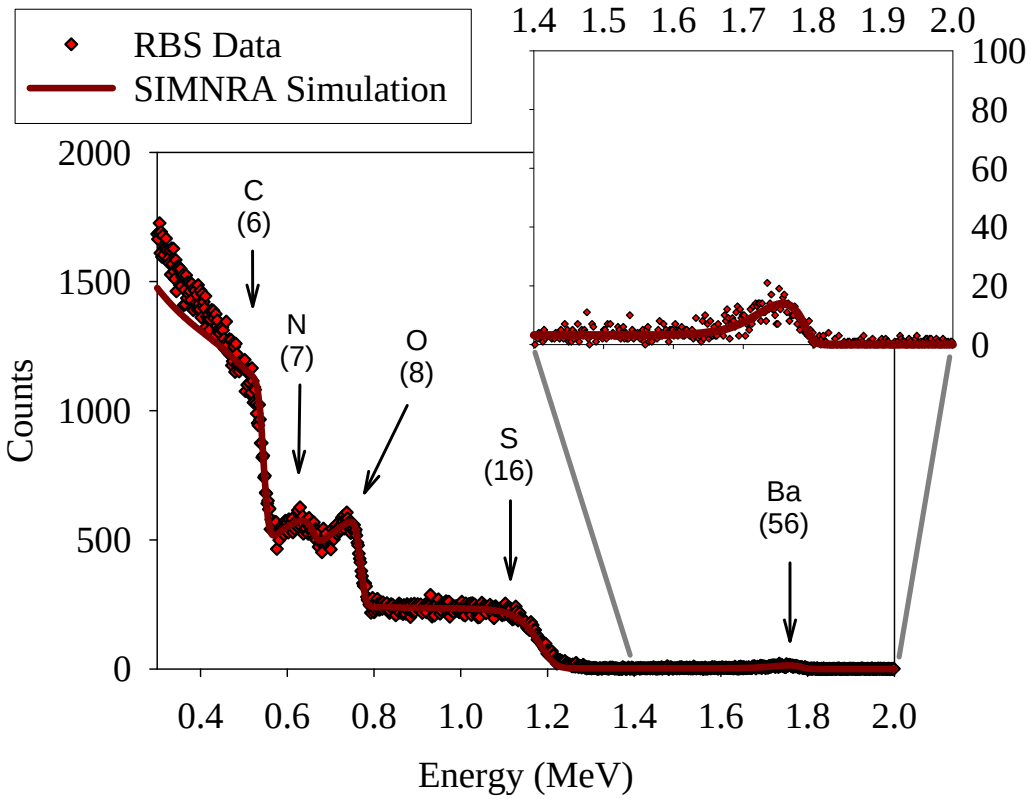
RBS Data
SIMNRA Simulation
Counts
Energy (MeV)
C (6)
N (7)
O (8)
S (16)
Ba (56)

**19Ba**

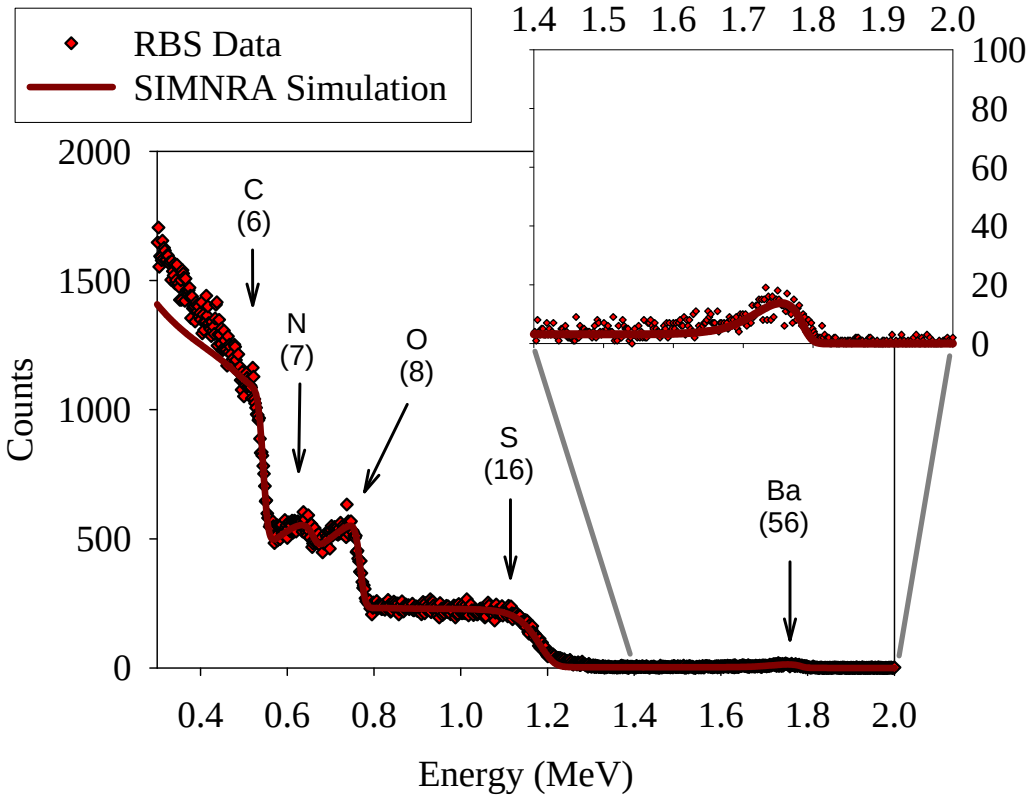
RBS Data
SIMNRA Simulation
Counts
Energy (MeV)
C (6)
N (7)
O (8)
S (16)
Ba (56)

**20Ba**

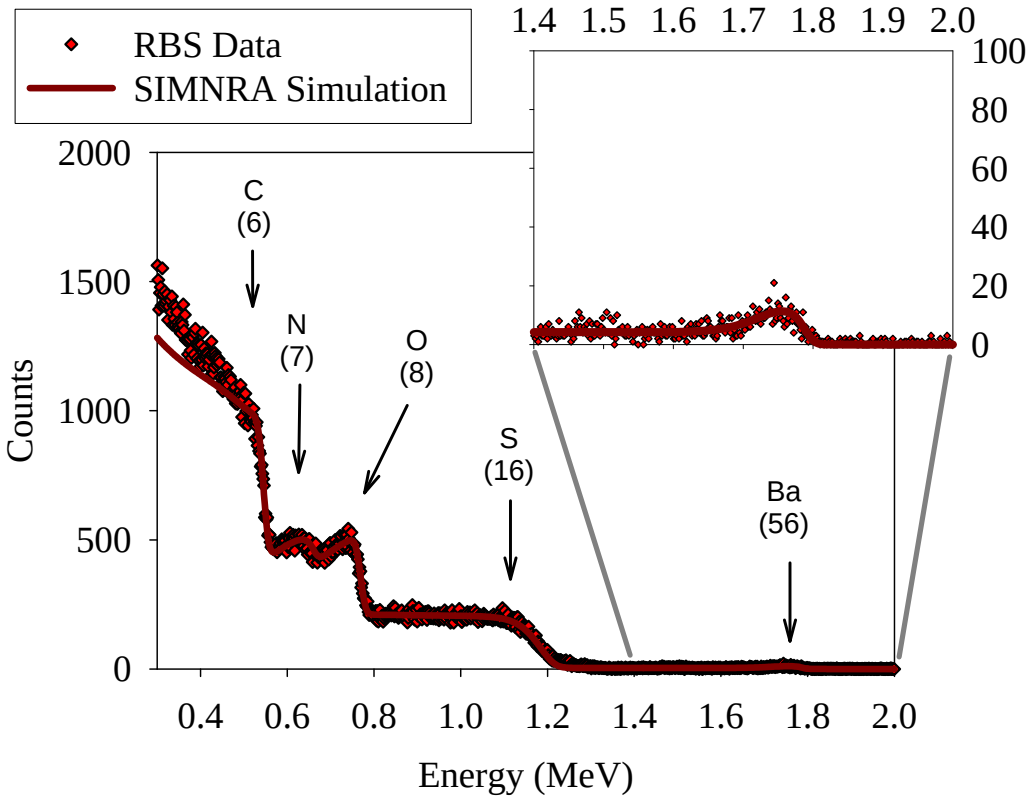
RBS Data
SIMNRA Simulation
Counts
Energy (MeV)
C (6)
N (7)
O (8)
S (16)
Ba (56)

**21Ba**

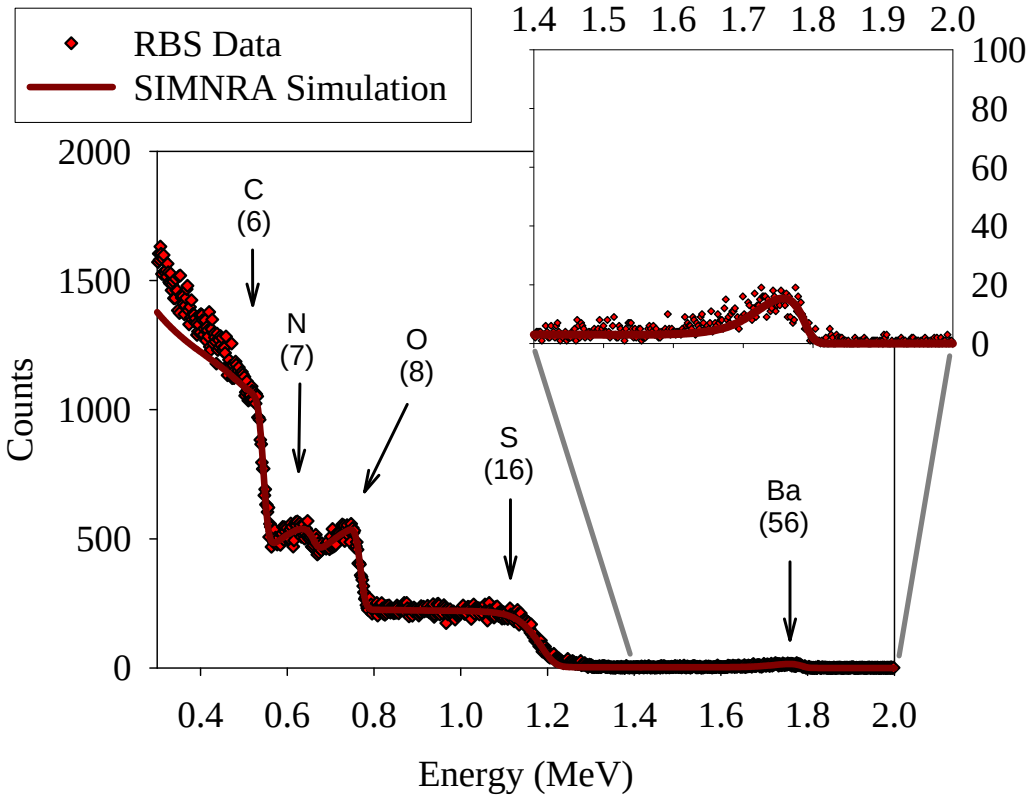
RBS Data
SIMNRA Simulation
Counts
Energy (MeV)
C
(6)
N
(7)
O
(8)
S
(16)
Ba
(56)
2000
1500
1000
500
0
0.4
0.6
0.8
1.0
1.2
1.4
1.6
1.8
2.0
1.4
1.5
1.6
1.7
1.8
1.9
2.0
100
80
60
40
20
0

*Appendix C.2.4. Re-analysis of Rutherford Backscattering Spectrometry (RBS) Data of FT30 Reverse Osmosis (RO) Membrane Samples Used for the Study of the Stoichiometry of Association between Barium ($Ba^{2+}$) Ion and Carboxylate ($R\text{-}COO^{-}$) Groups*

| | FT30-L2 | | | | | |
|---|---|---|---|---|---|---|
| | **Ionic exchange of Ag+ for Ba++ pH = 9.51** | | | | | |
| | **Treatment** | **pH1/pH2/pH3/pH4** | **Ba++ elemental ratio** | **Ba++ concentration [M]** | **Ag+ elemental ratio** | **Ag+ concentration [M]** |
| **1IX** | **FT30+IX 9.5** | 9.48/9.47/9.56/9.51 | 0.00050 | 0.06904 | 0.00118 | 0.16293 |
| **2IX** | | 9.48/9.47/9.56/9.51 | 0.00051 | 0.07042 | 0.00105 | 0.14498 |
| **3IX** | | 9.48/9.47/9.56/9.51 | 0.00054 | 0.07456 | 0.00125 | 0.17260 |
| | | | **Average** | 0.07134 | **Average** | 0.16017 |
| | | | **Std deviation** | 0.00287 | **Std deviation** | 0.01401 |
| | | | **(Std dev/Mean) x100** | 4.03 | **(Std dev/Mean) x100** | 8.75 |

| | **Ag+ pH = 9.53** | | | |
|---|---|---|---|---|
| | **Treatment** | **pH max/pH min/pH final** | **Ag+ elemental ratio** | **Ag+ concentration [M]** |
| **4IX** | **FT30+Ag 9.5** | 9.56/9.50/9.50 | 0.00197 | 0.27202 |
| **5IX** | | 9.60/9.48/9.53 | 0.00205 | 0.28306 |
| **6IX** | | 9.60/9.48/9.53 | 0.00192 | 0.26511 |
| | | | **Average** | 0.27340 |
| | | | **Std deviation** | 0.00905 |
| | | | **(Std dev/Mean) x100** | 3.31 |

**FT30-L3**

**Ionic exchange of Ag+ for Ba++ pH = 9.48**

| | Treatment | pH1/pH2/pH3/pH4 | Ba++ elemental ratio | Ba++ concentration [M] | Ag+ elemental ratio | Ag+ concentration [M] |
|---|---|---|---|---|---|---|
| 7IX | FT30+IX 9.5 | 9.90/9.44/9.52/9.48 | 0.00062 | 0.08561 | 0.00083 | 0.11461 |
| 8IX | | 9.90/9.44/9.52/9.48 | 0.00062 | 0.08561 | 0.00074 | 0.10218 |
| 9IX | | 9.90/9.44/9.52/9.48 | 0.00057 | 0.07871 | 0.00074 | 0.10218 |
| | | | **Average** | 0.08331 | **Average** | 0.10632 |
| | | | **Std deviation** | 0.00399 | **Std deviation** | 0.00717 |
| | | | **(Std dev/Mean) x100** | 4.78 | **(Std dev/Mean) x100** | 6.75 |

**Ag+ pH = 9.52**

| | Treatment | pH max/pH min/pH final | Ag+ elemental ratio | Ag+ concentration [M] |
|---|---|---|---|---|
| 10IX | FT30+Ag 9.5 | 9.52/9.35/9.52 | 0.00178 | 0.24578 |
| 11IX | | 9.52/9.35/9.52 | 0.00175 | 0.24164 |
| 12IX | | 9.52/9.35/9.52 | 0.00183 | 0.25269 |
| | | | **Average** | 0.24670 |
| | | | **Std deviation** | 0.00558 |
| | | | **(Std dev/Mean) x100** | 2.26 |

**FT30-L4**

**Ionic exchange of Ag+ for Ba++ pH = 7.58**

| | Treatment | pH1/pH2/pH3/pH4 | Ba++ elemental ratio | Ba++ concentration [M] | Ag+ elemental ratio | Ag+ concentration [M] |
|---|---|---|---|---|---|---|
| 13IX | FT30+IX 7.5 | 8.05/7.45/7.72/7.58 | 0.00036 | 0.04971 | 0.00038 | 0.05247 |
| 14IX | | 8.05/7.45/7.72/7.58 | 0.00034 | 0.04695 | 0.00038 | 0.05247 |
| 15IX | | 8.05/7.45/7.72/7.58 | 0.00032 | 0.04419 | 0.00046 | 0.06352 |
| | | | **Average** | 0.04695 | **Average** | 0.05615 |
| | | | **Std deviation** | 0.00276 | **Std deviation** | 0.00638 |
| | | | **(Std dev/Mean) x100** | 5.88 | **(Std dev/Mean) x100** | 11.36 |

**Ag+ pH = 7.54**

| | Treatment | pH max/pH min/pH final | Ag+ elemental ratio | Ag+ concentration [M] |
|---|---|---|---|---|
| 16IX | FT30+Ag 7.5 | 7.54/6.60/7.54 | 0.00088 | 0.12151 |
| 17IX | | 7.54/6.60/7.54 | 0.00089 | 0.12289 |
| 18IX | | 7.54/6.60/7.54 | 0.00083 | 0.11461 |
| | | | **Average** | 0.11967 |
| | | | **Std deviation** | 0.00444 |
| | | | **(Std dev/Mean) x100** | 3.71 |

**FT30-L5**

**Ionic exchange of Ag+ for Ba++ pH = 7.50**

| | Treatment | pH1/pH2/pH3/pH4 | Ba++ elemental ratio | Ba++ concentration [M] | Ag+ elemental ratio | Ag+ concentration [M] |
|---|---|---|---|---|---|---|
| 19IX | FT30+IX 7.5 | 8.25/7.49/7.51/7.50 | 0.00034 | 0.04695 | 0.00043 | 0.05937 |
| 20IX | | 8.25/7.49/7.51/7.50 | 0.00037 | 0.05109 | 0.00039 | 0.05385 |
| | | | **Average** | 0.04902 | **Average** | 0.05661 |
| | | | **Std deviation** | 0.00293 | **Std deviation** | 0.00391 |
| | | | **(Std dev/Mean) x100** | 5.98 | **(Std dev/Mean) x100** | 6.90 |

**Ag+ pH = 7.40**

| | Treatment | pH max/pH min/pH final | Ag+ elemental ratio | Ag+ concentration [M] |
|---|---|---|---|---|
| 21IX | FT30+Ag 7.5 | 7.65/7.05/7.40 | 0.00090 | 0.12427 |
| 22IX | | 7.65/7.05/7.40 | 0.00085 | 0.11737 |
| 23IX | | 7.65/7.05/7.40 | 0.00085 | 0.11737 |
| | | | **Average** | 0.11967 |
| | | | **Std deviation** | 0.00399 |
| | | | **(Std dev/Mean) x100** | 3.33 |

| | Ionic exchange of Ag+ for Ba++ pH = 10.26 | | | | | |
|---|---|---|---|---|---|---|
| | Treatment | pH1/pH2/pH3/pH4 | Ba++ elemental ratio | Ba++ concentration [M] | Ag+ elemental ratio | Ag+ concentration [M] |
| 24IX | FT30+IX 10.5 | 10.38/10.25/10.27/10.26 | 0.00062 | 0.08561 | 0.00187 | 0.25821 |
| 25IX | | 10.38/10.25/10.27/10.26 | 0.00064 | 0.08837 | 0.00195 | 0.26926 |
| | | | Average | 0.08699 | Average | 0.26373 |
| | | | Std deviation | 0.00138 | Std deviation | 0.00552 |
| | | | (Std dev/Mean) x100 | 1.59 | (Std dev/Mean) x100 | 2.09 |

| | Ag+ pH = 10.29 | | | |
|---|---|---|---|---|
| | Treatment | pH max/pH min/pH final | Ag+ elemental ratio | Ag+ concentration [M] |
| 26IX | FT30+Ag 10.5 | 10.35/10.20/10.29 | 0.00285 | 0.39353 |
| 27IX | | 10.35/10.20/10.29 | 0.00307 | 0.42391 |
| | | | Average | 0.40872 |
| | | | Std deviation | 0.01519 |
| | | | (Std dev/Mean) x100 | 3.72 |

**1IX**

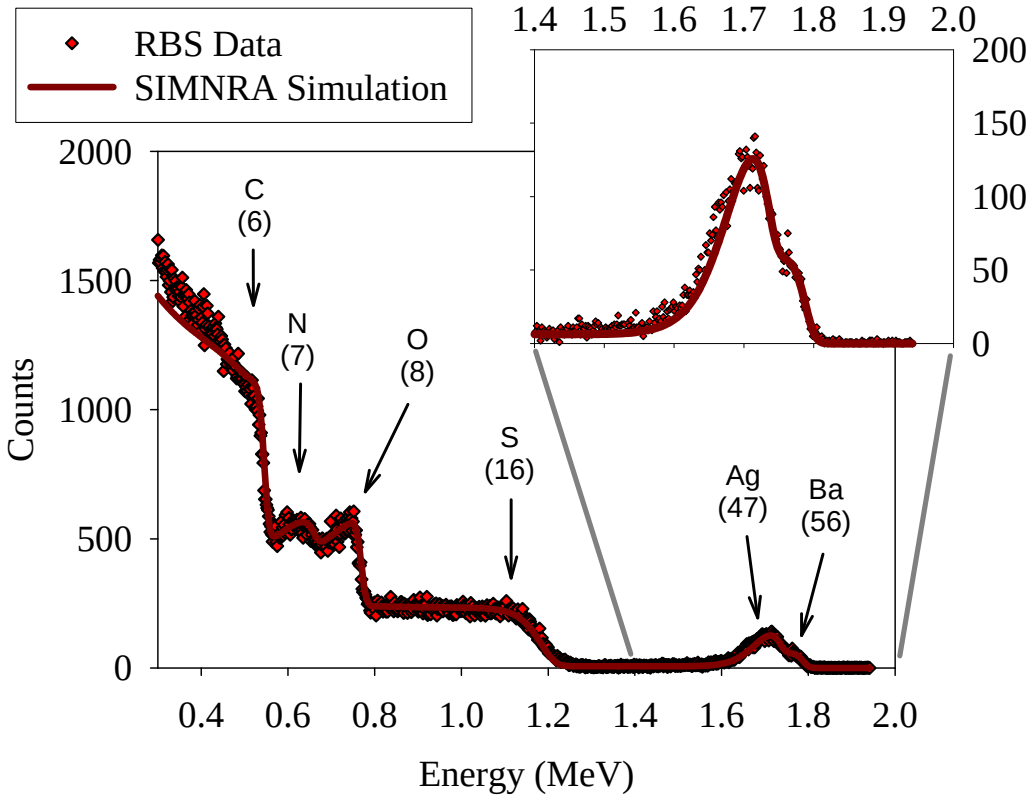
RBS Data
SIMNRA Simulation
Counts
Energy (MeV)
C (6)
N (7)
O (8)
S (16)
Ag (47)
Ba (56)

**2IX**

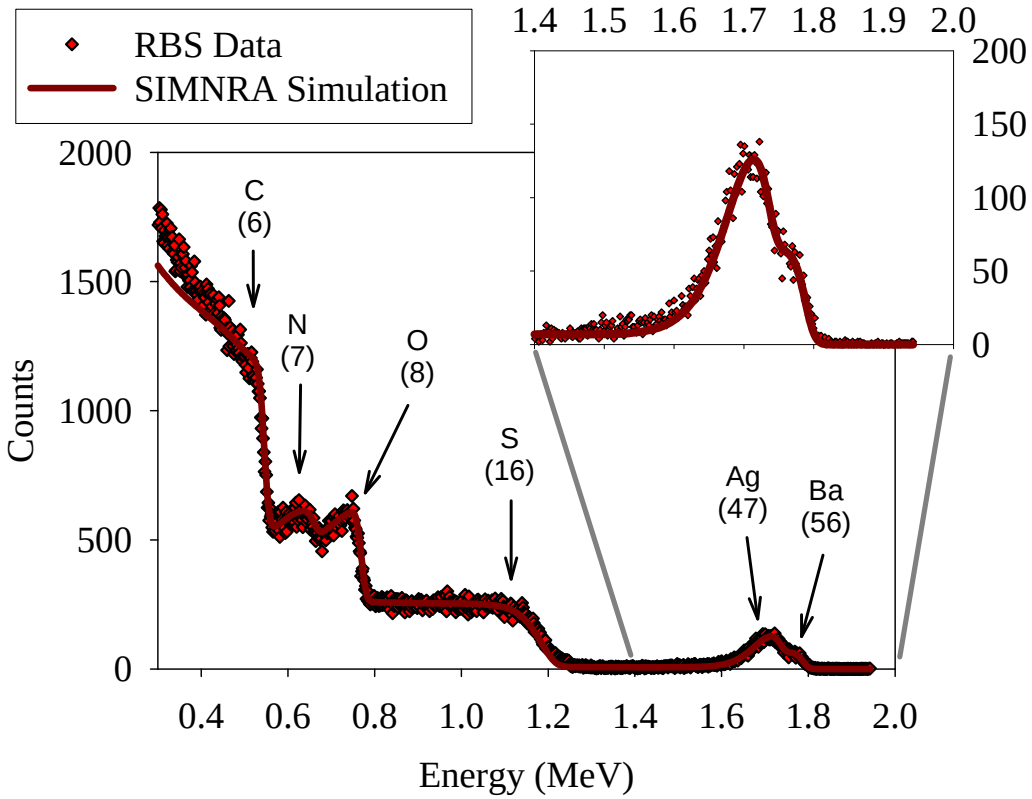
RBS Data
SIMNRA Simulation
Counts
Energy (MeV)
C (6)
N (7)
O (8)
S (16)
Ag (47)
Ba (56)

**3IX**

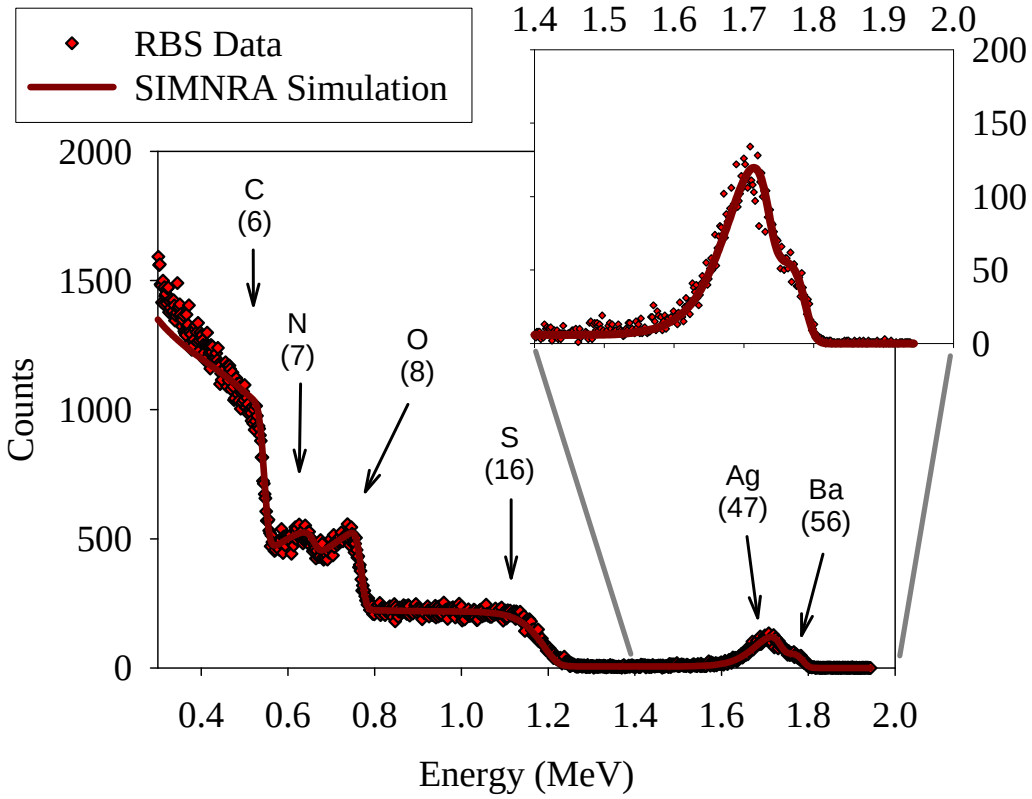
RBS Data
SIMNRA Simulation
Counts
Energy (MeV)
C (6)
N (7)
O (8)
S (16)
Ag (47)
Ba (56)

**4IX**

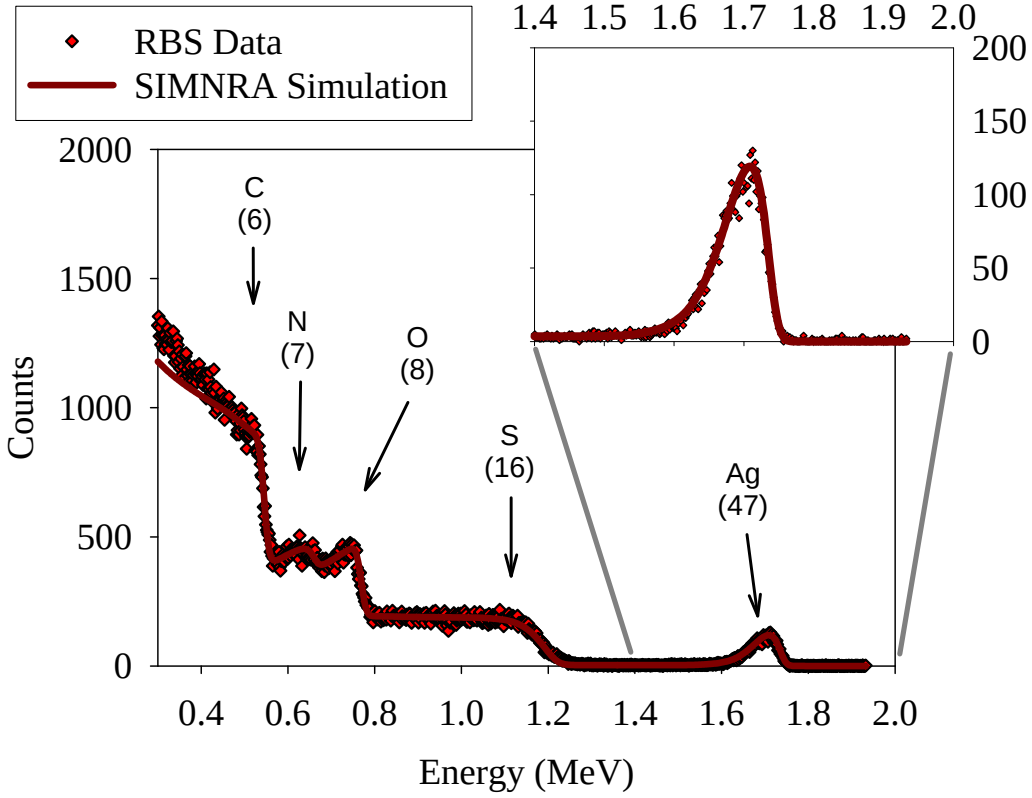
RBS Data
SIMNRA Simulation
Counts
Energy (MeV)
C (6)
N (7)
O (8)
S (16)
Ag (47)

**5IX**

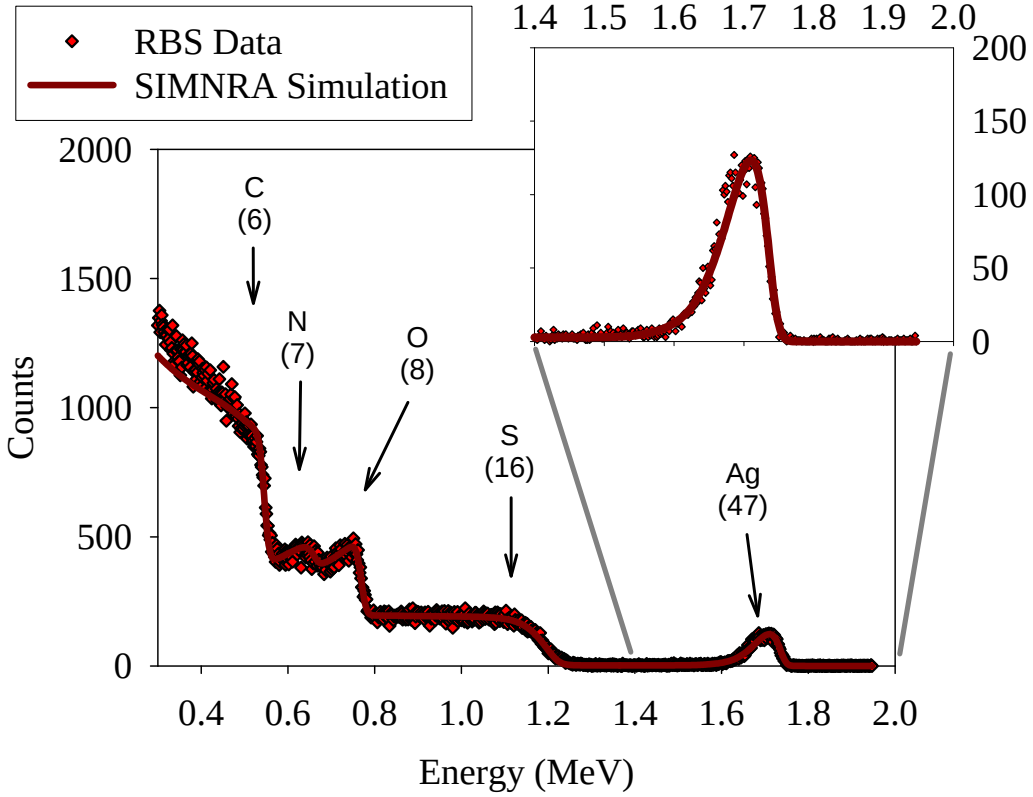
RBS Data
SIMNRA Simulation
Counts
Energy (MeV)
C (6)
N (7)
O (8)
S (16)
Ag (47)

**6IX**

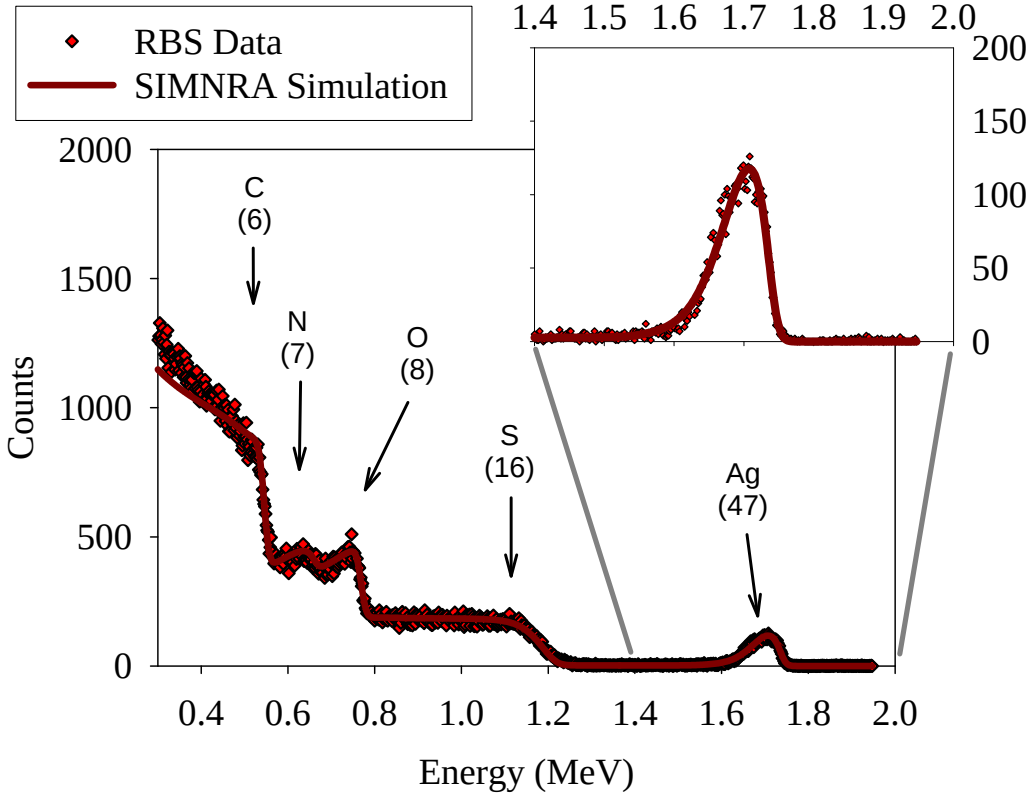
RBS Data
SIMNRA Simulation
Counts
Energy (MeV)
C (6)
N (7)
O (8)
S (16)
Ag (47)

**7IX**

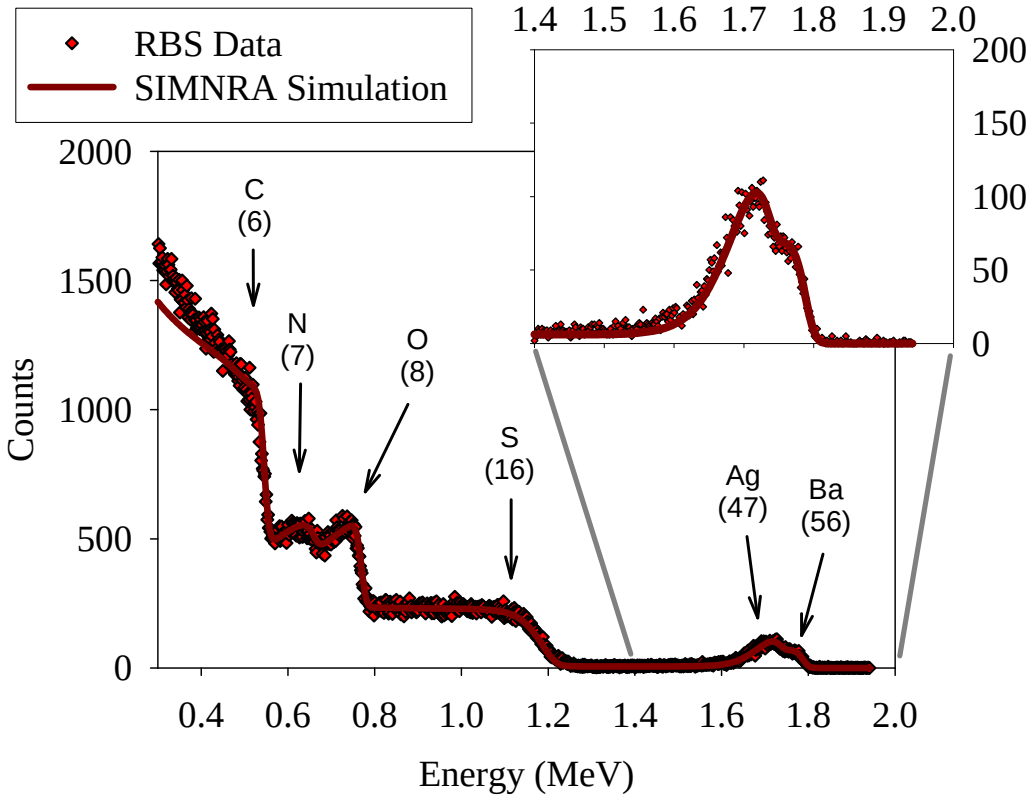
RBS Data
SIMNRA Simulation
Counts
Energy (MeV)
C (6)
N (7)
O (8)
S (16)
Ag (47)
Ba (56)

**8IX**

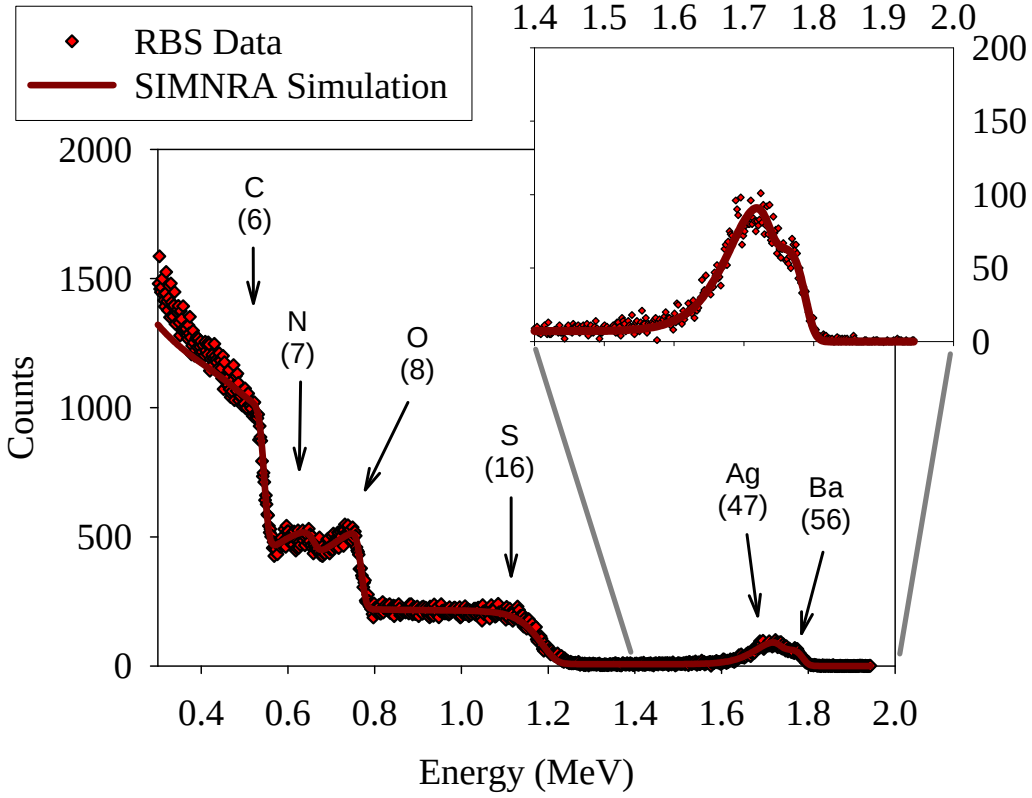
RBS Data
SIMNRA Simulation
Counts
Energy (MeV)
C (6)
N (7)
O (8)
S (16)
Ag (47)
Ba (56)

**9IX**

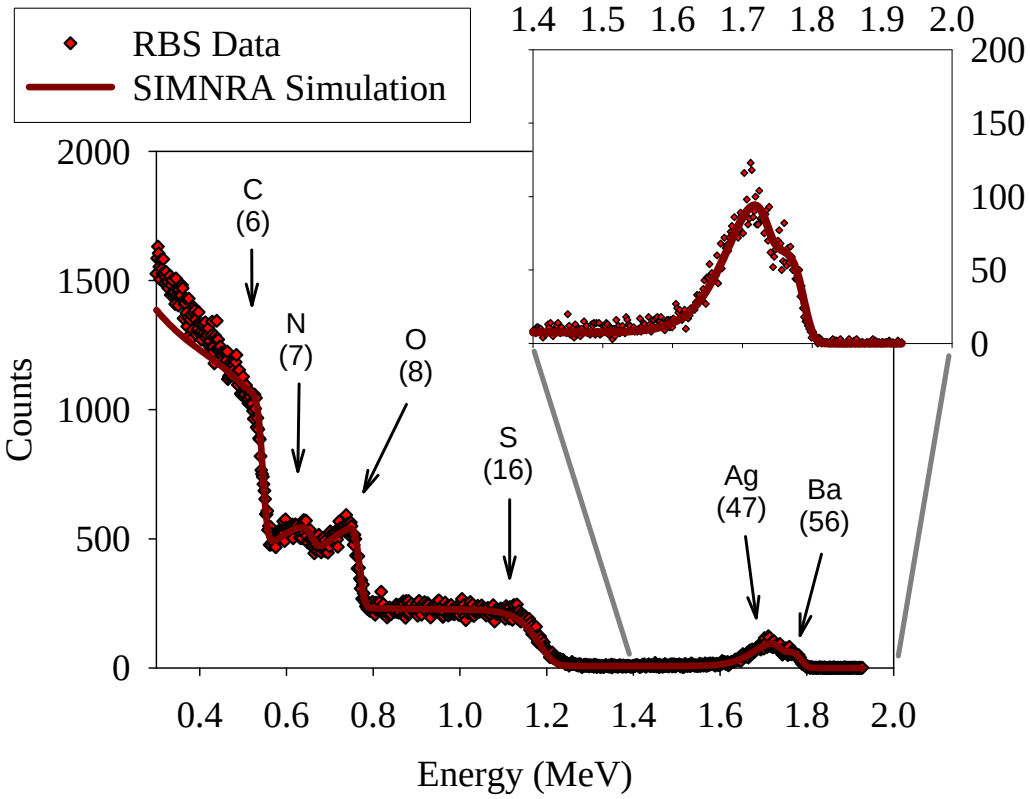
RBS Data
SIMNRA Simulation
Counts
Energy (MeV)
C (6)
N (7)
O (8)
S (16)
Ag (47)
Ba (56)

**10IX**

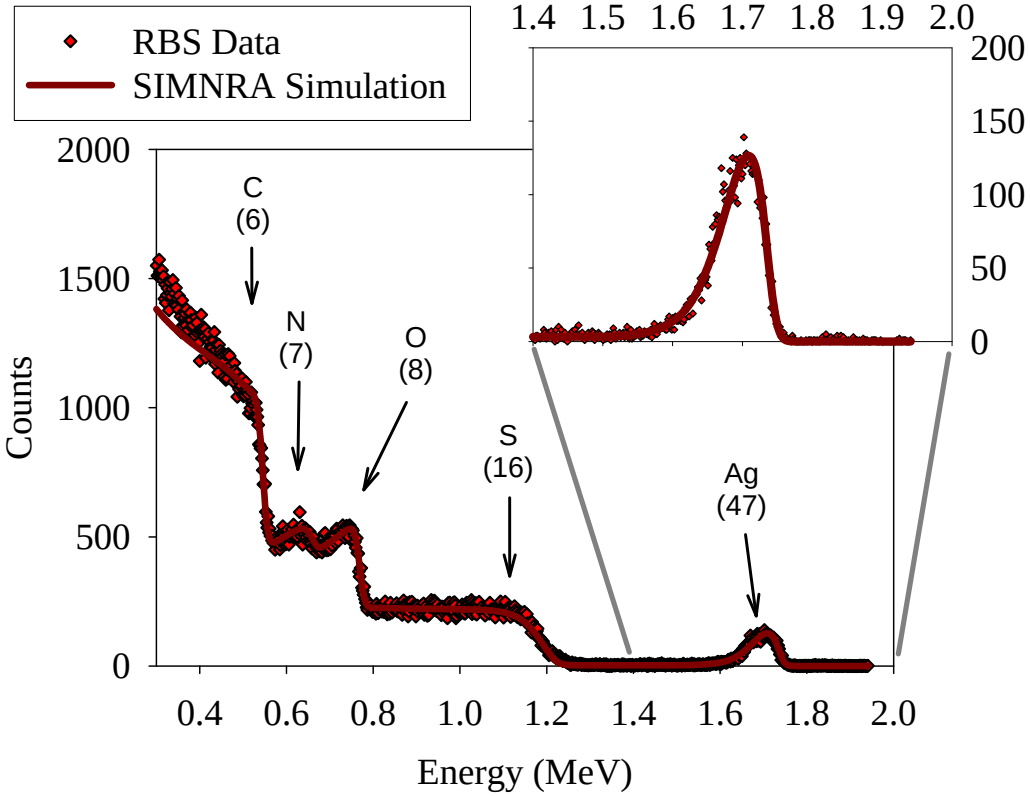
RBS Data
SIMNRA Simulation
Counts
Energy (MeV)
C (6)
N (7)
O (8)
S (16)
Ag (47)

**11IX**

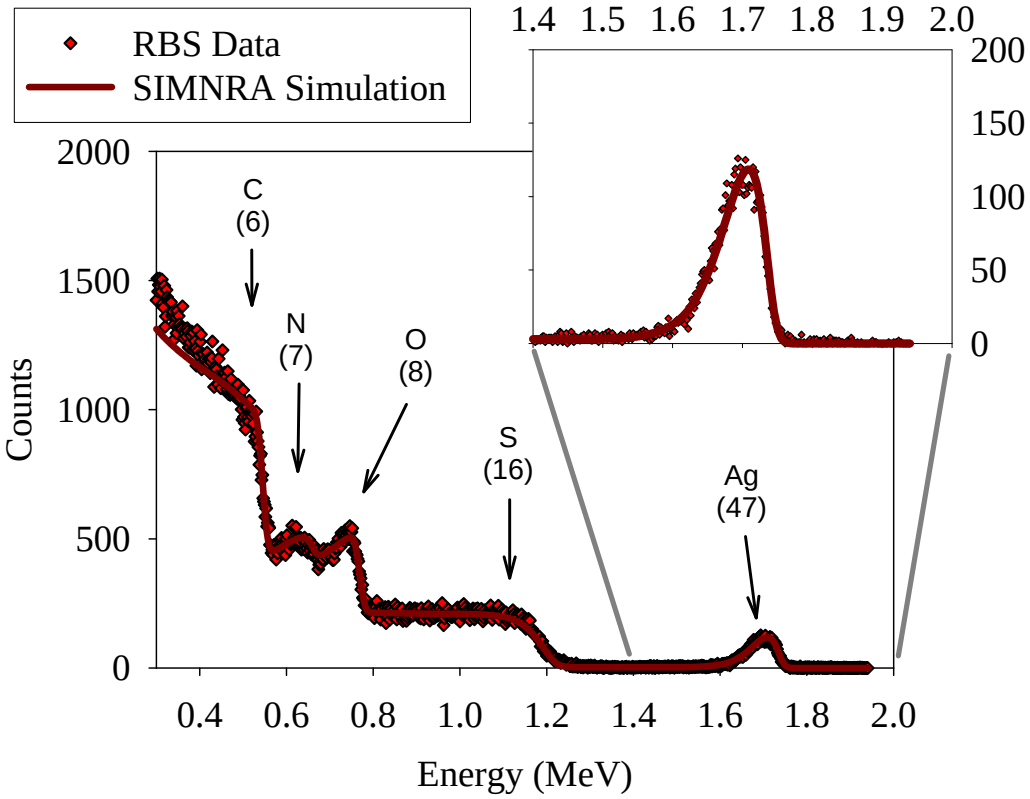
RBS Data
SIMNRA Simulation
Counts
Energy (MeV)
C (6)
N (7)
O (8)
S (16)
Ag (47)

**12IX**

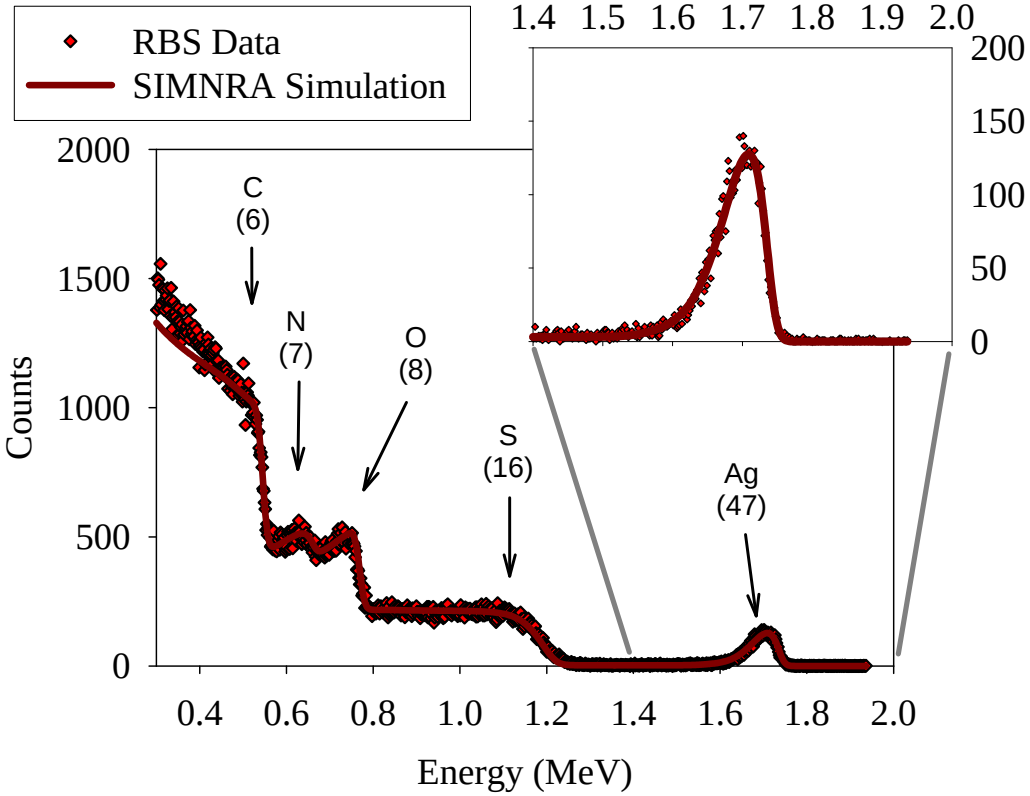
RBS Data
SIMNRA Simulation
Counts
Energy (MeV)
C (6)
N (7)
O (8)
S (16)
Ag (47)

**13IX**

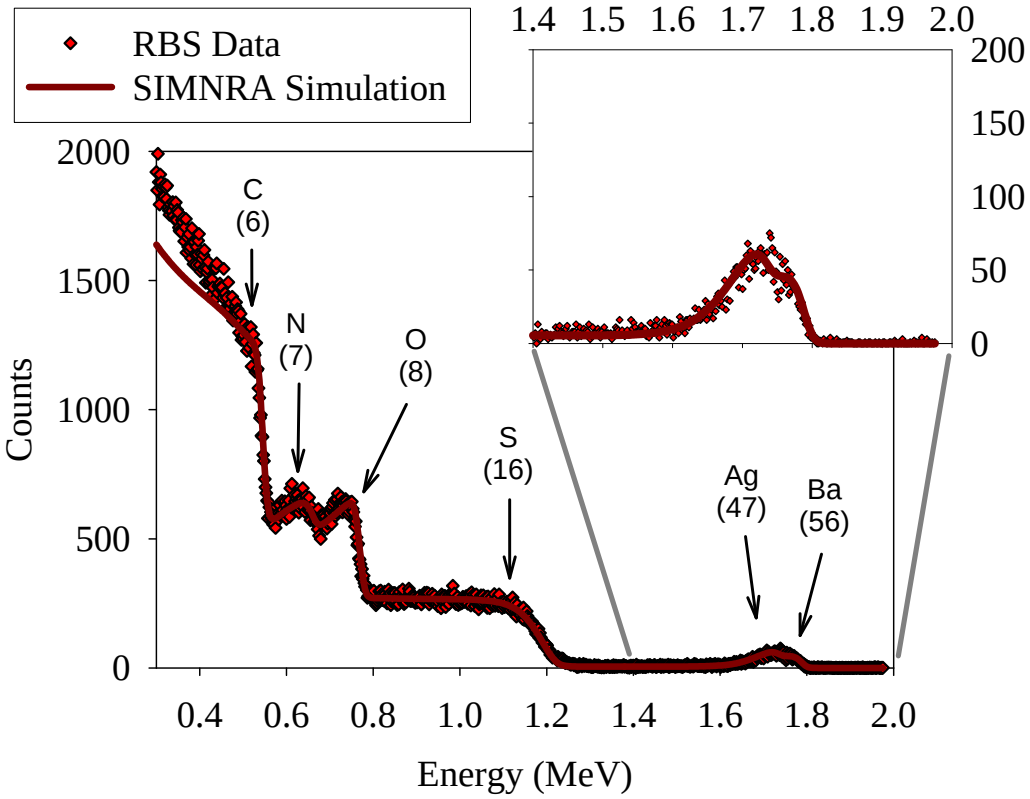
RBS Data
SIMNRA Simulation
Counts
Energy (MeV)
C (6)
N (7)
O (8)
S (16)
Ag (47)
Ba (56)

**14IX**

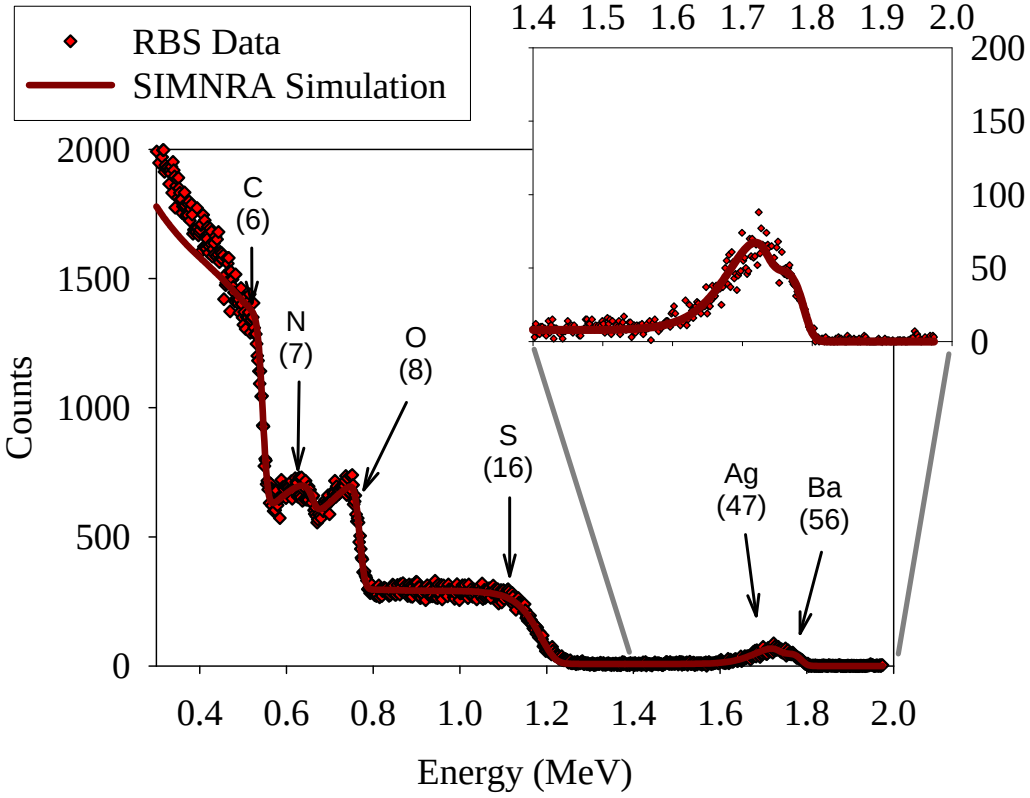
RBS Data
SIMNRA Simulation
Counts
Energy (MeV)
C (6)
N (7)
O (8)
S (16)
Ag (47)
Ba (56)

**15IX**

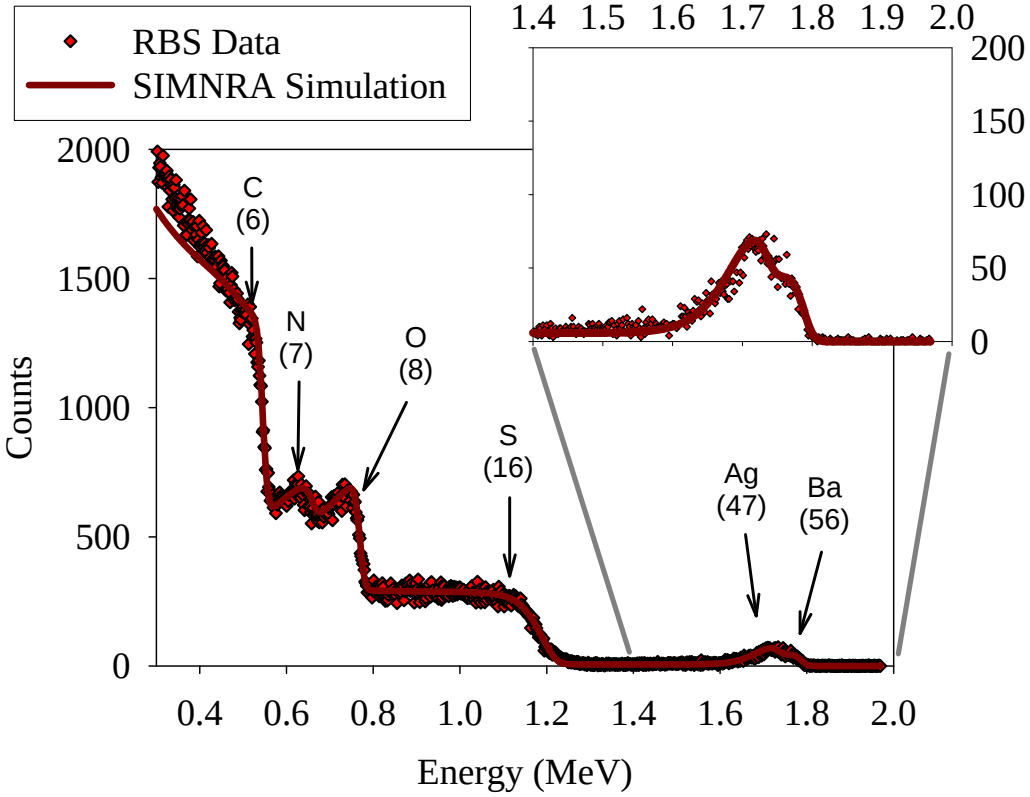
RBS Data
SIMNRA Simulation
Counts
Energy (MeV)
C (6)
N (7)
O (8)
S (16)
Ag (47)
Ba (56)

**16IX**

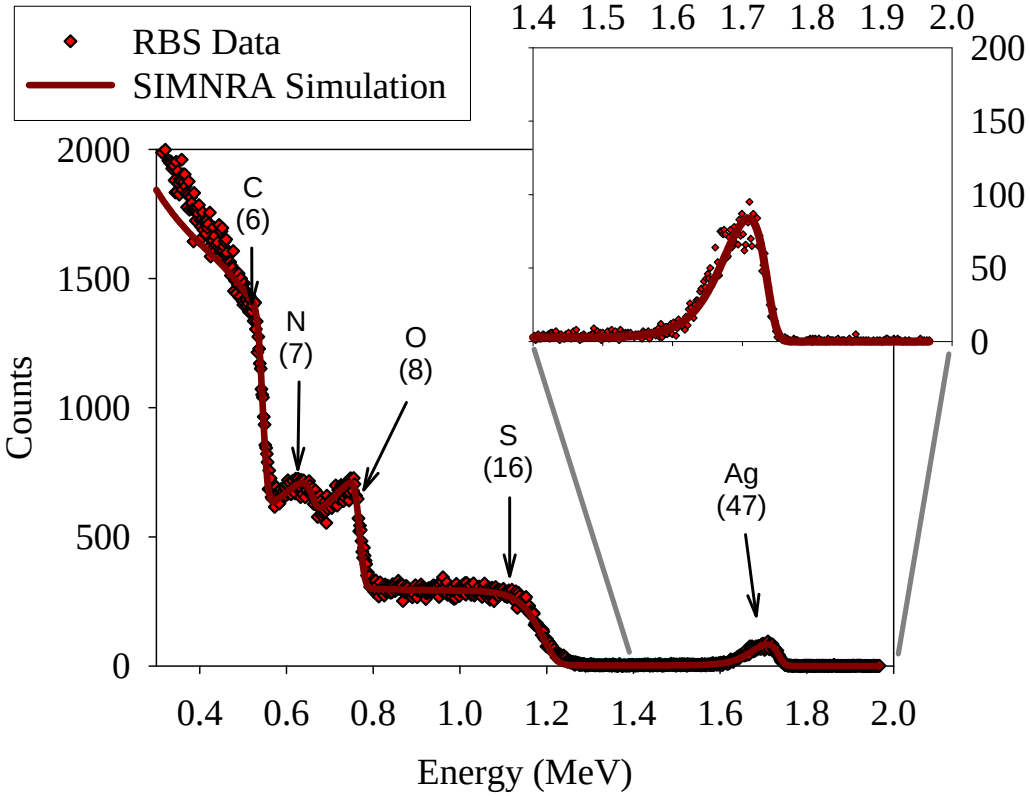
RBS Data
SIMNRA Simulation
Counts
Energy (MeV)
C (6)
N (7)
O (8)
S (16)
Ag (47)

**17IX**

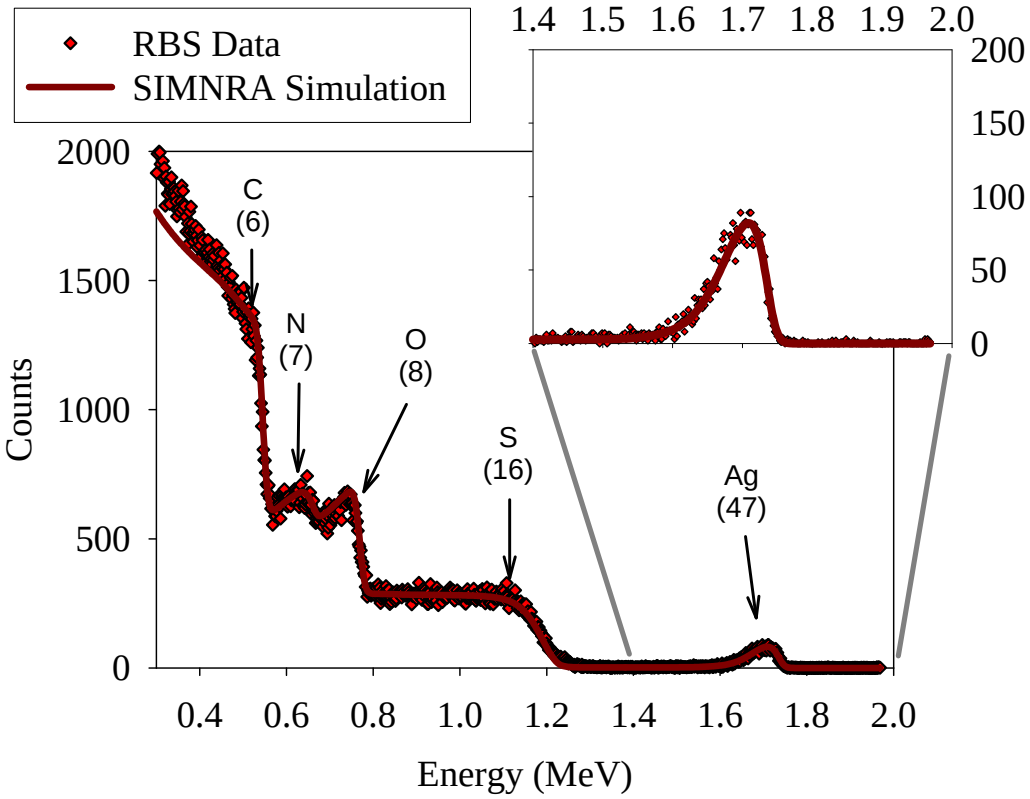
RBS Data
SIMNRA Simulation
Counts
Energy (MeV)
C (6)
N (7)
O (8)
S (16)
Ag (47)

**18IX**

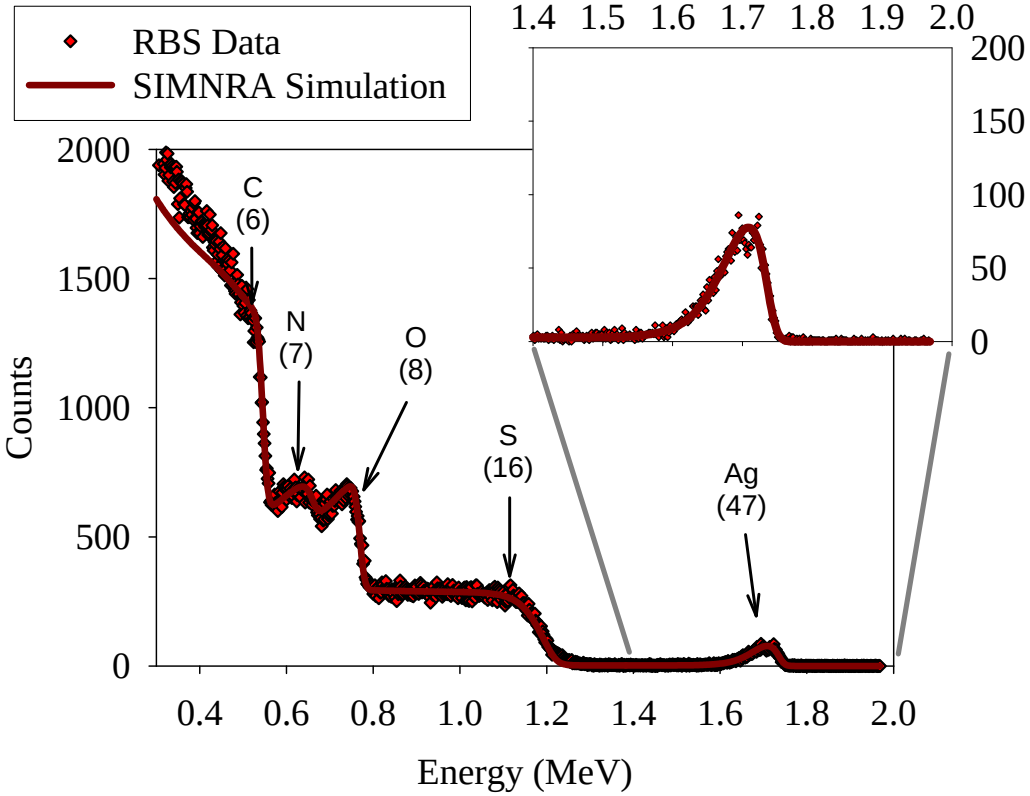
RBS Data
SIMNRA Simulation
Counts
Energy (MeV)
C (6)
N (7)
O (8)
S (16)
Ag (47)

**19IX**

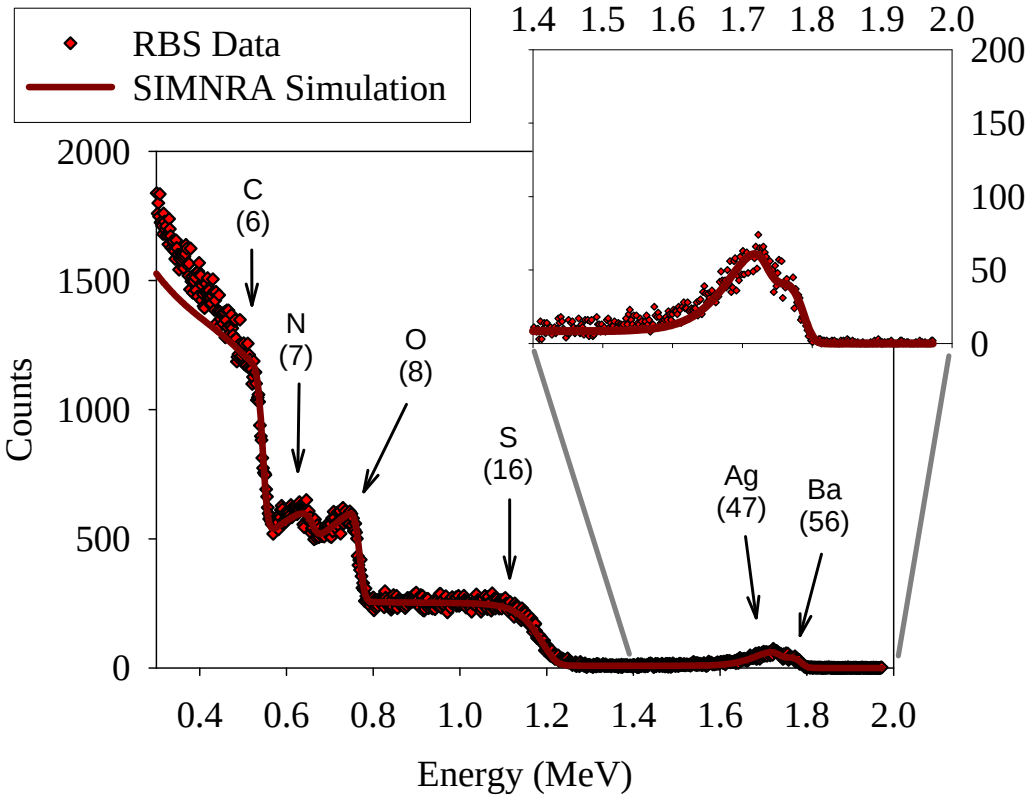
RBS Data
SIMNRA Simulation
Counts
Energy (MeV)
C (6)
N (7)
O (8)
S (16)
Ag (47)
Ba (56)

**20IX**

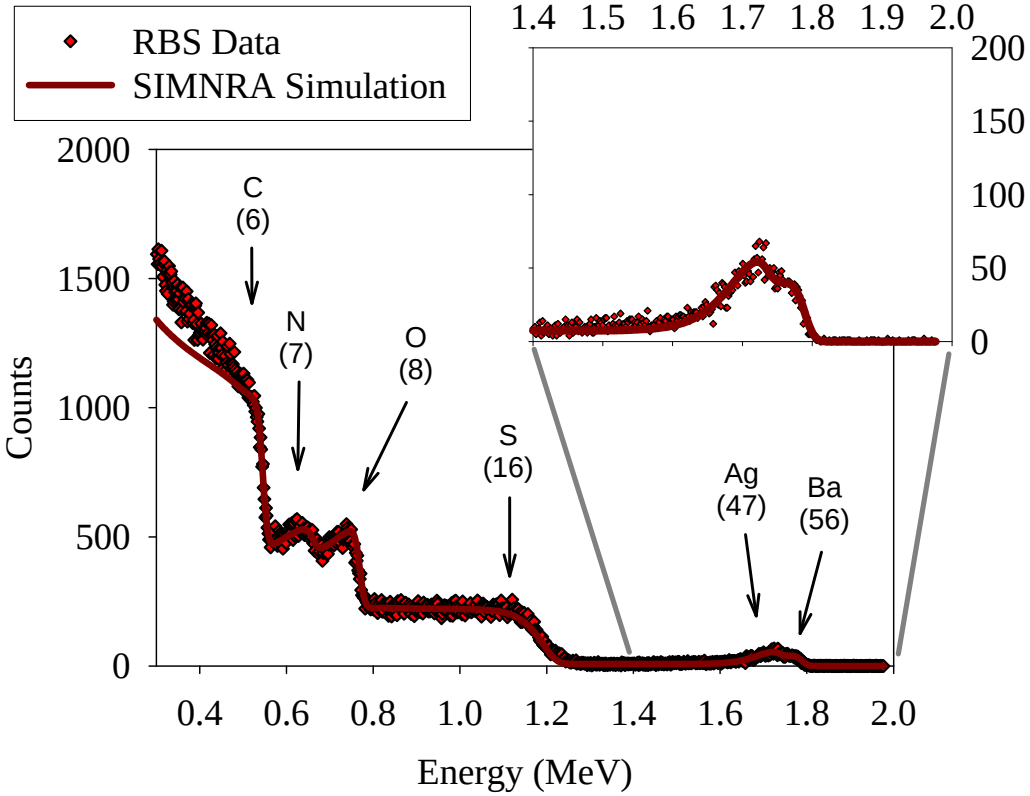
RBS Data
SIMNRA Simulation
Counts
Energy (MeV)
C (6)
N (7)
O (8)
S (16)
Ag (47)
Ba (56)

**21IX**

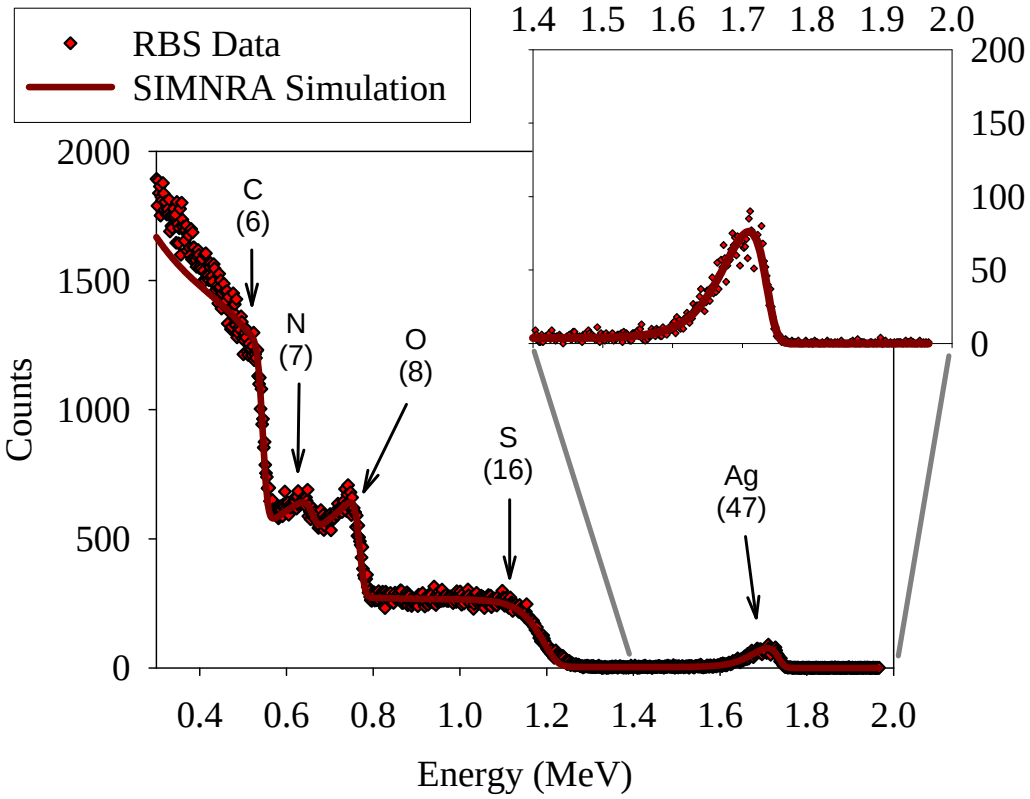
RBS Data
SIMNRA Simulation
Counts
Energy (MeV)
C (6)
N (7)
O (8)
S (16)
Ag (47)

**22IX**

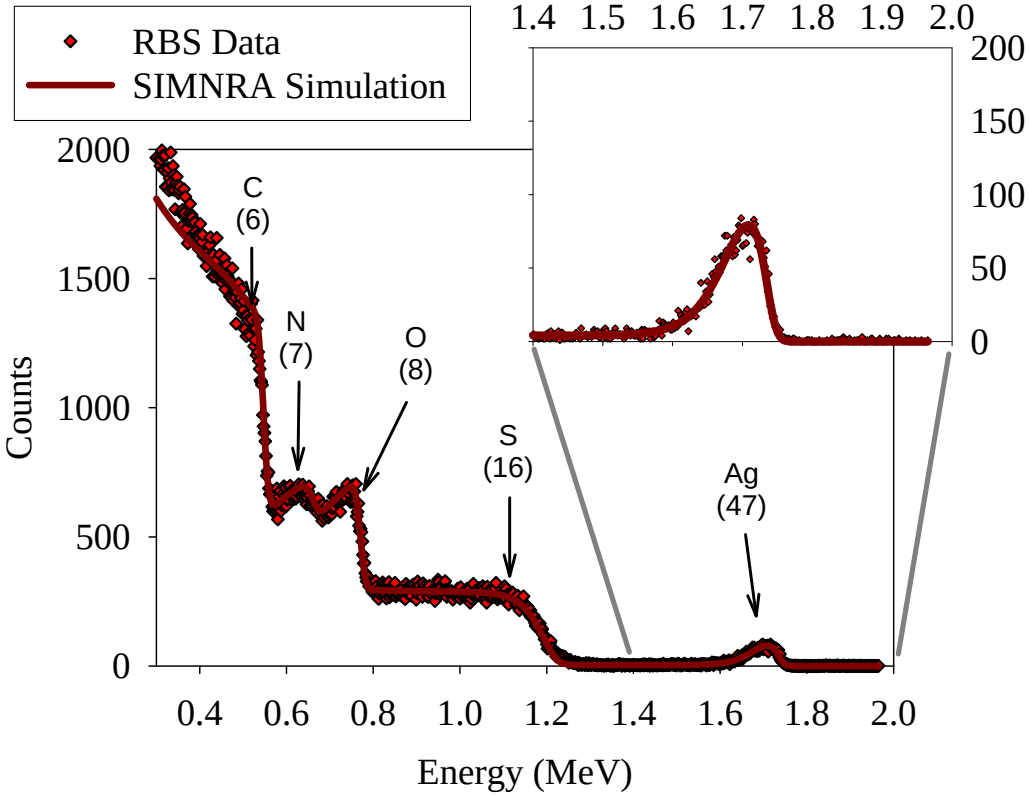
RBS Data
SIMNRA Simulation
Counts
Energy (MeV)
C (6)
N (7)
O (8)
S (16)
Ag (47)

**23IX**

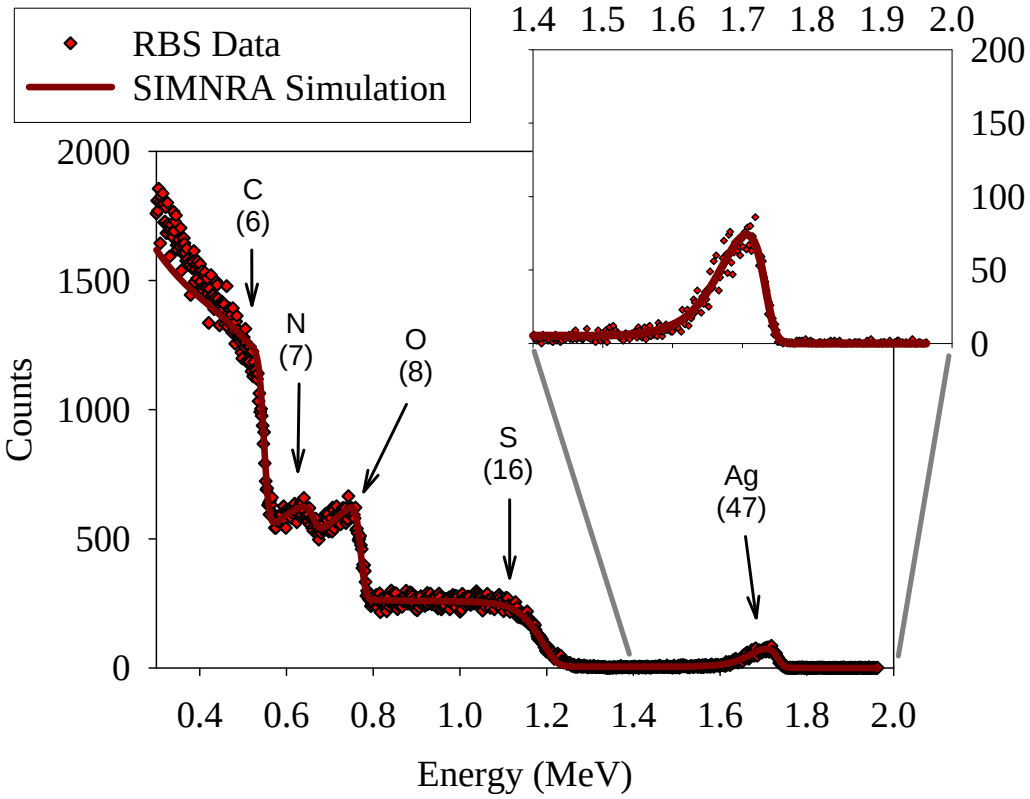
RBS Data
SIMNRA Simulation
Counts
Energy (MeV)
C (6)
N (7)
O (8)
S (16)
Ag (47)

**24IX**

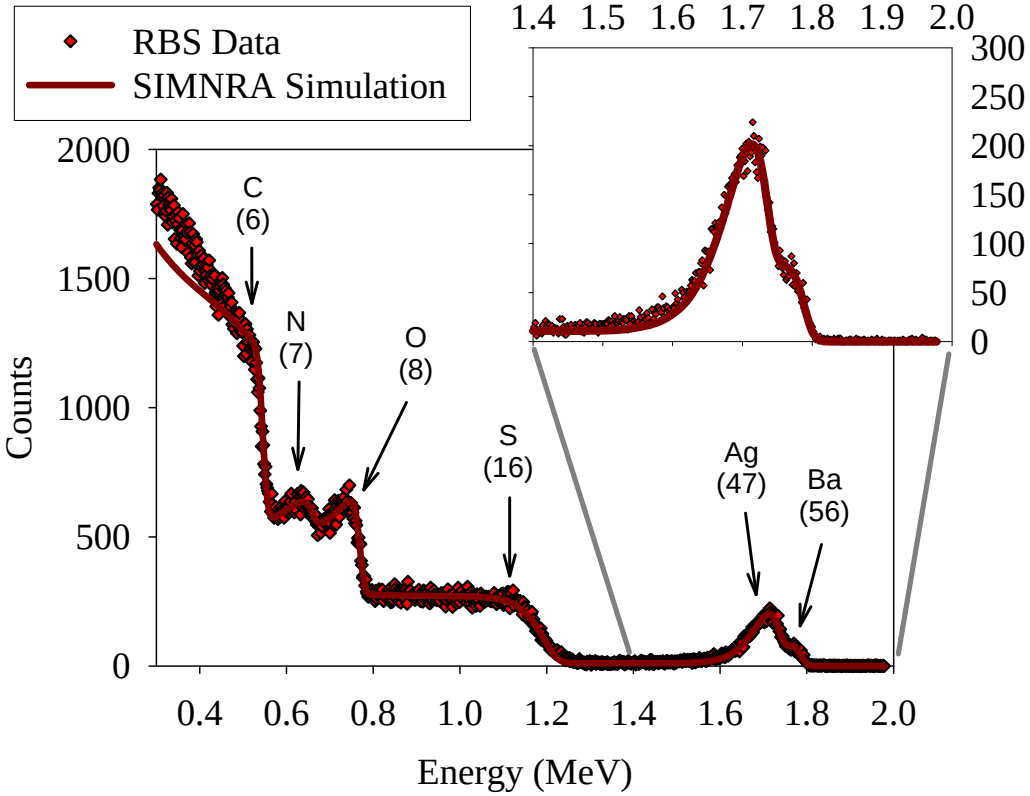
RBS Data
SIMNRA Simulation
Counts
Energy (MeV)
C (6)
N (7)
O (8)
S (16)
Ag (47)
Ba (56)

**25IX**

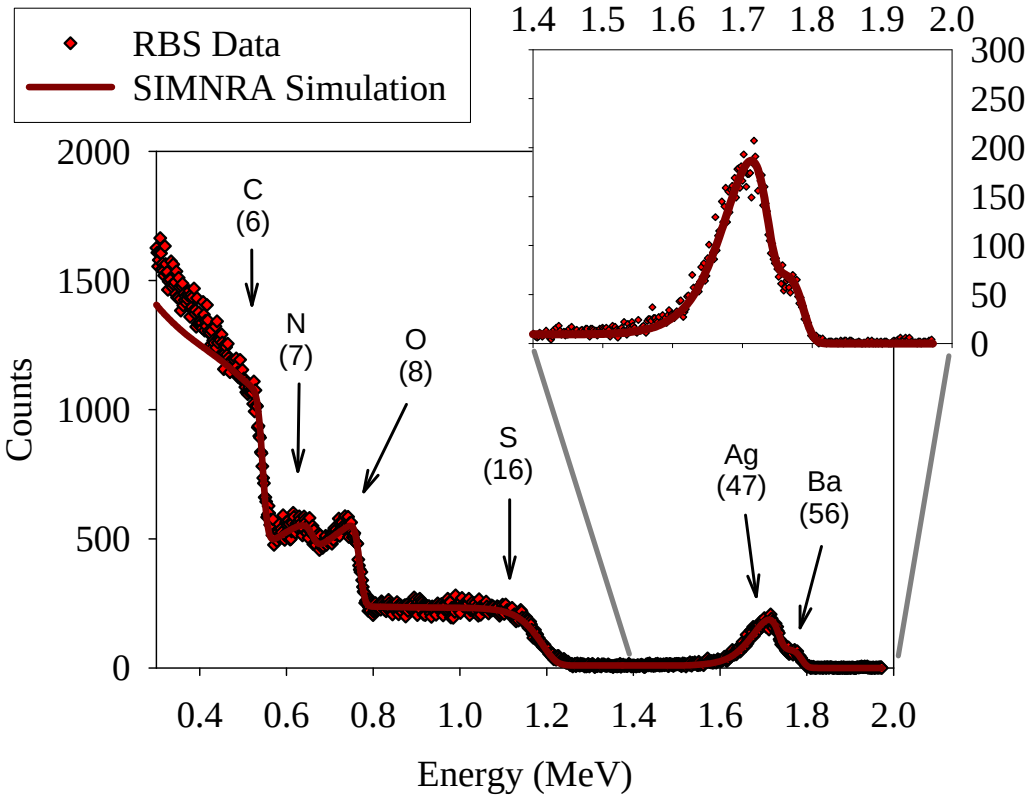
RBS Data
SIMNRA Simulation
Counts
Energy (MeV)
C (6)
N (7)
O (8)
S (16)
Ag (47)
Ba (56)

**26IX**

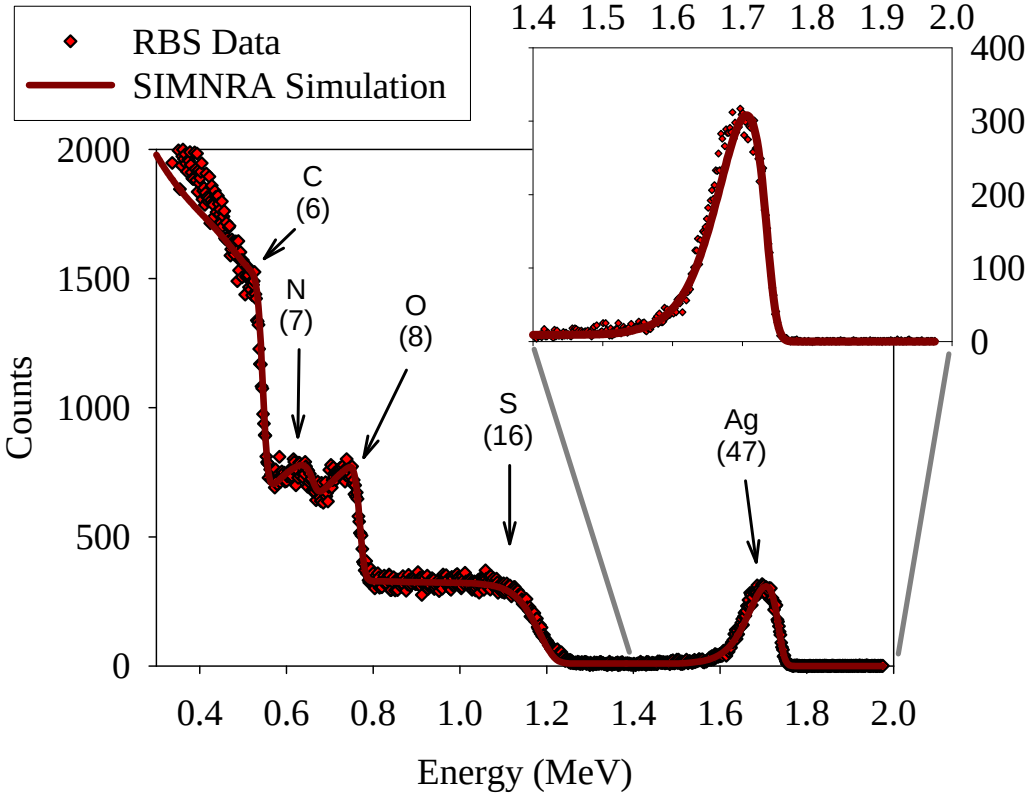
RBS Data
SIMNRA Simulation
Counts
Energy (MeV)
C (6)
N (7)
O (8)
S (16)
Ag (47)

**27IX**

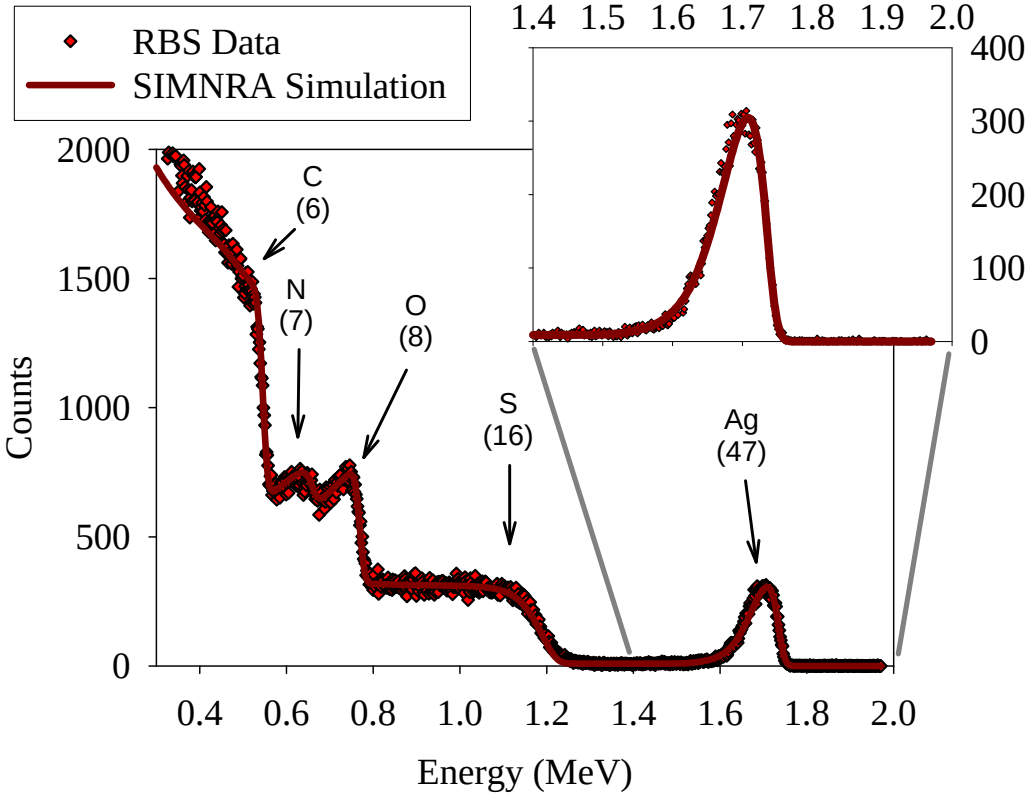
RBS Data
SIMNRA Simulation
Counts
Energy (MeV)
C
(6)
N
(7)
O
(8)
S
(16)
Ag
(47)
2000
1500
1000
500
0
0.4
0.6
0.8
1.0
1.2
1.4
1.6
1.8
2.0
400
300
200
100
0
1.4
1.5
1.6
1.7
1.8
1.9
2.0

# APPENDIX D

# APPENDIX FOR CHAPTER 5

**Supporting Information for Chapter 5**

**Summary of Contents:**

- Fourteen pages
- Section D.1. Calculation of the analysis depth of X-ray photoelectron spectroscopy (XPS) tests.
- Section D.2. Derivation of Equation 5.1 used to calculate the molar concentration of ionized carboxylic groups ($R–COO^-$) in the active layers.
- Figure D.1. Attenuated total reflectance Fourier transform infrared (ATR-FTIR) spectrometry analyses of SWC5 and ESPAB reverse osmosis (RO) membranes.
- Figure D.2. Rutherford backscattering spectrometry (RBS) spectra and corresponding simulations of virgin (a) SWC5 RO and (b) ESPAB RO membranes.
- Figure D.3. XPS signals of the (a) chlorine Cl2p, (b) silver Ag3d, and (c) barium Ba3d photoelectrons in a sample of ESPA3 RO membrane used for $Ag^+$–$Ba^{2+}$ displacement tests.
- Figure D.4. Atomic force microscopy (AFM) images (10×10 μm) of (a) ESPA3 RO, (b) SWC5 RO, (c) TFC–S NF, (d) ESNA NF, (e) ESPAB RO, (f) NF90 NF, (g) FT30 RO, and (h) LF10 RO membranes
- Figure D.5. Stoichiometry of association between the $R–COO^-$ groups neutralized by $Ba^{2+}$ ion in the polyamide (PA) active layers of ESPA3 RO and NF90 NF membranes and the $Ba^{2+}$ ions neutralizing them.
- **Note:** Bibliographic information for references cited in Appendix D can be found in Section 5.6 of this dissertation.

**Section D.1.** Calculation of the analysis depth of X-ray photoelectron spectroscopy (XPS) tests.

The analysis depth of XPS tests can be estimated based on the kinetic energy ($E_{Kinetic}$), take-off angle ($\theta$), and inelastic mean-free path ($\lambda$) of the photoelectrons generated in the test specimen by taking into account that photoelectrons ejected from deeper in the sample have a higher probability of experiencing scattering events on their path to the XPS detector, than those ejected from closer to the surface. Accordingly, the sample depth from which, for example, 95% of the XPS signal is generated ($D_{95\%}$) can be estimated as the travel distance necessary to reduce the intensity (I) of the ejected photoelectrons by 95%. Since the energy of the X-rays (photons) in our setup is $E_{Photon}$ = 1,253.6 eV and the electrons with the lowest binding energies ($E_{Binding}$) in the elements analyzed are ≈285 eV for carbon C1s and ≈200 eV for chlorine Cl2p, then the highest kinetic energy of photoelectrons generated is ≈1,000 eV (i.e., $E_{Kinetic} \approx E_{Photon} - E_{Binding}$, if we neglect the work function of the spectrometer (Briggs, D. *Surface analysis of polymers by XPS and static SIMS*. Cambridge University Press: New York, NY, 1998)). If we assume inelastic scattering only, and take into account that the inelastic mean-free path for a photoelectron with kinetic energy of 1,000 eV in a material with high carbon content is $\lambda \approx 1.8$ nm (Tanuma et al., *Surf. Interface Anal.* 1991, *17*, 911-926), and that the take-off angle of the photoelectrons in our setup is $\theta = 90^{o}$, we can use the Beer-Lambert law to estimate $D_{95\%}$ from the expression, $I/I_0 = 0.05 = \exp(-D/(\cos(90-\theta)\times\lambda))$. We obtain $D_{95\%}$ = 5.4 nm which indicates that 95% of the signal collected during XPS analyses comes from within ≈6 nm of the surface or less. Similar calculations performed for the silver Ag3d (≈367 eV) and barium Ba3d (≈780 eV) electrons indicate that 95% of their signals come from within ≈3 nm and ≈5 nm, respectively, of the sample surface or less.

**Section D.2.** Derivation of Equation 5.1 used to calculate the molar concentration of ionized carboxylic groups ($R-COO^-$) in the active layers.

From the definitions

$\rho_{PA}$ = 1.24 g/cm$^3$ [26] = Dry mass density of PA,
$\varepsilon_i$ = elemental fraction *including hydrogen* of element i in the active layer, where "*including hydrogen*" means that the summation of the $\varepsilon_i$ values of all elements in the sample including $\varepsilon_H$ equals one (i.e., $\sum \varepsilon_i = 1$), and
$M_i$ = molar mass of element i,

we have that the average mass of a mole of atoms in a fully protonated polyamide (PA) active layer is given by

$\Sigma(\varepsilon_i \times M_i)$,

where i represents any of the elements in the PA film at complete protonation (i.e., C, O, N, Cl, H). The molar concentration of atoms in the fully protonated PA active layer is thus given by

$$\frac{\rho_{PA}}{\sum(\varepsilon_i \times M_i)}$$

and the molar concentration of element j in the PA active layer by

$$\varepsilon_j \times \frac{\rho_{PA}}{\sum(\varepsilon_i \times M_i)}$$

Accordingly, the molar concentration of R–$COO^-$ groups in the active layers ([R–$COO^-$]) can be expressed as

$$[R-COO^-] = [Ag] = \varepsilon_{Ag} \times \frac{\rho_{PA}}{\sum(\varepsilon_i \times M_i)} \quad \text{(D.1)}$$

where it is assumed that the increase in the volume of the fully-aromatic PA active layer because of hydration is negligible, i.e., ≤5% [26]. Since the value of the PA density $\rho_{PA}$ = 1.24 g/$cm^3$ [26] was obtained with a PA active layer that did not contain heavy ions, then the denominator in Equation D.1 (and Equations D.3-D.5) refers to a fully protonated active layer (i.e., in the denominator the silver content is assigned to hydrogen). In other words, Equation D.1 (and Equations D.3-D.5) assumes that the active layer volume remains unchanged after the exchange of protons for $Ag^+$ ions.

If we represent the elemental fraction *excluding hydrogen* of element i in the active layer as $\varepsilon_i'$, where "*excluding hydrogen*" means that the summation of the $\varepsilon_i'$ values of all elements in the sample excluding $\varepsilon_H'$ equals one (i.e., $\sum \varepsilon_i' = 1 + \varepsilon_H'$), then

$$\varepsilon_i' = \frac{\varepsilon_i}{1-\varepsilon_H} \quad \rightarrow \quad \varepsilon_i = \varepsilon_i' \times (1-\varepsilon_H). \quad \text{(D.2)}$$

From Equations D.1 and D.2:

$$[R-COO^-] = \varepsilon_{Ag}' \times \frac{\rho_{PA}}{\sum(\varepsilon_i' \times M_i)} \quad \text{(D.3)}$$

Since only $\varepsilon_H'$ cannot be measured by XPS (Briggs, D. *Surface analysis of polymers by XPS and static SIMS*. Cambridge University Press: New York, NY, 1998) or RBS [18], for convenience Equation D.3 can be re-written as:

$$[R-COO^-] = \varepsilon_{Ag}' \times \frac{\rho_{PA}}{\sum_{C,O,N,Cl}(\varepsilon_i' \times M_i) + (\varepsilon_H'/\varepsilon_C') \times \varepsilon_C' \times M_H} \quad \text{(D.4)}$$

where C and H indicate carbon and hydrogen, respectively.

For the estimation of the H:C = $(\varepsilon_H'/\varepsilon_C')$ ratio in the PA active layer we can take a look at the elemental composition of the polymer repeating units *n*, *x* and *y* in the PA structure that are fully crosslinked $(C_{36}H_{24}N_6O_6)_n$, that contain a carboxylic group $(C_{36}H_{25}N_6O_7)_x$

and that contain an amine group $(C_{36}H_{25}N_6O_6)_y$. If $n$ =1 or $x$ =1, then H:C = 0.67; if $y$ = 1, then H:C =0.69. Keeping in mind that $n+x+y$ =1, and that from our previous studies [4] we know that in fully-aromatic PA active layers $y_{max} \approx 0.05$, then H:C = 0.67 is a safe assumption regardless of the value of the $n$, $x$ and $y$ fractions. Moreover, even if the active layer or only its surface were a linear polyamide ($C_{15}H_{10}N_2O_4$) [31], as opposed to a crosslinked polyamide, the H:C ratio would be H:C = 0.67. Accordingly, $(\varepsilon_H^{'}/\varepsilon_C^{'})$ =0.67 and Equation D.6 becomes

$$[R-COO^{-}] = \varepsilon_{Ag}^{'} \times \frac{\rho_{PA}}{\sum_{C,O,N,Cl}\left(\varepsilon_i^{'} \times M_i\right) + 0.67 \times \varepsilon_C^{'} \times M_H} \qquad (D.5)$$

which corresponds to Equation 5.1 in the manuscript.

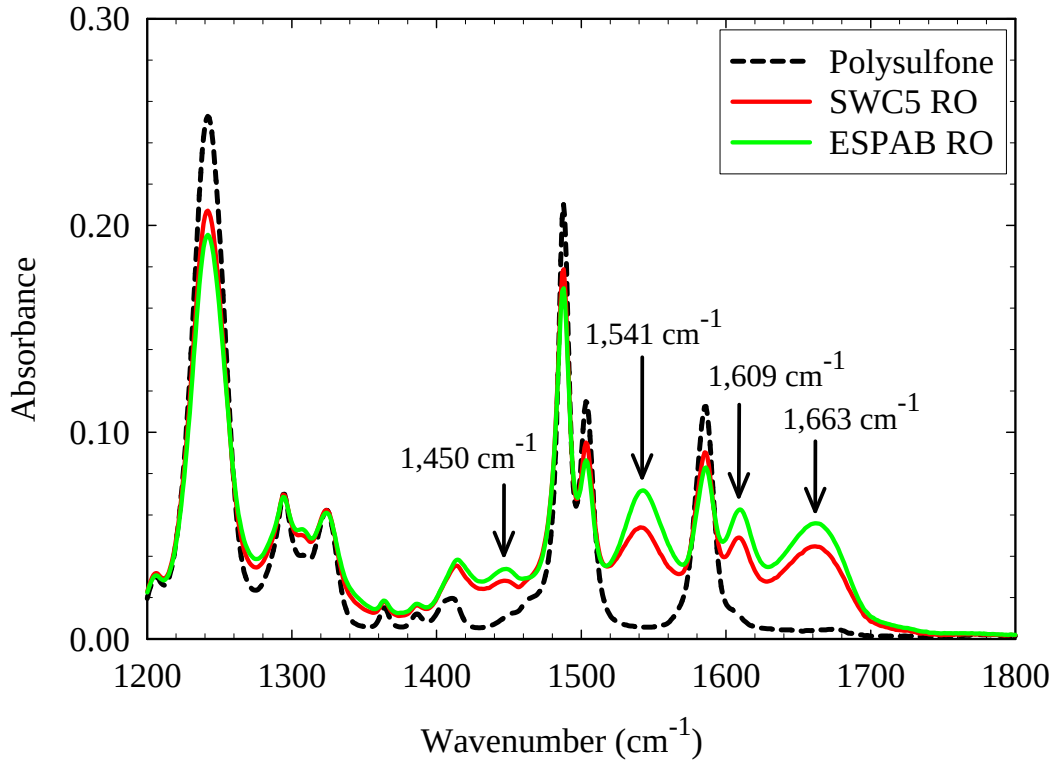


**Figure D.1.** Attenuated total reflectance Fourier transform infrared (ATR-FTIR) spectrometry analyses of SWC5 and ESPAB reverse osmosis (RO) membranes.

**Commentary:** The spectra reveal that both SWC5 RO and ESPAB RO have the three characteristic peaks of fully-aromatic polyamide (PA) [3]. We previously reported [4] similar ATR-FTIR spectra for the other membranes used in this study (i.e., ESPA RO, TFC–S NF, ESNA NF, NF90 NF, FT30 RO, and LF10 RO) that also showed that their active layers are fully-aromatic PA. The wavenumbers of the characteristic peaks for fully aromatic PA are [3] 1,663 $cm^{-1}$ (amide I band, secondary amide groups: C=O stretching, C–N stretching, and C–C–N deformation vibration), 1,609 $cm^{-1}$ (aromatic amide groups: N–H deformation vibration, and C=C ring stretching vibration), and 1,541 $cm^{-1}$ (amide II band, amide groups: N–H in-plane bending and N–C stretching vibration). The peak at wavenumber 1,450 $cm^{-1}$ is associated to carboxylic groups (C–O stretching/O–H bending (Rao et al., *J. Mem. Sci.* 2003, *211*, 13-24)). ATR-FTIR analyses were performed as reported previously [4] with a Nexus 670 FTIR spectrometer (Thermo Nicolet Corporation, Madison, WI) using an IR source with an incident angle of 45°, a Smart Golden Gate diamond ATR accessory, a DTGS-KBr detector, and a KBr beam-splitter. Prior to analyses, membrane samples were thoroughly rinsed with and stored in nanopure water, dried by applying fingertip pressure them between two qualitative-grade filter-paper circles, and dried in vacuum for ≥72 hours. For each membrane, five replicate ATR-FTIR spectra were averaged to obtain the spectra shown in the figure, with each of the five spectra being collected from a circular area of ≈2 mm in diameter as the average of 256 scans in the 650–4000 $cm^{-1}$ wavenumber range at 2 $cm^{-1}$ resolution.

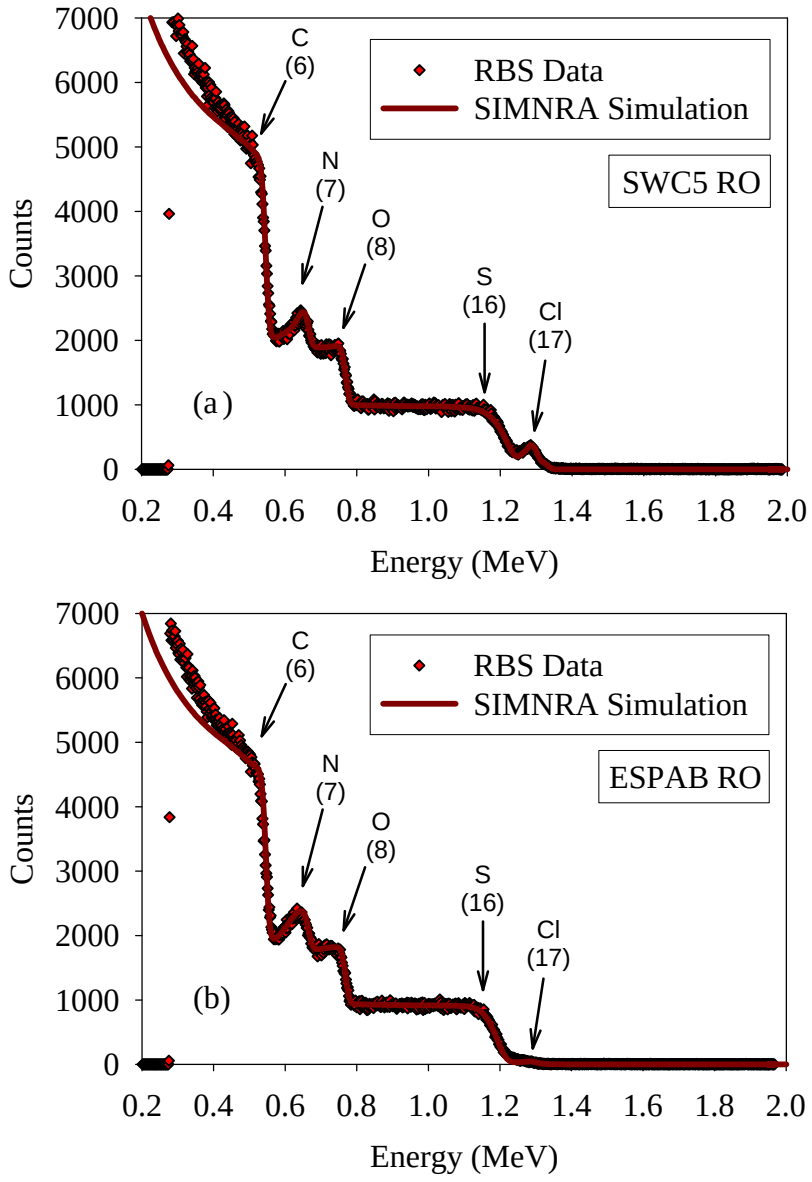


**Figure D.2.** Rutherford backscattering spectrometry (RBS) spectra and corresponding simulations of virgin (a) SWC5 RO and (b) ESPAB RO membranes. Symbols represent RBS data. Lines represent the fit obtained using the software SIMRA® [18].

**Commentary:** The existence of coats on the PA active layers of FT30 RO and LF10 RO was confirmed in our previous studies [4, 12] by analyzing the onset energy of the nitrogen peak in their RBS spectra. The presence of a coat layer makes the nitrogen peak recede to lower energies with the magnitude of the energy recession indicating the coat thickness (see ref [12] for details). Similar analyses performed for ESPA3 RO, TFC–S NF, ESNA NF and NF90 NF membranes in ref [4], and for SWC5 RO and ESPAB RO in this study using the spectra in Figure D.2, showed that the onset energy of the nitrogen peaks does not recede, and that as a result the PA active layer is the surface layer in each membrane (i.e., the membranes are not coated).

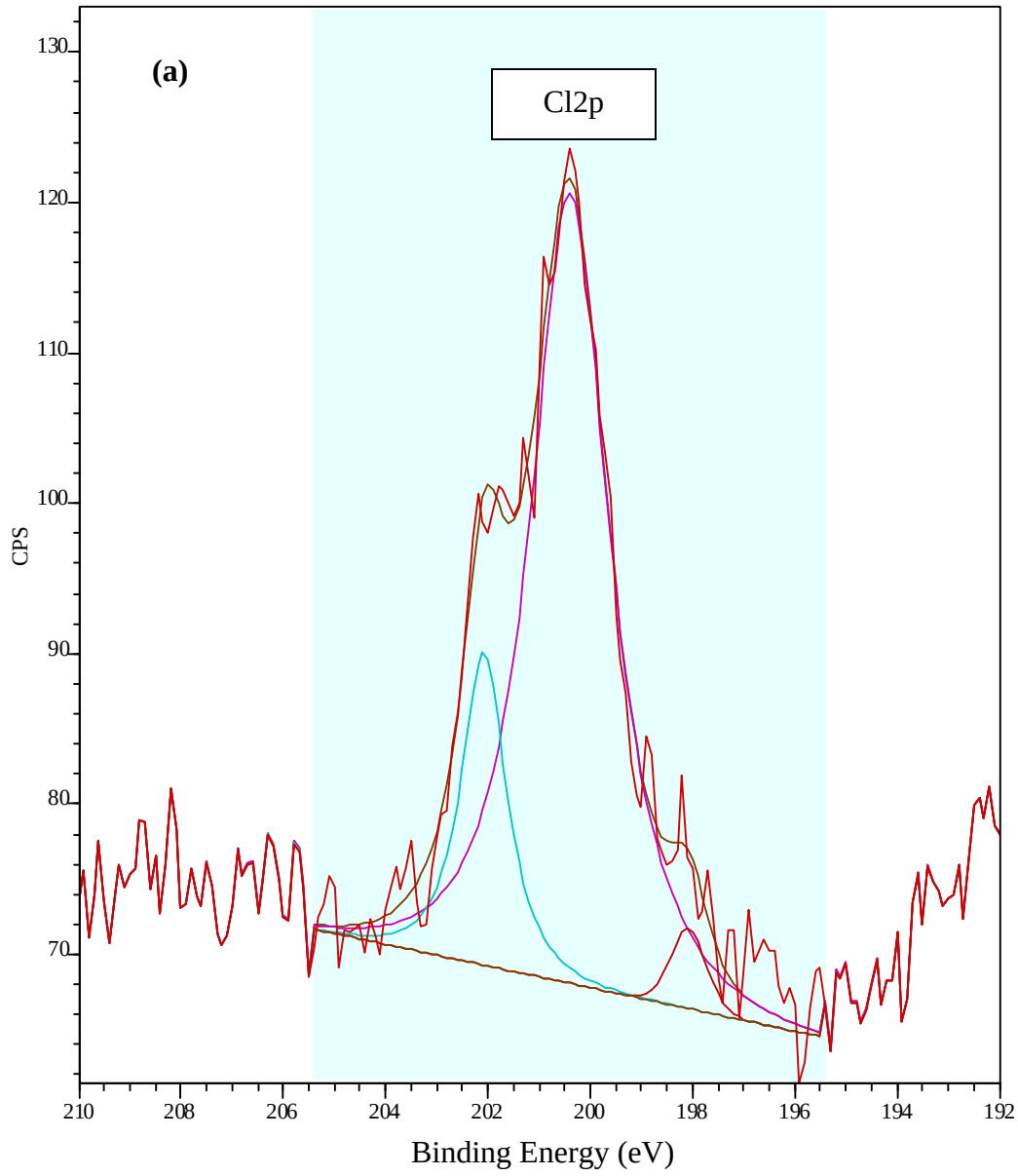
(a)
Cl2p
CPS
130
120
110
100
90
80
70
210
208
206
204
202
200
198
196
194
192
Binding Energy (eV)

**Figure D.3a**

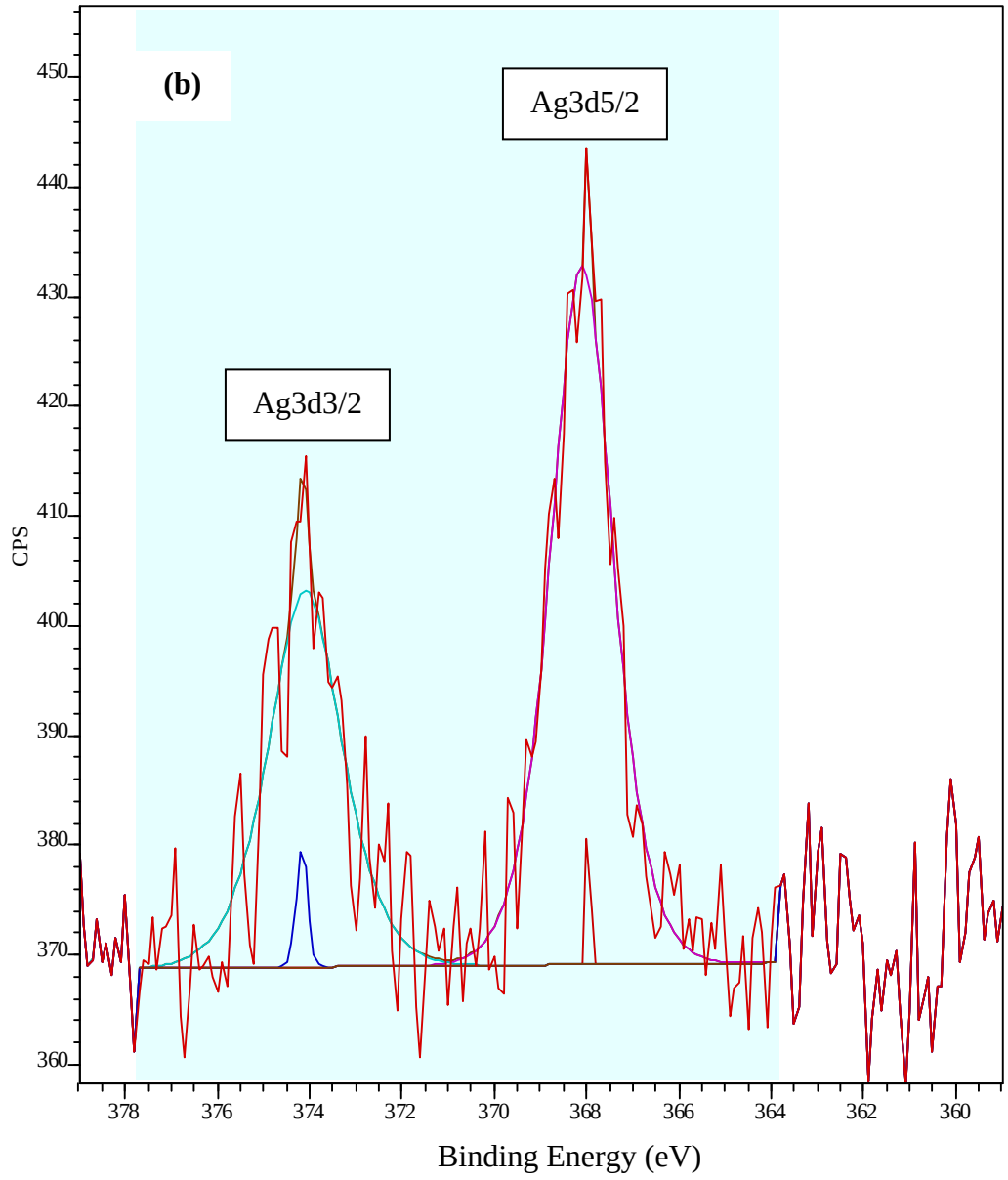
(b)
Ag3d5/2
Ag3d3/2
CPS
450
440
430
420
410
400
390
380
370
360
378
376
374
372
370
368
366
364
362
360
Binding Energy (eV)

**Figure D.3b**

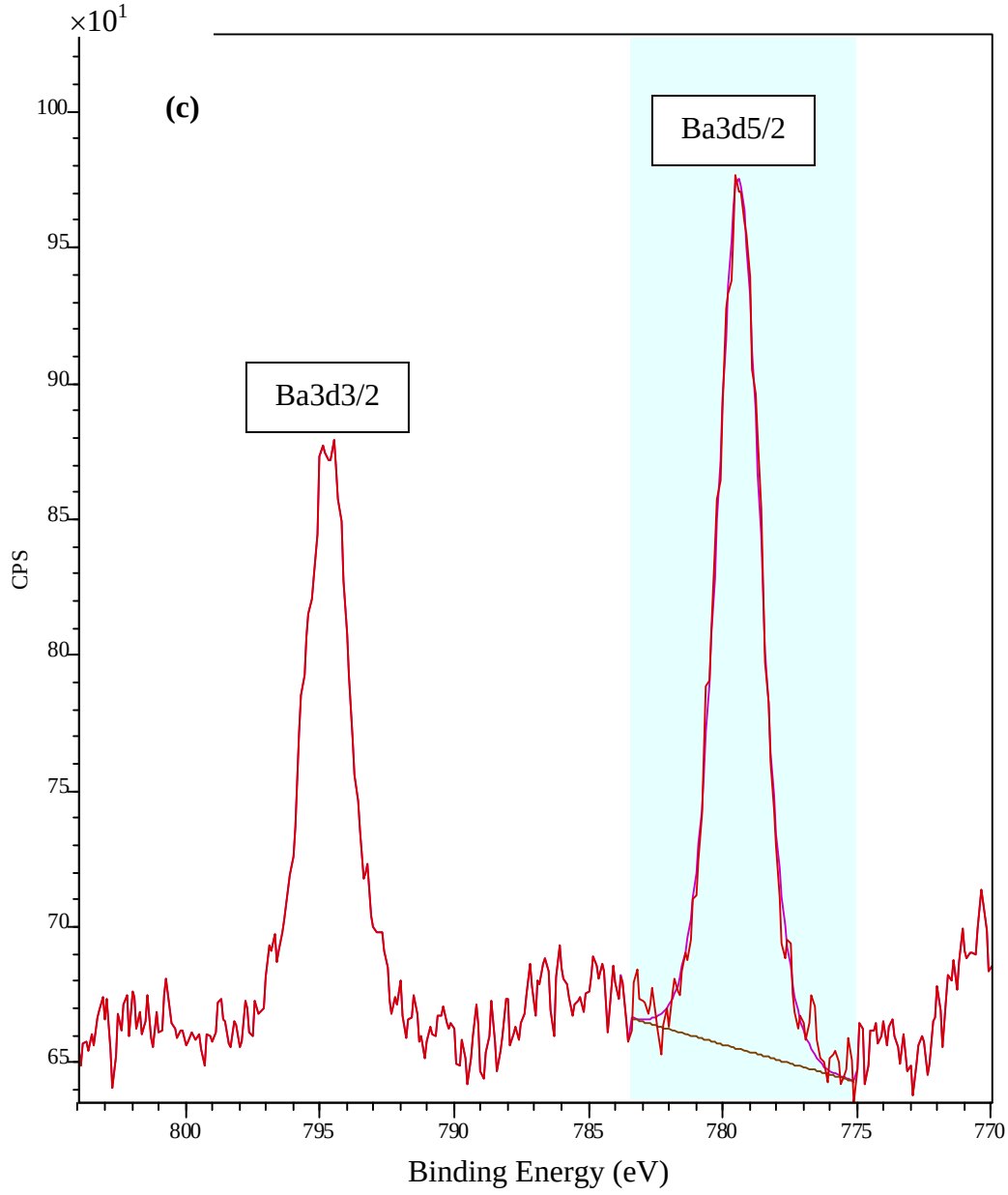


**Figure D.3**. X-ray photoelectron spectroscopy (XPS) signals of the (a) chlorine Cl2p, (b) silver Ag3d, and (c) barium Ba3d photoelectrons in a sample of ESPA3 RO membrane used for $Ag^{+}$–$Ba^{2+}$ displacement tests.

**Commentary:** The different peaks in the Cl2p signal are the result of different binding energies of the Cl2p photoelectrons due to energy shifting associated with, among other reasons, different locations of chlorine atoms in the polymer structure (Briggs, D. *Surface analysis of polymers by XPS and static SIMS*. Cambridge University Press: New York, NY, 1998). Chlorine was also detected in membrane samples not treated with ion-probe solutions. In all samples, the analysis of the silver signal was performed using both the Ag3d5/2 and Ag3d3/2 peaks, and the analysis of the barium signal was performed using only the Ba3d5/2, and not the Ba3d3/2 peak.

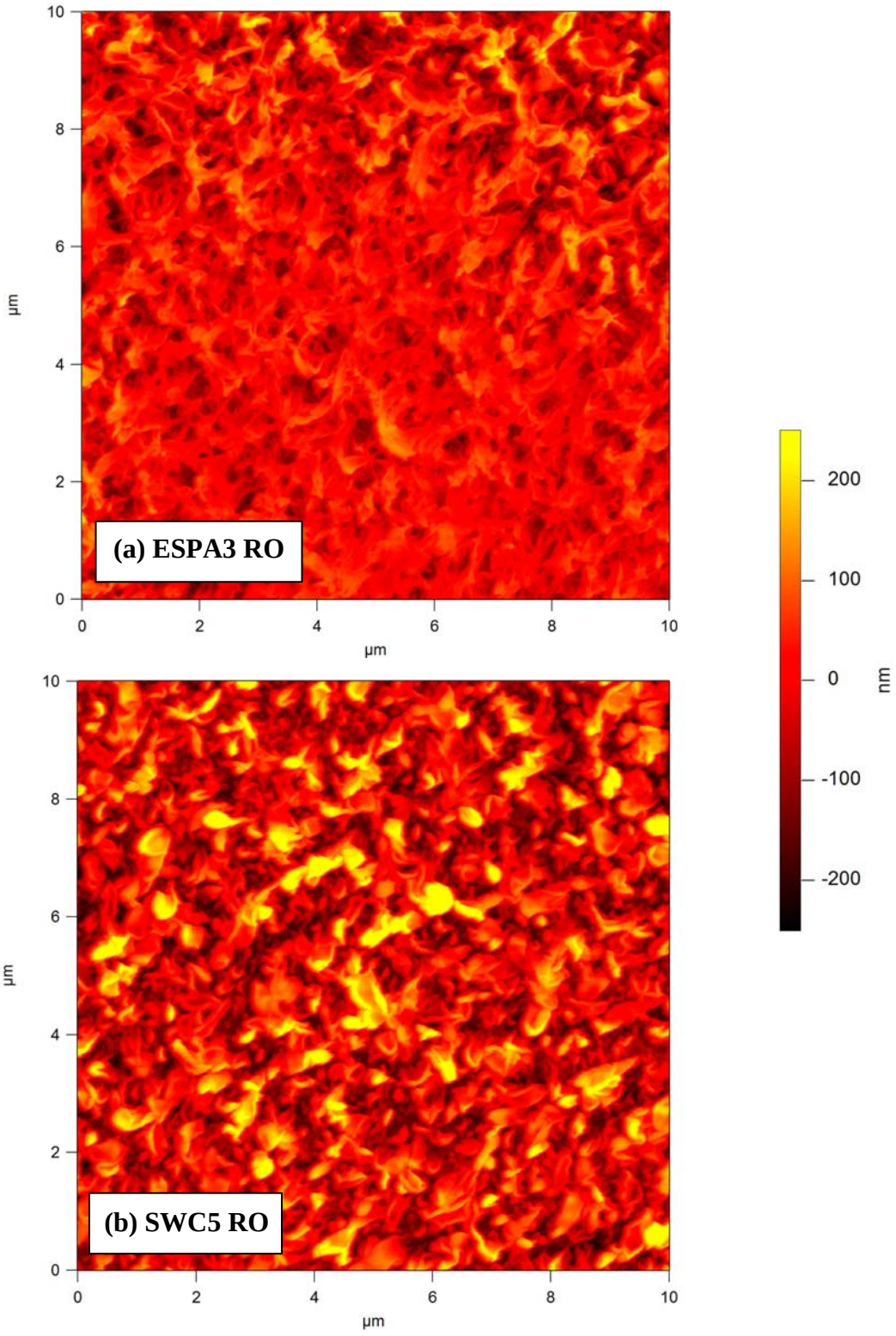


**Figure D.4a and D.4b**

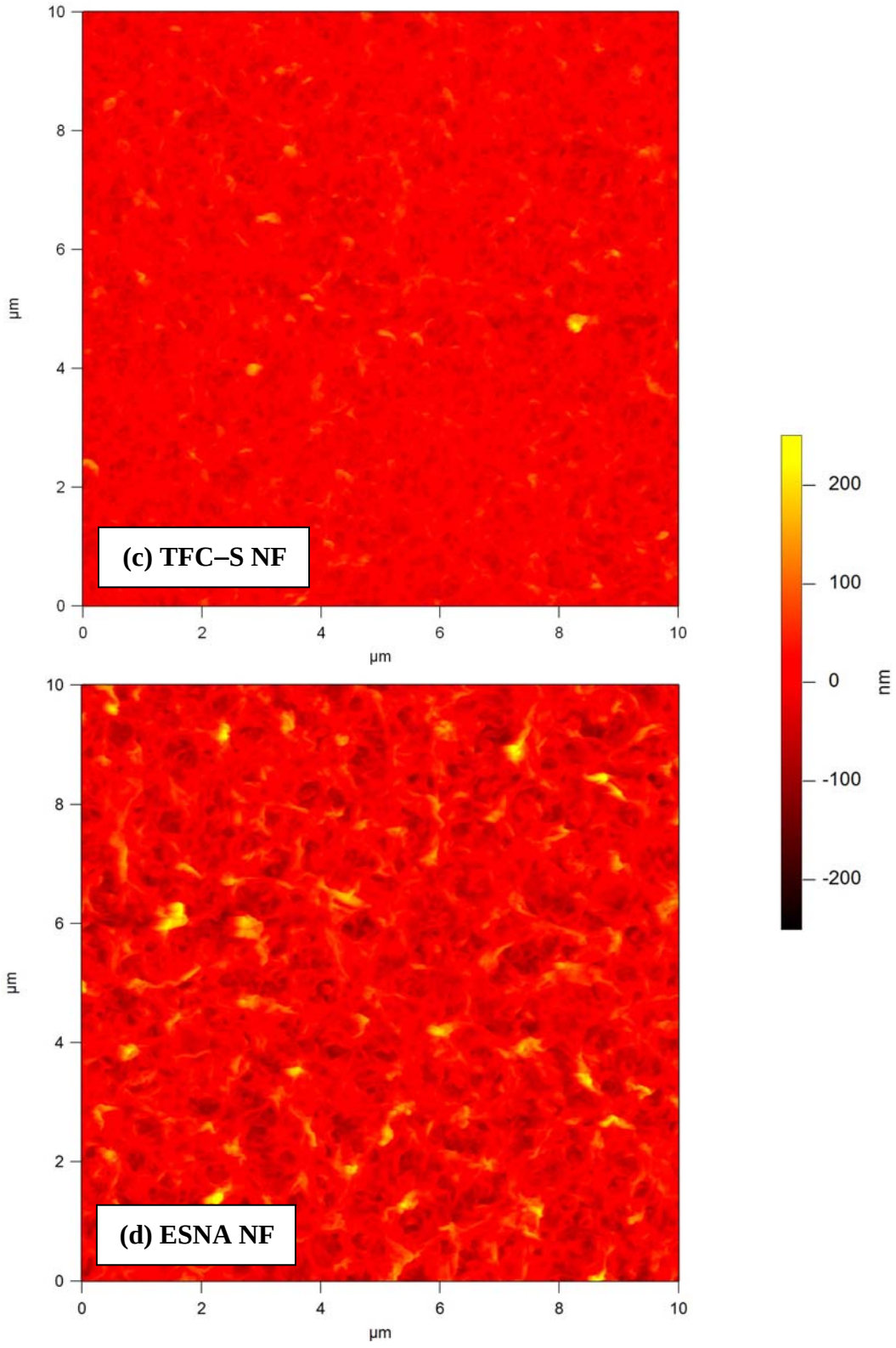


**Figure D.4c and D.4d**

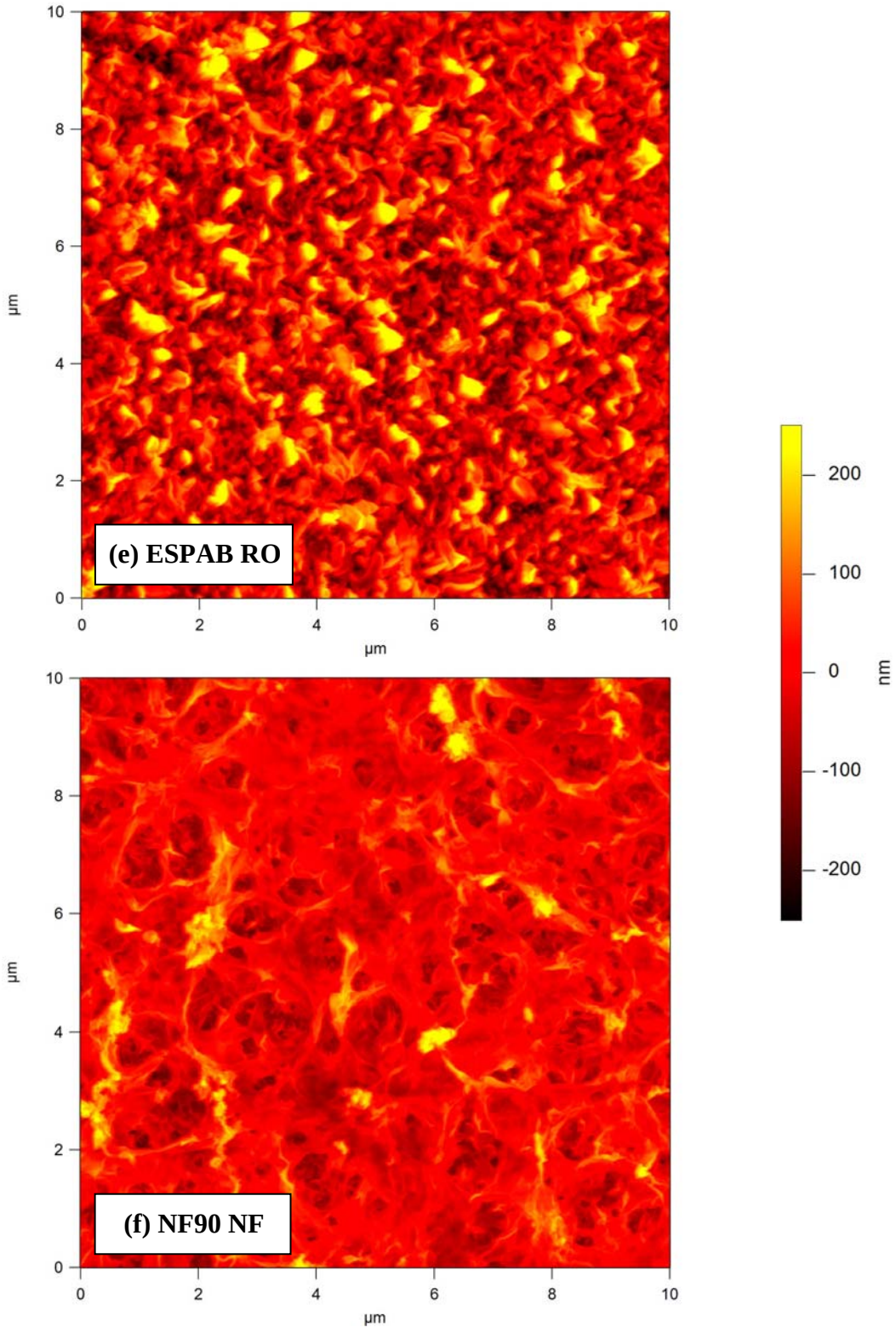


**Figure D.4e and D.4f**

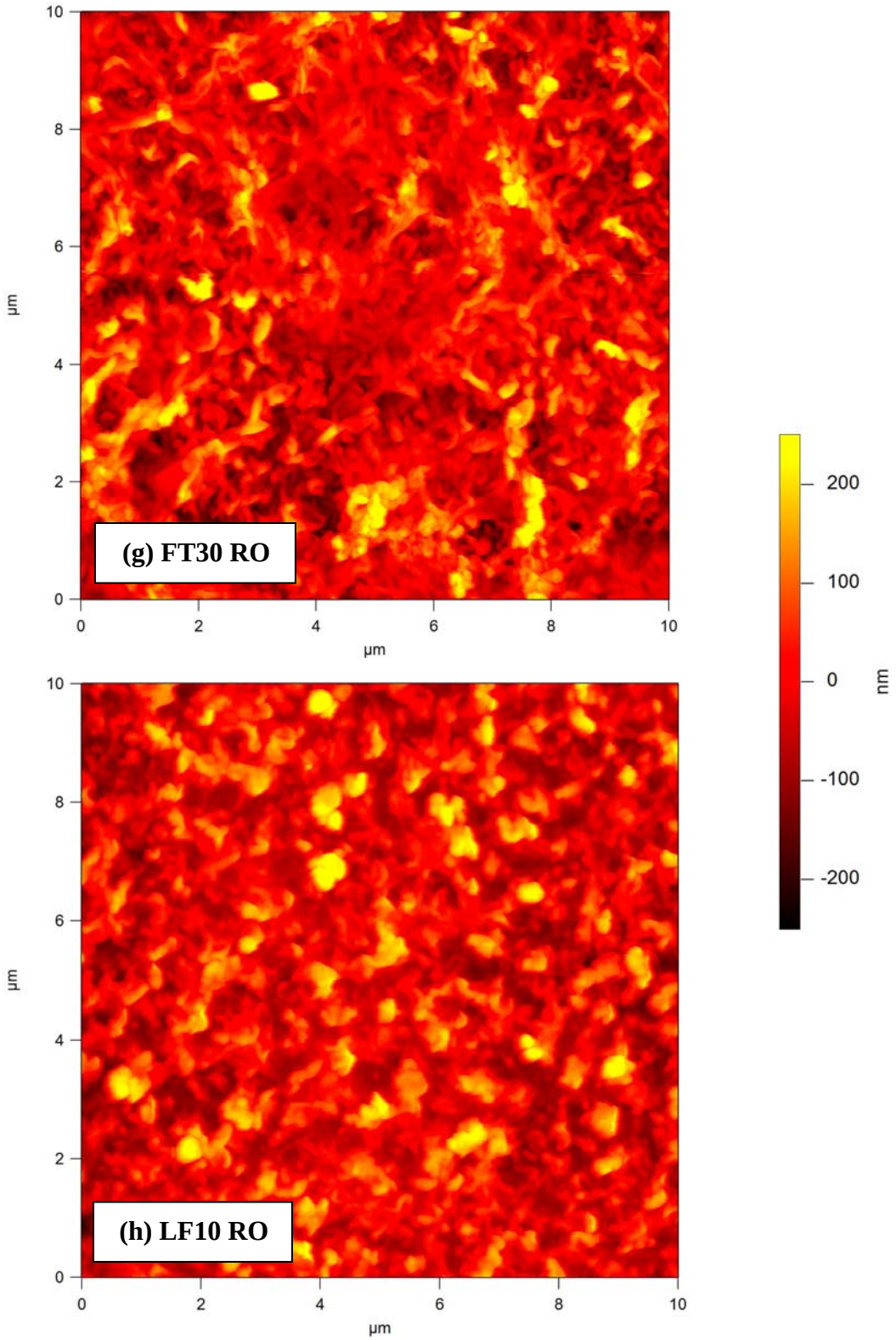


**Figure D.4.** Atomic force microscopy (AFM) images (10×10 µm) of (a) ESPA3 RO, (b) SWC5 RO, (c) TFC–S NF, (d) ESNA NF, (e) ESPAB RO, (f) NF90 NF, (g) FT30 RO, and (h) LF10 RO membranes.

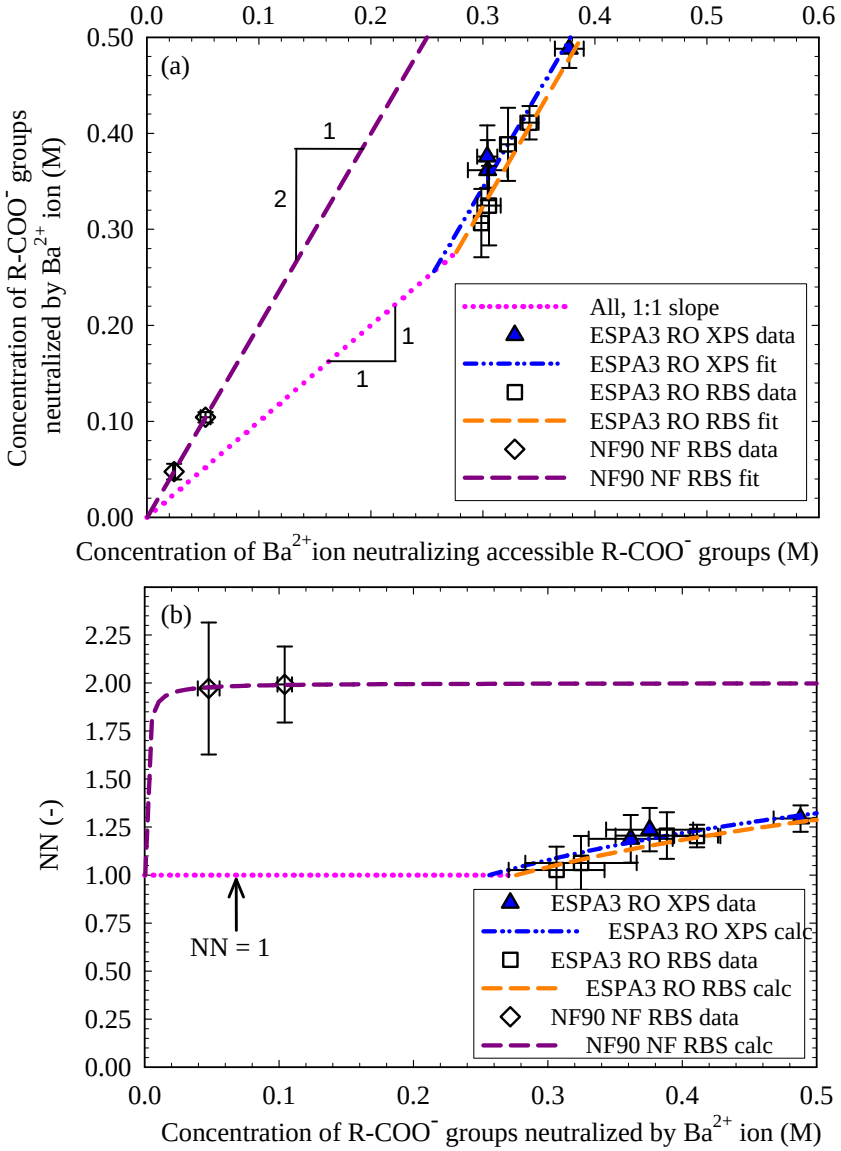


**Figure D.5.** Stoichiometry of association between the R–$COO^-$ groups neutralized by $Ba^{2+}$ ion in the polyamide (PA) active layers of ESPA3 RO and NF90 NF membranes and the $Ba^{2+}$ ions neutralizing them. (a) Limiting one-to-one (pink dotted line) and two-to-one (color dashed and dash-dot-dot lines) correspondence between neutralized R–$COO^-$ groups and $Ba^{2+}$ ion. Open symbols are experimental data from $Ag^+$–$Ba^{2+}$ displacement/RBS analyses and were reproduced from our previous work [4]. Solid symbols are experimental data obtained from $Ag^+$–$Ba^{2+}$ displacement/XPS analyses. The coordinates $(x,y) = (a,a)$ of the intersection of any 2:1 line with the 1:1 line correspond to the value of the $a$ parameter in Equation 5.6. For ESPA3 RO, $a_{XPS}$ = 0.13±0.01 M and $a_{RBS}$ = 0.14±0.01 M. For NF90 NF, $a_{XPS} = a_{RBS} \approx 0$ (see commentary below). For a given $(x,y)$ point, the corresponding NN was calculated as its $y/x$ ratio. (b) NN as a function of the concentration of R–$COO^-$ sites neutralized in the PA active layers of the

membranes studied. Symbols and lines are the calculated NN values of their corresponding plots in (a). Error bars indicate standard error.

**Commentary:** In Figure D.5a the *y*-coordinate represents the concentration of R–$COO^-$ groups neutralized by $Ba^{2+}$ ion calculated as the difference between the $Ag^+$ concentrations in the active layer before and after $Ag^+$ displacement by $Ba^{2+}$. The *x*-coordinate represents the concentration of $Ba^{2+}$ ions neutralizing a *y* concentration of R–$COO^-$ groups and was measured as the concentration of $Ba^{2+}$ ion in the active layer after ion displacement. $Ag^+$–$Ba^{2+}$ displacement tests were performed at different pH values, thus resulting in different (*x*,*y*) data points. We plotted the calculated average number of R–$COO^-$ groups neutralized per $Ba^{2+}$ ion, referred to as the neutralization number NN, in Figure 5.5b as a function of the concentration of R–$COO^-$ groups neutralized by $Ba^{2+}$ (i.e., the *x*-axis in Figure D.5a and the *y*-axis in Figure D.5b are the same). The data in Figure 5.5a was modeled based on only the parameter *a* as follows: $\Delta y/\Delta x = 1 \rightarrow y = x$ for $x \leq a$, and $\Delta y/\Delta x = 2 \rightarrow y = 2x - a$ for $x > a$. The *a* parameter represents the concentration of neutralized R–$COO^-$ groups at which the stoichiometry of association between the additional R–$COO^-$ sites that ionize ($\Delta y$) and the $Ba^{2+}$ ions that neutralize them ($\Delta x$) changes from 1:1 to 2:1. In our previous work [4], we showed that for the ESPA3 RO membrane $a_{RBS} = 0.14 \pm 0.01$ M. In this study, we found that $a_{XPS} = 0.13 \pm 0.01$ M indicating depth homogeneity in the stoichiometry of association between R–$COO^-$ groups and $Ba^{2+}$ ion in the active layer of ESPA3 RO membrane. For NF90 NF, we showed in our previous work [4] using RBS analyses that NN = 1.98±0.20 (i.e., $a_{RBS} \approx 0$) [4] across the entire pH range studied. Taking into account that (i) XPS analyses in the present study showed that the concentration of R–$COO^-$ groups at the active layer surface of NF90 is almost twice as much as that in average throughout the active layer, thus indicating a shorter average distance between R–$COO^-$ groups at the surface, and that (ii) the maximum value that NN can take is $NN_{Max} = 2$ (i.e., one $Ba^{2+}$ ion can neutralize at most two R–$COO^-$ groups), then we safely assumed that NN≈2 at the surface of the active layer of NF90 NF membranes (i.e., $a_{XPS} = a_{RBS} \approx 0$). .